Università degli Studi di Torino

Doctoral School of the University of Torino

PhD Programme in Chemical and Materials Sciences XXXV Cycle

Synthesis of NIR Dyes and Colorless Redox Couples for Near-Infrared Dye-Sensitized Solar Cells (NIR-DSSCs)

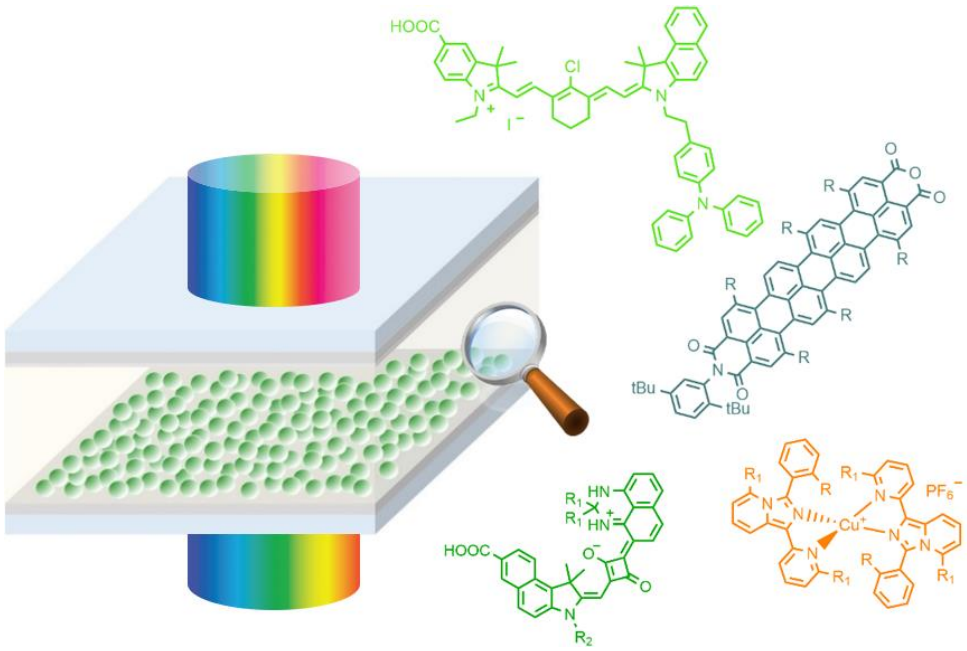

Marco Giordano

Supervisor:
Prof. Guido Viscardi

Università degli Studi di Torino

Doctoral School of the University of Torino

PhD Programme in Chemical and Materials Sciences XXXV Cycle

Synthesis of NIR Dyes and Colorless Redox Couples for Near-Infrared Dye-Sensitized Solar Cells (NIR-DSSCs)

Candidate: **Marco Giordano**

Supervisor: Prof. **Guido Viscardi**

Jury Members: Prof. **Andrea Fin**
Università degli Studi di Torino
Dipartimento di Chimica

Prof. **Luca Beverina**
Università degli Studi di Milano-Bicocca
Dipartimento di Scienza dei Materiali

Prof. **Stefano Caramori**
Università degli Studi di Ferrara
Dipartimento di Scienze chimiche, farmaceutiche ed agrarie

Head of the Doctoral School: Prof. Alberto Rizzuti
PhD Programme Coordinator: Prof. Bartolomeo Civalleri

Torino, 2023

TABLE OF CONTENTS

LIST OF FIGURES

LIST OF TABLES

LIST OF ABBREVIATIONS

2D – Two-Dimensional
5DI – Pentarylene-tetracarboxylic Diimides
acac – Tris(acetylacetonato)
ACN – Acetonitrile
AM – Air Mass
ARC – Anti Reflective Coating
ATR – Attenuated Total Reflection
AVs – Agrivoltaic System
AVT – Average Visible Transmittance
BASF – Badische Anilin und Soda Fabrik
BBARC – Broad Band Anti-Reflective Coating
BDT – Benzodithiophene
BI – Benzoindolenine
BIPVs – Building Integration Photovoltaics
bpy – 2,2'-Bipyridine
bpye – Bis(1,1-bis(2-pyridyl)ethane)
bpyPY4 – 6,6'-Bis(1,1-di(pyridin-2-yl)ethyl)-2,2'-bipyridine
bpy-pz – 6-(1*H*-pyrazol-1-yl)-2,2'-bipyridine
BQ – 2,2'-Biquinoline
bqp – 2,6-Bis(8-quinolinyl)pyridine
BTU – British Thermal Unit
CB – Conduction Band
CBI – Carboxy-benzoindolenine
CBI-SQ – Carboxy-benzoindolenine Squaraine
CDCA – Chenodeoxycholic Acid
CE – Counter Electrode
CI – Carboxyindolenine
CIGS – Copper Indium Gallium Selenide
CI-SQ – Carboxyindolenine Squaraine
COD – 1,5-Cyclooctadiene
COSY – Correlation Spectroscopy
CPDT – Cyclopentadithiophene
CPS – Count Per Second
CR – Croconine dye
CV – Cyclic Voltammetry
CY – Cyanine dye
CY3 – Trimethine cyanine
CY5 – Pentamethine cyanine
CY7 – Heptamethine cyanine
DAN – 1,5-Diaminonapthalene

dbbip – Bis[2,6-bis-(1'butylbenzimidazol-2'-yl)]pyridine
DBU – 1,8-diazabicyclo[5.4.0]undec-7-ene
DCA – Deoxycholic Acid
DCM – Dichloromethane
DDS – Dodecyl sulfate
DEPT – Distortionless Enhancement by Polarization Transfer
DE-SQ – 3,4-Diethoxycyclobut-3-ene-1,2-dione
DHP – 2,3-Dihydro-1*H*-perimidine
DHP-SQ – 2,3-Dihydro-1*H*-perimidine-based Squaraine
DIPEA – *N*,*N*-Diisopropylethylamine
DMF – Dimethylformamide
DMII – 1,3-Dimethyl-1*H*-imidazol-3-ium iodide
DMSO – Dimethyl Sulfoxide
DOPC – 1,2-Dioleoyl-*sn*-glycero-3-phosphocholine
DPK – Di(pyridine-2-yl)methanone
DPPC – 1,2-Dipalmitoyl-*sn*-glycero-3-phosphocholine
dppf – 1,1'-Bis(diphenylphosphino)ferrocene
DSSC – Dye-Sensitized Solar Cell
DTP – Dithienopyrrole
DTS – Silolodithiophene
DTT – Dithienothiophene
EIS – Electrochemical Impedance Spectroscopy
ESI – Electron-Spray Ionization
EtOAc – Ethyl Acetate
EtOH – Ethanol
EU – European Union
FF – Fill Factor
FSCV – Fast-Scan Cyclic Voltammetry
FT – Fourier transform
FTO – Fluorine-Tin Oxide
GuSCN – Guanidinium Thiocyanate
HBA – Hydrogen-Bond Acceptor
HBD – Hydrogen-Bond Donor
HCCA – *α*-Cyano-4-hydroxycinnamic Acid
HDI – Hexarylenetetracarboxylic Diimides
HMBC – Heteronuclear Multiple Bond Correlation
HOMO – Highest Occupied Molecular Orbital
HPE – High-Performance Electrolyte
HRMS – High-resolution Mass Spectrometry
HSQC – Heteronuclear Single Quantum Coherence
HTM – Hole Transport Material
hybeb – Diaminodiphenolate
Impy – Imidazo[1,5-*a*]pyridine

IPCE – Incident Photon to Current Conversion Efficiency
IR – Infrared
ITO – Indium-Tin Oxide
LEC – Light-emitting Electrochemical Cells
LED – Light Emitting Diodes
LUMO – Lowest Unoccupied Molecular Orbital
LUV – Large Unilamellar Vesicles
MALDI-TOF – Matrix-Assisted Laser Desorption/Ionization - Time-Of-Flight
MeOH – Methanol
MLARC – Multi-Layers Anti-Reflective Coating
MLCT – Metal-to-Ligand Charge-Transfer
mmt – Maleonitriledithiolate
Mp – Melting Point
MPN – 3-Methoxypropionitrile
MS – Mass Spectrometry
MW – Microwave
NAP – *N*-annulated Perylene
nbpbi – 2-(Pyridin-2-yl)-1*H*-benzo[*d*]imidazole
NHE – Normal Hydrogen Electrode
NIR – Near-Infrared
NIR-DSSC – Near-Infrared Dye-Sensitized Solar Cell
NLO – Nonlinear Optics
NMBI – Methylbenzoimidazole
NMI – Naphthalene Mono-Imide
NMP – *N*-Methyl-2-pyrrolidone
NMR – Nuclear Magnetic Resonance
NP – Nanoparticle
OFET – Organic Field-Effect Transistors
OSC – Organic Solar Cell
oxabpy – 6,6'-Bis(4-(S)-isopropyl-2-oxazolinyl)-2,2'-bipyridine
PC – Phthalocyanine
PCE – Photovoltaic Conversion Efficiency
PDI – Perylene Diimide
PDT – Photodynamic Therapy
PDTO – 1,8-Bis(2'-pyridyl)-3,6-dithiaoctane
PEDOT – Poly(3,4-ethylenedioxythiophene)
phen – 1,10-Phenantroline
PMA – Perylene Monoanhydride
PMI – Perylene Monoimide
PPCY – Pyrrolopyrrole Cyanine
PQ – Pyridil-quinoline
PSC – Perovskite Solar Cell
PTCDA – Perylene-3,4,9,10-tetracarboxylic Dianhydride

PTSA – *p*-Toluene sulfonic acid
py-pz – 2-(1*H*-yrazol-1-yl)pyridine
PY5Me$_2$ – 2,6-(Bis(bis-2-pyridyl)methylmethane)pyridine
QDI – Quaterrylenetetracarboxylic Diimides
QMA – Quaterrylene Monoanhydride
QDSC – Quantum Dots Solar Cell
QY – Quantum Yield
rGO – Reduced graphene oxide (rGO)
Rf – Retention Factor
RI – Refractive Index
RT – Room Temperature
salen – Salicylideneiminate
SBCC – (*E*)-2-(((2-((2-hydroxyethyl)amino)ethyl)imino)methyl)-4-methoxyphenol
SI – Supporting Information
SLARC – Single-Layer Anti-Reflective Coating
SQ – Squaraine dye
SS-DSSC – Solid-State Dye-Sensitized Solar Cell
T3P – Propylphosphonic Anhydride
TAS – Transient Absorption Spectroscopy
TBP – 4-*tert*-Butyl Pyridine
TCI – Tokyo Chemical Industries
TDI – Terrylenetetracarboxylic Diimides
TEA – Triethylamine
TEMPO – 2,2,6,6-tetramethylpiperidine-1-oxyl
terpy – 2,2',6',2''-Terpyridine
TFA – Trifluoroacetic Acid
THF – Tetrahydrofuran
TLC – Thin Layer Chromatography
TMS – Tetramethylsilane
TMSCl – Trimethylsilyl Chloride
TMTU – Tetramethyl Thiourea
TPA – Triphenylamine
TT – Thienothiophene
ttcn – Trithiacyclononane
UV – Ultraviolet
UV-PSC – Ultraviolet Perovskite Solar Cell
VB – Valence Band

INTRODUCTION

World energy consumption is steadily increasing and it is expected to increase of at least 50% by 2050 in respect to the current 600 British Thermal Unit (BTU). The strong socio-economic growth underway is leading to a race for energy inevitably still based on fossil fuels.[1] Regardless of their price, the use of fossil fuels cannot be a long-term solution because of their limited availability but in particular for their environmental impact. In the last fifty years several events, such as the oil crisis of the 1970s and 1990s, the Great Recession of 2008, the COVID-19 pandemic, the Russo-Ukrainian war alongside the increasingly frequent effects of climate change on daily life have forced the international community to consider the energy transition to renewable energies the only solution for sustainable global development.[2] Among all the renewable energy technologies, photovoltaic technology is considered the most promising.[3] Sun is the most powerful energy source among all renewable and non-renewable ones. Every year it provides the Earth with 174 PW; in other words: the sun provides more energy to the Earth in one hour than it consumes in a year.[4] Over the last twenty years, the photovoltaic technologies were driven to the centre of the international research and politics due to the almost "unlimited power", the global availability and its low cost.[5,6]

A photovoltaic cell (PV) is an electrical device that converts the sun's incident light directly into electricity by the photovoltaic effect. Based on this concept, several technologies have been developed over the years after the first crystalline silicon solar cell reported by Chapin *et al.* in 1954.[7] The first-generation solar cells are based on monocrystalline or polycrystalline silicon. They achieved efficiencies over 25% and they are currently dominating the PV global market.[8] While the sustainability of their production remains a limitation, the huge reduction costs' production is increasing its competitivity.[8,9] Over the years, different technologies have been developed in this scenario (Fig. 1): (i) thin-film solar cells, based on semiconductor materials such as gallium arsenide and copper indium gallium

selenide (CIGS),[10] and (ii) the latest third-generation technologies including Dye-Sensitized Solar Cells (DSSC),[11-13], Organic Solar Cells (OSC),[14-16] Quantum Dots Solar Cells (QDSC),[17-19] and Perovskite Solar Cells (PSC).[20,21]

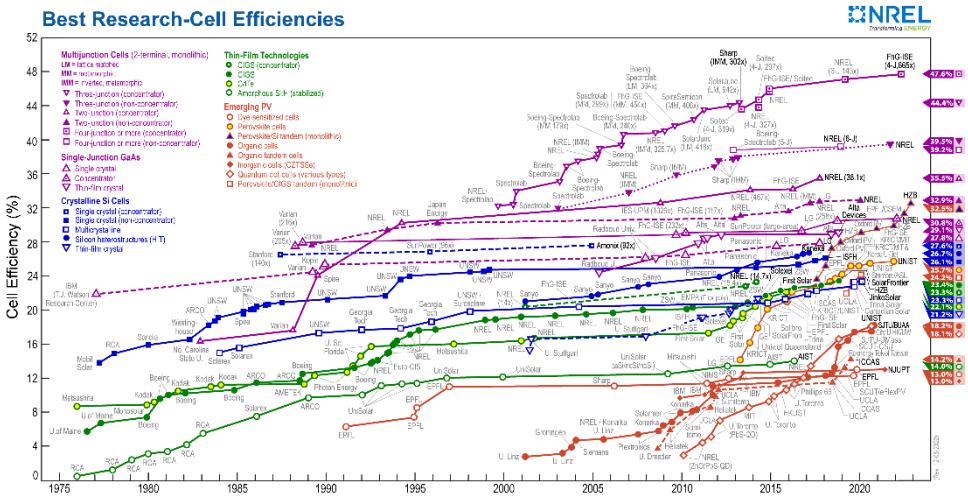

Figure 1 - Evolution of the certified record power conversion efficiency for each existing technology since 1976 (Source: National Renewable Energy Laboratory).[22]

Among them, DSSCs are nowadays the most consolidated technology reaching efficiencies above 14%.[23] Despite lower performance compared to other third generation technologies,[8] the low cost-material, scalable manufacturing, promising designs using multiple colours and patterns, as well as high performance and stability under low or diffuse light conditions are attractive features that are nowadays leading to the renaissance of DSSCs.[13,24,25,26] New interesting technology approaches like (i) the textile-DSSCs for wearable electronics,[27] (ii) the semi-transparent DSSCs for the application in Agrivoltaic system (AVs)[28] and (iii) the colorless and transparent DSSCs for the Building Integration Photovoltaics (BIPVs)[29] are in constant development. In this context, the EU funded IMPRESSIVE research project tried to develop transparent photovoltaic cells converting selectively UV and NIR part of the light while excluding the visible range to reach colourless and fully transparent devices. To reach this innovative objective, the approach was based on hybrid tandem UV-

perovskite solar cell (UV-PSCs) combined with a NIR-dye sensitised solar cell (NIR-DSSCs) (Fig. 2).

The present doctorate project is part of IMPRESSIVE project and is aimed to synthetize NIR dyes and colourless redox couples followed by their application and optimization in DSSC devices. In this thesis will be firstly report a general description about the state-of-art of the classic DSSCs in comparison with the NIR-DSSCs and after, the research work will be presented in four different chapters about: (i) the synthesis of extended-rylene dyes, (ii) the synthesis and the application as NIR-sensitizers of a new class of 2,3-dihydro-1*H*-perimidine-based squaraines (DHP-SQs), (iii) the synthesis of copper complexes as redox mediators, and finally (iv) the study of an interesting new class of squaraines with an hypsochromic absorption for the co-sensitization in classic DSSCs.

In addition, in the two final addenda will be report two small research works regarding the synthesis of an asymmetrical cyanine as NIR-sensitizer for the IMPRESSIVE project and the application of DHP-SQs as membrane probes.

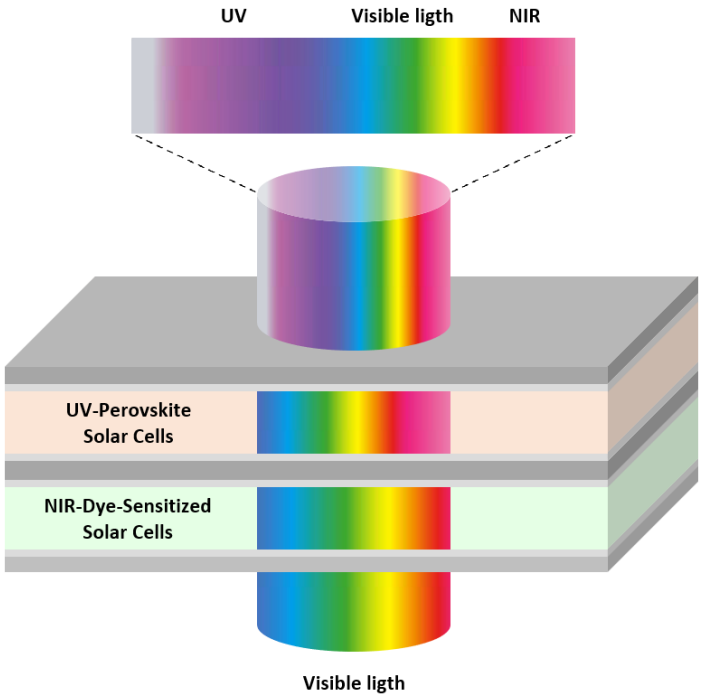

Figure 2 – Schematic overview of hybrid tandem cell based on UV-perovskite solar cell (UV-PSCs) combined with a NIR-dye sensitised solar cell (NIR-DSSCs).

CHAPTER 1 – Near Infrared Dye-Sensitized Solar Cells

A DSSC is a multicomponent photoelectrochemical device constituted by several components (Fig. 3): (i) a transparent glass sheet covered by a conductive indium-tin oxide (ITO) or fluorine-tin oxide (FTO) layer used as anode substrate, (ii) a mesoporous oxide semiconductors layer (typically TiO_2) deposited on the conductive substrate to transfer the electrons, (iii) a sensitizer adsorbed on the mesoporous oxide layer to harvest the incident light, (iv) an electrolyte for the regeneration of the sensitizer, typically I_3^-/I^- or Co(III/II) and Cu(II)/Cu(I) complexes, and (v) a counter electrode (CE) made of a conductive layer glass sheet coated with a catalyst, typically platinum, to catalyse the redox couple regeneration reaction and to collect the electrons from the external circuit.[13,30,31]

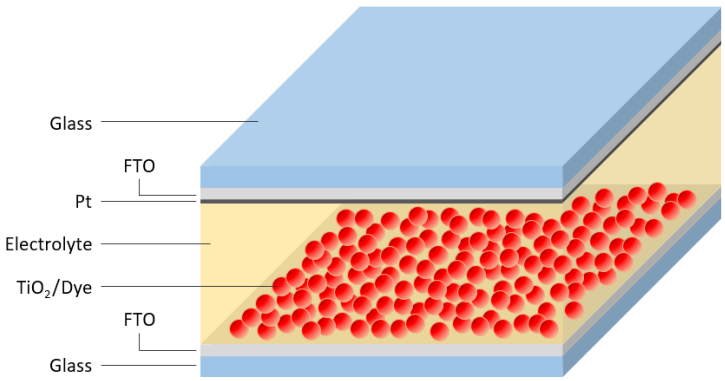

Figure 3 – Schematic overview of a classic DSSC.

The operating principle in a DSSCs under light involves four main processes with different time scales (Fig. 4): (i) the photoexcitation of the sensitizer followed by the electron injection from the dye excited-state to the conduction band (CB) of the semiconductor (fs up to ps), (ii) the dye regeneration (ns up to µs) (iii) the electron transport towards collection (ms) and (iv) the diffusion of the redox mediator to/from the counter electrode (ms up to s).[29] Unfortunately, beside to the described electron transfer processes some undesirable reactions as the

deactivation of the excited state of the dye, the geminate and the non-geminate electron recombination can occur resulting in efficiency's losses.[32-34]

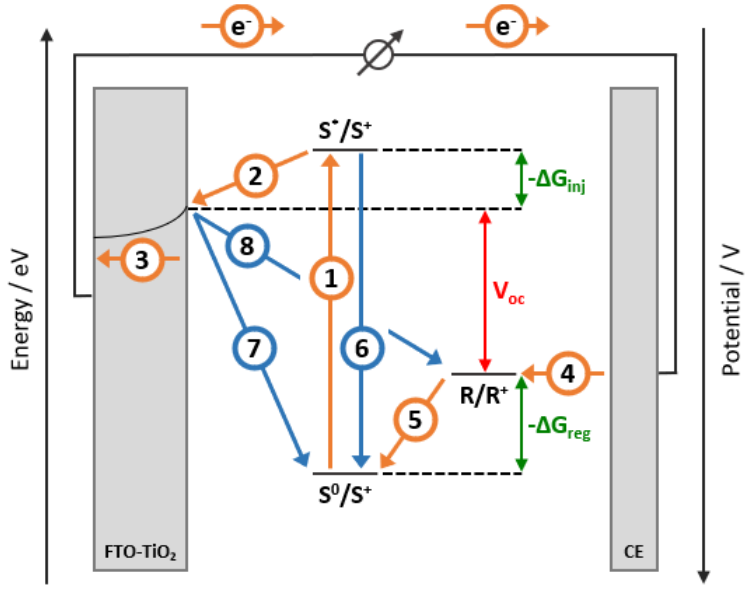

Figure 4 – Schematic overview of charge transfer processes in a DSSCs. (1) Photoexcitation, (2) electron injection, (3) electron migration, (4) redox couple regeneration, (5) dye regeneration, (6) deactivation of the excited state, (7) geminate electron recombination and (8) non-geminate electron recombination. $-\Delta G_{inj}$ and $-\Delta G_{reg}$, are the driving force energy for electron injection and dye regeneration, respectively. $-\Delta G_{inj}$ is defined by the potential difference between the conduction band of semiconductor and LUMO level of the dye while, $-\Delta G_{reg}$ is defined by the potential difference between the HOMO level of the sensitizer and the redox couple.

The photovoltaic conversion efficiency (PCE) is correlated to the short circuit photocurrent density (J_{SC}), the open circuit voltage (V_{OC}), the fill factor of the cell (FF) and the intensity of the incident light (P_{in}), as shown by the equation 1:

$$\eta = \frac{J_{SC}\, V_{OC}\, FF}{P_{in}} \qquad (1)$$

The fill factor is the ratio between the maximum power obtained with the device and the theoretical maximum power (J_{SC} V_{OC}), it can assume values between 0 and 1 and describe the electrical and electrochemical losses during cell's operation. Another fundamental measurement of the performance of a

DSSC is the “external quantum efficiency”, normally called the Incident Photon to Current Conversion Efficiency (IPCE). The IPCE value corresponds to the photocurrent density produced in the external circuit under monochromatic illumination of the cell divided by the photon flux that strikes the cell. IPCE values provide practical information about the monochromatic quantum efficiencies of a DSSC and is calculated by the equation 2:

$$\mathrm{IPCE} = 1240\ [eV\ nm]\frac{J_{SC}\ [mA\ cm^{-2}]}{\lambda\ [nm]\cdot P_{in}(\lambda)[mW\ cm^{-2}]} \qquad (2)$$

The successful production of current relies not only on reaching a quantitative yield of electron injection and dye regeneration but also requires the minimization of the undesired recombination processes. Each unfavorable deactivation path requires to be at least 10^3 times slower than the favorable pathway to reach 99+ % yield.[29] From the pioneer studies on DSSCs, the research was focused on the development of each component of the device and on their interactions to maximize the efficiency of desired electron transfer processes and reducing as much as possible any recombination pathways. If in the DSSC the fine optimization of every electron transfer process is challenging, in the NIR-DSSC is dramatically trickier. The main challenge is due to the integration of a lower bandgap NIR sensitizer able to favor both electron injection and regeneration steps. This restriction limits enormously the number of dyes that can be adapted to the benchmark TiO_2 nanoparticles and the conventional redox mediators introduced so far. For these reasons, the development of efficient colorless NIR-DSSC needs the design of transparent materials with tailored properties (Fig. 5).

In addition, a trade-off between high Average Visible Transmittance (AVT) and high efficiency renders the selection of the materials more complicated than for opaque technologies. In this chapter, the state-of-art of the different constituent materials of possible interest for the application in the NIR-DSSCs will be described, with particular attention to squaraine and cyanine sensitizers as well as metal-based redox mediators.

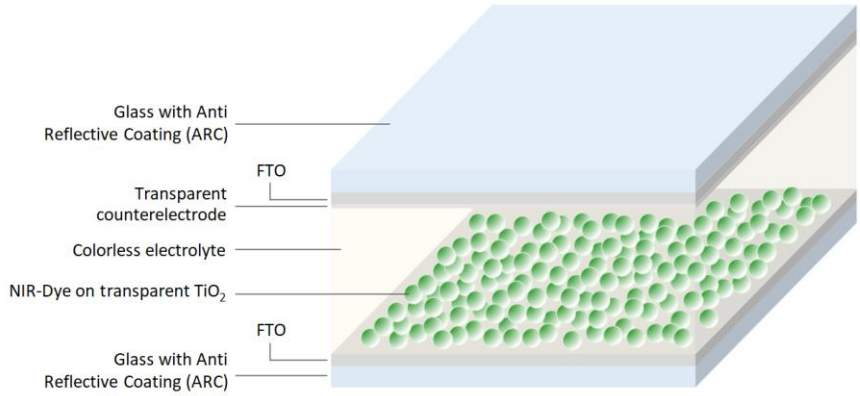

Figure 5 – Schematic overview of a NIR-DSSC.

1. NIR-Sensitizers

The development of NIR sensitizer is the main challenge of the development of NIR-DSSCs because it directly influences not only the performance of the device but also the final level of transparency and aesthetic. In a conventional visible-DSSC, the ideal photosensitizer should fulfil some essential characteristics: (i) the dye should have a panchromatic absorption spectrum with high molar extinction coefficient; (ii) strong anchoring groups are required to bind the dye onto the semiconductor surface; (iii) the LUMO level of the sensitizer should be higher in energy than the conduction band edge of semiconductor to lead to an efficient electron injection; (iv) the unfavourable aggregation of the dyes in the device should be avoided by an optimization of the molecular structure; (v) high photo- and thermal stability are required.[35] Many classes of dyes have been tested starting from the ruthenium-based complexes[36,37] with the goal to fulfil these requirements: porphyrins,[38,39] phthalocyanines,[40,41] metal-free organic dyes including coumarin dyes,[42] indoline dyes,[43] triarylamine dyes,[44] polymethine dyes,[45,46] perylene-based dyes[47,48] are just few examples.

However, to design a sensitizer capable to selectively harvests the light in the NIR region of the spectrum requires a reduction in the energy bandgap; as such, either stabilization of the LUMO levels or/and destabilization of the HOMO levels

is followed. Due this approach, both electron injection and oxidized dye regeneration rates will be affected, and therefore creating the first challenges in the optimization of such dyes. In order to assure an effective electron injection from the LUMO level of the sensitizers, the latter should be located at least 0.2 eV above the TiO_2 conduction band; this will place the LUMO level of the sensitizers at roughly -3.75 eV. At the same time, the selected dye should have a selective absorption in NIR part beyond 700 nm; this will place the HOMO level of the sensitizer close to -5.25 eV.[32] For these reasons, the classes of dyes possessing energetic levels that can ensure an efficient injection while being absorbers in the NIR region are limited. Among the above cited families of sensitizers, only polymethine and phthalocyanine dyes are well-known NIR sensitizers applied in DSSCs. These dyes are characterized by a sharp and strong absorption above 700 nm, making them suitable for devices targeting the NIR selectively.

1.1. Polymethine Dyes

Polymethine dyes are highly conjugated molecules with strong NIR absorption up to 1300 nm.[49] They are well-known in chemistry since 1873 when they have been first applied in photographic sensitization.[50] Their versatility has been widely exploited finding application as laser media,[51] as molecular switch,[52] as fluorescent probes,[53,54] in photodynamic therapy (PDT),[55] in non-linear optical (NLO) technologies[56] and obviously as sensitizers in DSSCs.[46,57] They are characterized by a high molar extinction coefficient and easily tunable properties through the modification of the polymethine central core or the lateral chromogenic units. Different polymethine core can be exploit allowing the synthesis of different class of dyes (Fig. 6a): (i) Cyanine dyes (CYs), (ii) Squaraine dyes (SQs) and (iii) Croconine dyes (CRs).

By varying the central core and thus the polymethine chain length it is possible to shift the $S_0 \rightarrow S_1$ transition from the visible towards the NIR region. For this reason, usually SQs are the worst sensitizer in terms of NIR-absorption selectivity

with absorption maxima at roughly 660-670 nm with molar extinction coefficient up to $3 \cdot 10^5$ $M^{-1}cm^{-1}$. The CRs usually have a more bathochromic shifted absorption around 790-800 nm due to the slightly more conjugated structure with similar molar extinction coefficient than SQs. Finally, CYs have the most selectiveness in the NIR-absorption but only in the case of the CY7 structure with absorption maxima beyond 810 nm and molar extinction coefficient up to $2.5 \cdot 10^5$ $M^{-1}cm^{-1}$. In addition, photophysical properties can be tuned by the further modification of the conjugated backbone with different lateral heterocyclic units (Fig. 6b).[46,58,59]

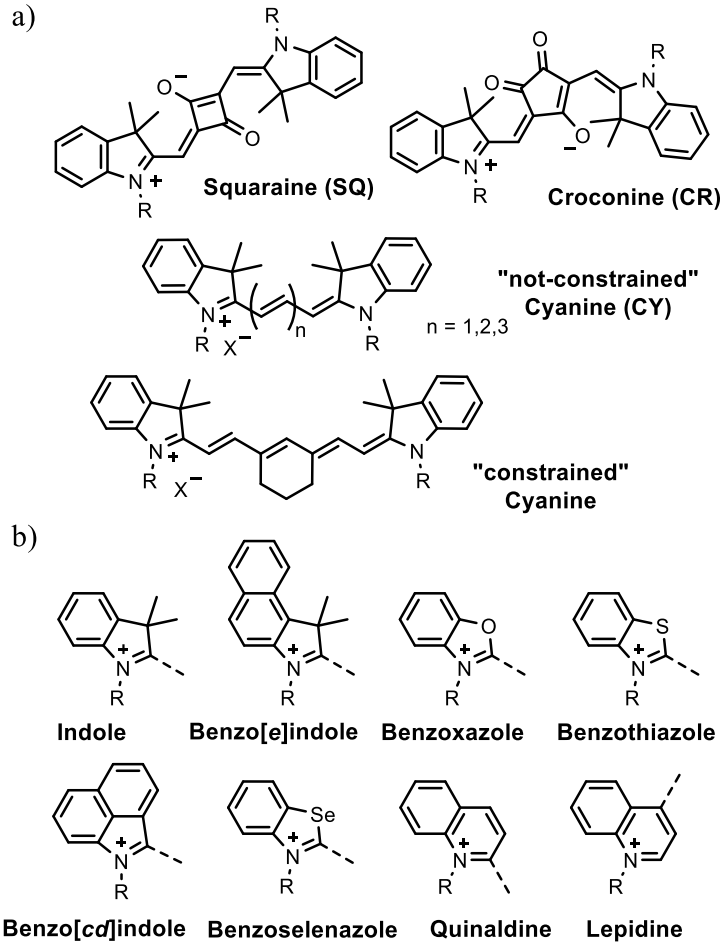

Figure 6 – a) General structure of Squaraine, Croconine and Cyanine dyes. In particular, CYs can be synthetize introducing a constrained polymethine structure that avoid any photoisomerization improving the general stability of longer cyanines. b) Schematic representation of the most used heterocyclic units to tune the photophysical properties of polymethine dyes.

Despite their suitable NIR-absorption, these sensitizers are well-known for their self-aggregation, mainly when anchored onto the semiconductor surface. Aggregates are very detrimental not only for the device performance but also for transparency level since they can induce absorption band broadening or even cause an onset of new absorption bands conferring device coloration. Aggregation can be reduced either by the co-sensitization approach, the addition of a disaggregating agent such as the chenodeoxycholic acid (CDCA) (see Appendix) or via the introduction of bulky lateral moieties or long alkyl chains.[60-62]

Beside to the right photophysical properties, a sensitizer should be also thermo- and photostable; however, polymethine dyes, in particular croconines and "not-constrain" cyanines, are well-known for their poor stability. For this reason, squaraines and the "constrained" cyanines are nowadays the only widely used polymethine dyes in DSSCs.

1.1.1. Squaraines

Squaraine dyes are the most studied NIR-sensitizers in DSSCs due to the large versatility offered by their structures toward new molecular designs (Fig. 7).

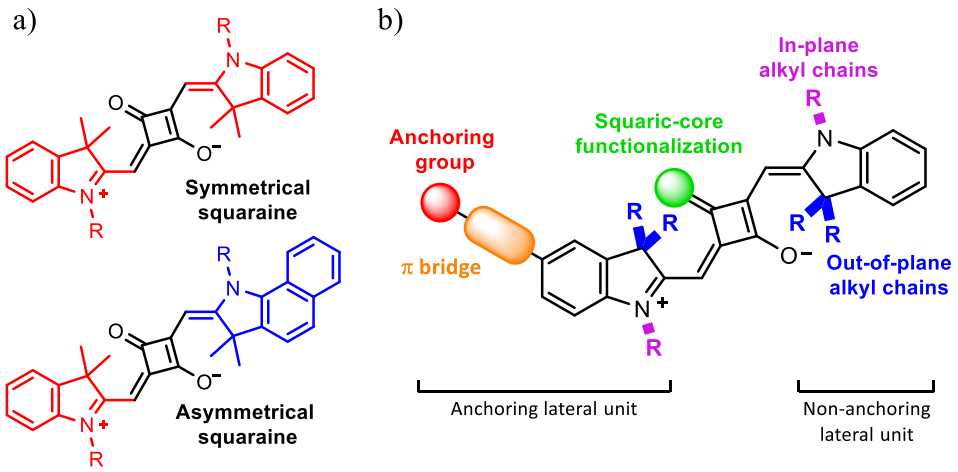

Figure 7 – a) Comparison between symmetrical and asymmetrical squaraines. b) General structure of unsymmetrical squaraine sensitizer with all the possible structural variations.

Over the years, a wide variety of structural motifs have been explored to tune any characteristic of the dyes, from the photophysical and electronic properties up to their solid-state behavior on the surface of the semiconductor.[46,57,63-66] The core of the structure is a four-membered aromatic ring derived from squaric acid. Depending on the lateral units, they are categorized as symmetrical or asymmetrical (Fig. 7a).

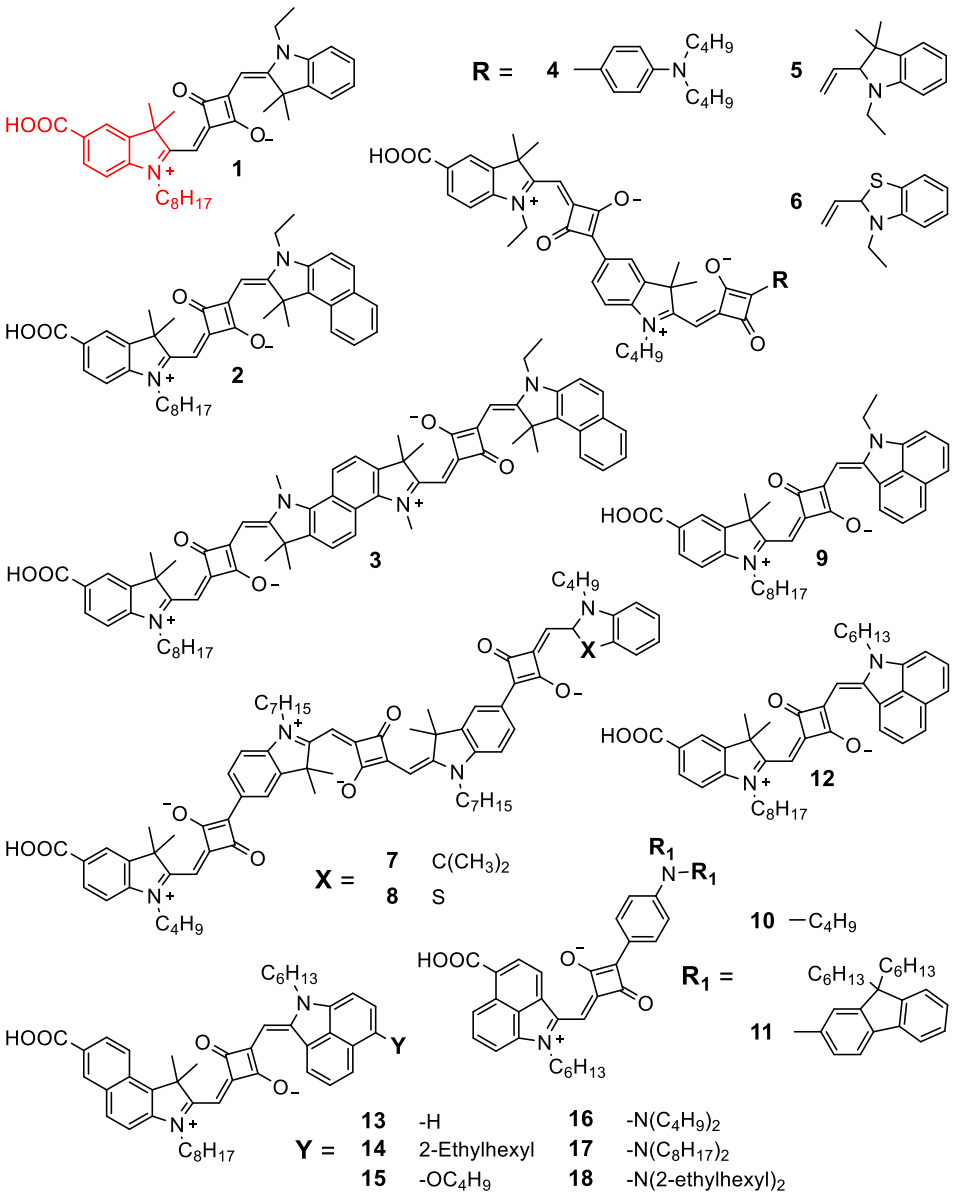

Figure 8 – Squaraine dyes with π-conjugated extended lateral units.

The latter ones were initially accounted the best choice to achieve good performance due to the directionality created in the excited state, allowing better electron injection.[29] The first example of DSSCs with a squaraine-based sensitizer was reported in 2007 with *SQ01* dye (**1**). In squaraine **1** an in-plane $-C_8$ alkyl chain was attached on the carboxyindolenine unit (CI), highlighted in red in Fig. 8, to reduce dye aggregation on the semiconductor's surface, achieving a PCE of 4.5% (Tab. 1).[67] However, this sensitizer is not-redshifted enough because the maximum absorption is only at 636 nm. The addition of one aromatic ring in the indolenine structure leading to the benzo[*e*]indole unit, inducing a bathochromic shift of roughly 25 nm for *SQ02* squaraine (**2**). This modification improves both photovoltage and photocurrent leading to an overall 5.4% PCE.[68] Despite the efficiency improvement, the flatter benzo[*e*]indole structure causes a more pronounced π-π stacking and don't push enough the absorption toward the NIR. However, stating form the encouraging result obtained with *SQ02*, the extension of the π-conjugation structure of the "non-anchoring lateral unit", was the first effective strategy exploited to shift the absorption toward the NIR. The dimeric squaraine *BSQ01* (**3**) has a strong absorption at 730 nm, slightly 100 nm more shifted compared to the monomeric *SQ01* (**1**). The presence of two chromophores squaric units in the structure leads to a very high molar extinction coefficient of $3.9 \cdot 10^5$ M^{-1} cm^{-1}. However, the PCE of **3** is only 1.3% probably due to the stronger π-π stacking compared to the monomeric squaraines **1** and **2**.[69] Following this concept, Maeda *et al.* firstly proposed the *LSQ* dimer squaraine series (**4**-**6**) that reached 2.26% PCE for dye **4** with strong absorption beyond 770 nm, and after the *TSQ* trimer series (**7**-**8**) with an outstanding absorption at roughly 850 nm, achieving 2.43% PCE for dye **8**. Despite the slightly efficiencies improvement due to the conjugation extension, the approach of oligomerization of squaraines was not further explored because of the high synthetic complexity and also due to the increasing of the absorption in visible region raising the structure's extension.[70,71] In addition, these pioneering studies have been demonstrated how the extension of the π-conjugation and the planarization of

the dye-structure to shift the absorption toward the NIR, unfortunately also raises the self-aggregation tendency.

Table 1 – Photovoltaic performance and photophysical properties of squaraines with π-conjugated extended lateral units.

Dye	λ_{max} (solvent) [nm]	ε [M^{-1} cm^{-1}]	J_{SC} [mA/cm^2]	V_{OC} [mV]	FF	PCE [%]	Ref.
1	636 (EtOH) 647 (DMF)	158 500 292 200	10.50	603	0.71	4.5	67 68
2	662 (DMF)	319 000	11.3	667	0.72	5.4	68
3	730 (DMF)	389 000	3.11	545	0.76	1.3	69
4	777 ($CHCl_3$)	174 000	9.05	460	0.54	2.26	70
5	779 ($CHCl_3$)	180 000	8.64	410	0.57	2.01	70
6	800 ($CHCl_3$)	189 000	9.01	400	0.51	1.82	70
7	856 ($CHCl_3$)	336 000	8.05	450	0.59	2.13	71
8	848 ($CHCl_3$)	347 000	8.89	450	0.61	2.43	71
9	768 (EtOH)	-	7.29	350	0.43	1.10	72
10	790 (DMF) 778 ($CHCl_3$)	83 180 69 180	2.47	230	0.55	0.32	73
11	763 (DMF) 852 ($CHCl_3$)	43 650 64 570	0.54	200	0.36	0.04	73
12	771 (EtOH)	103 000	4.39	300	0.56	0.74	74
13	728 (EtOH)	110 000	6.22	300	0.47	0.89	74
14	796 (EtOH)	116 000	9.20	315	0.45	1.31	74
15	806 (EtOH)	94 100	3.81	266	0.56	0.56	74
16	818 (EtOH)	102 000	1.77	276	0.59	0.29	74
17	820 (EtOH)	110 000	1.45	289	0.60	0.25	74
18	815 (EtOH)	97 700	2.05	279	0.52	0.30	74
19	640 (EtOH)	118 430	2.0	630	0.67	0.85	75
20	648 (EtOH)	144 370	1.26	660	0.66	0.55	75
21	673 (EtOH)	87 200	9.06	391	0.55	1.96	76
22	686 (EtOH)	92 400	9.25	374	0.51	1.77	76
23	643 (DMSO)	139 000	13.39	473	0.53	3.50	77
24	643 (DMSO)	86 200	13.64	480	0.57	3.75	77
25	673 (ACN)	61 000	20.77	486	0.68	6.82	78
26	673 (ACN)	69 000	20.35	526	0.67	7.16	78
27	674 (ACN)	65 000	20.00	540	0.66	7.09	78
28	692 (DCM)	129 000	6.86	558	0.69	2.63	79
29	715 (DCM)	111 000	9.62	558	0.69	3.68	79
30	754 (DCM)	135 000	10.02	576	0.72	4.15	79
31	665 (DCM)	220 000	12.6	652	0.70	5.75	80
32	666 (DCM)	300 000	13.8	657	0.71	6.42	80
33	679 (DCM)	240 000	8.98	643	0.70	4.05	80
34	681 (DCM)	350 000	12.1	633	0.70	5.37	80

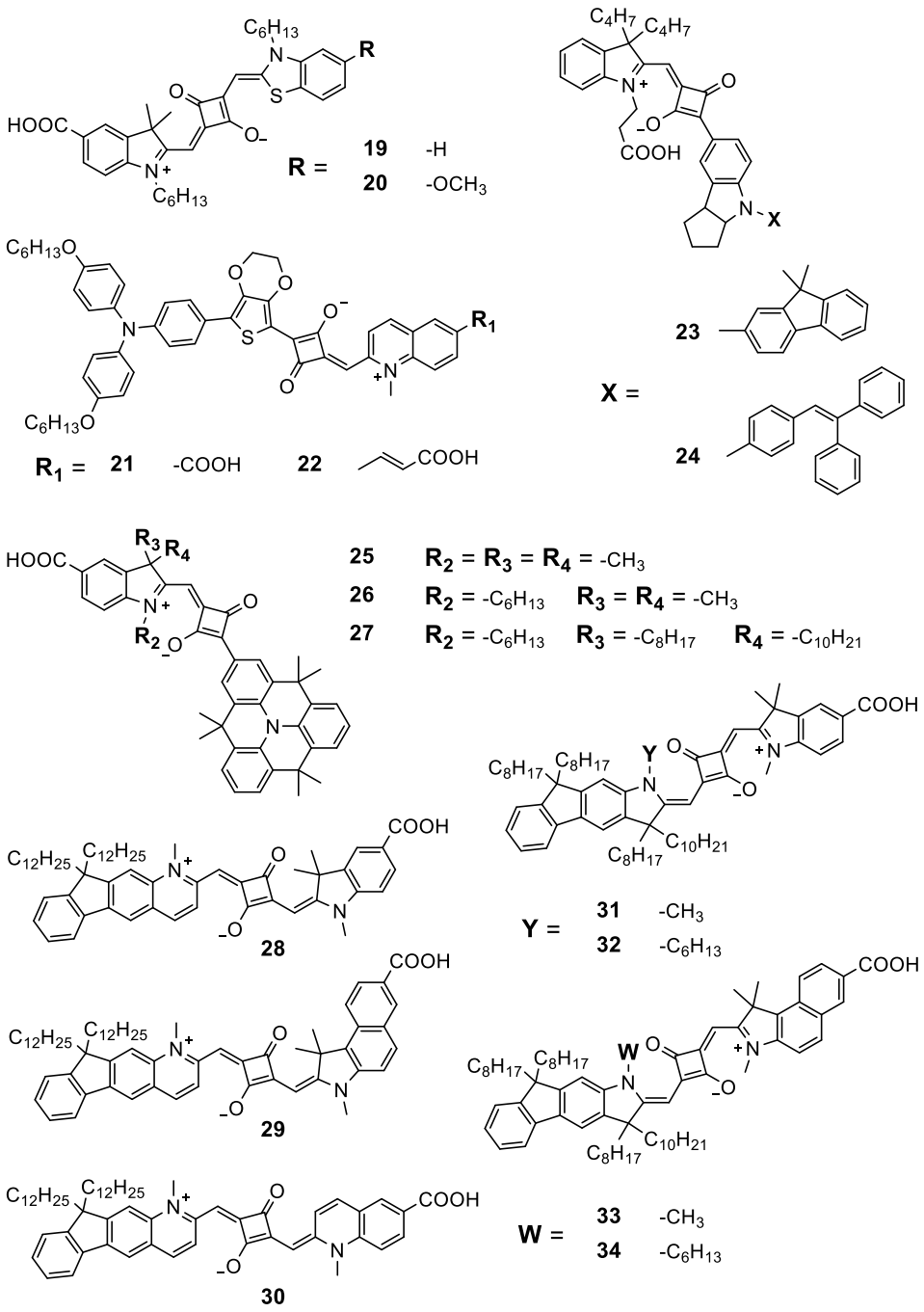

Figure 9 – Squaraine dyes with other π-conjugated extended lateral units.

For these reasons, the research studied different non-anchoring lateral units able to strongly red-shift the absorption but with a less self-aggregation tendency. Benzo[*cd*]indole was the first example of lateral unit able to

considerably shift the absorption in the NIR. Squaraine *VG5* (**9**) has a maximum absorption at 768 nm, roughly 130 nm red-shifted compared to the similar *SQ01* (**1**). However, the benzo[*cd*]indole unit exhibit a higher self-aggregation tendency limiting the efficiency of **9** that achieved only the 1.1%.[72] To improve the PCE different strategies have been proved. Maeda *et al.* tried to use the benzo[*cd*]indole as anchoring group exhibiting lateral unit (**10**-**11**). However, compared to the classic carboxyindolenine-based squaraine like **1**, dyes **10** and **11** does not show good performances mainly due to a very low electron injection.[73] Another idea has been the introduction of bulky-groups in 6 position of benzo[*cd*]indole, instead. It was demonstrated that the additional group positively influence either the self-aggregation tendency and the photophysical properties. Squaraines **12**-**18** exhibit a lower π-π stacking compared to **9** and absorption maxima up to 820 nm. Nevertheless, the PCEs of these series of dyes were still low, with a best result of 1.3% achieved by **14**.[74] Following the same strategy, many other extended π-conjugate structure has been tried as lateral unit like benzothiazole (**19**-**20**),[75] quinoline (**21**-**22**),[76] hexahydrocyclopenta[*b*]indole (**23**-**24**),[77] heterotriangulene (**25**-**27**),[78] indenoquinaldine (**28**-**30**),[79] and fused fluorenylindolenine (**31**-**34**) (Fig. 9).[80] However, it was demonstrated that the use of different heterocycle-based lateral units is only a good strategy to tune the photophysical properties of the squaraines but it's not the best way to reach a breakthrough in the PCE.

Squaraine dyes are well-known for their photoisomerization processes involving the *cis*-*trans*-configuration (Fig. 10a), limiting their performance in DSSCs.[81] To avoid the photoisomerization, different strategies have been proposed: (i) the addition of a second anchoring group that provides a stronger and double electronic coupling with the semiconductor surface (Fig. 10b), (ii) the functionalization of the squaric-core unit to lock the structure in the *cis*-configuration (Fig. 10c) and finally, even if less effective, (iii) the insertion of a long in-plane alkyl chain that increases the steric hindrance, thus preventing intramolecular rotation.[46,82,83] The first strategy was demonstrated by Park *et al.* by the comparison of the classic unsymmetrical squaraine **1** with its symmetrical

counterpart **35** (Fig. 11). Both squaraine have the same energy difference between the *trans*- and *cis*-conformation (about 0.8 kJ mol^{-1}) suggesting the co-existence of either in solution. However, the *cis*-conformation of **35** has higher polarity, indicating a higher charge separation and thus a possible higher electron injection then the asymmetrical squaraine **1**. The photovoltaic performances of dye **35** are roughly the same of **1** with an efficiency of 4.6% *vs.* 4.2%, respectively.[84]

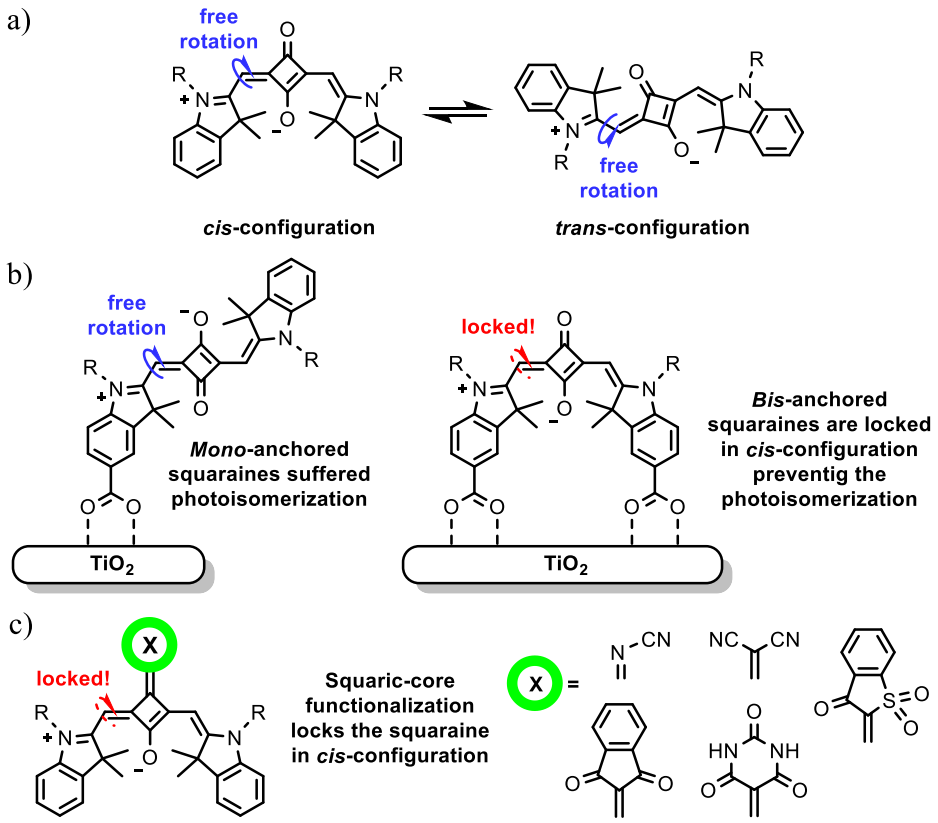

Figure 10 – a) Isomerization equilibrium between *cis*- and *trans*-conformation in squaraine dye. b) The different behaviour between a mono- and bis-anchored squaraine dye on the semiconductor surface. c) The effect of the squaric-core functionalization on the photoisomerization process.

Even if both asymmetrical **1** and symmetrical **35** squaraines exhibit comparable efficiencies, the latter has undoubtedly advantaged with an easiest synthesis alongside better photophysical properties. Usually, symmetrical

squaraines have a more red-shifted absorption compared to the asymmetrical counterpart (roughly 10-15 nm) and a slightly higher molar extinction coefficient.[64,84,85] In addition, it was also demonstrated that symmetrical bis-anchoring squaraine leading to a more stable devices due to the stronger electronic coupling with the semiconductor surface able to suppress the dye-desorption.[86] The insertion of two carboxylic anchoring moieties in squaraine dyes was further investigated by Park *et al.* using the more extended benzo[*e*]indole lateral unit, achieving the record efficiency of 6.2%. Even in this case the symmetrical squaraines **36** and **37** show higher PCEs than to the asymmetrical one **38**.[87]

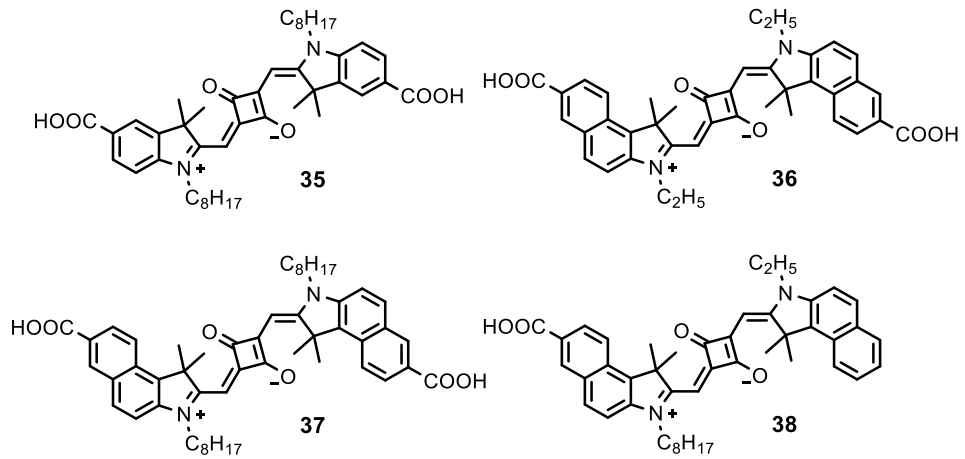

Figure 11 – Squaraines investigated by Park *et al.* to demonstrate the advantages of the symmetrical bis-anchoring squaraine *vs.* the asymmetrical mono-anchoring ones.

Table 2 – Photovoltaic performance and photophysical properties of squaraines investigated by Park *et al.*

Dye	λ_{max} (solvent) [nm]	ε [M^{-1} cm^{-1}]	J_{SC} [mA/cm^2]	V_{OC} [mV]	FF	PCE [%]	Ref.
35	646 (EtOH)	295 120	9.4	629	0.77	4.6	84
36	669 (EtOH)	240 000	14.3	623	0.69	6.18	87
37	673 (EtOH)	280 000	13.6	641	0.70	6.10	87
38	665 (DCM)	270 000	12.1	665	0.68	5.50	87

In the first strategy we saw as the presence of two anchoring groups on the dye structure promotes a strong electronic coupling with the semiconductor surface, inducing the squaraine in the *cis*-conformation. However, this behavior is closely related to the interaction of the dye with the semiconductor surface; in solution, these symmetrical squaraines continue to show the *cis-trans* isomerization, indeed. For this reason, another approach was developed to avoid or at least decrease the photoisomerization even in solution. The functionalization of the squaric-core unit is a well-known strategy to lock the squaraine structure in the *cis*-conformation as figure out in Fig. 10c. In addition, it was demonstrated that the addition of electron-withdrawing groups on the squaric-core unit leads to a bathochromic shift of the maximum absorption of almost 50 nm.[83,88] The first example of core-functionalized squaraine as sensitizer in DSSC was reported by Beverina *et al.* using the diethylthiobarbiturate moiety as electron-withdrawing group on the squaric-core.[89]

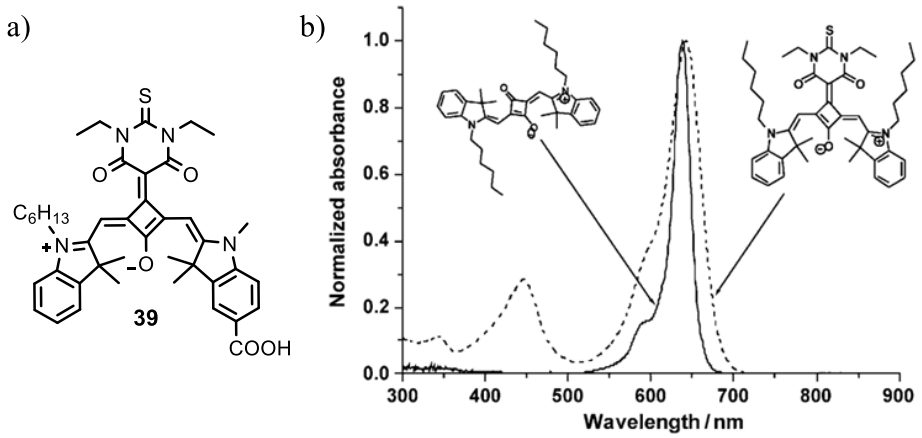

Figure 12 – a) Structure of core-functionalized squaraine **39**. b) UV/vis absorption spectra (in ACN) comparison between a classical squaraine (solid line) and its core-functionalized counterpart (dashed line).[89]

Compared to the classic squaraines, dye **39** (Fig. 12a) shows at 646 nm a slightly broader strong absorption band arising from the cyanine-like transition associated with the delocalization of the nitrogen lone pair over the main conjugation axis. In addition, squaraine **39** has another characteristic high-energy

absorption band at roughly 450 nm due to the presence of the electron-withdrawing diethylthiobarbiturate group on the core (Fig. 12b).[89,90] In terms of efficiency, the core-functionalized squaraine **39** achieved a PCE of 4.7% (J_{SC} = 11.87 mA/cm^2, V_{OC} = 576 mV, FF = 0.68), slightly higher than its unsubstituted counterpart.[89] Following this concept, other electron-withdrawing groups were investigated to functionalize the squaric-core such as the dicyanovinyl residue and cyano-esters with alkyl chains of different length. However, for the purpose to develop NIR-DSSCs the core-functionalized squaraines are not suitable as NIR-sensitizers due to their not negligible absorption in the visible region.[86,91-94]

As mentioned before, also the in-plane alkyl chains can affect the *cis-trans* photoisomerization process; in particular, the insertion of longer alkyl chains favors the *cis*-conformation.[87,95] However, this strategy is much less effective to tune the *cis-trans* isomerization equilibrium compared to the effect resulting from squaraines with two anchoring groups or with functionalized squaric-core.

In-plane alkyl chains are well-known not only for their effect on the isomerization but for their key-role to prevent the dye-aggregation and to reduce the charge recombination process between the injected electrons and the oxidized electrolyte.[96] In the pivotal work of Pandey *et al.* it was investigated the effect of in-plane alkyl chain length in squaraines **40**-**45** (Fig. 13a). The results demonstrate that alkyl chain length more than butyl is necessary to prevent the dye-aggregation and dodecyl alkyl substituent was found to be optimum giving highest V_{OC}.[97] Squaraines with longer alkyl chains (**43**-**44**) exhibit enhanced adsorption of the dyes on the semiconductor leading to a better passivation of surface traps. The enhanced surface passivation is fundamental to increase the electron lifetime and the electron diffusion length, respectively.[96] For these reasons, squaraines **43**-**44** have higher J_{SC} and V_{OC} than dyes with shorter alkyl chains (**40**-**42**) (Fig. 13b-13c). In addition, the comparison between squaraines **41** and **45** demonstrated how a judicious selection of fluoroalkyl substituents can be exploited to tune the HOMO and LUMO energy levels. The presence of the trifluoromethane residue in **45** leads to the energy stabilization of both HOMO and LUMO energetic levels (Fig. 13d).

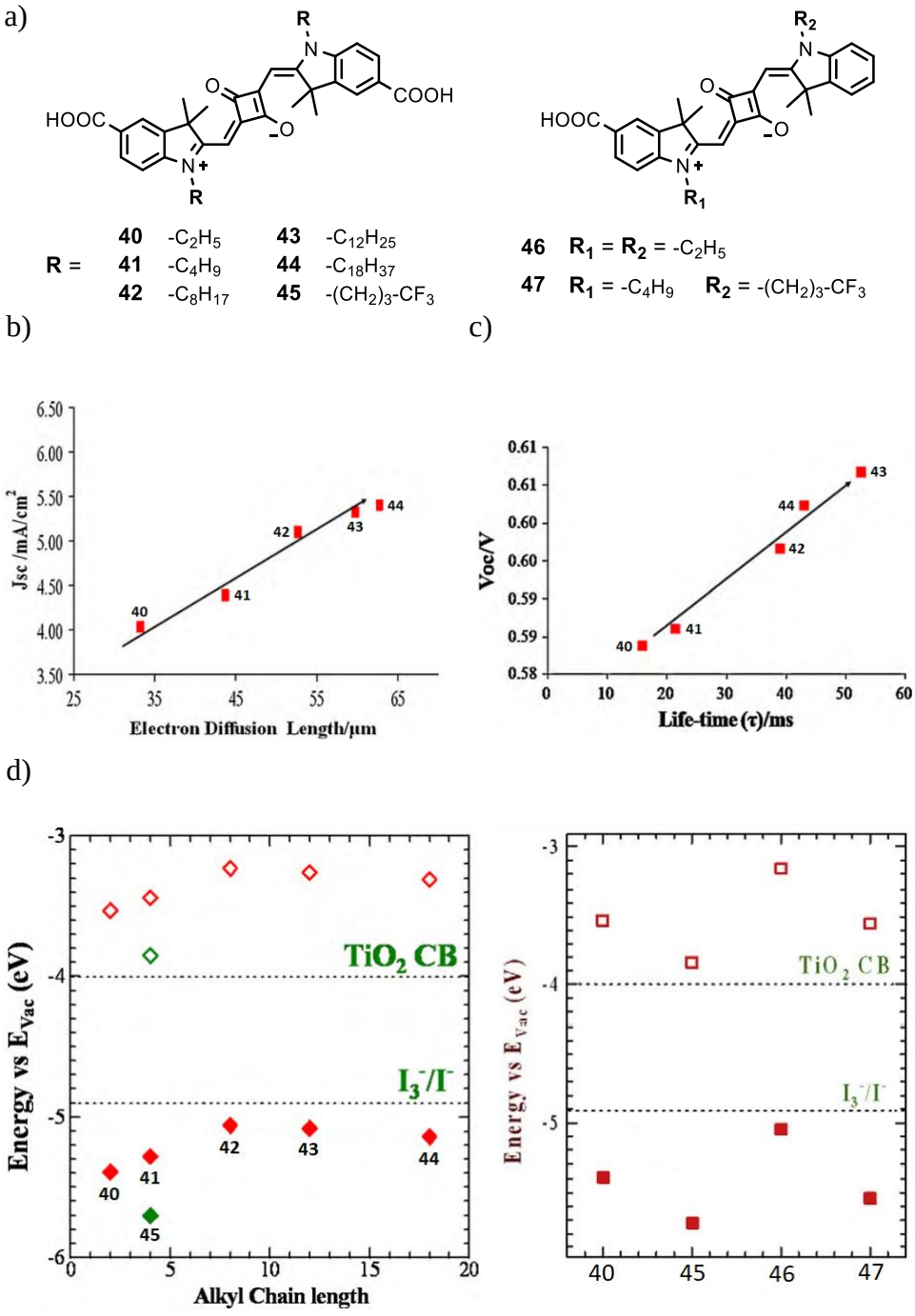

Figure 13 – a) Squaraines investigated by Pandey *et al.* to demonstrate the effect of the in-plane alkyl chain length. b) Correlation between measured electron diffusion length and J_{SC} for DSSC based on alkyl substituted model squaraine dyes. c) Relationship between measured electron lifetime and observed V_{OC} for DSSC based on squaraine dyes having variable alkyl chain length. d) HOMO and LUMO energy level of squaraines **40**-**47**.[97,98]

Following the same strategy, Pandey *et al.* investigated the effects on the DSSCs' performance of the in-plane alkyl chain length and fluoroalkyl substituents in asymmetrical squaraines **46**-**47**. Interestingly, the comparison between the symmetrical squaraines **40** and **45** with the asymmetrical ones **46** and **47** demonstrates how the molecular asymmetry plays an important role in controlling the HOMO/LUMO energy level of the sensitizers. The introduction of molecular asymmetry leads to a destabilization of both HOMO/LUMO energy levels (Fig. 13d) raising the $-\Delta G_{inj}$ alongside the overall efficiency (Tab. 3).[98]

Table 3 – Photovoltaic performance and photophysical properties of squaraines investigated by Pandey *et al.*

Dye	λ_{MAX} (solvent) [nm]	ε [$M^{-1}cm^{-1}$]	J_{SC} [mA/cm^2]	V_{OC} [mV]	FF	PCE [%]	Ref.
40	640 (DMF)	-	4.03	560	0.64	1.46	97
	650 (DMF)	320 000	6.36	570	0.68	2.46	98
41	641 (DMF)	-	4.39	580	0.65	1.66	97
	652 (DMF)	355 000	7.13	590	0.66	2.76	98
42	641 (DMF)	-	5.09	600	0.69	2.09	97
43	-	-	5.31	610	0.67	2.17	97
44	643 (DMF)	-	5.40	600	0.71	2.29	97
45	650 (DMF)	295 000	6.63	570	0.70	2.65	98
46	645 (DMF)	250 000	7.68	600	0.67	3.08	98
47	645 (DMF)	420 000	7.50	620	0.72	3.36	98

The demonstration of the key role of the long alkyl chains to decrease the dye's aggregation represented the first turning point in the development of high performance DSSCs based on squaraine sensitizers. However, the real breakthrough was reached by the addition in the squaraines' structure of a π-bridge between the dye and the anchoring group (Fig. 7b). In the pivotal work of Shi *et al.*, the well-known *SQ01* (**1**) was modified by the insertion of a thiophen as a π-bridge and the replacement of the carboxylic acid anchoring-group with strong π-accepting carboxycyanovinyl moiety (**48**) (Fig. 14).[99] In this strategy, the role of the π-bridge is: (i) to increase the molecule's polarity and thus the charge separation to favor higher electron injection, (ii) to extend the distance between

the injected electron and the generated positive charge on the dye to reduce the charge recombination rate and (iii) to control the orientation of the dye on the semiconductor surface.

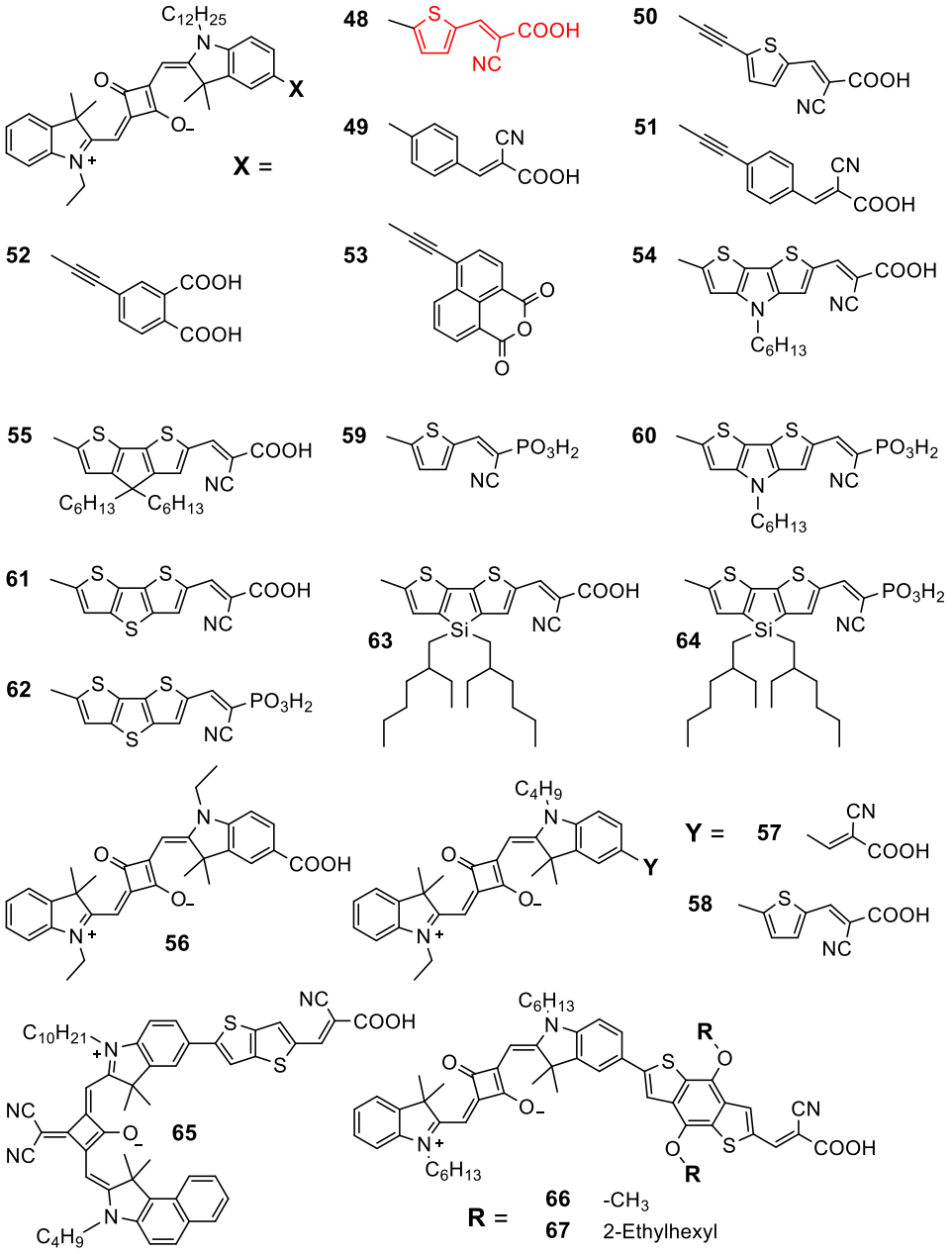

Figure 14 – Squaraine dyes with π-bridge.

Compared to dye **1**, squaraine **48** exhibits a red shifted absorption at 659 nm with stronger molar extinction coefficient (Tab. 4) due to the effect of the extended conjugation. Moreover, the insertion of the thiophen-cyanoacrylic acid moiety (in red in Fig. 14) adds other high-energy bands in the absorption of the squaraine. The larger and stronger absorption alongside the higher charge separation in **48** leading to a better photocurrent density than squaraine **1**, achieving a record PCE of 6.74%.[99]

Table 4 – Photovoltaic performance and photophysical properties of squaraines with π-bridges.

Dye	λ_{max} (solvent) [nm]	ε [$M^{-1}cm^{-1}$]	J_{SC} [mA/cm^2]	V_{OC} [mV]	FF	PCE [%]	Ref.
48	659 (EtOH) 671 ($CHCl_3$)	279 000 275 000	14.8	642	0.71	6.74	99 100
49	656 ($CHCl_3$)	316 000	7.80	605	0.74	3.49	100
50	664 ($CHCl_3$)	322 000	8.53	613	0.74	3.85	100
51	658 ($CHCl_3$)	332 000	7.26	604	0.74	3.27	100
52	653 ($CHCl_3$)	289 000	2.77	563	0.73	1.14	100
53	662 ($CHCl_3$)	285 000	2.88	524	0.69	1.04	100
54	678 ($CHCl_3$)	160 000	13.1	622	0.73	5.95	100
55	680 ($CHCl_3$)	230 000	16.4	635	0.70	7.30	100
56	636 (EtOH)	-	6.71	580	0.72	2.82	102
57	653 (EtOH)	-	11.53	630	0.69	5.03	102
58	663 (EtOH)	-	6.93	580	0.66	2.67	102
59	655 (EtOH)	311 000	9.6	644	0.72	4.6	103
60	670 (EtOH)	204 000	5.9	642	0.73	2.8	103
61	662 (EtOH)	231 000	13.1	644	0.72	6.0	103
62	661 (EtOH)	259 000	3.7	621	0.76	1.8	103
63	667 (EtOH)	257 000	19.1	682	0.68	8.9	103
64	666 (EtOH)	214 000	10.4	676	0.70	5.0	103
65	720 ($CHCl_3$)	246 000	15.0	560	0.69	5.86	104
66	664 ($CHCl_3$)	218 000	19.03	490	0.58	5.43	105
67	664 ($CHCl_3$)	239 000	18.53	538	0.67	6.72	105

Starting from these results, many other different π-bridges were investigated on the same squaraine-structure. A carefully comparation of the effect on optical and electrochemical properties of benzene (**49**), ethynyl thiophene (**50**), ethynyl benzene (**51**), ethynyl phthalic (**52**), ethynyl naphthalene anhydride (**53**), *N*-(*n*-

hexyl)dithienopyrrole (DTP) (**54**) and di-*n*-hexyl-substituted cyclopentadithiophene (CPDT) (**55**) groups as π-bridge was performed by Delcamp *et al.*[100] Squaraines **48**-**55** exhibits absorption maxima between 653 and 680 nm (Table 4). Dyes with thiophene or fused thiophene bridges (**48**, **50**, **54** and **55**) shows more red-shifted absorbance likely owing to the lower degree of aromaticity of thiophene when compared with benzene-based π-bridges. Among the latter ones, the naphthalene-anhydride anchor (**53**) is the most red-shifted, although the color range between the dyes with different benzene-based π-bridges (**49**-**53**) is modest. For all dyes, the molar extinction coefficient exhibits typical values for squaraine dyes between 1.5 and $3.5 \cdot 10^5$ M^{-1} cm^{-1} with lower absorptivities measured for sensitizers with thiophene-fused π-bridges (**54** and **55**). In addition, the latter ones show a not negligible absorption band around 500 nm with molar extinction coefficients up to 25 000 M^{-1} cm^{-1}.[100] The analysis of the photovoltaic performances of all these dyes (**48**-**55**) allowed to define which are the fundamental characteristics required to achieve high efficiencies.

A critical aspect to dye design is positioning the LUMO close to the TiO_2 surface for efficient electron injection and the HOMO sufficiently far from the TiO_2 surface to inhibit the recombination of electrons in the semiconductor CB. Usually, the squaraine LUMO is often significantly delocalized on the whole squaraine core, which is spatially separated from the TiO_2 surface. However, in the case of **53**, the LUMO is predominately located on the acceptor and π-bridge regions of the sensitizers, decreasing the charge separation and thus more favoring the electron recombination processes.

The ethynyl linker in dyes **50**-**53** were investigated to eliminate the steric interactions between the π-spacer and squaraine core. As expected, the alkyne-containing sensitizers show a minimal dihedral angle (<4°) due to the absence of steric hinderance. However, the efficiencies of the squaraines with (**50**-**51**) and without the ethynyl linker (**48**-**49**) are comparable. This trend may indicate a balance between the beneficial effect of a planarized conjugated π-system on donor-acceptor communication and the possible detrimental effects of an

increased propensity for aggregation. For this reason, ethynyl linker is scarcely exploited in the π-bridges design for squaraine-based sensitizers.

The investigation of the dihedral angle between π-bridges and the squaraine core also demonstrate the main drawback of the benzene-based bridges. Thiophene- and fused-thiophene based dyes (**48**, **54** and **55**) in which the steric interactions are between 6- and 5- membered rings, the dihedral angles are roughly 25° while in the benzene-based dyes (**49**) is much higher (36°). In terms of performance, dye **48** has a J_{SC} of 14.1 mA/cm^2 with a PCE of 6.21% while squaraine **49** has a much lower J_{SC} of 7.80 mA/cm^2 with only 3.49% of efficiency.[100] The higher performance of **48** is mainly due to the lower dihedral angle of the thiophene-based linker resulting in a flatter structure which therefore allows for better electronic communication through the π-bridge.

Finally, Delcamp *et al.* demonstrated for the first time how the out-of-plane alkyl chains (depicted in Fig. 7) can be useful to effectively reduce the squaraines self-aggregation and thus improve the PCE. In dyes **54** and **55**, a DTP and a CPDT units were used like π-bridges, respectively. In DTP-based bridge, the pyrrole's nitrogen is functionalized with an in-plane *n*-hexyl chain while in CPDT-based one, the sp^3 carbon is decorated with two out-of-plane 2-ethylhexyl groups. The more hindered environment guarantees by the two out-of-plane 2-ethylhexyl groups in squaraine **55** better hamper the self-aggregation than the in-plane *n*-hexyl in **54**; for this reason, squaraine **55** exhibit a higher J_{SC} of 16.4 mA/cm^2 and an efficiency record of 7.30%.[100,101]

The introduction of π-bridges in the sensitizers' structures certainly lead to better performance but the outstanding record achieved by **55** it's not only owing by the presence of the π-bridge. If we compare the two squaraines **57** and **58**, it's possible to determine how even the thiophene-based bridges favor the self-aggregation causing a relevant drop in the photocurrent density. Squaraine **57** without the thiophene bridge and with only the cyanoacrylate anchoring group achieves an efficiency of 5.03% while dye **58** reaches only 2.67%.[102] This gap is mainly due to the clear difference in photocurrent density between the two dyes

(Tab. 4) caused by the more self-aggregation tendency of dye **58**. In addition, the comparison between classic squaraine **56** with **58**, demonstrates how the insertion of π-bridge in a squaraine's structure decorated with not enough bulky substituents (like the ethyl and the butyl chain in **58**) could be detrimental don't leading to any improvement in device's performance. However, a carefully tailored π-bridge in relation to the dye structure can allow for outstanding results. Starting from the pivotal work of Delcamp *et al.*, Jradi *et al.* investigated squaraines (**61**-**64**) bearing two new fused-thiophene bridges based on the dithienothiophene (DTT) and the silolodithiophene (DTS).[103] In addition, all the thiophene and the fused-thiophene based π-bridges described so far, have also been investigated using a phosphonic acid-type anchoring group (**59**, **60**, **62** and **64**), known to give enhanced device stability.[82] DTT- and DTS-based squaraines (**61**-**64**) have almost the same photophysical properties of similar DTP- and CPDT-based dyes (**54**-**55**) reported before with a maximum absorption between 660-670 nm and a molar extinction coefficient between 2.0 and $2.5 \cdot 10^5$ $M^{-}1$ cm^{-1}. Even in these cases, the insertion of the DTT and the DTS π-bridge cause the appearance of a not negligible absorption band in the visible around 440 nm for DTS-based squaraines (**63**-**64**) and 470 nm for DTT-based dyes (**61**-**62**), respectively. The comparison between the performances of the two series based on DTS- and DTT-bridges given a further confirmation about the importance of the presence of bulky substituents in the dye's structure, in particular the presence of out-of-plane alkyl chains. Dyes with DTS bridges achieved an outstanding record efficiency of 8.9% in the case of the carboxylic anchoring group (**63**) and 5.0% in the case of the phosphonic anchoring group (**64**). The higher efficiencies mainly depend by the presence of the two bulky 2-ethylexhyl groups attached on the silicon atom that guarantee (i) lower dye aggregation, (ii) slower recombination rates improving the J_{SC} and (iii) a lower interaction of the electrolyte with the TiO_2 surface increasing the V_{OC}.[103] In the case of DTT-based squaraines (**61**-**62**), the absence of bulky substituents mainly results in lower electron injection rate and thus in lower PCEs. Finally, squaraines with

phosphonic acid anchoring group shows lower efficiencies than ones bearing the carboxylic group, as expected from the literature.[82]

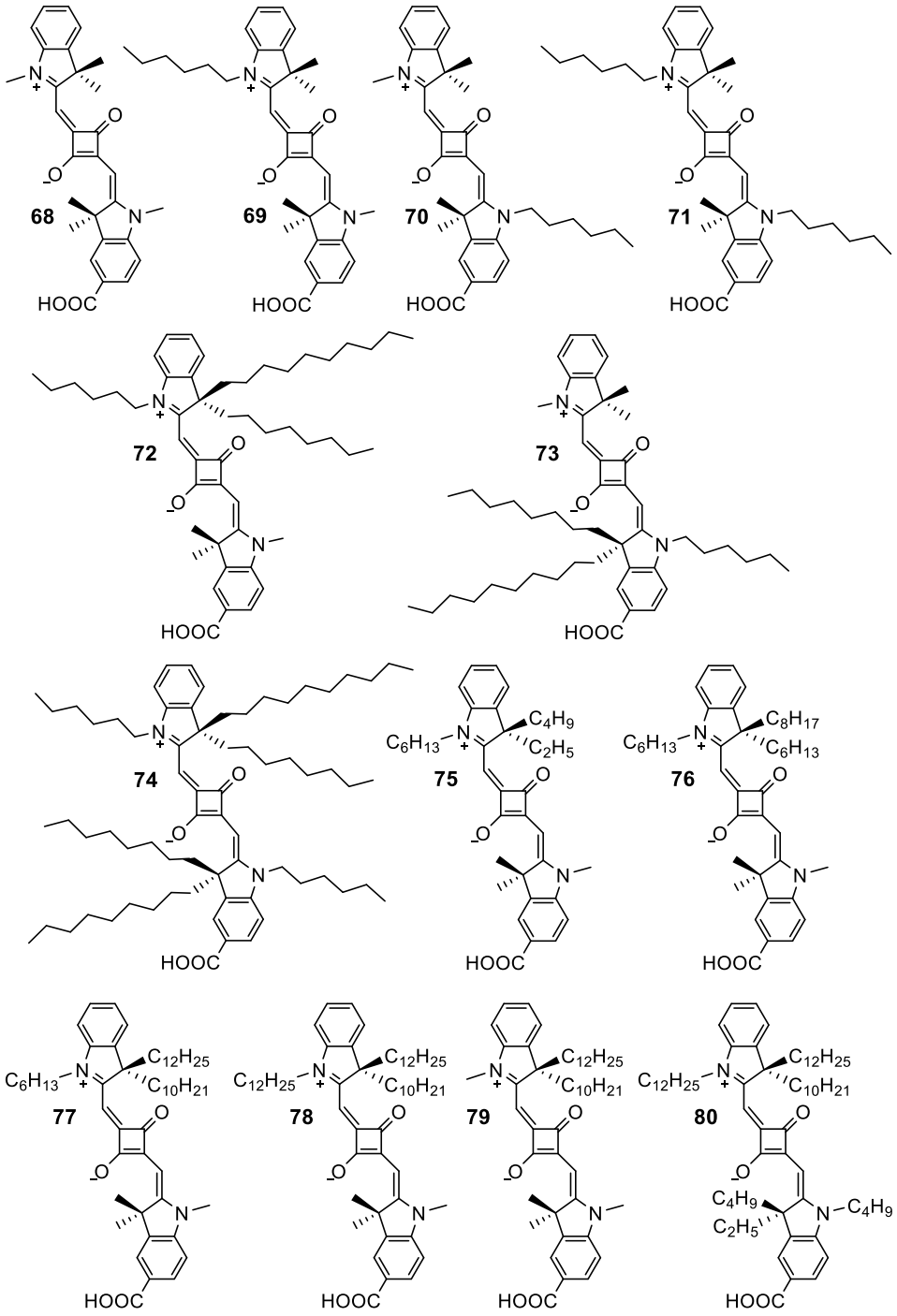

Figure 15 – Squaraine dyes with out-of-plane alkyl chains on the indolenine core.

Following the same strategies, other π-bridges based on fused-thiophene have been investigated like the thienothiophene (TT) (**65**) and the benzodithiophene (BDT) (**66**,**67**) but neither approached the PCE record achieved by DTS-based squaraine **63**.[104,105]

The definitive confirmation of the smashing importance of the out-of-plane alkyl chains in squaraines were demonstrated by Nithyanandhan's group in their pivotal work on the effect of out-of-plane alkyl groups' position in DSSCs efficiency.[106] Firstly, squaraines **68**-**74** was assessed by varying the position of in-plane and out-of-plane alkyl groups on the two indoline units (Fig. 15). In particular, was evaluated the effect of: (i) the presence and position of in-plane hexyl chain in dyes **68**-**71**, (ii) the role of out-of-plane alkyl chains in relationship of the presence of the in-plane hexyl group in **69** and **72** and (iii) the presence and position of out-of-plane alkyl chains on both indoline units in **72**-**74**. Thought in solution squaraines **68**-**74** exhibit almost the same absorption centered roughly between 640-650 nm, when they are adsorbed on TiO_2 the dye-aggregation plays an important role on the photophysical properties of these sensitizers. Generally, squaraines **68**-**74** have broadened and blue-shifted absorptions in relationship of their structures. Model dye **68** without any bulky substituents exhibit a two peaks absorption shape, in which the first one with higher intensity at 575 nm corresponds to the H-aggregates and the other one at 628 nm to the monomer absorption.[107] By introducing in-plane hexyl group in nitrogen atom, the aggregate and monomer peaks appear slightly red-shift, and especially the H-aggregate's peak intensity becomes lower than the monomer peak (Fig. 16) Other changes are observed in peak positions by the insertion of the out-of-plane alkyl chains, in these cases the absorption was further red-shifted up to reach the case of dye **74** where there aren't significant changes in both solution and on TiO_2 surface. However, the addition of CDCA in dye-loading solution as co-adsorbent tunes the intensity ratio between the monomer and the H-aggregate absorption and thus the final aesthetic of the photoanode. For our purpose, the addition of out-of-plane alkyl chains on the dye-structure could be a useful tool not only to

decrease the charge recombination as demonstrated before by **55** and **63** but also to tune the absorbance of the sensitizer on TiO_2 surface toward the development of colorless and transparent NIR-DSSCs.

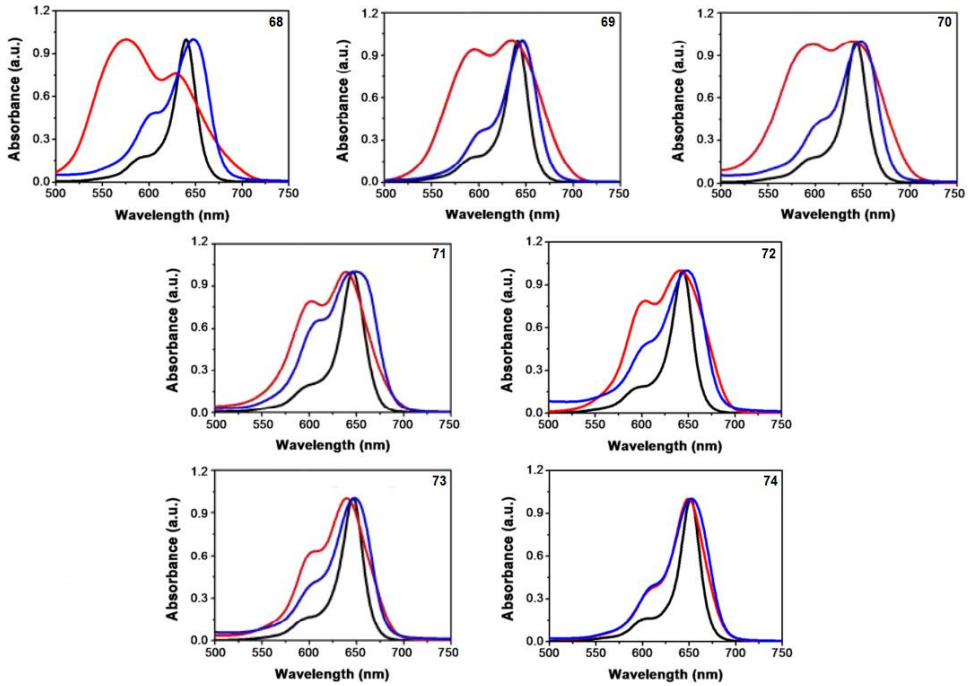

Figure 16 – UV-Vis absorption spectra of squaraines **68**-**74** in solution (black), on TiO_2 (red), and in presence of CDCA on TiO_2 (blue).[106]

In terms of photovoltaic performances, squaraine **69** achieved higher efficiency than other dyes having only the in-plane hexyl chain on their structure (**68**-**71**) (Tab. 5). In particular, when the in-plane alkyl chain is attached on the indoline unit far from the TiO_2 surface, squaraine **69** exhibit a remarkable efficiency of 5.71% higher than the 3.78% of its isomer **70** and the 4.15% of the double-substituted dye **71**. Though **69** and **70** are isomeric in structure, the position of in-plane hexyl chain makes significant impact on the adsorption on TiO_2 surface because the presence of bulky groups near to the anchoring group in the squaraine-based sensitizers, like **70**, passivate the surface besides blocking the anchoring sites (Fig. 17). This means that sensitizers with large surface coverage leads to a lower amount of active dye resulting in a poor J_{SC}.[106]

Table 5 – Photovoltaic performance and photophysical properties of squaraines with out-of-plane alkyl chains on the indolenine core.

Dye	λ_{max} (solvent) [nm]	ε [M^{-1} cm^{-1}]	CDCA [eq.]	J_{SC} [mA/cm^2]	V_{OC} [mV]	FF	PCE [%]	Ref.
68	640 (DCM)	140 000	0	7.33	568	0.68	2.85	106
			20	8.33	579	0.71	3.43	
69	641 (DCM)	210 000	0	10.41	609	0.69	4.37	106
			20	12.49	647	0.71	5.71	
70	643 (DCM)	184 000	0	8.38	595	0.69	3.45	106
			20	8.97	601	0.70	3.78	
71	646 (DCM)	209 000	0	8.72	614	0.69	3.72	106
			20	9.31	636	0.70	4.15	
72	644 (DCM)	210 000	0	17.97	637	0.67	7.70	106
			5	19.72	655	0.69	9.00	
			20	17.14	647	0.69	7.68	
73	647 (DCM)	220 000	0	12.35	633	0.68	5.28	106
			20	10.99	639	0.71	4.97	
74	652 (DCM)	100 000	0	14.06	640	0.68	6.13	106
			20	14.67	654	0.70	6.75	
75	643 (DCM)	350 000	0	7.64	668	0.71	3.62	108
			5	9.36	695	0.74	4.81	
76	643 (DCM)	330 000	0	8.89	683	0.77	4.67	108
			10	9.77	694	0.76	5.15	
77	643 (DCM)	320 000	0	10.95	706	0.75	5.80	108
			1	12.35	710	0.74	6.49	
78	643 (DCM)	300 000	0	11.55	715	0.70	5.78	108
			3	12.96	712	0.76	7.01	
79	642 (DCM)	290 000	0	8.78	671	0.77	4.53	108
			1	9.80	695	0.76	5.17	
80	650 (DCM)	310 000	0	11.95	717	0.71	6.08	108
			1	12.92	716	0.73	6.75	
81	705 (DCM)	150 000	0	13.33	567	0.67	5.15	110
			10	17.07	577	0.70	6.93	
82	715 (DCM)	230 000	0	11.99	575	0.70	4.81	110
			10	16.93	579	0.70	6.84	
83	665 (DCM)	220 000	0	7.2	621	0.70	3.21	80
			3	12.6	652	0.70	5.75	
84	666 (DCM)	300 000	0	9.21	634	0.71	4.12	80
			3	13.8	657	0.71	6.42	
85	679 (DCM)	240 000	0	5.3	616	0.69	2.25	80
			3	8.98	643	0.70	4.05	
86	681 (DCM)	350 000	0	8.3	591	0.69	3.38	80
			3	12.1	633	0.70	5.37	

Moreover, comparison between **70** and **71** gives a further confirmation about the key-role of the in-plane alkyl chain on the suppression of the charge recombination of the injected electron and the oxidized electrolyte. Even if both dyes have comparable surface coverage, the presence of two alkyl chains in **71** guarantee a better charge recombination suppression resulting in higher V_{OC} and thus in PCE (Fig. 17).

Beside to the effect due to the in-plane hexyl group, when the same indoline unit far from the TiO_2 is modified with out-of-plane branching alkyl chains, squaraines, like **72**-**74**, achieved outstanding efficiencies: sensitizer **72** outperformed all the high-efficiency squaraine-based DSSCs with an impressive J_{SC} of 19.82 mA/cm^2, V_{OC} of 660 mV and efficiency of 9.0%.[106] Even in the case of the out-of-plane alkyl chains, dyes with bulky groups too near to the anchoring site has a lower the dye-loading on TiO_2 (Fig. 17). The record efficiency achieved by **72** is mainly due to the outstanding ability of the out-of-plane alkyl chains in the suppression of the charge recombination, allowing both higher J_{SC} and V_{OC}.

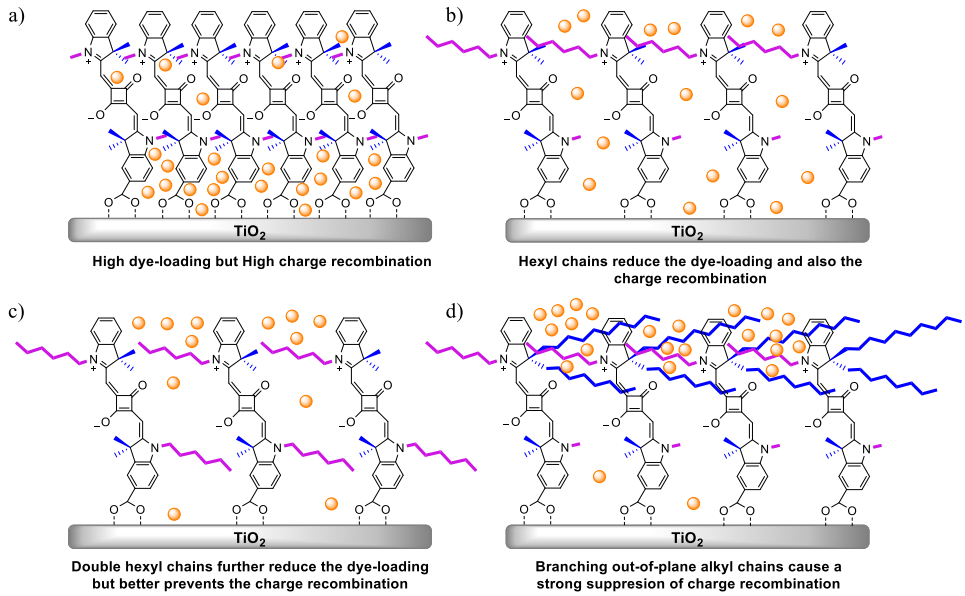

Figure 17 – Diagrammatic representation of monolayer formation with dyes **68** (a), **69** (b), **71** (c) and **72** (d) on the TiO_2 surface. Orange balls represents oxidized electrolyte, in purple the in-plane alkyl chains while in blue the out-of-plane ones.

Starting from these outstanding results, the Nithyanandhan's group further investigate the effect of out-of-plane alkyl chain on the DSSCs efficiency. After studied the effect of the position on the device's performance, Singh *et al.* investigated: (i) the effect of different length out-of-plane alkyl chains in dyes **75**-**77** and (ii) the performance's variations compared to the length modification of both in-plane and out-of-plane groups in dyes **78**-**80** (Fig. 15).[108] Photophysical properties of **75**-**80** are substantially the same than dyes **68**-**74** with absorptions centered roughly between 640-650 nm in DCM. Moreover, same behaviors on TiO_2 surface of the series **68**-**74** were noticed even for squaraines **75**-**80**.

The electrochemical properties of squaraines **75**-**80** on the TiO_2 surface indicate that self-hopping of charges can be controlled systematically by varying the out-of-plane chain lengths that is away from the TiO_2 surface. Such an observation helps in increasing the DSSCs performance by (i) effective charge injection from the self-assembled squaraine dyes and (ii) effectively passivating the surface of TiO_2, which helps in avoiding the charge recombination process.[108] Squaraine **75** having shorter both out-of-plane and in-plane alkyl chains shows an a PCE of 4.9% with a V_{OC} of 696 mV, whereas dye **78** exhibits a PCE of 7.1% with V_{OC} of 715 mV, with CDCA. However, the key role of the in-plane alkyl chain in this type of squaraines emerged by the investigation of dye **79** that has an efficiency of 5.17% due to the low V_{OC} of 671 mV. The comparison of all the performances of the series **68**-**80** demonstrated the presence of a correlation between the both in-plane and out-of-plane alkyl chains length in the observed open circuit voltage, as figured out in Fig. 18.

To resume, both in-plane and out-of-plane alkyl chains are fundamental in the structures of squaraines-based sensitizers for high efficiency DSSCs because they allow to reduce the charge recombination and they control the aggregation of the dye on the TiO_2 surface.[97,98,106,109] However, it was demonstrated that the achievement of high efficiency depends from a carefully optimization of the length of the in-plane alkyl chain in relationship with the length of the out-of-plane ones and also in relationship with the amount of CDCA used.[106,109]

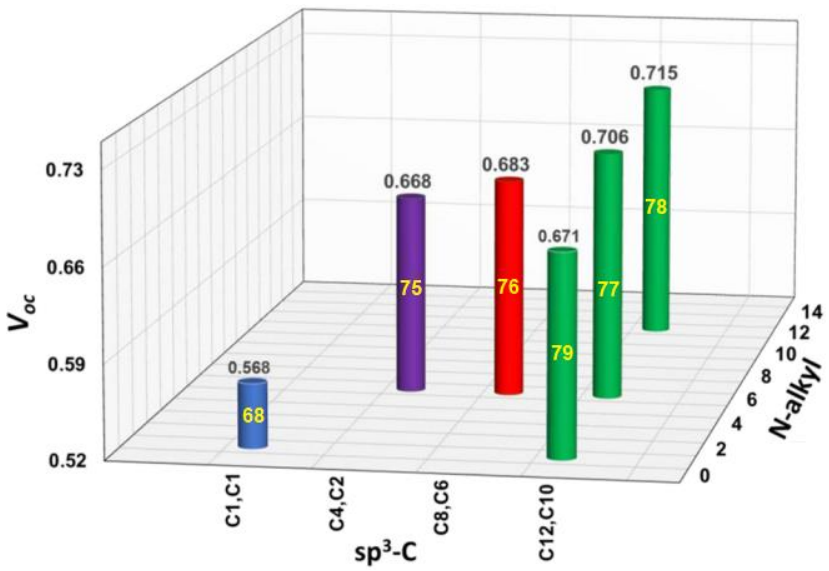

Figure 18 – Three-dimensional V_{OC} plot of squaraines decorated with different length out-of-plane alkyl chains (data obtained without CDCA).[109]

After the investigation of the key-roles of the two types of alkyl chains, new squaraines have been developed to study the relationship between the out-of-plane alkyl chains and the other structural modifications such as the squaric-core functionalization, the insertion of a π-bridge and the π-conjugated extended lateral units (Fig. 19).[80,109] In squaraines **81**-**82** the effect of both squaric-core functionalization by the dicyanovinyl group and the insertion of thiophene-based π-bridge was studied. The two dyes structures differ only for the anchoring moiety, a carboxylic acid in **81** and a cyanoacrylic acid in **82**, respectively. They exhibit a maximum absorption beyond 700 nm and the second lower intense absorption band between 400-500 nm cause by the dicyanovinyl core-functionalization. In devices, squaraines **81**-**82** achieved efficiencies near to 7% but their performance was limited due to non-optimal V_{OC} values around 570 mV. The low V_{OC} achieved are probably ascribable to the intrinsic structure of these squaraines.[109]

In the other series (**83**-**86**), the fused fluorenylindolenine lateral unit was exploited both to shift the absorption toward the NIR and to provide another sp^3

carbon atom where to insert additional out-of-plane alkyl chains.[80] Using three equivalents of CDCA as co-adsorbent, squaraines **83**-**86** achieved efficiencies from 4% up to the 6.4% of **84**. The lower performances than the other dyes decorated with the out-of-plane chains are mainly due to the higher surface coverage of these squaraines: while usually other ones (**68**-**82**) have an average dye-loading of 2-2.5·10^{-7} mol/cm^2, dyes **83**-**86** have values below 9·10^{-8} mol/cm^2.[80] A lower amount of dye heavily affects photocurrent density resulting in low PCEs compared to the outstanding results over 7% exhibit by the other squaraines with the out-of-plane alkyl chains.

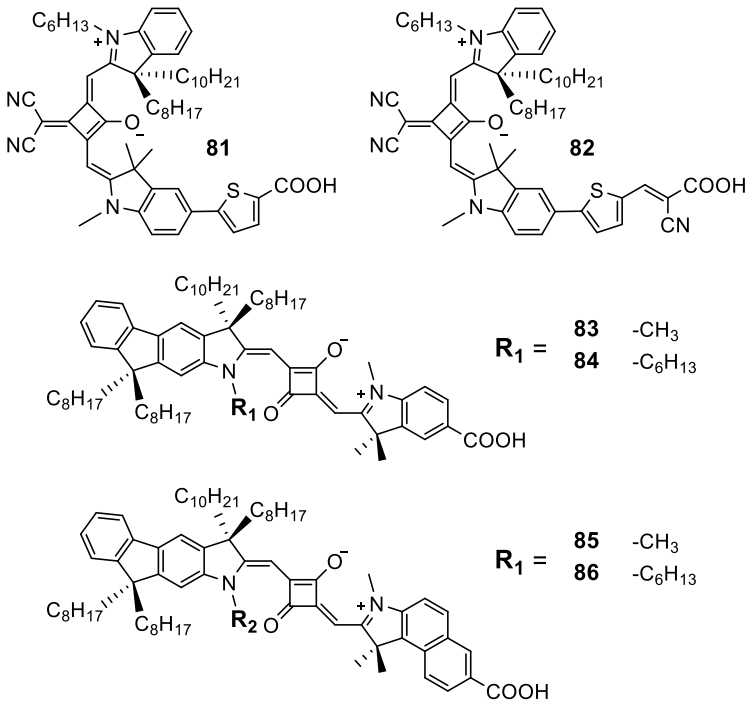

Figure 19 – Squaraine dyes with out-of-plane alkyl chains on the indolenine core and other structural modifications (core-functionalized, π-bridges, extended lateral unit).

Beside to the main strategies reported in this paragraph, many other structural modifications have been investigated to enhance the performance of squaraine-based DSSCs. Regarding the anchoring groups, it has been investigated the effect on the electron injection of the placement of the carboxylic group as terminal group in the in-plane alkyl chain.[110-112] Compared to classical squaraines

discussed so far, the dyes with no-conjugate anchoring groups doesn't achieve good performance mainly due to the too low electron injection cause by the poor electron transfer through the non-conjugated part of the dye's structure.[82] In addition, it has been studied the relationship between the DSSCs' efficiency and the position of the anchoring group on the indolenine lateral unit.[113] It has been demonstrated how the placement in different site on the indolenine ring sharply change the surface coverage of the dyes influencing the dye loading and thus the DSSCs' performance. Another interesting structural modification has been studied for the synthesis of amphiphilic squaraines able to perform with both organic-based and aqueous-based electrolytes.[114] However, all these structural modifications didn't lead to relevant improvement in squaraines-based DSSCs' efficiency.

In this paragraph a comprehensive revision of the state-of-art of the squaraine dyes in DSSCs was reported. The analysis demonstrates how between all the structural modification discussed so far, the modulation of the in-plane and the out-of-plane alkyl chains is surely the most effective to improve the DSSCs performance. This strategy has been exploited in our research to developed new squaraine-based sensitizers for NIR-DSSC application that will be discussed in Chapter 3.

1.1.2. Cyanine

Cyanines are a class of organic functional dyes characterized by a chemical structure in which two nitrogen atoms are linked through a single or multiple methine group to form a delocalized system containing an odd number of atoms. Cyanines are generally named according to the length of the chain between the two nitrogen atoms. Dyes with one, three, five and seven methine units are called (i) monomethine, (ii) trimethine (CY3), (iii) pentamethine (CY5), and (iv) heptamethine (CY7), respectively (Fig. 20a). In addition, a further classification is commonly reported based on the chemical structure of the groups bearing the nitrogen atoms (Fig. 20b). Cyanines without any terminal heterocyclic groups are

named streptocyanines, those with only one terminal heterocycle are hemicyanines and, those with two heterocycles at the chain edges are called closed chain cyanines.[115,116]

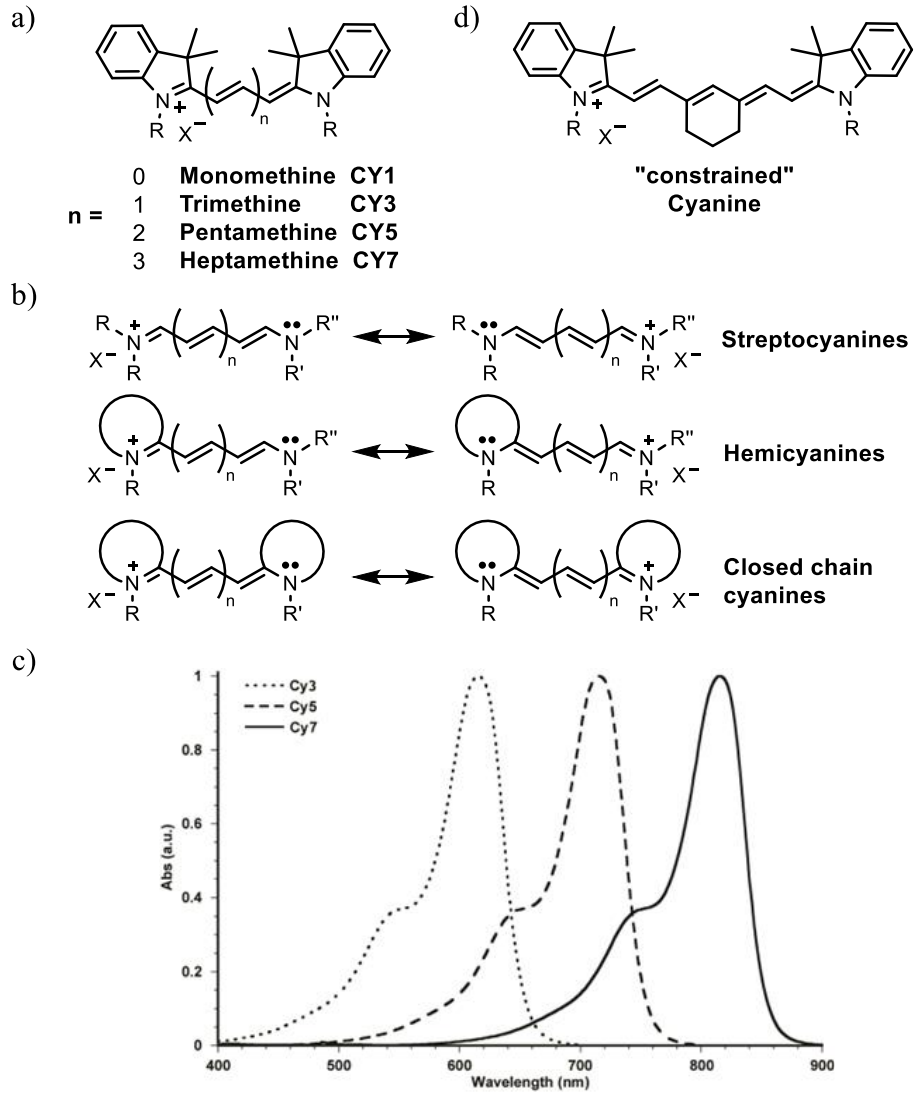

Figure 20 – a) General structure of different length cyanines. b) Schematic representation of the different cyanines as a function of the terminal groups. c) Bathochromic shift of the absorption spectra of cyanines by extending the length of the methine bridge from tri-, to penta- and finally hepta- CYs. d) General structure of constrained cyanines.[58]

The overall structure is fully conjugated with the π electrons delocalized along the whole molecular backbone.[58,117-120] By a structural point of view, the

conjugated carbon bridge plays a key role on the photophysical properties of cyanines leading to a bathochromic shift of around 100 nm upon each addition of a methylene unit (Fig. 20c).[118,120] Cyanines can thus cover a large part of the visible spectra by simply tuning the length of the polymethine bridge. This strategy allows to prepare CY7s with a strong absorption beyond 800 nm and with outstanding photophysical properties that could be suitable to prepare NIR-DSSCs. However, elongation of the conjugated polymethine bridge is detrimental for the stability of cyanines. The presence of more insaturations leads to a lower chemical stability and higher trend to the *cis-trans* photoisomerization processes.[118] For this reason, CY7 are generally decorated with a constrained polymethine bridge by the introduction of cycloalkenyl structure able to improve the chemical stability as well as to reduce the photoisomerization process on the insaturations (Fig. 20b).[120] In addition, the variation of the cycloalkenyl structure may be exploited to further tune the absorption of CY7s varying between cyclopentenyl, cyclohexenyl and cycloheptenyl.[121] The peculiar tunability of the absorption along with the remarkable molar extinction coefficients between 1.5-3.0·10^5 M^{-1} cm^{-1} made cyanines one of the most explored class of chromophores for various applications among which there are the DSSCs.[46,58,122-127]

The cyanines were introduced as sensitizers in DSSCs for the first time in 2001 when a detailed study about the adsorption on nanocrystalline TiO_2 of various di-carboxylated CYs was reported. The study has demonstrated that combinations of cyanine dyes could be used to sensitize solar cells over the entire visible spectrum.[128] For these reasons, all the first research works on cyanines as sensitizers in DSSCs were focused on the application of CY3 and CY5 standalone or in co-adsorption with each other to achieve a final device with a panchromatic absorption. The first ever DSSC based on cyanine dyes has been developed in 2003 by the Arakawa group.[129] Cyanines **87**-**89** (Fig. 21) were tested stand alone and in co-adsorption with each other. They have a symmetrical structure with carboxyindolenine lateral units and all in-plane and out-of-plane alkyl chains are methyl.

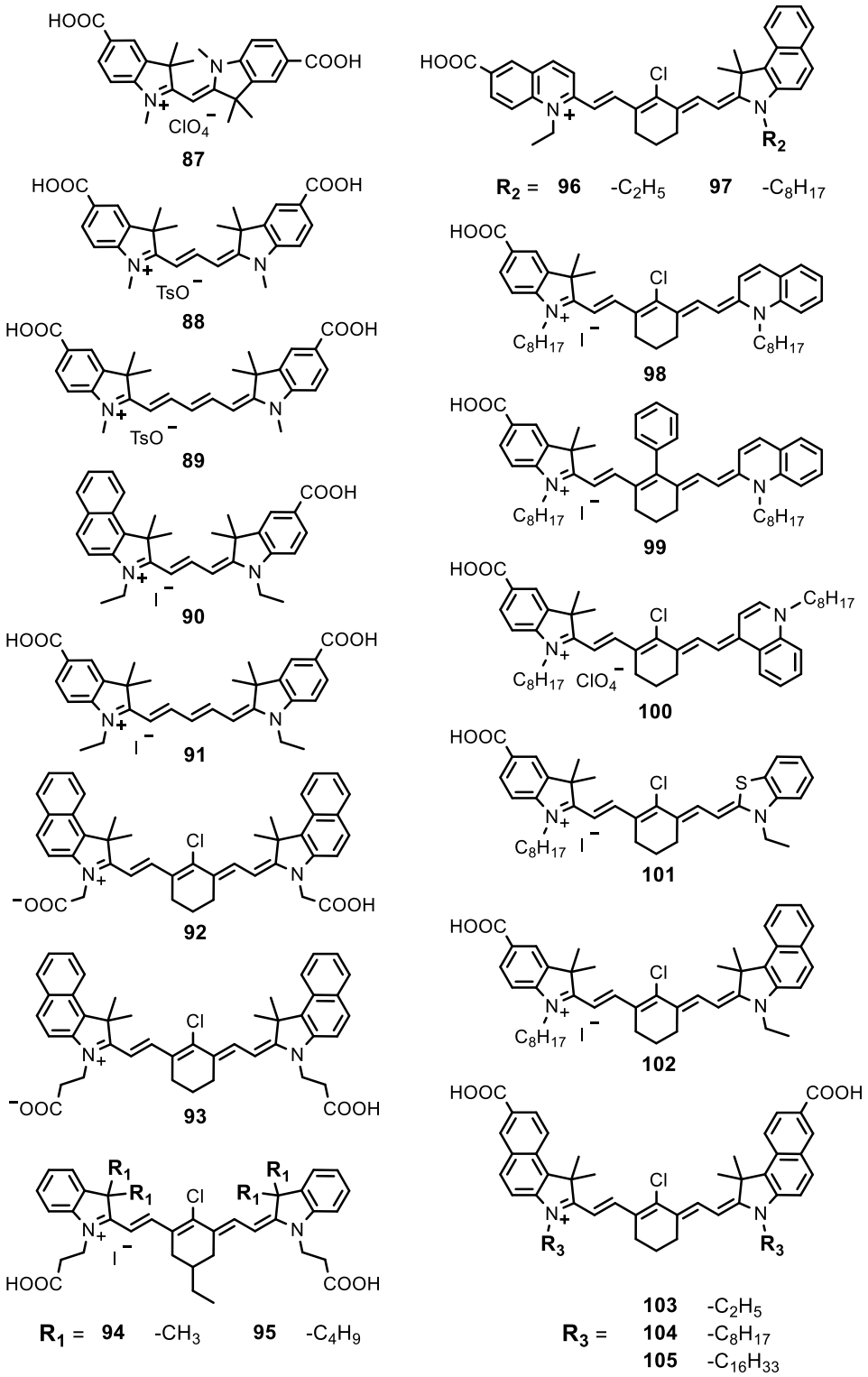

Figure 21 – Cyanines as sensitizer in DSSCs.

As mentioned before, the elongation of the polymethine bridge cause a 100 nm bathochromic shift as well demonstrated by the maximum absorptions of **87**-**89** (Tab. 6). Devices based on **87**-**89** without CDCA achieved efficiencies of 0.6%, 1.5% and 1.2%, respectively while for dye **88**-**89** with CDCA it has been founded an improvement of the performance reaching 2.5% and 1.5% respectively. The very low efficiency of **87** in mainly due to its worst photophysical properties that resulting in a low photocurrent density; the lower performance of **89** than **88** depends by different reasons, contrarily. The comparison of the redox potentials of **87**-**89** demonstrated as the increase of the methine chain length cause a detrimental shift of both HOMO and LUMO levels resulting in a decrease of the driving force of both the oxidized-dye regeneration process and the electron injection one.[129] In addition, it was reported the co-sensitization of both three dyes in presence of 1 equivalent of CDCA led to a record PCE of 2.6% for a DSSC based on cyanine sensitizers.

A further improvement in PCE was achieved by changing the cyanine structure from symmetrical to asymmetrical one. In CY3 **90** the non-anchoring lateral unit is a more π-conjugated benzoindolenine unit while on the other anchoring side there is a classic carboxyindolenine unit. Compared to CY3 **88**, dye **90** has a slightly red-shifted absorption due to the benzoindolenine unit with absorption maximum at 571 nm. However, the greater difference between dyes **88** and **90** is in the photovoltaic performance: the asymmetrical CY3 **90** guarantees a higher electron injection due to its intrinsic push-pull structure leading to a better efficiency of 2.9%. Even in this case, a further improvement in terms of performance was achieved by the co-sensitization of **90** with a longer pentamethine cyanine **91**, achieving the 3.4% with a dye-loading ratio **90**/**91** of 3/1 equivalents.[130]

The higher efficiencies achieved by the co-sensitization of the two or more cyanine dyes leads the development of a new type of multi-chromophore system in which another chromogenic moiety is attached on the cyanine structure by a π-spacer. The strategy allows the synthesis of dyes with broad absorption bands

able to cover the whole visible spectrum and thus to mime the results obtained by the co-sensitization with two or more dyes. Following this strategy, different chromogenic moiety like naphthalene mono-imide (NMI),[131-133] triphenylamine (TPA),[134-135] fluoranthene,[136] and perylene diimide (PDI)[137] were investigate in DSSCs. However, all the cyanines CY3 and CY5 discussed so far have not suitable photophysical properties for our purpose.

Table 6 – Photovoltaic performance and photophysical properties of cyanines in DSSCs.

Dye	λ_{max} (solvent) [nm]	ε [M^{-1} cm^{-1}]	CDCA [eq.]	J_{SC} [mA/cm^2]	V_{OC} [mV]	FF	PCE [%]	Ref.
87	443 (EtOH)	-	0	2.0	520	0.66	0.6	129
88	555 (EtOH)	-	0	5.1	480	0.61	1.5	129
			1	6.9	560	0.64	2.5	
89	660 (EtOH)	-	0	4.7	390	0.62	1.2	129
			1	6.5	420	0.56	1.5	
90	571 (EtOH)	101 000	0	5.5	470	0.46	2.9	130
91	651 (EtOH)	213 000	0	3.85	390	0.45	1.3	130
92	822 (EtOH)	146 000	0	2.57	310	0.63	0.5	138
			100	5.64	340	0.57	1.1	
			≈ 300	8.85	450	0.58	2.3	
93	824 (EtOH)	146 000	≈ 14	1.49	305	0.52	0.24	139
			≈ 140	2.51	375	0.49	0.46	
94	787 (EtOH)	263 000	0	0.12	380	0.63	0.03	140
			10	1.59	450	0.68	0.49	
95	780 (EtOH)	280 000	0	1.20	460	0.78	0.43	140
			2	3.34	490	0.76	1.23	
99	643 (DCM)	320 000	-	3.22	480	0.78	1.22	141
103	828 (EtOH:DMSO 9:1)	118 000	500	7.1	328	0.62	1.5	61
104	831 (EtOH:DMSO 9:1)	136 000	500	10.1	336	0.55	1.9	61
105	834 (EtOH:DMSO 9:1)	154 000	500	12.0	343	0.58	2.5	61
				11.5[a]	402[a]	0.58[a]	2.6[a]	
				11.2[b]	422[b]	0.65[b]	3.1[b]	

[a] Sensitization at 4 °C, [b] Sensitization at -20 °C

The first pioneer study of a NIR-sensitizer based on heptamethine cyanine was reported by the Arakawa *et al.* in 2009 with the investigation of symmetrical CY7 **92**.[138] Cyanine **92** has a strong absorption in the NIR at 822 nm with a molar

extinction coefficient of 146000 M^{-1} cm^{-1}. Compared to the cyanines discussed so far, dye **92** has the anchoring groups on the in-plane alkyl chains. In terms of efficiency, **92** achieves 2.3% with a J_{SC} of 8.85 $mAcm^{-2}$ in presence of ca. 300 eq. of CDCA. Interestingly, in presence of lower amount of CDCA or in completely absence of it, the efficiency decreases due to the dramatically drop-down of the photocurrent density values (Tab. 6). This behaviour confirms the strong tendency of cyanine dyes to the self-aggregation on the TiO_2 surface and the key-role of CDCA to contrast it.[60,138] A further confirmation about the key-role of the CDCA was reported by ultrafast laser spectroscopy study led by Ziółek *et al.* on cyanine **93**. Even if the final performance achieved has been lower, they demonstrated how the increase of the CDCA alongside the increase of the concentration of lithium iodide in the electrolyte solution led to sharply improvement of the device performance reaching an efficiency of 0.46%.[139]

In cyanines **94** and **95** the structure has been decorated with out-of-plane butyl chains as well as with an ethyl chain on the cycloalkenyl moiety of the constrained polymethine bridge to reduce the self-aggregation. In this study, the TiO_2 semiconductor was replaced with porous ZnO achieving 1.23% of efficiency for cyanine **95** decorated with out-of-plane butyl chains.[140]

All the heptamethine cyanine discussed so far have a symmetrical structure with carboxylic anchoring group located on the in-plane alkyl chains. Nüesch *et al.* synthetized a series of asymmetrical CY7 (**96**-**102**) in which a carboxylic anchoring group is located on quinaldine or indolenine lateral unit while on the other side of the structure different type of lateral units such as benzoindolenine, quinaldine, lepidine and benzothiazole were studied.[141] A comparative analysis between cyanines **96**-**102** and their symmetrical counterparts demonstrated how the symmetrical ones, similarly to squaraines, offers a red-shifted absorption and higher molar extinction coefficients. In addition, it has been demonstrated how the substitution of the chlorine atom on the polymethine bridge with an electron-donor phenyl group cause a sharply modification of the HOMO and LUMO energy levels. Cyanine **99** has a larger bandgap than **98** and their HOMO and LUMO levels

have higher and lower energy, respectively. The energetic levels exhibited by **99** are more suitable to guarantee better electron injection as well as dye-regeneration processes; for this reason, cyanine **99** has been applied as sensitizer in the first example of almost colorless and transparent NIR-DSSC achieving a PCE of 1.22% and a transmittance > 50% between 500-1000 nm (Fig. 22).[141]

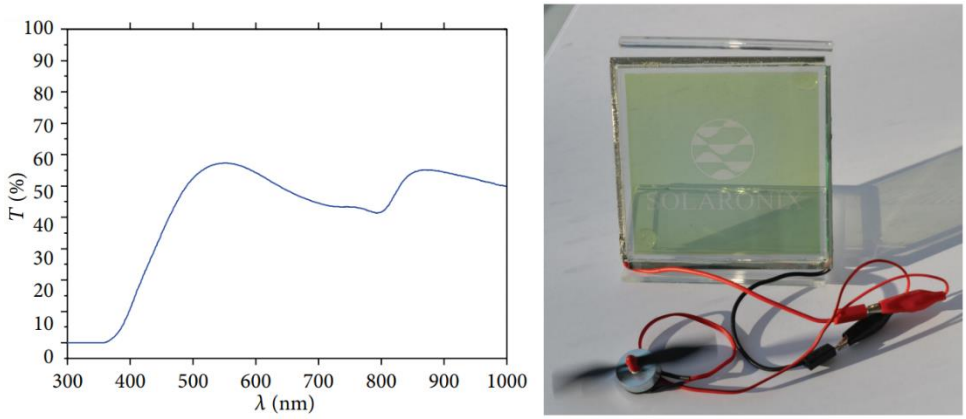

Figure 22 – (left) Transmission of large-area NIR-DSSC with **95**. (right) Photograph of working large-area NIR-DSSC sensitized with **95**.[141]

An outstanding improvement in performance of NIR-DSSC has been achieved with a series of heptamethine cyanines **103**-**105** reported by Sauvage *et al.* in their pivotal work on transparent and colorless NIR-DSSCs (Fig. 21).[61] In this work a series of symmetrical cyanines decorated with carboxy-benzoindolenine lateral units has been investigated to understand the relationship between the in-plane alkyl chain length and the photovoltaic performance. In addition, a carefully optimization of all the different components of a DSSC was made toward the realization of a fully transparent and colorless NIR-DSSC. Cyanines **103**-**105** has been decorated with ethyl, octyl and hexadecyl in-plane alkyl chains, respectively. First of all, it has been noticed that different chains length slightly influences the absorption properties: longer alkyl chains lead to a more red-shifted absorption and increase the molar extinction coefficient. In addition, it has been demonstrated that different alkyl chains length doesn't Influence the energy positions of both HOMO and LUMO. To avoid the well-known strong self-

aggregation of cyanines, 500 eq. of CDCA have been used as co-adsorbent with dyes **103**-**105** in the sensitization process reaching PCEs of 1.5%, 1.9% and 2.5%, respectively. The PCE achieved by **105** without any optimization was double than the previous record of 1.22% achieved by **95**.[141] However, this result has been further improved by the optimization of the dye-loading process. The sensitization temperature modifies dye packing on the TiO_2 surface as already demonstrated on ruthenium-based sensitizers: even in this case the different temperature sensitization causes a variation of the photovoltaic parameters of **105**.[142] In particular, lower temperature slightly reduces the photocurrent density while considerably improves both open circuit voltage and fill factor. The sensitization of **105** at -20 °C for 7 days allows to achieve the outstanding record efficiency of 3.1%. Beside to the photovoltaic performance, Sauvage *et al.* achieved an impressive maximum AVT of 76%, very close to the characteristic AVT of a standard double-glazed window which is 78% (Fig. 23).[143]

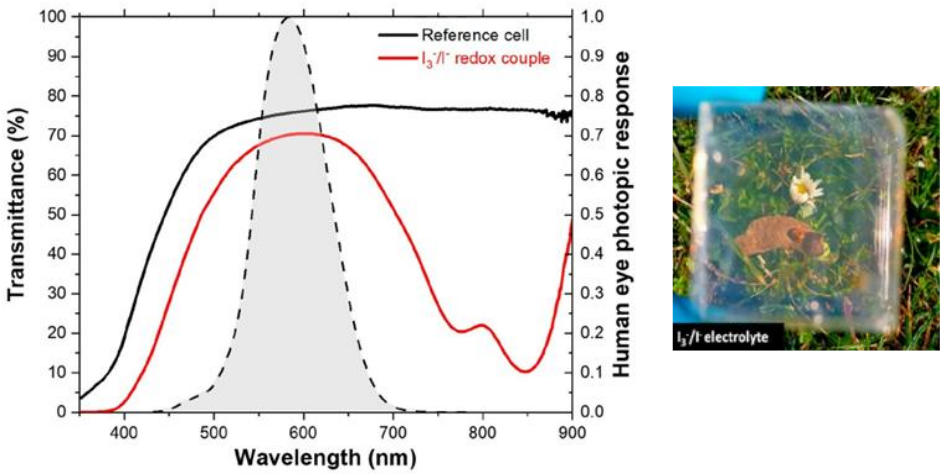

Figure 23 – (left) Comparison of total cell of a reference cell without dye and with an optimized electrolyte based on I_3^-/I^- redox couple (black curve) and **105** based devices constituted by an optimized electrolyte formulation based on the I_3^-/I^- redox couple (red curve). Black dashed line represents the photopic response of the human eye. (right) Photograph of colorless and transparent NIR-DSSC with **105**.[61]

As mentioned before, the stability is one of the main weaknesses of polymethine dyes and in particular of the cyanines. Recently, for the first time

Odobel *et al.* demonstrated the potentialities of a new class of cyanine-based sensitizers for NIR-DSSC with higher stability: the pyrrolopyrrole cyanines (**106**-**107**) (Fig. 24a).[144] Pyrrolopyrrole cyanines (PPCYs) is a class of NIR dyes first reported by Daltrozzo *et al.*, [145-147] that over the years has mainly been used for biological applications such as optical and photoacoustic imaging.[148-151] As cyanines, PPCYs display intense and narrow absorption bands located in the NIR part of the spectrum (between 700-800 nm depending on the substituents) and they exhibit usually high fluorescence quantum yields around 40-60%.[146-147] Compare to the CY7s, dyes **106**-**107** display a blue-shifted absorption at 710 and 758 nm respectively (Tab. 7).

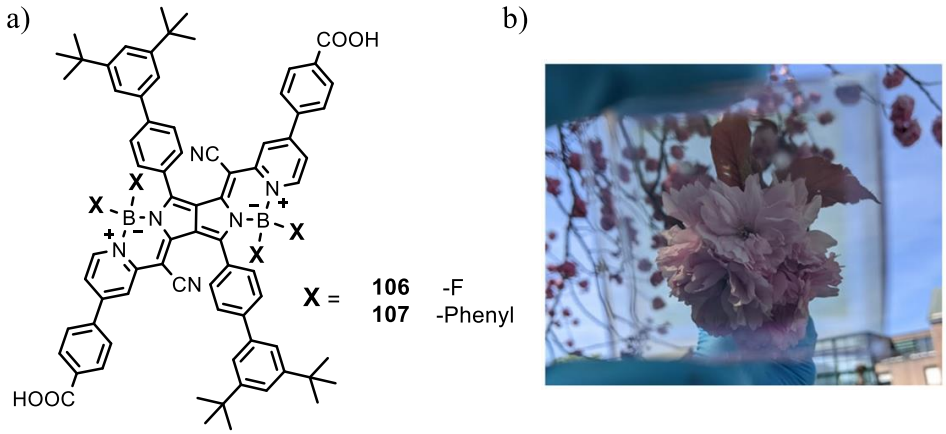

Figure 24 – a) Pyrrolopyrrole cyanines investigated by Odobel *et al.* b) Photograph of colorless and transparent NIR-DSSC with **107**.[144]

The planarity of the pyrrolopyrrole core obviously magnify the self-aggregation of this class of sensitizers. For this reason, usually they are decorated with bulky groups able to hamper the detrimental self-aggregation. The relevance of bulky groups is demonstrated by the sharply difference of photovoltaic performance obtained for dyes **106** and **107** (Tab. 7). Dye **107** decorated with bulky phenyl groups on the boron atoms achieved a PCE of 3.2% without CDCA while dye **106** achieved only the 1.2% even in the presence of 500 eq. of CDCA.[144] The carefully optimization of sensitization process of **107** has been allowed to

achieve the outstanding efficiency of 3.9%, the higher between the dyes absorbing beyond 750 nm. In addition, the removal of the scattering-layer on the photoanode has been allowed to obtain a completely transparent and colorless NIR-DSSC with a PCE of 2.5% and an AVT of 75% (Fig. 24b).[144]

Table 7 – Photovoltaic performance and photophysical properties of pyrrolopyrrole dyes investigated by Odobel *et al.*

Dye	λ_{max} (solvent) [nm]	ε [M^{-1} cm^{-1}]	CDCA [eq.]	J_{SC} [mA/cm^2]	V_{OC} [mV]	FF	PCE [%]	Ref.
106	710 (DCM)	55 000	500	5.18	333	0.62	1.2	144
			0	15.7	348	0.57	3.2	
107	758 (DCM)	138 000	50	16.5	394	0.58	3.9	144
			50	10.9[a]	408[a]	0.56[a]	2.5[a]	

[a] DSSC build without scattering layer

In this paragraph a revision of the state-of-art of cyanine dyes in DSSCs was reported. The analysis demonstrates how between all the cyanines discussed so far, only the heptamethine and the pyrrolopyrrole ones have the optimal photophysical properties for NIR-DSSC application. In addition, the key-role of CDCA in cyanine-based DSSCs to avoid the self-aggregation was demonstrated. Following the outstanding results obtained by cyanine **105**, in Addendum 1 will be briefly discussed the synthesis work made to obtain a heptamethine cyanine able to overcome the limits exhibited by dye **105**.

1.2. Phthalocyanine dyes

Phthalocyanines (PCs) are thermally and chemically stable 2D tetrapyrrolic macroheterocycles containing 18 delocalized π-electrons well-known for their strong absorption close to the NIR region of the solar spectrum (Fig. 25). Phthalocyanines exhibit peculiar absorption spectra with the Soret- and the Q-band.[152,153] In particular, compared to the other tetrapyrrolic structures like porphyrins, phthalocyanines display very intense Q-bands, with high molar extinction coefficients up to $3.0 \cdot 10^5$ M^{-1} cm^{-1} make them interesting candidates

as NIR-sensitizers for NIR-DSSCs. In addition, the Q-band can be single or split depending on the symmetry of the macrocycle structure and the maximum as well as the bandwidth of absorption can be tune by the incorporation of different substituents.[152] Obviously, the high planarity of these conjugated aromatic structure causes the formation of J- or H-aggregates by strong π-π supramolecular interactions.[154] The physical and optical properties of phthalocyanines make them interesting for many applications such as organic electronics,[155,156] OSCs,[41,157] catalysis,[158] PDT,[159] and obviously as sensitizers in DSSCs.[40,160-162]

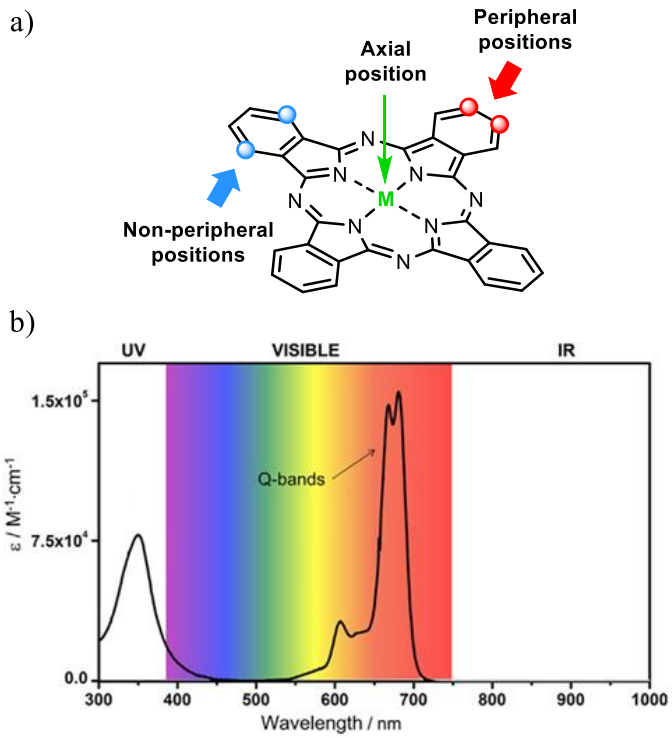

Figure 25 – a) General structure of phthalocyanine. b) Typical absorption spectrum of phthalocyanine dyes.[40]

Phthalocyanines hold several interesting properties to be suitable sensitizers in DSSCs for their photophysical properties, as well as their thermal and chemical stability and the relatively easy tunability of their redox properties. Several structural-modification strategies can be exploited to improve the photovoltaic

parameters: (i) the optimization of peripheral and (ii) non-peripheral substitutions patterns, (iii) the modification of the anchoring group, (iv) the insertion of different π-spacer between the macrocycle and the anchoring site, (v) the investigation of different metal and (vi) the functionalization of the axial sites (Fig. 25).

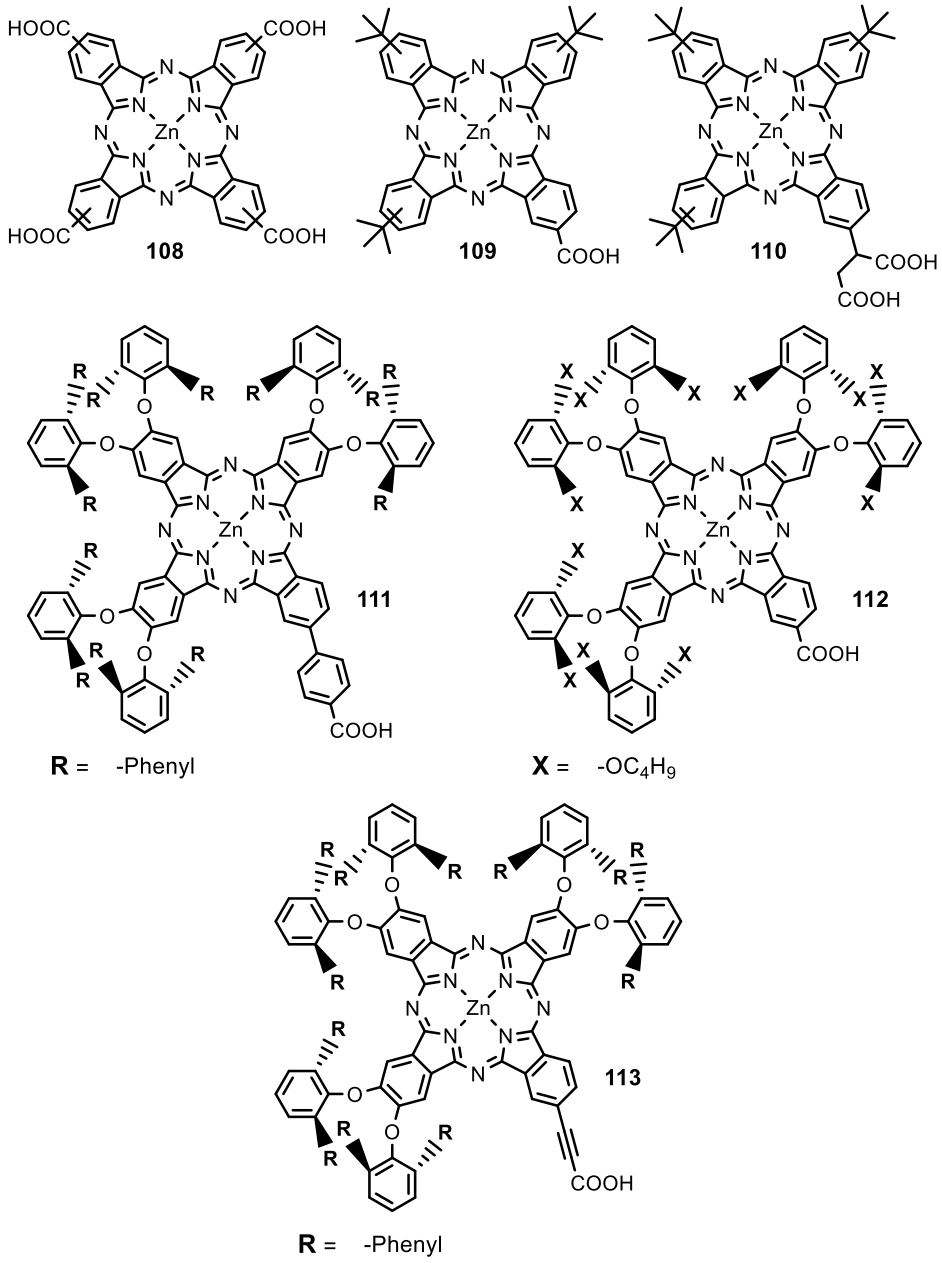

Figure 26 – Most important phthalocyanine dyes in DSSCs.

In this paragraph, will be reported a briefly survey of the evolution of the phthalocyanines' structures as sensitizers in DSSCs, highlighting the most important progress made towards the current efficiency record of 6.4%.[163]

Complete surveys on the structural evolution and the structure-performance relationship of the phthalocyanine-based dyes in DSSCs can be found in literature.[40,160-162]

The phthalocyanines were introduced as sensitizers in DSSCs for the first time in 1995 when a detailed study about the adsorption on nanocrystalline TiO_2 of tetra-carboxylated phthalocyanine **108** was reported by Shen *et al.* (Fig. 26).[164] The sensitization of the TiO_2 with **108** led to IPCE of 4% at 690 nm. Even if very poor result has been achieved, the phthalocyanine dye-uptake on the semiconductor surface has been demonstrated. Starting from this result, the interest of phthalocyanine dyes in DSSCs rapidly raise and in 1999, Nazeeruddin *et al.* demonstrated the first ever phthalocyanine-based DSSC over 1% of efficiency using dye **108** (Tab. 8).

Table 8 – Photovoltaic performance and photophysical properties of most important phthalocyanine dyes in DSSCs.

Dye	λ_{max} (solvent) [nm]	ε [M^{-1} cm^{-1}]	J_{SC} [mA/cm^2]	V_{OC} [mV]	FF	PCE [%]	Ref.
108	686 (EtOH)	33 000	5.5	416	0.45	1.0	164
109	680 (THF)	160 000	7.6	617	0.75	3.5	166
110	692 (EtOH)	191 000	6.5	635	0.73	3.05	167
111	684 (THF)	81 300	10.4	630	0.70	4.6	190
112	695 (Toluene)	93 300	15.1	600	0.71	6.4	163
113	698 (THF)	89 100	12.3	638	0.70	5.5	194

Beside to the record efficiency, the Nazeeruddin *et al.* pioneer work investigated the differences between several symmetrically and non-symmetrically substituted phthalocyanines. The results highlighted the advantages of developing unsymmetrically and peripheral-substituted phthalocyanines: (i) the asymmetry leads to a "push-pull" structure that improves

the directionality of intramolecular charge transfer processes and injection into TiO_2 surface, while (ii) the peripheral-substituents, especially if bulky, improves the solubility of the dye and decrease the detrimental strong self-aggregation of phthalocyanines.[165] Following these concepts, the asymmetrical phthalocyanine **109** and **110** decorated with peripheral *tert*-butyl substituents led to a huge improvement achieving efficiencies above 3% with an IPCE over 75% at 700 nm.[166,167] However, **109** and **110** are still affected by strong self-aggregation, despite the presence of the *tert*-butyl group, which limits the further improvement of performances since the aggregation drastically drop-down the electron injection efficiency. As already displayed for polymethine dyes, the first strategy to effectively decrease the self-aggregation issue in phthalocyanine dyes was the use of CDCA as co-adsorbent. However, in phthalocyanine sensitizers the beneficial effect of CDCA is achieved for ratio dye/CDCA higher (1:100 – 1:2000) compared for example to squaraine dyes (1:1 – 1:20).[40] The larger CDCA concentration resulting in very low total amount of dye-molecules that can be chemisorbed on the semiconductor's surface and thus in low photocurrent density. To tackle the self-aggregation issue, over the years several bulky substituents on both peripheral and non-peripheral sites were investigated.[168-189] The breakthrough stemmed by the introduction of the 2,6-diphenylphenoxy bulky groups at the peripheral positions of phthalocyanine **111** (Fig. 26) as reported by Kimura *et al.*[190] The presence of the 2,6-diphenylphenoxy groups completely suppress the self-aggregation of the phthalocyanine and allowing to decrease the necessary amount of CDCA. Dye **111** achieves an outstanding PCE of 4.6%, which is 1% higher compared to the previous PCE record of **110** (3.5%). In addition, it has been demonstrated how the presence of heteroatom donating groups directly linked to the phthalocyanine macrocycle improve both optical and energetic properties. In particular, it causes a further intensification of the "push-pull" effect and a further slight red-shift of the Q-band absorption.[191,192] The intense development of new dyes decorated with a wide library of bulky substituents similar to 2,6-diphenylphenoxy group, led to a constant

improvement in performances over the years so far to reach the current record efficiency of 6.4% with the phthalocyanine **112**.[163] The presence on peripheral sites of 2,6-dibutoxyphenol groups allow to reach a photocurrent density of 15.1 $mAcm^{-2}$, 50% higher than dye **111**.

Beside to the optimization of the peripheral- and non-peripheral substituents, an extensive investigation was also made to optimize the anchoring group and to study the possibility to insert a π-spacer between the main structure and the anchoring site. As previous demonstrated for squaraine dyes, even in phthalocyanine dyes the phosphonic acid group lead to a lower solar conversion efficiency but exhibits stronger binding properties than the carboxylate anchoring group, improving the durability of the DSSCs.[193] More promising results have been achieved by the insertion of π-spacer, instead. Torres *et al.* reported a sterically hindered phthalocyanine **113** with a PCE of 5.5%, having the same structure of **112** except for the presence of an ethynyl spacer. The comparison between the two dyes demonstrated how the ethynyl group improves the push-pull effect allowing a better electron injection and thus higher photocurrent density (Tab. 8).[194] Following the promising results achieved by dye **113**, several π-spacer have been investigated.[170,195-202]

As reported, phthalocyanine-based DSSCs achieve a maximum efficiency near to 6%, by a rational design of the dye's structure, but despite the several major advances and the great number of molecules tailored over the years, the performance remains significantly lower compared to other NIR-dyes like the squaraines. In addition, compared to polymethine dyes, the phthalocyanines exhibit worst photophysical properties alongside an intrinsic lower tunability of own absorption properties. For these reasons, polymethine dyes result more suitable for our purpose to develop a fully transparent and colorless NIR-DSSC.

2. Fully-Transparent Photoanode

In a DSSC, the photoanode is composed by a sensitizer adsorbed on a semi-conductor oxide layer and has the key-role to harvest the incident light, leading

to the formation of a charge separation. In particular, the semiconductor oxide has the fundamental role to transfer the electron charges from the sensitizer to the external circuit. Its features like the chemical composition and the morphology, heavily influence both dye-loading process and charge transfer. To achieve high efficiencies, it's necessary to reduce the amount of the internal energy losses. For this reason, the electronic coupling between the excited states of the dye and the large bandgap semiconductor must be as efficient as possible.[13] In addition, beside to these important features that impact on the device performance, in NIR-DSSCs it's necessary to taking account also of the aesthetic aspects in terms of transparency and coloration. In particular, NIR-DSSC required not only a dye free of absorption bands in the visible range to ensure no coloration features, but it also need a large bandgap semiconductor greater than 3.0 eV and nanocrystals free of aggregates to avoid light scattering accordingly to Mie-scattering theory which would be detrimental for the AVT value.[29,202]

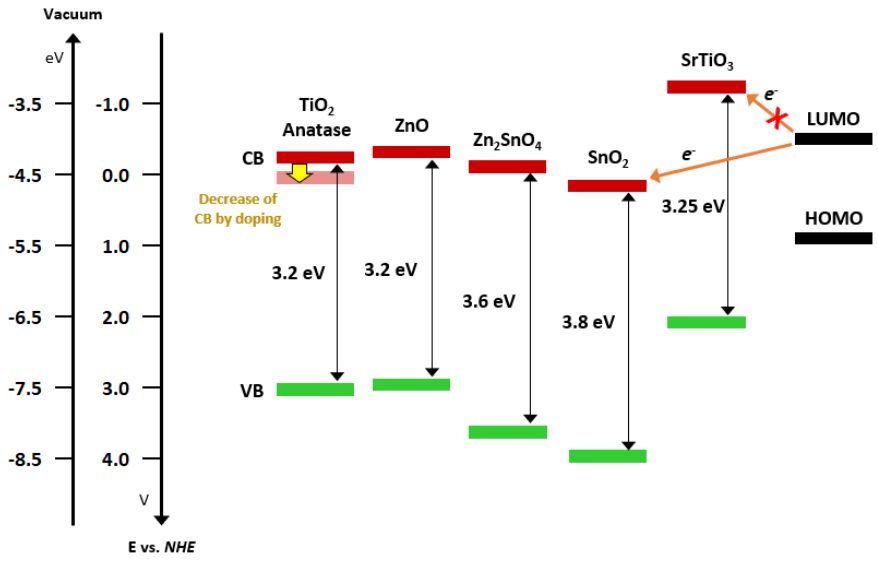

Figure 27 – Valence Band (VB) and Conduction Band (CB) position of different metal-oxide semiconductors used in DSSC, compared with average HOMO and LUMO levels of NIR sensitizers. In addition, the effect of hypervalent cation doping on the TiO_2 CB is depicted.

Typically, the photoanode is based on a mesoporous layer of anatase TiO_2 nanoparticles (NPs) with a thickness of few micrometers. Anatase TiO_2 is well-

known for its high chemical stability, low cost, low toxicity and versatile ways of synthesis.[203-207] In addition, it's characterized by high transparency in the visible and NIR-region due to its large bandgap of 3.2 eV, makes it suitable for NIR-DSSCs (Fig. 27). Since the pivotal work of O'Regan and Grätzel in 1991, the key to the breakthrough for DSSCs was the use of a mesoporous layer.[30] Mesoporous morphology of TiO_2 is fundamental to allow the adsorption of a larger amount of sensitizer, dramatically improving the harvesting of the incident light. In addition, over the years a deeply investigation has been made on the nanostructuration of the mesoporous TiO_2 layer, spanning from random assemblies of nanoparticles to organized arrays of nanotubes and single-crystalline nanorods.[204,208-212] The nanoparticle random assemblies exhibit surface traps through the interconnected small particles, resulting in detrimental charge recombination between electrons and either the oxidized dye molecules or electron-accepting species in the electrolyte during the charge transfer. Contrarily, the organized nanostructures can supply a straightforward pathway for the electron transport, improving the electron mobility and the transfer rate as well as reducing the recombination processes (Fig. 28). However, ordered nanostructures are generally affected by low sensitization due the small specific surface area.[210,213]

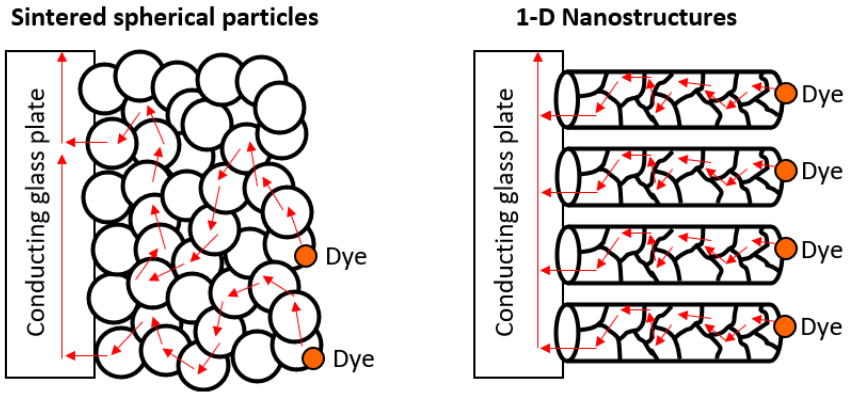

Figure 28 – Schematic of electron diffusion between sintered spherical nanoparticles (left) and one-dimensional (1-D) nanostructures. Electron diffusion spherical nanoparticles is according to random walk model. Though diffusion is in accordance with the random walk in 1-D structures also, the electrons are constrained to move directionally.[214]

Even if anatase TiO_2 is the most explored and efficient semiconductor oxide in DSSCs, its application in NIR-DSSCs may be limited by two main drawbacks: (i) the conduction band of TiO_2 is too close to the LUMO levels of the most NIR sensitizers, strongly limiting the electron injection kinetic (Fig. 27), and (ii) the low electron mobility with values between 0.1-1.0 $cm^2 V^{-1} s^{-1}$.[29,215] While the latter property cannot be easily improved, the former can be widely tune by the carefully doping of the anatase TiO_2 structure.[204,214,216,217] The $3d^0$ electronic configuration of the Ti^{4+} confers a high sensitiveness to impurities and doping that will affect the optoelectronic characteristics of TiO_2. A broad range of dopants has been investigated but not all meet the requirements for NIR-DSSCs applications as the CB varies its position depending on the dopant nature. Consequently, anatase's optical bandgap and electron injection rate can be affected.[29,217] In literature, promising results for NIR-DSSCs are reported with hypervalent cations such as V^{5+}, W^{6+}, Ta^{5+} and Nb^{5+}, able to decrease the CB position of the TiO_2 by few tens mV.[217] Generally, the introduction of hypervalent cation into the anatase crystal structure produces donor levels and shallow traps below the CB, which can favor the electron injection in the particular case where the lack of driving force limits the injection yield. The dopants can be introduced either in substitution of the Ti^{4+} if ionic radii are comparable or can be placed in the interstitial sites, thus generating excess oxygen stoichiometry as charge compensation mechanism.[29] In addition, the doping can be also exploited to tune the transparency of the photoanode as demonstrated by Chandiran *et al.* They demonstrated as the Nb^{5+} doping of anatase TiO_2 is a successful strategy to increase the photoanode transparency by 5-10% as a result of the Burstein-Moss effect.[218]

Beside the investigation of TiO_2 anatase, different alternative semiconductor oxides have been explored such as ZnO,[219-221] SnO_2,[222,223] Nb_2O_5,[224] brookite and the other TiO_2 polymorphs,[225] or ternary metal oxides such as the spinel Zn_2SnO_4,[226,227] or the Perovskite $SrTiO_3$.[228] Between the above-mentioned alternative semiconductor oxides, ZnO has been the first explored due to the very

similar bandgap compared to TiO_2 and for its higher electron mobility of 1-5 $cm^2 V^{-1} s^{-1}$.[229] However, ZnO is affected by rapid corrosion phenomena due to the contact with iodine-based electrolyte, and lower chemical stability under acidic and basic conditions. These issues strongly limit both the stability and the performance of the DSSCs but in perspective, ZnO could become interesting in devices using free-iodine electrolytes.

SnO_2 is another very interesting semiconductor oxide suitable for NIR-DSSC application due to its highest transparency in the visible range compared to the other semiconductor oxides abovementioned. Compared to the anatase, SnO_2 has a more oxidized CB as well as higher bandgap (3.8 eV) than TiO_2 (Fig. 27). The more oxidized CB better fits the LUMO of the most common NIR dyes, not requiring the doping of the semiconductor's structure to decrease the CB as in the case of anatase. In addition, SnO_2 has a very higher electron mobility reaching values up to 100-200 $cm^2 V^{-1} s^{-1}$. However, the efficiency of SnO_2 is affected by fast electron recombination processes with both oxidized redox mediator and sensitizer cation.[230-232] The use of SnO_2 in NIR-DSSCs could be very promising but a carefully optimization of NIR dyes' structure is requested to prevent the fast electron recombination processes.

Intermediate properties between TiO_2 and SnO_2 in terms of CB position and bandgap value is the spinel zinc stannate. The application in classic DSSCs demonstrated as Zn_2SnO_4 is affected by large energy losses due to the inefficient electron injection. However, compared to ZnO it has a higher chemical stability and electron mobility (ca. 10-15 $cm^2 V^{-1} s^{-1}$).[233,234]

The analysis of the different semiconductor oxide investigated in DSSCs has been proved how the main issue of all of them is due to the electron recombination processes that noticeably affect the final efficiency. While the geminate recombination is usually faced up by a careful optimization of sensitizers' structure, the non-geminate recombination processes can be reduced by a surface modification of the nanostructured semiconductor oxide.[29] It has been proved how a sub-nanometer thick laker of wide bandgap material such as

MgO, SiO_2, Al_2O_3, ZrO_2, Ga_2O_3 or $BaCO_3$ can help to increase all the photovoltaic parameters as demonstrated by Naim et. al in association with the cyanine NIR-dyes **105**.[61] The authors observed an improvement of both J_{SC} and V_{OC}, achieving an efficiency of 2.3% with a shell of 0.1 nm of Ga_2O_3 on the TiO_2 layer (PCE of 1.9% was achieved without Ga_2O_3 treatment).

Beside to the investigation of new materials, the manufacturing of the semiconductor oxide layer is a crucial aspect toward highly efficient DSSCs. In addition, the fabrication of the conductive film dramatically influences the devices' aesthetic resulting extremely important to obtain a fully transparent photoanode for NIR-DSSCs. In standard DSSCs, TiO_2 film preparation can have up to four different phases in which they are produced: (i) the compact TiO_2 "under-layer", (ii) the nanocrystalline active layer, (iii) the microcrystalline light-scattering layer and (iv) the compact TiO_2 "over-layer" (Fig. 29).[235]

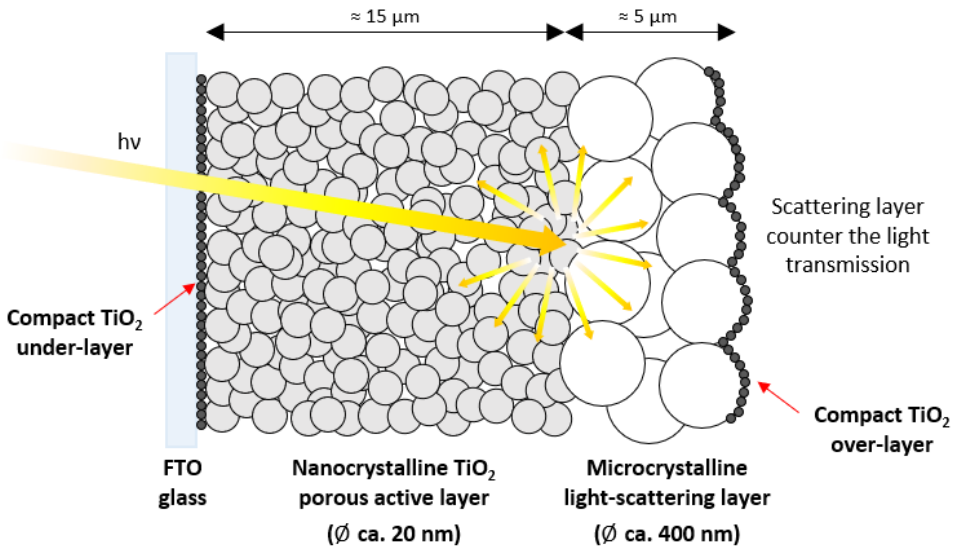

Figure 29 – Schematic representation of photoanode with the four different hierarchical layers. The presence of larger particles (ca. 400 nm) in the light-scattering layer hampers the light-transmission, trapping the scattered light and thus enhancing the probability of the absorption by the sensitizer.

The nano- and the microcrystalline TiO_2 layer are usually prepared by the screen-printing techniques while the two compact TiO_2 layers are prepared by

chemical bath deposition with $TiCl_4$ solution. While it has already been discussed the key-role of the active layer on the devices' PCE, the other ones contribute to improve the efficiency in different ways. The two compact TiO_2 layers are prepared in two precise moments of the photoanode manufacturing procedure, the first one prior to the screen-print of the active layer, and the second one after the preparation of the scattering layer.[236,237] The compact TiO_2 "under-layer" positively influences the photoanode in two manners: (i) enhances the bonding strength between the FTO substrate and the porous-active layer and (ii) blocks the charge recombination between electrons proceed from the FTO and the oxidized species in the electrolyte. Instead, the compact TiO_2 "over-layer" enhance the surface roughness factor of the scattering-layer's TiO_2 particles improving dye adsorption and thus the photocurrent.[237]

The light-scattering layer, also known as photon-trapping layer, was used to improve the photocurrent exploiting the scattering phenomena between the incident light and the larger TiO_2 particles (≈ 400 nm) to reduce the light transmission through the photoanode.[238,239]

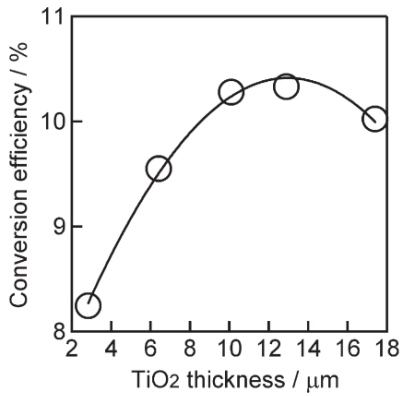

Figure 30 – Photoconversion efficiency as a function of nanocrystalline TiO_2 layer thickness. Layer with too small thickness doesn't allow the adsorption of enough dye's molecules while layer with too large thickness lead to longer pathways for the excited electrons resulting in detrimental enhancement of electron recombination processes.[235]

As previously mentioned, the key-role of the photoanode is to support the sensitizers and transfer the photoexcited electrons toward the conductive FTO

glass. For this reason, the thickness of the photoanode is a crucial factor in the performances of DSSCs. In the pivotal work of Grätzel *et al.*, it has been demonstrated a relationship between the nanocrystalline TiO_2 film thickness and the resulting PCE, finding an optimum thickness of 12-14 μm (Fig. 30).[235,240] However, to obtain a fully colorless and transparent NIR-DSSC with AVT > 70% it's necessary to reduce the global thickness of the photoanode, achieving the best possible compromise between the aesthetic requirements and high efficiencies.

3. Redox couples for NIR-DSSCs

The redox electrolyte is one of the key components of a DSSC and its properties directly influence both the efficiency and the stability of the devices. Generally, the redox electrolyte used in DSSCs can be classified into three main categories: liquid electrolyte, quasi-solid electrolyte and solid-state hole conductors.[241-243] In the electrolyte, the main component is the redox couple that has the function to transfer electrons from the counter electrode to the oxidized dye to regenerate it and thus close the electrochemical circuit. In a conventional DSSC, the ideal redox couple should fulfil several properties like: (i) redox potential close enough to the HOMO energy level of the dye to avoid energy losses and meanwhile to guarantee a sufficient driving force to regenerate the oxidized dye quantitatively, (ii) ability to regenerate the oxidized dye with low reorganization energy, (iii) fast electron transfer rate at the counter electrode, (iv) fast mass transport through the electrolyte, (v) slow recombination process between the oxidized form of the redox couple and the injected electron from the photoanode, (vi) high thermal, photo- and chemical stability, (vii) high solubility in organic solvents, (viii) low molar extinction coefficient (< 1000 M^{-1} cm^{-1}) to avoid parasitic absorption of the incident light.[242] However, for the manufacturing of colorless transparent NIR-DSSCs the redox potential of the mediators needs to comply particular characteristics. As mentioned in the Section 1 of this chapter, suitable NIR-sensitizers for NIR-DSSCs required HOMO and

LUMO energy levels with precise values. In particular, HOMO energy level should be located around -5.25 eV (≈ +0.85 V). For this reason, it has been estimated that optimally redox mediator for NIR-DSSCs should have a formal redox potential in the range of 0.40-0.65 V *vs*. *NHE* to reach high level of performances in conjunction with the already explored NIR-dyes. In addition, suitable redox couple for NIR-DSSCs highly required level of transparency without any parasitic absorption in the visible part of the spectrum.[29,244]

Over the years, in classical DSSCs the I_3^-/I^- electrolyte was the most commonly used redox mediator. This redox couple exhibits suitable properties for the efficient functioning of the DSSCs: the forward electron donation by I^- is sufficiently fast to ensure efficient dyes regeneration while the reduction of I_3^- at the photoanode is slow enough to allow for high carrier collection efficiencies. These features as well as their excellent stability made sure for long time that triiodide/iodide redox couple been the best candidate in DSSCs. However, I_3^-/I^- mediator is affected by noticeable drawbacks that avoided to achieve high efficiencies: (i) I_2 species in equilibrium with I_3^- is volatile, affecting the long-term stability of the cell, (ii) I_3^-/I^- requires a detrimental overpotential of ca. 400 mV due to the two-electron transfer bond creation, (iii) I_3^- is darkly red colored with strong absorption below 450 nm that limits the light harvesting efficiency of the dye, (iv) I_3^- in solution can forms poly-iodide species like I_5^-, I_7^-, and I_9^- having a further parasitic absorption of the incident light, (v) large photovoltage loss due to poor matching between its redox potential (+0.35 V *vs*. *NHE*) and the oxidized dye's redox potential (usually ca. +1.0 V *vs*. *NHE* for classic dyes and ca. +0.85 V *vs*. *NHE* for NIR-sensitizers), (vi) I_3^-/I^- is corrosive thus able to corrode the Ag- and Cu-based current collectors.[241,245-247] For these reasons, over the years several attempts have been made to replace the iodide/triiodide with most efficient redox couples. In this context, the metal-based redox mediators quickly caught on in DSSCs due to their fast mono-electronic redox processes as well as the easily tunability of the redox potentials and optoelectronic properties by the carefully modification of their structures.[248] Beside to metal-complexes, another class of

mediators based on pure organic molecules has been investigated. Highly transparent and non-corrosive redox couple like nitroxide and disulfide/sulfide system successfully found application in DSSCs.[241]

In this section, the state-of-art of metal-based and fully-organic redox couples will be described, highlighting the suitable candidates for the application in NIR-DSSCs (Fig. 31).

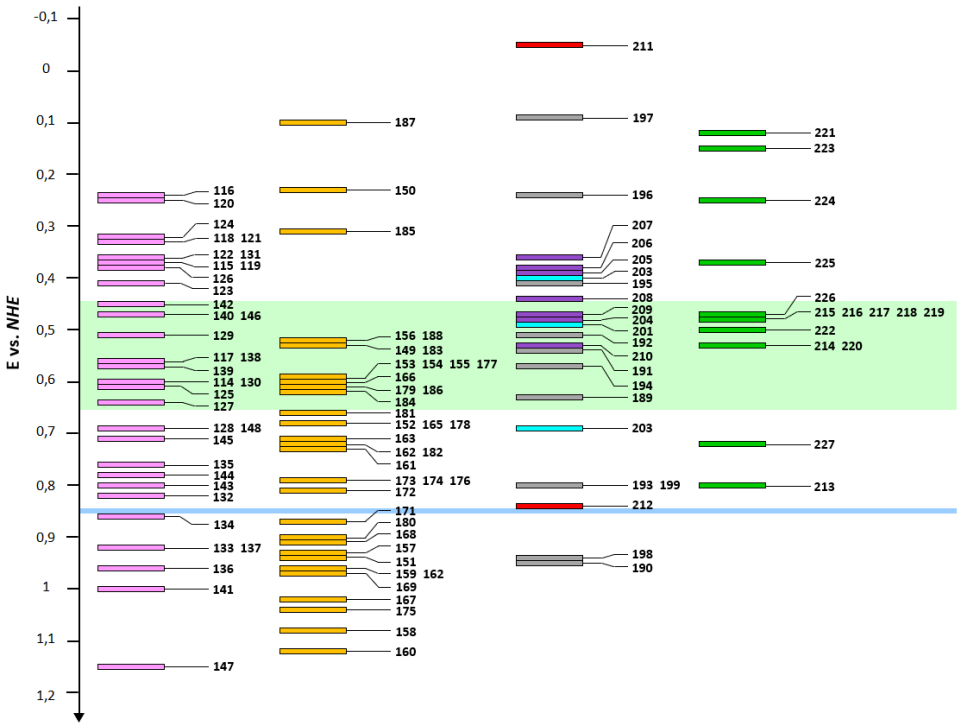

Figure 31 – The dispersion of redox potentials of the different types of redox mediators discussed in this section: cobalt (pink), copper (orange), iron (grey), manganese (cyan), nickel (purple), vanadium (red), fully organic (green). Light-green area identify the suitable range of redox potentials that redox mediators should have for efficient regeneration in NIR-DSSCs. The light-blue line denotes the average position of the HOMO level for most common NIR-sensitizers.

3.1. Metal-based Redox Couples

Metal-based redox couples are currently the most used and efficient redox mediators in DSSCs. Their main advantage is due to the easy tunability of their properties by a carefully selection of the metal core and the structure of ligands.

The choice of the metal core and ligands mainly depends by the specific electrochemical and photophysical properties (i.e., redox potential, diffusion, absorption) required by the sensitizer apply in the device. However, the choice also depends by practical and economic reasons: the electrolyte solution requires a high concentration of redox couple (0.1-0.5 M). For this reason, the choice of metal and ligands should be fall on a metal in the first raw of the d-block and on cheap, easily synthesized ligands.[241,245]

3.1.1. Cobalt-based Redox Couples

Historically, cobalt complexes represented the first successful strategy to replace triiodide/iodide redox couple. The cobalt is a transition metal commonly found in the Co(II) or Co(III) oxidation states, possessing d^7 and d^6 electronic structure with a paramagnetic nature for Co(II) and a diamagnetic nature for Co(III), respectively. Cobalt complexes usually form stable compounds with a coordination number of six, exhibiting an octahedral geometry. Due to its structure, cobalt can form organometallics complexes with both bidentate of tridentate ligands. The physical properties of cobalt-based redox couples strongly depends by their spin states.[249] Co(III) complexes are characterized by a closed-shell electron structure without unpaired electrons, which results in a low-spin state. For this reason, Co(III) is relatively stable and required a careful optimization of the catalytic activity of the counter electrode to guarantee an efficient redox-couple regeneration.[249,250] Contrarily, Co(II) are commonly in the high spin state resulting more reactive.

However, Co(II) complexes have a less straightforward situation because the energy difference between the high-spin and low-spin state configuration is relatively low. As such, spin-crossover processes can occur leading to a decreasing of formal redox potential and higher internal reorganization energy.[251] This spin-crossover upon oxidation of Co(II) to Co(III) is expected to have detrimental effects in the operational mechanism of DSSCs. As the oxidized dye has to be regenerated by the Co(II) coordination complex, the energy required to perform

the spin change resulting from this redox reaction is added to the inherent reorganization energy required to rearrange the cobalt-complexes structure. For this reasons, cobalt-based mediators should preferably be close to the Co(II) states spin-crossover point to achieve high dye-regeneration rates and thus high efficiencies.[29,248,251]

The first ever cobalt-based redox mediator in DSSCs was reported in 2001 by Nusbaumer *et al.* with complex **114** based on the tridentate bis[2,6-bis-(1'butylbenzimidazol-2'-yl)]pyridine ligand (*dbbip*) (Fig. 32).[252] Complex **114** exhibits a redox potential of 0.60 V *vs*. *NHE* and both Co(II) and Co(III) species have a very low absorption in the visible (Tab. 9). This pivotal work has been demonstrated the first advantages of cobalt-based redox couples: both Co(II) and Co(III) complexes haven't relevant parasitic absorptions in the visible part of the spectrum. Further investigation on **114** has been made to understand the effect of the counter ion.[253] The investigation of **114** with a series of counter ions such as triflate (OTf^-), perchlorate (ClO_4^-), dodecyl sulfate (DDS^-) and hexafluoro phosphate (PF_6^-), has demonstrated as the different counter ions do not influence the V_{OC} of DSSC while lead to strong fluctuations of the J_{SC}. Bulkier counter ions like DDS^- heavily affects the diffusion of the complex giving low J_{SC} values, whereas smaller ions like PF_6^- providing higher J_{SC}.[253] In addition, an electrochemical study on **114** reported by Cameron *et al.* demonstrated two of the main drawbacks of cobalt complexes.[254] It has been discovered that complex **114** exhibit slow electron exchange kinetics at the counter electrode as well as a very low diffusion coefficient compared to I_3^-/I^- redox couple. The lowering of charge transfer resistance at the counter electrode can be obtained by increasing the thickness and/or the active area of the counter electrode or choosing different electrode materials, whereas the improvement of diffusion coefficient can be obtained by carefully optimization of the cobalt-complexes structure using less bulky ligands.[29,248,254]

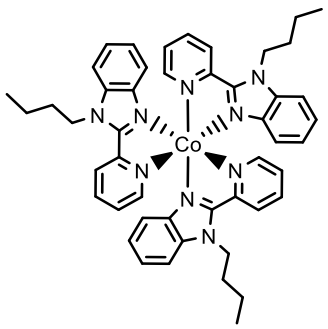

114

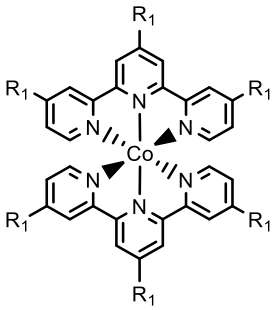

R1 = **115** -C_2H_5; **116** -*tert*-butyl; **129** -H

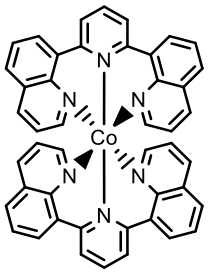

138

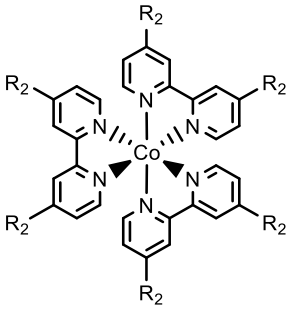

R2 = **117** -H; **118** -CH_3; **121** -*tert*-butyl; **122** -phenil; **123** -3-pentyl; **124** -*n*-nonyl; **131** -OCH_3; **141** -CN

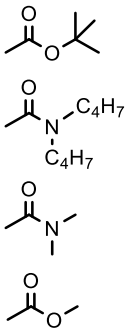

127; **128**; **139**; **140**

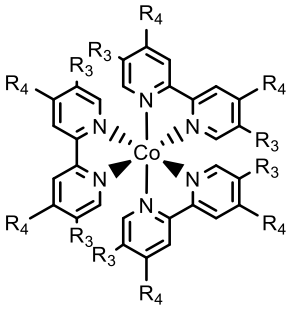

R3 = -H **R4** = -CH_3 **119**

R3 = **R4** = -CH_3 **120**

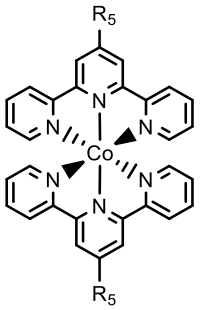

R5 = **130** -Cl; **142**

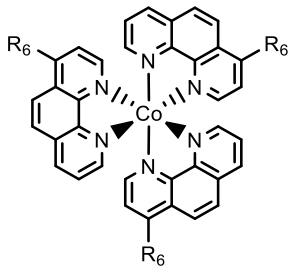

R6 = **125** -H; **126** -phenil; **132** -Cl; **133** -NO_2

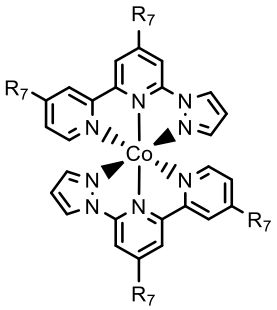

R7 = **134** -H; **135** -CH_3

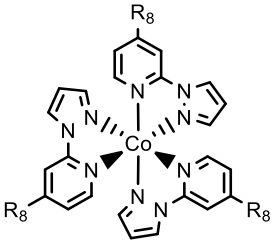

R8 = **136** -H; **137** -CH_3

Figure 32 – Cobalt-based redox couples with pyridyl-based ligands in DSSCs.

Table 9 – Electrochemical and photophysical properties of cobalt-based redox couples in DSSCs.

Redox couple	Redox potential *vs*. *NHE* [V]	Absorption in the visible region [M^{-1} cm^{-1}]	Suitable redox potential for NIR-DSSCs application	Ref.
114	0.60	ε_{450} = 310	Yes	252
115	0.37	-	Too low	255
116	0.24	ε_{450} = 1 400	Too low	255
117	0.56	ε_{450} = 90 [256]	Yes	255
118	0.33	ε_{450} < 150 [257]	Too low	255
119	0.37	-	Too low	255
120	0.25	-	Too low	255
121	0.33	ε_{440} = 140	Too low	255
122	0.36	-	Too low	255
123	0.41	ε_{440} = 110	Yes	255
124	0.32	ε_{440} = 110	Too low	255
125	0.61	ε_{450} = < 90 [257]	Yes	255
126	0.38	-	Too low	255
127	0.64	-	Yes	255
128	0.69	ε_{440} = 150	Too high	255
129	0.51	ε_{450} = < 1 500 [259]	Yes	258
130	0.60	ε_{450} = < 900	Yes	260
131	0.37	ε_{450} = < 120 [261]	Too low	258
132	0.72	ε_{450} = < 200 [257]	Too high	258
133	0.85	ε_{450} = < 200 [257]	Too high	258
134	0.86	ε_{450} = < 100 [262]	Too high	258
135	0.76	-	Too high	258
136	0.96	ε_{450} = < 100 [263]	Too high	258
137	0.92	-	Too high	258
138	0.56	ε_{450} = < 1 500	Yes	259
139	0.51	ε_{450} = 180	Yes	266
140	0.72	ε_{450} = 300	Too high	266
141	0.90	ε_{450} = 120	Too high	266
142	0.46	-	Yes	267
143	0.80	-	Too high	269
144	0.78	ε_{450} < 100	Too high	269
145	0.71	ε_{450} < 100	Too high	269
146	0.47	-	Yes	270
147	1.15	-	Too high	271
148	0.69	ε_{500} ≈ 100	Too high	273

Following these concepts, Sapp *et al.* reported a series of cobalt-based redox couples **115**-**128** with different ligands such as 2,2',6',2''-terpyridine (*terpy*), 2,2'-bipyridine (*bpy*) and 1,10-phenantroline (*phen*).[255] All these complexes exhibit a

very low visible absorption and redox potentials between 0.24 and 0.69 V. This series demonstrates how the modification of the ligand structure slightly influence the photophysical properties of the complexes while can dramatically change their redox potential, allowing a fine tunability of the electrochemical properties of the redox couples. The introduction of electron-donor groups on ligand structure causes the decrease the redox potential of the complex whereas electron-withdrawing groups increase it. For this reason, complexes **127** and **128**, bearing the *tert*-butyl ester and the *di*-butylamide respectively, exhibit higher redox potential (Tab. 9). In addition, according to the report of Cameron *et al.* even these complexes have a very poor electrochemistry activity at the counter electrode.

Despite the advantages compared to I_3^-/I^- redox couple, cobalt-based mediators exhibit lower efficiency in conjunction with ruthenium(II) sensitizers due to the undesired formation of an ion pair between the negatively charged dyes and the positively charged Co complexes.[251] For this reason, cobalt-based mediators never achieved high efficiency in DSSCs with ruthenium(II) sensitizers. However, the application and the efficiency of cobalt-based redox couples dramatically raised-up with the advent of organic dyes. The pivotal work of Feldt *et al.* reported a DSSCs with a record PCE of 6.7% using **117** in conjunction with dyes *D29* and *D35* (see Appendix).[264] The authors demonstrated the key-role of the choice of the optimal combination sensitizer-redox mediator to achieve higher efficiency. Studying a series of cobalt-complexes with increased bulkiness (**117**, **118** and **121**) they demonstrated that the non-geminate recombination processes can be decrease using long alkyl chains on the sensitizer structure and not on the cobalt-complexes, thus avoiding the decreasing of the diffusion coefficient of the mediators. Following the concepts discussed so far, several cobalt-based redox mediators (**129**-**142**) have been investigated over the year, studying different chemical modification of classic ligands such as *bpy*, *terpy* and *phen* as well as exploring new structure derived from 6-(1*H*-pyrazol-1-yl)-2,2'-bipyridine (*bpy-pz*), 2-(1*H*-pyrazol-1-yl)pyridine (*py-pz*) and 2,6-bis(8-

quinolinyl)pyridine (*bqp*) (Fig. 32).[258-260,265-267] The analysis of all these cobalt-complexes allows to rank the naked ligands in base to the redox potential achieved by their respective cobalt-complexes: *py-pz* (0.96 V) > *bpy-pz* (0.86 V) > *phen* (0.61 V) > *bqp* (0.56 V) > *bpy* (0.56 V) > *terpy* (0.51 V). This rank demonstrated how ligands such as *py-pz* and *bpy-pz* have too high redox potential to be suitable for NIR-DSSCs whereas *bpy*, *terpy* and *phen* present suitable redox potential. In particular, *bpy* ligands are the best candidate to synthetize efficient cobalt-based redox mediators due to their easier synthesis and structural modifiability.

When dealing with Co-based electrolytes, despite the very high efficiency reached over the years and their many advantages over the I_3^-/I^- redox couple, one should not forget that a major problem is the limited stability of the cobalt complexes under prolonged irradiation conditions. Their lack of stability is mainly cause by: (i) dissociation of the complexes and ligand exchange, (ii) cobalt complex adsorption on TiO_2, and (iii) slow irreversible oxidation of Co(II) by dissolved oxygen in the solvent.[268] To improve the electrochemical stability of cobalt-based redox mediators, the modification of the denticity and spatial arrangement of the ligands can be exploited.

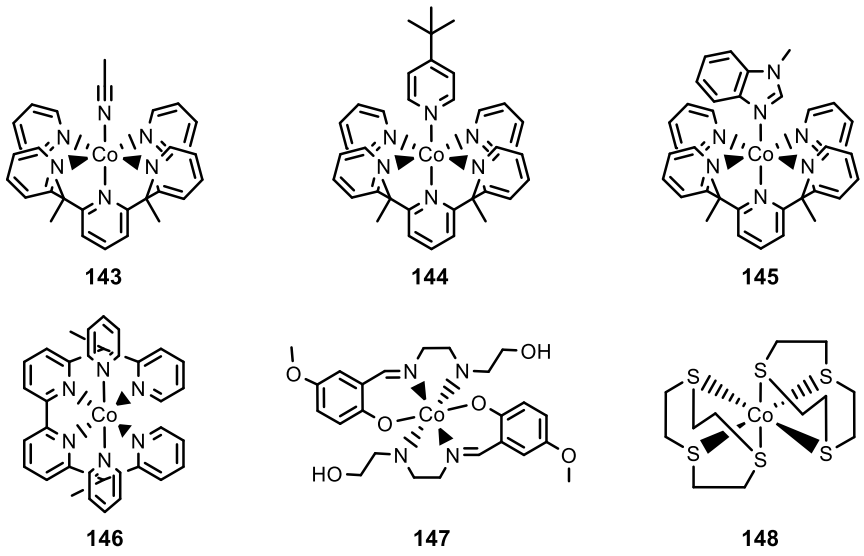

Figure 33 – Cobalt-based redox couples with rigid ligands and with not-polypyridine based ligands.

In particular, rigid ligands can be suitable in improving the electrochemical stability of cobalt-complexes in DSSCs. Following this concept, Bach *et al.* proposed a series of cobalt-based mediators **143**-**145** with pentadentate ligand 2,6-(bis(bis-2-pyridyl)methylmethane)pyridine (*PY5Me$_2$*) (Fig. 33).[269] In their work, the authors hypothesized that the 6th remaining coordination site would be occupied by a coordinating Lewis base such as 4-*tert*-butylpyridine (TBP) and methylbenzoimidazole (NMBI) that could ultimately tune the redox properties of the complex. It has been demonstrated as stronger Lewis's basicity allows to shift-down the redox potential and moreover leads to a better photovoltaic performance. Device with Co(*PY5Me$_2$*)(NMBI) **145** in conjunction with dye *MK2* (see Appendix) achieved a PCE of 8.3% whereas that with Co(*PY5Me$_2$*)(TBP) **144** only 6.1%. The lower efficiency of DSSC with **144** is due to the higher redox potential of **144** that exhibits a faster non-geminate recombination.[269] This behavior demonstrates as getting too close the HOMO level of the dye with the mediator's redox potential can be detrimental even if the sensitizer is tailored to avoid the electron recombination.

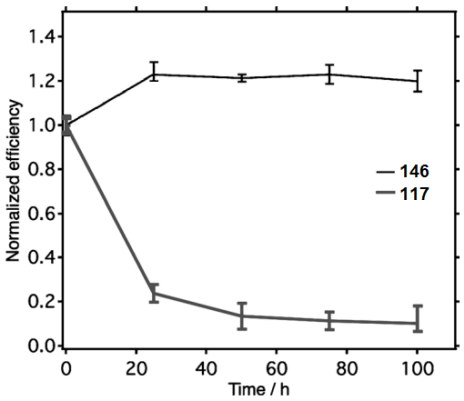

Figure 34 – Normalized efficiencies of the devices under full sun irradiation aging experiment with a 400 nm UV-cut off filter. Comparison between device with cobalt-based mediators **146** and reference redox couple Co(bpy)$_3$ **117**.[271]

Following this strategy, Bach *et al.* reported a more rigid cobalt-complex **146** based on the hexadentate ligand 6,6'-bis(1,1-di(pyridin-2-yl)ethyl)-2,2'-bipyridine

(*bpyPY4*).[270] Compared to cobalt-based mediators with pentadentate ligands **143**-**145**, complex **146** exhibited a lower redox potential at 0.46 V *vs*. *NHE* leading to a device with a lower V_{OC} compared to **144** and **145** (**144** V_{OC} = 993 mV, **145** V_{OC} = 940 mV, **146** V_{OC} = 757 mV). However, complex **146** achieves comparable efficiency of **145** due to its lower electron recombination. Despite the similar photovoltaic performance, devices with **146** exhibit as outstanding stability: the increased chelating effect of *bpyPY4* lead to very thermodynamically stable complex (Fig. 34).

In addition to polypyridine-based ligands, other examples of cobalt-based mediators with different ligands have been reported in literature. Nasr-Esfahani *et al.* reported the synthesis of cobalt-based mediators **147** with (*E*)-2-(((2-((2-hydroxyethyl)amino)ethyl)imino)methyl)-4-methoxyphenol ligand (*SBCC*) (Fig. 33). This complex was developed starting from the structure of the salcomine, a cobalt complex well known for its robust coordination structure and its oxygen carrier ability.[271,272] Complex **147** exhibits an outstanding redox potential of 1.15 V *vs*. *NHE* able to manage a very high V_{OC} in device but due to poor fill factor and low photocurrent, *SBCC*-based mediator in DSSC achieves a PCE of only 2.5%. The lower performance is mainly due to an increased charge transfer resistance at the counter electrode, confirming how the selection of the CE is crucial to achieve an efficient regeneration and strongly depends by the redox mediator apply in the device.

Another interesting example of cobalt-based mediators was reported by Hamann *et al.* using the trithiacyclononane ligand (*ttcn*) to obtain a low-spin Co(II) complex **148**.[273] Complex **148** has a redox potential of 0.69 V *vs*. *NHE* and no parasitic absorption with $\varepsilon_{500} \approx 100\ M^{-1}\ cm^{-1}$. The rigid structure of *ttcn* ligand is meaningful in lowering reorganization energy by hampering the spin crossing but unfortunately, DSSC with **148** suffered fast non-geminate recombination process leading to a poor PCE of 1.55% with dye *LEG4* (see Appendix).

Nowadays, cobalt-based complexes have completely undermined the iodine-based mediator and have a key-role in the manufacturing of high performance

DSSCs as demonstrated by the current overall record of 14.3% achieved with **125**.[23] However, in NIR-DSSCs I_3^-/I^- redox couple still results the most attractive to achieved better efficiencies despite its limitations, as demonstrated by Naim *et al.* with the cyanine dye **105**. (PCE with I_3^-/I^- = 3.1%, PCE with **117** = 2.3%).[61] In addition, cobalt-based mediators still suffer relevant long-term stability issue but above all, they are a penalizing point for future industrialization step due to the poor sustainability of the cobalt, classified as Critical Raw Material.[274] For these reasons, novel redox mediators based on more sustainable metals like copper and iron have been developed and they will be discussed in next paragraphs.

3.1.2. Copper-based Redox Couples

In the last years the use of copper-complexes in DSSCs to replace the cobalt-based redox couples dramatically grown. Copper-based redox couples are particularly interesting as mediators due their high efficiency in both liquid and solid-state DSSCs (SS-DSSCs) as well as their better sustainability.[275-277] However, two main issues hamper the application of copper-based mediators in NIR-DSSCs. The first one is due to their large reorganization energy between the two oxidation states while the second one is related to their much more absorption in the visible region that influences the aesthetic of the NIR-DSSCs hampering the manufacturing of colorless device. Over the years, the thoughtful engineering of ligand structures has been allowed to overcome the issue of the large reorganization energy while isn't possible to get through the non-negligible absorptions in the visible region in any way. However, as will be discussed in detail in the introduction of Chapter 4, copper-based redox mediators could be equally useful in the manufacturing of NIR-DSSC for the IMPRESSIVE project. For these reasons, despite the well-known pale-orange coloration of copper-based mediators, they will be equally discussed in this paragraph as possible redox mediators in NIR-DSSCs for IMPRESSIVE project.

For many years, copper complexes were not considered as mediators in DSSCs because it was well-known that Cu(II)→Cu(I) redox switch is generally

accompanied by significant variation in the geometry of the central atom, with concomitant high inner reorganization energy, due to the different preferred geometries assumed by copper in the two oxidation states. Copper(I) has a d^{10} electronic configuration preferring a tetrahedral disposition of the ligands whereas copper(II) mainly prefers a tetragonal geometry which minimizes the energy of its d^9 electronic configuration, with possibility to expand its coordination sphere from four to up to six. This intrinsic behavior slows down the electron transfer rates, reducing the undesired charge recombination but at the same time hampering the dye regeneration which has to as fast as possible to minimize the direct recombination by the oxidized sensitizer.[278] However, as often happens, nature provides the inspiration to solve issues. Copper is well-known to be involved in many natural systems like in the "copper blue proteins", in which it is responsible of very efficient electron transfer processes due to a specific chemical environment around the copper atom.[279-281] In the "copper blue proteins" the coordination geometry of the copper is essentially blocked by the protein folding, hampering any significant variation from the distorted tetragonal geometry that represents a compromise between the two preferred ones.[278] Following this concepts, Hattori *et al.* reported in their pioneer work the first application of copper-based redox mediators in DSSCs. They investigated the performances of the heteroleptic complex **149** with sparteine and maleonitriledithiolate (*mmt*) ligands mimics the "blue copper protein" centers, and to carry out a comparison the phenanthroline-based complexes **150** and **151** (Fig. 35).[282] By using dye *N719* (see Appendix) they demonstrated how mediators without hindered ligands, as in the case of **150**, afforded a dramatically lower efficiency (PCE = 0.12%) than mediators **149** and **151** (PCE = 1.3% and PCE = 1.4%, respectively). This trend provides evidence of the key-role of bulky groups near to the coordinated nitrogen atoms. In particular, while complex **150** with the naked-phenanthrolines can easily change its coordination geometry, in complex **151** the methyl substituents increase the bulkiness of the structure fixing the coordination in an intermediate distorted geometry.

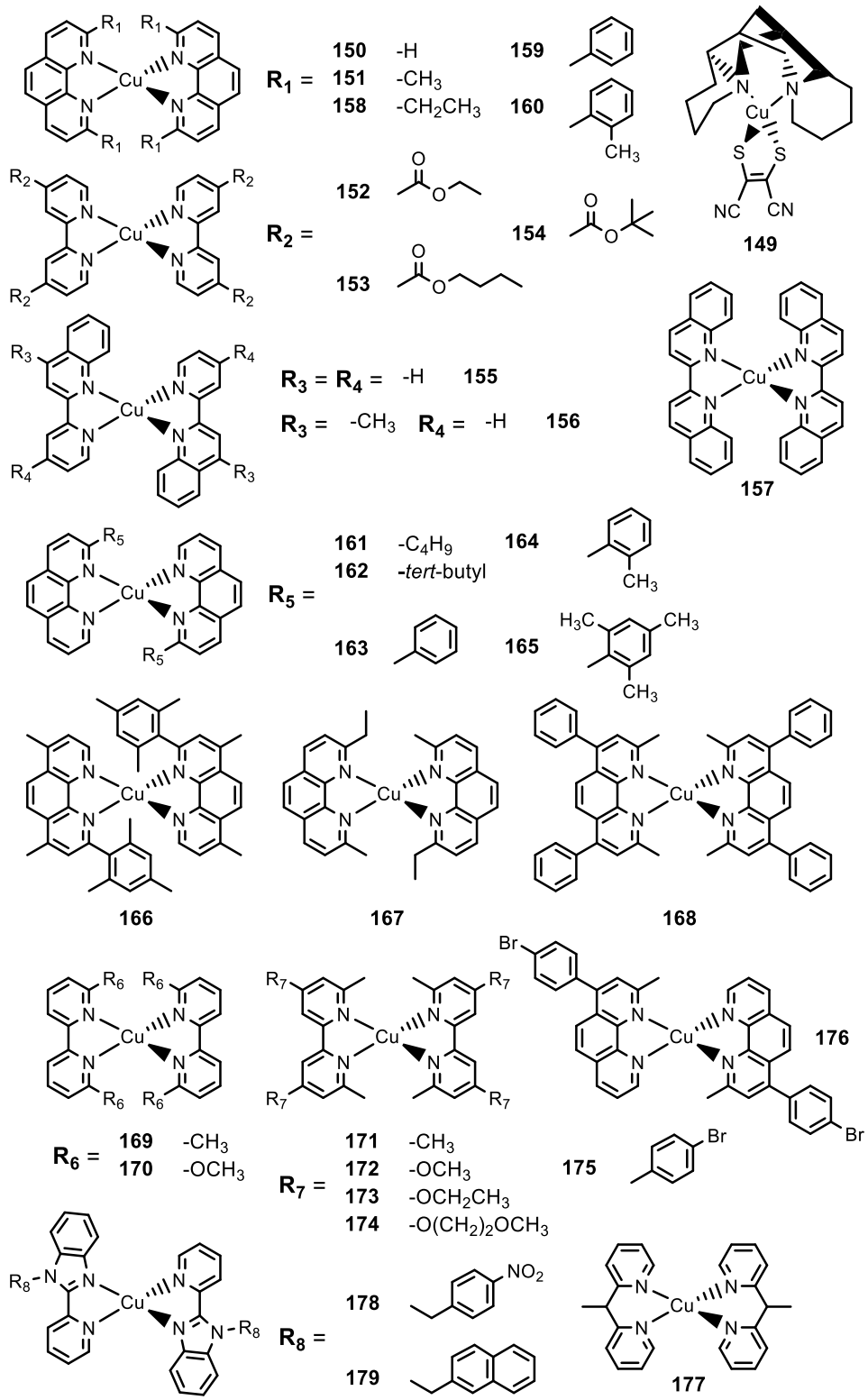

Figure 35 – Copper-based redox couples in DSSCs.

Table 10 – Electrochemical and photophysical properties of copper-based redox couples in DSSCs.

Redox couple	Redox potential *vs*. *NHE* [V]	Absorption in the visible region [M^{-1} cm^{-1}]	Suitable redox potential for NIR-DSSCs application	Ref.
149	0.53	-	Yes	282
150	0.14	-	Too low	282
151	0.90	$\varepsilon_{460} \approx 7\,300$ [283]	Too high	282
152	0.68	-	Too high	286
153	0.59	-	Yes	286
154	0.59	-	Yes	286
155	0.59	-	Yes	286
156	0.52	-	Yes	286
157	0.93	-	Too high	286
158	1.08	-	Too high	287
159	0.96	-	Too high	287
160	1.12	$\varepsilon_{470} \approx 4\,500$	Too high	288
161	0.73	$\varepsilon_{450} \approx 6\,200$	Too high	289
162	0.96	$\varepsilon_{430} \approx 2\,200$	Too high	288
163	0.72	$\varepsilon_{440} \approx 4\,600$	Too high	288
164	0.71	$\varepsilon_{450} \approx 4\,600$	Too high	288
165	0.68	$\varepsilon_{450} \approx 4\,100$	Too high	290
166	0.60	$\varepsilon_{450} \approx 5\,000$	Yes	291
167	1.02	-	Too high	287
168	0.91	$\varepsilon_{450} \approx 23\,000$	Too high	291
169	0.97	$\varepsilon_{450} \approx 6\,900$	Too high	283
170	0.68	$\varepsilon_{440} \approx 2\,400$	Too high	295
171	0.87	$\varepsilon_{450} \approx 5\,300$	Too high	283
172	0.81	$\varepsilon_{450} \approx 5\,500$	Too high	297
173	0.79	$\varepsilon_{440} \approx 5\,000$	Too high	298
174	0.79	$\varepsilon_{440} \approx 5\,200$	Too high	298
175	1.04	-	Too high	297
176	0.79	$\varepsilon_{460} \approx 7\,400$	Too high	297
177	0.59	$\varepsilon_{450} < 200$	Yes	302
178	0.68	$\varepsilon_{400} \approx 3\,200$	Too high	303
179	0.61	$\varepsilon_{400} \approx 5\,900$	Yes	303
180	0.90	-	Too high	309
181	0.66	$\varepsilon_{420} \approx 1\,500$	Too high	310
182	0.72	$\varepsilon_{465} \approx 4\,400$	Too high	311
183	0.53	$\varepsilon_{440} \approx 1\,300$	Yes	311
184	0.62	-	Yes	311
185	0.31	$\varepsilon_{350} \approx 2\,000$	Too low	312
186	0.61	$\varepsilon_{400} \approx 2\,000$	Yes	312
187	0.10	$\varepsilon_{400} \approx 2\,300$	Too low	313
188	0.52	$\varepsilon_{400} \approx 2\,300$	Yes	313

Beside to the devices' performance improvement, careful design of hindered ligands can dramatically raise the redox potentials toward values up to 1.0 V (Tab. 10). While for classical DSSCs this outstanding property has been exploited to achieve efficiencies beyond 13%,[284,285] for NIR-DSSCs application it's necessary remembered the upper-limit of 0.65 V (*vs*. *NHE*) imposed to guarantee an efficient dye-regeneration processes.

Starting from the pivotal work of Hattori *et al.*, over the years several copper-complexes have been investigated, testing different ligand structures with different bulkiness. Bignozzi *et al.* reported the synthesis of copper-based mediators **152**-**157** exploiting different type of ligands such as 2,2'-bipyridine (*bpy*), 2,2'-pyridil-quinoline (*PQ*) and 2,2'-biquinoline (*BQ*).[286] However, the authors followed a different strategy to minimize the back electron-transfer rates, providing copper-complexes with not-hindered ligands and thus having high reorganization energies. As expected, the relevant re-arrangement occurring in these complexes decreases the recombination rates but at the same time resulting in very slow dye regeneration processes. In addition, it has been demonstrated as complexes **152**-**154** bearing 4,4'-disubstituted *bpy* ligands exhibit very slow electron transfer kinetic and the bulky groups in the same position are not suitable to suppressing the recombination.

The breakthrough of copper-based mediators in DSSCs arrived with their application in conjunction with organic dyes bearing bulky alkyl-chains able to slow-down the recombination processes. In particular, PCEs of 7.0% and 8.3% was reached with **151** in combination with dyes *C218* and *LEG4* (see Appendix), respectively.[299,300] The outstanding results confirmed the key-role of hindered ligands to reduce the reorganization energy of copper complexes and raise their redox potentials, providing DSSCs with V_{OC} up to 1.0 V. Starting from these concepts, over the years several sterically hindered phenanthroline- and bipyridine-based copper complexes have been explored **158**-**176**.[287-298] As mentioned before, all these copper-based mediators exhibit a not negligible absorption in the visible; in particular, Cu(I) complexes exhibit *MLCT* (*Metal-to-*

Ligand Charge-Transfer) absorption band with molar extinction coefficients between 2.0-6.0·10^3 M^{-1} cm^{-1} at 450 nm while Cu(II) ones shows weaker absorption bands among 600-750 nm (<1.5·10^3 M^{-1} cm^{-1}), ascribable to *d-d* transitions.[301] However, compared to more colorless cobalt-based redox couples, copper complexes have almost three-fold higher diffusion coefficients, leading to faster regeneration processes.[283]

Beside to the most used *phen* and *bpy* ligands, interesting results have been achieved with copper complexes bearing other bidentate ligands such as bis(1,1-bis(2-pyridyl)ethane) (*bpye*) **177** and 2-(pyridin-2-yl)-1*H*-benzo[*d*]imidazole (*nbpbi*) **178**-**179**.[302,303] In particular, copper-based mediator **177** has a very low absorption with molar extinction coefficients for both Cu(I) and Cu(II) species below 100 $M^{-1}cm^{-1}$ in whole visible region. In addition, **177** has suitable redox potential for NIR-DSSCs application as well as it has been demonstrated to be an efficient mediator in conjunction with dye *LEG4* achieving an efficiency of 9.0%.[302] Even *nbpbi*-based copper complexes **178**-**179** shows suitable redox potentials for NIR-DSSCs application but compared to **177**, they have higher absorption in the early part of the visible region with molar extinction coefficients between 3.0-6.0·10^3 M^{-1} cm^{-1} at 400 nm.[303]

Recently, a different approach to lock the coordination geometry of copper complexes has been exploited to reduce the energetic loss which follows the oxidation Cu(I)→Cu(II). Beyond to most used polypyridyl ligands, copper complexes with tetra- and pentadentate ligands have been developed (Fig. 36). However, the necessity to reduce the high reorganization energy wasn't the only reason to promote the introduction of tetra- and pentadentate ligands in copper-based mediators. Several experimental observations demonstrated that the TBP, the most frequently used Lewis' base additive in the electrolytes, can coordinate to the Cu(II) species, negatively impacts on the electrochemical behavior and the stability of the redox mediators and thus the overall device performance. It has been assumed that tetra- and pentadentate ligands can lead to the formation of

copper complexes with a cage structure able to prevent the detrimental coordination of the TBP on Cu(II) species.[295,304-308]

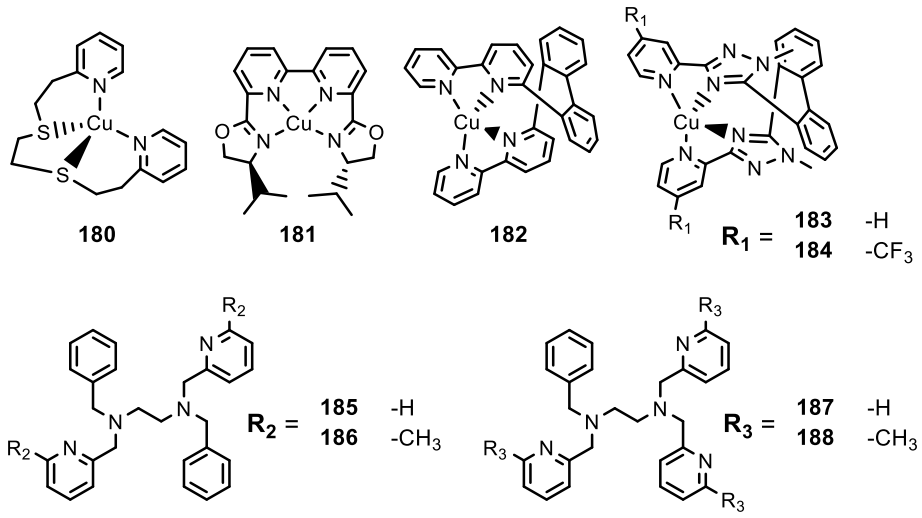

Figure 36 – Copper-based redox couples with rigid tetra- and pentadentate ligands. For complexes **185**-**188** we reported only ligands due to the tricky tridimensional structures of their copper complexes.

The first example of copper-based mediator bearing tetradentate ligand has been reported by Hoffeditz *et al.* using the 1,8-bis(2'-pyridyl)-3,6-dithiaoctane (*PDTO*) **180**.[309] However, the less coordination ability of sulfur atoms leads to destabilization in Cu(II) species favoring the TBP coordination. A more stable copper-based mediator with tetradentate ligand 6,6'-bis(4-(S)-isopropyl-2-oxazolinyl)-2,2'-bipyridine (*oxabpy*) **181** has been reported by Michaels *et al.*[310] Complex **181** exhibits square-planar geometry providing a low reorganization energy. Interestingly, despite authors obtained **181** as viscous gel-like solution, it provided an enhancement of charge transport compared to the currently most efficient copper-based mediator **171**. However, in terms of device's performance, all the cell's parameters with mediator **181** are lower than the reference DSSC with **171**, only achieving a PCE of 6.2%.

Other copper-based mediators with tetradentate ligands have been reported by Rodrigues *et al.* **182**-**184**.[311] In these complexes, the biphenyl moiety on the

ligand forced the four nitrogen atoms in a pseudo-tetrahedral arrangement which allowed the chelation of the metal center while preventing the coordination geometry variation during the oxidation. Authors demonstrate as complexes **183**-**184** with tetradentate ligands having methyltriazole donor in their structure leads to better performance, achieving efficiencies of 4.4% and 4.8% in conjunction with *Y123* (see Appendix), respectively.

The breakthrough in copper-based mediators with tetradentate ligands has been achieved by Wang *et al.* with the investigation of a new class of copper complexes containing diamine-bipyridine tetradentate ligands **185**-**186**, the former without any substituents while the latter with two methyl groups to enhance the steric hinderance.[312] The introduction of methyl groups in **186** positively shifts by 0.30 V the redox potential compared to the naked-structure of **185**. However, the main effect of methyl groups is the decreasing of the internal reorganization energy that increases the dye regeneration yield, achieving a PCE of 9.2%, the highest so far in devices with tetradentate-based copper complexes. In addition, it has been demonstrated that complexes **185**-**186** have a good air, photo, and electrochemical stability, resulting in longer lifetime of the whole DSSC. Following these concepts, Sun *et al.* further improved the performances by using similar, but stiffer ligands based on the diamine-tripyridine pentadentate structures **187**-**188**.[313] Compared to previous **185**-**186**, in ligands **187**-**188** a phenyl is replaced by a pyridine ring which confers an additional coordination site. Even in this case, both complexes with the unsubstituted and the methyl-decorated ligands have been investigated. Obviously, pentadentate ligands providing more rigid copper-complexes compared **185**-**186**, further diminishing the internal reorganization energy and thus achieving higher PCEs of 9.4% for **187** and 10.3% for **188**. In addition, authors demonstrate the outstanding ability of pentadentate ligands to completely avoid the detrimental parasitic coordination of the TBP (Fig. 37). Nowadays, copper-based complexes are the most promising redox-mediator for the future industrialization step of DSSCs due to their very high performance as well as their

sustainability.[274] Contrarily, in colorless NIR-DSSCs application copper-based electrolyte are not suitable due to their pale-orange coloration.

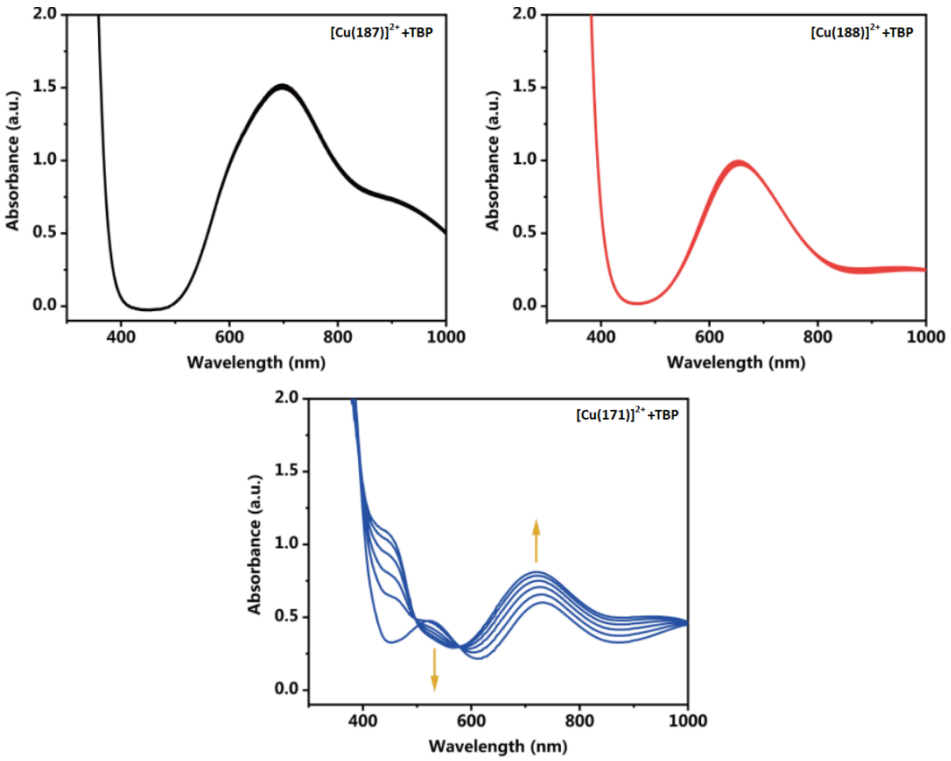

Figure 37 – UV-vis absorption spectra of copper(II) complexes with ligands **187** (black), **188** (red), **171** (blue) in presence of 0.2, 0.4, 0.6, 0.8 and 1.0 molar eq. of TBP in acetonitrile. TPB has no effect on the coordination structure of complexes with pentadentate ligands **187**-**188** whereas strongly influences the structure of the reference copper complex with tetramethyl-bpy ligand **171**.[313]

As mentioned before, despite their not negligible absorption, copper-based redox mediators could be equally useful in the manufacturing of NIR-DSSC for the IMPRESSIVE project. However, the development of new sterically hindered ligands with lower redox potentials between 0.40-0.65 V (*vs*. *NHE*) it's necessary. For these reasons, a new class of copper complexes based on different imidazo[1,5-*a*]pyridine ligands (*Impy*) were studied, which will be detailly discussed in Chapter 4.

3.1.3. Iron-based Redox Couples

Generally, the use of iron for material development has attracted a great deal of interest due to its high abundance, low cost and relatively low toxicity, making the iron-based redox couples the most sustainable so far.[274,277] Iron-based mediators are considered the holy grail of DSSCs due to their suitable photophysical features like cobalt-based mediators, as well as the possibility to obtain several iron complexes with very high redox potential (> 1.0 V *vs*. *NHE*), which can potentially lead to achieved theoretical V_{OC} values up to 1.4-1.6 V. However, the few examples reported in literature well described the difficult application of iron-based mediators in DSSCs.

The first iron-based mediator studied in DSSCs has been the ferrocenium/ ferrocene (Fc^+/Fc) **189** redox couple due to its fast kinetic properties (Fig. 38). The ferrocene molecule consists of a sandwich structure with an iron(II) ion between two negatively charged cyclopentadienyl rings, providing a very stable 18-π electron system. Ferrocenes are well-known for their high stability to temperature, air and water as well as for their fully reversable and solvent-independent redox potential. Beside to these interesting properties, the main attractiveness of ferrocene-based mediators to the application in DSSC is related to their very fast monoelectronic redox process which does not involve high-energy intermediate species, leading to negligible energy losses.[314,315]

The pioneer work of Gregg *et al.* demonstrated as ferrocene-based electrolytes wouldn't be suitable for DSSCs due to their too fast non-geminate electron recombination. For these reasons, different strategies were applied to tackle-down the fast recombination. However, only photovoltaic performance below 0.4% were achieved.[316,317] The breakthrough in ferrocene-based mediator was achieved by Spiccia *et al.* with **189** in conjunction with dye *Carbz-PAHTDTT* (see Appendix) reaching a sensational efficiency of 7.5%.[318] The dramatically improvement of performance compared to previous reported devices, is due to the carefully optimization of dye-structure: the bulky structure of *Carbz-PAHTDTT* slowing-down the recombination kinetic, favoring better injection and thus higher efficiency.

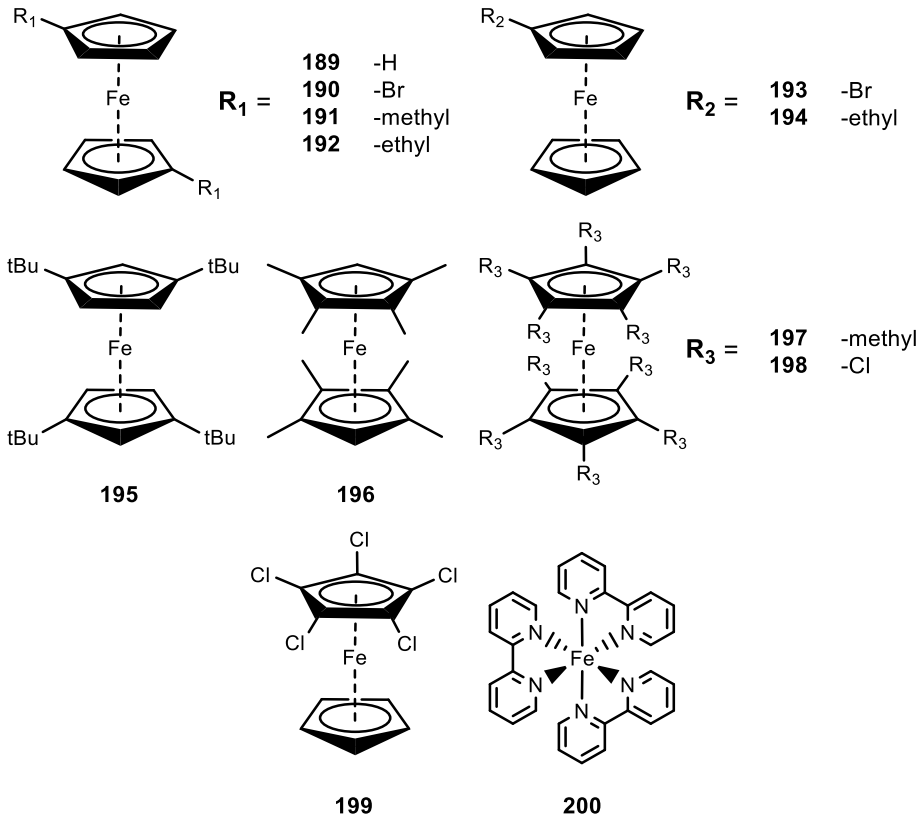

Figure 38 – Iron-based redox couples in DSSCs.

Table 11 – Electrochemical and photophysical properties of iron-based redox couples in DSSCs.

Redox couple	Redox potential *vs. NHE* [V]	Absorption in the visible region [M^{-1} cm^{-1}]	Suitable redox potential for NIR-DSSCs application	Ref.
189	0.62	$\varepsilon_{442} \approx 95$	Yes	318
190	0.94	-	Too high	322
191	0.54	Fc $\varepsilon_{438} \approx 96$ Fc^+ $\varepsilon_{462} \approx 105$	Yes	321
192	0.51	-	Yes	322
193	0.80	-	Too high	322
194	0.57	-	Yes	322
195	0.41	Fc $\varepsilon_{462} \approx 95$ Fc^+ $\varepsilon_{750} \approx 380$	Yes	321
196	0.24	Fc $\varepsilon_{428} \approx 95$ Fc^+ $\varepsilon_{750} \approx 380$	Too low	321
197	0.09	Fc $\varepsilon_{423} \approx 97$ Fc^+ $\varepsilon_{778} \approx 488$	Too low	321
198	0.95	-	Too high	320
199	0.80	-	Too high	320
200	1.37	-	Too high	325

However, ferrocene-based redox couples remain less apply in DSSCs than Co- and Cu-based mediators, mainly due to their intrinsic rapid recombination processes. In addition, there are other two relevant drawbacks that hamper the efficient application of ferrocene-based mediators: (i) ferrocenium species are poorly stable as being very sensitive to oxygen leading to the formation of undesired binuclear iron complexes and (ii) both ferrocene and ferrocenium species present low solubility in organic solvents which are today the most used in the electrolyte's formulation.[242,315]

Despite their lower attractiveness in classic DSSCs, ferrocene-based mediators could be the most interesting redox couples for colorless NIR-DSSCs application. As mentioned before, both ferrocene and ferrocenium species have suitable photophysical features with molar extinction coefficients below 500 $M^{-1}cm^{-1}$ in whole visible region as well as suitable redox potentials for the regeneration of most NIR-dyes (Tab. 11). Interestingly, the redox potential of ferrocene can be easily tuned through the functionalization of the cyclopentadienyl rings with a variety of electron donating or withdrawing substituents.[315] Over the years, this approach allowed the development of several ferrocene-based mediators **190**-**199** with redox potentials between 0.1-1.0 V *vs*. *NHE*.[319-322] In addition, it has been demonstrated that the introduction of electron donor units lead to the electronic enrichment of the iron 3d orbitals providing higher stability to the ferrocenium species.[315]

Beside to ferrocene-based mediators, over the year other different iron-complexes have been studies as redox couples in DSSCs.[323-325] Between them, bpy-based iron complex **200** is the most important. In 2018 Rodrigues *et al.* reported the investigation of a DSSCs applying **200** as redox mediator in conjunction with bulky dye *RR9* (see Appendix), achieving the highest ever V_{OC} of 1.42 V in DSSCs.[325] Despite the incredible photovoltage achieved and the use of a bulky sensitizer like *RR9*, authors only reached a PCE of 1.9%, confirming how the fast electron recombination remains the main issue to overcome for to allow an efficient application of iron-based mediators in DSSCs.

3.1.4. Other Metal-based Redox Couples

Over the years, beside to cobalt, copper and iron, other transition metals such as manganese, nickel and vanadium have been investigated to the preparation of new redox mediators.

Analogously to iron-based complexes, the natural abundance of manganese and its low toxicity makes the search for Mn-based mediators very interesting. Like the other metals discussed so far, even manganese function as one-electron outer-sphere redox shuttles, and by ligand engineering the redox potential as well the absorption coefficient can be tuned. Manganese is well-known for their tricky redox chemistry including several possible oxidation states, from +2 to +7. Between theses oxidation states, the most relevant for reversible electron transfer reactions include the pairs Mn(III)/Mn(II) or Mn(IV)/Mn(III). The high oxidation state Mn(IV) can act as a strong Lewis acid and can be reduced by solvents or ligands as well as undergo hydrolysis if water is present in the media. In addition, it can easily bind oxygen atoms, as known from the photosynthesis reactions involving the Mn–Ca cluster. On the other hand, the Mn(III) species can act as strong oxidant, undergoing disproportionation to Mn(II) and MnO_2.[248,326] In addition, both oxidation states can be stabilized by ligands with donor atoms such as nitrogen and oxygen, with hard Lewis-acid features. As a result, the occurrence of two different metal-center electron-transfer reactions with the pairs Mn(IV/III) and Mn(III/II) are possible, but difficult to distinguish.

The first DSSC with a manganese-based mediator was reported by Perera et. al based-on Mn complexes with oxidation states +3/+4 and ligand the tris(acetylacetonato) (*acac*) **201** (Fig. 39).[327] Mediators **201** has a redox potential of 0.49 V *vs*. *NHE* and low absorption in the visible, features make it suitable for possible NIR-DSSC application (Tab. 12). In conjunction with *MK2* dye, authors achieved a PCE of 4.4%. The poor performance is mainly due to the high recombination rate which affects **201**, resulting in a lower J_{SC} of 8.5 mA cm^{-2} and thus in low performance. Following these interesting results, Carli *et al.* attempted to improve the performance of manganese-based mediators by

modifying the *acac* structures.[328] Authors reported the synthesis and the application of two new Mn-complexes **202**-**203**, bearing on *acac* structure both phenyl and difluoromethyl groups in **202** and only phenyl groups in **203**. Authors determine the redox potentials of both electron-transfer reactions Mn(III)/Mn(II) and Mn(IV)/Mn(III) for **202**-**203**. For mediators **202**, the presence electron withdrawing groups like the difluoromethyl, raises the redox potentials at 0.69 V *vs*. *NHE*, higher than **201**. In addition, authors determined a redox potential of 1.57 V *vs*. *NHE* for Mn(IV)/Mn(III) electron-transfer reactions. Whereas couples **203**, bearing six donor phenyl groups, exhibit lower redox potentials for both electron-transfer reactions, achieving 0.41 V *vs*. *NHE* for Mn(III)/Mn(II) and 1.20 V *vs*. *NHE* for Mn(IV)/Mn(III). However, Mn(IV)/Mn(III) electron-transfer reactions are unsuitable for the regeneration of most the sensitizers, due to the mismatch of the redox potential with the sensitizers HOMO level. Devices with **202** and **203** achieved PCEs of only 2.6% and 1.5% respectively, due to the above-mentioned fast recombination processes that affected manganese-based redox mediators.

Nickel(II) complexes are well-known for their high redox potentials, up to 1 V *vs*. *NHE*, but for many of them the oxidation process occurs on the ligand instead on the central nickel atom, making them unattractive for the manufacturing of stable mediators for DSSC application.[248,329] However, Li *et al.* demonstrated the possible application on nickel-based mediators in DSSCs by the investigation of redox couples Ni(III)/(IV) bis(dicarbolide) **204** featuring by two η^5- deboronated (nido-2) *o*-carborane ligands, with a fast and reversible one-electron transfer process (Fig. 39). This nickel-based mediator has low corrosivity and exhibit low electron-exchange rates since the electron transfer process requires a *cis*-to-*trans* conformational rotation, resulting in high reorganization energies. For this reason, a poor PCE of 1.5% was reached in conjunction with *N719* dye.[330,331] The performance this type of redox mediator was improved by Spokoyny *et al.* by the functionalization of the bis(dicarbolide) moiety in the B(9/12) positions with different aryl electron-donating and withdrawing groups in order to tune the redox potentials (**205**-**210**).[332]

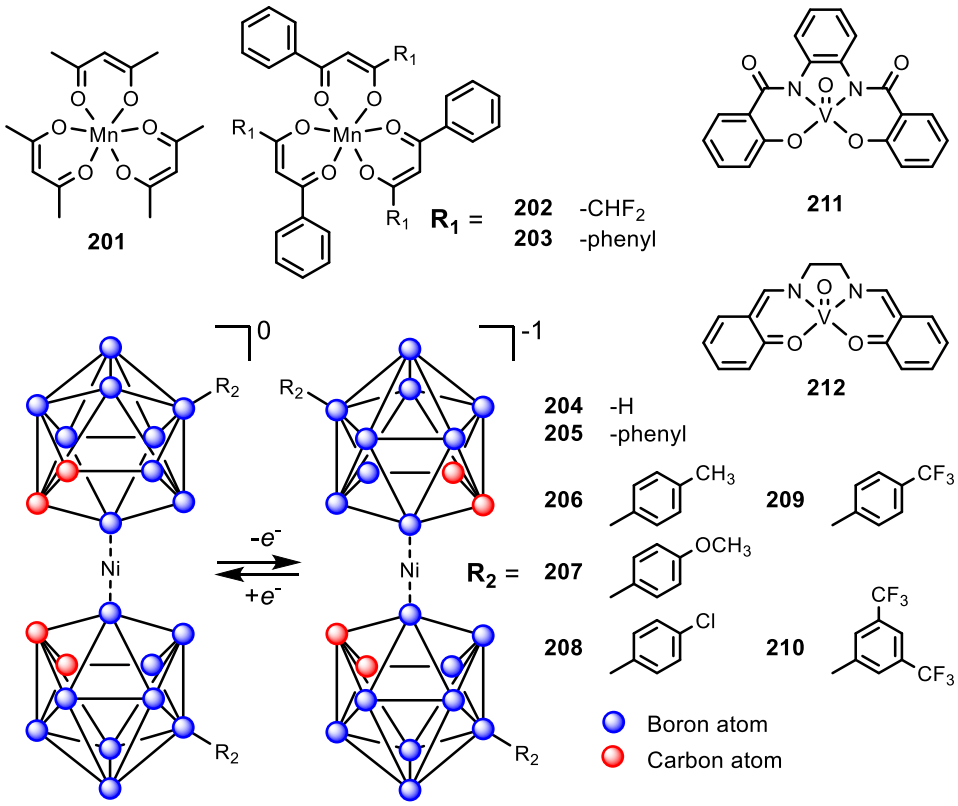

Figure 39 – Other metal-based redox couples in DSSCs.

Table 12 – Electrochemical and photophysical properties of other metal-based redox couples in DSSCs.

Redox couple	Redox potential *vs. NHE* [V]	Absorption in the visible region [M^{-1} cm^{-1}]	Suitable redox potential for NIR-DSSCs application	Ref.
201	0.49	$\varepsilon_{450} \approx 500$	Yes	327
202	0.69	$\varepsilon_{450} \approx 1\,200$	Too high	328
203	0.41	$\varepsilon_{450} \approx 1\,200$	Yes	328
204	0.48	-	Yes	330
205	0.40	-	Yes	332
206	0.38	-	Too low	332
207	0.36	-	Too low	332
209	0.44	-	Yes	332
209	0.47	-	Yes	332
210	0.54	-	Yes	332
211	-0,05	-	Too low	333
212	0.84	-	Too high	334

As expected, lowest redox potentials were obtained for the complexes with electron-donor groups and the highest redox potentials were obtained for the groups with higher electron-withdrawing effect. In conjunction with dye *N719*, Ni-bis(dicarbolide) mediators achieved PCEs between 0.7-2.0%, with the best efficiency achieved by **206**.

Finally, other interesting results have been obtained by the application of vanadium-based mediators. Apostolopoulou *et al.* reported the first application of vanadium-based mediator by using the oxovanadium(IV) reversible redox couple **211** with the tetradentate diaminodiphenolate ligand (*hybeb*).[333] Mediator **211** has a fast self-exchange rate providing high dye regeneration rate but unfortunately, it has a very low redox potential of -0.05 *vs*. *NHE* leading to an overall very low V_{OC} in device. Redox couples **211** in conjunction with dye *N719* achieved a poor PCE of 2%. In addition, mediator **211** is very sensitive to the water-content in the electrolyte even in trace, complicating the manufacturing of the device. Starting from this interesting result, Oyaizu, *et al.* improved the performance of DSSCs with vanadium-based electrolytes by introducing mediator **212** with salicylideneiminate ligand (*salen*).[334] Vanadium-based mediator **212** has a redox potential of 0.8 V *vs*. *NHE* and a fast electron exchange rate, resulting in a PCE of 5.4%, the highest efficiency between the mediators based-on other transitional metals.

3.2. Organic redox couple

Next to the metal-based redox couples, purely organic redox mediators represent an important sake for the application in selective NIR-DSSC to achieve colorless devices and overcome the limitations displayed by the metal-based redox couples in terms of more transparency and improved sustainability compared to transition metal complexes. Organic-based redox molecules are generally easier to synthesize and recycle. It can take advantage of relatively cheap starting materials and fewer synthetic steps, thus resulting in more cost-effective and sustainable redox mediators.[274]

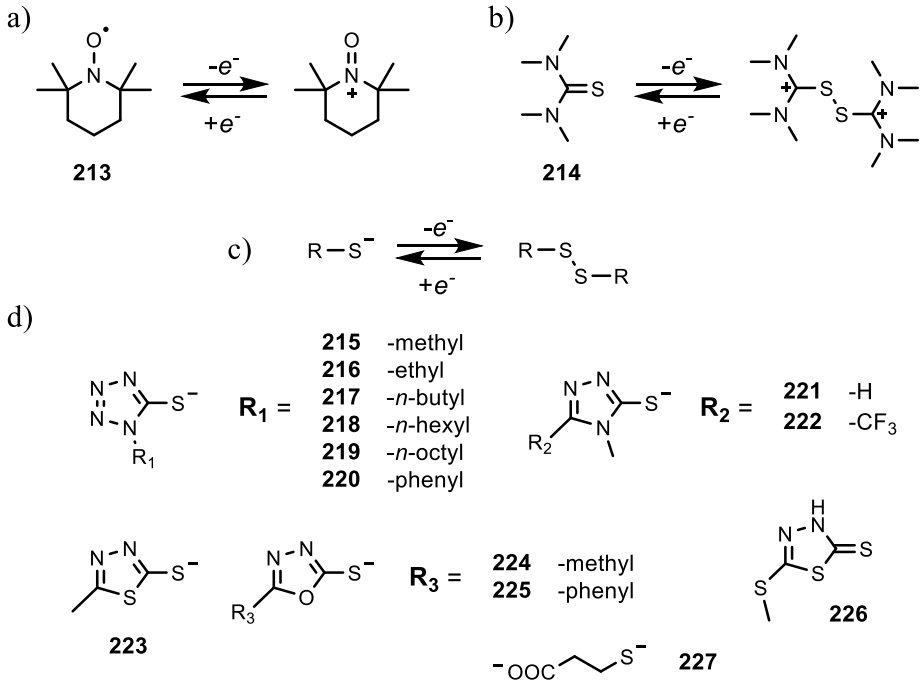

Figure 40 – a) Structure of TEMPO redox couple **213** and its oxidation process. b) Structure of TMTU redox couple **214** and its oxidation process. c) General oxidation process of disulfide/thiolate-based redox couples. d) Disulfide/thiolate-based mediators in DSSCs.

Table 13 – Redox potentials of fully-organic redox couples in DSSCs.

Redox couple	Redox potential *vs*. *NHE* [V]	Suitable redox potential for NIR-DSSCs application	Ref.
213	0.80	Too high	335
214	0.53	Yes	336
215	0.48	Yes	337
216	0.48	Yes	338
217	0.48	Yes	339
218	0.48	Yes	339
219	0.48	Yes	339
220	0.53	Yes	340
221	0.12	Too low	341
222	0.50	Yes	342
223	0.15	Too low	343
224	0.25	Too low	344
225	0.37	Too low	344
226	0.47	Yes	345
227	0.72	Too high	346

The first application of an organic redox couple in DSSCs was reported by Grätzel *et al.* in 2008 using the 2,2,6,6-tetramethylpiperidine-1-oxyl (TEMPO) **213** (Fig. 40) achieving a PCE of 5.4%.[335] TEMPO is a radical-type redox mediator which involves a fast one-electron process at 0.80 V *vs*. *NHE* (Tab. 13). This type of radical redox couple affords to have transparent electrolyte and optimally limits internal energy losses as it has no reorganization energy while displaying all the features of a very rapid redox system. It has a greater diffusion coefficient, between 10^{-5} to 10^{-4} cm^2 s^{-1} compared to less than 10^{-5} cm^2 s^{-1} for the metal-based redox couples.[248] Unfortunately, TEMPO-based electrolytes are penalized by faster nongeminate recombination and well-known instability of the oxidized $TEMPO^+$, which affects not only the device performance and stability but also limiting the application of this type of redox mediators. In addition, TEMPO-based mediators have very high redox potentials between 0.7-1.1 V *vs*. *NHE*, make them unusable for NIR-DSSCs.[29]

Alongside nitrosyl-based couples, disulfide/thiourea and disulfide/thiolate-based redox couples are highly interesting in NIR-DSSCs since their redox potential is sufficiently more positive than the HOMO energy level of most common NIR sensitizers. Li *et al.* reported the first example of disulfide-based mediators applying non-corrosive electrolyte based on tetramethyl thiourea (TMTU) **214**.[336] TMTU and its oxidized counterpart are completely colorless and highly soluble in common organic solvents. **214** has a two-electron redox process to lead to the disulfide bridge formation for the oxidized species with a reversible redox potential at 0.53 V *vs*. *NHE*. This different feature leads to the formation of electronic interstates resulting in higher reorganization energies. Compared to iodine-based electrolyte, disulfide-base mediators have a lower activity with Pt-based counter electrodes. For these reasons the development of new materials is required for the efficient application of these colorless organic mediators. Closely related to TMTU behavior, disulfide/thiolate redox couple are another interesting class of fully-organic mediators. Compared to TMTU system, this class has the same negligible absorption in the visible range and has an easier tunability

of the redox potentials. Over the years, several disulfide-based redox couples have been developed based on tetrazole (**215**-**220**),[337-340] triazole (**221**-**222**),[341,342] thiadiazole (**223**),[343] oxadiazole (**224**-**225**),[344] thiadiazole-thione (**226**)[345] and thiopropionic acid (**227**).[346]

Among all the fully-organic redox couples reported in literature, mediators **216** and **220** have been interestingly applied in combination with fully transparent counter electrode based on Poly(3,4-ethylenedioxythiophene) (PEDOT) and nickel sulfide, achieving PCEs above 6% in association with dye *N719*, respectively.[338,347]

4. Fully Transparent Counter Electrode

The counter electrode is the last important component of DSSCs and play a key-role in the regeneration of the reduced form of the redox mediator as well as to close the photoelectrochemical cell circuit. The features of the counter electrodes influence the device performance, in particular fill factor well describe the counter electrodes behaviour. Generally, counter electrode is formed by FTO glass support coated by a nanolayer of catalyst to reduce the charge transfer resistance. The type of electrocatalyst strongly depends on the redox couple used in the electrolyte solution. Ideal counter electrode required electrocatalyst with: (i) high electrochemical catalytic activity able to guarantee an efficient reduction process as well as to avoid electrode polarization, (ii) chemical stability with respect to the electrolyte components and (iii) high thermal- and photostability.[348-351] Alongside these features, in NIR-DSSCs the counter electrode also requires a high level of transparency which can be achieved either by an ultrathin electrocatalyst layer or via a transparent conducting material.

In classical DSSCs, platinum coated FTO glass is the most employed counter electrode so far due to its best electrocatalytic activity to reduce the triiodide to iodide. However, is affected by corrosion in presence of iodine-based electrolytes, in particular with formulations without guanidinium thiocyanate.[352]

Platinum-based counter electrodes are usually prepared by the deposition of a nanometric/sub-nanometric layer of platinum exploiting the screen-printing or drop-casting techniques.[353,354] Usually, classical platinum-based counter electrodes display relatively high optical reflectance, enhancing the light confinement in the device and thus raising the harvesting of incident light. However, this feature is detrimental for NIR-DSSCs application, negatively affecting the transparency of devices.

As mentioned before, the thickness of the electrocatalyst layer is one of the main strategies to control the aesthetic features of counter electrodes.[350] For platinum-based CEs, Otaka *et al.* demonstrated as a Pt-layer with a thickness of only 0.5 nm provides a very good transmittance in the visible region without any negative impact on the photovoltaic performance, displaying appealing features for NIR-DSSCs.[355] Alternative strategy toward fully transparent CEs is the selection of new materials as electrocatalysts with intrinsic high visible transmittance. However, it is important to emphasize that both transmittance and sheet resistance feature strictly depend by the deposition techniques and the conditions of the thermal post-treatments applied in the manufacturing of the CEs.[350] Among alternatives to platinum, carbonaceous materials,[356,357] conducting polymers,[358] and metal oxides, sulfides or selenides,[359] can provide excellent catalytic properties while remaining low cost and sustainable (except for the Co-based ones). However, most of them do not comply with the transparency standard required for NIR-DSSCs application.

Over the years, some interesting examples of fully transparent counter electrodes have been reported in literature (Tab. 14). In the following section will be briefly discuss the main advantages and drawbacks of different materials used in these fully transparent CEs.

Among carbonaceous materials, the graphene and the reduced graphene oxide (rGO) exhibit very interesting features, combining excellent electrical and thermal conductivity with high optical transparency at the sub-nanometer thickness.[356,357] However, the deposition of graphene sheets onto FTO glass

remains challenging. In addition, the preparation of multi-sheets layers (with more than 4-5 sheets) to raise the electrocatalyst activity of the CE strongly decrease both its transmittance and conductivity.[357]

Conductive polymers are an incredibly wide category of materials which play a key-role in many photovoltaic applications such as PSCs and OSCs. However, in the last years conductive polymers finding interesting application also in DSSCs due to their good catalytic activity, excellent stability, and ease of tuning their properties through simple synthetic modifications.[358] However, conductive polymers have an intrinsic higher surface resistivity and a lower catalytic activity, resulting in the necessity to increase them to the detriment of the transparency of the counter electrode. In particular, the improvement of catalytic activity can be achieved raising the thickness of the polymeric film while the surface resistivity can be decreased by doping.[358]

Table 14 – Different transparent counter-electrodes with transmittance > 75% that could be suitable for the application in NIR-DSSCs.

Material	Transmittance	Electrolyte	PCE [%]	Ref.
rGO	81%	I_3^-/I^-	3.6	360
Graphene	85%	I_3^-/I^-	2.3	361
CoS	80%	I_3^-/I^-	8.5	362
NiS	82%	I_3^-/I^-	7.4	363
NiSe	88%	I_3^-/I^-	8.0	364
FeSe	78%	I_3^-/I^-	9.2	365
MoS_2	79%	I_3^-/I^-	7.4	366
$Mo_{0.6}Se$	85%	I_3^-/I^-	8.0	365
CuSe	100%	I_3^-/I^-	6.0	367
$Cu_{2-x}Se$@N-doped	83%	Co-based	7.6	368

An interesting alternative has been proposed by Grätzel *et al.* in 2009 by the introduction off a new class of counter electrode based on transition metal materials like sulfides, selenides, phosphides, nitrides, carbides and oxides.[359] Sulfides, selenides and oxide are the most widely investigated alternative electrocatalysts as being easily synthesizable even for large areas together with

being thermally, chemically, and electrochemically robust whereas nitrides and carbides usually exhibit very good electrocatalytic activity, especially with I_3^-/I^- redox couple, although they are less robust than their oxide- and sulfur-based counterpart.

As presented by Grifoni *et al.*, the absence of literature about the coupling of transparent CE and alternative redox mediator prevents to draw very specific conclusions. The absence of literature about the coupling of transparent CE and alternative redox mediator prevents us to draw very specific conclusions. Indeed, each redox mediator has its own electrochemistry and the CE should be tailored to assure the highest electrocatalytic behaviour and the longest longevity. Among the different materials proposed, the most promising results have been obtained with carbon-based materials, especially graphene and its derivatives. They have also been proven to work properly with Co-based redox systems. However, importantly for the NIR-DSSC application, they often required a trade-off between transparency and catalytic activity. Very promising results have also been obtained with sulfide-based and selenide-based CE. The beneficial effect assured by their good catalytic properties with respect to conventional I_3^-/I^- based electrolyte combined to high optical transmittance could be jeopardized by stability issues when organic-based redox mediators are used. In the case of sulfide/thiolate redox couple, one should consider that the reduced species of the electrolyte could irreversibly bind on the CE surface leading to a dramatic decrease in cell performances. Similar issue could arise from the implementation of a metal based redox system, especially if they are based on atom with good affinity with sulfur or selenium, as copper, iron, and cobalt.[29]

5. Anti-Reflective Coatings for NIR-DSSC

In the previous paragraphs all the necessary requirements for each component to the creation of an efficient NIR-DSSC have been reported. However, to achieve the specifications in terms of transparency, the introduction

of Anti-Reflective Coatings (ARCs) on the external surface of device it's necessary. The ARCs allow to reduce optical losses due to the reflection phenomena owing to refractive index (RI) mismatch between glass (n_{glass} ≈ 1.52) and air (n_{air} = 1.00) accordingly with Fresnel's law (equation 3).[369]

$$R = \left|\frac{1 - n_{glass}}{1 + n_{glass}}\right|^2 \qquad (3)$$

The corresponding reflection in contact with air is 4.3% per interface, resulting in a total optical loss of 8.6% only by light reflection only considering the two external interfaces. However, same consideration but with different values of reflection loss will be apply for each interface inside the device: (i) FTO glass/electrolyte, (ii) TiO_2/electrolyte, (iii) FTO glass/TiO_2, (iv) counter electrode/electrolyte.[29]

ARC usually is a submicrometric thickness layer able to tone down the refractive index change between the air and the FTO glass, reducing the reflection phenomena and thus increasing the device's AVT and the PCE. Typically, ARCs can reduce the reflection per interface down to 1% level, thus increasing the transmission by 7-8%. The ARCs can be classified in three main categories: (i) the single-layer (SLARC), (ii) the multilayers (MLARC), and (iii) "moth-eye".[370] Obviously, as mentioned before for the semiconductor layer, even in ARC its necessary avoid any film's defect with a diameter in the range of the incident wavelengths to avoid the detrimental light scattering accordingly to Mie-scattering theory.

SLARC is a layer with controlled thickness and RI value between the air's RI and glass' ones. The SLARC's RI mainly depend by the chemical nature of the material but can be further tuned by the carefully fabrication of the layer's structure (Fig. 41). For a SLARC, the total thickness (*d*) is crucial to obtain destructive interferences between the reflected light between air/ARC interface and ARC/ glass interface. For this reason, a so-called "quarter-wave" layer is needed (equation 4).

$$n_{ARC} \times d = \frac{\lambda}{4} \qquad (4)$$

The simplification of Fresnel equation for the air/ARC interface allows the easy calculation of the best ARC refractive index to reduce light reflection following the equation 5.

$$n_{ARC} = \sqrt{n_{air} \times n_{sub}} \qquad (5)$$

Applying the above-mentioned equations in the case of NIR-DSSCs, an efficient SLARC can be designed with a material exhibiting a refractive index of 1.23 and a thickness of 114 nm.[29,370,371]

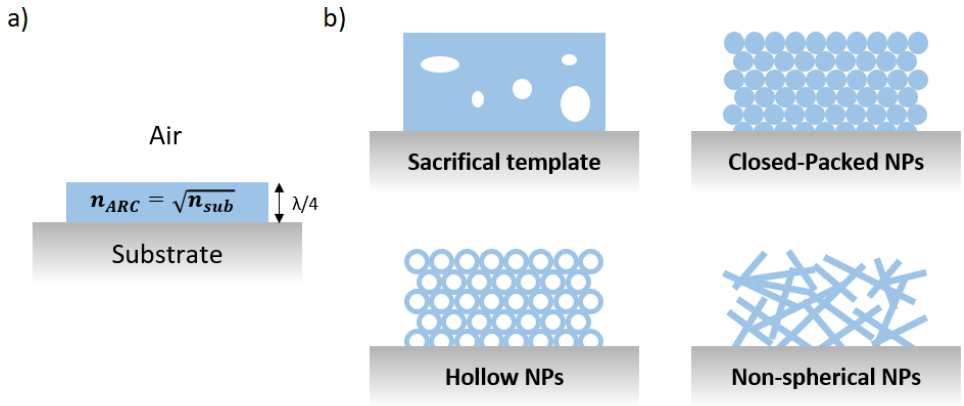

Figure 41 – a) Schematic illustration of "quarter-wave" SLARC. b) Schematic illustration of different structure morphologies of SLARC layer.

MLARC consist of a periodic multilayer quarter-wave coating or a multilayer stacking of materials with different refractive indexes (Fig. 42a). In the simplest quarter-quarter stack design, the external layer is made with a lower refractive index material in comparison with the internal layer in contact with the substrate. The optimal refractive index for these two layers can be calculated for a specific wavelength following the equation 6 in which n_L and n_U are the RI of the lower and the upper quarter-wave coatings, respectively.[372]

$$\frac{1}{n_{sub}} = \left(\frac{n_U}{n_L}\right)^2 \qquad (6)$$

However, to minimize the reflection on a broader wavelength range, an evolution of MLARC has been developed: the Broad Band Anti-Reflective Coating (BBARC) Contrarily to MLARC, BBARC has an additional third layer called "absentee layer" (n_2) composed of a dielectric material with a thickness equal to λ/2, inserted between the two quarter-wave layers (n_1 and n_3) (Fig. 42b). Based on Fresnel's theory, the continuous transition of refractive index from 1 to 1.5 is mandatory to achieve BBARC from visible to NIR range.[372]

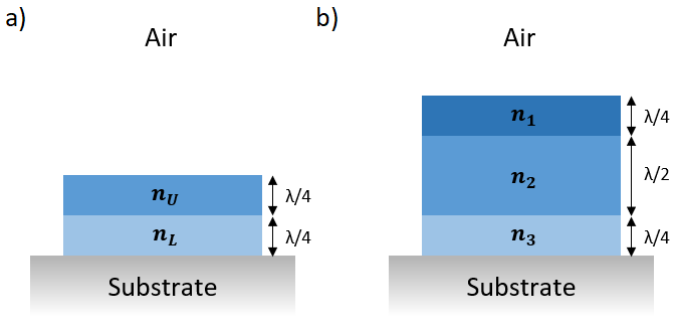

Figure 42 – a) Schematic illustration of MLARC with quarter-quarter stack design. b) Schematic illustration BBARC coating.

Finally, the third design of ARCs is the "moth-eyes" like texture which is able to limit the reflection phenomena due to the presence of a spatially ordered array of sub-micrometric dots (Fig. 43). This strategy is based on the formation of a periodic framework with several types of geometry, such as nanohemisphere, cones, and pyramidal, directly on the glass substrate.

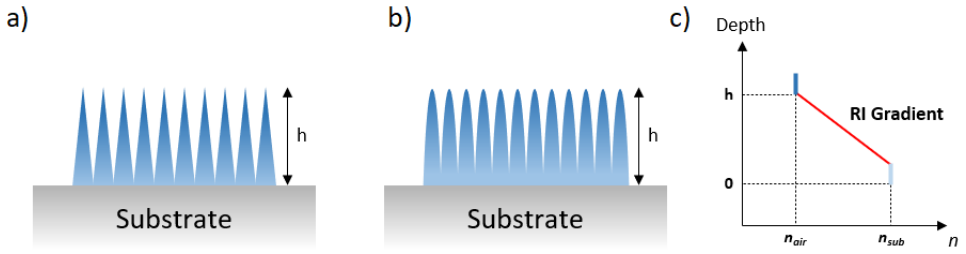

Figure 43 – Schematic illustration of a) cones-based and b) nanohemisphere-based "moth-eyes" like textures. c) Schematic illustration of gradient variation of RI. The slope of the RI gradient (in red) depends by the types of geometry used in the periodic framework.

When incident light penetrates the ordered lattice, the refractive index progressively enhances due to the increased volume ratio of material/air with depth. The geometric profile of the “dots” directly determines the refractive index gradient profile which can be tuned by the selection of different types of geometry.[373]

As mentioned before, the refractive index of ARCs mainly depends by the material used for their fabrication. Over the years, several examples of ARCs are reported in literature with polymer-based materials, inorganic compounds, or a mix of these two. In particular, polymers-based film have been widely discussed due to their relatively easy processability, low cost, flexibility and their tunable refractive indexes.[370,373-379]

Regardless of the transparency gain achieved by the application of ARCs in DSSCs, their use unfortunately displays two main drawbacks. In polymer-based and nanotextured ARCs, the mechanical strength and durability versus external conditions such as solar irradiation are important issues. In addition, complex multi-layer or nanotextured structures require multistep process for their preparation, raising the final cost of devices. For these reasons, considering the fabrication of efficient NIR-DSSCs as well as the possible future industrialization of the classic visible-DSSCs, it’s necessary the development of ARCs with a good compromise between high anti-reflective efficiency and low-cost production to be easily applicable in large-scale production.

CHAPTER 2 – Extended-rylene as NIR Sensitizers for NIR-DSSCs

As mentioned in Chapter 1, phthalocyanine and polymethine dyes are the only two families of sensitizers could be interesting for the fabrication of NIR-DSSCs. However, both of them present not negligible drawbacks like the worst photophysical properties and the lower tunability displayed by the phthalocyanines, as well as the intrinsic low photostability of the polymethine dyes. For these reasons, in the context of the IMPRESSIVE research project it has been decided to sieve the literature to understand if there was the possibility to develop a new class of NIR sensitizers or the possibility to modify an already existing one to fulfill the requirement needed.

Among the several types of sensitizers applied in classic DSSCs over the years, the perylene tetracarboxylic diimides (PDIs) (Fig. 44) caught our attention due to their: (i) remarkable photophysical properties,[380,381] (ii) their outstanding conductive behaviour,[382,383] (iii) exceptional chemical, thermal and photostability[380-385] in (iv) combination with the possibility to easily tune their optical and physical properties.[381,386-393].

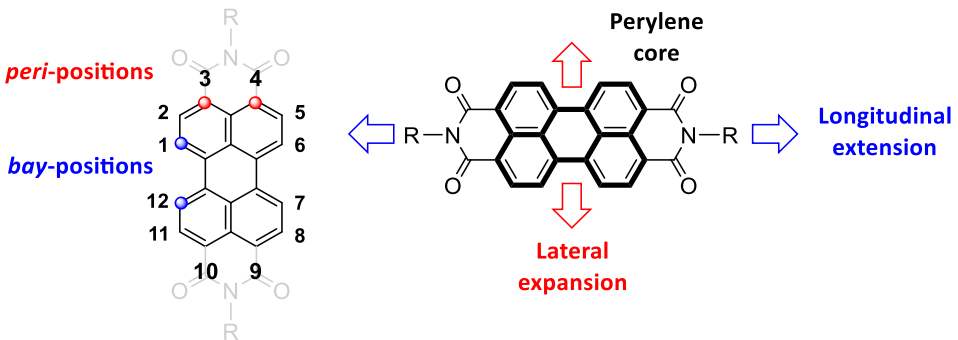

Figure 44 – Structure of PDI with the schematic illustration of the possible strategies to modify the perylene-core.

Over their application as sensitizer in DSSCs, their properties have been also widely exploited in fully-organic solar cells (OSCs),[16,47,394-396] in organic field-effect transistors (OFETs) technologies[397] and in bioimaging applications.[398,399]

Unfortunately, PDIs are not suitable for NIR-DSSCs application due to their strong visible absorption with maxima at ca. 525 nm and molar extinction coefficients approaching 10^5 M^{-1} cm^{-1}. In addition, PDIs exhibiting very strongly fluorescence emission with quantum yield approaching 100%.[384] However, even if the PDIs are completely useless for the IMPRESSIVE project purpose, they caught our attention due to the possibility to modify their structure to obtain the so-called "extended-rylene" dyes (Fig. 45a), well-known for their outstanding stability and their strong absorption in the NIR-region. It has been demonstrated that the longitudinal extension of the rylene-core (Fig. 44), gradually moves of ca. 100 nm the maximum absorption toward the NIR region for each unit of naphthalene added (Fig. 45b). Moreover, even molar extinction coefficients dramatically raise from $5 \cdot 10^4$ M^{-1} cm^{-1} up to $2.5 \cdot 10^5$ M^{-1} cm^{-1} (Fig. 45c).[388,390,400]

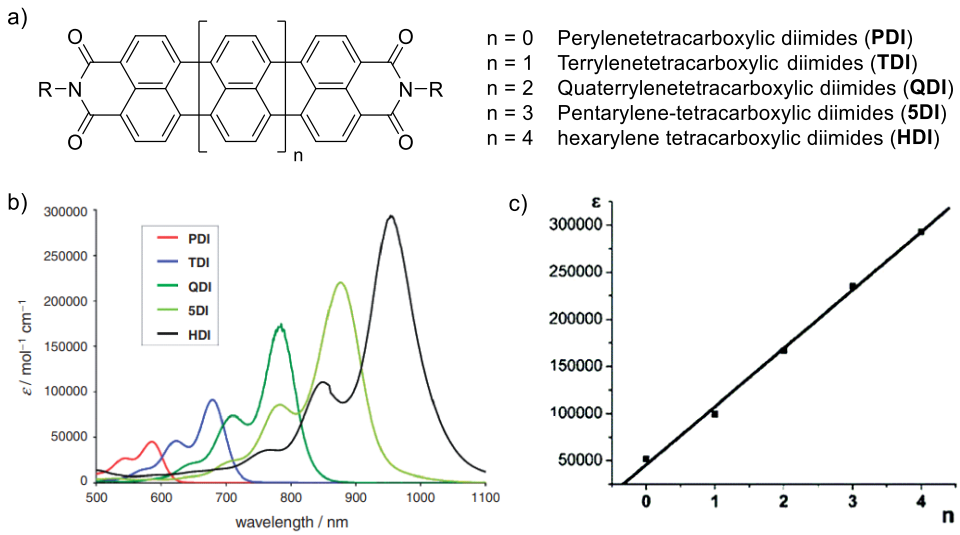

Figure 45 – a) Schematic illustration of longitudinally-extended rylene diimides. b) Comparison of absorption spectra of extended-rylene diimides. c) Correlation between the number of naphthalene units and the molar extinction coefficient in extend-rylenes.[388,400]

Beside to the bathochromic shift of the absorption, the longitudinal extension of rylene-core unfortunately causes the detrimental increase of the intramolecular π-π stacking, dramatically reducing the solubility of extended-

rylenes. Obviously, these features make the synthesis, processing, and characterization of this class of materials rather difficult.[388] In addition, will be reported in this chapter as also the fabrication and the photovoltaic performances of the DSSCs will be affected by the above-mentioned features.

Before to discuss the results achieved in this first part of research project, will be provide an overview on the main synthetic strategies to modify the PDIs and following, will be give an overview on the state-of-art of PDIs as sensitizers in classic DSSCs, highlighting the relationship between the dye-structure development and the PCEs improvement to furnish a useful "instruction manual" for the design of new NIR extended-rylene dyes.

1. Synthesis and Structural Modifications of PDIs

The PDIs chemistry starting in 1912 in the colorants industry when perylene-3,4,9,10-tetracarboxylic dianhydride (PTCDA) **228** has been synthetized for the first time. PTCDA is a red pigment and it is the pivotal starting material for the synthesis of all perylene imides derivatives.[380,401] PTCDA is a red pigment and it is the pivotal starting material for the synthesis of all perylene imides derivatives (Fig. 46). The imidization (**228**→**229**) has been the first modification performed on PTCDA to obtain the PDIs such as *Pigment Red 179* and *Pigment Red 149* (see Appendix). This approach led to the development of high-performance industrial pigments.[380,402] These molecules are insoluble in most organic solvents as many pigments, therefore to improve their solubility alkyl or aryl substituents at the PDI's imide positions have been exploited.[387] Long branched alkyl chains or ortho-substituted aryl groups are particularly effective solubilizers because they are forced out of the PDI-structure's plane preventing the π-π stacking.[387,403,404] The solubility of these bulky-substituted PDIs is good in halogenated solvents such as dichloromethane, chloroform and aryl halide. Contrarily, PDIs show a very poor solubility in polar solvents such as alcohols and water therefore these solvents are often exploited to precipitate and collect the desired product.

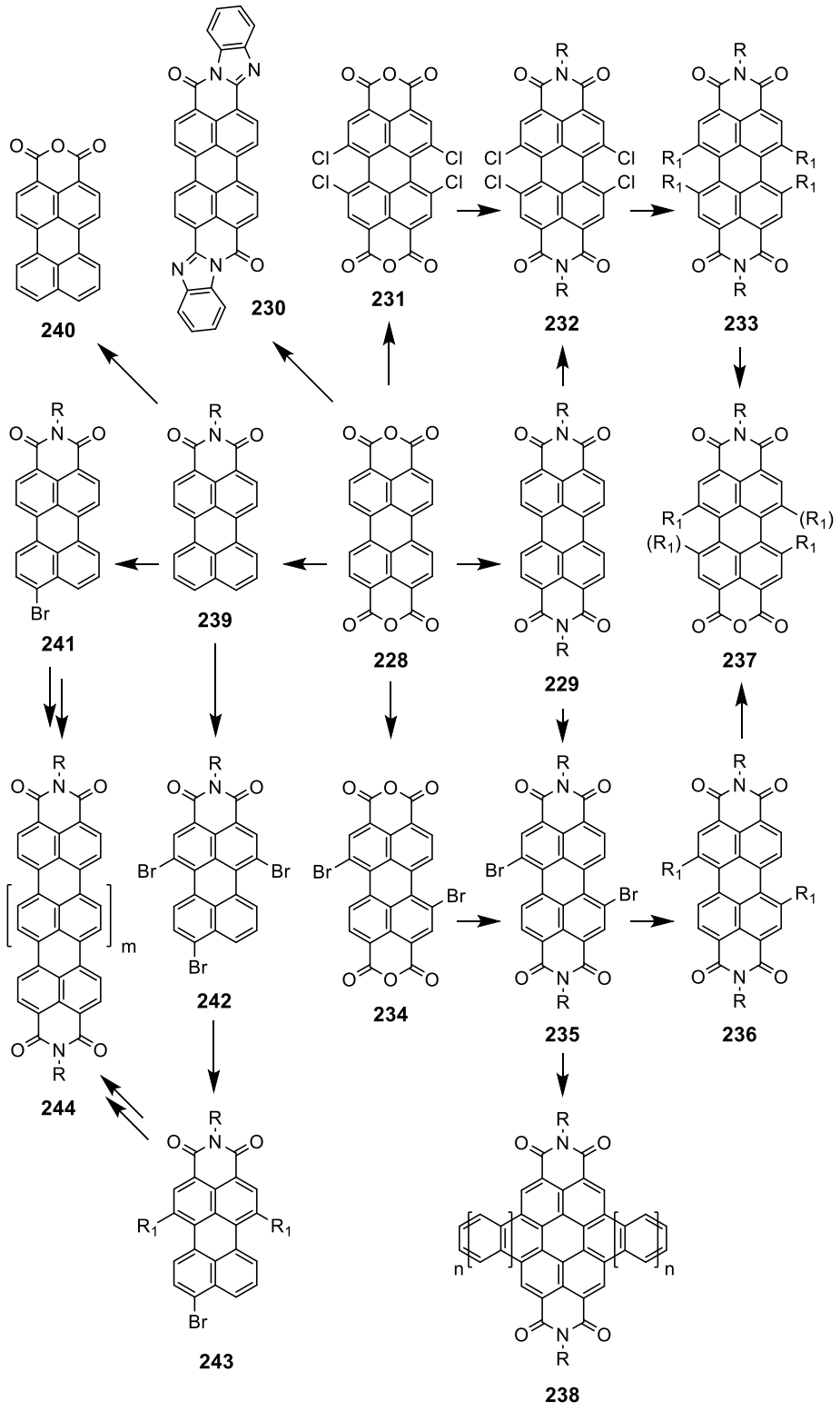

Figure 46 – Synthesis and modification of PDIs derivatives.

PDIs (**229**) are commonly synthetized by the condensation reaction of PTCDA (**228**) with aniline or aliphatic primary amine at high temperature (> 160 °C) in high-melting solvents such as imidazole or quinoline with zinc acetate as catalyst. This synthetic approach allows large scale production with high yields (> 80%) and usually the product purification is relatively easy.[381,387,391]

Solubility and supramolecular interactions can be tuned by different functionalization of the imide positions, but any variation on these sites is not sufficient to modify the other fundamental properties of the PDIs such as absorption, fluorescence and HOMO/LUMO energies. However, photophysical properties can be improved by imidization of PTCDA (**228**) with aromatic amines decorated with an adjacent amino group (**228**→**230**). The extension of the aromatic system in perylene tetracarboxylic acid dibenzimidazole (**230**) lead to a dramatic bathochromic shift and higher molar extinction coefficients than a classic PDI (**229**).[389]

The great breakthrough for properties manipulation of PDIs derivatives was the discovery of a synthetic pathway to halogenate PTCDA.[405] As a consequence of the reactivity of the PTCDA, the electrophilic aromatic substitution occurs selectively at the bay positions.

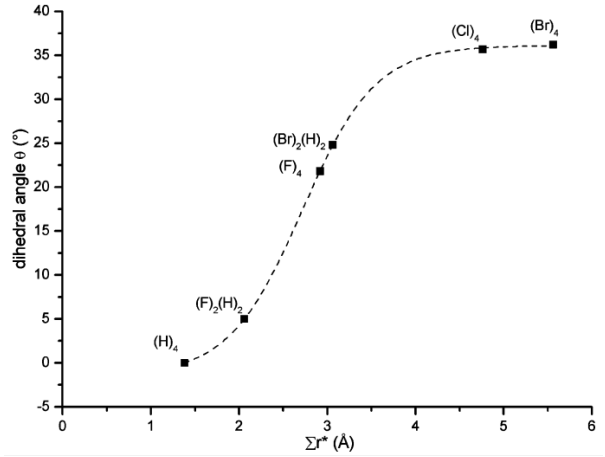

Figure 47 – Dependence of the dihedral angle and the apparent overlap for different halogen-substituted PDIs (substituents with numbers are given). The reported values are the average of the two dihedral angles.

The halogenation of perylene core always led to the distortion of the originally planar structure as reported by Würthner *et al.* The dihedral angle in the bay area increases with the number and size of halogen atoms (Fig. 47).[406]

Tetrachlorinated PTCDA (**231**) is commonly synthetized from PTCDA (**228**) by electrophilic substitution with chlorosulfonic acid and a catalytic amount of iodine at 70 °C for 20 h. This procedure leads almost to a quantitative yield but a slightly amount of penta-chlorinated side-product can be found.[407] Same procedure can be used to chlorinate PDIs to relative tetra-chlorinated derivative (**229**→**232**).[408] Dibrominated PTCDA (**234**) is usually synthetized according to the procedure developed by *BASF*. PTCDA (**228**) is treated with bromine in fuming sulfuric acid at high temperature (> 80 °C) for 18 h.[409] This reaction lead to a regioisomers mixture of 1,7-dibrominated-PTCDA and 1,6-dibrominated-PTCDA along with a tribrominated derivative in a ratio of 76:20:4. The total insolubility of these compounds does not allow their separation which is carried out later on the more soluble imidized products.[410] The common imidization procedure of halogenated PTCDAs (**231**→**232** and **234**→**235**) employs *N*-Methyl-2-pyrrolidone (NMP) as solvent and a catalytic amount of acetic or propionic acid. Imidization procedures with aromatic amines usually requires higher temperatures and prolonged time than imidization with primary alkyl amines.[391] Dibrominated-PDIs (**7**) can be obtained also with a mild bromination of unsubstituted PDI (**2**) with bromine in chloroform and the resulting regioisomers mixture can be purified by repetitive crystallization.[411]

The halogenated PDIs (**232** and **235**) pave the way to further solubility improvements and to tune the properties by functionalization of the bay positions (**233** and **236**). Traditional nucleophilic substitution as well as metal-catalysed coupling reaction, such as Suzuki, Stille, Sonogashira and Heck coupling are just some of the possible exploitable reactions.[391] The bay-functionalization with phenols, thiophenols and alcohols allow to red-shift the absorption maximum of a few tens of nanometres preserving an intensive fluorescence. Whereas amines substituents lead to a huge maximum red-shift but they reduce

considerably the fluorescence property and the photostability.[381,384,412] Furthermore, dibrominated PDI (**235**) is the key building block for the lateral extension of the perylene core. Lateral extended PDIs (**238**), such as coronene diimide (n = 0) and dibenzo coronene diimide (n = 1) (Fig. 46), can be synthetized coupling various 1-alkynes by Sonogashira reaction to obtain the substituted PDIs which are subsequently treated with 1,8-diazabicyclo[5.4.0]undec-7-ene (DBU) to promote the aromatization.[389,390]

As seen in Chapter 1, a strong anchoring group is a crucial characteristic of an efficient sensitizer for DSSC application. The best anchoring moiety in perylene imides derivatives is the anhydride group.[82]

The substituents in the imide positions improve the solubility s facilitating both synthetic and purification processes. Therefore, the hydrolysis of the imide group to the corresponding anhydride group is always the last synthetic step. The hydrolysed derivatives (**237** and **240**) can be obtained by a two steps procedure: the imide group hydrolyse to the corresponding salified diester with KOH in *tert*-butanol, the resulting product is refluxed in acidic condition to prepare the closing dianhydride moiety.[381]

The poor push-pull effect of the PDIs derivatives does not allow to achieve the high photovoltaic performance. Despite the possibility to give a partial push-pull effect adding strong donor groups in the bay position, these modifications are not sufficient to reach the desired requirements. Perylene monoimide derivatives (**239**) are the key structures to achieve the desired push-pull effect. Compared to the imidization process of PTCDA (**228**→**229**) already known in the 1910s, the first synthesis of perylene monoimide derivative dates back to 1980s.[413,414] The breakthrough for the synthesis of monoimide derivatives was the discovery of a single-step procedure reported by Langhals *et al.*[415] The procedure (**228**→**239**) provides the mono-imidization of PTCDA with the desired amine and zinc acetate as catalyst. Imidazole and a small amount of water are used as solvent. The reaction is carried out in autoclave due to the required high temperature (180-190 °C), long reaction-time (almost one day) and an optimal

pressure of 15 bar. Reactions with hindered aromatic amines such as 2,5-di-*tert*-butylphenylamine or 2,6-di-*iso*-propilphenylamine lead to the desired products in better yield (almost 50%) than reactions whit aliphatic amines (< 30%).[415,416]

Perylene monoamide (**239**) could be selectively brominated in 9-position (**241**) in chloroform at low temperature or treated in harsher condition (60 °C) to yield the tri-brominated derivative (**242**).[417,418] These derivatives are outstanding and versatile building blocks. The bromine in *peri*-position is usually exploited to attach strong donor group by metal-catalysed coupling reactions, such as Suzuki-Miyaura, Stille, Sonogashira and Buchwald-Hartwig, while both bromine in the *bay*-positions are useful to selectively attach bulky substituents such as phenol, thiophenol or triphenylamine. Obviously, the selective functionalization occurs with poor yields generally lower than 35%.[388]

Perylene monoimide is also a key building block for the longitudinal extension of the perylene core. High rylene diimides such as terrylene diimide (TDI) (m = 1), quaterrylene diimide (QDI) (m = 2), pentarylene diimide (5DI) (m = 3) and hexarylene diimide (HDI) (m = 4) (Fig. 46), have excellent photophysical properties but very poor solubility in many organic solvents. The longitudinal extension requires always a multi-step procedure (**241** or **243**→**244**): (i) a coupling reaction between two properly functionalized perylene monoimide lead to a twisting structure, (ii) a cyclization by dehydrogenation lead to the fully aromatized structure.[390,419]

π-extended heteroarenes containing nitrogen or chalcogens in fused aromatic rings are deeply investigate for their optoelectronic properties and their potential application in organic field-effect transistors (OFETs), light emitting diodes (LEDs) and photovoltaic devices.[420] *N*-annulated perylene (NAPs) derivatives are one of the most important classes of π-extended heteroarenes and over the years they have been successfully employed in DSSCs (Fig. 48). The electron-rich nature of *N*-annulated perylene makes it an ideal electron donor that can be further easily functionalized. However, structural modification of NAPs doesn't allow to shift enough the absorption toward the NIR region and for this reason it has been

decided to focus the attention only on extended-rylenes for the development of new NIR-sensitizers for NIR-DSSC application.

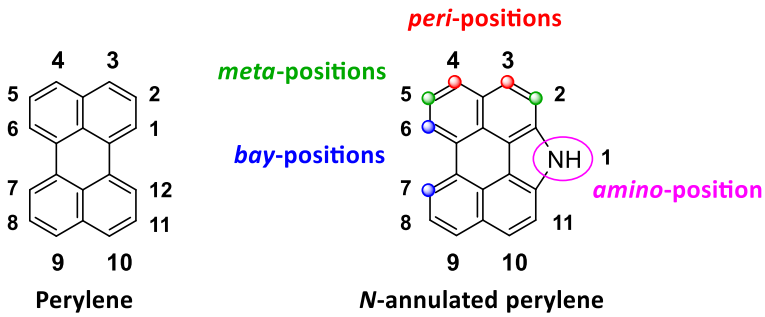

Figure 48 – Comparison between the structures of perylene and *N*-annulated perylene.

2. PDIs as Sensitizers in DSSCs

Perylene-based dyes were introduced as sensitizes for the first time in 1996 when an electron injection rate of 190 fs was discovered for 2,5-bis(*tert*-butyl)-9-methylphosphonic acid perylene (*PE dye*) (see Appendix) adsorbed on nanocrystalline TiO_2.[421] This brilliant result confirmed the versatility of perylene derivatives: their high emission can facilitate the time-related emission experiments used to measure charge injection rates opening up the development of perylene dyes in dye-sensitized solar cells.

The first ever photovoltaic application of rylene-based dyes began with the sensitization of **245**-**247** onto SnO_2 (Fig. 49).[422] The sensitizers were deposited on a 2.5 µm thick nanoporous SnO_2 film on FTO glass through their carboxylic acid groups. DSSC with sensitizer **246** achieved a maximum IPCE of approximately 30% between 460 nm and 490 nm, and an overall PCE of 0.89% was achieved (Tab. 15). In the same work the relevance of the position of anchoring groups has been demonstrated. Indeed dye **247**, holding the carboxylic acid groups on the phenyl ring, strongly adsorbed onto SnO_2 and it shows similar spectral properties of **246** but exhibits a small short-circuit photocurrent density. This feature may be related to its different orientation on the surface because the phenyl ring bearing the anchoring group is perpendicularly oriented to the perylene core.[422] Although

the lower efficiency compared to the optimized ruthenium complexes-based devices, this first work opened the way to PDI-based derivatives as sensitizers in DSSCs.

To better understand the sensitizing feature of PDI derivatives, Li *et al.* studied TiO_2 nanocrystalline films sensitized by dye **246** and **248**.[423] They reported a maximum IPCE of 40% for **246** and of 14% for **248**. Moreover, for the first time it has been demonstrated in detail bromine-doping of the TiO_2 nanocrystalline film. The doping caused the decreasing of IPCE values (about a tenth compared to the untreated) while the maximum absorption was more red-shifted by approximately 20 nm compared to the non-doped films.

In the previous pioneer works, only carboxylic groups on the PDI scaffold were tested as anchoring group. However, PDIs are able to strongly interact with inorganic semiconductors, such as TiO_2, exploiting the anhydride groups on the PDI scaffold.[82] For this reason, anhydride group was deeply investigated as efficient anchoring group in PDI-based sensitizers. Icli *et al.* reported a series of PDI sensitizers **249**-**253** and tried to understand how different substituents within the imide groups of perylene monoimide monoanhydride influence the photovoltaic performance in DSSCs.[424] It has been demonstrated as dyes with longer and branched alkyl chains were able to achieve higher PCEs. Hindered alkyl chains prevent self-aggregation of the dye as well as reduced the charge recombination with the electrolyte.[60,425] Sensitizer **249** achieved the highest PCE of 1.61% (Tab. 15). Moreover, it has been demonstrated the importance of the electronic behaviour of the different substituents. Dye **252** yields about twice better efficiency compared to **253** because aromatic ring is a stronger electron donor in comparison to the cyclohexyl moiety. This effect results in better electron injection into TiO_2 conduction band for **252**.[424] The results achieved with series **249**-**253** pointed out that these sensitizers do not have an intermolecular push-pull effect since they are all lacking electron donor group: they consist only of an ordinary chromophore with an anchoring group. Therefore, the electron transfer from the sensitizer to the conduction band of the semiconductor is not efficient enough.

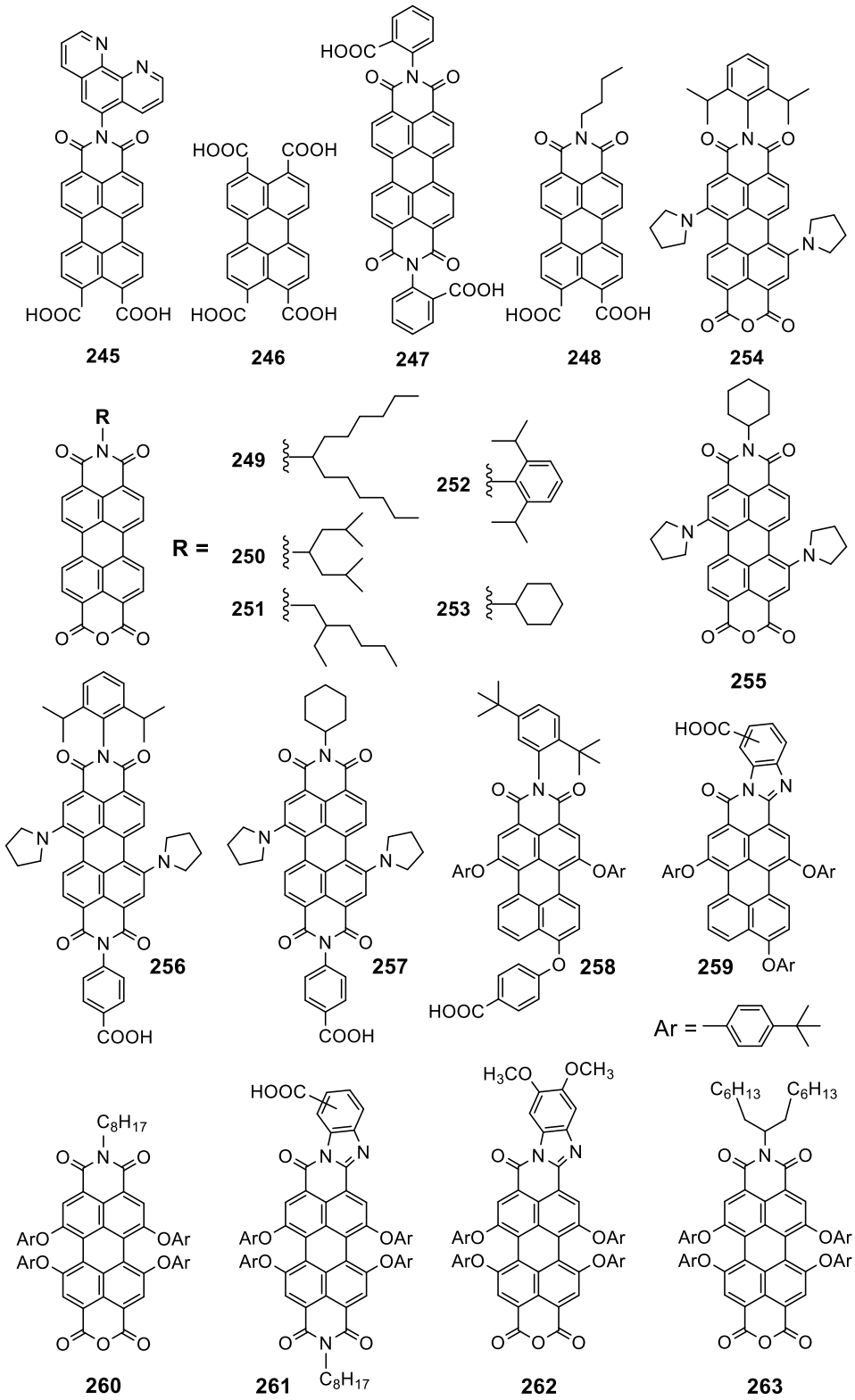

Figure 49 – First-generation of PDI-based sensitizers in DSSCs (Part 1).

Table 15 – Photovoltaic performance and photophysical properties of first-generation of PDI-based sensitizers in DSSCs.

Dye	λ_{max} (solvent) [nm]	ε [M^{-1} cm^{-1}]	J_{SC} [mA/cm^2]	V_{OC} [mV]	FF	PCE [%]	Ref.
245	479 (NMP)	-	3.26	450	0.45	0.89	422
246	480 (NMP)	-	-	-	-	-	423
247	-	-	-	-	-	-	422
248	-	-	-	-	-	-	423
249	-	-	9.79	300	0.55	1.61	424
250	-	-	8.40	300	0.46	1.16	424
251	-	-	6.73	260	0.37	0.65	424
252	524 (Toluene)	-	4.1	251	0.58	0.60	424
253	-	-	0.24	273	0.60	0.37	424
254	708 (DCM)	45 600	7.8	540	0.63	2.6	426
255	708 (DCM)	35 870	4.6	510	0.64	1.5	426
256	708 (DCM)	42 000	-	-	-	< 0,02	426
257	704 (DCM)	42 300	-	-	-	< 0,02	426
258	517 (DCM)	31 900	2.6 0.6[a]	424 440[a]	0.66 0.83[a]	0.72 0.22[a]	427
259	560 (DCM)	37 400	0.9 0.13[a]	336 369[a]	0.71 0.79[a]	0.21 0.04[a]	427
260	578 (DCM)	45 600	5.3 4.1[a]	443 520[a]	0.63 0.76[a]	1.47 1.64[a]	427
261	602 (DCM)	66 000	1.0 0.3[a]	434 461[a]	0.60 0.81[a]	0.26 0.11[a]	427
262	626 (DCM)	27 400	2.9 2.9[a]	0.401 456[a]	0.65 0.71[a]	0.76 0.96[a]	427
263	581 (DCM)	27 800	6.8 6.2[a]	494 550[a]	0.62 0.67[a]	2.09 2.29[a]	427
264	692 (DCM)	18 000	5.9 4.9[a]	380 450[a]	0.48 0.64[a]	1.08 1.42[a]	427
265	648 (DCM)	11 300	7.6 3.2[a]	412 433[a]	0.62 0.69[a]	1.96 0.96[a]	427
266	698 (DCM) 680 (ACN)	23 400 -	-	-	-	-	428
267	683 (DCM)	22 900	-	-	-	-	428
268	580 (DCM)	-	9.20	520	0.66	3.15	430
269	510 (THF)	-	10.8	680	0.61	4.48	431
270	543 ($CHCl_3$)	-	0.289	350	0.47	0.067	433
271	528 ($CHCl_3$)	-	0.07	320	0.42	0.009	433
272	528 ($CHCl_3$)	-	0.099	390	0.47	0.018	433
273	527 ($CHCl_3$)	-	0.117	410	0.52	0.025	433
274	586 ($CHCl_3$)	35 600	2.13	635	0.72	1.00	437
275	588 ($CHCl_3$)	44 900	2.89	638	0.69	1.30	437

[a] 0.1 M 4-*tert*-butyl-pyridine in the electrolyte.

To overcome the poor electron injection and to improve the PCE of perylene-based sensitizers, Imahori *et al.* introduced pyrrolidines as electron-donating groups in the 1,6-*bay*-position of the perylene core (**254**-**257**) (Fig. 49).[426] The studies around these structures lead to the following benefits: (i) The strong electron-donating ability of the pyrrolidine groups shifts both first oxidation and reduction potentials. This shift leading to a more exothermic electron injection from the excited singlet state to the conduction band of TiO_2 electrode and to a huge bathochromic shift of the maximum absorptions. (ii) The *bay*-substituents prevent the dye aggregation on the TiO_2 surface lowering the intermolecular charge recombination. The highest PCE of 2.6% was achieved with **254** (Tab. 15). The results can be emphasized considering the remarkable difference between the device with **254** and the previous one with **252**,[424] confirming the effect of the pyrrolidines substituents. Moreover, the comparison between dyes linked to TiO_2 via anhydride group (**254**-**255**) and via benzoic acid groups (**256**-**257**) shows a remarkable difference (100 times) in device's PCE, according to the results reported by Gregg *et al.*[422] Such difference depends by the larger distance between the perylene core and the anchoring site that led to a slower electron injection.

Following the work of Imahori *et al.*,[426] it has been reported a series of sensitizers **258**-**265** (Fig. 49 and Fig. 50) to investigate the effect of (i) the position of the anchoring groups, (ii) the presence of a fused benzimidazole moiety and (iii) the nature of electron-donating substituents (phenoxy or piperidine) on the perylene core on the final performance of the devices.[427] DSSCs with the sensitizers **258**-**265** reached PCEs between 0.2% and 2.3% (Tab. 15). (i) The large variation of the efficiency values is mostly related to the position of anchoring group. The highest PCEs were systematically obtained with the sensitizers anchored through the dianhydride acid group (**260**, **262**-**265**) which exhibit better electronic communication with the TiO_2 conduction band. The notable difference for dyes **258** and **261** depends on the presence of electron-rich groups, such as phenoxy and benzimidazole, and their positions compared to the anchoring site.

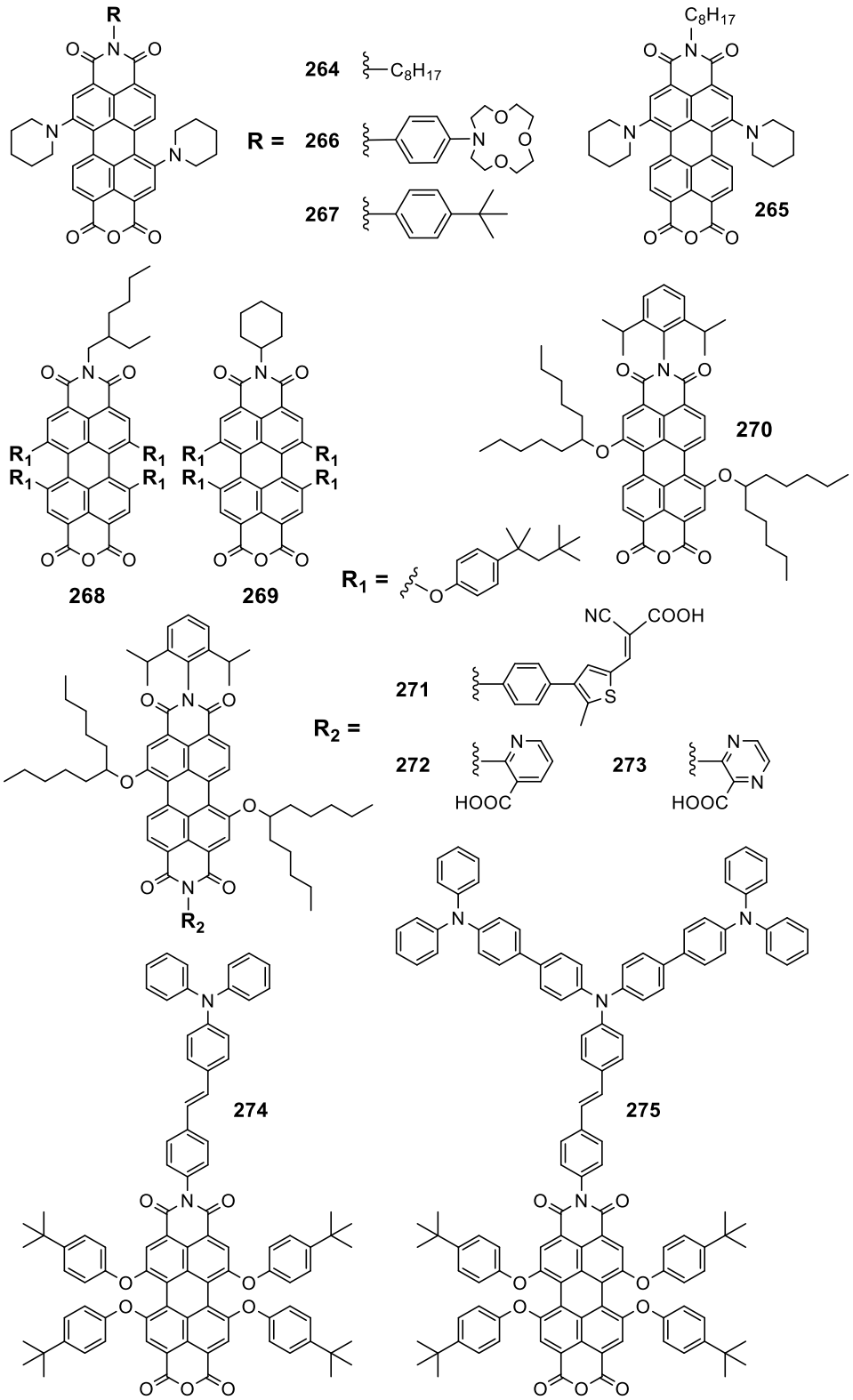

Figure 50 – First-generation of PDI-based sensitizers in DSSCs (Part 2).

As result, the electronic coupling in the excited-state is reduced, since the electronic density shifts away from the electron rich moieties to reach the most electron-withdrawing group that unfortunately is too distant from the TiO_2 surface. (ii) The presence of fused-benzimidazole moiety enlarges the conjugated systems leading to a bathochromic shift of the absorption. Cause its electron-rich nature, fused-benzimidazole moiety should be placed at the opposite side of the anchoring group. (iii) The presence of the four phenoxy groups (**260**-**263**) or the two piperidine groups (**264**-**265**) in the perylene *bay*-positions lead to similar effect noticing only that the latter ones easily aggregate generating a slightly lower photovoltaic performance. According to the reported results by Imahori *et al.*,[426] *N*-piperidinyl substituents introduce a strongest electron density compared to the tetra *O*-aryl substituted perylenes. In conclusion, it is interesting to observe how the two isomer dyes **264** and **265** exhibit a slightly different behaviour. The trans *N*-piperidinyl substituents **264** destabilize more the HOMO level than the *cis*-isomer, this involves a lower energy gap compared to the other one isomer and thus results in a red-shifted transition and a lower oxidation potential. Vice versa, the *cis*-*N*-piperidinyl substituents better prevent the aggregation on TiO_2 surface. These differences explain the best efficiency of the *cis* isomer **265**.

Another two piperidine-substituted perylene sensitizers (**266**-**267**) were presented by Palomares *et al.* (Fig. 50).[428] Dye **266** contains a complexing azacrown ether unit capable of a selective binding of lithium ions. The supramolecular control of the lithium ions contained in the electrolyte is well known to be the key to device improvement.[429] Under simulated sun light, the DSSC assembled with **266** shown higher voltages but lower photocurrent compared to the devices bearing **267** (Fig. 51). This behaviour leads to a shift of the TiO_2 conduction band edge due to the complexation of the lithium ions with the azacrown ether, which could be responsible of the formation of dipole at the semiconductor surface.

As already discussed, the bulky substituents on the *bay*-position of the perylene core prevent the self-aggregation on the TiO_2 surface and reduce the

charge recombination. In the following part of this paragraph, some studies on different *bay*-substituents will be reported. The 4-*tert*-octylphenoxy substituent introduced for the first time by Müllen *et al.* on the perylene core,[400] represents one of the better bulky-substituents to prevent the aggregation. Using sensitizers bearing such substituent, Palomares *et al.*[430] and Sharma *et al.*[431] reported the relationship between the dye loading and the charge recombination and the effect of the deoxycholic acid (DCA) (see Appendix) on the photovoltaic performance. These are the first detailed studies explaining such effects for devices with perylene-based sensitizers.

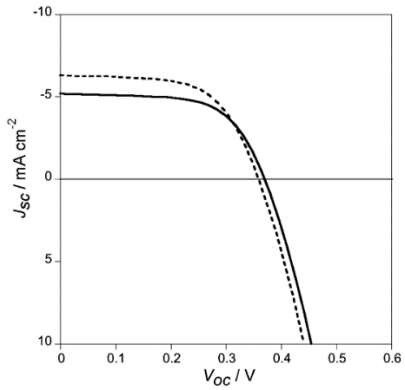

Figure 51 – Current *vs*. Voltage (*I-V* curve) for the **266** (straight line) and **267** (dashed line) DSSCs.[428]

Sensitizers **268** was deposited on a 12 µm thick TiO_2 film with different dye-loading times. The highest efficiency of 3.15% was achieved for the film sensitised for 5 hours.[430] Shorter dye-loading time showed less photocurrent and also less voltage, demonstrating the key role of the recombination between the photo-injected electrons and the oxidised electrolyte on the overall device efficiency. Interestingly, longer dye-loading time does not involve either a decrease of the electron injection and of the cell voltage in contrast with the usual trend of other organic dyes.[60]

Another crucial parameter to improve the photovoltaic performance is the use of DCA as co-adsborber.[432] To evaluate its effect, a 12 µm thick TiO_2 film was dyed by a solution of sensitizer **269** 0.5 mM in THF with and without DCA (10 mM) 24

h. The co-adsorption of DCA provides a significant improvement of photocurrent and slight increases the open circuit voltage which lead to an overall better PCE. An interesting PCE of 4.48% was achieved, which represents the highest value among the DSSCs with first-generation of PDI-based sensitizer.[431]

The first photovoltaic application of dyes bearing an O-alkyl branched substituents on the *bay*-position was reported by Dinçalp *et al.*[433] The devices with the sensitizers **270**-**273** achieved PCEs between 0.009% and 0.067% (Fig. 50). The lower efficiencies found are related to the strong electron-withdrawing nature of imide group, leading to limit the photo generated electrons transfer from the donor-side to the anchoring-side of the dye. Despite the poor performance, it was found a notable difference between the photovoltaic values of **272**-**273** and **271**. Dyes with pyridine and pyrazine anchoring moieties lead to overall better photovoltaic parameters compared to the sensitizer with cyanoacrylic acid anchoring group. These improvements can be related to the lower LUMO level of **272** (-3,61 eV) and **273** (-3.58 eV) compared to **271** (-3.75 eV). The shorter distance between the perylene core and their anchoring site play a role also in this case. Obviously, the better efficiency was achieved by dye **270** with standard the dianhydride acid group anchoring site, stressing their already reported advantages.

Among the latest strategies applied to improve the device's performance, there is the asymmetrical imide site functionalization with a strong electron-donating group such as triphenylamine. This group is already known to prevent dye-aggregation and to improve the intramolecular electron transfer, leading to an overall improvement of the photovoltaic performance.[44,434-436] Insuasty *et al.* reported PCEs of 1.00% and 1.30% applying the sensitizers **273** and **275**, respectively.[437] These results further highlight the effect of the electron-donating group on the photovoltaic performance. However, compared to **254** and **255**, the latest sensitizers show worse efficiency. This trend proves the better effect of the insertion of the electron-donating group on the *bay*-position than on the imide one.

The first-generation of PDI-based sensitizers showed good results, opening the development of perylene-based dyes in the DSSCs. However, they are affected by the presence of electron-withdrawing groups on both sides of the molecule which prevents a strongly directed photo-generated charge transfer from the molecule towards the conduction band of the metal oxide. This represents the main drawback of the first-generation of PDI-based sensitizers. However, this limitation was successfully overcome by the development of a second-generation of sensitizers based on the perylene monoimide scaffold (PMI), providing dyes with strong push-pull effect (Fig. 52).

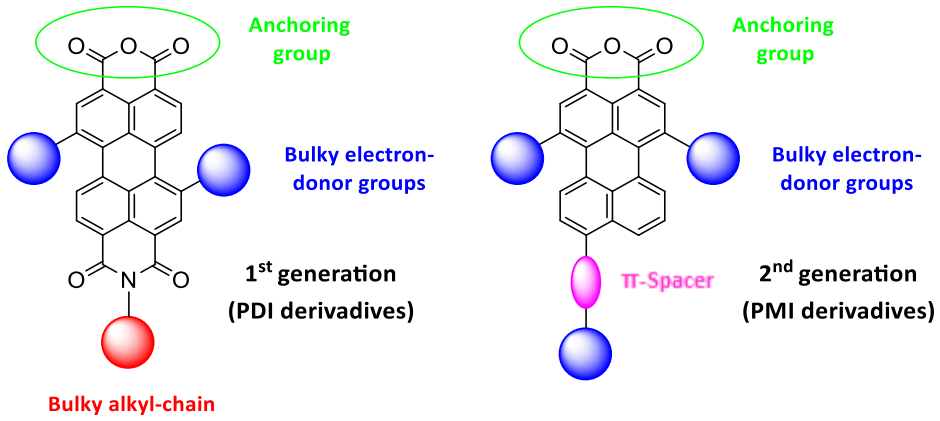

Figure 52 – Comparison between chemical structures of PDI-based first-generation sensitizers and PMI-based second-generation sensitizers.

The success of the second-generation of perylene-based dyes over the first one, can be easily explained by the analysis of the behaviour of well-known ruthenium-complexes sensitizers. Ru(II) complexes display as the charge separation in the sensitizers is fundamental to achieve an efficient charge transfer. Spatial separation of the positive charge left on the dye and the injected electrons after the MLCT decreases the rate of recombination phenomena between injected electrons and oxidized dye molecules considerably.[438] Transposing this information to the organic dyes, the orbital partitioning can only be achieved by a push-pull design, combining a strong donor with a strong acceptor and thus creating a strong intramolecular dipole. In the PMI derivatives,

a right molecular design can lead to a LUMO located on the perylene core and/or on the anchoring group, thus close to the metal oxide, whereas the HOMO is predominantly located on the donor part, close to the electrolyte. Such as approach will firstly help the intramolecular charge transfer and the electron injection from the LUMO of the excited dye to the conduction band of the metal semiconductor, but it is even useful for the dye's regeneration by the electrolyte. In addition, it has been known how the dye's aggregation is detrimental on the overall PCE. PMI were well-known for their strong tendency to aggregate.[439] Taking account of this information, the attachment of bulky strong electron-donating groups in position 9 was the first structure modification made on the PMI core. The first application of PMI-base sensitizers in DSSCs was reported by Gregg *et al.*[440,441] A series of four sensitizers were synthetized to evaluate the effect of different bulky alkyl chains as well as the effect of the position of the anchoring group. Dyes **276** and **277** are classic push-pull type molecules: the alkyl amine attached in the *peri*-position cause a strong coupling of the HOMO on the electron-donating amine group while the LUMO is on the perylene monoanhydride (PMA) core (Fig. 53). Obviously, the greater steric effect of *N*,*N*-dioctylamine substituents lead to a best efficiency: dye **277** achieved a PCE of 1.92%. Sensitizer **278** carries the same donor as **277** but instead of the anhydride, the typical carboxylic acid anchoring group was introduced in the imide site. The change of the anchoring group influences: (i) the orientation of the dye on the surface resulting in final different morphologies of the film and (ii) the photophysical properties of the dyes adsorbed on TiO_2. The anhydride anchoring group lead to a small hypsochromic shift in the dye's absorption, while the carboxylic acid group produces a small bathochromic shift. The comparison of efficiencies displays as the anhydride anchoring group lead to a better photovoltaic performance: dyes **278** achieves higher photocurrent than **277** but a lower voltage, resulting in lower PCE of 1.2% (Tab. 16). Finally, the position of the anchoring group is evaluated. Dye **279** presents the carboxymethyl-anchoring group in the *peri*-position instead of the electron-donating group. This sensitizer shows a similar photovoltaic performance to **278**, resulting in a PCE of 1.3%.

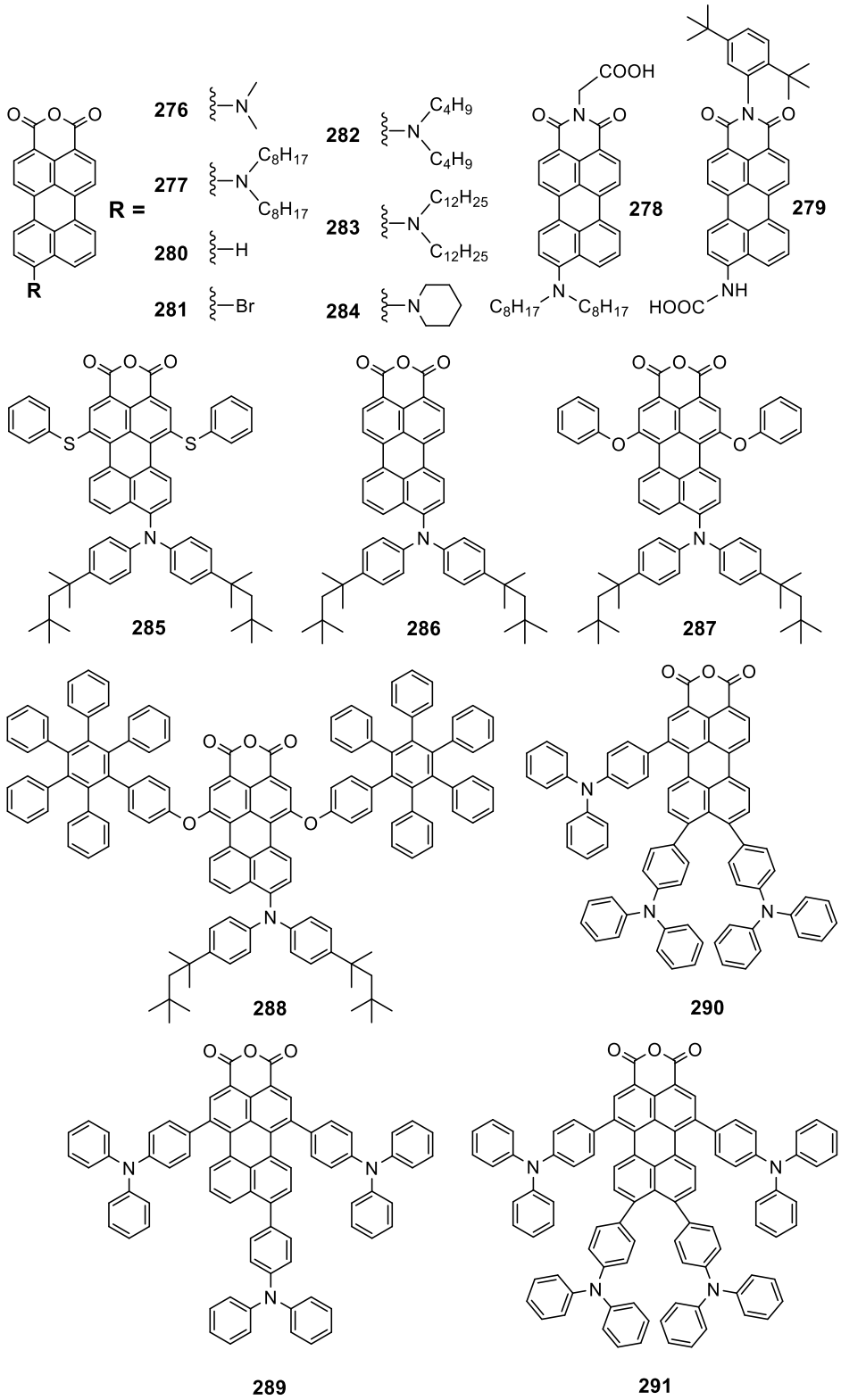

Figure 53 – Second-generation of PMI-based sensitizers in DSSCs (Part 1).

Table 16 – Photovoltaic performance and photophysical properties of second-generation of PMI-based sensitizers in DSSCs.

Dye	λ_{MAX} (solvent) [nm]	ε [M^{-1} cm^{-1}]	J_{SC} [mA/cm^2]	V_{OC} [mV]	FF	PCE [%]	Ref.
276	556 (ACN)	-	4.0	410	-	0.59	440
			1.0[a]	540[a]	-	0.26[a]	
	561 (DMSO)	25 000	0.66[b]	370[b]	0.67[b]	0.16[b]	442
277	560 (ACN)	-	8.9	540	-	1.92	440
			3.1[a]	630[a]	-	0.92[a]	
	564 (DMSO)	22 700	0.70[b]	440[b]	0.63	0.20[b]	442
278	500 (ACN)	-	9.7	400	-	1.2	440
	550 (DCM)	-	0.16[a]	540[a]	-	0.052[a]	
279	506 (DCM)	-	9.8	410	-	1.3	440
			2.7[a]	500[a]	-	0.68[a]	
280	495 (DMSO)	38 100	1.44[b]	450[b]	0.65[b]	0.42[b]	442
	489 ($CHCl_3$)	10 000	7.6	450	0.63	2.2	443
281	503 (DMSO)	35 200	1.78[b]	460[b]	0.64[b]	0.52[b]	442
282	561 (DMSO)	22 100	0.81[b]	410[b]	0.64[b]	0.21[b]	442
283	566 (DMSO)	22 400	0.70[b]	440[b]	0.63[b]	0.20[b]	442
284	544 ($CHCl_3$)	16 000	7.7	570	0.70	3.1	443
285	620 (DCM)	22 700	12.6	730	0.74	6.8	444
286	605 (DCM)	21 000	8.99	580	0.55	2.9	445
			10.4	651	0.58	3.9	447
287	606 (DCM)	25 200	7.52	640	0.57	2.7	445
288	606 (DCM)	18 800	6.99	630	0.56	2.5	445
289	582 ($CHCl_3$)	-	2.22	590	0.69	0.95	446
290	595 ($CHCl_3$)	-	2.07	570	0.69	0.85	446
291	624 ($CHCl_3$)	-	3.08	530	0.67	1.14	446
292	599 (DCM)	32 000	7.96	696	0.59	3.2	447
293	540 (DCM)	35 000	6.13	651	0.55	2.2	447
294	568 (DCM)	35 000	7.50	598	0.54	2.4	447
295	574 (DCM)	-	5.0	580	0.74	2.1	448
296	588 (DCM)	-	5.6	600	0.74	2.1	448
297	595 (DCM)	-	6.5	610	0.72	2.9	448

[a] Parameter achieved without UV treatment.

[b] DSSCs with ZnO as semiconductor.

Another series of PMI-based sensitizers (**276**-**277**, **280**-**283**) was reported by Matsui *et al.* In their experiments ZnO was used as semiconductor.[442] As expected, the push-pull structure of dyes **276**, **277**, **282** and **283** exhibit more bathochromic absorptions. Contrarily, the best photovoltaic performance was not achieved by dyes bearing bulkier amine-substituents but by the bromo-

substituted **281**, reaching a PCE of 0.52%. The unexpected result could be due to the dyes' higher fluorescence quantum yield but authors do not have any explanation regarding why this property should have a positive effect on the overall PCE.

A major improvement has been achieved by Otsuki *et al.* with a similar molecular design: dye **284** bearing a piperidine-substituent as electron-donating group achieved a PCE of 3.1%.[443]

As mentioned before, bulky electron-donating group in the 9-position of PMI scaffold give a push-pull effect to the dye improving the PCE. However, the simple spatial separation between the HOMO and LUMO levels is not enough to reach useful photovoltaic performance. A certain minimum driving force is required to have both efficient electron injection and dye-regeneration processes (at least 0.2 eV).[13] Obviously, the HOMO and LUMO levels of the dyes and therefore the driving forces involved can be tuned by the right molecular design. In PMI derivatives, the *bay*-functionalization (in particular in the 1,6-positions) allows to optimize the desired photophysical and electrochemical properties as well as to prevent the undesired aggregation phenomena.[386,439]

Following this concept, Nazeeruddin *et al.* synthetized dye **285** bearing a bis(4-(2,4,4-trimethylpentan-2-yl)phenyl)amine donor in the *peri*-position and phenylthio-groups in the *bay*-position (Fig. 53).[444] The optimized device with dye **285** achieved the outstanding PCE of 6.8%. PCE achieved by **285** is the highest among the DSSCs with PMI-based sensitizers. In addition, authors have been also tested dye **285** in Solid-State DSSCs (SS-DSSCs) achieving a PCE of 1,8%; *spiro-MeOTAD* (see Appendix) has been used as hole transport material (HTM).

To understand the relationship between photovoltaic performance and the size of the *bay*-substituents, Müllen *et al.* studied the sensitizers **286**-**288** (Fig. 53) which held gradually larger substituents.[445] Starting by the photophysical data, it was found that all the reported sensitizers show a very similar absorption spectra but once loaded on TiO_2, they show a strong decrease in absorption correlated with their increasing molecular weight and size. Moreover, the smallest dye (**286**)

exhibits a very broad absorption compared to **287** and **288**, demonstrating the higher aggregation rate due to the smallest size of the *bay*-substituents. Photovoltaic performances display a direct correlation between the PCE and the molecular size: smallest dyes achieve better results. DSSCs with **286**, **287** and **288** achieved PCEs of 2.9%, 2.7% and 2.5%, respectively. In particular, authors explain that the great tendency to aggregate shown by the unsubstituted dye **286** *vs*. **287**-**288**, was compensated by the greater dye loading on TiO_2 surface resulting in better photovoltaic performance.

Also, the number of substituents on the PMA core can modify the photovoltaic performance. To evaluate this effect Valiyaveettil *et al.* studied a series of sensitizers **289**-**291** bearing a different number of TPA substituent in different positions.[446] The comparison between the tri-substituted dyes **289** and **290** shows as the different positions of the TPA group on the PMA core doesn't affect the PCE. Sensitizers **289** and **290** achieve PCEs of 0.95% and 0.85%, respectively. Increasing the number of the substituents, contrarily, improves the photovoltaic performance, instead. The sensitizer **291** exhibits a PCE of 1.14%, probably due to the greater intramolecular charge transfer induced by the higher number of donors on the perylene acceptor core. Moreover, these dyes allow to introduce the concept of the spacer unit between the donor- and acceptor-part of the sensitizer.

Another important molecular design strategy is the insertion of a spacer between the donor and acceptor part of the sensitizer. The spacer can have two opposite effects: (i) If it takes part in the conjugation between the donor and acceptor it can enhance absorption. (i) If it hinders conjugation either due by twist or by an interruption of the aromatic conjugation system it will lead to a stronger orbital separation, resulting in a better intramolecular charge transfer.

Following these goals, Edvinsson *et al.* reported a series of sensitizers **286**, **292**-**294** (Fig. 53 and Fig. 54), to investigate for the first time the effect of different spacers on the photovoltaic performance.[447] A fully rigid conjugated acetylene spacer and an aromatic flexible phenylene one is employed in dyes **293** and **294**,

respectively. The phenylene spacer in **293** increases the distance between the amine donor and the anhydride acceptor but it also weakens the donor ability of the diphenylamine by twisting it out of the plane and thus limiting the conjugation. This is clearly reflected in a worse intramolecular charge transfer process showed by **293** and thus in a lower PCE than **294**. The devices prepared with **286**, **292**-**294** achieved PCEs of 3.9%, 3.2%, 2.4% and 2.2%, respectively.

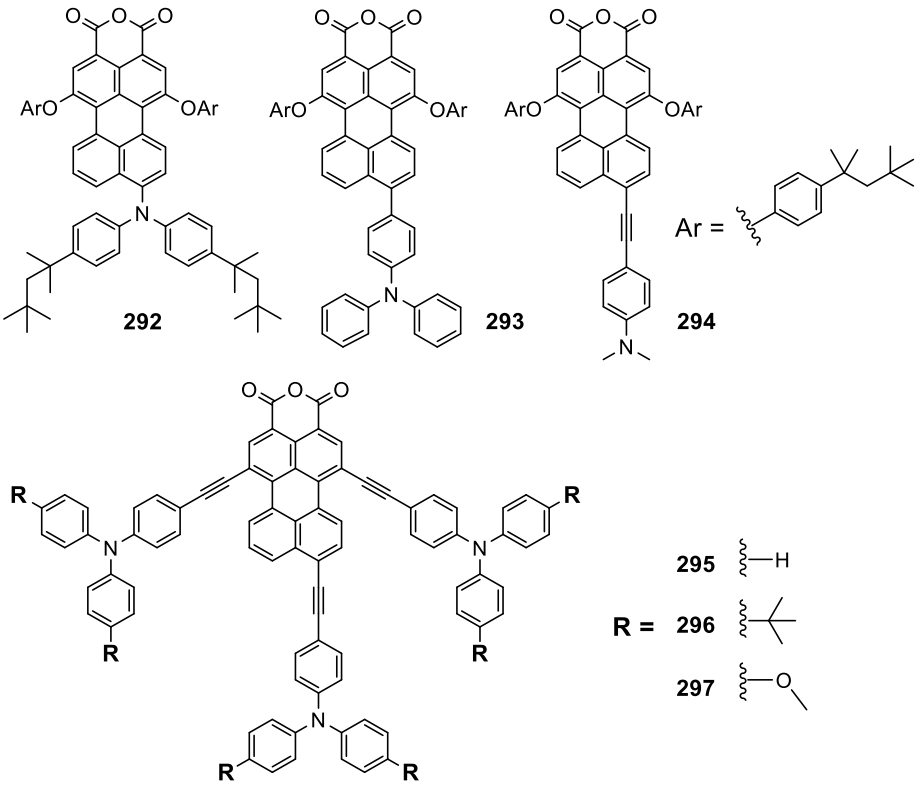

Figure 54 – Second-generation of PMI-based sensitizers in DSSCs (Part 2).

Interestingly, sensitizer **286** bearing only a *peri*-substituent without any spacer nor *bay*-functionalization, shows the best result compared to the other sensitizers of the series probably due to its higher concentration on TiO_2 surface. The spacer is an effective tool for molecular design, but the multiple parameters involved in real devices require a compromise combination regarding this aspect for achieving best results.

Another demonstration of the effectiveness of the spacer on the photovoltaic performance was reported by Imahori *et al.* In dyes **295**-**297**, an acetylene spacer was introduced between the three triphenylamine substituents and the acceptor PMI core.[448] Moreover, the para-position of the amine donor were decorated with different substituents increasing the donor strength. Compared to the previous reported dye **293**, where the twisted phenylene spacer decreased the donor influence, the presence of the acetylene bridge in sensitizers **295**-**297** separated and aligned the phenylene moieties with the conjugation plane of the perylene and acetylene allowing the increasing donor strength. In accordance with the improved electron donor effect, a best PCE of 2.9% was achieved with dye **297** (Tab. 16). The other sensitizers **295** and **296** both exhibit PCEs of 2.1%. Moreover, another prove to the effect of the spacer on the photovoltaic performance can be easily achieved with the comparison of dye **295** with the previous one (**289**) without the acetylene spacer which display a lower PCE of 0.95%.

PMI-based sensitizers demonstrated easy tunability of photophysical and electrochemical properties. Higher PCEs has been achieved compared to the first-generation PDI-based sensitizers mainly due to the dye-structure evolution. It has been demonstrated as (i) the modification of the *peri*-position allows to reach a more suitable push-pull design able to better partition the HOMO and LUMO levels, (ii) the modification of *bay*-positions allows to prevent the dye aggregation, (iii) too bulky substituents could dramatically reduce the dye-loading and (iv) the insertion of right spacer could improve the molecule push-pull effect providing better PCEs.

3. Project-proposal

As mentioned before, an efficient sensitizer for NIR-DSSCs required specific characteristics: (i) LUMO energy level located at -3.75 eV, (ii) HOMO energy level located at -5.25 eV and (iii) a selective NIR-absorption beyond 700 nm.[29,32]

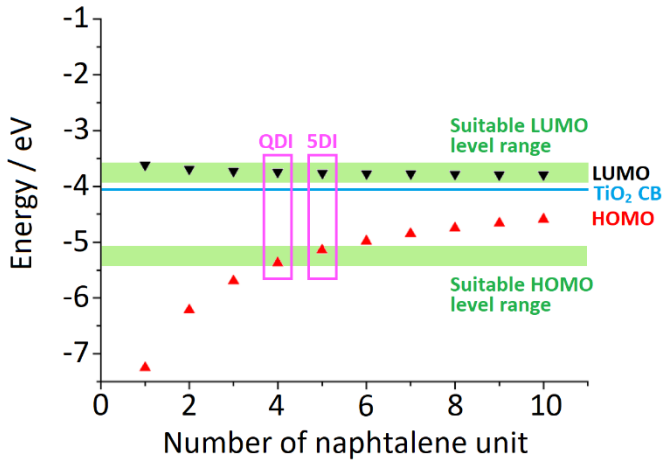

Figure 55 – Theoretical HOMO and LUMO energy levels of extended-rylenes diimide.[449]

Among the extended-rylenes, the QDIs and the 5DIs are the only two classes displaying suitable HOMO/LUMO energy levels and absorption features (Fig. 45b a Fig. 55).[388,400,449] However, even if both QDIs and 5DIs meet all the specific requirements to design an efficient NIR-sensitizer, the former ones are easier to synthetize and are relatively more soluble providing an easier manipulation. For these reasons, QDI and QMA classes have been selected as target scaffolds to design new NIR-sensitizers.

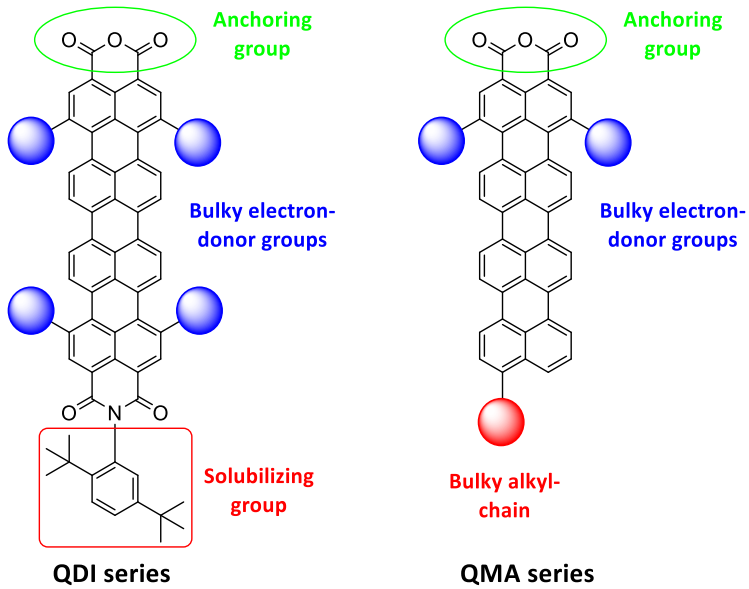

Figure 56 – Comparison between chemical structure of QDI-based and QMA-based dyes.

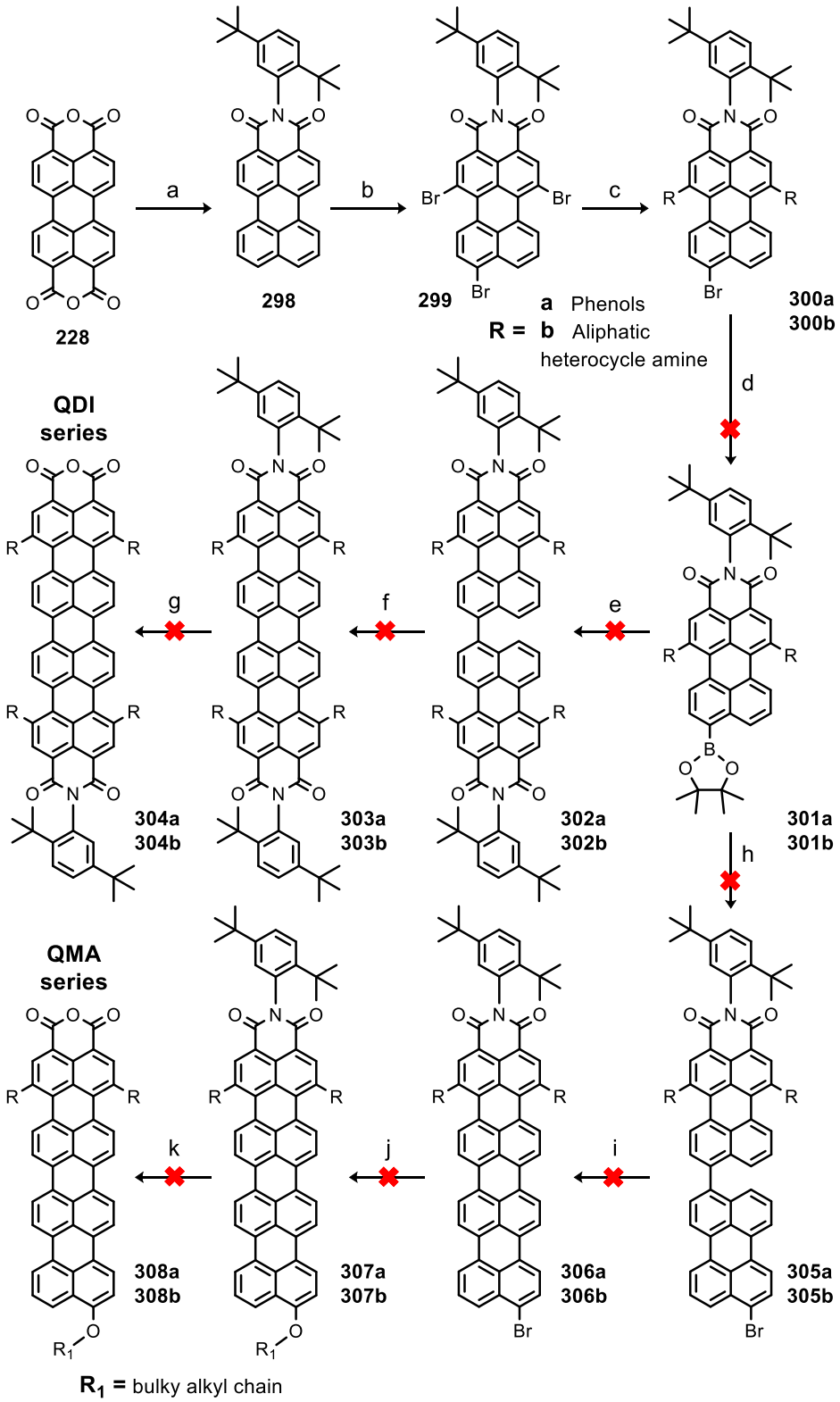

Figure 57 – Proposed synthetic scheme (reaction conditions reported in the next page).

a) 2,5-di-tert-butylaniline, $Zn(CH_3COO)_2$ $2{\cdot}H_2O$, imidazole, H_2O, 190 °C, 23 h, ≈ 15 bar. b) Br_2, K_2CO_3, $CHCl_3$, reflux, 6 h. c) Phenol derivative or aliphatic heterocycle amine, K_2CO_3, NMP, reflux, overnight. d) Bis(pinacolato)diboron, $Pd(dppf)_2Cl_2$, CH_3COOK, 1,4-dioxane, 70 °C, 2 h. e) **300a** or **300b**, $Pd(PPh_3)_4$, K_2CO_3, toluene/EtOH/H_2O 25/1/1, 80 °C, 24 h. f) K_2CO_3, ethanolamine, 120 °C, 24 h. g) KOH, *tert*-butanol, reflux, 1 h. CH_3COOH, RT, 2 h. h) 3,9-dibromoperylene, $Pd(PPh_3)_4$, K_2CO_3, toluene/EtOH/H_2O 25/1/1, 80 °C, 24 h. i) K_2CO_3, ethanolamine, 120 °C, 24 h. j) Sodium alkoxy, CuBr, NMP, 120 °C, overnight. k) KOH, *tert*-butanol, reflux, 1 h. CH_3COOH, RT, 2 h.

In particular, it has been decided to try the development of two different series of NIR-sensitizers: (i) the "QDI-series" and the (ii) "QMA-series" (Quaterrylene Monoanhydride) (Fig. 56). QDI-series mimics the PDI-based sensitizers while the QMA-series the PMA-based ones. Both series will be functionalized in the *bay*-positions with bulky electron-donor groups, such as phenols and aliphatic heterocycle amines, to prevent the self-aggregation and to red-shift the absorption.[386,436,439] In addition, QMA-series will be further functionalized in 13 *peri*-position with bulky alkoxy group to prevent both aggregation and non-geminate recombination (Fig. 56). The synthesis of the two series of quaterrylene-based sensitizers has been carried out following the synthetic plan displayed in Fig. 57. However, as will be discussed in next section, the QMA-series has been not synthetized due to the too drawbacks met in the synthesis procedures.

4. Synthesis

Following the synthetic scheme previously reported (Fig. 57), the synthesis of QDI-based sensitizers began with the preparation of the PMI derivative **298** from the commercially available PTCDA (**228**). Synthesis was carried out in autoclave following the reported procedure (reaction **a** in Fig. 57).[415] 2,5-Di-*tert*-butylaniline was selected due to its twofold effect: it has been demonstrated as this amine provides the highest conversion in desired PMI **298** (a yield > 50% has been achieved) as well as improving its solubility in chlorinated solvents.[415] However, the large-scale production of **298** represented the first trouble in the preparation

of quaterrylene-based sensitizers. In the preliminary phase of the project, the available autoclave's 30 mL vessel limited the reaction's production at roughly 0.9 g of **299** per day (with a yield of 62%). This issue dramatically slowed-down the production of a satisfying amount of stock-material to perform and optimize the next synthetic steps. To overcome the scalability limitation as well as decrease the reaction time, it has been tried to mimic the autoclave-reaction conditions in a microwave reactor. Over the years, it has been demonstrated as several reactions can be dramatically optimized, improving the final yield and reducing the reaction's time.[450] For the preparation of **298**, different molar ratio and reaction's conditions were tested (Tab. 17).

Table 17 – Different reaction's setups for PMI **298**.

Trial	PTCDA [eq]	Amine [eq]	Zinc acetate [eq]	Temperature [°C]	Time [min]	Yield [%]
1	1	0.9	0.04	190	30	**298** – No formation **309** – 27% **310** – No formation
2	1	0.55	0.4	190	30	**298** – No formation **309** – 5% **310** – 26%
3	1	0.55	0.8	190	40	**298** – No formation **309** – No formation **310** – 22%

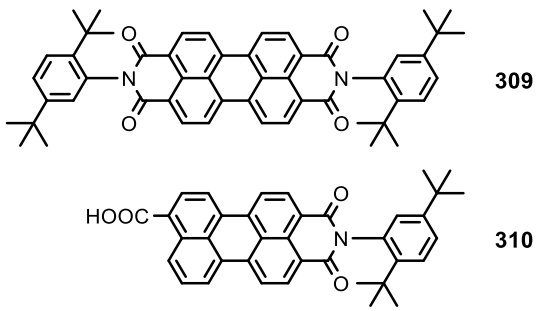

Figure 58 – Chemical structure of side products **309** and **310**.

However, no performed methods led to the desired product **298**. The PDI **309** and the non-decarboxylated PMI **310** were found as side products in different yields, instead (Fig. 58). To avoid the formation of the PDI **309**, we tried to reduce the amine equivalents whereas to push the decarboxylation of **310**, we tried to increase the amount of zinc acetate. However, both strategies didn't provide any successfully results. The only way to overcome the reaction-scalability limitation has been the synthesis in series of large number of batches until we were able to set up the mono-imidization reaction in a bigger autoclave. New autoclave's 125 mL vessel provided the dramatically improvement of the production-rate achieving roughly 3 g per day.

After the optimization and scale-up of the production of **298**, the preparation of tri-brominated PMI **299** (reaction **b** in Fig. 57) was another bottleneck. Adapting to our substrate the reported synthetic procedure, the tri-bromination reaction was performed in different scales (100 mg, 300 mg, 1 g, 7 g of starting material **298**).[418] The reaction-scalability was the first serious limitation in the preparation of **299**: while 100 and 300 mg scale reactions were carried out without any issues, 1 g and especially 7 g ones, resulted dangerous. The increased reaction-scales led to a slightly loss of material in the 1 g scale reaction due to the soiling of the condenser, while the 7 g one led to an uncontrollable outflow of material from the reactor (Fig. 59).

Figure 59 – Uncontrollable outflow of 7 g scale tri-bromination reaction.

The reaction runaway probably occurred due to the presence of the insoluble potassium carbonate which could hampered the homogeneous stirring. Beside its experimental issues on large-scale synthesis, tri-bromination reaction leads to a mixture of tri-brominated regioisomers: the desired 1,6,9-tribrominated derivative and the 1,7,9 one (Fig 60a).

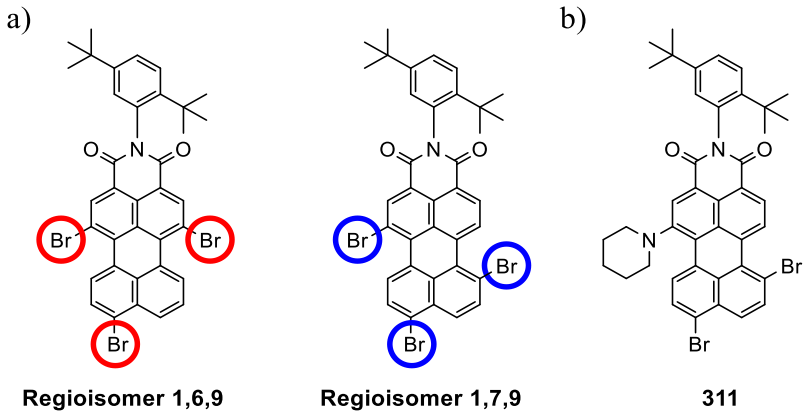

Figure 60 – a) Chemical structure of the 1,6,9-tribrominated isomer and the 1,7,9-tribrominated one. b) Chemical structure of mono-piperidine derivative **311** (compound isolated as regioisomeric mixture).

To isolate the desired compound, it has been necessary perform an oversize chromatography column, consuming a large quantity of solvents to obtain only few hundred milligrams of **299** (more than 5 litres were usually used to obtain roughly 100 mg of **299**) (COSY spectrum of **299** in SI - Fig. 145). The scalability limitation it has not been overcome, requiring a multiple reactions series to achieve a satisfying amount of **299**. Contrarily, the purification of the two isomers mixture has been optimized, finding as the substitution of the classic *n*-hexane/DCM mixture as mobile phase with a new one based on *n*-hexane/toluene, dramatically improved the separation's resolution.

As mentioned before, properly *bay*-positions functionalization allows the improvement of the solubility as well as tuning the photophysical properties of PMI derivatives. The *p*-propylphenol (**300a**) and piperidine (**300b**) were chosen as substituents; both groups should improve the solubility and provide a red-shift of

the absorption, in particular with piperidine groups. The synthesis of **300a** and **300b** required a carefully control of the molar ratio of the starting material and *p*-propylphenol or piperidine. This is necessary to avoid the undesired substitution of the bromine in the *peri*-position.

Adapting to our substrate the reported procedure, the synthesis of **300a** was performed by nucleophilic aromatic substitution in NMP at 120 °C for six hours, using a slightly excess of *p*-propylphenol (2.2 eq).[418] The reaction led to a tricky mixture of compounds (at least four main spots are detectable by the TLC) in which the desired product is only present in a very small amount. Increasing the equivalents of *p*-propylphenol leads to the undesired tri-substituted derivative while longer reaction's times leads to trickier mixtures from which the **300a** cannot be separate in relevant amount. As in the case of **299**, the isolation of pure **300a** requires oversize chromatographic purification with a dramatically consumption of solvents (at least 15 liters of solvents were usually used to obtain roughly 20-30 mg of **299**). The difficulty of the reaction alongside the tricky purification have been allowed to only achieve a final yield of 7% for a 200 mg scale reaction.

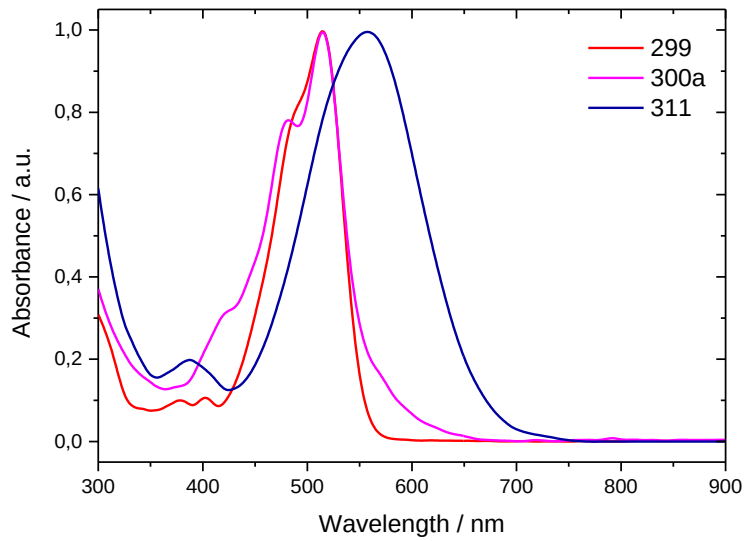

Figure 61 – Absorption spectra of the functionalized-PMI derivatives (in DCM).

About the synthesis of bis-piperidine substituted derivate **301b**, few attempts have been performed but unfortunately, we were able to isolate only the mono-piperidine substituted compound **311** in which is detectable the presence of another regioisomer difficult to separate (Fig. 60b).

As expected, the functionalization of the PMI scaffold improved the solubility: while **299** is completely insoluble in polar solvent like MeOH, **300a** and also the mono-piperidine derivative **311** become relatively soluble in alcoholic solvents. In addition, core-functionalization cause appreciable variation of photophysical properties (Fig. 61). Both *p*-propylphenol and piperidine substituent broadening the absorption band and in particular, derivative **311** exhibit a red-shifted absorption due to the higher electron-donor strength of piperidine.

As reported in the initial synthetic scheme (Fig. 57), the production of quaterrylene-based sensitizers requires multi-step synthesis, seven for QDI-series and eight for QMA-series, respectively. After only three synthetic steps, the common ones to both series, we decided to re-design our synthetic strategy due to the dramatically issues faced in the preparation and purification of both tribrominated-PMI **299** and disubstituted-PMI **300a,b**. In the previous reported strategy, the PMI scaffold is functionalized in the first phase of the synthetic procedure and after it is longitudinally extended in the second phase. To avoid the tri-bromination and the di-functionalization reactions, it has been proposed a new synthetic strategy in which in the first phase the PMI-scaffold is extended to form the quaterrylene structure and after occurs its functionalization (Fig. 62). Following this new strategy, the sensitizers **316** and **319** have been synthetized and preliminary tested in DSSCs to investigate if they can be suitable candidate for NIR-DSSCs.

Contrarily to the previous strategy, PMI-scaffold **298** is mono-brominated in *peri*-position 9 to obtain **312** (COSY spectrum of **312** in SI - Fig. 150). The synthesis of **312** was firstly attempted adapting a reported procedure.[417] However, this procedure using 1.5 eq. of bromine in chlorobenzene at 60 °C for 3 hours leads to a complex mixture of brominated compounds hardly to separate.

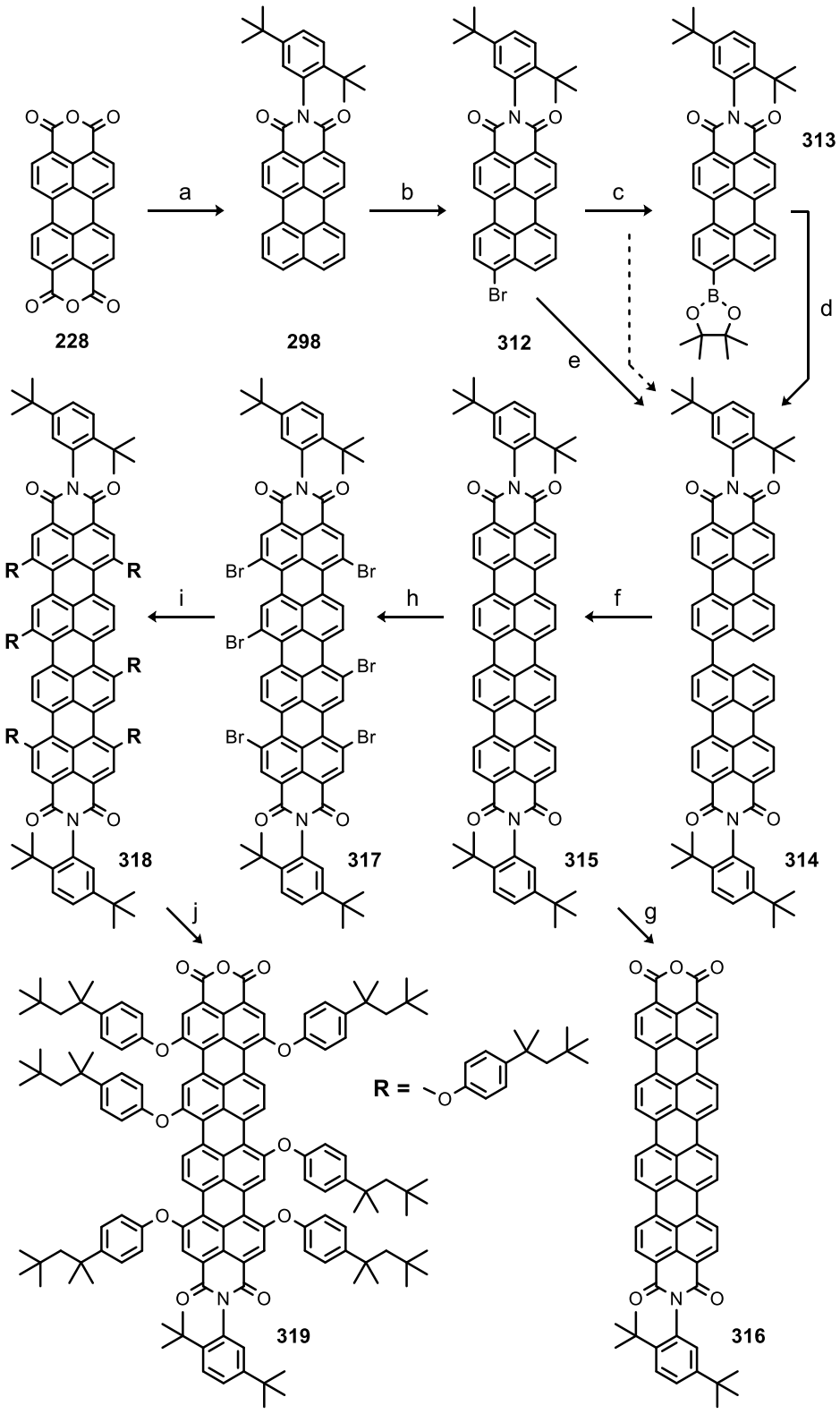
228
298
312
313
314
315
316
317
318
319
a
b
c
d
e
f
g
h
i
j
Br
R
R =

Figure 62 – New synthetic strategy (reaction conditions reported in the next page). a) 2,5-di-tert-butylaniline, $Zn(CH_3COO)_2$ $2{\cdot}H_2O$, imidazole, H_2O, 190 °C, 23 h, ≈ 15 bar. b) Br_2, K_2CO_3, $CHCl_3$, reflux, 6 h. c) Bis(pinacolato)diboron, $Pd(dppf)_2Cl_2$, CH_3COOK, 1,4-dioxane, 70 °C, 2 h. d) **312**, $Pd(PPh_3)_4$, K_2CO_3, toluene/EtOH/H_2O 25/1/1, 80 °C, 24 h. e) $Ni(COD)_2$, cyclooctadiene, 2,2'-bipyridine, DMF, 65 °C, 36 h. f) K_2CO_3, ethanolamine, 120 °C, 24 h. g) KOH, *tert*-butanol, reflux, 1 h. CH_3COOH, RT, 2 h. h) Br_2, $CHCl_3$, reflux, 48 h, dark. i) 4-*tert*-octylphenol, K_2CO_3, NMP, 120 °C, 72 h. j) KOH, *tert*-butanol, reflux, 1 h. CH_3COOH, RT, 2 h.

To easily synthetize **312**, we tried bromination via *N*-bromosuccinimide without any results. Finally, it has been optimized a straightforward mono-bromination process which allows the synthesis of **312** with almost quantitative yield without any purification (**b** in Fig. 62). Mono-brominated PMI **312** is the key building block to longitudinally extend the rylene core by a Suzuki-Miyaura cross-coupling reaction between it and **313** (**d** in Fig. 62). Borolane derivative **313** has been synthetized using standard procedure with bis(pinacolato)diboron (**c** in Fig. 62) Interestingly, the reaction toward **313** leads to the formation of derivative **314** as side product (dashed reaction in Fig. 62). Beside to the classic Suzuki-Miyaura cross-coupling reaction, it has been tried to directly synthetize **314** from **312** with a homocoupling reaction mediated by $Ni(COD)_2$ as catalyst (**e** in Fig. 62). Even if the latter strategy required only one step of synthesis and purification, the more air sensitiveness of catalyst and the longer reaction-time required convinced us to prefer the multi-step procedure via Suzuki-Miyaura cross-coupling reaction. As reported in literature, the twisted-structure **314** exhibits a slightly red-shifted absorption compared to the starting material **312** ($\boldsymbol{\lambda_{max}}$ = 508 nm for **312** and $\boldsymbol{\lambda_{max}}$ = 527 nm for **314**) and roughly triple molar extinction coefficient (ε_{508} = 37392 for **312** and ε_{527} = 99135 for **314**).[451] The twisted structure of **314** still provides a good solubility in chlorinated solvent, allowing a straightforward purification.

Starting from **314**, the fully aromatized QDI-structure **315** has been synthetized exploring two different cyclization by dehydrogenation reactions (**f** in Fig. 62).[419,452] The first method is carried out in ethanol using KOH as base and D-(+)-glucose as catalyst, while the second one is carried out in ethanolamine using

K_2CO_3 as base. Among two methods, in the second one the conversion of **314** into **315** is faster and exhibited higher yield. The cyclization in ethanolamine led to a noticeable colour variation due to the huge red-shift of the maximum-absorption: compound **314** shows a maximum absorption at 527 nm while **315** exhibits one at 764 nm in DCM (Fig. 63).

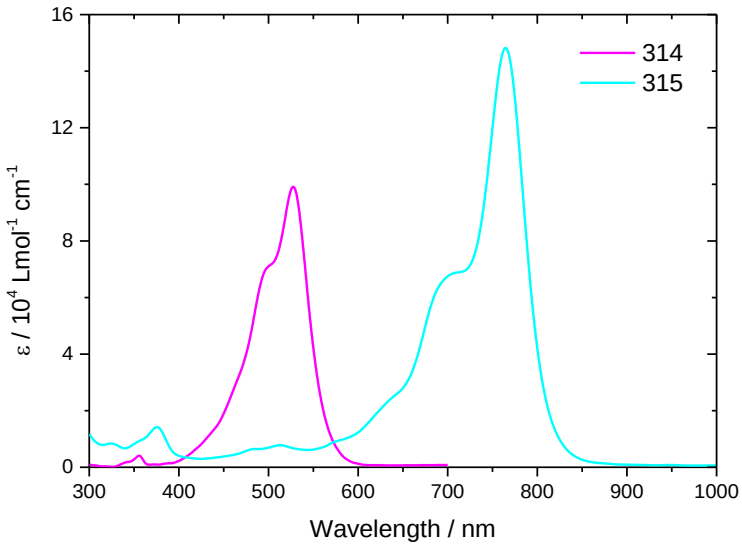

Figure 63 – Absorption spectra of **314** and **315** in DCM.

As mentioned before, extended rylene dyes as well-known for their outstanding photophysical properties but unfortunately also for their dramatically poor solubility. Starting from compound **315**, every synthetic- and purification-step as well as the chemical characterization became really tricky just due to very poor solubility. In particular, to fully understand how is difficult the investigation of the extended-rylenes, in literature it has been demonstrated as QDIs, similar to **315**, exhibit a solubility < 1 mg/mL (at 25 °C) and their chemical characterization by ^{1}H-NMR spectroscopy can be performed only at high temperatures (above 120 °C) in very expensive deuterated 1,2-dichlorobenzene-d4 (> 80 €/mL).[451] Thin-layer chromatography (TLC), UV-Vis spectroscopy, ATR-IR

spectroscopy and MALDI-TOF have been the only techniques that we could exploit to characterize these compounds and to evaluate their purity.

Starting from **315**, the first QDI-based NIR sensitizers **316** has been synthetized by the partial hydrolysis of one of the two imide groups (**g** in Fig. 62). Obviously, the removal of one di-*tert*-butylphenyl moiety further decrease the solubility.

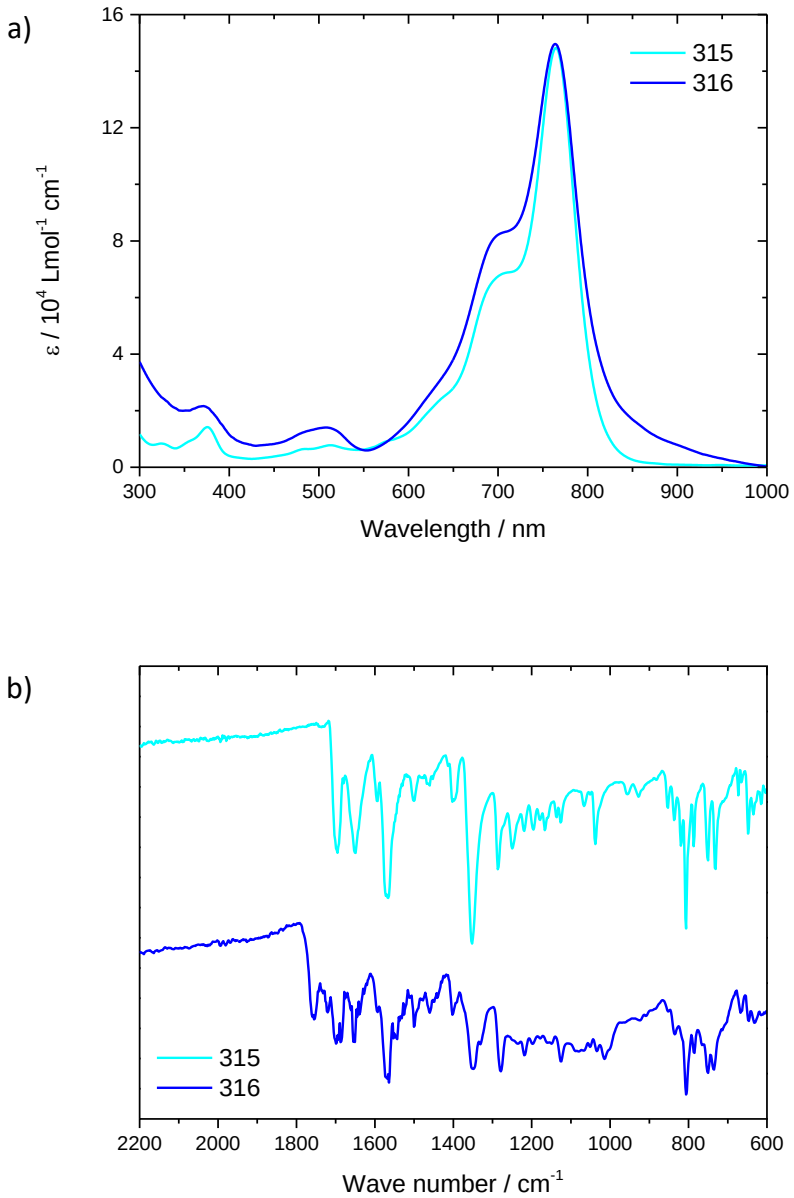

Figure 64 – a) UV-Vis absorption spectra in DCM and b) ATR-IR spectra of **315** and **316**.

To check the reaction's progress and verify the formation of hydrolysed compound **316**, IR- and UV-Vis spectroscopy have been exploited. Comparison between absorption spectra showed as **316** exhibits a broadening of the absorption band than **315** (Fig. 64a), in according with the features shown by the similar terrylene-based compounds.[452] In addition, IR spectrum of **316** exhibits the typical vibrational signals of anhydride group: (i) the *ν*(C═O) at 1750 cm^{-1} and the *ν*(O–C–O) between 1000-1200 cm^{-1} (Fig. 64b). Based on these results, we were confident about the hydrolyzation reaction occurred on **315** but we were not able to determine if the hydrolysis reaction led to the asymmetrical structure **316**. To confirm the formation of the desired compound, MALDI-TOF experiment was performed, confirming the formation of **316** (spectrum in SI - Fig. 155).

As previously reported, the only available strategy to improve the solubility is the functionalization of the quaterrylene-core with bulky substituents. For this reason, we synthetized the brominated derivative **317** as starting material for the following functionalization. Compound **317** was synthetized adapting a reported procedure. To avoid any risk due to the dramatically large amount of bromine used (420 eq.), the reaction was carried out in small scale (20 mg) (**h** in Fig. 62).[453] The bromination reaction led to a tricky mixture of regioisomers and polybrominated compounds that are impossible to separate by flash-chromatography. However, **317** exhibits a very good solubility in chlorinated solvents. According to what reported by Würthner *et al.*, the polybrominated compound **317** exhibits an hypsochromic shift compared to **315** due to the distortion of the originally planar quaterrylene-scaffold.[384]

Due to the impossibility to separate the different side-products, the crude material was directly used for the following functionalization step without any purification. Starting from **317**, it has been synthetized **318** by aromatic nucleophilic substitution reaction (**i** in Fig. 62). The 4-*tert*-octylphenol was selected as solubilizing agent. The purification of **318** has been very difficult due to the presence of different poly-substituted compounds, requiring multiple columns. The outstanding improvement of solubility allowed to perform ^{1}H-NMR spectroscopy (spectrum in SI - Fig. 156), demonstrating as **318** displays the

presence of a mixture of hexa-brominated regioisomers due to the poor selectivity of the previous bromination. However, we have been confident that the different hexa-substituted compound would similarly worked in device.

Following the same method previously reported for **316**, the mono-hydrolysis was carried out to synthetize **319** (**j** in Fig. 62). Like **316**, sensitizer **319** exhibits broad absorption band than its diimide counterpart **318**. Unfortunately, the very small amount achieved for **319** didn't allow to perform IR- and ^{1}H-NMR spectroscopy to confirm the formation of the desired mono-hydrolysed compound. Even in this case, the purity was confirmed performing a MALDI-TOF experiment (spectrum in SI - Fig. 157).

5. Photo- and Electrochemical Characterization

As mentioned in Chapter 1, suitable sensitizers for NIR-DSSCs application require selective absorption beyond 700 nm and specific HOMO and LUMO energy levels.[32] QDI-based sensitizers **316** and **319** exhibit strong absorption maxima at 763 and 784 nm, respectively with molar extinction coefficients near to $1.5 \cdot 10^5\ M^{-1}\ cm^{-1}$(Fig. 65).

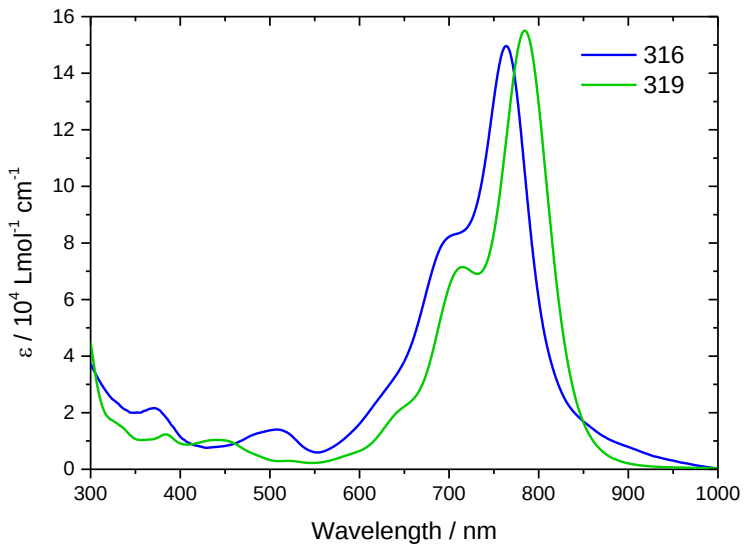

Figure 65 – Absorption spectra of QDI-based NIR-sensitizers **316** and **319** in DCM.

However, even if both dyes' absorptions are largely located in the NIR region, they also presented not-negligible absorptions between 400-600 nm, with molar extinction coefficients ≈ 10000 M^{-1} cm^{-1}. Obviously, these parasitic visible-absorptions will influence the aesthetic of NIR-DSSCs that will not be completely colorless.

Beside the photophysical characterization, cyclic voltammetry (CV) on **316** and **319** was performed to evaluate the HOMO and LUMO energy levels (voltammogram for **316** and **319** are reported in Section 3.1 of SI - Fig. 320). Before display the results, the methodology applied to determine the HOMO and LUMO energy levels will briefly be discussed. For dyes **316** and **319** we performed CV experiments to identify both first oxidation and reduction peaks. The determination of peak's redox potential can be obtained by the equation:

$$E_{1/2} = \frac{E_{ox} + E_{red}}{2} \qquad (7)$$

Where E_{ox} is the potential of the anodic peak while E_{red} is the potential of the cathodic one. After the determination of the $E_{1/2}$ referred to Fc^{+}/Fc ($E_{1/2}$ = +0,624 V *vs*. *NHE*),[454] it can be converted to electronvolt (eV):

$$HOMO\ o\ LUMO\ [eV] = -\left(5.1 + E_{1/2}\ vs.Fc|Fc^{+}\right) \qquad (8)$$

Where $E_{1/2}$ can be calculated from the CV experiment and 5.1 is a tabulated constant which corresponds to the energy necessary to oxidized ferrocene toward ferrocenium calculated in the vacuum. Knowing the $E_{1/2}$ for both oxidation and reduction peaks, by equation 8 is possible to calculate the HOMO and LUMO energy levels. However, usually it's not straightforward to determine the $E_{½}$ of the reduction peak for the sensitizers. For this reason, it is possible to exploit the "optic method". The main difference of the "optic method" compared to the previous one is the strategy applied to the calculation of the LUMO energy level. LUMO energy level is calculated by equation 9:

$$LUMO = HOMO + E_{0-0} \qquad (9)$$

The LUMO level can be easily obtained performing CV experiment while the optic band-gap ($E_{0\text{-}0}$) can be determined by UV-Vis and fluorescence spectroscopic measurements. Assuming all the necessary approximations, the optic band-gap corresponds to the intersection of the absorption and the steady state emission spectrum. The wavelength at which this intersection takes place is associated with a specific energy value through Planck's law. In particular, the optical band-gap, expressed in eV can be calculated using the equation 10:

$$E_{0-0}\,[eV] = \frac{1240}{\lambda_{0-0}\,(nm)} \qquad (10)$$

Where $\lambda_{0\text{-}0}$ is the wavelength in which there is the intersection between the absorption and steady state emission spectra, and 1240 is a constant provided by the merging of the Planck constant (*h*), the speed of light (*c*) and the elementary charge of electron (*e*).

Following the "optic method", the HOMO and LUMO energy levels of both NIR-sensitizers **316** and **319** were calculated (Tab. 18).

Table 18 – HOMO and LUMO energy levels calculated for NIR-sensitizers **316** and **319**.

Dye	$E_{0\text{-}0}$ [nm] [a]	$E_{0\text{-}0}$ [eV]	HOMO [V *vs*. Fc/Fc^+] [b]	LUMO [V *vs*. Fc/Fc^+] [b]	HOMO [eV]	LUMO [eV]
316	760	1.63	+0.44	-1.39	-5.54	-3.71
319	770	1.61	+0.54	-1.18	-5.64	-3.92

[a] Absorption and steady state emission spectra were performed in DCM.
[b] CVs experiments were performed as described in SI using DCM as solvent.

Either dye **316** and **319** exhibit suitable HOMO and LUMO energy levels, nearby to the target values -5.25 eV and -3.75 eV, respectively. In particular, among the two dyes, **316** exhibits a better LUMO energy level due to the higher gap between it and the CB of the TiO_2 (0.4 eV for **316** and 0.2 eV for **319**, respectively). From a theoretical point of view, dye **316** should provide a better electron injection process. However, as reported in Chapter 1, the dye's self-

aggregation plays a key-role in the electron injection process, dramatically hampering the achievement of efficient process. For this reason, despite the theoretical lower driving force exhibited by **319**, its bulky substituents should be preventing the detrimental aggregation guaranteeing a more efficient electron injection and thus a better PCE.

6. Photovoltaic application

The possible application of quaterrylene-based dyes **316** and **319** as NIR-sensitizers for NIR-DSSCs application was tested. To investigate their features into devices, the preliminary studies were performed in classic DSSCs using a transparent 6 μm thickness TiO_2 photoanode (without blocking layer), iodine-based HPE (High-Performance Electrolyte) and standard Pt-based CE (detailed description about DSSCs fabrication with **316** and **319** is reported in Section 8.1 of SI). As expected, the sensitization of photoanodes has been very difficult, requiring long dye-loading times. In literature, sensitization's time > 24 h has been used to prepare DSSCs with shorter terrylene-based dyes.[452] In addition, the small available amount of both pure dyes limited our possibilities to deeply investigate and optimize the sensitization process (for **319** only ≈ 2 mg was available). For these reasons, we decided to carry out the sensitization processes in DCM at RT for 48 h, using a 0.5 mM dye's solution. Moreover, to prove the beneficial effect of *tert*-octylphenol substituents to reduce the self-aggregation, the CDCA was not used as co-adsorbent.

Interestingly, the above-mentioned dye-loading conditions allowed the sensitization of dye **316**, providing a photoanode with a 60% of transmittance at 600 nm (Fig. 66a), whereas no-sensitization it has been found for dye **319**. Even extending the dye-loading time up to one week, sensitization of **319** didn't occur. Two main hypotheses have been made regarding the no-sensitization of **319**: (i) the mono-hydrolyzation reaction didn't occur (reaction **j** in Fig. 62) and (ii) *tert*-octyl phenols substituents are too bulky, preventing the sensitization. However,

both of them probably are not the cause of the no-sensitization because (i) the formation of the mono-hydrolysed **319** was confirmed by MALDI-TOF experiment (spectrum in SI - Fig. 157) while (ii) the successfully use of *tert*-octylphenol substituents it has been already demonstrated in literature for terrylene-based sensitizers.[452]

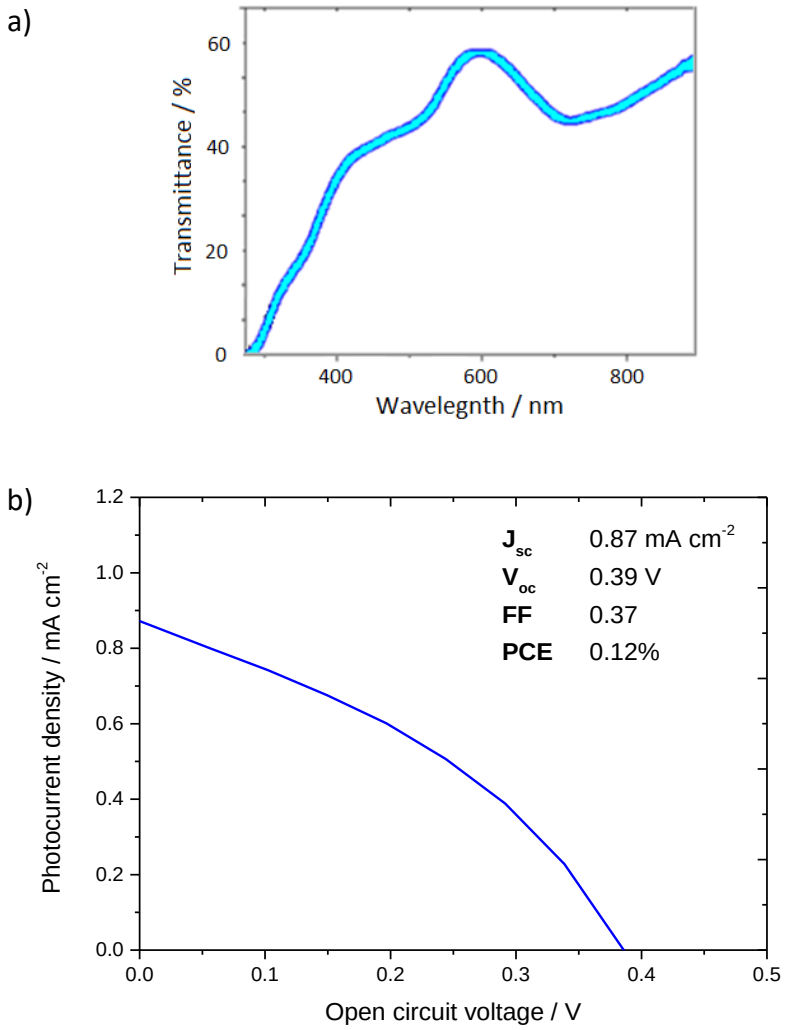

Figure 66 – a) Transmittance spectra of **316** on 6 µm thickness TiO_2 photoanode. b) *I-V* curve of DSSC with **316** under AM 1.5 solar light.

The DSSC realized with **316** achieved a very low PCE of 0.12%. As expected, the lack of bulky groups on the quaterrylene scaffold favours the dye's self-aggregation, affecting the overall photovoltaic parameters: a very low values of

photocurrent density of 0.87 mA cm^{-2} and open circuit voltage of 0.39 V have been achieved (Fig. 66b).

7. Conclusions and Future Outlook

In this chapter the synthesis and the application of two quaterrylene-based NIR-sensitizers have been reported. Both dyes displayed outstanding stability and the solubility issue related to the quaterrylene scaffold has been successfully overcame by the carefully core-functionalization. Sensitizer **316** has been preliminary investigated in DSSC achieving a PCE of 0.12% and as far as we know from the literature, **316** is the first example of quaterrylene-based DSSC.

However, the comparison with other common NIR-sensitizers like polymethine dyes and phthalocyanines, has been clearly demonstrated as the extended-rylenes cannot be able to compete in terms of photovoltaic performances and in terms of aesthetic features. In particular, the extended-rylenes (i) exhibit dramatically trickier synthetic procedures which are poor sustainable and that cannot be safely scaled, (ii) display tricky sensitization processes requiring more extended dye-loading times (e.g., 48 h for **316** *vs*. 6-8 h for polymethine dyes) and (iii) achieve lower aesthetic properties with AVT < 70%, inadequate values for the preparation of transparent and colorless NIR-DSSCs.

For these reasons, in the context of the IMPRESSIVE project we decided to leave the development of the extended-rylene NIR-sensitizers to focus our attention on the development of a new class of squaraine-based NIR-sensitizers, surely less stable but easier to synthetise.

Although the DSSC with **316** displayed a PCE of only 0.12%, further improvement could be achieved optimizing the dye-loading process: we are enough confident that CDCA co-adsorption can improve the PCE preventing the self-aggregation that strongly afflicts **316**. Another interesting strategy to improve the PCE could be the integration of a scattering-layer on the photoanode to increase the harvesting ability at the expense of the aesthetic features of the final device.

CHAPTER 3 – DHP-based Squaraine as NIR-Sensitizers for NIR-DSSCs

As mentioned in Chapter 1, squaraine dyes are the most studied NIR-sensitizers in DSSCs due to the versatility offered by their structures toward new molecular designs. Squaraines usually exhibit absorption's maxima between 650-700 nm with molar extinction coefficients between 1.5-3.0 M^{-1} cm^{-1}. As already reported in the Chapter 2 for extended-rylene dyes, a suitable NIR-sensitizer for the IMPRESSIVE project requires (i) LUMO energy level located at -3.75 eV, (ii) HOMO energy level located at -5.25 eV and (iii) a selective NIR-absorption beyond 700 nm.[29,32]

In Section 1.1.1 of Chapter 1, it has been reported as over the years several synthetic strategies have been developed allowing the shift of the absorption toward the NIR: i) the extension of the π-conjugated backbone by new lateral units, (ii) the squaric-core functionalization and (iii) the insertion of a π-bridge between the donor-part of the dye's structure and its anchoring group. However, to develop NIR-sensitizers suitable for IMPRESSIVE project, only the first one method guarantees to obtain squaraines with significantly red-shifted absorption. In addition, the key-points in the squaraine's structure to achieve high efficiencies are: (i) an asymmetrical push-pull molecule's architecture to improve the electron injection, (ii) the presence of out-of-plane alkyl chains to prevent the non-geminate recombination and (iii) the presence of π-bridge to positively influence both the electron injection and the non-geminate recombination.

Starting from the main goal to develop a new class of squaraine sensitizers with absorption > 700 nm, we thought that a lateral unit was not only able to allow the achievement of adequate absorption characteristics but was also able to satisfy the structural key points just mentioned.

In this context, the 2,3-dihydro-1*H*-perimidine moiety (DHP) has proven to be very interesting into development of new squaraine-based NIR-sensitizers. The

perimidine-derivatives chemistry starting in 1909 when an extensive study on their reactivity and their properties was reported by Sachs.[455] Perimidine-derivatives are well-known for their versatility in terms of reactivity, photophysical and biological properties. For these reasons, over the years DHP-based derivatives found application (i) in the synthesis of dyes for the fibres and plastic manufacturing,[456] (ii) in the development of anticancer, antimicrobial, antifungal, antiulcer, antioxidant drugs as well as anti-inflammatory agent,[457-460] and (iii) in development of fluorescent chemo-sensors.[461]

DHP is a tricyclic heterocycle containing two nitrogen atoms in the position 1 and 3 which by their electronic lone pairs increase the delocalization of π-electrons, mainly located on the naphthalene core (Fig. 67). In addition, the lone pairs confer interesting reactivity features enabling reactions on the two nitrogen atoms via both electrophilic and nucleophilic mechanisms.[462]

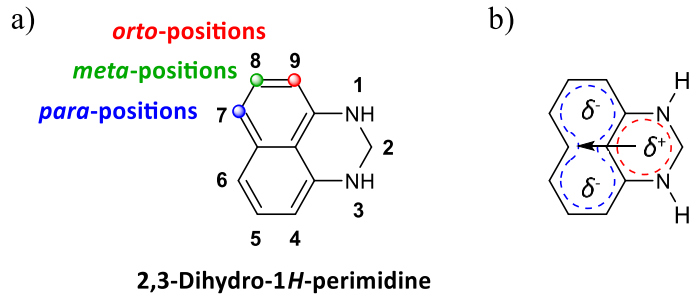

Figure 67 – a) Chemical structure of DHP. b) Charge distribution in the DHP.

For our purpose, the DHP can help us in the development of asymmetrical squaraines with a strong push-pull effect and bearing the fundamental out-of-plane alkyl chains. Interestingly, DHPs have been already exploited for the synthesis of particular SQ-based dyes called Squarylium dyes (Fig. 68). Compared to the squaraines' structures reported in Section 1.1.1 of Chapter 1, in the squarylium dyes the lateral units are directly bonded to the squaric-acid core without any methylene spacers. Usually, squarylium dyes exhibit slightly ipsochromic absorptions compared to a classical squaraine like *SQ01* (**1**) as well as display an increased tendency to the self-aggregation.[64,463]

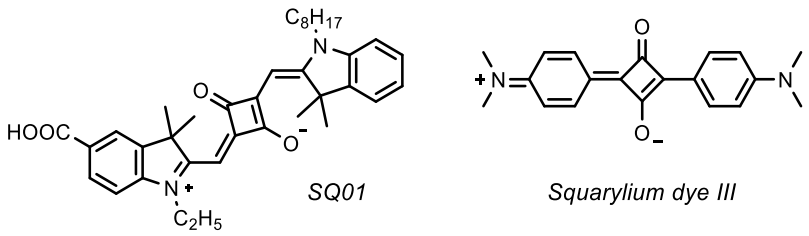

Classical squaraine **Squarylium dye**

Figure 68 – Comparison between chemical structures of classical squaraine and squarylium dyes.

The first DHP-based squarylium dye has been reported by Griffith *et al.* in 1993, demonstrating the outstanding ability of DHP to enlarge the π-conjugation backbone pushing the absorption toward the NIR.[464] In particular, while classical aniline-based squarylium dyes exhibit absorptions between 650-700 nm with molar extinction coefficients between 3.0-3.5·10^5 M^{-1} cm^{-1}, the DHP-based squarylium dyes display bathochromic absorptions beyond 800 nm alongside molar extinction coefficients nearby 1.5·10^5 M^{-1} cm^{-1}.[464] Over the years, the outstanding photophysical NIR features and the chemical versatility provided by the DHP moieties made DHP-based squarylium dyes very interesting for different application such as NLO technologies, chemical sensors, photography and fluorescence imaging.[465-473]

1. Project-proposal

As mentioned before, DHP-based squarylium dyes display strong absorptions in the NIR region beyond 800 nm. However, their structures are not suitable for the development of a sensitizer for NIR-DSSCs for different reasons: (i) the well-known self-aggregation affects the dye-loading process and is detrimental for the electron injection, (ii) DHP-based squarylium dyes are not characterized by a push-pull structure and (iii) it's not possible place a suitable anchoring group in conjugation with the dye's structure. For these reasons, we decided to try to develop a new class of asymmetrical intermediate structure between a classic

squaraine DSSC's sensitizer and a DHP-based squarylium dye in which the "classic indolenine-based moiety" will behave as acceptor bearing the carboxylic anchoring group whereas the "DHP-based part" will behave as donor, hosting the fundamental out-of-plane alkyl chains (Fig. 69).

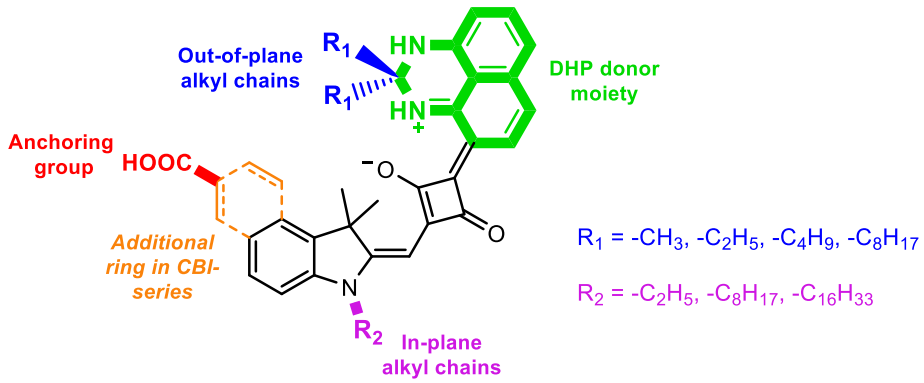

Figure 69 – General structure of the two synthetized series of DHP-based squaraines with the various structural variations (R_2 is always $-C_2H_5$ when R_1 is not $-C_8H_{17}$).

In particular, we decided to develop two different series of squaraines, the first one (*SQ-CI series* **341**-**344**) based on the CI lateral unit, while the second one with the more π-conjugated CBI moiety (*SQ-CBI series* **345**-**350**) (Fig. 70). Both series have been decorated with out-of-plane alkyl chains with progressive length to evaluate their effect on photovoltaic performance. In addition, the more efficient sensitizer (**348**) (as will be described in Section 5 of this chapter), it has been further modified to evaluate the effect of different in-plane alkyl chain length in comparison with the out-of-plane $-C_8$ ones.

All squaraines have been fully characterized studying their photo- and electrochemical properties in solution and analyzing their solid-state absorption features on TiO_2 semiconductor. Following, the squaraines have been tested in DSSCs, evaluating the effect of the out-of-plane alkyl chains on the sensitization process and on the photovoltaic performance. In addition, for the most performer sensitizer (**348**) the further optimization of the electrolyte solution has

been carried out. The synthesis of the two series of DHP-based squaraines has been carried out following the synthetic plan displayed in Fig. 70.

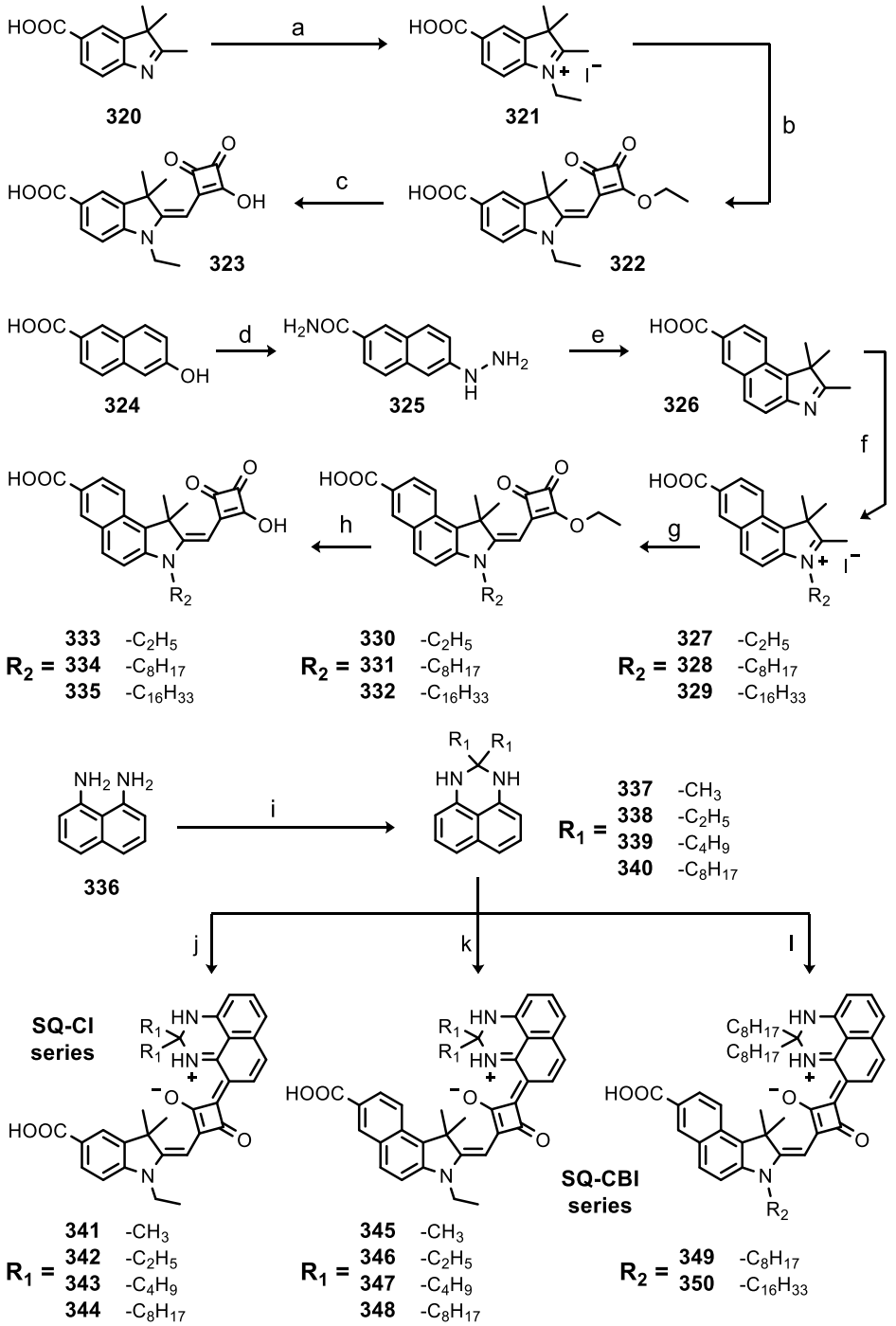

Figure 70 – Proposed synthetic scheme (reaction conditions reported in the next page).

a) Iodoethane, ACN, MW 155 °C, 20 min. b) DE-SQ, TEA, EtOH, reflux, 15 min. c) HCl 2.0 N in water, acetone, reflux, 8 h. d) Monohydrate hydrazine, 0 → 130 °C, 24 h under argon. e) CH_3COOH, 3-methyl-3-butanone, 0 → RT, overnight. f) 1-iodo alkyl, ACN, reflux, 48 h. g) DE-SQ, TEA, EtOH, reflux, 12 h. h) HCl 2.0 N in water, acetone, reflux, 8 h. i) Ketone, PTSA, toluene, reflux, 16 h in Dean-Stark apparatus. j) **323**, DHP (**337**-**340**), *n*-butanol/toluene, MW 160 °C, 30 min. k) **333**, DHP (**337**-**340**), *n*-butanol/toluene, MW 160 °C, 40 min. l) **334** or **335**, **340**, *n*-butanol/toluene, MW 160 °C, 40 min.

2. Synthesis

Following the reported synthetic scheme (Fig. 70), the synthesis of DHP-based squaraines started with the preparation of the indolium iodide salts **321** and **327**-**329** to activate the reactivity of the α-methyl of the indoline-derivatives.

The synthesis of **321** has been carried out with the carboxy indolenine (CI) **320**, while **327**-**329** salts have been prepared starting from the carboxy benzoindolenine (CBI) **326**. However, while CI **320** is commercially available, CBI **326** has been easily prepared in large scale (> 30 g) following a reported two-steps procedure.[87] In the first step, the 6-hydroxy-2-naphthoic acid **324** is transformed in the 6-hydrazineyl-2-naphthamide **325** by hydrate hydrazine (reaction **d** in Fig. 70) and in the second step, the CBI is prepared by the classic Fisher indole synthesis (reaction **e** in Fig. 70).

The indolium iodide salts **321** and **327**-**329** have been generally prepared by nucleophilic substitution in presence of the respective alkyl-iodide in refluxing ACN (reaction **f** in Fig. 70).[84] However, the synthesis of CI indolium salt **321** has been also carried out in microwave (MW) reactor following a reported procedure (reaction **a** in Fig. 70).[474]

Generally, in the synthesis of symmetrical squaraine dyes, such as **40**-**45**, an excess of indolium iodide salt (usually 2.1-2.5 eq.) has been directly reacted with one equivalent of squaric acid. Contrarily, in the synthesis of asymmetrical SQs, the direct synthetic strategy is not exploitable because the reaction of an equimolar mixture of the desired two lateral units with one equivalent of squaric acid leads preferably to formation of the symmetrical SQ, deriving from the more reactive intermediate (Fig. 71). For these reasons, the asymmetrical squaraines

require a multi-step synthesis via emisquarate or emisquaraine derivatives. Starting from the indolium iodide salts **321** and **327**-**329**, the synthesis of the respectively emisquarate derivatives **322** and **330**-**332** was carried in refluxing ethanol using the 3,4-diethoxycyclobut-3-ene-1,2-dione (DE-SQ) (see Appendix) as source of squaric-core and the triethylamine (TEA) as catalyst to active the indole's α-methyl (reaction **b** ang **g** in Fig. 70).

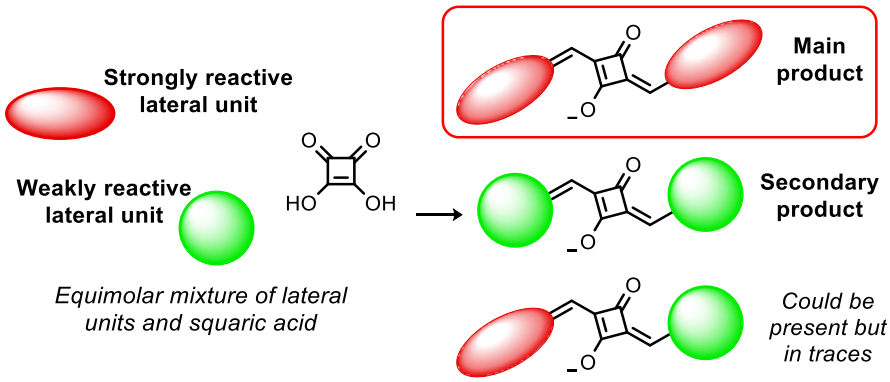

Figure 71 – Schematic representation of the most probable products' distribution in a one-pot synthesis for the preparation of asymmetrical squaraines.

Compared to the indolium iodide salts, the extension of the conjugation with the introduction of squaric-core gives interesting photophysical feature to the emisquarates. Usually, they display absorption maxima at roughly 420-450 nm with molar extinction coefficients between 7.0-8.0·10^4 M^{-1} cm^{-1}. It has been demonstrated that emisquarates can be directly used to synthetize asymmetrical squaraines, reacting with another lateral unit. Viscardi *et al.* reported successfully reactions between emisquarates and indolium iodide salts carrying out synthesis in MW reactor.[474] This direct strategy is advantageous, avoiding the synthesis and the purification of emisquaraines.

Following the same idea, the synthesis of **342** has been carried out in the MW reactor using the emisquarate **322** and the diethyl-DHP **338**. Despite several trials have been made, increasing the reaction time, the temperature and the concentration's ratio **322**/**338**, no formation of the desired compound has been

found. Probably, the less reactivity of either DHP-based derivatives and emisquarates does not allow the direct formation of desired asymmetrical squaraine. For these reasons, emisquarates have been easily converted in emisquaraines **323** and **333**-**335** by acid hydrolysis (reactions **c** and **h** in Fig. 70). Applying the same reaction conditions previously studied in the synthesis with the emisquarates, in the case of the emisquaraines the procedure led to the desired asymmetrical DHP-based squaraines (DHP-SQs).

Before cover the synthesis of squaraines in detail, will be reported a briefly discussion about the synthesis of DHP-derivatives. DHP derivatives are usually prepared by a condensation cyclization reaction of the 1,8-diaminonaphthalene **336** with an aldehyde or a ketone in presence of acid- or metal catalyst. In literature, several methods are reported in detail described by Sahiba *et al.*[462] For the preparation of our DHPs, we decided to develop a large-scale (≈ 3-5 g) acid-catalyzed method. DHPs **337**-**340** have been synthetized with a slightly excess (1.1 eq.) of aldehyde or ketone in presence of a catalytic amount of *p*-toluene sulfonic acid (PTSA) in refluxing toluene (reaction **i** in Fig. 70). The reactions have been carried out in Dean-Stark apparatus to promote the reaction's conversion removing the water. Generally, DHP synthesis exhibits almost complete conversions with reaction's yields between 80-90%. However, in some cases such as the mono-substituted DHPs and the di-substituted DHPs bearing short alkyl chains (**337**-**338**), yields are lower (ca. 50-60%) due to the formation of undesired side-product not easily to separate by flash chromatography. To improve the yields of these DHPs, we try to evaluate if the purification of the 1,8-diaminonaphthalene **336** starting material can decrease the formation of the side products. 1,8-diaminonaphthalene has been purified by sublimation procedure, affording pure crystals of **336**.[475] However, the comparison between reactions carried out with crude and pure **336**, displayed similar results. For these reasons, DHPs have been synthetized without any starting material purification.

As mentioned before, the synthesis of DHP-SQs (**341**-**350**) have been carried out in a MW reactor (reactions **j**, **k** and **l** in Fig. 70). DHP-SQs are prepared by a

condensation reaction between 1.0 eq. of emisquaraine and a slight excess of the desired DHP (1.5 eq.). In the reaction, the mixture *n*-butanol/toluene (1:1) has been used as solvent. In particular, toluene is used to improve the solubility of the starting materials, while the *n*-butanol has two main functions: (i) (i) in combination with toluene allows the azeotropic removal of the water (ternary azeotrope) (ii) increases the polarity of the mixture improving the MW absorption. Generally, DHP-SQs have been obtained with yields between 25-65%; the variability of yields is not due to the different reaction's activity of the emisquaraines or DHPs but depends by the purification procedure. The reactions toward DHP-SQs led to complex mixtures of side-products. Despite the desired squaraine is the main compound, the wide variety of side-products complicates the flash chromatography purification, leading to a decrease of the final yield.

3. Structural Study of DHP-SQs

As discussed in the introduction of this chapter, the DHP unit has been introduced in squaraines' synthesis in 1993 by Griffith *et al.* In their original work and in the following publications, the DHP-based SQs have been always reported with the structure display in Fig. 72a. In this structure, the lateral DHP units are linked to the squaric-core by the position 6.

However, in 2000 Busman *et al.* presented a patent in which has been reported a correction of the linkage of the lateral DHP unit with the four-membered squaric cycle but without any analytical evidence, leading to the revised structure in Fig. 72b).[476] In this revised structure, the lateral DHP units are linked to the squaric-core by the position 4. The comprehensive explanation of the real structure of DHP-based squarylium dyes has been provided by Hennig and Kiel *et al.* by means of a careful one-dimensional and two-dimensional NMR spectroscopy study on dye **351** (Fig. 72c).[472-473] In their investigations, they demonstrated as the DHP moiety is linked to the squaric core by the position 4. This structure configuration allows the formation of intramolecular hydrogen

bond interaction between one of the two perimidine-NH proton and the negatively charged oxygen of the squaric-core, leading to a more stable structure.

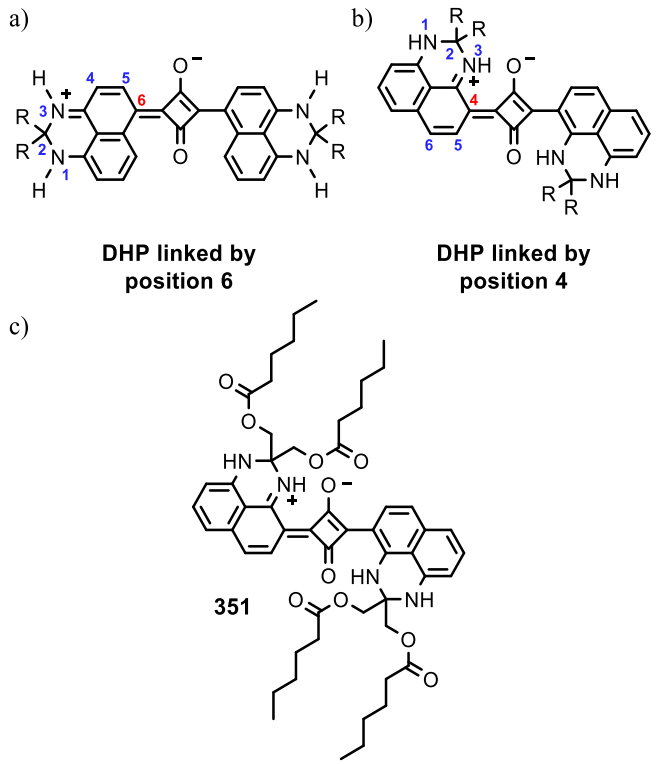

Figure 72 – a) DHP-based squarylium dye with DHP unit linked by position 6. b) DHP-based squarylium dye with DHP unit linked by position 4. c) Squarylium dye investigated by Hennig and Kiel *et al.*

In the case of our DHP-SQs, a same analysis approach has been performed to identify the real structure and to confirm that the lateral DHP units are linked to the squaric-core by the position 4 or by the position 6. For this reason, DHP-SQ **342** has been fully characterized by ^{1}H, ^{13}C, COSY, DEPT-135, COSY, HSQC and HMBC NMR experiments (all the spectra are reported in Section 1.10 of SI - Fig. 202-207). In this section, the numeration of carbon and hydrogen atoms is referred to the structure of **342** in Fig. 73.

The question whether the DHP lateral unit is linked at its position 4 or at its position 6 cannot be unambiguously answered with one-dimensional nuclear magnetic resonance spectroscopy alone (^{1}H,^{13}C and DEPT-135). For these

reasons, the two-dimensional nuclear magnetic resonance spectroscopic techniques have been performed (COSY, HSQC, HMBC).

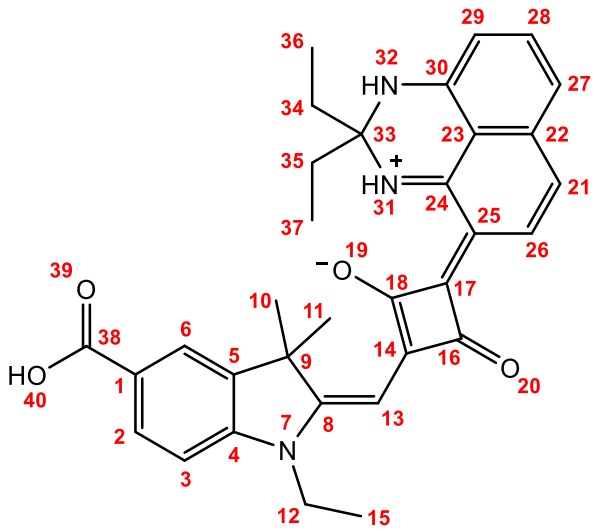

Figure 73 – Numeration of atoms in the assumed structure of SQ **342**.

To simplify the results' interpretation, we initially assigned the signals related to the carboxy indolenine moiety of the molecule (zoomed COSY, HSQC and HMBC spectra are reported in Fig. 74-76, respectively): (i) C-6 and H-6 at 123.37 and 8.09 ppm, (ii) C-2 and H-2 at 130.35 and 7.99 ppm, (iii) C-3 and H-3 at 110.63 and 7.50 ppm, (iv) C-1 at 126.60 ppm due to the ^{3}J coupling with H-3 and the absence of its signal in DEPT-135, (v) C-4 at 145.15 ppm due to the ^{3}J coupling with H-2 and the absence of its signal in DEPT-135, (vi) C-5 at 141.97 ppm due to the ^{3}J coupling with H-3 and the ^{3}J coupling with H-10, (vii) C-9 at 49.04 ppm due to their up field chemical shift and the absence of its signal in DEPT-135, (viii) C-10/C-11 and H-10/H11 at 26.07 and 1.72 ppm, (ix) C-12 and H-12 at 38.72 and 4.23 ppm, (x) C-15 and H-15 at 11.96 and 1.30 ppm, (xi) C-8 at 171.11 ppm due to the ^{2}J coupling with H-13 and the ^{3}J coupling with H-12, (xii) C-13 and H-13 at 88.22 and 5.90 ppm.

After the interpretation of the CI's signals, it has been easier to interpret the signals of the DHP moiety.

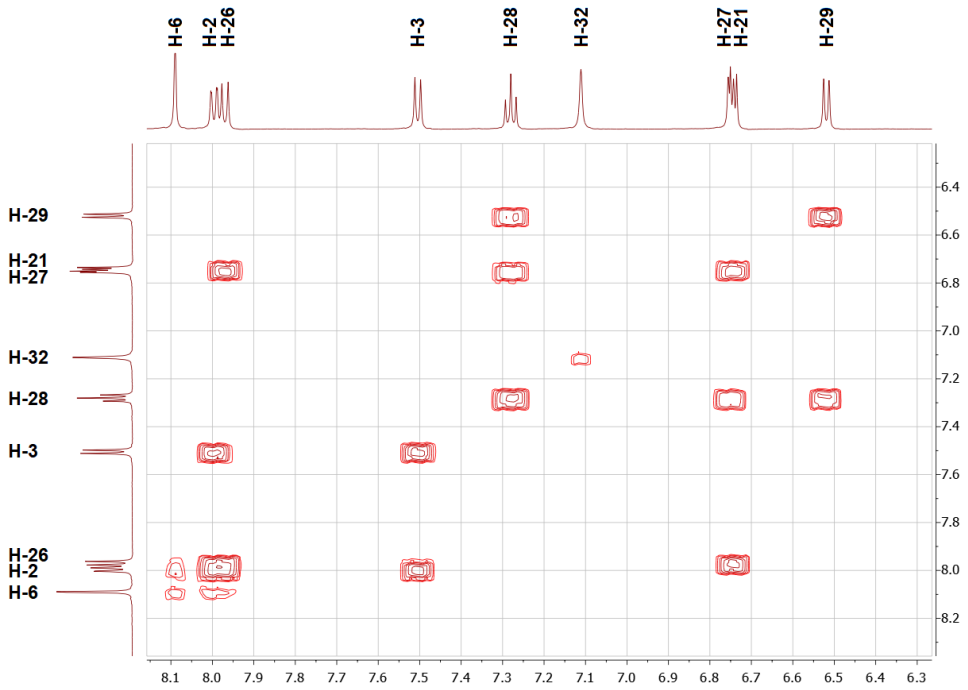

Figure 74 – Zoomed COSY of **342** (in DMSO-d_6).

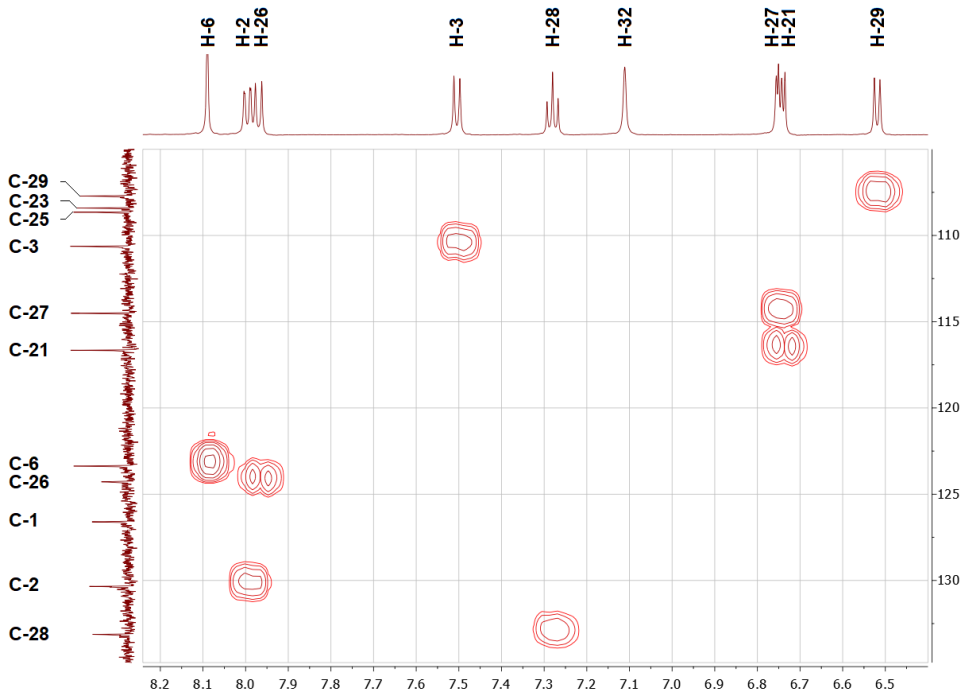

Figure 75 – Zoomed HSQC of **342** (in DMSO-d_6).

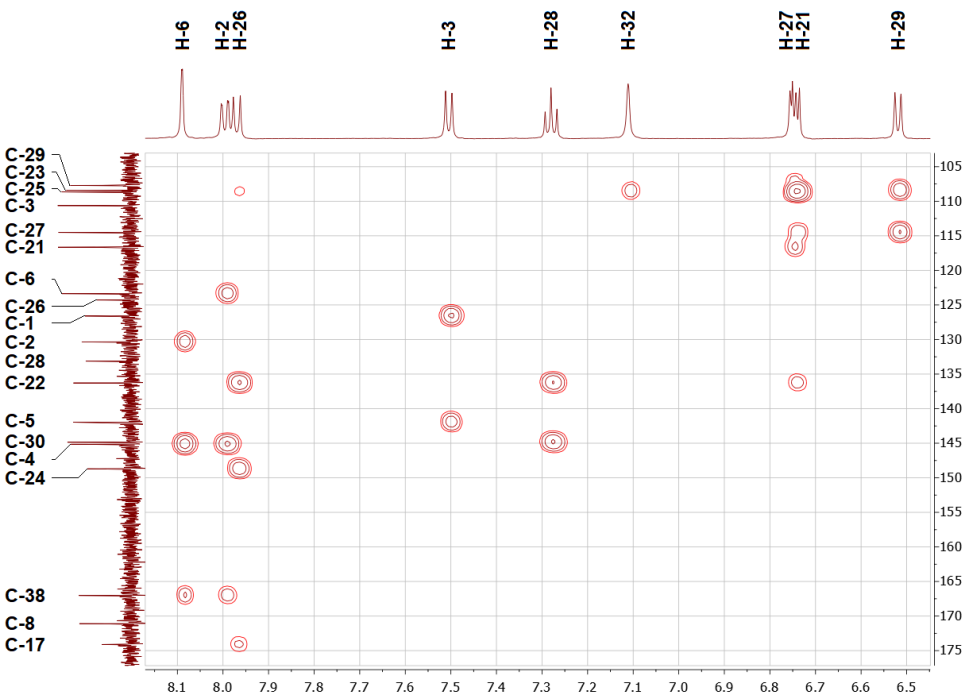

Figure 76 – Zoomed HMBC of **342** (in DMSO-d_6).

The lone triplet at 7.28 ppm can be unambiguously assigned to H-28 because is the only hydrogen atoms able to provide a signal with this multiplicity. It shows a ^3J coupling with the quaternary carbons C-30 at 144.86 ppm and C-22 at 136.29 ppm. The latter one exhibits a ^3J coupling with the doublet at 7.97 ppm, assigned at H-26. In addition, the latter doublet a 7.97 ppm is correlated by a ^3J coupling with the other quaternary carbon C-24 at 148.70 ppm. At this point, the signals assignment provides the keystone to define the real structure of SQ **342**. The two -NH protons exhibit two different singlet signals: the shielded one at 7.11 ppm (H-32) and the deshielded one at 10.52 ppm (H-31), respectively. Both signals display a ^3J coupling with the quaternary carbon C-23 at 108.41 ppm, furthermore the deshielded H-31 also exhibit an additional ^3J coupling with another quaternary carbon atom: C-25. This is possible only in the case of a SQ structure in which DHP unit is linked to the squaric core by the position 4 because otherwise, C-25 should be a tertiary carbon atom and thus exhibits a signal in DEPT-135 (Fig. 77).

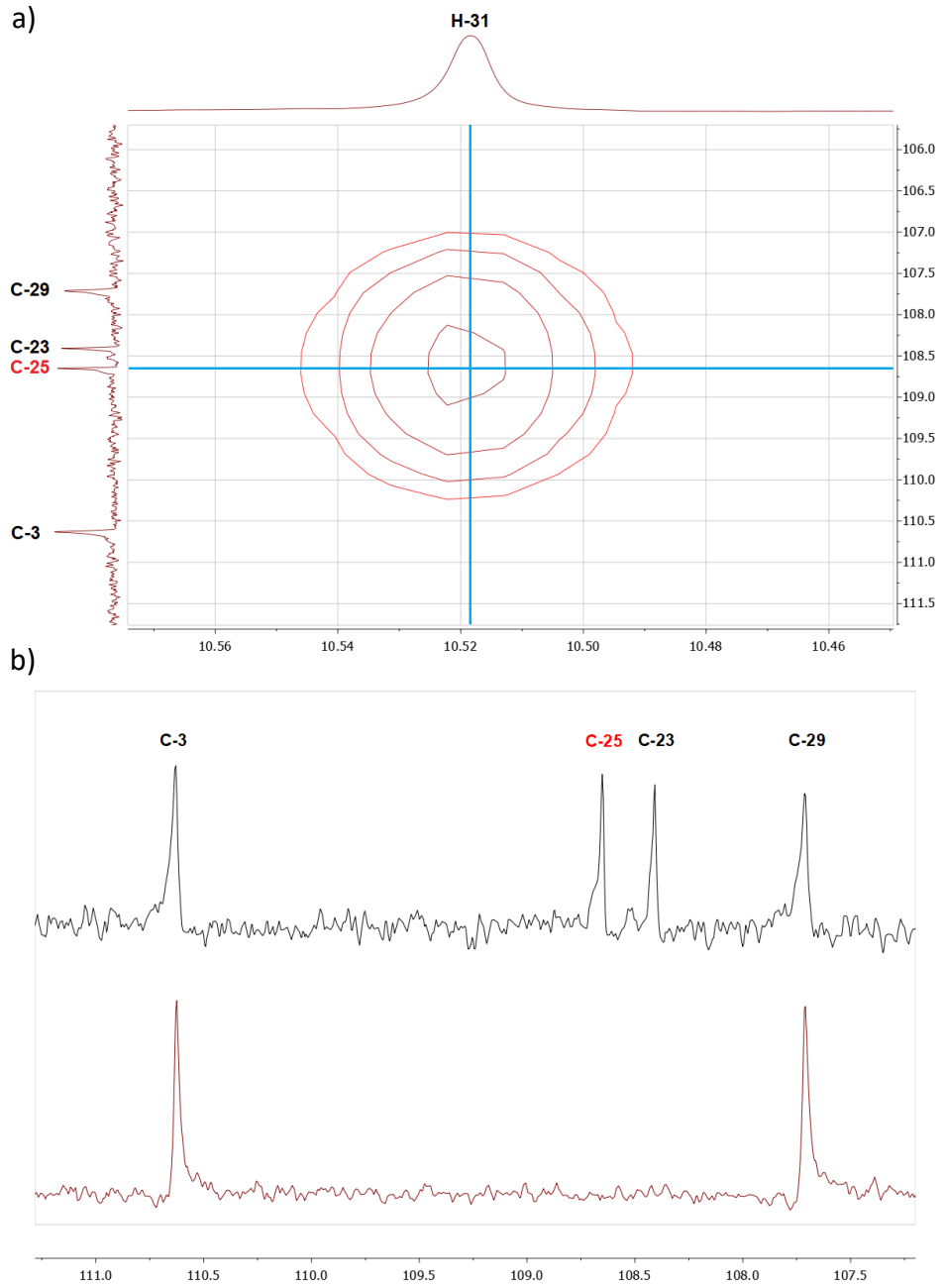

Figure 77 – a) Cross-peak between C-25 and H-31 in HMBC experiment. b) Particular of DEPT-135 spectrum in which C-25 doesn't exhibit any signal, confirming that is a quaternary carbon and thus involved in the linkage with the squaric core.

Finally, the remaining DHP's proton signals have been easily assigned as follow: (i) the triplet at 0.95 ppm at H-36 and H-37, (ii) the multiplet a 1.74-1.82

ppm at H-34 and H-35, (iii) the doublet at 6.52 ppm at H-29 and (iv) the multiplet at 6.74-6.76 ppm (with an integration of 2) is due to the overlap of the two doublets of H-21 and H-27.

The analysis of the ^{1}H-NMR spectra of the different DHP-SQs (**341**-**350**) demonstrated as all the structure are characterized by a connection DHP-squaric core in position 4 without any difference between the squaraines based on the CI unit or the CBI one.

4. Photo- and Electrochemical Characterization

The photophysical properties of all DHP-SQs **341**-**350** have been evaluated in ethanol (Tab. 19 and Fig. 78). In addition, their solvent-dependent behaviors have been qualitatively investigated in eight different solvents. In Fig. 79 are reported the absorption and steady state emission spectra of **342** in different solvents (absorption and steady state emission spectra of the other DHP-SQs and their Reichardt's plots are reported in Section 2.1 of SI; voltammogram for **341**-**350** are reported in Section 3.1 of SI - Fig. 321-322).

Table 19 – Photo- and electrochemical properties of DHP-SQs **341**-**350**.

Dye	λ_{max} [nm]	ε [M^{-1} cm^{-1}]	$E_{0\text{-}0}$ [nm] [a]	$E_{0\text{-}0}$ [eV]	HOMO [V *vs*. Fc/Fc^{+}] [b]	HOMO [eV]	LUMO [eV]
341	733	109 343	754	1.64	+0.07	-5.17	-3.53
342	746	108 086	762	1.63	+0.08	-5.18	-3.55
343	745	107 612	761	1.63	+0.08	-5.18	-3.55
344	744	93 359	760	1.63	+0.08	-5.18	-3.55
345	743	95 370	765	1.62	+0.03	-5.13	-3,51
346	749	102 549	767	1.62	+0.02	-5.12	-3.50
347	749	101 239	767	1.62	+0.03	-5.13	-3,51
348	744	102 695	767	1.62	+0.10	-5.20	-3.58
349	755	99 072	772	1.61	+0.10	-5.20	-3.59
350	756	95 794	772	1.61	+0.12	-5.22	-3.61

[a] Absorption and steady state emission spectra were performed in EtOH.

[b] CVs experiments were performed as described in SI using DCM as solvent.

All DHP-SQs exhibit a narrow absorption peak with a weak vibronic band, centered respectively around 740-750 nm and 680-700 nm. Molar extinction coefficients around $1.0 \cdot 10^5$ M^{-1} cm^{-1} were observed in ethanol for all DHP-SQs, independently by the alkyl chains length or indole *vs*. benzoindole moiety. The main band at ca. 740-750 nm can be attributed to a π-π* charge-transfer transition of the conjugated system.[75] Despite the more π-conjugation in the structures of CBI-based DHP-SQs **345**-**350**, no significant differences in absorption maxima are reported compared to the less conjugated CI-based DHP-SQs **341**-**344**. Interestingly, DHP-SQs with the shorter -C_1 out-of-plane alkyl chains (**341** and **345**) exhibit a slight blue-shift of absorption maximum as well as a slight enlargement of the absorption band causing the change of the peak-shape with the almost disappearing of the shoulder related to the vibronic band. This feature could be due to the higher propensity of SQs **341** and **345** to form H-aggregates in ethanol compared to other DHP-SQs bearing more bulky alkyl chains able to hamper the aggregation.[477]

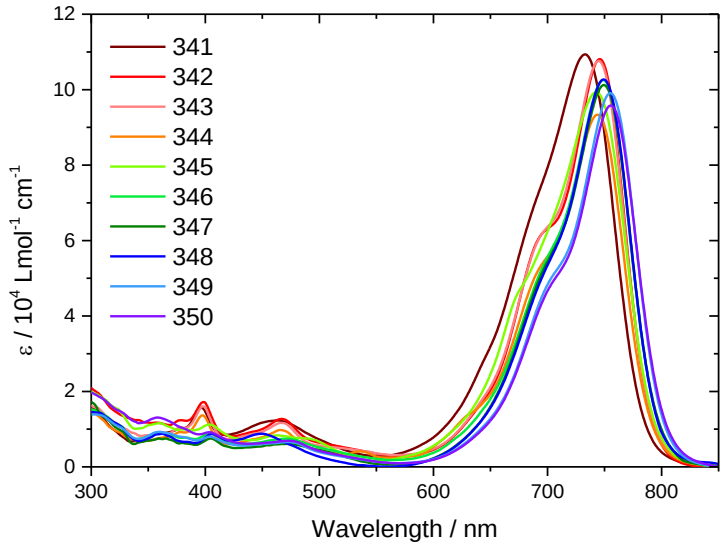

Figure 78 – Absorption spectra of DHP-SQs **341**-**350** in ethanol.

Similar behavior has been also observed in the solvatochromism studies. In particular, in aprotic polar solvents like ACN, DMF and acetone, DHP-SQs exhibit

blue-shifted absorption maxima as well as wider absorption bands with the almost disappearing of the vibronic band. Contrarily, increasing the non-polarity of the solvent, the absorption maximum is more narrow and red-shifted with the vibronic band well visible (Fig. 78). This behavior can be observed for all DHP-SQs (solvatochromism data for other DHP-SQs are reported in Section 2.1 of SI - Tab. 33-42), even for those ones bearing bulkier alkyl chains, suggesting solvents like ACN, DMF and acetone could be unsuitable for the dye-loading process due to their propensity to favor the aggregation in solution.

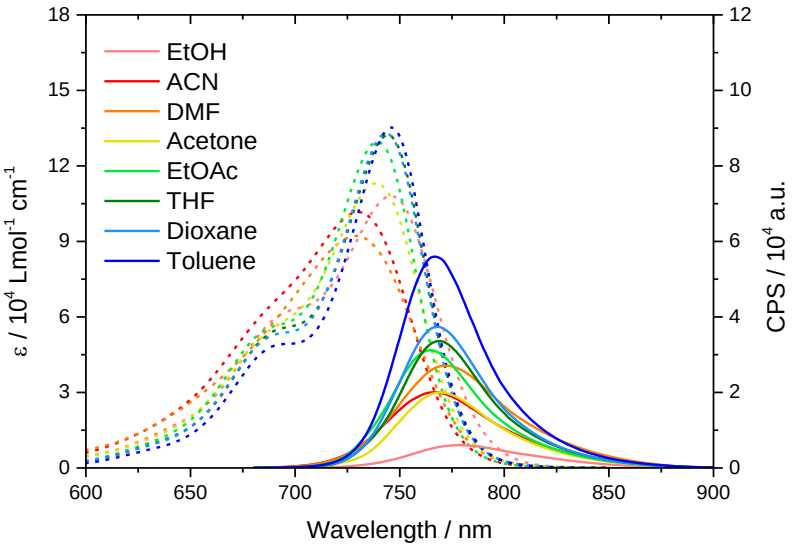

Figure 79 – Absorption (dashed) and steady state emission spectra of DHP-SQ **342** in different solvents. The emission spectra were normalized at 0.1 intensity at the excitation wavelength.

Even if not required for the application as sensitizers in DSSCs, the investigation of the steady state emission spectra in different solvents has been performed for all DHP-SQs, evaluating their fluorescence quantum yields (QY) (steady state emission spectra for all DHP-SQs are reported in Section 2.1 of SI - Fig. 297-305). This investigation was performed to evaluate the possible application of DHP-SQs as NIR fluorescent probes. A briefly structure-activity photophysical investigation in liposomes of DHP-SQs **341**-**348** will be reported in Addendum 2.

The emission profiles display the same trend above-mentioned: all DHP-SQs generally provide weaker QYs in polar solvents (QYs between ca. 1-4%) while higher QYs (> 7%) have been achieved in non-polar solvents, confirming the higher propensity of this SQs to the aggregation in polar solvents. In particular, higher QYs have been reached for **349** and **350**, the squaraines with the bulkier alkyl chains in the series. In addition, all SQs exhibit more red-shifted emission maxima alongside higher Stokes shifts with increasing polarity of the solvent (in SI - Tab. 33-42 and Fig. 306-315). The observed data for the DHP-SQs demonstrated as: (i) the positive solvatochromic behaviour of the absorption profiles that occurs upon environmental non-polarity increase, highlights the ability of non-polar solvents (e.g., toluene, 1,4-dioxane, THF, EtOAc) to stabilize better the LUMO then the HOMO, in agreement with data already reported for cyanines chromophores;[478] (ii) the higher Stokes shifts exhibit upon environmental polarity increase, demonstrate the sensitivity of the excited states to the solvent relaxation effects, confirming the polarity of the asymmetrical structure of the DHP-SQs.

As sensitizers for NIR-DSSCs, DHP-SQs **341**-**350** exhibit suitable strong absorption maxima beyond 700 nm. However, the absorption spectra show not negligible absorption in the visible between 350-600 nm (with an absorption background at 15000 M^{-1} cm^{-1}) and over 650 nm where is located the absorption tail of the vibronic band. For these reasons, these dyes can be adopted in NIR-DSSCs although probably will not allow the fabrication of completely colorless devices.

To evaluate their HOMO and LUMO energy levels, the procedure previously reported in Section 4 of Chapter 2 has been adopted. CV experiments have been performed to evaluate the HOMO energy level of DHP-SQs, while the LUMO levels were calculated by the “optic method”, using the optical band-band gap. As reported in Tab. 19, all DHP-SQs exhibit HOMO levels between -5.12 eV and -5.22 eV as well as LUMO levels between -3.50 eV and -3.61 eV. Compared to the previous reported QDI-based sensitizers **316** and **319**, DHP-SQs exhibit more

suitable HOMO levels, perfectly centred in the range set by the IMPRESSIVE project, while LUMO levels are slightly higher. As previously discussed in Chapter 1, at least 0.2 eV difference between the CB of the TiO_2 and the LUMO of the sensitizer is necessary to achieve an efficient electron injection: lower values do not allow the injection while higher ones lead to detrimental energy losses.[13] As far as DHP-SQs are concerned, they exhibit energy difference between 0.5-0.6 eV, acceptable to achieve efficient electron injection. These slightly higher differences compared to the optimum theoretical value of 0.2 eV, suggested us to investigate the possibility to use the TBP in the electrolyte solution to raise the TiO_2 CB and thus the V_{OC} of final devices with DHP-SQs.[479]

5. Photovoltaic application

DHP-SQs have been tested as NIR-sensitizers for NIR-DSSCs application. Contrarily to the previous QDI-based dyes, in this case a deeply investigation of the sensitizers' behavior has been possible, studying and optimizing the dye-loading processes and the formulation of the electrolyte solution. In this section will firstly comment the CDCA concentration on the dye-loading process of the two series of DHP-SQs: the CI-series (**341**-**344**) and the CBI-series (**345**-**348**). Following, the most efficient squaraine sensitizer **348** has deeply studied to further improve its efficiency by the optimization of the time and the temperature of the dye-loading process and by the optimization of the electrolyte solution. Finally, the effect of longer in-plane alkyl chain on photovoltaic performances has been evaluated in the DHP-SQ series **348**-**350**.

5.1. The Effect of CDCA Concentration on Photovoltaic Performances

As mentioned before in Section 1.1.1. of Chapter 1, the achievement of high PCE in squaraine-based DSSCs requires the prevention of the detrimental aggregation phenomena by (i) the insertion of bulky alkyl chains in the dye's structure and (ii) the introduction of CDCA as co-adsorbent.[60,62,80,106,108]

For this reason, the synergistic effect of out-of-plane alkyl chains of different lengths and of different CDCA concentrations on photovoltaic performance have been studied. The investigation was performed using transparent 4 µm thickness TiO_2 photoanodes (without blocking layer). The dye-loading solutions were prepared mixing the specific amounts of dye' stock solution (in ethanol abs.) and CDCA saturated solution (in ethanol abs.) to obtain five solutions with specific ratio CDCA/dye for each squaraines **341**-**348**: (i) 0, (ii) 50, (iii) 100, (iv) 250 and (v) 500 eq. It has been decided to the sensitizers with a concentration of 0.1 mM which usually is the benchmark for squaraine sensitizers.[78-80,106-109] The study suggested for several squaraine-based sensitizers that higher dye-concentration in the sensitization promote the formation of H-aggregates even performing short-time dye-loading processes.[60]

With the above-mentioned solutions, the dye-loading processes were performed for 6 h, at RT and in the dark. For each dye-loading solution, four photoanodes were dipped. After the sensitization, the solid-state absorption of photoanodes has been measured and then they were used to make the devices (detailed description of solid-state absorption measurement procedure and of DSSCs fabrication with **341**-**348** is reported in Section 7 and Section 8 of SI).

In Fig. 80a-81a are reported the solid-state absorption spectra of photoanodes sensitized with squaraines substituted with the shortest (**341** and **345**) and the longest (**344** and **348**) out-of-plane alkyl chains (data of other squaraines in Section 7.1 of SI - Fig. 324-325). In general, all the solid-state absorption spectra of DHP-SQs **341**-**348** on TiO_2 exhibit a broad band due to the presence of a new absorption component at roughly 690-700 nm related to the H-aggregates.[106,107] In particular, in the case of the squaraines with shortest chains, the absorption component of H-aggregates is prevalent and can be reduced only by high concentration of CDCA as co-adsorbent (> 250 eq.). CDCA as co-adsorbent causes the reduction of the H-aggregates' absorption component at 700 nm, allowing to achieve similar or lower absorbance values compared to the monomer band at roughly 750-760 nm. As shown in Fig. 80a, the ability of CDCA to prevent the H-

aggregation is similar for DHP-SQs with shortest alkyl chains (**341** and **345**). Contrarily, in the case of squaraines with longest alkyl chains (**344** and **348**), it seems that CDCA has a greater effect in the case of CBI-based squaraine **348**.

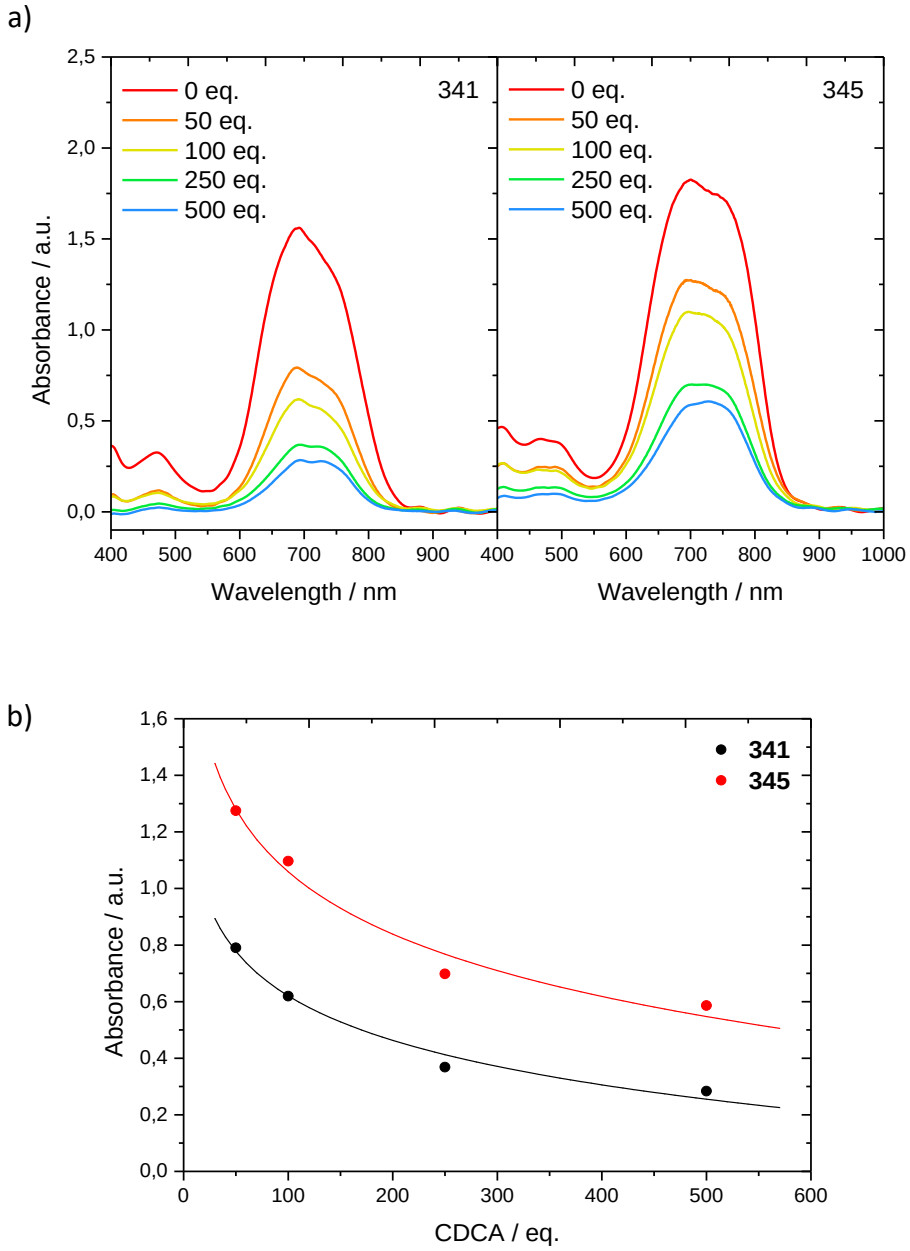

Figure 80 – a) Solid-state absorption spectra of photoanodes sensitized with **341** (left) and **345** (right) in presence of different concentrations of CDCA. b) Solid-state absorbance *vs*. CDCA concentration trend for the photoanodes sensitized with **341** and **345**.

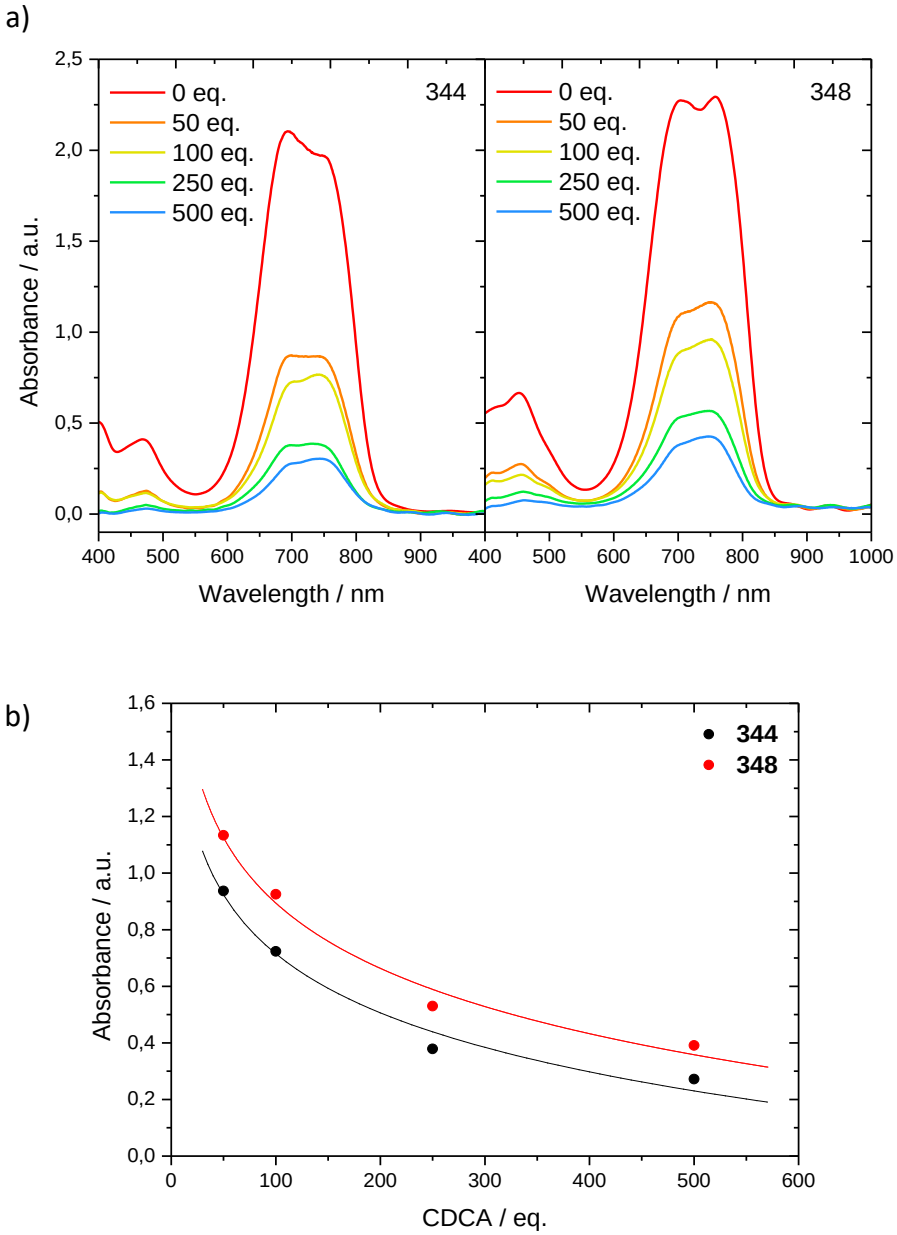

Figure 81 – a) Solid-state absorption spectra of photoanodes sensitized with **344** (left) and **348** (right) in presence of different concentrations of CDCA. b) Solid-state absorbance *vs*. CDCA concentration trend for the photoanodes sensitized with **344** and **348**.

The analysis of the absorption spectra in Fig. 81a demonstrate the key-role of the longer out-of-plane alkyl chains to counter the H-aggregates formation: in the case of **344** and **348**, 50 eq. of CDCA are already enough to lowering the

absorption contribute of H-aggregates compared to band absorption of the monomer. This trend is also confirmed by the solid-state absorption spectra of other squaraines on TiO_2: generally, squaraines with -C_4 out-of-plane chains (**343** and **347**) required less CDCA eq. to reduce the H-aggregation compared to squaraines with -C_2 chains (**342** and **346**) (see spectra in SI - Fig. 320). In addition, considering the variation of absorbance *vs*. the CDCA concentration of DHP-SQs (Fig. 80b-81b for **341**, **344**, **345**, **348** and SI - Fig. 324-325 for **342**, **343**, **346**, **347**) it is possible to see as CBI-based squaraines exhibit higher absorption, suggesting us that they could be the best choice to achieve higher photovoltaic performance. Finally, the comparison of solid-state absorption spectra also confirms that longer out-of-plane alkyl chains do not negatively affect the amount of dye loaded on TiO_2 surface, as demonstrate by Nithyanandhan *et al.* (Fig. 17).[106]

After the evaluation of the effect of CDCA concentration on the solid-state absorption spectra of DHP-SQs, we evaluated its effect on the photovoltaic performances (detailed description about DSSCs fabrication with **341**-**348** is reported in Section 8 of SI). In Fig. 82a-b are reported the PCEs as a function of CDCA concentration and as a function of the length of out-of-plane alkyl chains for CI-based squaraines **341**-**344** and for CBI-based ones **345**-**348** are reported. We can easily see that CBI-based squaraines (Fig. 82b) generally exhibit higher PCEs over CI-based SQs at almost any CDCA concentration. However, the most important trend showed is the higher PCEs achieved for squaraines bearing the longest out-of-plane alkyl chains (**344** and **348**) at any CDCA concentrations, confirming the key-role of these longer chains in preventing the aggregation and thus allowing the achievement of better photovoltaic performances.

A more detailed analysis of photovoltaic parameters of DHP-SQs **341**-**348** (Tab. 20) demonstrated as the great differences in terms of PCEs found between the two series (SQ-CI *vs*. SQ-CBI series) but also between the squaraines of the same series bearing different length alkyl chains, are mainly due to the large variation of the photocurrent density. This variation is well described by the comparison between **347** and **348**; **348** almost always exhibits double photocurrent density at any CDCA concentration.

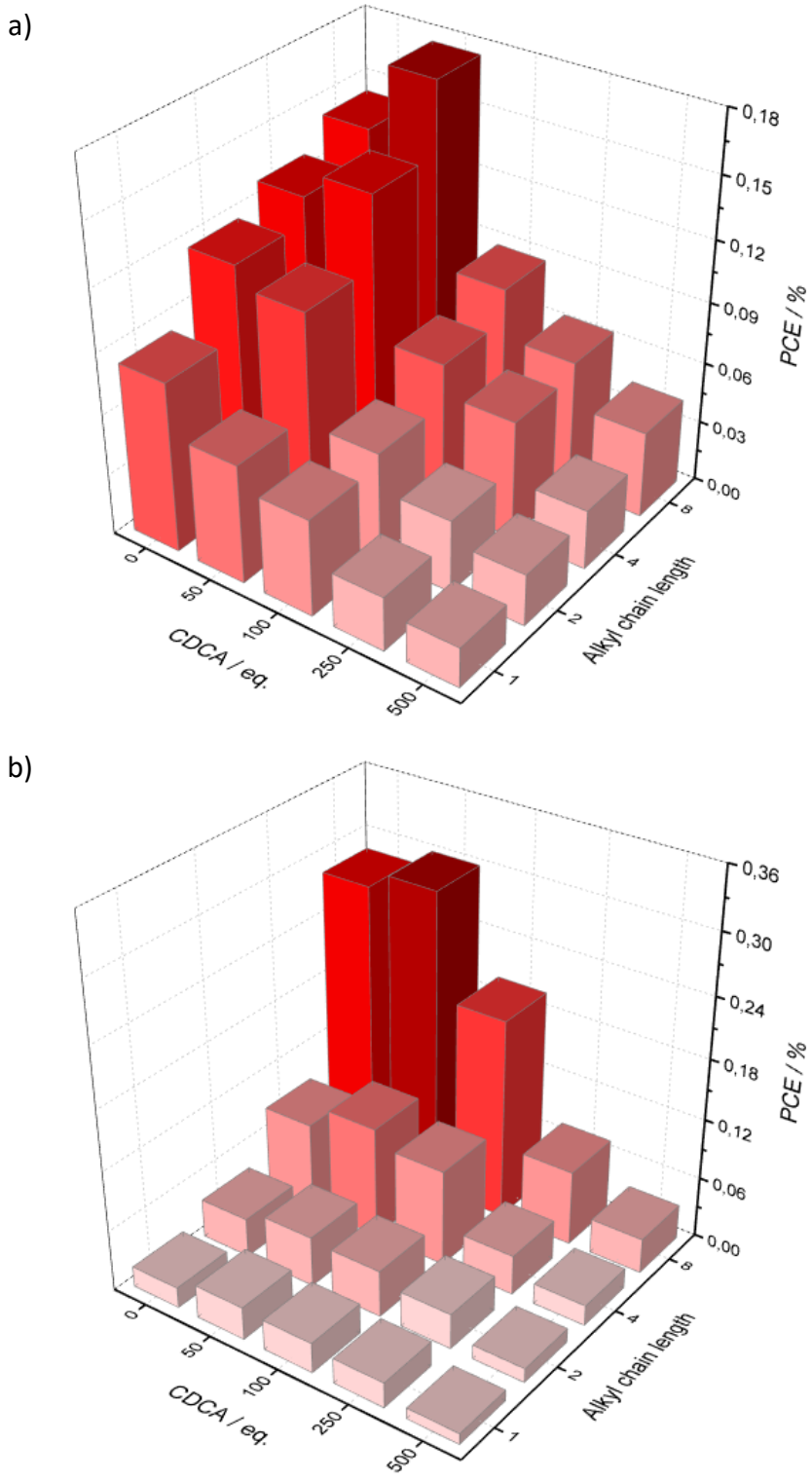

Figure 82 – 3D-plots PCE *vs*. CDCA concentration *vs*. alkyl chains length of (a) SQ-CI series and (b) SQ-CBI series.

Table 20 – Average photovoltaic parameters of DSSCs based on dyes **341**-**348** obtained performing dye-loading processes with different concentrations of CDCA as co-adsorbent.

Dye	CDCA [eq.]	J_{SC} [mA/cm^2]	V_{OC} [mV]	FF	PCE [%]
341	0	0.32 ± 0.02	436 ± 5	0.60 ± 0.01	0.08 ± 0.00
	50	0.23 ± 0.01	430 ± 4	0.58 ± 0.01	0.06 ± 0.00
	100	0.21 ± 0.01	414 ± 6	0.56 ± 0.01	0.05 ± 0.00
	250	0.13 ± 0.00	399 ± 7	0.53 ± 0.02	0.03 ± 0.00
	500	0.10 ± 0.01	392 ± 12	0.50 ± 0.04	0.02 ± 0.00
342	0	0.44 ± 0.02	439 ± 7	0.61 ± 0.01	0.12 ± 0.01
	50	0.37 ± 0.01	453 ± 7	0.63 ± 0.01	0.11 ± 0.01
	100	0.22 ± 0.01	421 ± 6	0.57 ± 0.02	0.05 ± 0.00
	250	0.16 ± 0.01	411 ± 7	0.54 ± 0.02	0.04 ± 0.00
	500	0.12 ± 0.01	404 ± 9	0.53 ± 0.01	0.03 ± 0.00
343	0	0.47 ± 0.02	446 ± 5	0.61 ± 0.01	0.13 ± 0.01
	50	0.46 ± 0.01	464 ± 11	0.66 ± 0.01	0.14 ± 0.01
	100	0.27 ± 0.02	444 ± 7	0.60 ± 0.02	0.07 ± 0.01
	250	0.23 ± 0.02	434 ± 6	0.59 ± 0.02	0.06 ± 0.01
	500	0.13 ± 0.01	416 ± 2	0.55 ± 0.01	0.03 ± 0.00
344	0	0.47 ± 0.01	475 ± 5	0.64 ± 0.01	0.14 ± 0.00
	50	0.54 ± 0.01	483 ± 5	0.67 ± 0.01	0.18 ± 0.01
	100	0.30 ± 0.01	472 ± 8	0.62 ± 0.01	0.09 ± 0.01
	250	0.25 ± 0.03	436 ± 7	0.59 ± 0.02	0.06 ± 0.01
	500	0.18 ± 0.03	430 ± 7	0.56 ± 0.03	0.04 ± 0.00
345	0	0.13 ± 0.01	365 ± 12	0.44 ± 0.01	0.02 ± 0.00
	50	0.18 ± 0.03	371 ± 13	0.49 ± 0.01	0.03 ± 0.01
	100	0.16 ± 0.01	388 ± 12	0.48 ± 0.00	0.03 ± 0.00
	250	0.13 ± 0.02	411 ± 11	0.47 ± 0.01	0.03 ± 0.00
	500	0.06 ± 0.02	368 ± 7	0.46 ± 0.01	0.01 ± 0.00
346	0	0.20 ± 0.01	402 ± 8	0.48 ± 0.01	0.04 ± 0.00
	50	0.24 ± 0.01	413 ± 9	0.49 ± 0.01	0.05 ± 0.00
	100	0.21 ± 0.02	415 ± 8	0.54 ± 0.03	0.05 ± 0.01
	250	0.15 ± 0.02	425 ± 7	0.54 ± 0.03	0.04 ± 0.00
	500	0.08 ± 0.01	369 ± 4	0.49 ± 0.01	0.01 ± 0.00
347	0	0.37 ± 0.00	441 ± 4	0.54 ± 0.01	0.09 ± 0.00
	50	0.43 ± 0.02	450 ± 14	0.57 ± 0.01	0.11 ± 0.01
	100	0.38 ± 0.02	439 ± 16	0.57 ± 0.01	0.10 ± 0.01
	250	0.16 ± 0.02	428 ± 4	0.56 ± 0.01	0.04 ± 0.01
	500	0.10 ± 0.01	391 ± 18	0.50 ± 0.02	0.02 ± 0.00
348	0	0.97 ± 0.02	471 ± 21	0.62 ± 0.01	0.29 ± 0.01
	50	0.97 ± 0.04	475 ± 8	0.66 ± 0.02	0.30 ± 0.02
	100	0.62 ± 0.05	476 ± 9	0.68 ± 0.01	0.20 ± 0.02
	250	0.27 ± 0.05	456 ± 11	0.58 ± 0.03	0.07 ± 0.02
	500	0.15 ± 0.02	421 ± 10	0.55 ± 0.01	0.03 ± 0.01

Average and standard deviation calculated on four independent repetitions.
Electrolyte: 1.0 M DMII, 0.05 LiI, 0.03 M I_2, 0.1 M GuSCN, ACN/MPN 85/15.

In addition, even the open circuit voltage and FF achieved higher values in squaraine with longer chains although the variations are less remarkable than those displayed by the photocurrent density (3D plots of other photovoltaic parameters are reported in Section 9 of SI - Fig. 328-330). For these reasons, after this analysis we decided to select the squaraine **348** as best candidate for the fabrication of DSSCs. To further improve the PCE of **348** we decided to optimize the dye-loading process studying the effect of time and temperature on the photovoltaic performance.

5.2. The Effect of the Dye-loading Time and Temperature

As above-mentioned, squaraine **348** with 50 eq. of CDCA in dye-loading solution achieved the best PCE of 0.30%. To further improve the photovoltaic performances, the effect of the time and the temperature on the dye-loading process of squaraine **348** with 50 eq. of CDCA has been investigated.

It is well known that time and temperature can deeply influences the dye-loading process, modifying the dye-packing on the TiO_2 surface.[60] Long times can promote the adsorption of higher amount of dye on the TiO_2 surface but if the process is too extended, the dye-aggregation is favoured resulting in lower photovoltaic performances. In the case of sensitization temperature, it has been demonstrated for different type of sensitizers, like ruthenium complexes and cyanines, that low temperatures can positively modify the dye-packing on TiO_2 surface, slowing-down the tendency to the formation of aggregates.[61,142] Obviously, the low temperatures influence the kinetic of the adsorption process and for this reason usually the sensitizations at low temperature requires extended dye-loading times.

For these reasons, we performed different dye-loading processes at 16 and 24 hours at two different temperatures: 2 °C and RT. For each dye-loading different condition, three photoanodes were dipped.

In Tab. 21 and Fig. 83 are reported the photovoltaic performances of DSSCs made performing different dye-loading processes. The data demonstrate that

extended dye-loading times generally raise all the photovoltaic parameters, demonstrating as the adsorption process on TiO_2 of DHP-SQ **348** has a slow kinetic. Particularly, low temperature dye-loading processes leading to impressive FFs over 0.72.

Table 21 – Average photovoltaic parameters of DSSCs based on sensitizer **348** obtained performing dye-loading processes with different times and temperatures.

Temperature	Time [hours]	J_{SC} [mA/cm^2]	V_{OC} [mV]	FF	PCE [%]
RT	6	0.97 ± 0.04	475 ± 8	0.66 ± 0.02	0.30 ± 0.02
	16	1.14 ± 0.12	502 ± 4	0.66 ± 0.01	0.38 ± 0.04
	24	1.80 ± 0.13	513 ± 7	0.72 ± 0.01	0.67 ± 0.04
2 °C	6	1.35 ± 0.15	505 ± 11	0.72 ± 0.01	0.49 ± 0.04
	16	1.38 ± 0.04	503 ± 3	0.72 ± 0.02	0.50 ± 0.03
	24	1.86 ± 0.15	517 ± 3	0.73 ± 0.00	0.70 ± 0.05

Average and standard deviation calculated on three independent repetitions.
Electrolyte: 1.0 M DMII, 0.05 LiI, 0.03 M I_2, 0.1 M GuSCN, ACN/MPN 85/15.

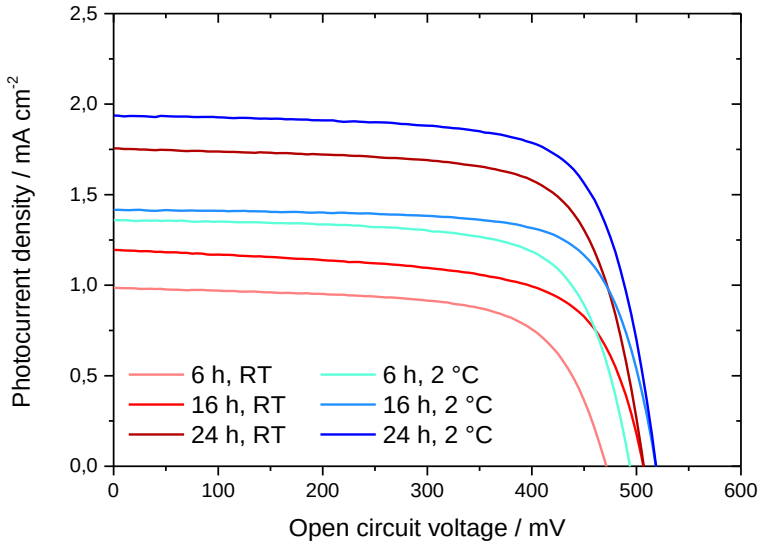

Figure 83 – I-V curves of DSSCs with **348** obtained performing dye-loading with different times and temperatures.

In addition, the improvement of all photovoltaic parameters is even found in low temperature sensitization procedures, highlighting that DHP-SQ **348** suffers

of detrimental aggregation phenomena: at RT the aggregates formation is probably favoured both thermodynamically and kinetically (the trends of photovoltaic parameters *vs*. dye-loading times and at different temperatures are reported in Section 9 of SI - Fig. 331-334).

For these reasons, after the investigation of time and temperature on the dye-loading process, we select the sensitization process at 2 °C for 24 h as best procedure for the fabrication of a NIR-DSSC based on DHP-SQ **348**.

5.3. The Effect of Low CDCA Concentration on DSSCs with 348

As displayed in Fig. 82b, **348** exhibits J_{SC} around 1 mA cm^{-2} in both 0 and 50 eq. of CDCA. The investigation of other CDCA concentrations inside the range 0-50 eq. could allow to further optimize the dye-loading process leading to higher photovoltaic performance. Following the same sensitization procedure described in Section 5.1 of this chapter, four additional dye-loading solutions with specific concentration's ratio CDCA/**348** have been prepared: (i) 5, (ii) 10, (iii) 15 and (iv) 25. Even in this case, for each dye-loading solution, four photoanodes were dipped.

Solid-state spectra performed with the new photoanodes confirmed as even less concentrations of CDCA are able to decrease the absorption contribute of H-aggregates (see spectra in Section 7.2 of SI - Fig. 326). This behaviour could be fundamental, highlighting the possibility to prevent the formation of H-aggregates using a less concentration of CDCA as co-adsorbent and thus allowing to increase the amount of sensitizer on the TiO_2 surface.[79,106]

In terms of photovoltaic performances, the less concentration of CDCA in the dye-loading process causes a further improvement in PCEs, achieving the record of 0.77% with 10 eq. of CDCA (Tab. 22). In particular, I-V curves in Fig. 84 displayed that low concentration of CDCA increases both photocurrent density and open circuit voltage (the trends of photovoltaic parameters *vs*. CDCA concentration are reported in Section 9 of SI - Fig. 335-338).

Table 22 – Average photovoltaic parameters of **348** obtained with low concentrations of CDCA as co-adsorbent.

CDCA [eq.]	J_{SC} [mA/cm^2]	V_{OC} [mV]	FF	PCE [%]
0	0.97 ± 0.04	475 ± 8	0.66 ± 0.02	0.30 ± 0.02
5	1.05 ± 0.15	513 ± 11	0.61 ± 0.01	0.33 ± 0.04
10	2.14 ± 0.03	502 ± 6	0.71 ± 0.00	0.77 ± 0.01
15	2.01 ± 0.05	504 ± 4	0.70 ± 0.01	0.71 ± 0.02
25	1.80 ± 0.16	509 ± 5	0.73 ± 0.01	0.67 ± 0.05
50	0.97 ± 0.04	475 ± 8	0.66 ± 0.02	0.30 ± 0.02

Average and standard deviation calculated on four independent repetitions.
Electrolyte: 1.0 M DMII, 0.05 LiI, 0.03 M I_2, 0.1 M GuSCN, ACN/MPN 85/15.

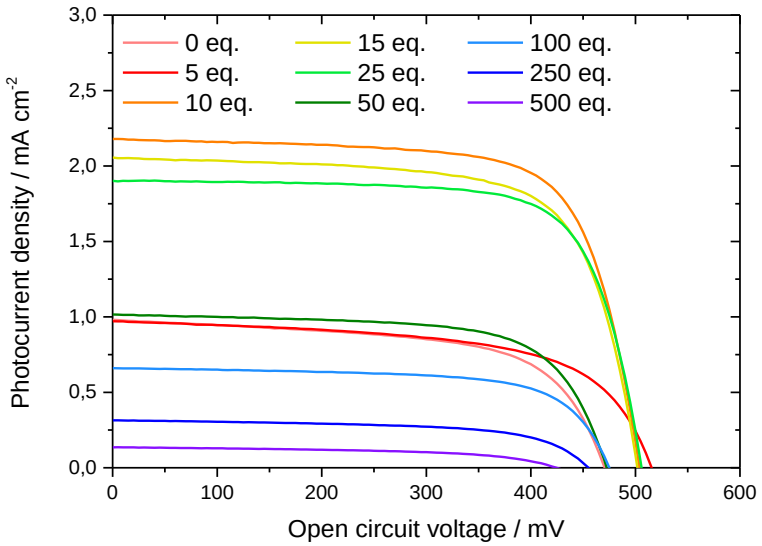

Figure 84 – I-V curves of DSSCs with **348** obtained performing dye-loading with different concentrations of CDCA.

The CDCA concentration in the dye-loading solution can be a useful tool not only to raise the photovoltaic performances but also to control the aesthetic of the device. As displayed in Fig. 85, high concentration of CDCA (> 250 eq.) leads to the fabrication of almost colorless devices. However, we already reported that the higher concentration of CDCA fall-down the device's performance. Contrarily, less amount of CDCA leads to better photovoltaic performances but is

disadvantageous in terms of aesthetic: devices are transparent but exhibit a bright-green coloration.

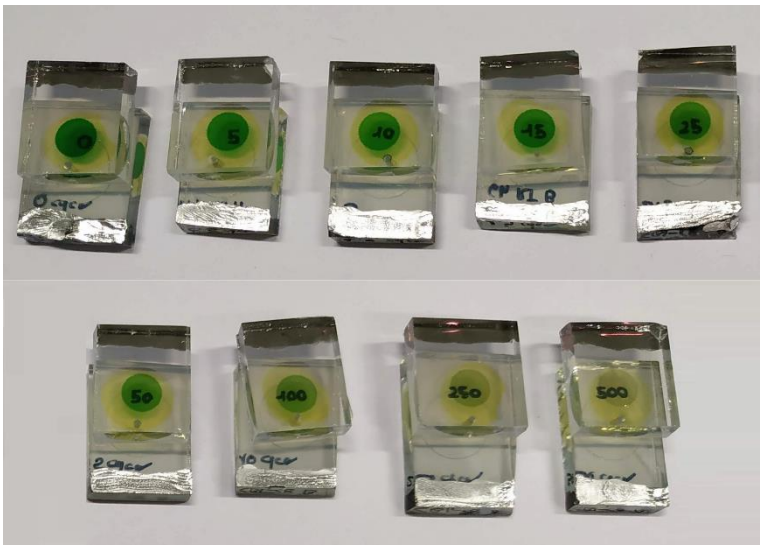

Figure 85 – Photography of DSSCs based on sensitizer **348** obtained using different concentrations of CDCA in the dye-loading solution. The numbers in black are written on the paper below the devices, demonstrating their transparency.

5.4. The Effect of 4-*tert*-Butyl Pyridine Concentration in the Electrolyte

As mentioned in Chapter 1, to assure an effective electron injection from the LUMO level of the sensitizers, the latter should be located at least 0.2 eV above the TiO_2 conduction band. In the case of **348**, it has been reported an energy gap of 0.5 eV between its LUMO energy level and the CB of TiO_2. This slightly higher difference compared to the optimum theoretical value of 0.2 eV, suggested us to investigate the possibility to use the TBP in the electrolyte solution to raise the TiO_2 CB and thus the V_{OC} of final device with **348**.

The 4-*tert*-butyl pyridine (TBP) is one of the most frequently used additive able to significantly improve the open-circuit voltage of the DSSC. However, even the photocurrent density is affected by the addition of TBP, usually resulting in a slightly decreased of it.[479] Over the years, several mechanisms have been proposed to explain the observed effects. Nazeeruddin *et al.* showed that the dark current, due to reduction of triiodide by electrons in TiO_2, was suppressed

by addition of TBP.[236] This was attributed to a blocking effect due to adsorption of TBP on active sites at the TiO_2 surface. Huang *et al.* estimated that addition of TBP and similar compounds decreased the electron-triiodide recombination rate by 1-2 orders of magnitude.[480] Schlichthörl *et al.* found that TBP addition led to a shift of the TiO_2 conduction band edge as well as an increased electron lifetime.[481] Nakade and co-workers, on the other hand, found no significant influence of TBP on the electron lifetime and attributed the increased V_{OC} solely to a shift of the band edge.[482] Boschloo *et al.* found that addition of TBP led to a decreased response in the red part of the photocurrent spectrum, which is in accordance with a band edge shift of TiO_2.[483]

To understand the effect of TBP on the open-circuit voltage and thus on the photovoltaic performance of DSSC with **348**, it has been decided to study three different electrolyte solutions containing respectively: (i) 0.1, (ii) 0.25 and (iii) 0.5 M of TBP. For comparison, all devices were fabricated using the non-optimized dye-loading procedure at RT for 6 h in presence of 50 eq. of CDCA.

Table 23 – Average photovoltaic parameters of **348** obtained with different concentrations of TBP in the electrolyte.

TBP [mol L^{-1}]	J_{SC} [mA/cm^2]	V_{OC} [mV]	FF	PCE [%]
0	0.97 ± 0.04	475 ± 8	0.66 ± 0.02	0.30 ± 0.02
0.1	0.74 ± 0.06	518 ± 7	0.65 ± 0.01	0.25 ± 0.02
0.25	0.46 ± 0.05	530 ± 10	0.63 ± 0.02	0.16 ± 0.03
0.5	0.35 ± 0.04	538 ± 2	0.62 ± 0.01	0.12 ± 0.02

Average and standard deviation calculated on three independent repetitions.
Dye-loading: **348** 0.1 mM in EtOH at RT for 6 h in presence of 50 eq. of CDCA.
Electrolyte: TBP (in Tab. 23), 1.0 M DMII, 0.05 LiI, 0.03 M I_2, 0.1 M GuSCN, ACN/MPN 85/15.

In Tab. 23 and Fig. 86 are reported the photovoltaic performances of DSSCs made using the electrolytes with different TBP-content. The data demonstrated that the higher concentrations of TBP improve the open-circuit voltage, from 475 mV without TBP up to 538 mV in the case of electrolyte with 0.5 M of TBP. However, higher concentration of TBP leads fall-down the photocurrent density

as well as involves a slight decrease of FF values resulting in worsening of photovoltaic performance (the trends of photovoltaic parameters *vs*. TBP concentration in the electrolyte solution are reported in Section 9 of SI - Fig. 339-342). In particular, the clear fall-down of photocurrent density is probably due to the too up-shifting of the TiO_2 conduction band, leading to a too lower energy gap between the LUMO energy level of **348** and the TiO_2 CB (less than 0.2 eV) and thus to a lower electron injection efficiency.

For these reasons, to achieve NIR-DSSC based on DHP-SQ **348** with high PCEs, we decided to not use TBP in the formulation of the electrolyte solution.

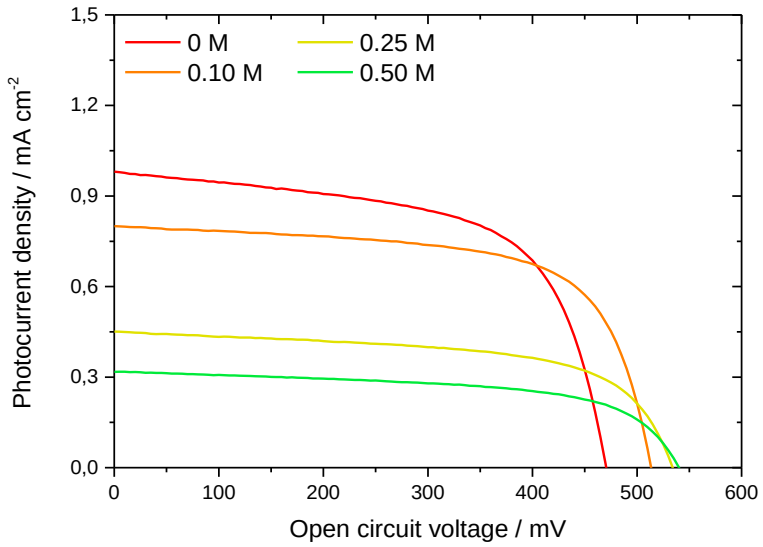

Figure 86 – I-V curves of DSSCs with **348** obtained using different concentration of TBP in the electrolyte solution.

5.5. The Effect of LiI Concentration in the Electrolyte

In the previous sections, we demonstrated as the optimization of dye-loading process of squaraine **348** allows to achieve a PCE of 0.77%. Despite the improvement of all photovoltaic parameters, the PCE resulted significantly low (Tab. 22): while the open-circuit voltage and FF displayed suitable values to reach high PCE, the photocurrent densities are very low and do not allow the achievement of higher PCEs.

In literature, it has been already demonstrated that in these cases, especially with low band-gap dyes like the NIR sensitizers, the proper formulation of the electrolyte solution can dramatically improve the photovoltaic performances. Naim *et al.* reported an improvement of the PCE higher than 1% with the cyanine **105** (Fig. 21) by the removal of the guanidinium thiocyanate (GuSCN) and the addition of high concentration of lithium iodide In the electrolyte.[61]

Usually, the GuSCN is used as additive in electrolyte due to its ability to suppress the surface recombination and to shift the conduction band to positive potentials. In addition, it is also known for its key role in the improvement of the devices' stability.[484] However, in our case it has been demonstrated that its presence in the electrolyte is absolutely detrimental: the DSSC obtained using an electrolyte with the same formulation but without the GuSCN, achieved an impressive PCE of 0.92%, three times compared the PCE of DSSC with 0.1 M of GuSCN in the electrolyte (Tab. 24 and Fig. 87). Due to its ability to suppress the surface recombination and to shift the conduction band to positive potentials, we expected to achieve an improvement in PCE due to a probable better electron injection and at the same time, to find a lower value of open-circuit voltage. However, in our case the removal of GuSCN caused an improvement of all photovoltaic parameters. Currently, the available data are insufficient to hypothesize the reason behind the dramatically improvement achieved simply removing the GuSCN from the electrolyte. Probably, additional measurements by transient absorption spectroscopy (TAS) and electrochemical impedance spectroscopy (EIS) might shed some light on this behavior.

Small alkali cation, like Li^+, are well-known for their specific adsorption on TiO_2 surface. The interaction of Li^+ with the surface of TiO_2 nanocrystals increases the flat band potential value, which moves the conduction band edge and surface traps down proportionally to the Nernst equation, 59 mV per decade of concentration.[61,485,486] Usually, the variation on Li^+ concentration in the electrolyte affects both open-circuit voltage and photocurrent density, in particular the former decreases while the latter achieves higher values.[486] The

effect of different Li^+ content in the electrolyte has been already studied in polymethine-based DSSC, studying its effect with squaraine **35** (Fig. 11) and cyanine **105** (Fig. 21).[61,487] In particular, in the case of squaraine **35** a 0.05 M concentration of Li^+ causes a slightly improvement of the photocurrent density and thus of the PCE while in the case of cyanine **105**, the higher Li^+ content in the electrolyte (1.0 M) leads to an impressive improvement of J_{SC} and PCE (J_{SC} with 0 M Li^+ = 5.5 mA cm^{-2}, J_{SC} with 1.0 M Li^+ = 12.1 mA cm^{-2}). In addition, in both cases the open-circuit voltage decreases, in accordance with the literature. Novelli *et al.* demonstrated that the introduction of Li^+ in the electrolyte solution of squaraine-based DSSC, affords notably decreased electron recombination. However, they have been demonstrated that an excessive concentration of lithium in the electrolyte drastically harms the device performance with squaraine dyes because lithium cation slows the rate of dye regeneration without accelerating the charge injection. Various experimental highlighted that lithium plays the role of complexing agent and that the negatively charged oxygen of the squaric core likely induces the formation of detrimental aggregate-like particles within the self-assembled monolayer upon the TiO_2 surface.[487]

Table 24 – Average photovoltaic parameters of **348** obtained with different concentrations of LiI in the electrolyte.

LiI [mol L^{-1}]	J_{SC} [mA/cm^2]	V_{OC} [mV]	FF	PCE [%]
0.05 (0.1 M GuSCN)	0.97 ± 0.04	475 ± 8	0.66 ± 0.02	0.30 ± 0.02
0.05	2.49 ± 0.15	509 ± 5	0.73 ± 0.01	0.92 ± 0.04
0.25	3.22 ± 0.28	441 ± 18	0.67 ± 0.01	0.95 ± 0.03
0.5	2.42 ± 0.15	368 ± 7	0.63 ± 0.01	0.56 ± 0.05
1.0	2.19 ± 0.31	334 ± 6	0.61 ± 0.01	0.45 ± 0.06

Average and standard deviation calculated on three independent repetitions.
Dye-loading: **348** 0.1 mM in EtOH at RT for 6 h in presence of 50 eq. of CDCA.
Electrolyte: 1.0 M DMII, LiI (in Tab. 24), 0.03 M I_2, ACN/MPN 85/15.

Starting from these interesting results, it has been decided to investigate the effect of Li^+ content in the DSSC with **348** to improve the photocurrent density

and thus the PCE. It has been investigated four different electrolyte solutions containing respectively: (i) 0.05, (ii) 0.25, (iii) 0.5 and (iv) 1.0 M of LiI. For comparison, all devices were fabricated using the non-optimized dye-loading procedure at RT for 6 h in presence of 50 eq. of CDCA.

In Tab. 24 and Fig. 87 are reported the photovoltaic performances of DSSCs made using the electrolytes with different LiI-content.

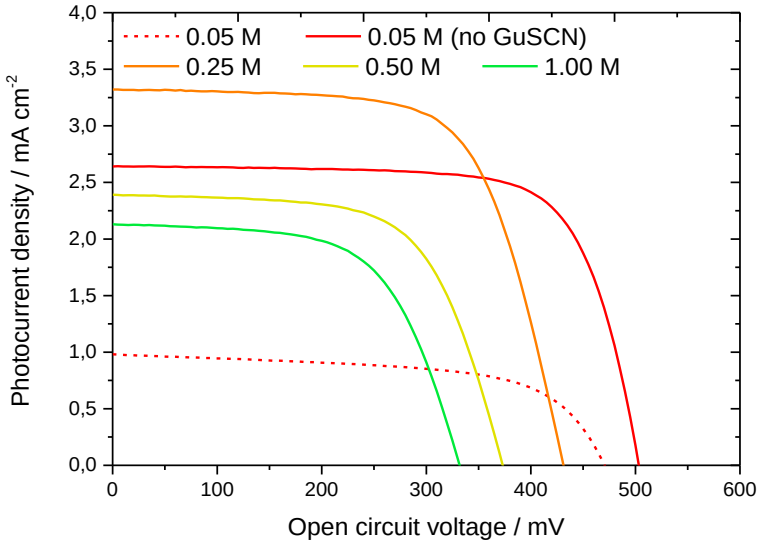

Figure 87 – I-V curves of DSSCs with **348** obtained using different concentration of LiI in the electrolyte solution.

In accordance with the literature, the data demonstrate that higher concentrations of LiI cause the fall-down of the open-circuit voltage, from 509 mV with 0.05 M of LiI up to 334 mV in the case of electrolyte with 1.0 M of LiI; moreover, the photocurrent density raised, achieving the highest value of 3.22 mA cm^{-2} in presence of 0.25 M of LiI. In particular, in the electrolyte containing LiI 0.25 M, it has been achieved the record PCE of 0.95%. As reported by Novelli *et al.*,[487] even **348** negatively suffers the high concentration of lithium cations, reporting the fall-down of all photovoltaic parameters in presence of 0.5 and 1.0 M of LiI (the trends of photovoltaic parameters *vs.* LiI concentration in the electrolyte solution are reported in Section 9 of SI - Fig. 343-346).

After the investigation of the effect of GuSCN and LiI content in the electrolyte solution, to achieve NIR-DSSC based on DHP-SQ **348** with high PCEs, we decided to use an electrolyte solution without GuSCN and with 0.25 M of LiI.

5.6. The Effect of Different Length In-plane Alkyl Chains

In the previous sections of this chapter, it has been reported our effort in the optimization of the dye-loading process and the electrolyte solution formulation to obtain a DSSC based on squaraine **348** with a high PCE. In this section, they will be firstly reported the photovoltaic performance achieved applying all the optimized conditions and after, it will be exhibited the investigation of the effect of different length in-plane alkyl chains on the photovoltaic performances using the squaraines **349** and **350**.

In Tab. 25 are reported the photovoltaic performances of DSSCs made following the optimized dye-loading process and using the optimized electrolyte solution. All the optimization allows to achieve for squaraine **348** a PCE of 1.51%. The remarkable improvement of PCE is mainly due to the high photocurrent density achieved with values above 4.0 mA cm^{-2} (in the cases of DSSCs obtained with dye-loading processes applying 10 and 25 eq. of CDCA, respectively).

Despite the outstanding improvement from the PCEs of the preliminary tests (0.30%), it was felt that further improvements could be achieved by modifying the structure of squaraine **348**. As reported in Section 1.1.1. of Chapter 1, over the years several structural modifications have been tested to improve the photovoltaic performances of squaraines. In particular, the breakthrough in terms of efficiency was achieved by the out-of-plane alkyl chains but previously, even the in-plane alkyl chains have been demonstrated to play a key-role in the improvement of the photovoltaic performances. Several examples demonstrated that longer in-plane alkyl chains prevent the dye-aggregation and reduce the charge recombination process between the injected electrons and the oxidized electrolyte leading to higher PCEs.[96-98]

Table 25 – Average photovoltaic parameters of DSSCs based on dyes **348**-**350** obtained performing dye-loading processes with different concentrations of CDCA as co-adsorbent and using the optimized electrolyte.

Dye	CDCA [eq.]	J_{SC} [mA/cm²]	V_{OC} [mV]	FF	PCE [%]
348	5	3.92 ± 0.11	489 ± 12	0.67 ± 0.01	1.28 ± 0.05
	10	4.56 ± 0.39	481 ± 6	0.68 ± 0.01	1.51 ± 0.14
	25	4.21 ± 0.21	467 ± 8	0.68 ± 0.01	1.33 ± 0.10
	50	3.02 ± 0.21	460 ± 16	0.65 ± 0.01	0.91 ± 0.07
349	5	5.64 ± 0.32	510 ± 4	0.70 ± 0.02	2.02 ± 0.09
	10	4.90 ± 0.35	525 ± 10	0.67 ± 0.02	1.73 ± 0.04
	25	3.58 ± 0.64	479 ± 6	0.70 ± 0.04	1.19 ± 0.12
	50	2.88 ± 0.21	444 ± 15	0.70 ± 0.02	0.90 ± 0.06
350	5	2.45 ± 0.21	429 ± 9	0.48 ± 0.05	0.49 ± 0.07
	10	2.40 ± 0.26	431 ± 9	0.50 ± 0.01	0.52 ± 0.03
	25	1.89 ± 0.14	411 ± 4	0.48 ± 0.05	0.37 ± 0.02
	50	1.59 ± 0.25	406 ± 12	0.51 ± 0.04	0.33 ± 0.02

Average and standard deviation calculated on three independent repetitions.
Dye-loading: **348** or **349** or **350** 0.1 mM in EtOH at 2 °C for 24 h in presence of CDCA (see Tab. 25).
Electrolyte: 1.0 M DMII, 0.25 M LiI, 0.03 M I_2, ACN/MPN 85/15.

For these reasons, it has been decided to synthetize two novel squaraine bearing -C_8 out-of-plane alkyl chains like **348** but with longer in-plane alkyl chains, such as -C_8 for **349** and -C_{16} for **350**, respectively (Fig. 70). The insertion of longer in-plane alkyl chains obviously changes the behaviors of squaraines **349** and **350** in the dye-loading process: we expect to achieve similar photovoltaic performances using a less amount of CDCA. However, it is important highlights that too longer in-plane alkyl chains could also negatively influences the dye-loaded amount of sensitizer and thus the ability of the photoanode to harvest the incident light, as demonstrated by Nithyanandhan *et al.*[108]

For these reasons, to be sure to find the optimal dye-loading conditions, it has been decided to investigate the effect of four different concentration's ratio CDCA/dye for both squaraine **349** and **350**: (i) 5, (ii) 10, (iii) 25 and (iv) 50.

In Tab. 25 and Fig. 88 are reported the photovoltaic performances of DSSCs with **349**-**350** compared to **348**. In accordance with the literature, the photovoltaic parameters of squaraine **350** bearing the longer in-plan -C_{16} alkyl

chain are clearly worse compared to **348** and **349**. However, while the lower photocurrent densities achieved by **350** are due to the lower amount of adsorbed dye on the photoanode due to the too bulky in-plane alkyl chain (the reason is well figure-out in Fig. 17), it's not clear the motif behind the lower values of open-circuit voltage and FF. It has been supposed that the low solubility of **350** in polar solvents (it was not possible performed ^{1}H-NMR in DMSO-d_6 and prepared the stock solution for the photophysical characterization in DMSO) alongside the low-temperature of the dye-loading procedure, can lead to the formation of undesired aggregates onto the TiO_2 surface, decreasing the photovoltaic performances.

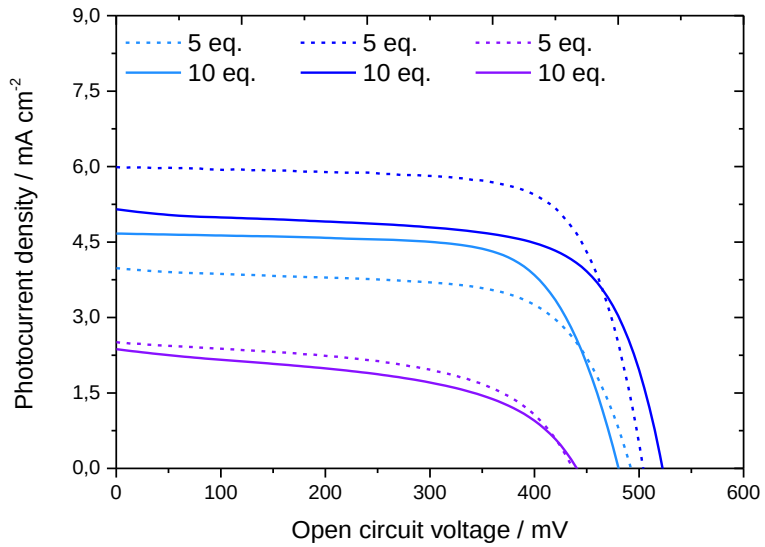

Figure 88 – I-V curves of DSSCs with **348** (light-blue), **349** (blue) and **350** (purple) obtained performing dye-loading with different concentrations of CDCA: 5 eq. (dashed) and 10 eq. (solid).

Contrarily, squaraine **349** with -C_8 in-plane alkyl chain achieved the record PCE of 2.02%, exceeding the previous record of 1.51% achieved by **348**. In presence of 5 and 10 eq. of CDCA in the dye loading solutions, the DSSCs with **349** achieving higher PCE compared to **348**, mainly due to the higher photocurrent densities exhibited. These results are due to the synergic effect of the in-plane and out-of-

plane alkyl chains to prevent the self-aggregation and the electron recombination: in the case of **349**, the in-plane -C_8 chain further improve this synergic effect resulting in better photovoltaic parameters (the trends of photovoltaic parameters *vs*. CDCA concentration are reported in Section 9 of SI - Fig. 347-350). However, for higher concentrations of CDCA in the dye-loading solutions, squaraine **348** come back to display better photovoltaic performances. This is mainly due to the more sensitiveness of **349** toward the CDCA content. A too high concentration of CDCA in the dye-loading solutions compete with the dye-adsorption leading to a lower amount of dye's molecules on the photoanode. The increase of the length of in-plane alkyl chain, the above-mentioned effect becomes more and more relevant leading to worse photovoltaic performances.[108]

6. Conclusions and Future Outlook

In this chapter the synthesis and the application of a series of DHP-SQs sensitizers has been reported.

Between the two series of squaraines, the CBI-series demonstrated to be the most performing and in particular, a record PCE of 2.02% was achieved with **349**. The optimization of dye-loading process and the electrolyte solutions suggested different important tools for the fabrication of efficient DSSCs with these novel DHP-based squaraines: (i) a concentration of 5-10 eq. of CDCA is necessary in the dye-loading solution to prevent the self-aggregation and the electron recombination, (ii) dye-loading procedure performed with longer time and lower temperature provide better photovoltaic performance due to the probable less tendency of these dyes to the self-aggregation at low temperatures, (iii) the TBP must be removed from the electrolyte solution to avoid the shift of the TiO_2 CB to values too near to the LUMO energy level of squaraine sensitizers, (iv) the removal of GuSCN and the concentration of 0.25 M of LiI allow to achieve better photocurrent densities and thus PCEs and finally (v) the insertion of too longer in-plane alkyl chains, like -C_{16} in **350**, fall-dawn the photovoltaic performances.

Despite the optimization, the comparison of DHP-SQs with other squaraines dyes, clearly demonstrated their lower performances: currently, squaraine-based DSSC achieved a record PCE of 9.0%.[106] However, it is important highlight that our results were achieved using thin photoanode (only 4 μm) without scattering-layer and above-all, using squaraines with a lower band-gap and with absorption maxima centered at roughly 750 nm in which the incident light is lower energetic.

Although DHP-SQs probably will never reach the efficiencies of the most performing squaraine-based sensitizers, we are confident about the possibility to further improve the photovoltaic performances of DHP-SQs.

Recently, it has been demonstrated for squaraine **78** (Fig. 15) bearing a -C_{12} in-plane, a -C_{10} and -C_{12} out-plane alkyl chains, that the solvent selected for the dye-loading can strongly influence the formation of the sensitizer' mono-layer leading to very different photovoltaic performances: in particular, high efficiencies are obtained using acetonitrile as solvent in the dye-loading procedure.[488] Following this concept, the most performing DHP-SQs **348** and **349** could be tested using the ACN as solvent for the dye-loading procedure.

Beside to the optimization of the sensitization procedure, another improvement could be reached by the structural modification of squaraines **348**-**349** by the insertion of different anchoring moiety like the cyanoacrilic group, well-known for their strongly electron-withdrawing property. The substitution of the classic carboxylic acid group with the cyanoacrilic one, could improve the push-pull effect of the structure resulting in higher electron injection and thus in higher PCEs.

To conclude, in the context of the IMPRESSIVE project, DHP-SQs are not suitable as clearly figure-out in Fig. 85: even if they allow the fabrication of transparent devices, they present not negligible absorption in the visible that compromises the realization of colorless devices.

CHAPTER 4 – *Impy*-based Copper Complexes as Possible Redox Mediators for NIR-DSSCs

In the last 10 years, there was a renaissance of DSSCs following the development of a new class of efficient redox mediators based on copper complexes.[25,489] As mentioned before in Chapter 1, the copper complexes are currently the most performer redox mediators in DSSCs, achieving PCEs over 13%. Their success is due to the possibility to achieve high redox potentials (over 1.0 V *vs*. *NHE*) and thus high open-circuit voltages (up to 1.2 V), by the fine tuning of the complexes structure.[284,285] Hindered ligands reduced the reorganization energy of copper complexes and raise their redox potentials, providing DSSCs with V_{OC} up to 1.0 V.[287,288] In addition, contrarily to the cobalt-based redox mediators, copper complexes are more sustainable and cheaper.[274] For these reasons, novel redox mediators based on copper-complexes have been developed for the IMPRESSIVE project. Although the copper(I) complexes generally exhibit a not negligible absorption in the visible region at roughly 400-450 nm due to the MLCT band, they can be equally exploited for the fabrication of NIR-DSSC for the IMPRESSIVE project.[301]

As discussed in the Introduction, the goal of the IMPRESSIVE project was the development of a hybrid tandem device able to convert selectively UV and NIR part of the light while excluding the visible range to reach colourless and fully transparent device. In particular, the configuration of this hybrid tandem device (Fig. 2) shows as the incident light is previously harvest by a UV-PSC and after by a NIR-DSSC. In this configuration, the PSC device acts like an optical filter that theoretically collects only the UV part of the incident light. Practically, the UV-PSCs developed for the IMPRESSIVE project exhibit not negligible absorptions tail up to 440-450 nm. This means that any redox mediators with absorptions below 440-450 nm are suitable to develop a NIR-DSSC for the IMPRESSIVE project.

Besides to the optical properties, the development of novel copper-based redox mediators requires the fine tuning of the electrochemical properties. As

mentioned before in Chapter 1, the very promising results achieved by DSSCs with copper complexes as redox mediators are due to their outstanding redox potentials up to 1.0 V *vs*. *NHE*. However, these values are too high to meet the HOMO energy levels of the most common NIR dyes that usually required mediators with lower redox potentials between 0.40-0.65 V (*vs*. *NHE*). For these reasons, it has been decided to develop a novel class of copper(I) and copper(II) complexes based on different imidazo[1,5-*a*]pyridine ligands (*impy*).

The imidazo[1,5-*a*]pyridines are a wide class of heterocycles known for their versatility: over the years they are successfully applied in different research field such as medicinal chemistry, bioimaging, chemicals sensor, confocal microscopy, optoelectronics and organometallic chemistry.[490] The imidazo[1,5-*a*]pyridine scaffold, depicted in Fig. 89a, can be easily functionalized by the introduction of substituents in different positions. In particular, it has been demonstrated as the functionalization of the positions 1 and 3 of the *impy* core strongly influences their optical and electrochemical properties.[491]

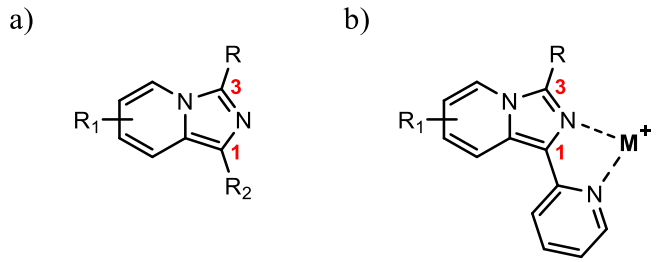

Figure 89 – a) General imidazo[1,5-*a*]pyridine core structure. b) General structure of *impy* bidentate ligands and their coordination modality.

Generally, the *impy* derivatives exhibit main absorption peaks in the wavelength range between 250-380 nm with almost no absorption beyond 450 nm. The corresponding molar extinction coefficients are usually between 0.5-2.5·10^4 M^{-1} cm^{-1}.[492,493] *Impy* derivatives are well-known for their intense emission in the green-blue spectrum region. Typically, *impy* derivatives exhibit quantum yields around 20-25% even if many of them achieving higher values up to 50%. Their characteristic emission spectra are featured by remarkable Stoke shift up to

100-150 nm.[493-498] The electrochemical properties of *impy* ligands are peculiar, displaying a mono-electronic oxidation (generally reversible) at roughly 400 mV *vs*. Fc/Fc^{+}.[295,499,500] Interestingly, the insertion of pendant pyridine group in position 1 provides the typical bidentate ligand motif, which is well-known for allowing suitable complexation reactions (Fig. 89b). In literature, *impy* derivatives have been successfully applied as alternative to the commonly *bpy*, *terpy* and *phen* ligands, in the complexation of a large variety of metal ions: silver(I),[501] cobalt(II),[502] nickel(II),[503] palladium(II),[503] zinc(II),[504] rhenium(I),[499] iridium(III),[500] and copper(I).[295,505] Currently, copper(I) complexes based on *impy* ligands have been applied in light-emitting electrochemical cells (LECs) and have been proposed as redox mediators in classic DSSCs.[295,505-507]

1. Project-proposal

As mentioned in Chapter 1, for many years copper-based mediators haven't been considered due to their poor performance related to their intrinsic high inner reorganization energy between the copper(I) and copper(II) species. However, the insertion of sterically hindered ligands, such as the 6,6'-di-substituted-2,2'-bipyridines or the 2,9-disubstituted-1,10-phenantrolines, leads to the formation of copper-based mediators exhibiting a low reorganization energy between the copper(I) and copper(II) species and thus displaying higher photovoltaic performances.[282,283]

In literature many examples of sterically hindered bidentate ligands are reported (Fig. 31) but only few of them have a suitable redox potential to regenerate the most common NIR-sensitizers. In particular, a suitable copper-based mediators for NIR-DSSCs should be exhibit a redox potential between 0.40-0.65 V (*vs*. *NHE*). For these reasons, a novel series of homoleptic copper(I) complexes based on a series of *impy* ligands (**353**-**356**, **361**, **362**, **368**) has been developed. In particular, a series of mono-substituted *impy* ligands (**353**-**356**) and a series of more sterically hindered tris-substituted ones (**361**, **362**, **368**) have

been synthetized to evaluate if also the *impy*-based copper complexes are subjected to bulky ligands effect.

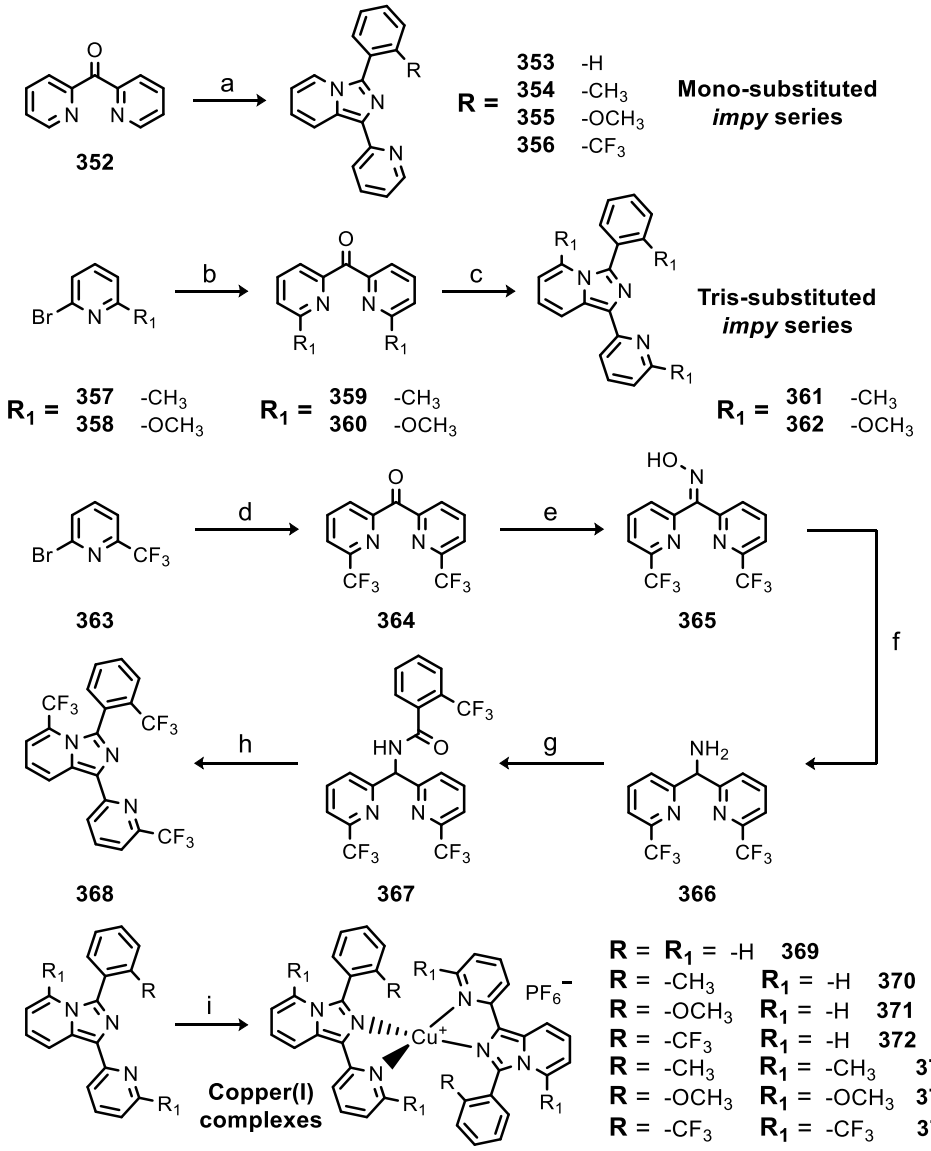

Figure 90 – Synthetic scheme. a) 2-Substituted-benzaldehyde, ammonium acetate, acetic acid, reflux, 6 h. b) *n*BuLi, THF, -78 °C, 1 h. Diethyl carbonate, -78 °C → RT, 2 h. c) 2-Substituted-benzaldehyde, ammonium acetate, acetic acid, reflux, 6 h. d) *n*BuLi, THF, -78 °C, 1 h. Ethyl chloroformate, -78 °C → RT, 2 h. e) Hydroxylamine hydrochloride, TEA, ethanol, RT → reflux, 24 h. f) Zinc dust, ammonium acetate, ammonium hydroxide 25%, ethanol, reflux, 3 h. g) 2-(Trifluoromethyl)benzoic acid, T3P (50% in ethyl acetate), butyl acetate, reflux, 16 h. h) T3P (50% in ethyl acetate), MW 180 °C, 1 h. i) Tetrakis(acetonitrile)copper(I) hexafluorophosphate, DCM, under Ar, reflux, 2 h.

The methyl, the methoxy and the trifluoromethyl groups have been selected as substituents to study if their different electronic inductive effect can influence the optical and the electrochemical properties of the relative copper complexes.

All *impy* ligands synthetized and the relative copper(I) complexes have been fully characterized studying their photo- and electrochemical properties. The synthesis of the *impy* ligands and the relative copper(I) complexes has been carried out following the synthetic plan displayed in Fig. 90.

2. Synthesis and Characterization of *Impy* Ligands

Over the years, several synthetic methods have been developed to synthetize imidazo[1,5-*a*]pyridine-based compounds as revised by Volpi *et al.*[508] Generally, these strategies required multi-step reactions using sensitive reagents and Lewis's acid catalysts, such as Schiff bases, triflates and boron trifluoride, and resulted in the preparation of impy ligands only in low yields (usually < 30%).[508-510] However, the breakthrough in the preparation of imidazo[1,5-*a*]pyridine-based compounds was achieved in 2005 by Wang *et al.* who reported the first example of one-step synthesis toward *impy* ligands. In their synthetic method the commercially available di(pyridine-2-yl)methanone (DPK) reacts with an aromatic aldehyde in presence of ammonium acetate in acidic media.[511] Exploiting the Wang method, the mono-substituted *impy* ligands **353**-**356** were synthetized in good yield (from 79% to 94%) (reaction **a** in Fig. 90). Even the tris-substituted *impy*-ligands **361** and **362** were prepared using the same method but, in their case, the synthesis of the starting di-substituted DPKs **359**-**360** (reaction **c** in Fig. 90) was necessary. The di-substituted DPKs were prepared by nucleophilic acyl substitution reaction (reaction **b** in Fig. 90) in which the diethyl carbonate reacts with two equivalents of an organo-lithium derivative, previously prepared treating a 2-bromo-6-substituted pyridine (**357**-**358**) with *n*-butyl lithium solution.[496]

Despite the Wang method allowed us the straightforward preparation of both mono- and tris-substituted *impy* ligands, it didn't enable the synthesis of tris-substituted ligand **368** bearing the trifluoromethyl groups. Following the previously described synthetic procedure, it has been prepared the di-substituted DPK **364** (reaction **d** in Fig. 90) and after, it has been reacted with the 2-(trifluoromethyl)benzaldehyde in presence of ammonium acetate. However, no evidence of ligand **368**'s formation has been found even modifying the reaction conditions. We tried (i) to increase the reaction time from 12 h up to 48 h, (ii) to raise the aldehyde concentration from 1.5 eq. up to 6.0 eq. and (iii) to raise the ammonium acetate concentration from 5 eq. up to 20 eq.

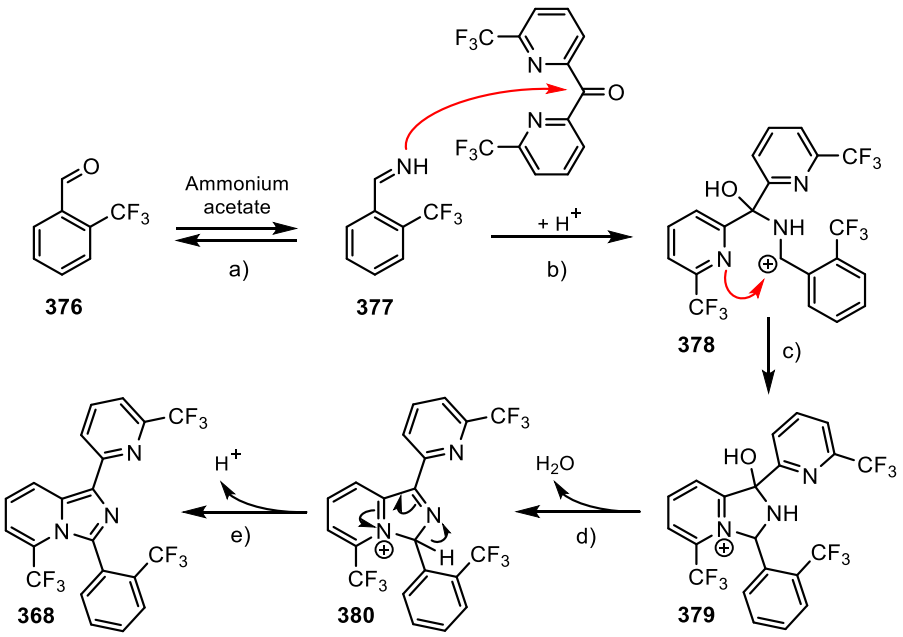

Figure 91 – Reaction mechanism proposed by Wang *et al.* for the one-step synthesis of *impy* ligands.[511] In figure, reaction mechanism was applied to the specific synthesis of tris-substituted trifluoromethylated *impy* ligand **368**. The red curved arrows described the probable problematic steps in the reaction mechanism.

To understand the possible reasons behind the failure of the direct cyclization reaction we analyzed the reaction's mechanism. As depicted in Fig. 91, the mechanism exhibits five steps: (i) the formation of the active nucleophilic species

377 (**a** in Fig. 91), (ii) the nucleophilic addition to the carbonyl group of the DPK derivative (**b** in Fig. 91), (iii) the intramolecular cyclization (**c** in Fig. 91), (iv) the dehydration reaction of ternary hydroxyl group (**d** in Fig. 91) and (v) the final charges rearrangement toward the desired *impy* ligand **368**. In the case of the synthesis of **368**, we supposed that the presence of a strong electron withdrawing group like the trifluoromethyl can negatively influences both the nucleophilic addition to the carbonyl group of the DPK derivative (**b** in Fig. 91) and the intramolecular cyclization (**c** in Fig. 91). In particular, the hypothesis of the failed nucleophilic addition to the carbonyl group of the DPK could be validated by the presence of unreacted DPK at the end of the reaction. Probably, the trifluoromethyl group in the *ortho*- position of the benzylimine **377**, strongly affects the nucleophilicity of the imine group, decreasing its reactivity and thus hampering the nucleophilic addition to the carbonyl group of the DPK.

For these reasons, we decided to try the preparation of **368** by a different synthetic strategy in which the carbonyl group of the 2-(trifluoromethyl)benzaldehyde **376** is not involved in the reaction mechanism as reactant (its derivative **377** is the nucleophilic agent) but it behaves as electrophile target.

One of the first synthetic strategy proposed for the preparation of imidazo[1,5-*a*]pyridine-based compounds was based on the reaction of a benzoic acid derivative and pyridyl methanamine derivative in presence of a dehydrating agent.[512-514] In particular, Crawforth *et al.* reported an efficient method based on benzoic acid and pyridyl methanamine derivatives in presence of the propylphosphonic anhydride (T3P) as dehydrating agent in butyl acetate.[514] As depicted in Fig. 92, the reaction mechanism of this synthetic method exhibits three steps: (i) the nucleophilic addition to the carbonyl group of the benzoic acid derivative (**381**) that leads to the formation of amide derivative **367** (**a** in Fig. 92), the intramolecular cyclization (**b** in Fig. 92) and the final dehydration reaction of ternary hydroxyl group catalysed by the presence of T3P (**c** in Fig. 92).

To prepare **368** following the latter described strategy, we performed the synthesis of the necessary amine derivative **366** (Fig. 90). Starting from bis-trifluoromethylated DPK **363**, the ketoxime derivative **365** has been synthetized following the general procedure in presence of hydroxylamine hydrochloride and triethylamine (reaction **e** in Fig. 90).[515,516] After, the ketoxime **365** was reduced using zinc dust in presence of ammonium acetate and ammonium hydroxide to obtain the desired amine **366** in almost quantitative yield (reaction **f** in Fig. 90).

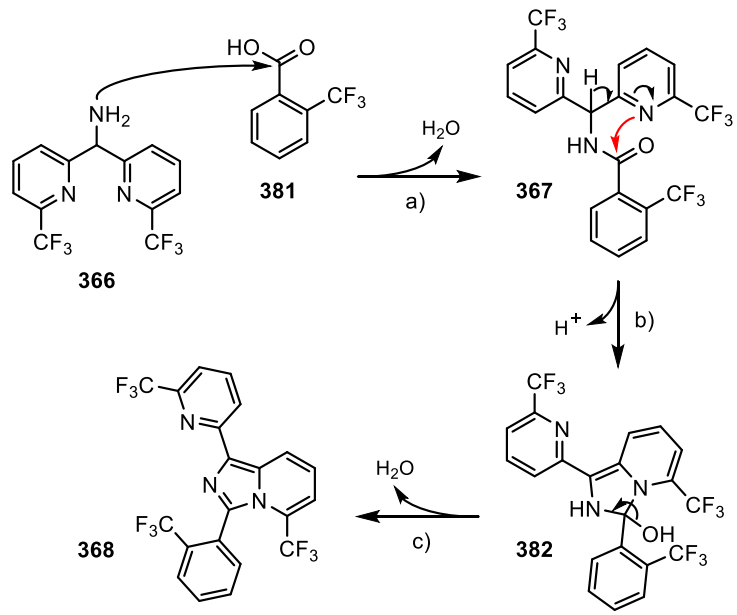

Figure 92 – Reaction mechanism proposed for the synthesis of *impy* ligands with the method based on the reaction between the benzoic acid and the pyridyl methanamine derivative.[508,514] In figure, reaction mechanism was applied to the specific synthesis of tris-substituted trifluoromethylated *impy* ligand **368**. The red curved arrow described the probable problematic steps in the reaction mechanism.

Following the general procedure reported by Crawforth *et al.*, the reaction between the pyridyl methanamine derivative **366** and the 2-(trifluoromethyl)benzoic acid **381** was carried out in presence of T3P in butyl acetate.[514] As expected, the change of mechanism provide the nucleophilic attack on the carbonyl of compound **381** but even in this case we were not able to isolate the desired *impy* ligand **368**. However, at the end of the reaction we found poor

amounts of starting materials. The analysis of the isolated compound confirmed the formation of the non-cyclized amide derivative **367** (reaction **g** in Fig. 90). Even in this case, the missed intramolecular cyclization reaction toward the desired *impy* ligand **368** is probably due to the trifluoromethyl group in *ortho*-respect to the pyridine's nitrogen involved in the cyclization reaction. The strong electron withdrawing effect of the trifluoromethyl group noticeably decreased the reactivity of the pyridine's nitrogen hampering the intramolecular cyclization (curved red arrow in Fig. 92). For this reason, we decided to further react the non-cyclized amide derivative **367** in stronger conditions performing the reaction in T3P in a MW reactor at 180 °C for 1 h (reaction **h** in Fig. 90). The stronger reaction conditions overcome the less reactivity of the pyridine's nitrogen leading to the synthesis of the desired *impy* ligand **368**.

2.1. Photophysical Characterization of *Impy* Ligands

After the synthesis, the photophysical properties of all *impy* ligands have been evaluated in DCM (Tab. 26 and Fig. 93).

All *impy* ligands exhibit two main absorption bands peaking at roughly 300 nm and 360-380 nm, with almost no absorption beyond 430 nm in accordance with the data reported for similar structures.[492,494,496]

Table 26 – Photophysical properties of *impy* ligands in DCM.

Ligand	λ_{max} [nm]	λ_{em} [nm]	ε [M^{-1} cm^{-1}]	Stokes shift [cm^{-1}]	QY [%]	Brightness [M^{-1} cm^{-1}]
353	323	463	11 615	9 361	18.3	2 125
354	319	460	17 003	9 609	32.0	5 440
355	317	454	17 247	9 519	53.2	9 171
356	328	454	12 982	8 461	33.1	4 291
361	366	445	15 677	4 850	58.8	9 212
362	375	435	22 601	3 678	41.8	9 437
368	296	490	16 192	13 376	66.9	10 826

Excluding the unsubstituted *impy* ligand **353** and those ones bearing the -CF_3 groups (**356** and **368**), the mono-substituted ligands generally exhibit a higher absorbance for the first peak at 300 nm with molar extinction coefficient values nearby $1.7 \cdot 10^4$ M^{-1} cm^{-1} while the tri-substituted ones display higher absorbance for the second peak at roughly 360-380 nm with molar extinction coefficient values > $1.5 \cdot 10^4$ M^{-1} cm^{-1}. Interestingly, the *impy* ligands bearing -CF_3 group exhibit hypochromic absorption.

The emission profiles have the typical shapes of the imidazo[1,5-*a*]pyridine-based compounds and exhibit variable Stokes shift from 60 to 190 nm. In accordance with the literature, all the substituted *impy* ligands (except for the reference unsubstituted one **353**) displayed high quantum yields due to the presence of sterically hindered groups in the ortho-positions of the phenyl ring that partially or completely block its rotation leading to a marked increase of the emission quantum yield.[496] In particular, the *impy* ligand **368** achieved an outstanding quantum yield of 66.9% and as far as we know from the literature, it is the highest quantum yield achieved by an imidazo[1,5-*a*]pyridine-based compound.

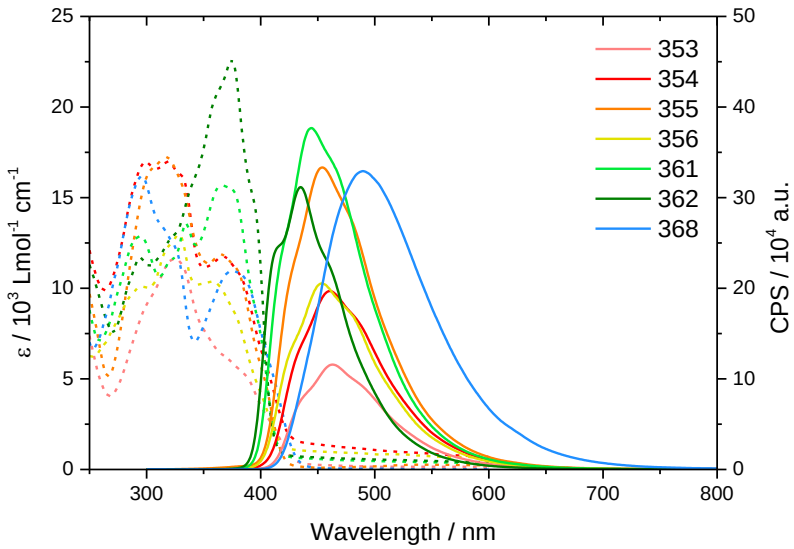

Figure 93 – Absorption (dashed) and steady state emission spectra of *impy* ligands in DCM. The emission spectra were normalized at 0.1 intensity at the excitation wavelength.

2.2. Electrochemical Characterization of *Impy* Ligands

The electrochemical properties of all *impy* ligands have been evaluated in DCM (Tab. 27 and Fig. 94). The *impy* ligands display a monoelectronic oxidation characterized by halfwave potential $E_{1/2}$ of about 1.0 V *vs*. *NHE* (except for the tris-substituted ligands **362** and **368**) in accordance with the literature.[499,500,517]

Table 27 – Electrochemical properties of *impy* ligands in DCM.

Ligand	Redox potential *vs*. Fc^+/Fc [V]	Redox potential *vs*. *NHE* [V]
353	0.43	1.06
354	0.42	1.05
355	0.36	0.99
356	0.50	1.13
361	0.39	1.01
362	0.25	0.87
368	1.05	1.67

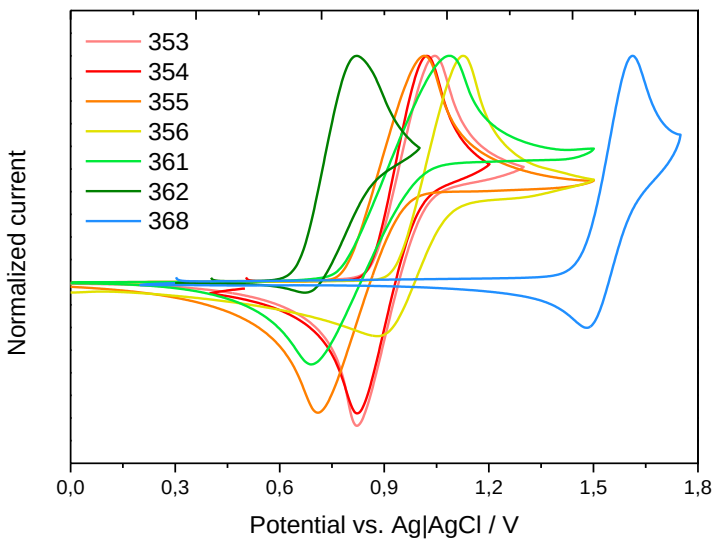

Figure 94 – Cyclic voltammetry curves of *impy* ligands in DCM. Scan rate: 50 mV/s.

In particular, in the case of ligands with electron donor groups **354** and **355**, the redox potential is slightly shifted toward more negative values while in the case of ligand with the $-CF_3$ electron withdrawing group (**356**), the redox potential

is positively shifted toward higher values. Obviously, also the number of substituents influence the redox potentials; in particular, ligand **362** with three methoxy groups displays the lowest redox potential at 0.87 V *vs*. *NHE* while the ligand **368** with the three trifluoromethyl groups exhibits the highest redox potential at 1.67 V *vs*. *NHE*.

3. Synthesis of Copper(I) Complexes

In literature, the synthesis of copper(I) complexes is carried out mainly using two different precursors, the copper(I) iodide and the tetrakis(acetonitrile)copper(I) hexafluorophosphate. The coordination reactions are usually performed using an organic solvent in which the ligand is highly soluble and in which the resulting copper(I) complex exhibits a lower solubility to easily recover it by precipitation and filtration.[283,291,292] Usually, to promote the coordination reaction, a slightly excess of ligand is used.

To synthetize *impy*-based copper(I) complexes **369**-**375**, the tetrakis(acetonitrile)copper(I) hexafluorophosphate has been selected over copper(I) iodide due to its higher stability and solubility in DCM. The synthesis of copper(I) complexes **369**-**375** (reaction **i** in Fig. 90) was carried out in refluxing DCM for 2 h under argon, achieving yields from 54% to 93%.

The purity of synthetized copper(I) complexes was evaluated by ^{1}H-NMR and ESI-HRMS. The mass spectra of all the obtained copper(I) complexes are consistent with the proposed structures: all spectra of Cu(I) complexes exhibit a main peak related to the singly charged molecular cation (all the HRMS spectra are reported in Section 1.17 of SI). Characteristic isotope patterns for copper - containing ions are clearly seen, confirming the elemental composition of the ions observed.

Interestingly, the ^{1}H-NMR spectra of copper(I) complexes are generally characterized by peculiar broad signals which were first related to the presence of traces of copper(II) species but, as just mentioned, the mass spectra did not exhibit any signals attributable to the presence of copper(II) species. Contrarily,

copper(I) complexes **369** and **373** exhibit sharper signals: in the case of compound **369**, signals are narrower compared to the other complexes but still slightly broad, whereas in the case of compound **373**, are very narrow and sharp (all the ^{1}H-NMR spectra are reported in Section 1.17 of SI).

The particular ^{1}H-NMR spectra obtained for copper(I) complexes forced us to stop the development of these structures for the application in DSSCs as redox mediators and pushed us to investigate in detail which are the reasons behind these peculiar behaviors.

For these reasons, copper(I) complexes **369**-**375** have been characterized performing additional NMR experiments at low temperature and studying their optical and their electrochemical properties. The obtained results will be discussed in the next section of this chapter.

4. Structural Study of *Impy*-based Copper(I) Complexes

As just mentioned, further characterizations of copper(I) complexes **369**-**375** were performed to understand the peculiarities found in the 1H-NMR spectra.

The analysis of all the collected data suggests us for the compounds **369**-**375** not the classical tetrahydric structure usually related to the copper(I) complexes but a different coordination's structure depending by the type of *impy* ligand used for their synthesis.

In particular, the comparison of the cyclic voltammetry curves with the ^{1}H-NMR spectra at low temperature allowed us to classify the copper(I) complexes **369**-**375** in four different categories on the bases of the coordination modes of the *impy* ligands, as depicted in Fig. 95.

Optical and electrochemical characterization has been performed in DCM due to its non-coordinating feature while to improve the solubility of copper(I) complexes and thus to allow the measurement of ^{1}H-NMR spectra at low temperature, deuterated acetone was used instead of deuterated chloroform.

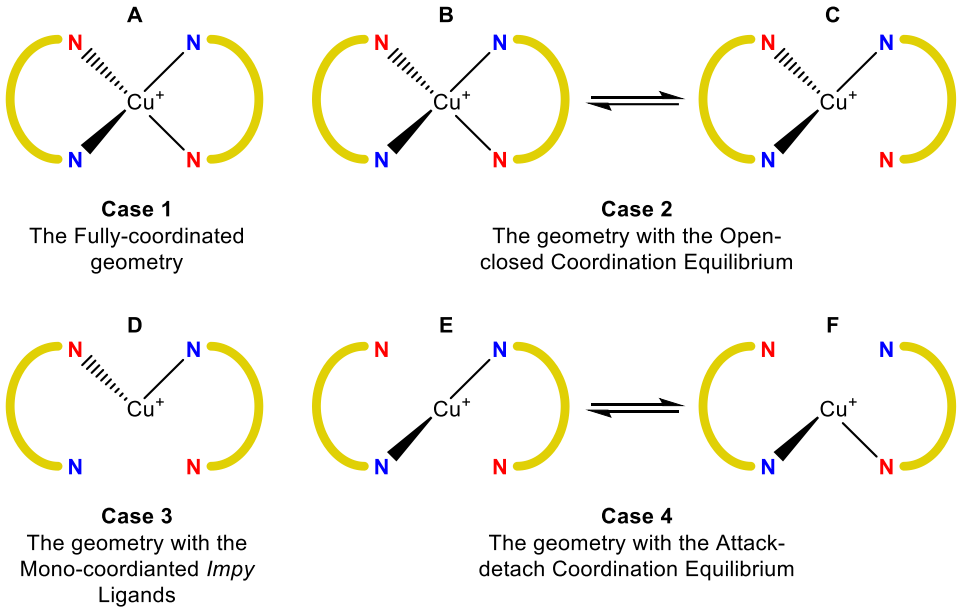

Figure 95 – Possible coordination modes of *impy* ligands around central metal cation in the copper(I) complexes **369**-**375**. In the scheme, red nitrogen atoms describe the nitrogen of the pending pyridine ring of the *impy* ligands, while the blue nitrogen atoms describe the nitrogen of the imidazo[1,5-*a*]pyridine scaffold. The semicircle represents a general *impy* ligand.

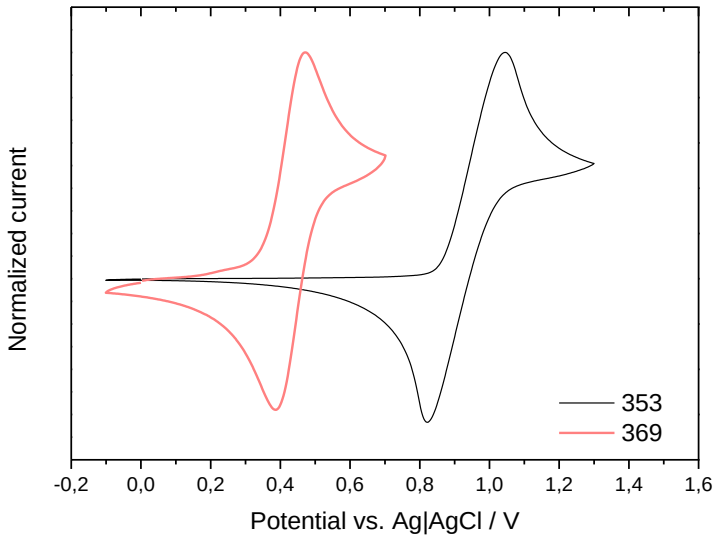

Figure 96 – Comparison of cyclic voltammetry curves of *impy* ligand **353** (black) and corresponding copper(I) complex **369** (pink) in DCM (scan rate: 50 mV/s).

Starting from the first copper(I) complex **369**, its cyclic voltammetry curve displays a mono-electronic fully reversible oxidation peak at 0.43 V *vs*. Ag/AgCl (0.63 V *vs*. *NHE*) (Fig. 96). The analysis of its ^{1}H-NMR spectra at low temperature demonstrates that the decrease in temperature causes the narrowing of all the NMR signals without any modification of their multiplicity and their integration values. In addition, the decrease in temperature does not lead to appearance of new signals (Fig. 97).

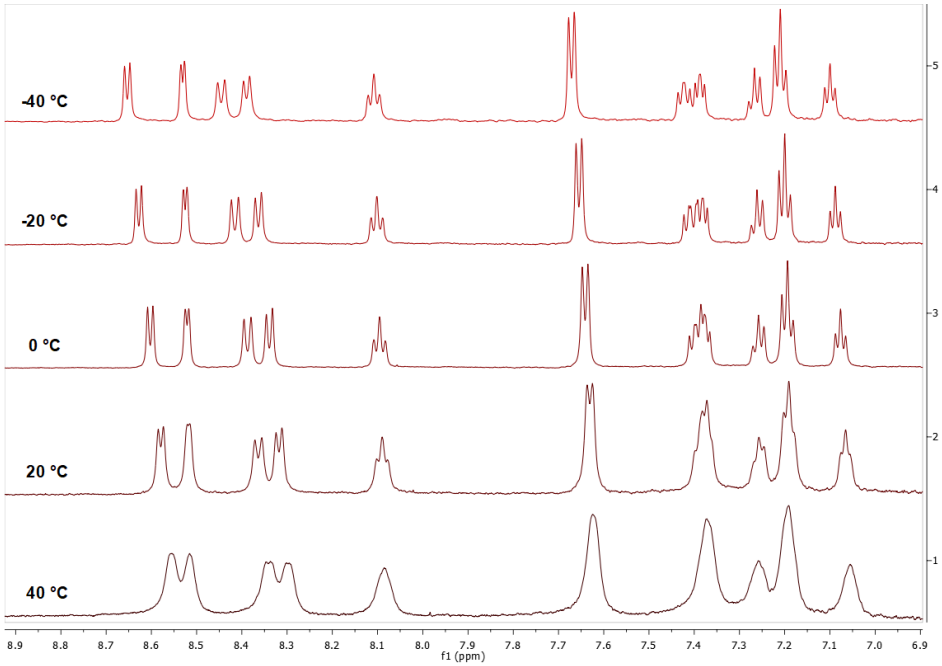

Figure 97 – Variable-temperature ^{1}H-NMR spectra in acetone-d_6 of **369**.

The data obtained from the CV curve and ^{1}H-NMR spectra at low temperature suggested us that copper(I) complex **369** based on the naked *impy* ligand (**353**) exhibits in solution a symmetrical structure (probably tetrahedral) in which the two bidentate *impy* ligands are fully coordinated to the copper(I) metal center (**A** in Fig. 95). Even if CV curve of **369** exhibits a single oxidation peak, the narrowing of the NMR signals while the temperature decreases suggest the probably presence of very fast coordination equilibria that are progressively slowed-down.

Further confirmation can be obtained by the evaluation of the ^{1}H-NMR spectrum at 40 °C of **369** that display broader signals.

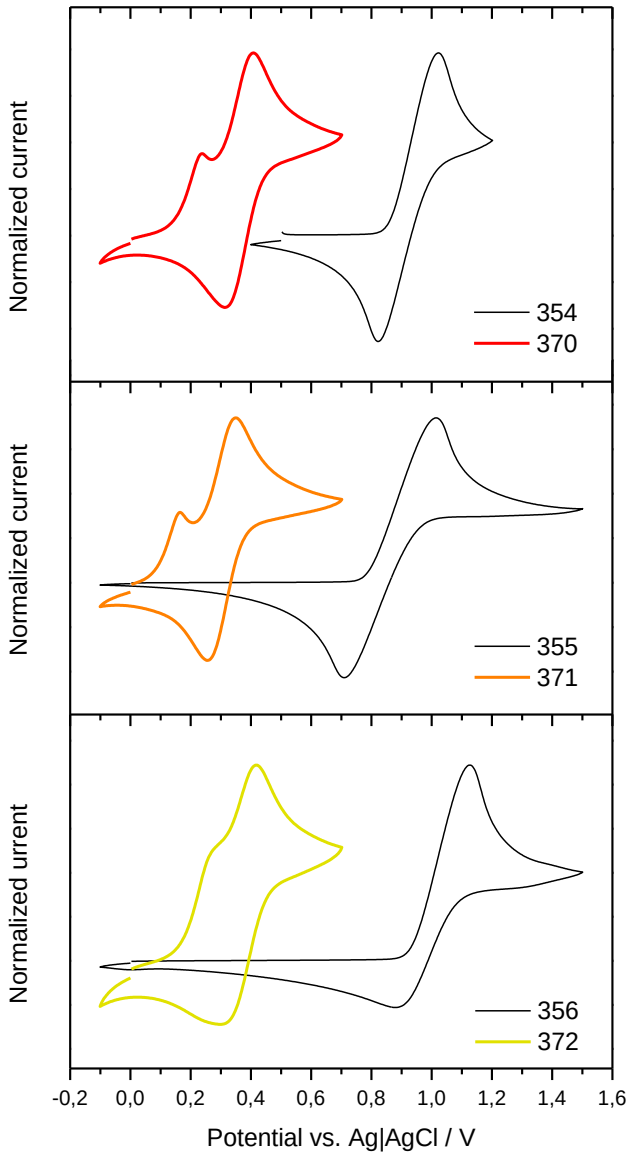

Figure 98 – Comparison of cyclic voltammetry curves of *impy* ligand **354**-**356** (black) and corresponding copper(I) complexes **370**-**372** (colored) in DCM (scan rate: 50 mV/s).

Contrarily, in the case of copper(I) complexes with more hindered mono-substituted ligands **370**-**372**, the cyclic voltammetry curves exhibit an oxidation's

signal with a particular shape in which is well distinguishable the presence of two peaks (Fig. 98): the comparison with a known-concentration solution of ferrocene demonstrated that each of the two signals describes a mono-electronic oxidation process. The CV curves of copper(I) complexes **370**-**372** suggested the presence of two different species having a similar structure and thus having a very similar redox potential.

With the aim to detect the presence of two different species, we recorded the ^{1}H-NMR spectra at low temperature for both copper(I) complexes. The ^{1}H-NMR spectra at low temperature of compound **370** displayed in Fig. 99 (^{1}H-NMR spectra at low temperature of **371** and **372** are reported in Section 1.17 of SI - Fig. 276 and Fig. 279), show narrower signals with the decreasing of temperature like the compound **369** displayed. However, in the case of compounds **370**-**372**, the spectra at -40 °C exhibit the presence of a second family of signals with a lower intensity (highlighted by blue asterisks in Fig. 99). The presence of a doubled peak in the CV curves and the appearance of a second family of signals in the NMR spectrum at -40 °C suggested us to hypothesize that copper(I) complexes **370**-**372** are characterized by two coordination forms in equilibrium between them: (i) the former could be the one in which all the two mono-substituted *impy* ligands are fully-coordinated to the metal center through all the four coordination sites, providing a fully symmetrical structure (**B** in Fig. 95) whereas (ii) the latter could be the one in which one of the two *impy* ligands is fully-coordinated and the second one is mono-coordinated through one of its two nitrogen coordination sites (**C** in Fig. 95), providing an asymmetrical structure that justifies the appearance of new signals in the ^{1}H-NMR spectrum at -40 °C. Compared to the previous case (**A** in Fig. 95), we hypothesized that in copper(I) complexes **370**-**372** it has been possible to detect the presence of the coordination equilibria in their structure because these equilibria have a slower kinetic due to the higher steric hinderance of the mono-substituted *impy* ligands (**354**-**356**).

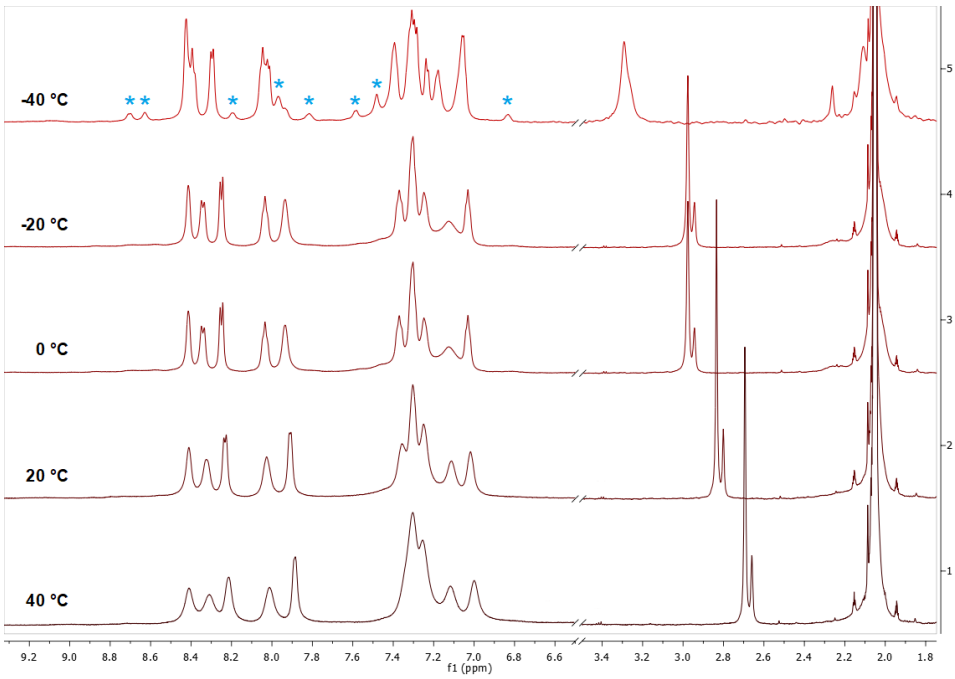

Figure 99 – Variable-temperature ^{1}H-NMR spectra in acetone-d_6 of **370**. Blue asterisks in the ^{1}H-NMR spectrum at -40 °C point out the additional signals of the asymmetrical structure **C** (Fig. 95) in which one of the two mono-substituted *impy* ligands is mono-coordinated.

Following the concept of a dynamic coordination equilibrium between the species **B** and **C** (Fig. 95), we tried to investigate what happen in the case of copper(I) complexes **373**-**375** bearing the more sterically hindered tris-substituted *impy* ligands (**361**, **362** and **368**). Two particular coordination modalities have been hypothesized: the Case 3 and 4 depicted in Fig. 95. The Case 3 (**D** in Fig. 95) has been defined for the copper(I) complex **373**.

In this complex we hypothesize that the high sterically hindered *impy* ligands are not able to fully coordinate the copper metal center trough both their nitrogen atoms, leading to the formation of a copper(I) complex in which both *impy* ligands are mono-coordinated to the copper metal center. In addition, the CV curve and the ^{1}H-NMR spectra at low temperature suggested us that the high steric hinderance of the *impy* ligand **361** prevents any possible coordination equilibria, leading to a locked structure.

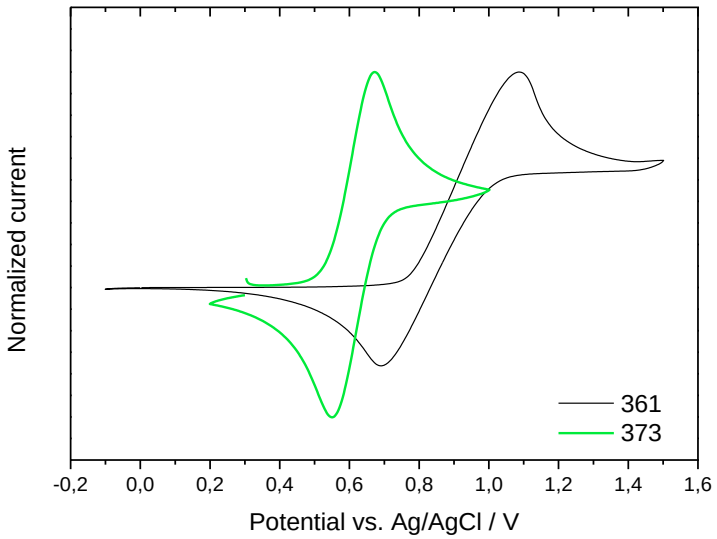

Figure 100 – Comparison of cyclic voltammetry curves of *impy* ligand **361** (black) and corresponding copper(I) complex **373** (light-green) in DCM (scan rate: 50 mV/s).

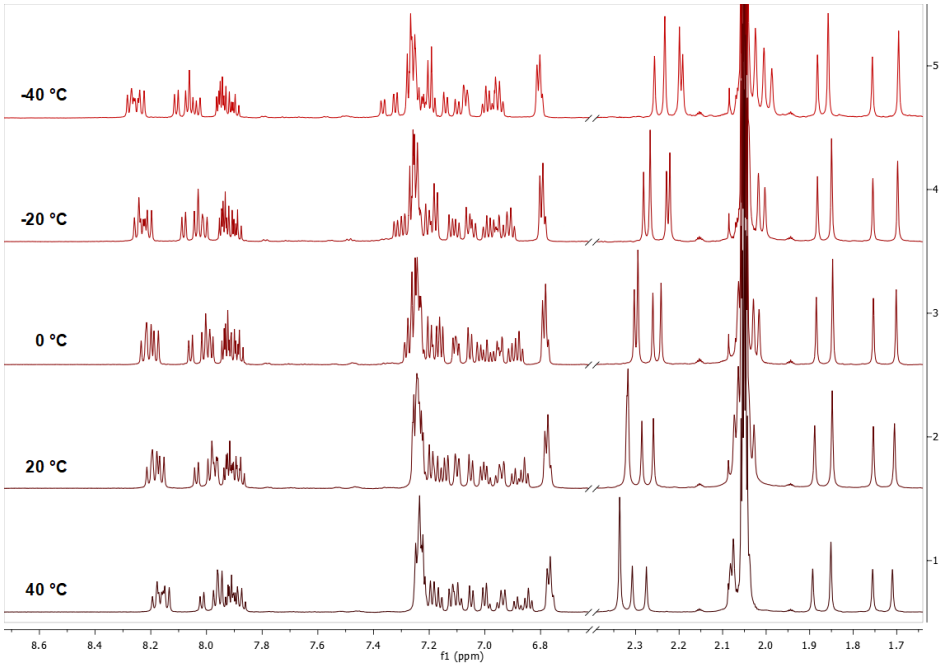

Figure 101 – Variable-temperature ^{1}H-NMR spectra in acetone-d_6 of **373**.

This hypothesize is supported by the CV curve (Fig. 100) of **373** that exhibits a reversible monoelectronic oxidation peak at 0.61 V *vs*. Ag/AgCl (0.81 V *vs*. *NHE*).

Further confirmations have been reported by the ^{1}H-NMR spectra at low temperature of **373** (Fig. 101): at any temperatures, NMR spectra display the same narrow signals confirming the hypothesize of the locked structure. The highly number of signals in the NMR spectrum of **373** is due to the different possible coordination geometries **D1**-**D3** of the two mono-coordinated *impy* ligands around to the copper metal center (Fig. 102).

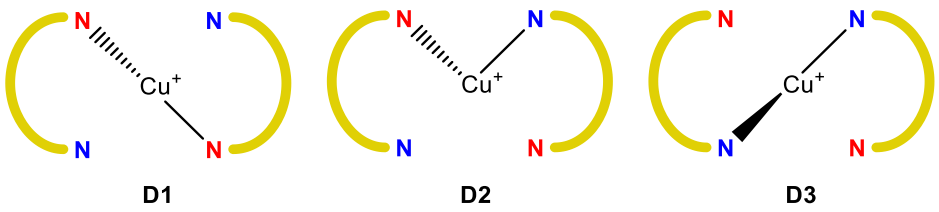

Figure 102 – Possible coordination modes of the two *impy* ligands **373** around the copper(I) metal center.

Finally, in the Case 4 we classified the copper(I) complexes **374** and **375** bearing the tri-methoxylated (**362**) and tris-trifluoromethylated (**368**) *impy* ligands, respectively.

In the Case 4, the copper complexes are subjected to the presence of a dynamic coordination equilibrium between the structure **E** and the structure **F** depicted in Fig. 95, where both the *impy* ligands are mono-coordinated to the copper metal center and in addition, one of them is able to change the coordination site between the pyridine ring's nitrogen and the imidazo[1,5-*a*]pyridine's nitrogen.

The presence of coordination equilibria in complexes **374**-**375** is confirmed by the ^{1}H-NMR spectra at low temperatures. As reported by the ^{1}H-NMR spectra at low temperature of compound **374** displayed in Fig. 103 (^{1}H-NMR spectra at low temperature of **375** are reported in Section 1.17 of SI - Fig. 286), the decrease in temperature lead to narrower signals like the case 2.

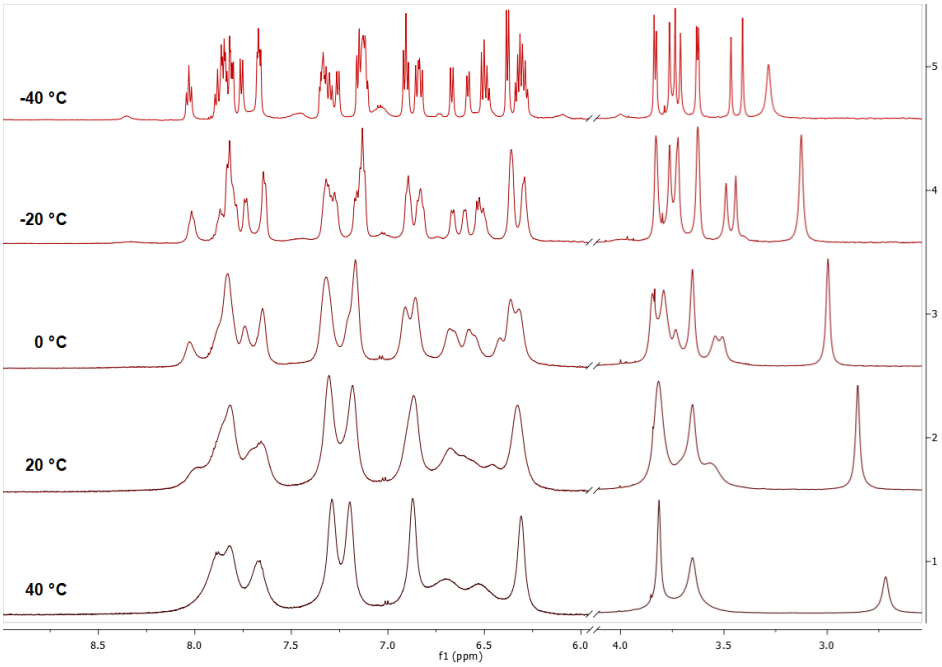

Figure 103 – Variable-temperature ^{1}H-NMR spectra in acetone-d_6 of **374**.

However, compared to the previous coordination equilibria found for compounds **370**-**372** (Case 2), the coordination equilibria hypothesized for complexes **374**-**375** seems to be faster; in fact, they do not no doubling of oxidation peak has observed. In particular, the CV curves of **374** and **375** display a reversible monoelectronic oxidation peak at 0.33 V *vs*. Ag/AgCl (0.53 V *vs*. *NHE*) and a quasi-reversible monoelectronic oxidation peak at 1.18 V *vs*. Ag/AgCl (1.38 V *vs*. *NHE*), respectively (Fig. 104).

Contrarily to the Case 3, in the Case 4 the complexes display the presence of coordination equilibria despite the steric hinderance of the tris-substituted *impy* ligands. However, we hypothesize that: (i) in the case of complex **374**, the less steric hinderance of the methoxy groups compared to the methyl ones,[518] provides higher mobility to the *impy* ligands and thus allows the presence of a coordination equilibrium between the species **E** and **F** (Fig. 95) whereas (ii) in the case of complex **375**, even if the trifluoromethyl groups are bulkier compared to the methyl ones, their strong electron-withdrawing effect weakens the

coordination strength of *impy* ligands **368** allowing the presence of the coordination equilibrium between the species **E** and **F**.

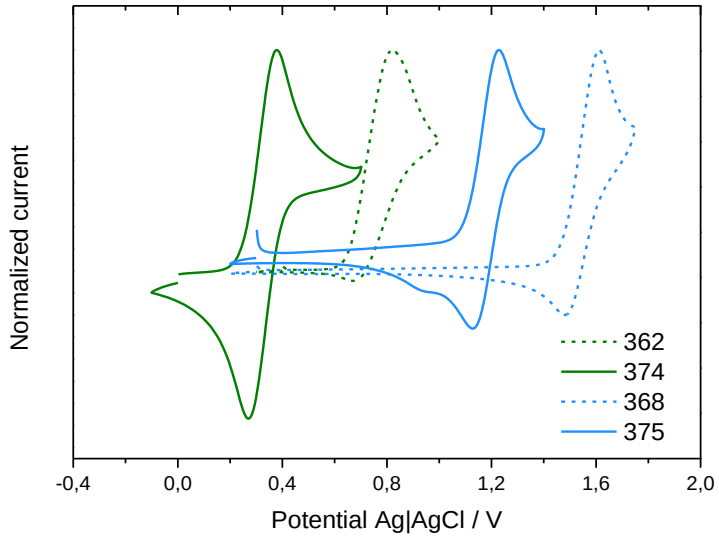

Figure 104 – Comparison of cyclic voltammetry curves of *impy* ligands **362** and **368** (dashed) and corresponding copper(I) complex **374**-**375** (solid) in DCM (scan rate: 50 mV/s).

5. Photophysical Characterization of Copper(I) Complexes

The photophysical properties of *impy*-based copper(I) complexes **369**-**375** (Tab. 28 and Fig. 105) have been evaluated.

All copper(I) complexes exhibit two main absorption bands peaking at roughly 300-330 nm and 360-370 nm, with almost no absorption beyond 450 nm (Fig. 105). The absorption maxima can be attributed to a π-π* charge-transfer transition of the imidazo[1,5-*a*]pyridine scaffold.[295] Excluding complex **372**, it is possible to see that generally the complexes **369**-**371** with the mono-substituted *impy* ligands exhibit a higher absorbance for the first peak at 300-330 nm with molar extinction coefficient values between 3.0-4.5·10^4 M^{-1} cm^{-1} while the complexes with the tri-substituted ones display higher absorbance for the second peak at roughly 360-370 nm with molar extinction coefficient values between 2.5-

$3.0 \cdot 10^4$ M^{-1} cm^{-1}. In addition, complex **375** with the tris-CF_3 *impy* ligand exhibits hypochromic absorption. Interestingly, these behaviours just described as similar to what has been found for free *impy* ligands.

Table 28 – Photophysical properties of copper(I) complexes in DCM.

Complex	λ_{max} [nm]	λ_{em} [nm]	ε [M^{-1} cm^{-1}]	Stokes shift [cm^{-1}]	QY [%]	Brightness [M^{-1} cm^{-1}]
369	303	460	46 973	11 264	0.9	431
370	297	458	33 151	11 836	4.4	1 451
371	298	454	34 466	11 531	12.6	4 342
372	369	454	31 692	5 074	9.0	2 862
373	375	444	24 918	4 144	15.2	3 777
374	375	434	29 409	3 625	25.3	7 432
375	296	488	18 122	13 376	13.5	2 442

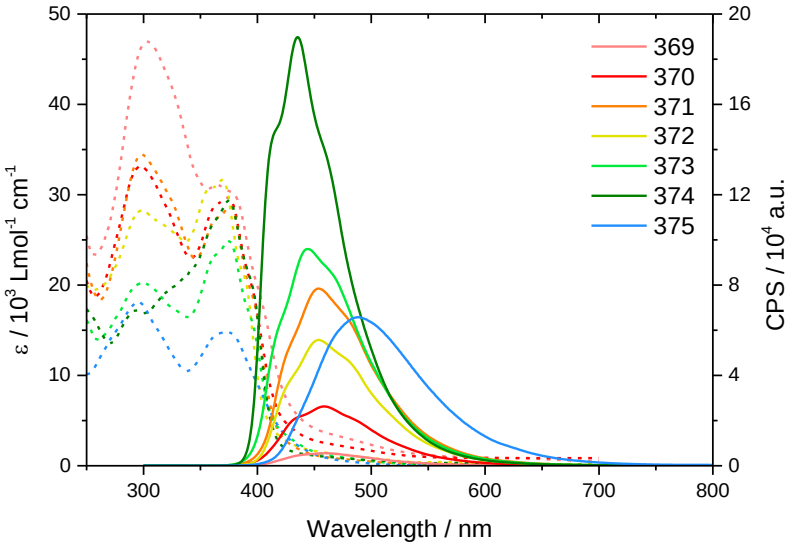

Figure 105 – Absorption (dashed) and steady state emission spectra of copper(I) complexes based on *impy* ligands in DCM. The emission spectra were normalized at 0.1 intensity at the excitation wavelength.

Compared to the copper(I) complexes based on classical ligands such as bipyridines and phenanthrolines, the *impy*-based copper(I) complexes do not display a maximum for the MLCT transition. In copper(I) complexes **369**-**375** the

MLCT signal appears as a broad tail between 425-500 nm with low absorbance (ε < 4000 M^{-1} cm^{-1} after 450 nm) (Fig. 105).

The emission profiles have similar shapes compared to the relative *impy* free ligands and exhibit variable Stokes shift from 60 to 180 nm. With a very similar trend compared to the relative free *impy* ligands, copper(I) complexes are quite emissive whit quantum yield values up to 25% (Tab. 28).

6. Conclusions and Future Outlook

In this chapter the synthesis and the characterization of a novel series of *impy*-based homoleptic copper(I) complexes has been reported. Despite the aim of this work was the development of a series of novel potential redox mediators for the application in DSSCs, the peculiar results obtained during the chemical characterization of the synthetized copper(I) complexes forced us to lose sight of the application and to exploit our efforts to elucidate these particular features.

We demonstrated that the synthetized copper(I) complexes are characterized by different coordination geometries (depicted in Fig. 95) which can also display the presence of coordination equilibria. In particular, the experimental data pushed us to hypothesize that the coordination structures of copper(I) complexes **369**-**375** strictly depends on the structure of the corresponding *impy* ligand and in particular by its steric hinderance.

The results obtained for copper(I) complexes with *impy* ligands could become very interesting to elucidate the chemistry of hindered copper(I) complexes that is actually a hot-topic in literature due to the outstanding results achieved in DSSCs with redox mediators based on sterically hindered copper-complexes.

Despite our hypothesizes are currently quite surrounded by consistent experimental data, additional measurements of the electrochemical properties of copper complexes by Fast-Scan Cyclic Voltammetry (FSCV) could be perform to further understand the faster kinetic of the coordination equilibria involved in complexes **369** and **374**-**375**.

Finally, additional confirms about our hypotheses can be obtained performing ^{15}N-NMR spectra on copper(I) complexes synthetized starting from ^{15}N enriched *impy* ligands. Despite the synthesis of ^{15}N enriched *impy* ligands in straightforward and cheaper synthetic manner has been already reported in literature,[500] this strategy could be selectiveness applied to evaluate the ^{15}N enriched copper(I) complexes bearing respectively the mono- and the tris-methoxylated *impy* ligands.

CHAPTER 5 – Synthesis and Characterization of a Novel Class of DHP-based Squaraine with an Hypsochromic Absorption in the Visible

As reported in Section 1.1. of Chapter 1, polymethine-based sensitizers are generally affected by too fast charge recombination and slow regeneration rate of the dye that prevent the achievement of better performances. The too fast charge recombination can be reduced by the introduction of bulky groups such as the out-of-plane alkyl chains, while for the slow regeneration rate of the dye an effective strategy has not yet been found. However, Hirata *et al.* have been demonstrated for ruthenium-based sensitizer that the introduction of a non-conjugated triphenylamine (TPA) moiety could partially delocalize the positive charge density of the oxidized sensitizer, raising the distance between the negative charge and the positive one and simultaneously projecting the positive charge of the oxidized dye in the electrolyte solution, favouring its regeneration (Fig. 106).[519]

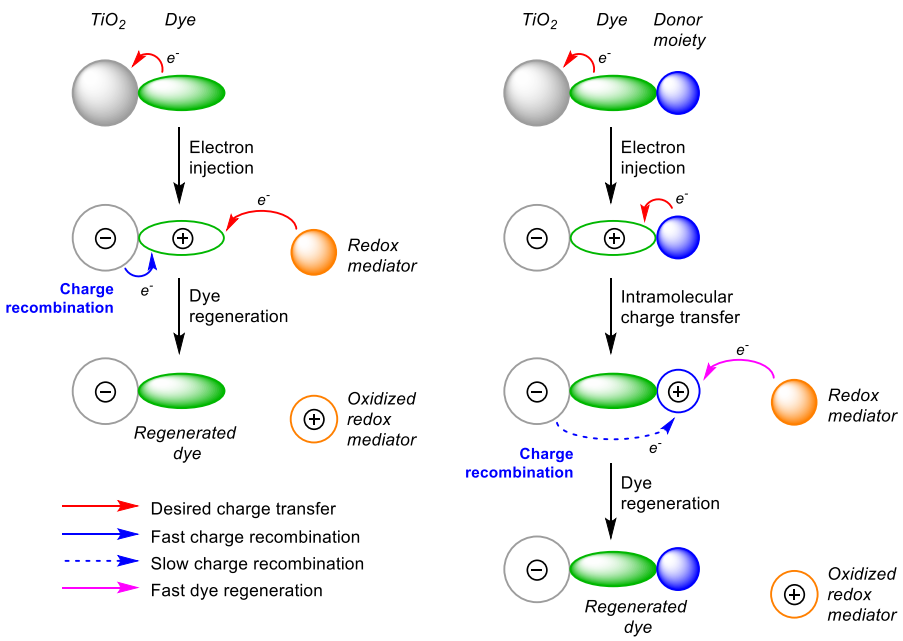

Figure 106 – Charge distribution on dye's structure during the electron injection processes in a classic sensitizer (left) and in a sensitizer bearing a non-conjugated TPA moiety (right).

Following the same strategy, we decided to develop a new series of DHP-SQs in which the DHP moiety is exploited to introduce a non-conjugated TPA group in the squaraine structure. In particular, we decided to develop a DHP-SQ bearing one non-conjugated TPA group **388** and two DHP-SQs bearing respectively a methyl **384** and a phenyl group **386** as reference.

To simplify the synthetic work, we decided to perform the investigation of the effect of the non-conjugated TPA group on the regeneration, starting from the more straightforward carboxyindolenine-based squaraines. The preparation of the squaraines **384**, **386** and **388** have been carried out following the synthetic plan displayed in Fig. 107.

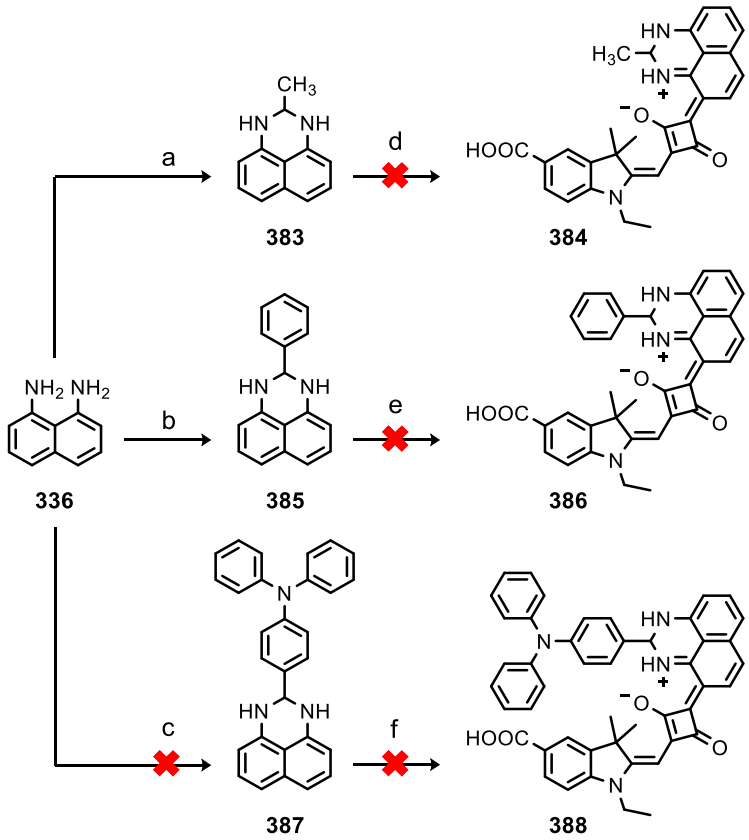

Figure 107 – Proposed synthetic scheme. a, b, c) Aldehyde (Acetaldehyde for **383**, Benzaldehyde for **385**, 4-Formyltriphenylamine for **387**) PTSA, toluene, reflux, 16 h in Dean-Stark apparatus. d, e, f) **323**, mono-DHP (**383** or **385** or **387**), *n*-butanol/toluene, MW 160 °C, 30 min.

1. Synthesis

Following the reported synthetic scheme (Fig. 107), the synthesis of the novel series of squaraine sensitizers started with the preparation of mono-substituted DHP derivatives **383**, **385** and **387**. Following the same procedure already reported in Section 2 of Chapter 3, the mono-substituted DHP have been synthetized by a condensation cyclization reaction of the 1,8-diaminonaphthalene **336** with the desired aldehyde in presence of a catalytic amount of PTSA (reactions **a** and **b** in Fig. 107). Compared to the di-substituted DHP previously discussed (**337**-**340**) the synthesis of mono-substituted DHP display a less reaction's conversion and they are slightly trickier to purify by flash chromatography. For these reasons, mono-substituted DHP synthesis exhibit yield of ca. 50%.

After the preparation of the firstly two mono-substituted DHP derivatives **383** and **385**, the synthesis of squaraines **384** and **386** were tested. Applying the same reaction conditions used for the synthesis of the previous CI-based squaraines (**341**-**344**), the synthesis of **384** and **386** was carried out in a MW reactor by the condensation reaction between 1.0 eq of emisquaraine **323** and a slight excess of the desired DHP (1.5 eq.) using the mixture *n*-butanol/toluene (1:1) as solvent media (reactions **d** and **e** in Fig. 107).

Surprisingly, at the end of both reactions we found a completely different situation compared to the synthesis of DHP-SQs (**341**-**344**): both reaction's media did not display the classic dark-green coloration but exhibit an intense dark-pink coloration. In addition, the isolation and the analysis (by TLC) of the two reactions' crudes demonstrated as the two synthesis are slightly different from each other: (i) in the case of the reaction with the mono-phenyl DHP derivative **386**, we found the presence of one main product with a bright pink spot in TLC (Fig. 108), while (ii) in the case of the reaction with the mono-methyl DHP derivative **384**, we found the presence of an additional product with a purple spot in TLC below to the pink one (Fig. 108). In literature, it has been already demonstrated that MW reactor is a useful and effective tool to easily prepare the squaraines but at the

same time, it has been demonstrated that its harsher reaction's conditions can also favor the formation of undesired side products.[474]

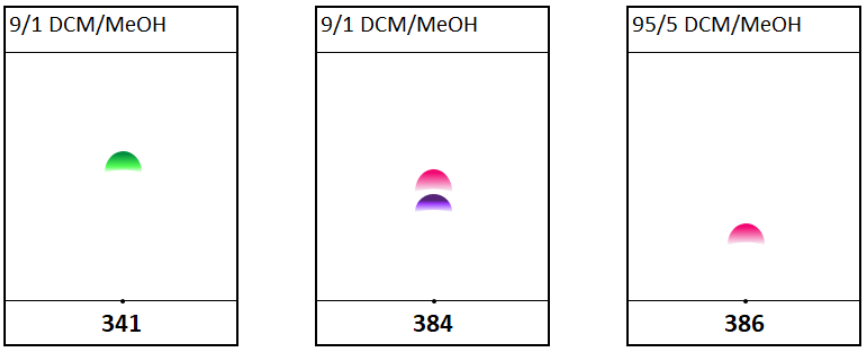

Figure 108 – TLC plates of the different reactions' crudes: synthesis of "*green*" DHP-SQ **341** (left) and the synthesis of "*pink*" DHP-SQs **384** (center) and **386** (right). The schemes of TLC plates of the reactions' crudes report only the spots of the main products (the additional spots of both unreacted starting materials (emisquaraine **323**, DHPs and PTSA) are omitted.

For these reasons, we decided to perform the same reactions toward **384** and **386** using the classic "thermal method" for the preparation of the squaraines, carrying out the synthesis in a Dean-Stark apparatus at reflux overnight.

However, even in the case of the "thermal method" we did not find any difference compared to the reactions performed in the MW reactor. For these reasons, we decided to stop the development of squaraine-based sensitizers bearing a non-conjugated TPA group and move our efforts to understand what happen in the synthesis of the squaraines when a mono-substituted DHP derivative is used instead to the di-substituted one.

To better understand the reaction's system, we decided to purify and isolate the different obtained compounds by flash chromatography. Henceforward, the squaraines synthetized in the Chapter 3 using the di-substituted DHP derivatives will be commonly called "*green*" while the obtained compounds using the mono-substituted DHP derivatives will be commonly called "*pink*" (the main product of both reactions with **383** and **385**) and "*purple*" (the additional product found in the reaction with **383**) (Fig. 108).

Firstly, the "*pink*" and "*purple*" compounds were analysed by mass spectrometry and compared to the known "*green*" squaraines. We performed and compared the MS spectra (ESI^-) of the unknown compounds with the "*green*" squaraine **341**. As reported in Fig. 109, the squaraine **341** has an exact mass of 506.21 and the desired mono-substituted SQ **384** (Fig. 107) should has 492.19.

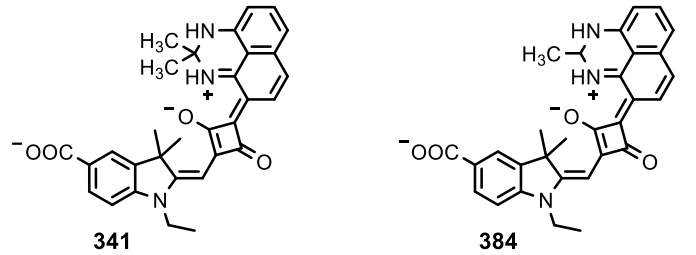

Chemical Formula: $C_{31}H_{28}N_3O_4^-$
Exact Mass: 506,21

Chemical Formula: $C_{30}H_{26}N_3O_4^-$
Exact Mass: 492,19

Figure 109 – Structures and exact mass of squaraines with the di-substituted DHP (**341**) and the mono-substituted DHP (**384**).

The "*pink*" and "*purple*" compound obtained from the reaction with **383** display mass values (ESI^--HRMS) of 492.1944 and 490.1781, respectively. "*Pink*" compound exhibits the exact mass of the desired target compound **384**, demonstrating that probably it has a regioisomeric structure in which the DHP moiety is connected to the squaric ring in a different manner. Contrarily, the "*purple*" compound displays a slightly different exact mass, suggesting that the mono-methyl DHP moiety is able to react with the squaric ring in two different manners, leading to different squaraine structures.

2. Structural Studies of "*Pink*" and "*Purple*" Squaraines

Following the same approach applied in Chapter 3, the "*pink*" and "*purple*" compounds have been fully characterized by ^1H, ^{13}C, COSY, DEPT-135, COSY, HSQC and HMBC NMR experiments to identify their structure (all the spectra are reported in Section 1.12). Even if the "*pink*" product provided by the synthesis with **385** will surely exhibit trickier NMR spectra due to the presence of additional

signals related to the phenyl ring, it has been selected because larger amount of pure compound was available due to its easier purification compared to the other "*pink*" derivative provided by the reaction with **383**. In addition, the performed ^{13}C, DEPT-135 and two-dimensional NMR experiments for the "*pink*" and "*purple*" derivatives required very long acquisition times (up to 16 hours) and the fine optimization of the relaxation delay: between the two "*pink*" products; considering all of that, the product obtained by the reaction with the mono-phenyl DHP **385** provided better NMR spectra.

Starting from the "*pink*" product, we hypothesized two possible regioisomers in which the DHP moiety is connected to the squaric ring in a different manner (Fig. 110).

In particular, we hypothesized that the different connection can be related to the DHP moiety or to the squaric ring. In the former case, we hypothesized that the DHP moiety reacts with the emisquaraine through one of the two secondary amine sites (**389** in Fig. 110), while in the other case we hypothesized that the DHP moiety reacts with the emisquaraine through the position 4 to form a 1,2-squaraine (**390** in Fig. 110).

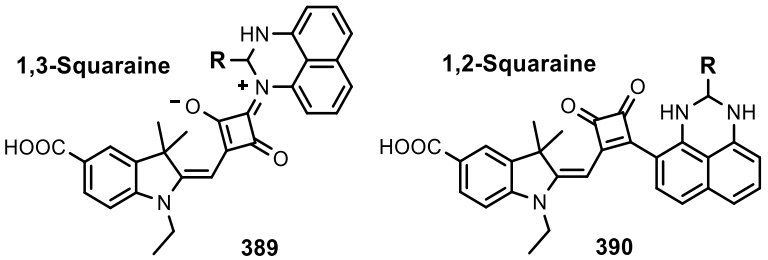

Figure 110 – Hypothesized regioisomeric structures for the "*pink*" products.

Interestingly, it is known from the literature that both 1,2-squaraines and 1,3-squaraines display strong absorptions between 500-550 nm, in accordance with the "*pink*" color noticed.[520-522]

As previously reported for "*green*" squaraines, the identification of the structure of the "*pink*" products cannot be unambiguously answered with one-

dimensional nuclear magnetic resonance spectroscopy alone (^{1}H,^{13}C and DEPT-135). For these reasons, the two-dimensional nuclear magnetic resonance spectroscopic techniques have been performed (COSY, HSQC, HMBC).

The investigation to identify the structure of the "*pink*" products started considering the squaraine **391** (Fig. 111) as possible target compound. Henceforward, the numeration of carbon and hydrogen atoms will be referred to the structure **391** in Fig. 111.

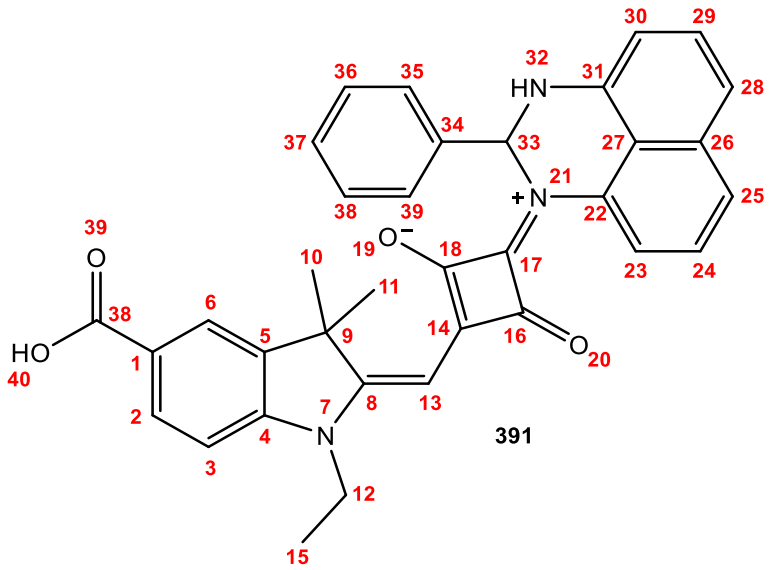

Figure 111 – Numeration of atoms in the assumed structure of SQ **391**.

Considering **391** as the possible structure, it is possible to make some considerations which, if satisfied, will give us the confirmation that the "*pink*" compounds have a general structure like **391**: (i) in the HSQC experiment should be only one signal without any ^{1}J coupling, refereed to hydrogen atom H-32 and (ii) excluding the quaternary carbon atoms of the emisquaraine moiety (C-4, C-5, C-8, C-9, C-14, C-16, C-17, C-18 and C-38), DEPT-135 spectrum should exhibits further five quaternary carbon atoms, four referred to the naphthalene scaffold (C-22, C-26, C-27 and C-31) and one referred to the phenyl ring (C-34). To simplify the results' interpretation, we initially assigned the signals related to the carboxy indolenine moiety of the molecule (zoomed HSQC, DEPT-135, HMBC and COSY

spectra are reported in Fig. 112-115, respectively): (i) C-6 and H-6 at 123.19 and 8.04 ppm, (ii) C-2 and H-2 at 130.32 and 7.96 ppm, (iii) C-3 and H-3 at 109.70 and one of the signals in the multiplet at 7.37-7.42 ppm, (iv) C-1 at 125.65 ppm due to the ^{3}J coupling with H-3 and the absence of its signal in DEPT-135, (v) C-4 at 145.46 ppm due to the ^{3}J coupling with H-2, the ^{3}J coupling with H-6 and the absence of its signal in DEPT-135, (vi) C-5 at 141.41 ppm due to the ^{3}J coupling with H-3 and the ^{3}J coupling with H-10 and H-11, (vii) C-9 at 48.35 ppm due to their up field chemical shift and the absence of its signal in DEPT-135, (viii) C-10/C-11 and H-10/H-11 at 26.57/26.83 and 1.69/1.73 ppm, (ix) C-12 and H-12 at 38.12 and 4.13 ppm, (x) C-15 and H-15 at 11.55 and 1.27 ppm, (xi) C-8 at 169.25 ppm due to the ^{2}J coupling with H-13 and the ^{3}J coupling with H-10 and H-11, (xii) C-13 and H-13 at 86.12 and 5.89 ppm.

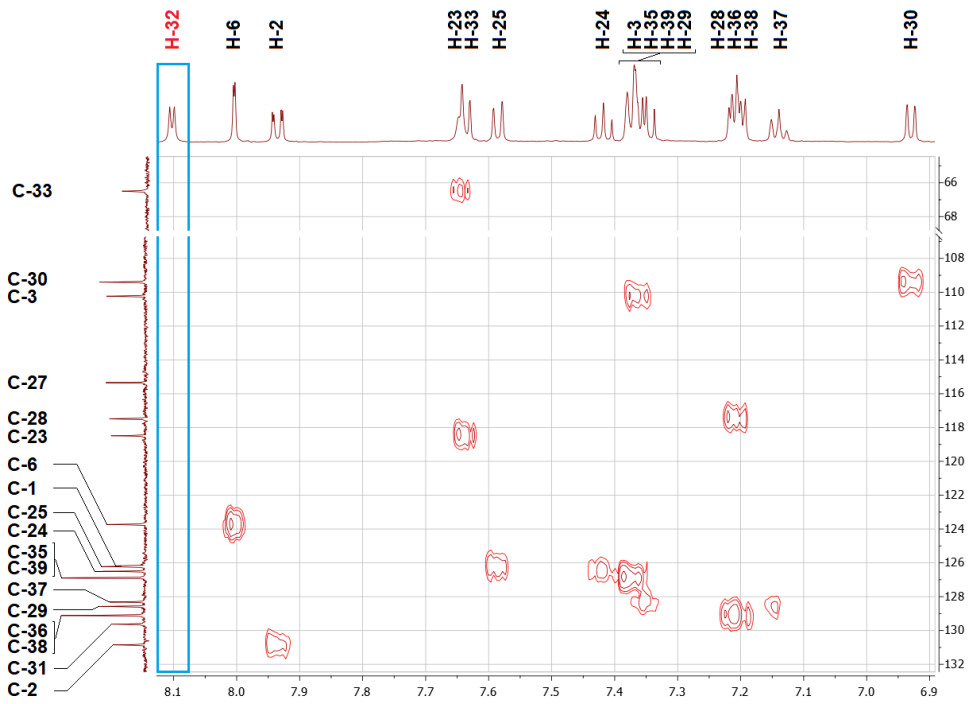

Figure 112 – Zoomed HSQC of "*pink*" product (in DMSO-d_6).

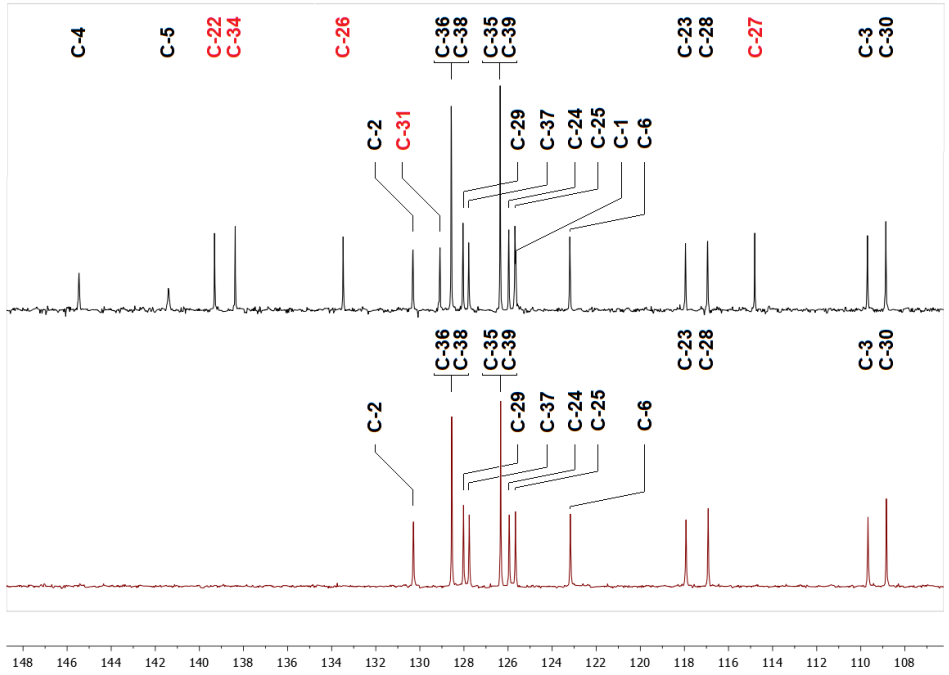

Figure 113 – Zoomed DEPT-135 of "*pink*" product (in DMSO-d_6).

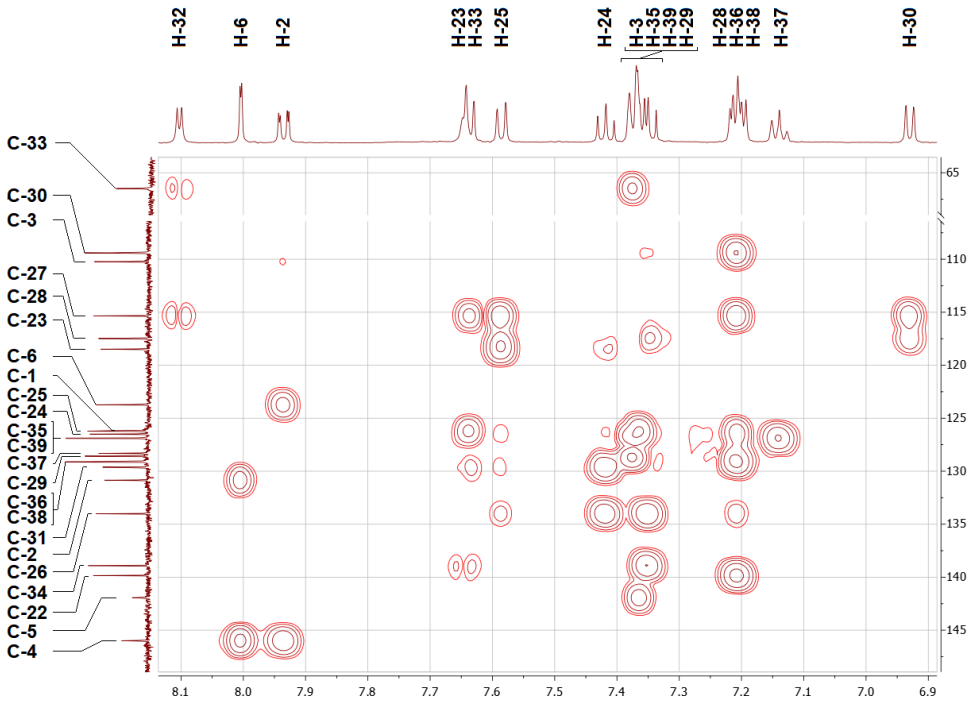

Figure 114 – Zoomed HMBC of "*pink*" product (in DMSO-d_6).

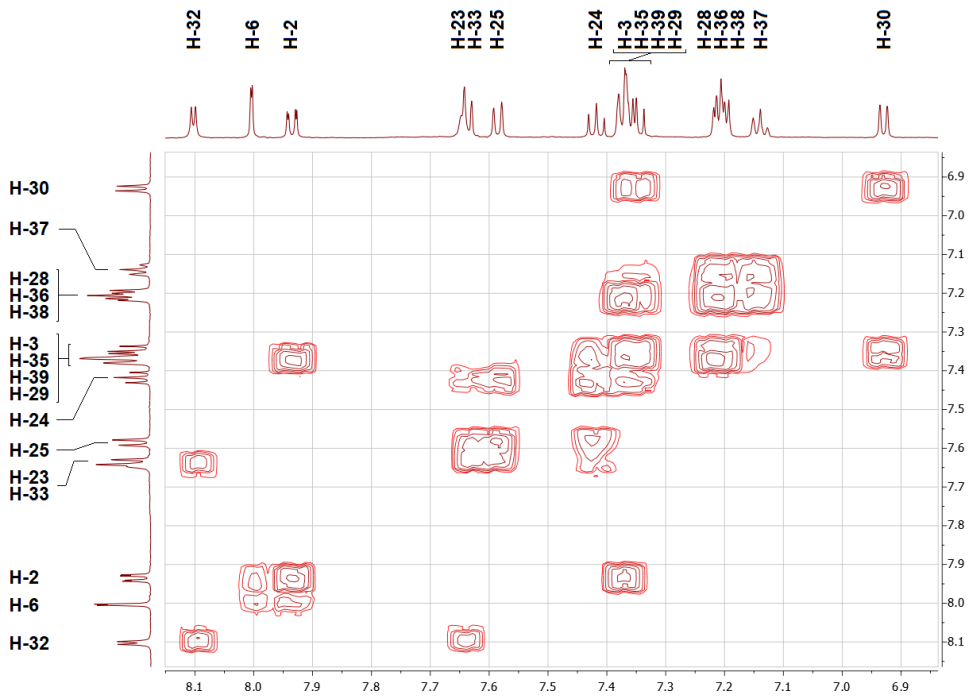

Figure 115 – Zoomed COSY of "*pink*" product (in DMSO-d_6).

After the interpretation of the CI's signals, we tried to verify if the two considerations previously reported were satisfied. The HSQC spectrum demonstrates that there is one signal at 8.14 ppm without any ^1J coupling (light-blue frame in Fig. 112) that can be attributed to the hydrogen atom (H-32) of the free amino group of the DHP moiety. In addition, DEPT-135 demonstrated that excluding the quaternary carbon atoms of the emisquaraine moiety, there six other quaternary carbon atoms (in red in Fig. 113). Both previously considerations are satisfied by the NMR experiments, suggesting that **391** can be the real structure of the "*pink*" products. To remove all doubts and to confirms the structure, the signals of the pending phenyl group and of the DHP moiety have been interpretated. The signals of the pending phenyl group have been thus assigned: (i) C-35/C-39 and H-35/H-39 at 126.36 and two of the signals in the multiplet at 7.37-7.42 ppm, this assignment is due to the ^1J coupling between H-35/H-39 and C-35/C-39 and due to the ^3J coupling between H-35/H-39 with C-33, (ii) C-36/C-38 and H-36/H-38 at 128.58 and two of the signals in the multiplet at

7.23-7.26 ppm, this assignment is due to the ^{3}J coupling between H-36/H-38 and H-35/H-39 and due to the ^{3}J coupling between H-36/H-38 with C-35/C-39, (iii) C-37 and H-37 at 127.78 and 7.15 ppm due to the ^{3}J coupling between H-37 and H-36/H-38, (iv) C-34 at 138.38 ppm due to the ^{3}J coupling with H-35/H-39 and H-33 and the absence of its signal in DEPT-135. After the attributions of the signals related to the phenyl ring, we assigned the signals of the DHP moiety: (i) C-27 at 114.81 ppm due to the ^{3}J coupling with H-23, H-25, H-28, H-30, H-32 and the absence of its signal in DEPT-135, (ii) C-26 at 133.48 ppm due to the ^{2}J coupling with H-25 and H-28, the ^{3}J coupling with H-24 and H-29 and the absence of its signal in DEPT-135, (iii) C-23 and H-23 at 117.95 and one of the two signals in the multiplet at 7.67-7.68 ppm due to the ^{3}J coupling between C-23 and H-25 and the ^{3}J coupling between H-23 and H-24, (iv) C-24 and H-24 at 125.97 and 7.45 ppm due to the multiplicity of the signals of H-24 and due to its ^{3}J coupling with H-23 and H-25, (v) C-25 and H-25 at 125.69 and 7.62 ppm, (vi) C-30 and H-30 at 108.86 and 6.96 ppm due to the ^{3}J coupling between C-30 and H-28 and the ^{3}J coupling between H-30 and H-29, (vii) C-29 and H-29 at 128.04 and one of the signals in the multiplet at 7.37-7.42 ppm, (viii) C-28 and H-28 at 116.95 and one of the signals in the multiplet at 7.23-7.26 ppm, (ix) C-22 and C-31 at 139.31 and 129.09 due to their chemical shifts (C-22 nearest to the charge nitrogen is more deshielded) and the absence of their signals in DEPT-135. Further confirmation is related to identification of only one signal without any ^{1}J coupling in the HSQC spectrum attributed to the -NH group; in the case of the connection by the position 4 of the DHP (**390** in Fig. 110), we should have to find two signals (like displayed by the "*green*" SQs).

The interpretation of NMR experiments confirms that the "*pink*" products are characterized by a general structure like **391** in Fig. 111. The selective formation of **391** in the reaction of the emisquaraine **323** and the mono-substituted DHP **385** suggests the possible regioselectivity of the reaction. In particular, when the DHP is di-substituted the synthesis leads to the "*green*" squaraine in which the emisquaraine reacts in the position 4 of the DHP scaffold, whereas when the DHP

is mono-substituted the synthesis leads to the "*pink*" regioisomer in which the emisquaraine reacts with one of the two secondary amine sites of the DHP scaffold.

However, in the case of the reaction with the mono-methyl DHP **383** it has been detected an additional "*purple*" product beside to the "*pink*" one. The formation of the "*purple*" product in this reaction could be a particular case due to the peculiar structure of **383**: the methyl substituent in α between the two secondary amine sites can be compared to the α-methyl of the indole salts used for the synthesis of the common squaraines. Starting from this consideration, we hypothesized that the "*purple*" compound is characterized by the structure **392** depicted in Fig. 116 in which the DHP is connected to the squaric ring by a methine. Henceforward, the numeration of carbon and hydrogen atoms will be referred to the structure **392** in Fig. 116.

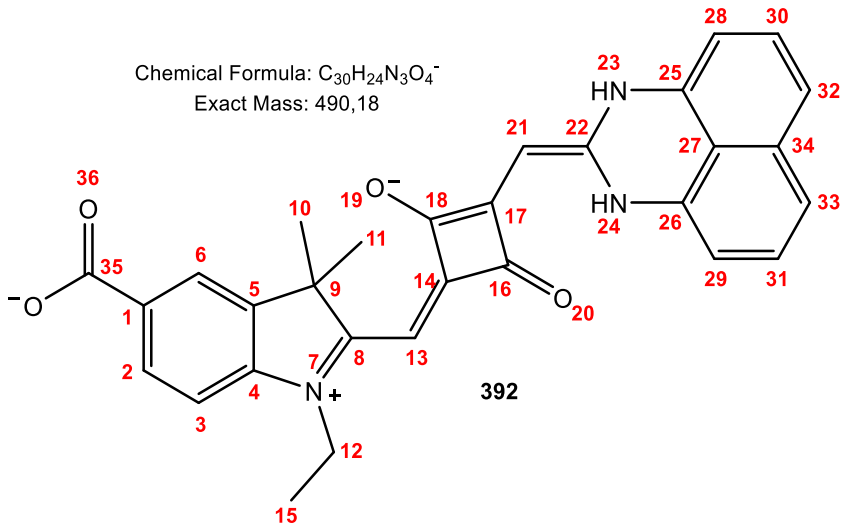

Figure 116 – Numeration of atoms in the assumed structure of SQ **392**.

Compared to the previous case, the identification of the structure of the "*purple*" compound has been easier owing to symmetry of DHP moiety. The first confirmation about the hypothesized structure has been provided by the ESI$^-$-HRMS spectrum (Fig. 117) that exhibited the expected mass value (490,1781) from structure **392**, while the unambiguously identification of the structure has

been achieved by the analysis of the ^{1}H-NMR and COSY spectra (additional NMR spectra are reported in Section 1.12 of SI - Fig. 228-233).

Considering **392** as the possible structure for the "*purple*" compounds, it is possible to make the following considerations (i) in ^{1}H-NMR should be two different singlet signals referred to H-13 and H-21, (ii) in COSY experiment should be two distinct families of coupled signals, one refereed to the hydrogen atoms of the carboxyindolenine (CI) part whereas the other one refereed to the DHP moiety.

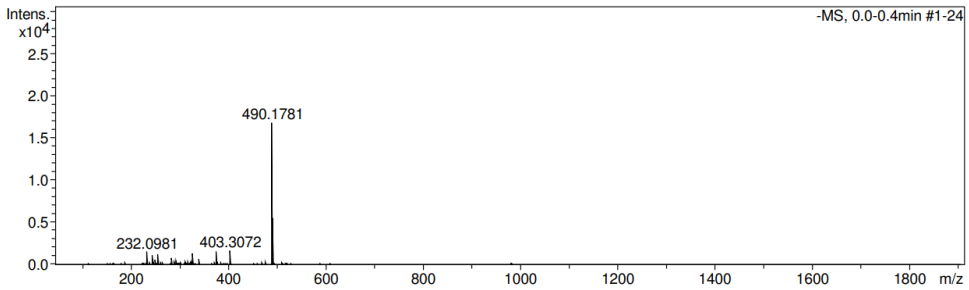

Figure 117 – ESI^{-}-HRMS spectrum of SQ **393** in methanol.

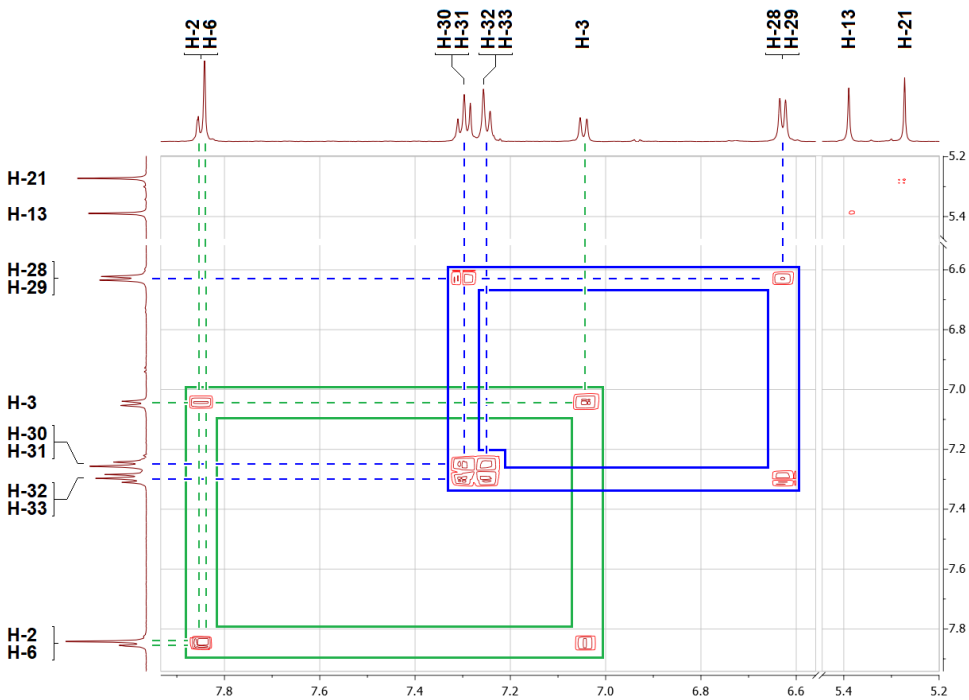

Figure 118 – Zoomed COSY of "*purple*" product (in DMSO-d_6).

As displayed in Fig. 118, COSY experiment exhibits the two peculiar singlet signals referred to H-13/H-21 and demonstrated the presence of two different families of coupled signals: (i) the green signals are referred to the hydrogen atoms of the CI part of the molecule while (ii) the blue ones to DHP moiety.

The structural identification of the "*pink*" and "*purple*" compounds confirmed that the substitution degree of the sp^3 carbon atom of the DHP can strongly influence the regioselectivity of the reaction with an emisquaraine in the synthesis of squaraines. In particular, the structural identification of the "*green*", "*pink*" and "*purple*" compounds suggested that: (i) when the DHP is di-substituted, the reaction with the CI-based emisquaraine leads to the formation of "*green*" squaraines in which the DHP is connected to the squaric ring by its position 4, (ii) when the DHP is mono-substituted, the reaction with the CI-based emisquaraine leads to the formation of "*pink*" squaraines in which the DHP is connected to the squaric ring trough one of its nitrogen atoms. In addition, it has been demonstrated that the mono-methylated DHP **383** provides the formation of additional "*purple*" squaraine **392** in which the DHP is connected to the squaric ring by a methine.

3. Project Proposal

After the identification of the structures, we decided to leave the development of the squaraine bearing the non-conjugated TPA group (**388**) and we focused our attention on the comparison of the photophysical properties of the classic DHP-based "*green*" squaraines and the new "*pink*" ones. For this reason, the di-phenyl DHP moiety **396** and the relative "*green*" squaraine **397** have been synthetized for the comparison with **391**. In addition, to confirm that the formation of "*purple*" product represents a particular case only related to the mono-methylated DHP **383**, we decided to synthetize the mono-ethylated DHP **394** and its relative squaraine **395** As expected, in the synthesis of **395** it has been not found any evidence about the formation of a *purple*-like squaraine, probably due the steric effect of ethyl. The preparation of the squaraines has been carried

out following the synthetic plan displayed in Fig. 119. Henceforward, squaraines **391**, **393** and **395** will be called “mono-substituted DHP-SQs” while squaraine **341**-**350** and **397** will be called “di-substituted DHP-SQs”.

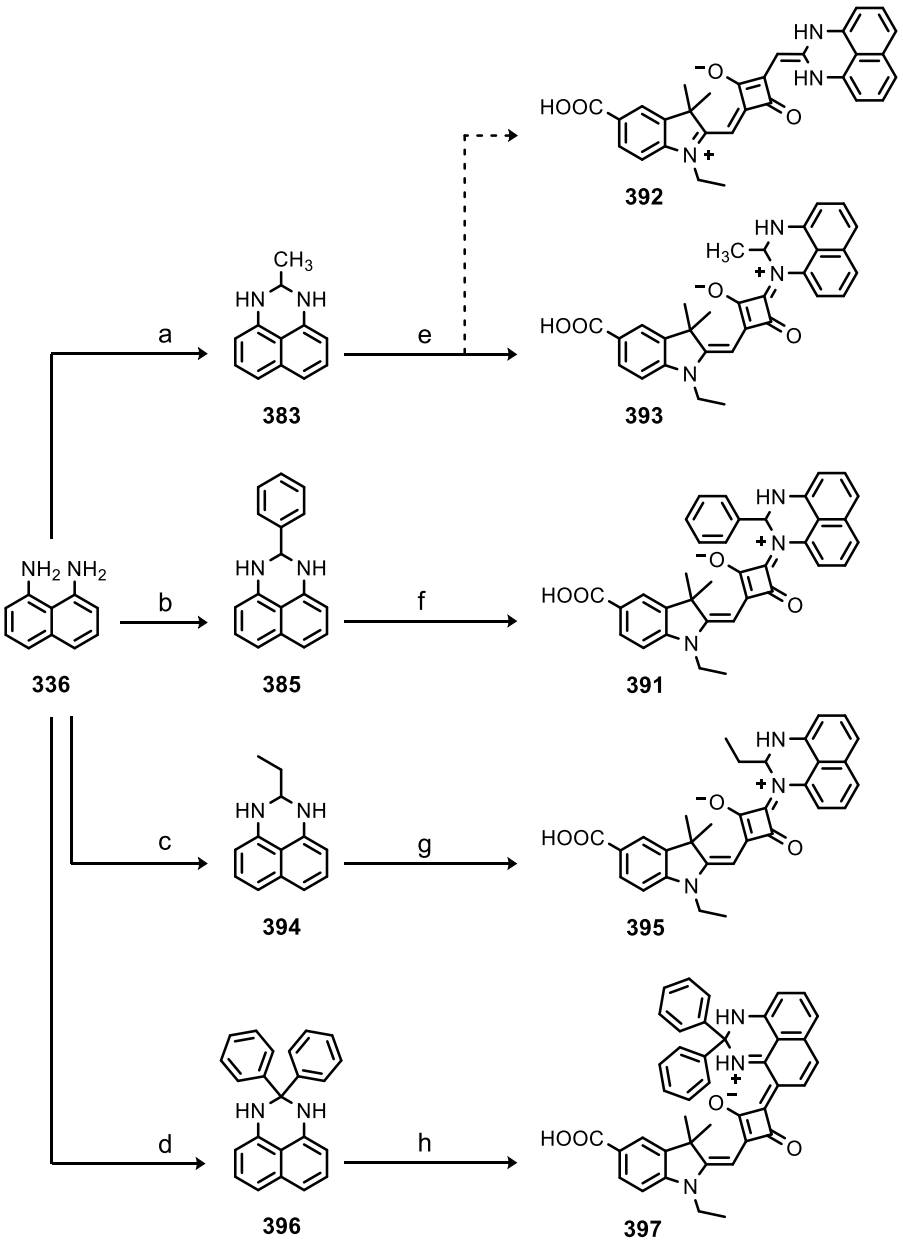

Figure 119 – Synthetic scheme. a, b, c) Aldehyde (acetaldehyde for **383**, benzaldehyde for **385**, propionaldehyde for **394**) PTSA, toluene, reflux, 16 h in Dean-Stark apparatus. d) Benzophenone, PTSA, toluene, reflux, 16 h in Dean-Stark apparatus. e, f, g, h) **323**, DHP (**383** or **385** or **394** or **396**), *n*-butanol/toluene, MW 160 °C, 30 min.

4. Photo- and Electrochemical Characterization

The photophysical properties of squaraines **391**-**393**, **395** and **397** have been evaluated in ethanol (Tab. 29 and Fig. 120). In addition, their solvent-dependent behaviors have been qualitatively investigated in eight different solvents. In Fig. 121 are reported the absorption spectra of **391** in different solvents (the data of all other squaraines are reported in Section 2.2 of SI, voltammogram for **391**-**393**, **395** and **397** are reported in Section 3.1 of SI - Fig. 323).

Table 29 – Photo- and electrochemical properties of all mono- and di-substituted DHP squaraines.

Dye	λ_{max} [nm]	ε [M^{-1} cm^{-1}]	$E_{0\text{-}0}$ [nm] [a]	$E_{0\text{-}0}$ [eV]	HOMO [V *vs.* Fc/Fc^+] [b]	HOMO [eV]	LUMO [eV]
391	546	71 618	561	2.21	+0.29	-5.39	-3.18
392	572	38 858	592	2.09	+0.04	-5.14	-3,05
393	542	44 511	555	2.23	+0.29	-5.39	-3.16
395	543	48 012	561	2.21	+0.29	-5.39	-3.18
397	732	93 693	757	1.64	+0.05	-5.15	-3.51

[a] Absorption and steady state emission spectra were performed in EtOH.

[b] CVs experiments were performed as described in SI using DCM as solvent.

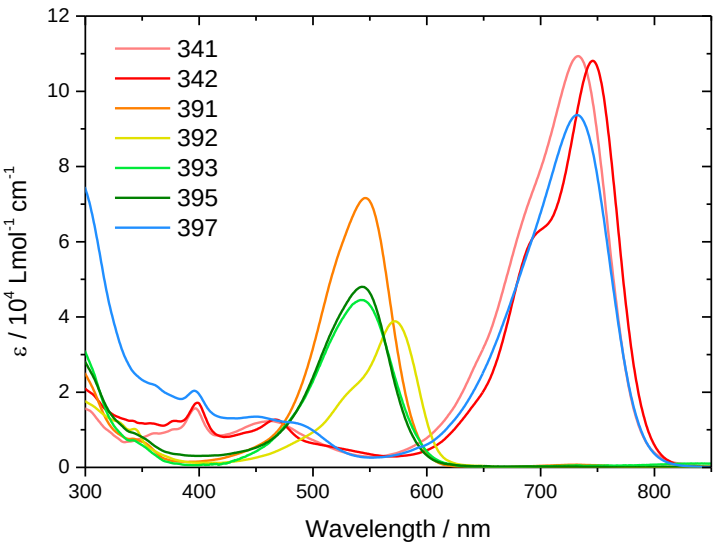

Figure 120 – Comparison between the absorption spectra of the di-substituted DHP-SQs **341**, **342**, **397** and the mono-substituted DHP-SQs **391**, **393**, **395** in ethanol. The spectrum of the "*purple*" squaraine **392** has been also reported.

The mono-substituted DHP-SQs **391**, **393** and **395** exhibit an absorption peak centered at 545 nm. Molar extinction coefficient around $4.5 \cdot 10^4$ M^{-1} cm^{-1} were observed in ethanol for squaraine bearing respectively the methyl (**393**) and the ethyl (**395**) groups, whereas **391** bearing the phenyl group display an hyperchromic absorption with a molar extinction coefficient up to $7.1 \cdot 10^4$ M^{-1} cm^1. The main band at ca. 545 nm can be attributed to a π-π* charge-transfer transition of the conjugated system.[522] The different π-conjugation scaffold between the mono-substituted DHP-SQs and the di-substituted ones strongly influences the absorption properties of the two series. In particular, the two series of squaraines exhibit a difference of absorption maxima of almost 200 nm.

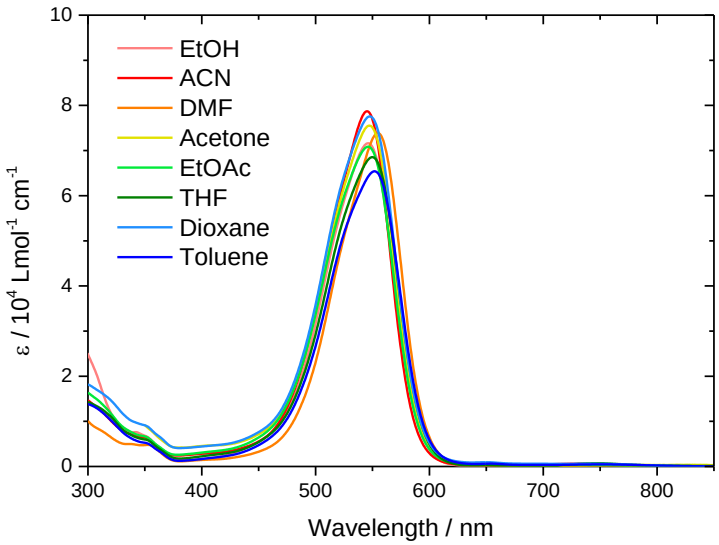

Figure 121 – Absorption spectra of **391** in different solvents.

In the case of **392**, the further slightly extension of the π-conjugation structure due to the presence of the methine bridge between the squaric core and the DHP moiety, causes a bathochromic shift of the absorption maximum compared to the "*pink*" squaraines. "*Purple*" squaraine **392** exhibit an absorption peak centered at 572 nm with a molar extinction coefficient of $3.9 \cdot 10^4$ M^{-1} cm^{-1}. The main band can be attributed to a π-π* charge-transfer transition of the conjugated system and in addition, **392** exhibit a weak vibronic band centred at 520-530 nm.

The di-substituted DHP-SQ **397** displays the classic absorption features of the "*green*" squaraines (**341**-**350**) with a maximum absorption at 732 nm with a molar extinction coefficient of $9.4 \cdot 10^4$ M^{-1}.

The solvatochromism of mono-substituted DHP-SQs (**391**, **393**, **395**) has been also evaluated. In Fig. 121 the absorption spectra of **391** in eight different solvents are reported. In the case of the "green" squaraines, it has been demonstrated that different solvents influence the peak-shape mainly acting on the vibronic band. Contrarily, in the case of the "*pink*" squaraines the absence of the vibronic band lead to a very low solvatochromic effect: the different solvents do not influence the peak-shape and do not cause considerable shifts of the absorption's maxima (solvatochromism data for other "*pink*" SQs are reported in Section 2.2 of SI - Fig. 316-317).

Even for **392** a solvatochromism study has been performed but, in this case, a huge solvent-dependency has been found (Tab. 30). In Fig. 122 are reported the absorption spectra of **392** in nine different solvents.

Table 30 – Absorption properties of squaraine **392**.

Solvent	λ_{max} [nm]	ε [M^{-1} cm^{-1}]
EtOH	572	38 858
ACN	476	18 895
DMSO	494	25 948
DMF	479	23 442
Acetone	571	22 725
EtOAc	576	39 764
THF	580	36 518
Dioxane	582	45 197
Toluene	582	41 941

In particular, it has been demonstrated that the polar protic solvent like ethanol and the apolar ones like ethyl acetate, THF, 1,4-dioxane and toluene, do not influence the peak-shape and do not cause considerable shifts of the absorption's maxima, as before described for the "*pink*" squaraines. Contrarily, in

polar aprotic solvents like ACN, DMF, DMSO and acetone, it has been found a huge solvatochromic effect that cause a peak-shape modification: (i) in the case of DMF and DMSO there is huge ipsochromic shift of the absorption maximum from ca. 570 nm to ca. 480-500, while (ii) in the case of ACN and acetone, **392** exhibits doubled absorption shape in which is possible to detect both the absorption components at 570 nm and at 480-500 nm.

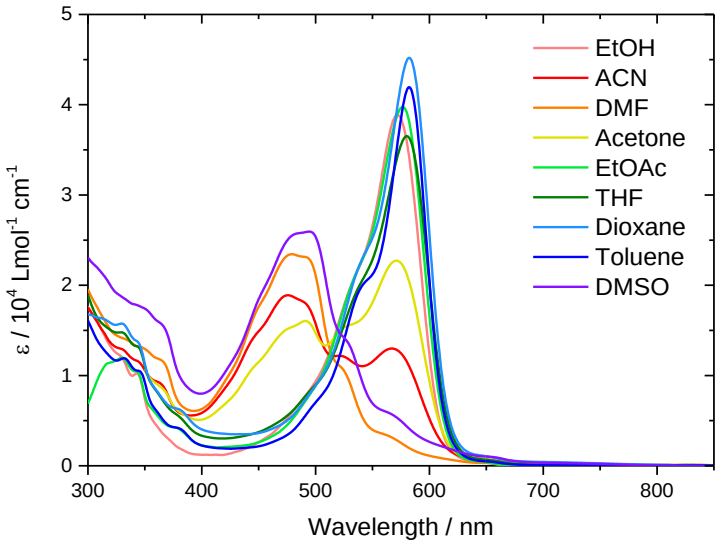

Figure 122 – Absorption spectra of **392** in nine different solvents.

Squaraine **392** has a highly planar structure that could suffer self-aggregation phenomena, leading to the formation of H-aggregates. It is well-known that the formation of H-aggregates in squaraines usually causes the ipsochromic shift of the absorption band.[477] Starting from these considerations, we hypothesized that in the case of aprotic polar solvents like ACN, DMF, DMSO and acetone, the squaraine's molecules are not well solvated and therefore they tend to form H-aggregates that cause the appearance of the absorption component at 480-500 nm (Fig. 122). Contrarily, increasing the apolarity of the solvents, the solvation of squaraine's molecule increases preventing the formation of H-aggregates. For this reason, in the more apolar solvents, **392** exhibits a sharp absorption band at ca. 570 nm. However, **392** exhibits the same optical behaviour even in a high polar

solvent like ethanol. The similar behaviour of **392** is probably due to the feature of ethanol to be a hydrogen-bond donor solvent (HBD), allowing the well solvation of squaraine trough the hydrogen-bonds between the solvent's molecules and the hydrogen-bond acceptor groups (HBA) of **392** such as the carboxylic and the carbonyl groups. According to the last hypothesis, the non-hydrogen-bond donor solvents as ACN, DMF, DMSO and acetone, confirms the weak solvation of these solvents toward **392**.

As mentioned before, squaraine **392** displays different behaviour in the four used aprotic solvents. While in DMF and DMSO there is only one main absorption contribute centred at 480-500 nm, in acetone and ACN **392** exhibits a doubled absorption shape. Interestingly, the absorption ratio between the two maxima is completely different between acetone and ACN: (i) in the case of acetone, prevails the second component at ca. 570 nm, while (ii) in the case of ACN, the uppermost is the first one at ca. 480-500 nm. To understand if the concentration influences the absorption shape, spectra of **392** at different concentrations have been performed in the four aprotic solvents (Fig. 123-124). In the case of DMF and DMSO, the concentration of **392** do not have any effect on the absorption shape (Fig. 123), demonstrating as these solvents have a poor solvation ability toward **392** even at low concentrations. For these reasons, in DMF and DMSO the absorption's contributes related to the H-aggregates are predominant.

Even in the case of acetone, the concentration of **392** has no effects on the absorption shape (Fig. 124a). However, even if it possible to find the absorption's component related to the presence of H-aggregates, the acetone seems to be able to be better in the solvation of **392**, as demonstrated by the predominant absorption's contribute at ca. 570 nm. Despite the features of **392** in ACN seems to be more similar to what seen in DMSO and DMF, its absorption spectra at different concentration proves that it behaves like in acetone. The increase of the concentration of **392** causes the modification of the absorption shape: while at low concentrations (≤ 14 μM) the absorption's component of the H-aggregates is

predominant, at high concentrations the uppermost is the absorption's contribute due to the single solvated molecule (Fig. 124b).

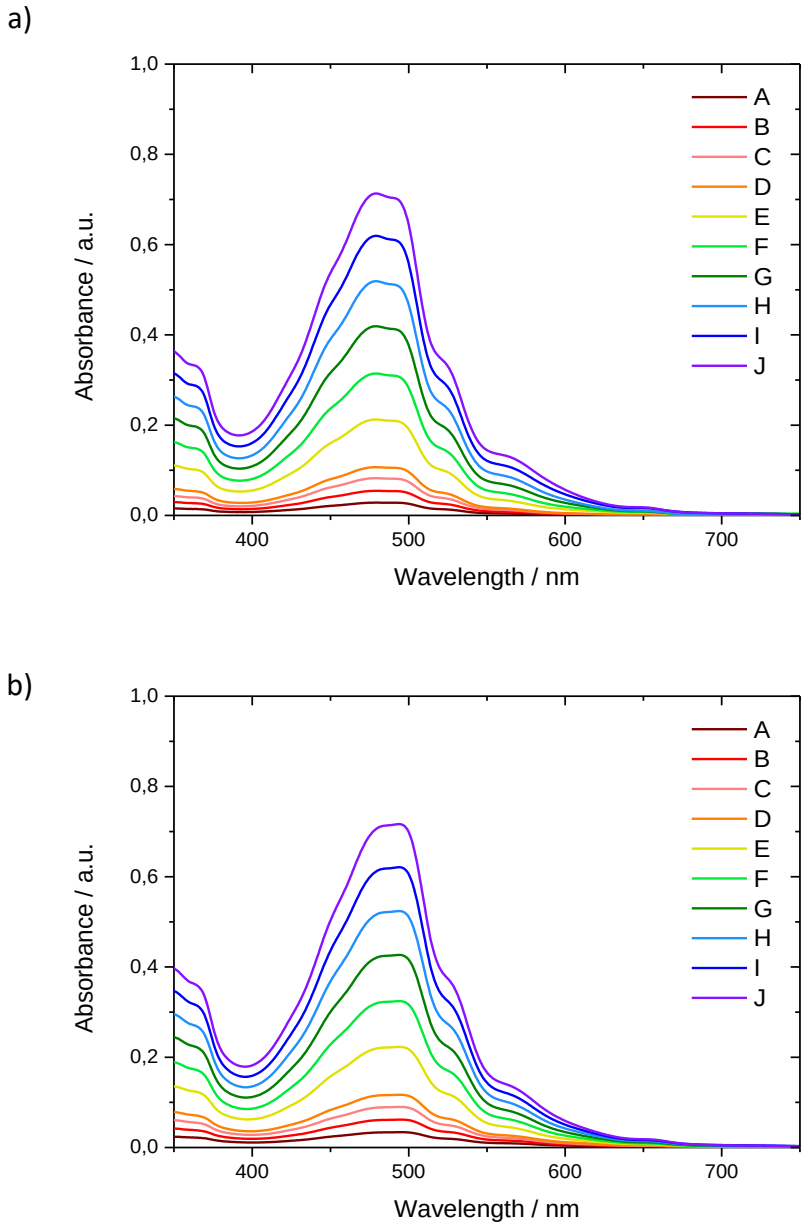

Figure 123 – a) Absorption spectra of **392** in DMF at different concentrations. b) Absorption spectra of **392** in DMSO at different concentrations. Concentrations: 1.2 µM (**A**), 2.3 µM (**B**), 3.5 µM (**C**), 4.6 µM (**D**), 9.2 µM (**E**), 14 µM (**F**), 18 µM (**G**), 23 µM (**H**), 28 µM (**I**), 32 µM (**J**).

a)

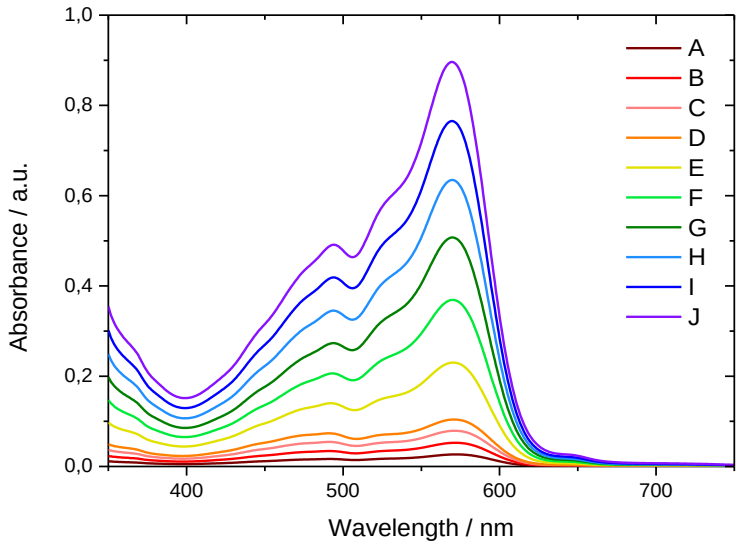

b)

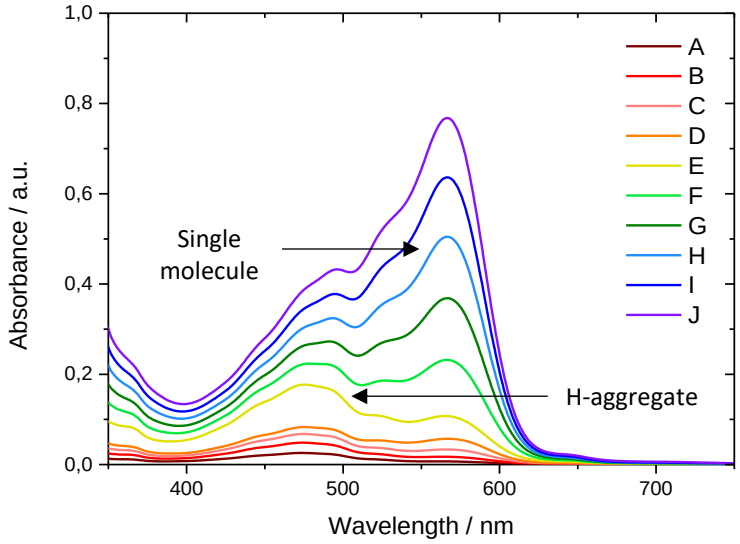

Figure 124 – a) Absorption spectra of **392** in acetone at different concentrations. b) Absorption spectra of **392** in ACN at different concentrations. Concentrations: 1.2 µM (**A**), 2.3 µM (**B**), 3.5 µM (**C**), 4.6 µM (**D**), 9.2 µM (**E**), 14 µM (**F**), 18 µM (**G**), 23 µM (**H**), 28 µM (**I**), 32 µM (**J**).

The results suggest that acetone and ACN to solvate better **392** compared to DMSO and DMF. In addition, we hypothesized that the absorption-shape variation in ACN could be due to the HBD feature of **392** (in its structure there are

two secondary amine sites and a carboxylic group). The increase of the concentration of **392** raises the probability to the formation of hydrogen-bond interactions among the squaraine's molecules, thus preventing aggregation phenomena. This behaviour is demonstrated by the predominant absorption's component at 570 nm of **392** in ACN.

Contrarily to the "*green*" SQs, the "*pink*" and the "*purple*" ones exhibit very weak fluorescence emission with QYs lower than 1% (the collection of the spectra required the widen of the slits from 5-10 nm to 20-20 nm, respectively). For these reasons, it has been decided to qualitatively evaluate their emission behaviours only in ethanol (Fig. 125 and Tab. 31). "*Pink*" SQs (**391**, **393**, **395**) exhibit broader and weaker emission peaks' compared to **392**. In addition, the "*purple*" SQ **392** has a slightly larger Stokes Shift (ca. 40 nm) compared to the "*pink*" ones that exhibit values around 25 nm.

Table 31 – Photophysical properties of "*pink*" and "*purple*" SQs in ethanol.

Dye	λ_{max} [nm]	λ_{em} [nm]	ε [M^{-1} cm^{-1}]	Stokes shift [cm^{-1}]
391	546	571	71 618	802
392	572	614	38 858	1196
393	542	568	44 511	845
395	543	570	48 012	872

Recently, similar squaraines have been tested as co-sensitizers in DSSC.[522] For this reason, the HOMO and LUMO energy levels of the "*pink*" and "*purple*" squaraines have been evaluated and compared to the other sensitizers presented in this thesis. To calculate the HOMO and LUMO energy levels, the procedure previously reported in Section 4 of Chapter 2 has been adopted. CV experiments have been performed to evaluate the HOMO energy level of **391**-**393** and **395**, while the LUMO levels were calculated by the "optic method", using the optical band-band gap. As reported in Tab. 29, the "*pink*" SQs (**391**, **393**, **395**) and the "*purple*" one (**392**) obviously display higher band-gap values compared to the "*green*" SQs.

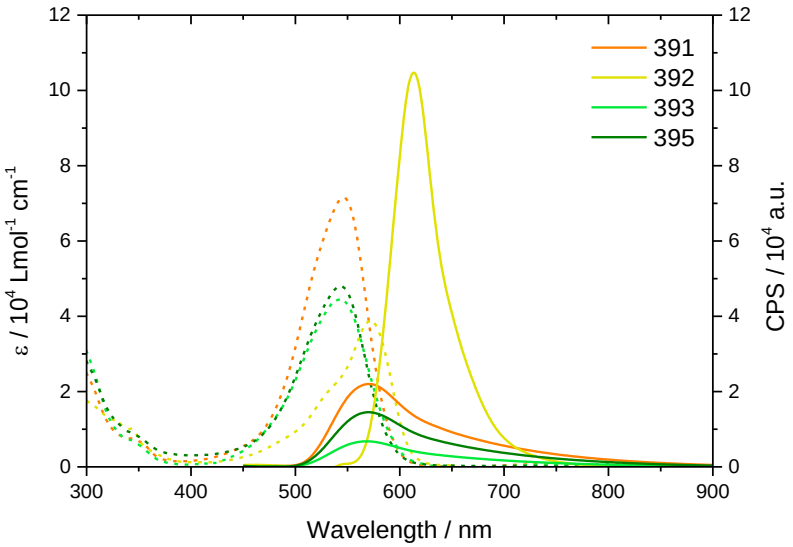

Figure 125 – Absorption (dashed) and steady state emission spectra of **391**-**393** and **395** in ethanol. The emission spectra were normalized at 0.1 intensity at the excitation wavelength.

In particular, "*pink*" SQs exhibit HOMO levels at -5.39 eV and LUMO levels between -3.16 eV and -3.18 eV, while **392** displays a HOMO level at -5.14 eV and a LUMO level at -3.05 eV. Compared to the "*green*" SQs, **392** exhibits almost the same HOMO level energy value while the "*pink*" SQs display lower values. As previously discussed in Chapter 1, at least 0.2 eV difference between the CB of the TiO_2 and the LUMO of the sensitizer is necessary to achieve an efficient electron injection: lower values do not allow the injection while higher ones lead to detrimental energy losses.[13] As far as "*pink*" SQs are concerned, they exhibit energy difference of 0.8 eV, high enough to achieve efficient electron injection. In the case of "*purple*" SQ **392**, the energy difference between the TiO_2 CB and its LUMO energy level it is even of 1.0 eV. The high energy gap between the TiO_2 CB and the LUMO levels of both "*pink*" and "*purple*" SQs suggested the possibility to use the 4-*tert*-butylpyridine (TBP) in the electrolyte solution to raise the TiO_2 CB and thus the V_{OC} of final devices with DHP-SQs.[479] Even if it has been demonstrated in the case of "*green*" SQs that the addition of TBP in the

electrolyte solution drop-down their photovoltaic performance, in the case of "*pink*" and "*purple*" SQs the presence of TBP could be useful due to the higher energy gaps between their LUMO levels and the TiO_2 CB.

5. Conclusions and Future Outlook

Despite the starting proposal of this work was the synthesis of a squaraine with a non-conjugated TPA moiety to enhance the dye-regeneration in DSSCs, in this chapter the synthesis of a novel series of DHP-based squaraine with an hypsochromic absorption in the visible has been reported.

Slightly modification of the DHP moiety dramatically change the reactivity of the system. Regioselectivity of the squaraines synthesis has been demonstrated in base of the structure of DHP moiety. In particular, performing reactions with the mono- or the di-substituted DHP moieties, it is possible to obtain two different regioisomers: (i) in the case of the mono-substituted DHP, the reaction with emisquaraine leads to the formation of "*pink*" SQ in which the DHP moiety is connected to the squaric ring by one of its nitrogen atoms, whereas (ii) in the case of the di-substituted DHP, the reaction with emisquaraine leads to the formation of "*green*" SQ in which the DHP moiety is connected to the squaric ring by its position 4 (as previous discussed in Chapter 3).

In addition, we demonstrated that the reaction between an emisquaraine and the mono-methylated DHP (**383**) lead to the formation of an additional product in which the DHP moiety is connected to the squaric ring by a methine (**392**). The comparison of the reactivity of the mono-methylated DHP (**383**) and the mono-ethylated one (**394**) confirmed that the formation of "*purple*" SQ like **392** is limited to the case of the reaction between an emisquaraine with the mono-methylated DHP (**383**).

HOMO and LUMO energy levels suggest that all "*pink*" and "purple" SQs could be applied in classic DSSC as co-sensitizers, as reported for similar structures by Singh *et al.*[522]

As reported, NMR studies allowed the structural identification of both "*pink*" and "*purple*" squaraines. However, they don't shed light on the reasons behind the dramatically reactivity difference between the mono- and di-substituted DHP moiety. For these reasons, to conclude the work and to shed the light behind the tricky reactivity of these compounds, the squaraines obtained using both mono- and di-methylated DHP moieties (the "*green*" one **341**, the "*pink*" one **391** and the "*purple*" one **392**) have been selected as target compounds to perform DFT-studies of the reaction mechanisms.

ADDENDUM 1 – Synthesis of TPA-based Asymmetrical Cyanine

As reported in Section 1.1. of Chapter 1, polymethine-based sensitizers are generally affected by too fast charge recombination and slow regeneration rate of the dye that prevent the achievement of better performances. As mentioned in the introduction of Chapter 5, Hirata *et al.* partially overcomes this issue by the introduction of a non-conjugated triphenylamine (TPA) group.[519] After tried without success to exploit this strategy in the DHP-SQs due to the peculiar reactivity of the mono-substituted DHP moiety, we tried to introduced a non-conjugated TPA group in a heptamethine cyanine to understand if this strategy can solve the regeneration issue met by the IMPRESSIVE's sensitizer **105** (Fig. 21). To prove the effect of the non-conjugate TPA moiety, we decided to synthetize the asymmetrical heptamethine cyanine **410**. Cyanine **411** was selected as reference, instead.

In the asymmetrical cyanine **410**, in a side there is the anchoring unit based on a carboxyindolenine (CI) moiety bearing a short ethyl in-plane alkyl chain while in the other side there is a benzoindolenine unit bearing the non-conjugated TPA group. The non-conjugation of the TPA group with the cyanine backbone is fundamental to avoid the appearance of parasitic absorption contributions in the visible. The choice of CI unit compared to the more conjugated CBI one depended by the less reactivity of CBI, that can raise the difficulty of the synthesis of the target cyanine **410**.[58] As "methine bridge", it has been used the well-known (and commercially available) "*Russian Bridge*" Schiff base (see Appendix) in which a cyclohexyl structure locks the *cis-trans* photoisomerization process of the polymethine bridge and guarantee an improved chemical stability.[120]

The preparation of cyanines **410** and **411** have been carried out following the synthetic plan displayed in Fig. 126. The synthesis of **410** has been very tricky due to the difficult preparation and purification of both main units: (i) the carboxy indolenine salt (CI-salt) bearing the non-conjugated TPA (**406**) and (ii) the hemicyanine (**409**).

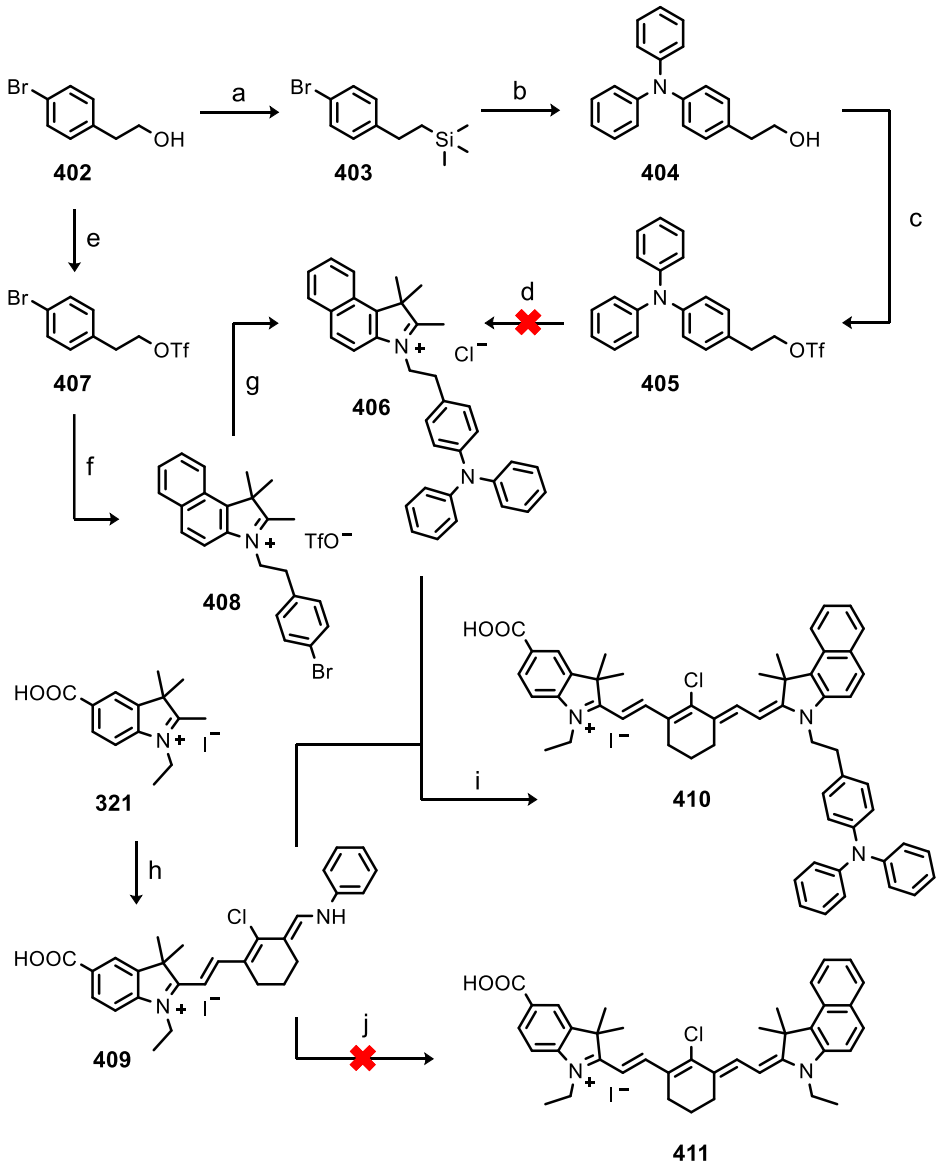

Figure 126 – Synthetic scheme for the preparation of **410** and **411**. a) DIPEA, TMSCl, DCM, 0 °C → RT, overnight. b) Tris(dibenzylideneacetone)dipalladium(0), sodium *tert*-butoxide 1.0 M of tri-*tert*-butyl phosphine in toluene, diphenylamine, toluene, reflux, overnight. c) 2,6-Lutidine, trifluoromethanesulfonic anhydride, DCM, -78 °C, 5 min. d) 1,1,2-Trimethyl-1*H*-benzo[*e*]indole, ACN, reflux, 1 h. e) 2,6-Lutidine, trifluoromethanesulfonic anhydride, DCM, -78 °C, 5 min. f) 1,1,2-Trimethyl-1*H*-benzo[*e*]indole, ACN, reflux, 1 h. g) Tris(dibenzylideneacetone)dipalladium(0), sodium *tert*-butoxide 1.0 M of tri-*tert*-butyl phosphine in toluene, diphenylamine, toluene, reflux, overnight. HCl 4 M in 1,4-dioxane, RT, 15 min. h) "*Russian bridge*", ethanol, reflux, 1 h. i) Potassium acetate, ethanol, reflux, overnight. j) 3-Ethyl-1,1,2-Trimethyl-1*H*-benzo[*e*]indole, potassium acetate, ethanol, reflux, overnight.

The synthesis started with the preparation of the CI-salt bearing the TPA **406**. Starting from **403**, the TPA group was synthetized by a Buchwald-Hartwig cross coupling reaction (reaction **b** in Fig. 126) following a reported procedure.[523,524] However, to avoid undesired side-reactions, the pendant hydroxyl group was previously protected (reaction **a** in Fig. 126). After the synthesis of the functionalized TPA **404**, the reactivity of hydroxyl group was improved transforming it in a triflate group (reaction **c** in Fig. 126) to favor the next nucleophilic substitution reaction with the benzoindolenine (BI) unit (reaction **d** in Fig. 126). However, reaction **d** did not occur. Several reaction conditions have been tested without any results. For these reasons, we decided to change synthetic strategy. In the first phase of the new strategy, we synthetized a TPA precursor benzoindolenine salt **408** (reaction **f** in Fig. 126), and after the TPA group has been obtained by Buchwald-Hartwig cross coupling reaction with diphenylamine (reaction **g** in Fig. 126). Even in this case, the reactivity of the hydroxyl group was enhanced by its transformation in a triflate group (reaction **e** in Fig. 126). The second strategy allowed the preparation of **406** but with a low overall yield of 14% starting from **402**.

After the synthesis of the TPA-based benzoindolenine salt **406**, we focused our synthetic effort on the preparation of hemicyanine **409**. Although at first sight the synthesis of **409** may seem very easy, its preparation was absolutely tricky. Usually, in literature the preparation of hemicyanines starting from the 1,1,2-trimethylindolenine was carried out using soft-base (like sodium or potassium acetate) in acetic anhydride with yields up to 50-60%.[58] However, in our case these reactions conditions did not allow the preparation of **409**. Several trials have been performed to optimize the synthesis of the hemicyanine and finally, despite our efforts we were able to synthetize **409** only with a 6% of yield. The synthesis of **409** was performed without any soft-base and in refluxing ethanol for one hour. The low yield is due by two main reasons: (i) the first one is the intrinsic too high reactivity of **409** due to the presence of the electron-withdrawing chlorine atom on the "*Russian bridge*" that lead to the further

reaction of **409** with **321** to form the undesired symmetrical cyanine **412** (Fig. 127), whereas (ii) the second one is the very tricky separation of the desired hemicyanine from the "*Russian bridge*" starting material.

Due to the impossibility to quench the reactivity of the hemicyanine **409**, we tried to improve the quality of the reaction's crude to simplify the purification procedure. To reduce the amount of unreacted starting material, we tried to performed reactions with longer times and with less amount of "*Russian bridge*" but in the same cases we found an improvement of the concentration of the undesired symmetrical cyanine **412**. Despite our attempts, no improvement was achieved and hemicyanine **409** was isolate after a very expensive and time-consuming purification procedure that required three flash chromatography purification steps (more than 300 g of SiO_2 and 15 L of eluent DCM/MeOH were used to isolate ca. 530 mg of **409** in which traces of "*Russian bridge*" were still detectable).

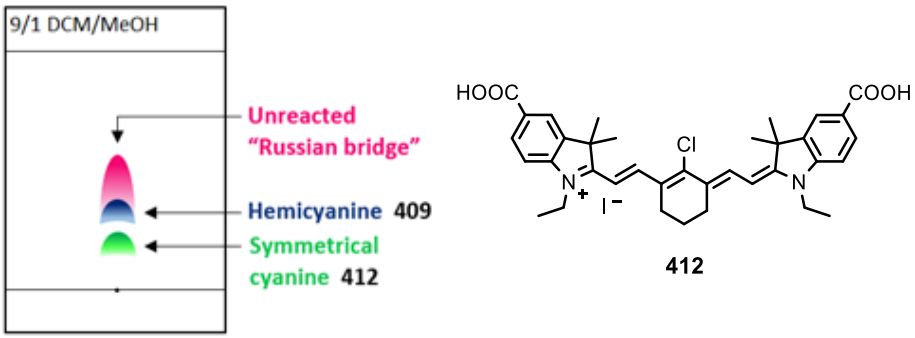

Figure 127 – TLC plate of the crude material at the end of the synthesis reaction (1 h). It displays the partial overlap of the desired hemicyanine **409** and the starting material.

Finally, the asymmetrical cyanine **410** has been prepared by classic synthetic methodology using potassium acetate in refluxing ethanol. Unfortunately, even in this last synthetic step we found relevant issues that dramatically hampered the production of the cyanine **410**, achieving a very low yield of only 2%. The analysis of the crude material at the end of the reaction showed the presence of three different cyanines (Fig. 128): (i) the symmetrical cyanine **413** in which **406**

reacted with the traces of the "*Russian bridge*" in the hemicyanine, (ii) the desired asymmetrical cyanine **410** and (iii) the undesired asymmetrical cyanine **414** in which the chlorine atom reacted with aniline leaving group coming from the reacted hemicyanine. Also in this case, the presence of the chlorine atom on the polymethine bridge negatively influences the reaction toward the target compound, leading to the formation of a very similar asymmetrical cyanine (**414**).

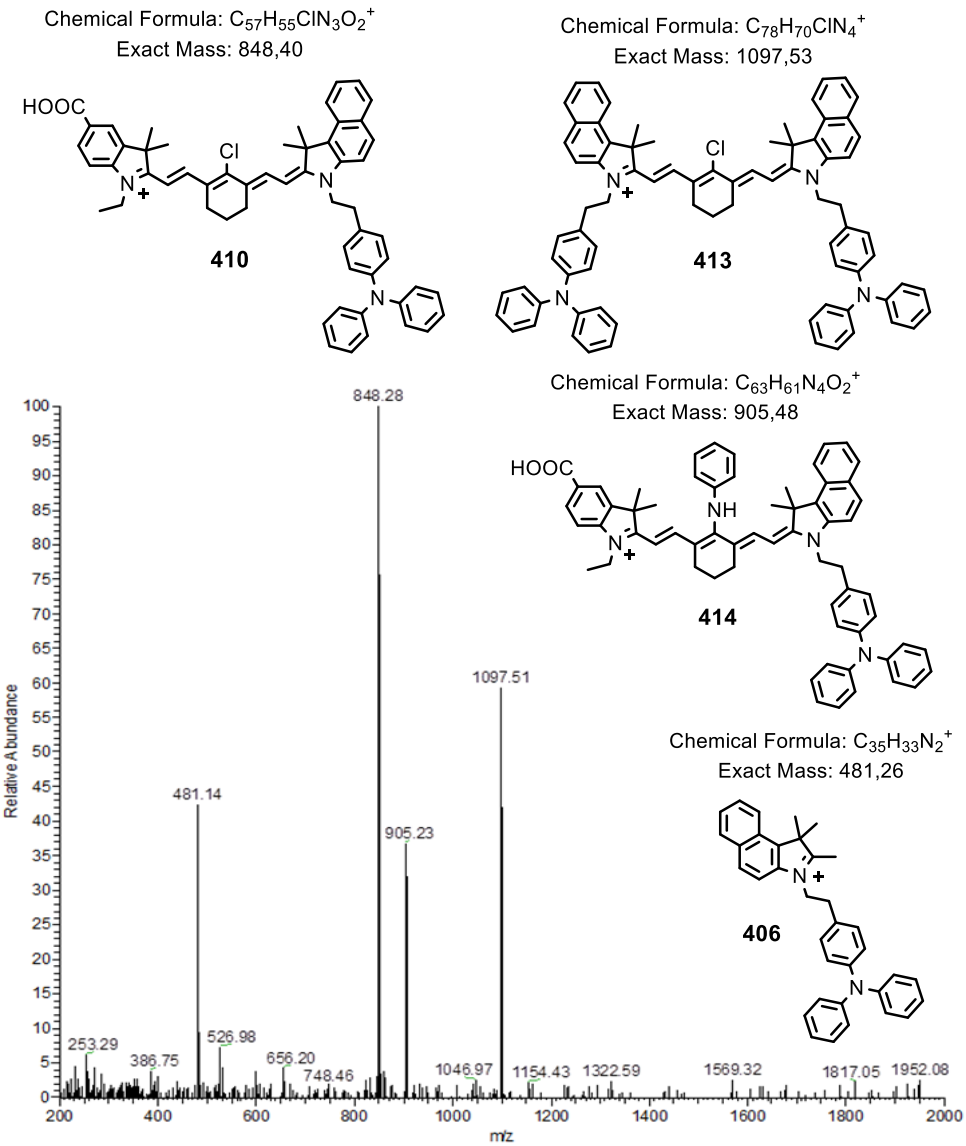

Figure 128 – MS-spectrum (in MeOH) of the crude of the reaction **i** (in Fig. 126) in which is it possible to detect the three different cyanines (**410**, **413** and **414**) and the residual unreacted starting material **406**.

The similarity between the target cyanine **410** and **414** really hampered the purification procedure: repeated flash chromatography purification steps allowed to isolate only 4 mg of **410**.

After the synthesis, the absorption behavior of **410** has been briefly studied to compare with the IMPRESIVE's cyanine sensitizer **105**. As display in Fig. 129, **410** exhibits a maximum absorption at 810 nm with a molar extinction coefficient of $1.4 \cdot 10^5$ M^{-1} cm^{-1}. Moreover, no parasitic absorptions are present in the visible region, confirming the suitable absorption properties of **410** for the application in NIR-DSSCs. Compared to **105** (Tab. 6), the asymmetrical cyanine **410** has a slightly hypsochromic absorption due to the less conjugated structure. For the same reason, it also exhibits a slightly lower molar extinction coefficient.[61]

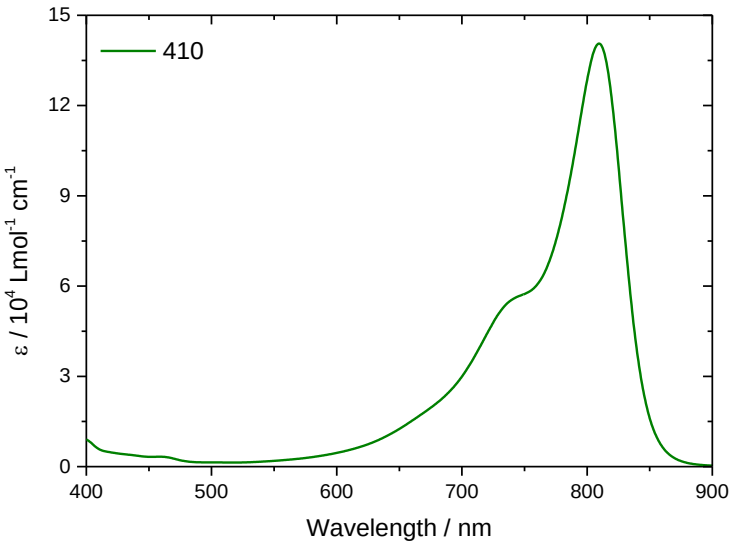

Figure 129 – Absorption spectra of **410** in ethanol.

To conclude, the reported synthetic work confirmed the possibility to functionalize the cyanine sensitizers with a non-conjugated TPA moiety. However, the several drawbacks met during the preparation the desired asymmetrical cyanine, related to the preparation and the purification of both hemicyanine **409** and target compound **410**, convinced us to rethink to the

structure of the target compound to obtain it in easier manner. For this reason, the reference cyanine **411** has not been synthetized and our synthetic efforts have been moved for the preparation of the new asymmetrical cyanine **419** (and **420** as reference), in which the problematic chlorine atom was removed by the polymethine bridge (Fig. 130). Synthetic work is still on-going but we are enough confident that this structure modification by the removal of the detrimental chlorine atom can settle all the synthetic drawbacks previously met.

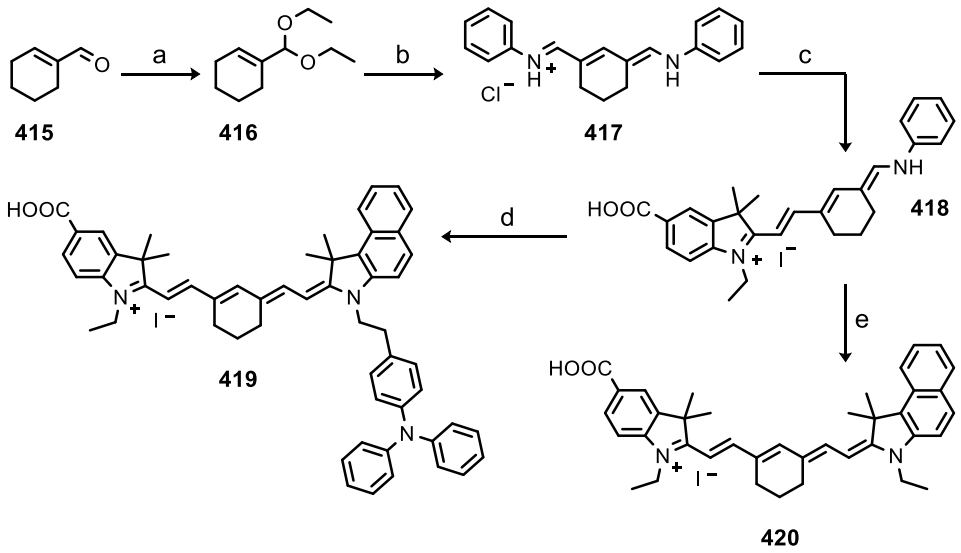

Figure 130 – New synthetic scheme for the preparation of **419** and **420**. a) Triethyl orthoformate, PTSA, ethanol, reflux, 6 h. b) Phosphoryl chloride, 0 °C, 30 min. DMF, 0 °C, 1 h. Aniline, 0 °C → RT, 1 h. c) **321**, Ethanol, reflux, 1 h. d) **406**, Potassium acetate, ethanol, reflux, overnight. e) 3-Ethyl-1,1,2-Trimethyl-1*H*-benzo[*e*]indole, potassium acetate, ethanol, reflux, overnight.

ADDENDUM 2 – Squaraine-Dyes as Possible Membrane Probes in Liposomes

Several crucial biochemical pathways are usually accompanied by changing in membrane lipidic composition and in membrane tension. The use of smart fluorescent organic dyes allows to visually highlight these phenomena, monitoring the cellular health status and important biophysical parameters like the hydration, membrane tension and fluidity.

Artificial Large Unilamellar Vesicles (LUVs) (also known as liposomes) have been used for studying *in vitro* membrane dynamics since they can act as membrane mimics. They are usually assembled by spontaneous self-organization from pure lipids or lipid mixtures in aqueous media upon several heating-cooling cycles.[525] In this work, 1,2-dioleoyl-*sn*-glycero-3-phosphocholine (DOPC) and 1,2-Dipalmitoyl-*sn*-glycero-3-phosphocholine (DPPC) (see Appendix) have been used due to their ability of creating two differently packed lipidic phases. While the DOPC create a fluid and hydrated phase, the DPPC-based liposomes are more ordered and tightly packed, providing a more hydrophobic local environment inside the vesicle.

The possibility of a staining into the NIR region of the electromagnetic spectrum is of fundamental importance due to the deep tissue penetration, negligible autofluorescence and low tissue degradation of light in this spectral area.[526] Several families of NIR dyes have been designed, synthesized and also proposed to the market for selective staining of PM along with a plethora of biological structures but proper modernization in the study of cutting-edge probes for PM is still a current challenge.[527,528] Klymchenko *et al.* have recently presented outstanding designs and application as membranes' fluorophores for both squaraine, merocyanine and cyanine dyes highlighting their potentialities and relevance due to singular lightness, specificity, and synthetic design.[529-533]

As mentioned before, squaraines have already been proposed to stain cell membranes,[529,530] but detailed investigations on the fluorophores' design and a preliminary structure to function study for novel bilayer membrane probes are

missing. Recently, our group presented the first rationally structure-activity photophysical investigation of a series of squaraines (**40**, **42**, **398**-**401**) in liposomes (Fig. 131).[534]

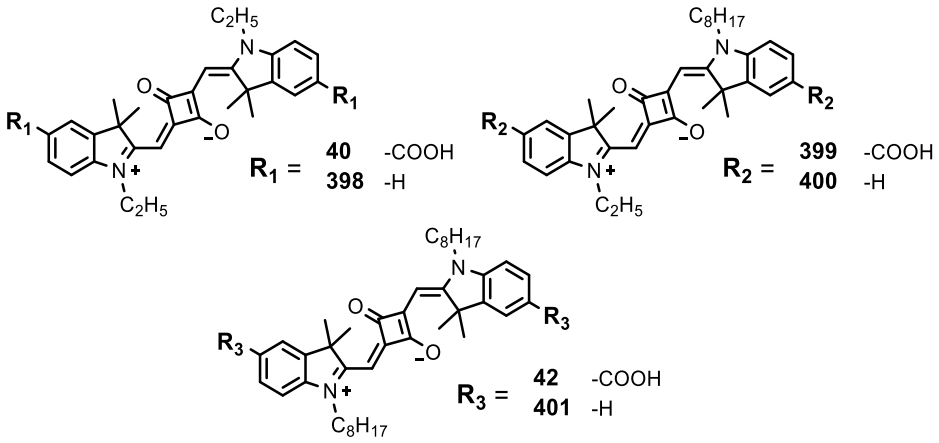

Figure 131 – Squaraines studied in liposomes by our research group.

It has been demonstrated the suitability of the squaraine scaffold as promising NIR probes, providing key-information for a better refining at the molecular design stage. The low dipole moment did not allow the dyes to discriminate between the differently packed lipidic phases, resulting in overlapping emission profiles not depending on the lipidic composition.[534] To overcome these issues, it has been decided to study the asymmetrical DHP-SQs **341**-**348** in which the higher dipole moment should be improve the sensitivity to phase-changes.

The DHP-SQs **341**-**348** behavior in DOPC and DPPC LUVs has been monitored by steady-state fluorescence spectroscopy. The probes' emission in aqueous buffer (black line in Fig. 132) is quenched, while a strong turn-on occurs upon the interaction with vesicles. The chains length and the presence of carboxyindolenine (CI)/carboxy benzoindolenine (CBI) moieties affect the probes ability for DOPC and DPPC stain (Fig. 132). Concerning the carboxyindolenine series (**345**-**348**), short chains allow the probe to equally stain DPPC and DOPC L_o (liquid ordered) and L_d (liquid disordered) phases while chains elongation provides a better response to the DPPC system.

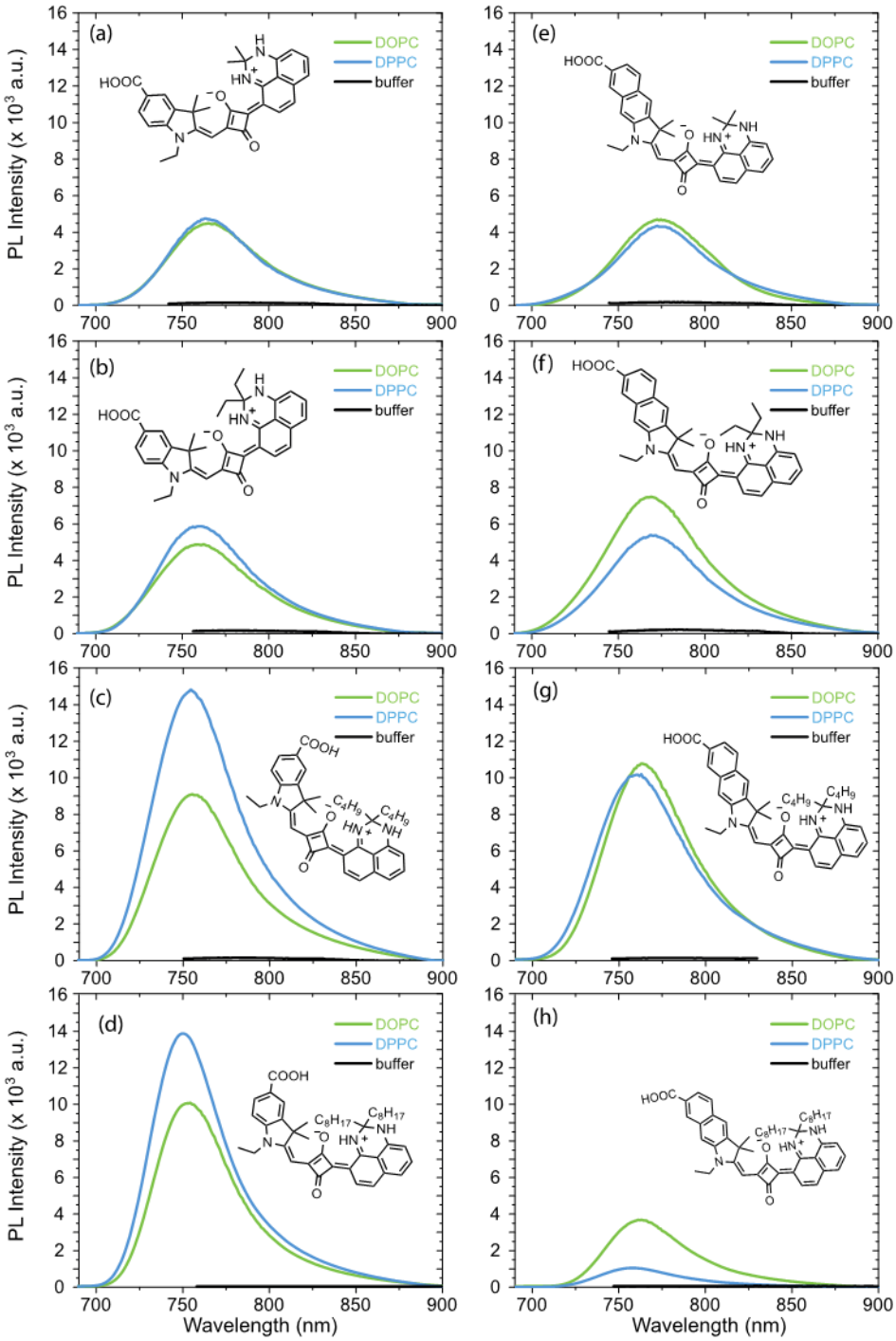

Figure 132 – Emission spectra of probes **341** (a), **342** (b), **343** (c), **344** (d), **345** (e), **346** (f), **347** (g), **348** (h) in buffer (black), DOPC (green), DPPC (blue) after their equilibration time.

The hydrophobic character of **343** and **344** squaraines makes the probe better fitting with the DPPC tighter packing, reducing the affinity with the more polar and hydrated DOPC. An additional phenyl fused ring in the CBI-series increases the overall probes hydrophobicity, resulting in a different phase staining compared to the CI analogues. While two methyl groups in **344** provide similar results to **341**, longer chains seem to favor the affinity in the more fluid and disordered DOPC phase. This trend might be related to the higher steric hinderance upon the additional fused phenyl ring, evidencing the importance of a proper probe molecular design and a fine structure-activity study. Additionally, longer aliphatic chains are necessary to increase the CI-series probes response in all the vesicles. In particular, the higher molecular similarity of **344** to the phospholipids structures prompt remarkable affinity of the probes to all the different membrane systems due to the more balanced and defined amphiphilic character. The polar head characterized by the carboxylic group provides moderate solubility in aqueous media allowing good diffusion towards the liposomes, while hindered hydrocarbon chains drive the hydrophobic interaction leading to an efficient partition inside the membrane bilayer. It is also worth noting that CI-series exhibit an increasing response moving from small methyl groups to the octyl chains, while the hindering CBI shape follows the same trend only until the butyl derivatives. The introduction of octyl chains dramatically reduces the solubility and the probe's diffusion into the aqueous medium, with a consequent drop in the detected fluorescence.

Then, the incorporation kinetics have been evaluated for all the probes in both kinds of vesicles. The full spectra are reported in Fig. 133 and Fig. 134, while Fig. 135 reports the turn-on effects variation over time, providing a smart overview on all the probes. Although the short aliphatic chains (**341**-**343**, **345**-**347**) allow an immediate response to the intercalation, they avoid the probe to accurately interact with the phospholipids hydrophobic tails. This reflects in a quick yet not stable fluorescence signal, since the system equilibrates over time displaying a lower emission intensity.

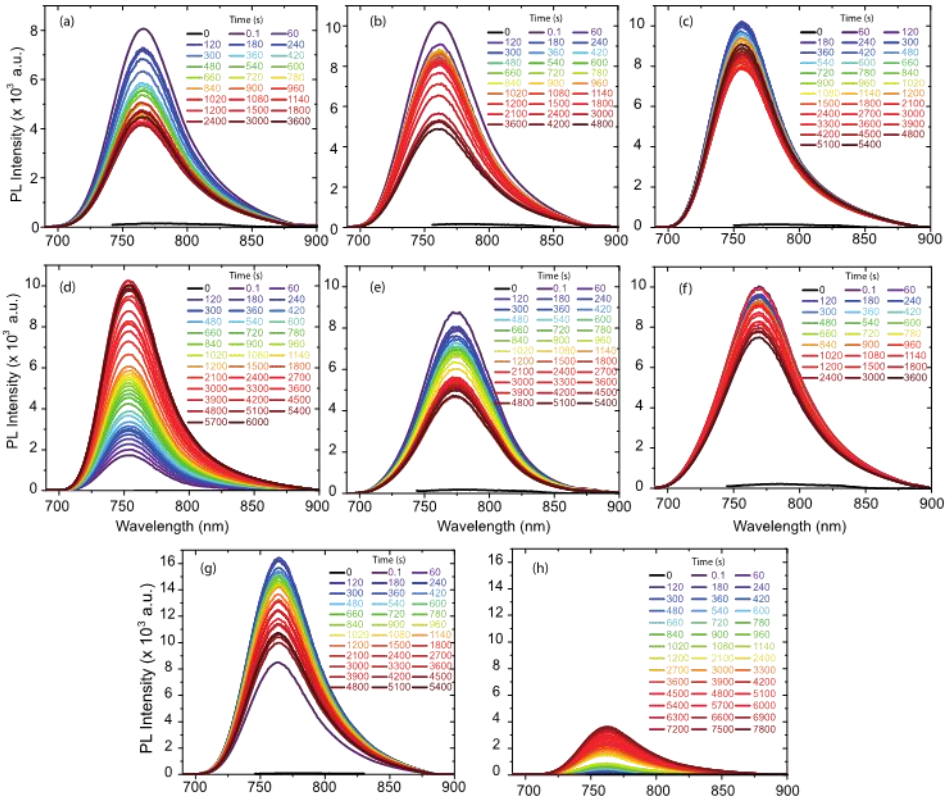

Figure 133 – Intercalation of probes **341** (a), **342** (b), **343** (c), **344** (d), **345** (e), **346** (f), **347** (g), **348** (h) into DOPC LUV vesicles.

Both DOPC and DPPC show this same issue, but the latter can better lock the fluorophore reducing the emission drop due to a higher packing degree. Although butyl chains can lower the trend and reduce the signal drop over time, longer octyl hydrophobic chains (**344**, **348**) are necessary to better stabilize the fluorophores within the lipidic bilayer. Additionally, the **344** quenched emission in aqueous buffer along with the remarkable detected fluorescence signal provide an outstanding turn-on effect (≈3500 in DPPC).

Upon equilibration, the intercalated probes into the liposome membranes were subjected to several heating-cooling cycles, since DPPC undergo to a phase transition at 41 °C.[535] The probes were warmed up to 55 °C and then cooled down to 25 °C several times to assess their response to the change of membrane fluidity.

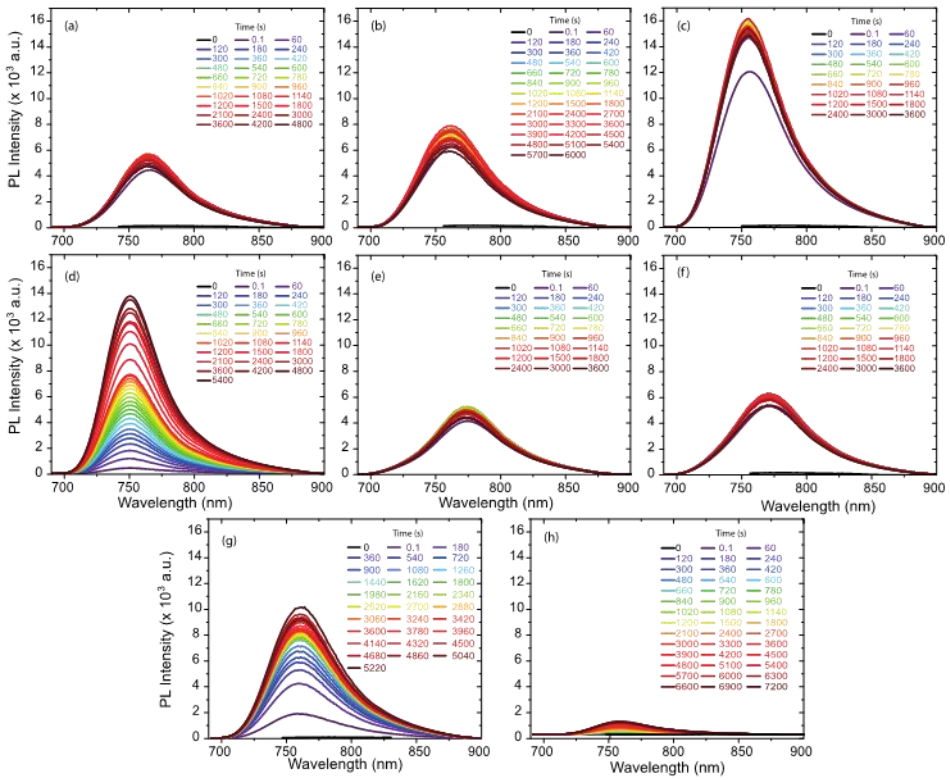

Figure 134 – Intercalation of probes **341** (a), **342** (b), **343** (c), **344** (d), **345** (e), **346** (f), **347** (g), **348** (h) into DPPC LUV vesicles.

DOPC liposomes were also tested as negative control, since they exhibit no transition phase in the explored temperature range. While no differences are detected for butyl and octyl chains bearing fluorophores, the resting probes' emission hypsochromically shifts upon warming the loaded DPPC vesicles at 55°C in a reversible manner, as confirmed by the occurring red shift upon cooling down to 25°C (Fig. 136). This shift can be rationalized by the π-system planarization occurring at room temperature, where the DPPC show a packed solid-ordered (S_o) phase. At 55°C, a phase transition creates a more fluid L_d phase, reducing the S_o planarization and resulting in a hypsochromically shifted emission. DOPCs have been tested as a negative control since any phase transition above room temperature (Fig. 137). Further support to this theory can be found looking at the excitation spectra recorded in DPPC (Fig. 138).

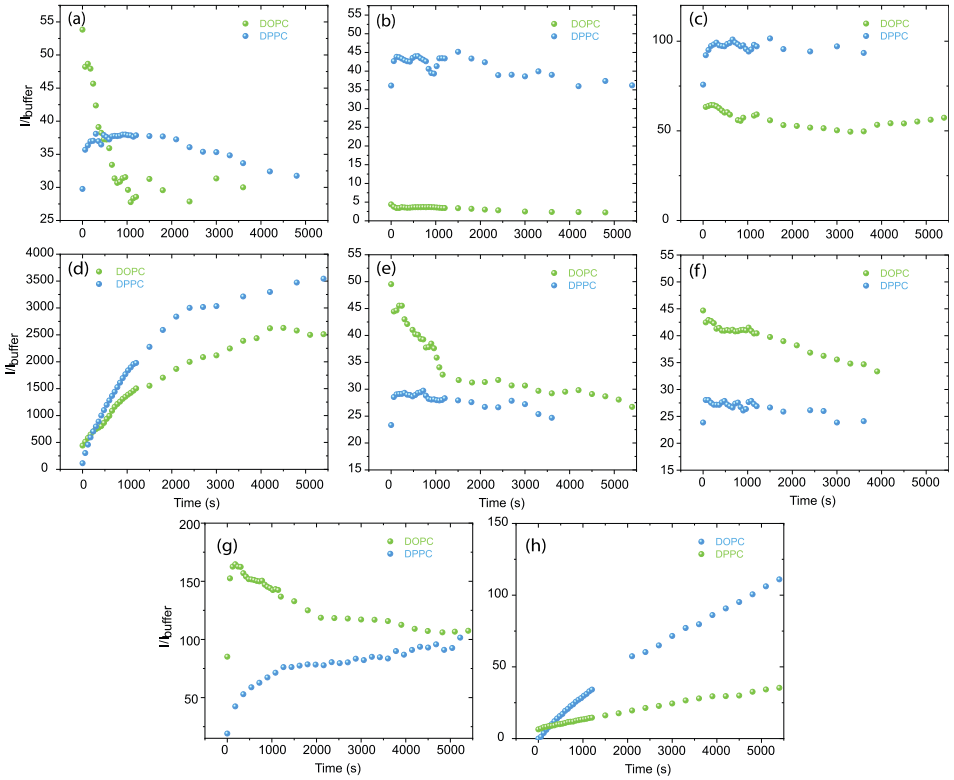

Figure 135 – I/I_{buffer} ratio plotted against time for all the probes. **341** (a), **342** (b), **343** (c), **344** (d), **345** (e), **346** (f), **347** (g), **348** (h).

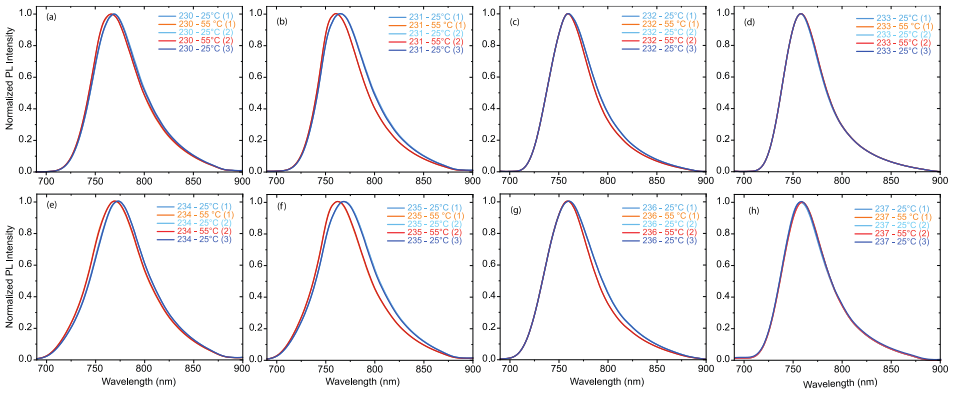

Figure 136 – Normalized emission spectra upon several heating-cooling cycles in DPPC vesicles for the probes. **341** (a), **342** (b), **343** (c), **344** (d), **345** (e), **346** (f), **347** (g), **348** (h).

$\Delta\lambda_{exc} > \Delta\lambda_{em}$ since the planarization is a phenomenon highly appreciable at the ground state (with the excitation spectra) and less at the excited state (with the

emission spectra). The not-occurring planarization for compounds **343**, **344** and **347**, **348** might be related to the bulkier emitters scaffold, whose planarization would require a higher membrane tension than the one provided by the DPPC S_o phase.

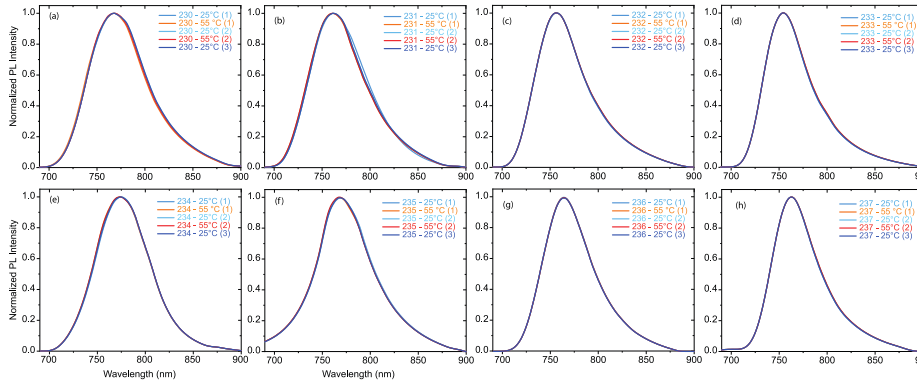

Figure 137 – Normalized emission spectra upon several heating-cooling cycles in DOPC vesicles for the probes. **341** (a), **342** (b), **343** (c), **344** (d), **345** (e), **346** (f), **347** (g), **348** (h).

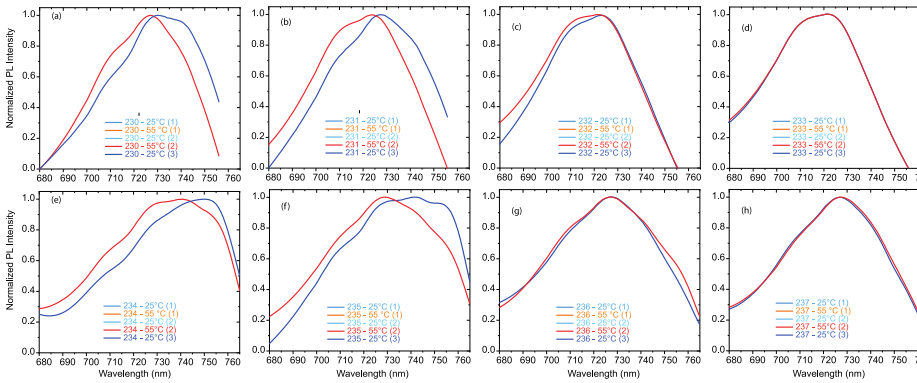

Figure 138 – Normalized excitation spectra upon several heating-cooling cycles in DPPC vesicles for the probes. **341** (a), **342** (b), **343** (c), **344** (d), **345** (e), **346** (f), **347** (g), **348** (h).

To conclude, in this section the series of novel DHP-SQs have been studied in LUVs. Their implementation into LUVs proved their intercalation into the lipid bilayer with particular outstanding results for octyl chain-bearing probes **344** and **348**. Their accentuated fluorogenic behavior and stability inside the bilayer make

them promising candidates to stain the cell membranes in a powerful spectral window. Additionally, the fluorophores bearing shorter alkyl chains proved to be sensitive to the membrane tension, undergoing p-system planarization upon viscosity increase. This finding suggests their use as a promising cellular tool to monitor many cellular pathways like the endocytosis and the apoptosis, where the membrane tension plays a key-role.

CONCLUSIONS

The negative effects of the climate change on daily life are constantly raising and the international community has to consider the energy transition towards renewable energies the only solution for a sustainable future. Among all the renewable energy technologies, photovoltaic technology is considered the most promising.

In this context, this work presented the research activities made as partner of the European funded IMPRESSIVE project with the aim to develop suitable materials for the realization of a NIR-Dye Sensitised Solar Cell (NIR-DSSCs). In particular, in this work we focused our attention on the synthesis of novel NIR sensitizers and novel colorless redox-couples. Our research was presented in four different chapters about: (i) the synthesis of extended-rylene dyes, (ii) the synthesis and the application as NIR-sensitizers of a new class of 2,3-dihydro-1*H*-perimidine-based squaraines (DHP-SQs), (iii) the synthesis of copper complexes as redox mediators, and finally (iv) the study of an interesting new class of squaraines with an hypsochromic absorption for the co-sensitization in classic DSSCs.

Despite we were not able to develop highly efficient NIR-sensitizers and fully colorless redox-mediators, in this work we achieved interesting milestones.

As far as we know from the literature, in Chapter 2 was reported the first example of quaterrylene-based DSSC with sensitizer **316**, achieving a PCE of 0.12%. Beyond the obtained result, this study demonstrated the unsuitability on extended rylene dyes as sensitizers for DSSC despite their high chemical and thermal stability.

In Chapter 3 a novel series of DHP-SQs has been presented and tested as sensitizers in NIR-DSSCs. The carefully optimization of device manufacturing allowed to achieve the respectable PCE of 2.0%. Starting from this encouraging result, we are confident that will be possible to further raise the performance of DHP-SQs by tailored structure-modifications and by the improvement of the

materials used to the devices manufacturing. In addition, it was also demonstrated the versatility of DHP-SQs by their successfully application as NIR-fluorescence membrane probes.

Beside to the studies of their different applications, in the last chapter the particular reactivity properties of different DHP-SQs were investigated. It was demonstrated that the substitution degree of the DHP moiety influences the regioselectivity of the squaraines formation reactions, leading to different products with dramatically different photophysical properties.

Finally, in the Chapter 4 a series of copper(I) complexes based on different *impy* ligands was presented. Despite we were not able to develop any colorless redox-mediators for NIR-DSSC application, the investigation of the chemical properties of these compounds provided interesting and precious information about the properties and the behaviour of the sterically hindered copper(I) complexes: we are enough confident that the reported results could be a useful tool for the rationalization of future novel copper-based mediators for DSSCs application.

To conclude, this work has not reported breakthrough results but we think it managed to provide useful tools for the future investigations about novel class of compounds like the DHP-SQs and copper(I) complexes.

APPENDIX

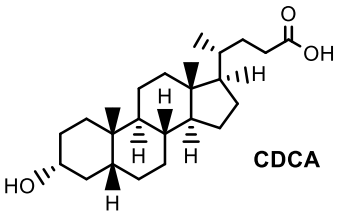

CDCA

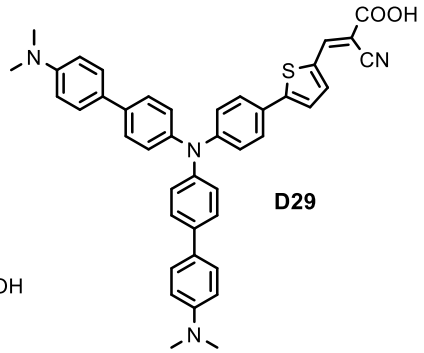

D29

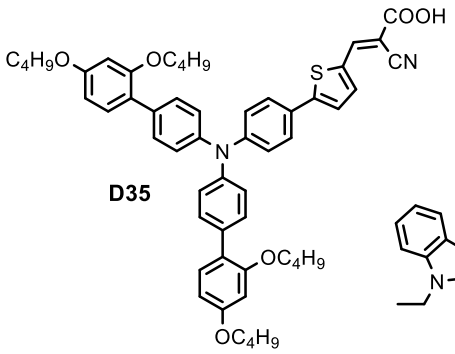

D35

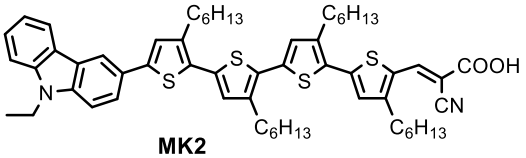

MK2

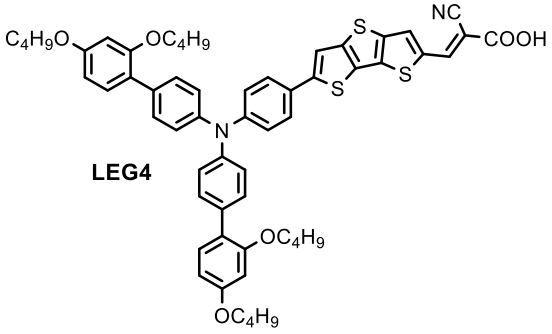

LEG4

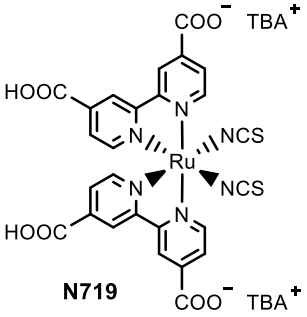

N719

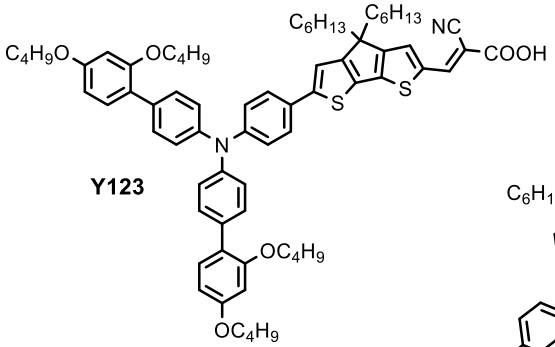

Y123

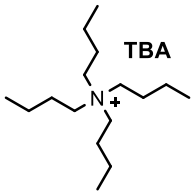

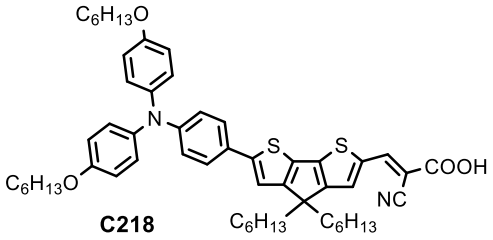

C218

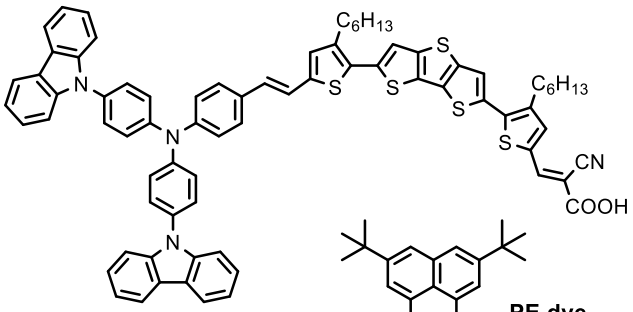

Carbz-PAHTDTT

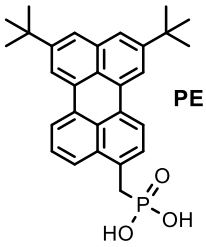

PE dye

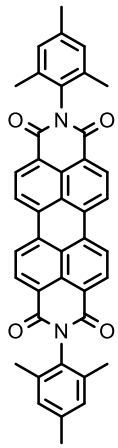

Pigment Red 149

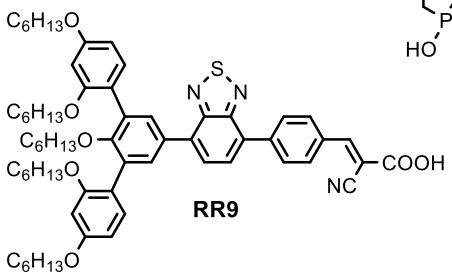

RR9

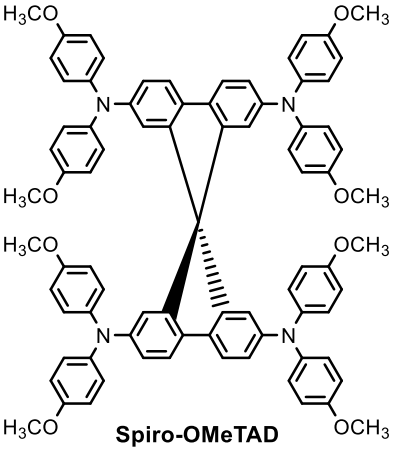

Spiro-OMeTAD

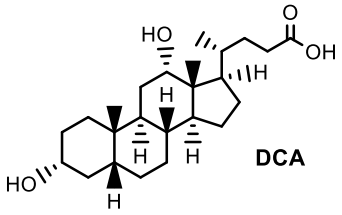

DCA

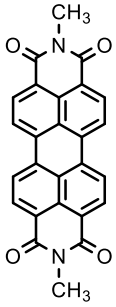

Pigment Red 179

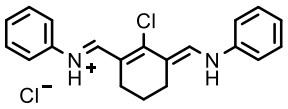

Russian bridge

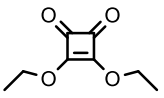

3,4-diethoxycyclobut-3-ene-1,2-dione

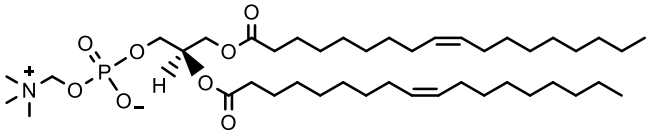

DOPC

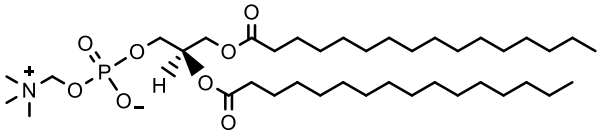

DPPC

SUPPORTING INFORMATION

1. Synthesis

1.1. Synthesis of Quaterrylene-based NIR-Sensitizers

Compound 298

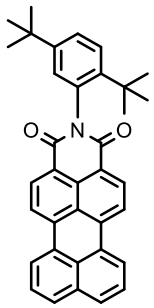

Synthesis of **298** was performed as described in literature.[415] A mixture of PTCDA **228** (4.4 g, 11.21 mmol), 2,5-di-*tert*-butylaniline (1.27 g, 6.17 mmol), zinc acetate dihydrate (1.60 g, 7.29 mmol), imidazole (22.9 g, 336 mmol) and deionized water (9.7 mL) was heated in a 125 mL autoclave at 190 °C for 24 h. The reaction mixture is washed out of the reaction vessel with water. The brown-red solid is collected by vacuum filtration. The brown cake was suspended in 200 mL of 2 N HCl in methanol and the resulting mixture is stirred for 15 min. The solution was filtered and the resulting dark brown cake was dissolved in 125 mL of chloroform and filtered on celite-545. The dark brown solution was concentered under vacuum and the title compound was obtained as a bright brown powder without any other purification (2.91 g, 51%). R_f (silica gel): 0.60 ($CHCl_3$). M_p: > 200 °C.

^{1}H-NMR (600 MHz, $CDCl_3$, RT): δ 8.61-8.62 (d, *J* = 7.8 Hz, 2H, Ar-H), 8.39-8.42 (m, 4H, Ar-H), 7.88-7.90 (d, *J* = 7.8 Hz, 2H, Ar-H), 7.59-7.63 (m, 3H, Ar-H), 7.45-7.47 (dd, *J* = 8.4 Hz, *J* = 2.4 Hz, 1H, Ar-H), 7.04 (d, *J* = 2.4 Hz, 1H, Ar-H), 1.34 (s, 9H, -CH_3), 1.30 (s, 9H, -CH_3) ppm.

^{13}C-NMR (151 MHz, $CDCl_3$, RT): δ 165.08, 150.13, 143.94, 137.52, 134.37, 133.23, 131.95, 131.03, 130.36, 129.27, 128.86, 128.01, 127.95, 127.13, 127.07, 126.28, 123.86, 121.38, 120.28, 35.66, 34.39, 31.87, 31.40 ppm.

MS (ESI$^+$, MeOH/$CHCl_3$ 1:1): *m/z* 510.73 $[M+H]^+$; calculated for $C_{36}H_{31}NO_2$: 509.24.

UV-Vis (DCM): λ_{max} (*ε*) = 484 (*34588*), 506 (*32896*) nm.

Fluorescence (DCM, λ_{exc} 470 nm): 553 nm. **ϕ:** 69%.

IR-Spectrum (cm^{-1}, ATR): 2960 *ν*(C–H aliphatic), 1696 *ν*(C═O), 1660 *ν*(C═O), 1590 *ν*(C═C aromatic), 1570 *ν*(C═C aromatic), 1350, 1245, 1185, 1140, 1035, 920, 810, 755.

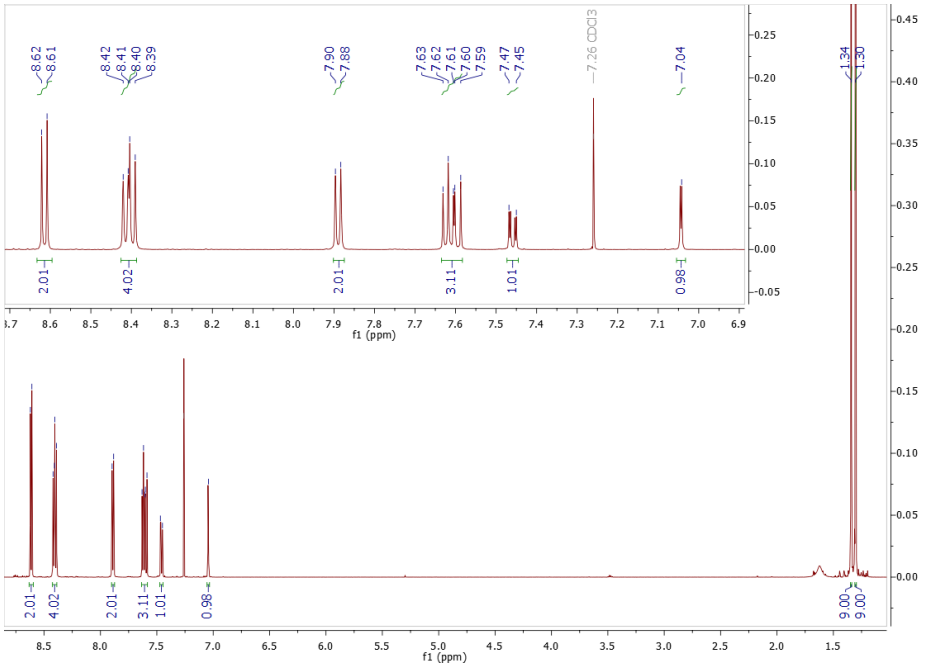

Figure 139 – ^{1}H-NMR in $CDCl_3$ of **298**.

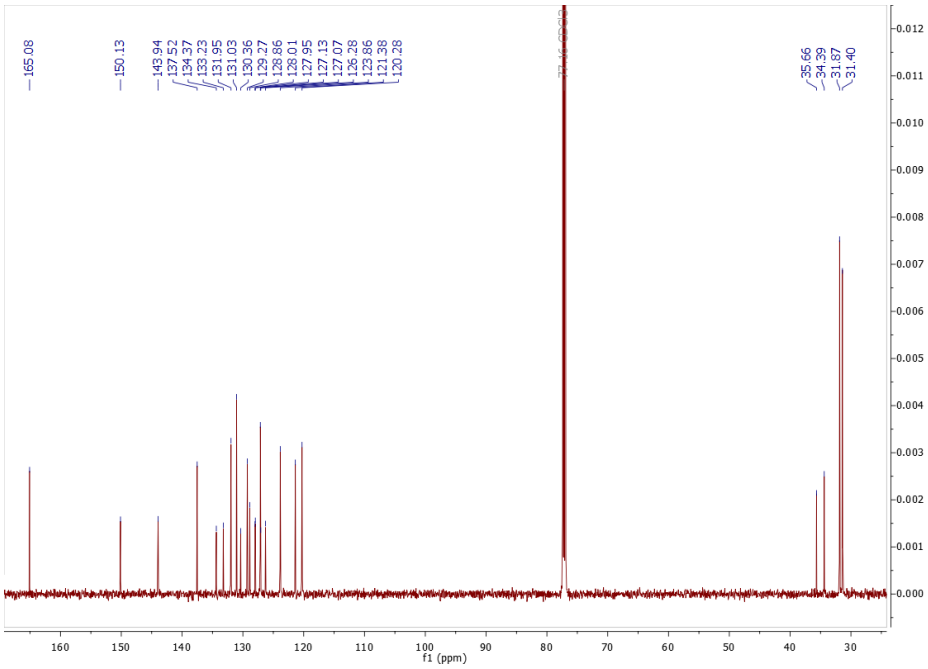

Figure 140 – ^{13}C-NMR in $CDCl_3$ of **298**.

Compound 309

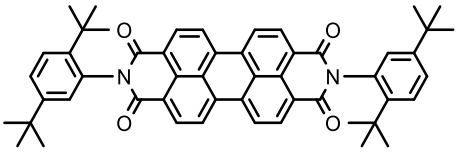

A mixture of PTCDA **228** (0.5 g, 1.27 mmol), 2,5-di-*tert*-butylaniline (0.236 g, 1.15 mmol), zinc acetate dihydrate (0.181 g, 0.83 mmol), imidazole (2.59 g, 38.1 mmol) and deionized water (1.4 mL) was introduced in a sealed 20 mL reaction vial and heated in a microwave reactor at 190 °C for 30 min. The reaction mixture is washed out of the reaction vessel with hot water. The red-purple solid is collected by vacuum filtration and the cake was suspended in 50 mL of 2 N HCl in methanol and the resulting mixture was stirred for 15 min. The solution was filtered and the resulting dark red crude was purified by flash chromatography on silica gel using dichloromethane as eluent (175 mg, 18%). The product was isolated as a bright red powder. R_f (silica gel): 0.35 ($CHCl_3$). M_p: > 200 °C.

^{1}H-NMR (200 MHz, $CDCl_3$, RT): δ 8.69-8.81 (m, 8H, Ar-H), 7.59-7.63 (d, *J* = 8.6 Hz, 2H, Ar-H), 7.45-7.50 (dd, *J* = 8.4 Hz, *J* = 2.2 Hz, 2H, Ar-H), 7.02-7.03 (d, *J* = 2.0 Hz, 2H, Ar-H), 1.34 (s, 18H, -CH_3), 1.31 (s, 18H, -CH_3) ppm.

^{13}C-NMR (151 MHz, $CDCl_3$, RT): δ 164.80, 150.56, 150.53, 144.14, 135.43, 135.38, 132.91, 132.32, 130.28, 130.23, 129.21, 128.07, 128.04, 127.20, 127.16, 126.76, 124.08, 123.68, 35.90, 34.62, 32.09, 31.57 ppm.

MS (ESI$^+$, MeOH/$CHCl_3$ + formic acid): *m/z* 767.52 $[M+H]^+$; calculated for $C_{52}H_{50}N_2O_4$: 766.38.

UV-Vis (DCM): λ_{max} (*ε*) = 459 (*18941*), 490 (*50752*), 526 (*83633*) nm.

Fluorescence (DCM, λ_{exc} 470 nm): 536 nm. **ϕ:** 96%.

IR-Spectrum (cm^{-1}, ATR): 2955 *ν*(C–H aliphatic), 1700 *ν*(C═O), 1665 *ν*(C═O), 1590 *ν*(C═C aromatic), 1575 *ν*(C═C aromatic), 1340, 1245, 1195, 1175, 970, 810, 750, 730.

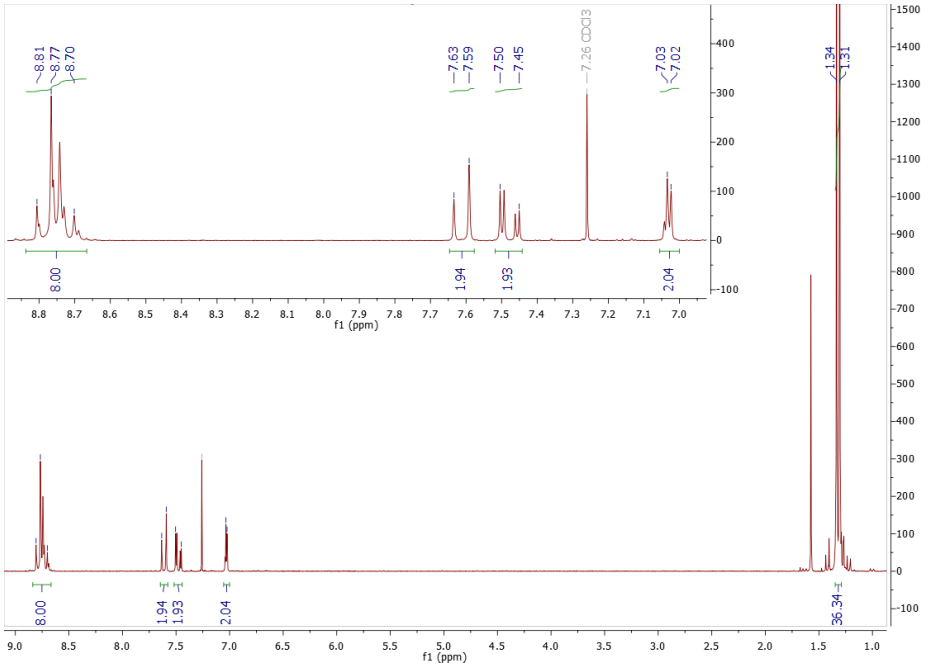

Figure 141 – ^{1}H-NMR in $CDCl_3$ of **309**.

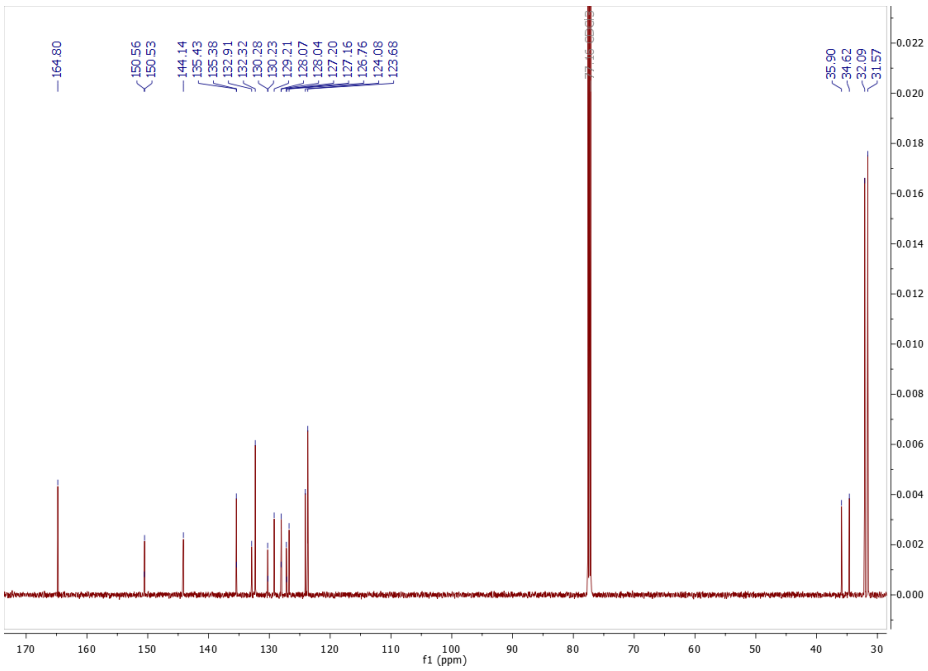

Figure 142 – ^{13}C-NMR in $CDCl_3$ of **309**.

Compound 299

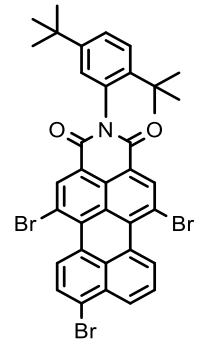

A mixture of **298** (0.1 g, 0.20 mmol), bromine (1.56 g, 10 mmol, 0.5 mL), potassium carbonate (0.35 g, 2.55 mmol) and chloroform (5 mL), was stirred in a sealed vial at 60 °C for 6 h. After cooling to room temperature, the reaction mixture was washed with a solution of 0.15 g KOH and 0.1 g sodium sulfite in 20 mL of water. The organic phase was separated and dried over sodium sulfate. Removing the solvent under the vacuum afforded a red-orange solid. The desired product was purified by flash chromatography on silica gel using *n*-hexane/toluene (6:4) as eluent (52 mg, 35%). R_f (silica gel): 0.50 (3:2 *n*-hexane/DCM). M_p: > 200 °C.

^{1}H-NMR (600 MHz, $CDCl_3$, RT): δ 9.31-9.32 (dd, *J* = 7.6 Hz, *J* = 0.7 Hz, 1H, Ar-H), 9.10-9.11 (d, *J* = 8.2 Hz, 1H, Ar-H), 8.90-8.92 (d, *J* = 8.3 Hz, 2H, Ar-H), 8.44-8.45 (dd, *J* = 8.3 Hz, *J* = 0.7 Hz, 1H, Ar-H), 7.98-7.99 (d, *J* = 8.2 Hz, 1H, Ar-H), 7.79-7.81 (t, *J* = 8.0 Hz, 1H, Ar-H), 7.59-7.61 (d, *J* = 8.6 Hz, 1H, Ar-H), 7.47-7.48 (dd, *J* = 8.6 Hz, *J* = 2.2 Hz, 1H, Ar-H), 6.98 (d, *J* = 2.2 Hz, 1H, Ar-H), 1.32 (s, 9H, -CH_3), 1.30 (s, 9H, -CH_3) ppm.

^{13}C-NMR (151 MHz, $CDCl_3$, RT): δ 163.63, 150.41, 143.93, 138.51, 138.47, 138.39, 135.45, 135.24, 135.14, 134.68, 132.46, 131.72, 131.04, 130.79, 130.47, 129.94, 129.73, 129.02, 129.01, 128.91, 127.79, 127.64, 127.07, 126.87, 126.80, 126.64, 123.93, 121.51, 121.37, 121.33, 119.36, 119.13, 35.69, 34.41, 31.89, 31.34 ppm.

MS (ESI$^+$, MeOH/$CHCl_3$ + formic acid): *m/z* 744.88 $[M+H]^+$; calculated for $C_{36}H_{28}Br_3NO_2$: 742.97.

UV-Vis (DCM): λ_{max} (ε) = 514 (*35918*) nm.

Fluorescence (DCM, λ_{exc} 495 nm): 571 nm. **ϕ:** 66%.

IR-Spectrum (cm^{-1}, ATR): 2955 *ν*(C–H aliphatic), 2860 *ν*(C–H aliphatic), 1700 *ν*(C═O), 1665 *ν*(C═O), 1590 *ν*(C═C aromatic), 1560 *ν*(C═C aromatic), 1540 *ν*(C═C aromatic), 1390, 1350, 1325, 1235, 1200, 1040, 920, 830, 805, 755.

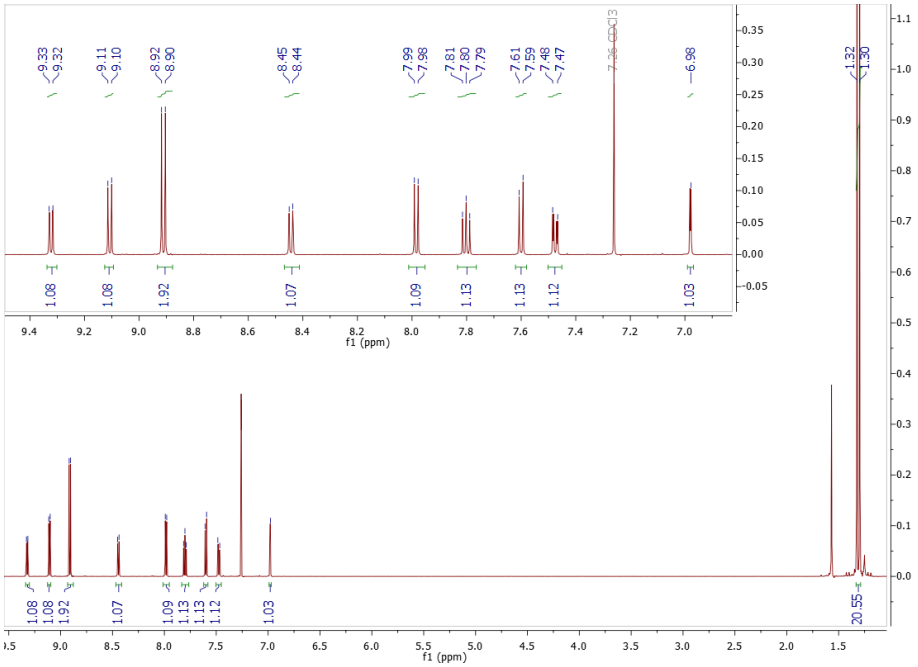

Figure 143 – ^{1}H-NMR in $CDCl_3$ of **299**.

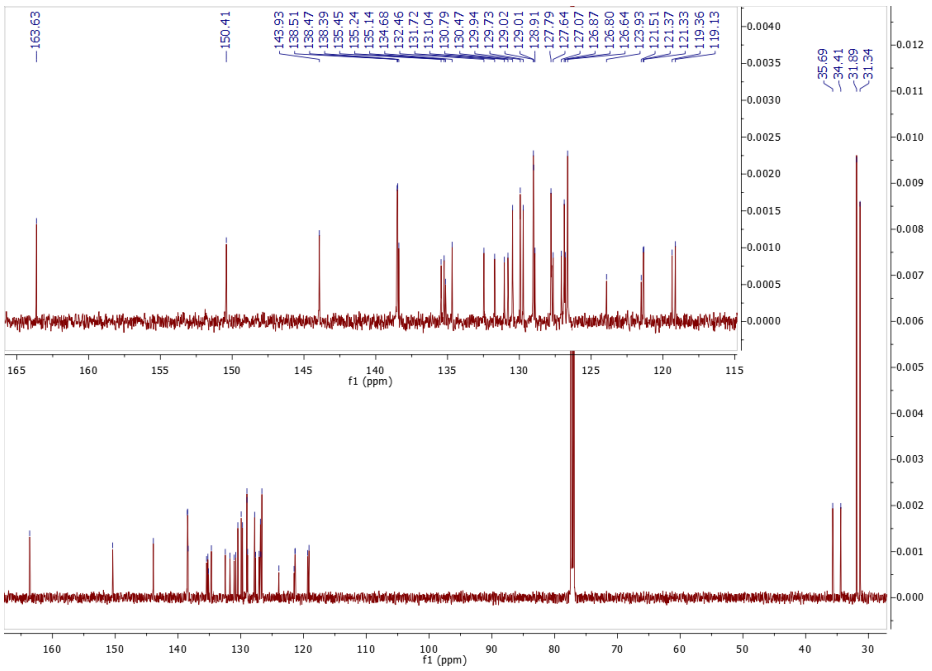

Figure 144 – ^{13}C-NMR in $CDCl_3$ of **299.**

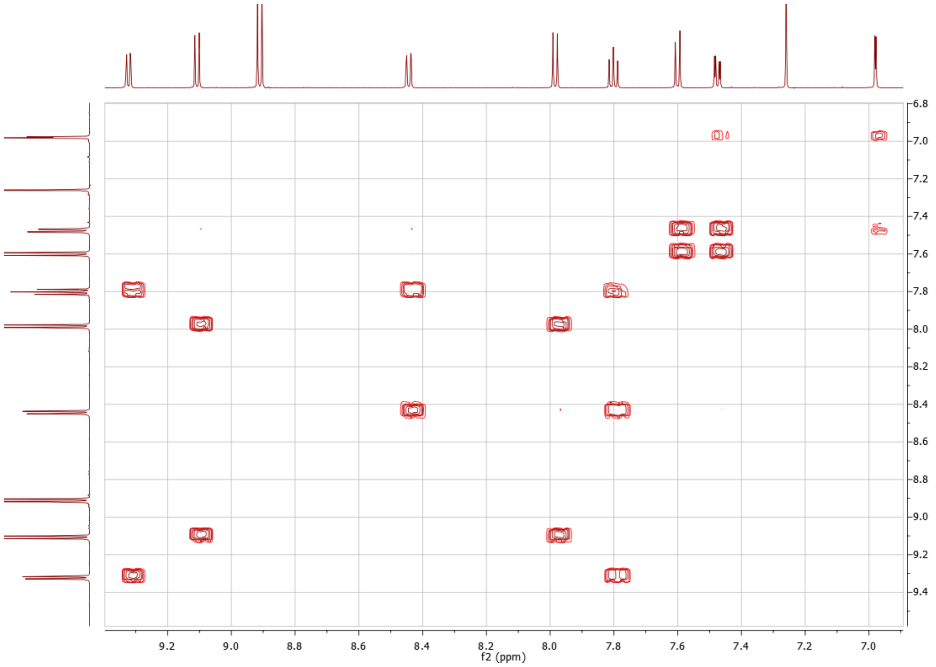

Figure 145 – COSY in $CDCl_3$ of **299**.

Compound 300a

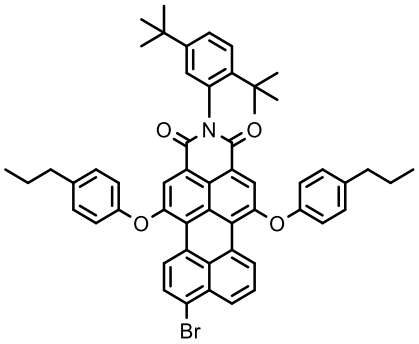

A mixture of **299** (0.2 g, 0.27 mmol), 4-propylphenol (80 mg, 0.60 mmol), potassium carbonate (0.11 g, 0.81 mmol) and NMP (8 mL) was stirred at 120 °C for 6 h. After cooling to room temperature, the reaction mixture was poured into 30 mL of solution water/HCl 37% (5:1). The resulting precipitate was filtered, washed with water, with diethyl ether and dried under vacuum. The desired product was purified by flash chromatography on silica gel using *n*-hexane/DCM (7:3) as eluent (16 mg, 7%). The product was isolated as a dark-red powder. R_f (silica gel): 0.60 (1:1 *n*-hexane/DCM). M_p: 198-200 °C.

^{1}H-NMR (600 MHz, $CDCl_3$, RT): δ 9.36-9.37 (d, *J* = 7.8 Hz, 1H, Ar-H), 9.12-9.13 (d, *J* = 8.4 Hz, 1H, Ar-H), 8.27-8.32 (m, 3H, Ar-H), 7.83-7.85 (d, *J* = 8.4 Hz, 1H, Ar-H), 7.64-7.68 (m, 1H, Ar-H), 7.55-7.56 (d, *J* = 8.4 Hz, 1H, Ar-H), 7.42-7.43 (d, *J* = 8.4 Hz, 1H, Ar-H), 7.20-7.22 (m, 4H, Ar-H), 7.03-7.07 (m, 4H, Ar-H), 6.96 (m, 1H, Ar-H), 2.58-2.61 (t, *J* = 7.8 Hz, 4H, -CH_2-), 1.63-1.69 (m, 4H, -CH_2-), 1.30 (s, 9H, CH_3), 1.27 (s, 9H, -CH_3), 0.96-0.98 (t, *J* = 7.2 Hz, 6H, -CH_3) ppm.

^{13}C-NMR: Not enough sample to perform the experiment.

MS (ESI$^+$, MeOH/$CHCl_3$ + formic acid): *m/z* 856.72 $[M+H]^+$; calculated for $C_{54}H_{50}BrNO_4$: 855.29.

UV-Vis (DCM): λ_{max} (ε) = 513 (*35517*) nm.

Fluorescence (DCM, λ_{exc} 495 nm): 568 nm. **ϕ:** 67%.

IR-Spectrum (cm^{-1}, ATR): 2955 *v*(C–H aliphatic), 2860 *v*(C–H aliphatic), 1700 *v*(C═O), 1665 *v*(C═O), 1590 *v*(C═C aromatic), 1560 *v*(C═C aromatic), 1495 *v*(C═C aromatic), 1350, 1200, 820, 805, 755.

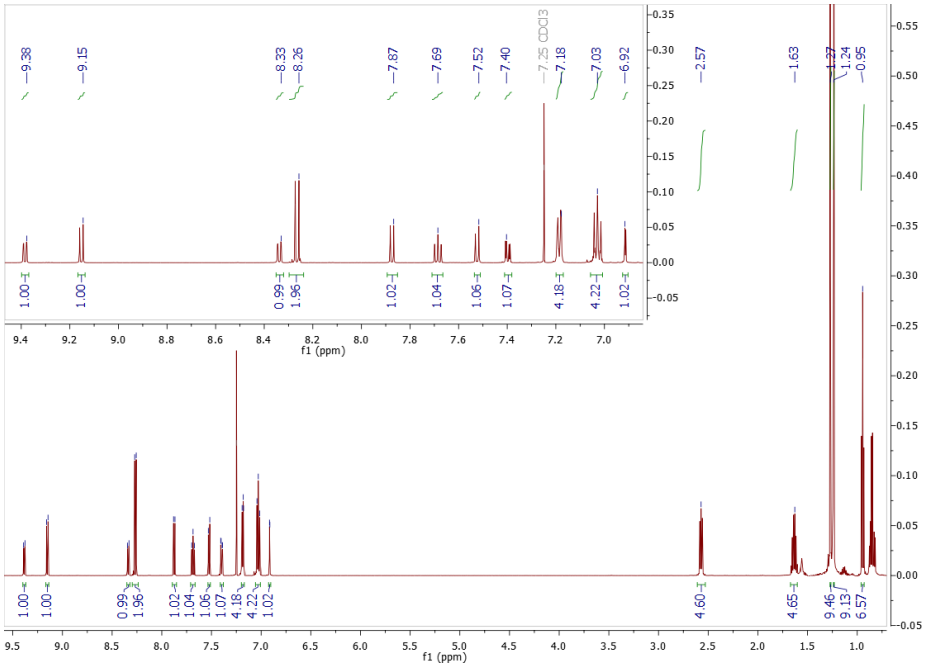

Figure 146 – ^{1}H-NMR in $CDCl_3$ of **300a**.

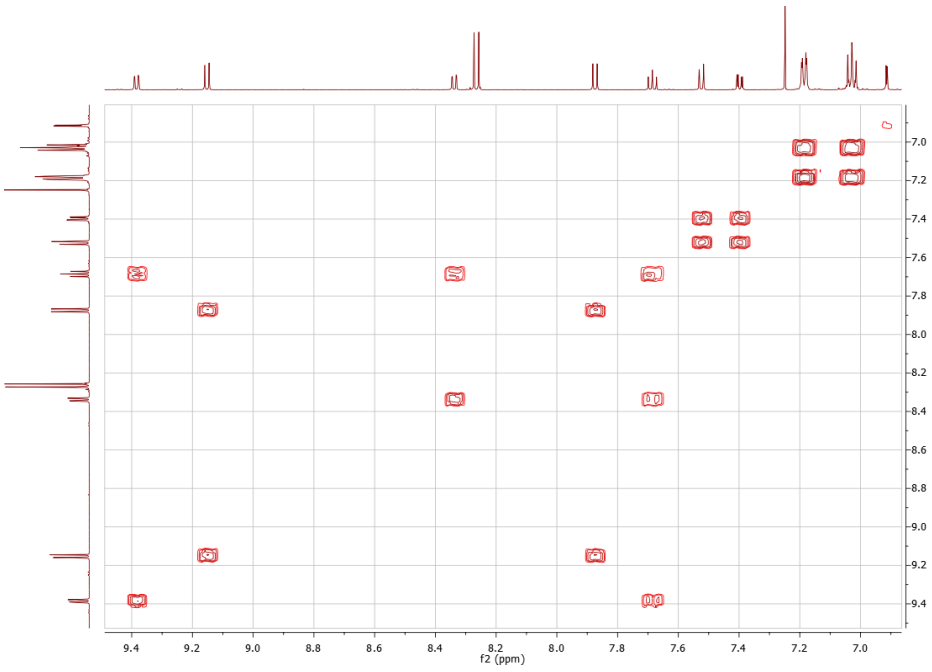

Figure 147 – COSY in $CDCl_3$ of **300a**.

Compound 312

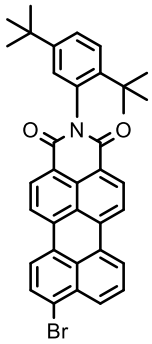

A mixture of **298** (1.6 g, 3.14 mmol), bromine (0.81 g, 5.03 mmol, 0.26 mL), potassium carbonate (1.82 g, 13.19 mmol) and 80 mL of dichloromethane was stirred at 0 °C for 20 min. The reaction mixture was poured into 50 mL of cold saturated sodium sulfite solution and stirred for 30 min. The desired product was extracted with dichloromethane and dried over sodium sulfate. The dark red solution was concentered under vacuum and the title compound was obtained as a red powder without any other purification (2.89 g, 98%). R_f (silica gel): 0.70 (DCM). M_p: > 200 °C.

^{1}H-NMR (600 MHz, $CDCl_3$, RT): δ 8.62-8.65 (m, 2H, Ar-H), 8.45-8.46 (d, *J* = 8.0 Hz, 1H, Ar-H), 8.42-8.43 (d, *J* = 8.2 Hz, 1H, Ar-H), 8.37-8.38 (d, *J* = 8.2 Hz, 1H, Ar-H), 8.28-8.29 (d, *J* = 8.3 Hz, 1H, Ar-H), 8.19-8.21 (d, *J* = 8.2 Hz, 1H, Ar-H), 7.88-7.89 (d, *J* = 8.0 Hz, 1H, Ar-H), 7.69-7.72 (m, 1H, Ar-H), 7.59-7.60 (d, *J* = 8.6 Hz, 1H, Ar-H), 7.45-7.47 (dd, *J* = 8.6 Hz, *J* = 2.3 Hz, 1H, Ar-H), 7.03 (d, *J* = 2.3 Hz, 1H, Ar-H), 1.33 (s, 9H, -CH_3), 1.30 (s, 9H, -CH_3) ppm.

^{13}C-NMR (151 MHz, $CDCl_3$, RT): δ 164.94, 150.20, 143.91, 136.74, 136.61, 133.10, 132.86, 132.00, 131.92, 131.22, 131.02, 130.15, 130.05, 129.54, 129.05, 128.98, 128.88, 128.11, 127.96, 126.56, 126.34, 126.25, 124.37, 123.70, 121.77, 120.72, 120.45, 120.26, 35.67, 34.40, 31.89, 31.39 ppm.

MS (ESI$^+$, MeOH/$CHCl_3$ + formic acid): *m/z* 588.29 $[M+H]^+$; calculated for $C_{36}H_{30}BrNO_2$: 587.15.

UV-Vis (DCM): λ_{max} (*ε*) = 484 (*37005*), 508 (*37392*) nm.

Fluorescence (DCM, λ_{exc} 490 nm): 547 nm. **ϕ:** 61%.

IR-Spectrum (cm^{-1}, ATR): 2955 *ν*(C–H aliphatic), 2870 *ν*(C–H aliphatic), 1700 *ν*(C═O), 1655 *ν*(C═O), 1590 *ν*(C═C aromatic), 1560 *ν*(C═C aromatic), 1495, 1355 *δ*(O–H), 1245, 1175, 1035, 925, 820, 800, 750, 735.

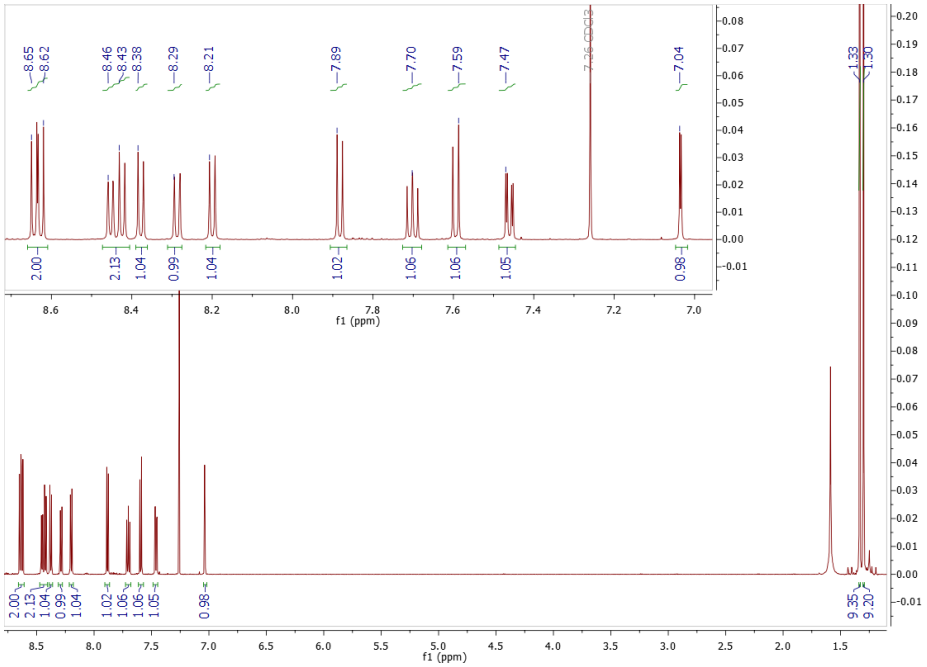

Figure 148 – ^{1}H-NMR in $CDCl_3$ of **312**.

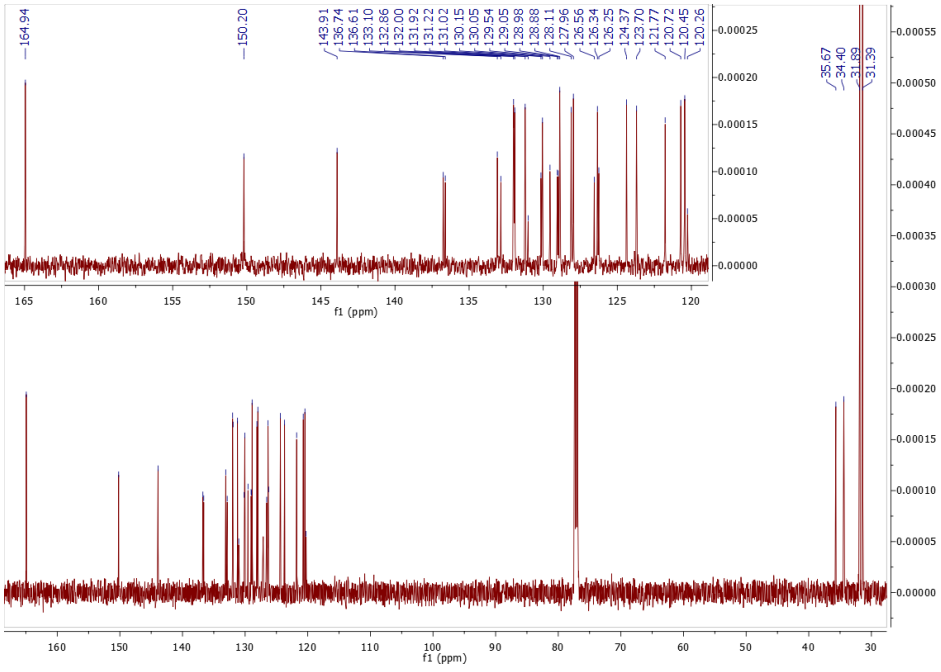

Figure 149 – ^{13}C-NMR in $CDCl_3$ of **312**.

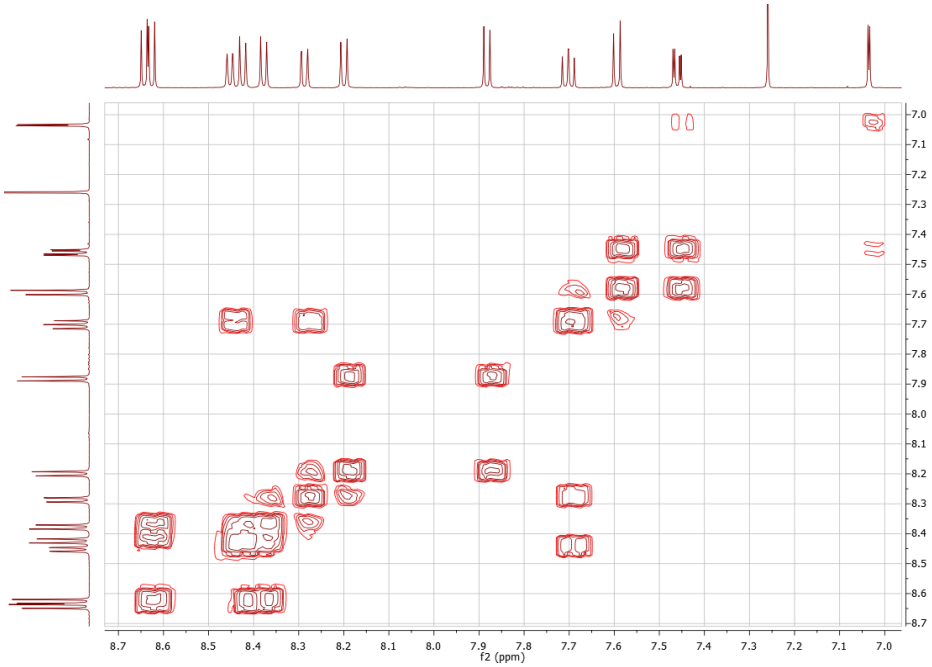

Figure 150 – COSY in $CDCl_3$ of **312**.

Compound 313

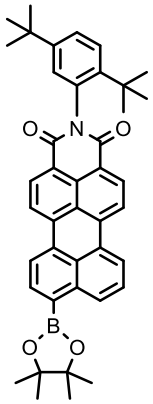

A mixture of **312** (400 mg, 0.68 mmol), bis(pinacolato)diboron (330 mg, 1.29 mmol), Pd(dppf)Cl_2 (50 mg, 0.07 mmol), potassium acetate (290 mg, 2.92 mmol) and 1,4-dioxane (15 mL) was stirred at 70 °C for 2 h under argon. Removing the solvent under the vacuum afforded a dark red solid. The desired product was purified by flash chromatography on silica gel using *n*-hexane/DCM (1:1) as eluent (177 mg, 41%). R_f (silica gel): 0.65 (DCM). M_p: > 200 °C.

^{1}H-NMR (600 MHz, $CDCl_3$, RT): δ 8.84-8.86 (dd, *J* = 8.4 Hz, *J* = 0.7 Hz, 1H, Ar-H), 8.61-8.63 (m, 2H, Ar-H), 8.40-8.43 (m, 3H, Ar-H), 8.36-8.37 (d, *J* = 7.7 Hz, 1H, Ar-H), 8.16-8.17 (d, *J* = 7.5 Hz, 1H, Ar-H), 7.63-7.66 (t, *J* = 7.6 Hz, 1H, Ar-H), 7.59-7.60 (d, *J* = 8.7 Hz, 1H, Ar-H), 7.45-7.47 (dd, *J* = 8.7 Hz, *J* = 2.3 Hz, 1H, Ar-H), 7.04-7.05 (d, *J* = 2.2 Hz, 1H, Ar-H), 1.47 (s, 12H, -CH_3), 1.34 (s, 9H, -CH_3), 1.31 (s, 9H, -CH_3) ppm.

^{13}C-NMR (151 MHz, $CDCl_3$, RT): δ 165.11, 150.13, 143.94, 138.11, 137.94, 137.42, 136.36, 133.24, 132.09, 131.92, 131.85, 131.77, 130.31, 129.11, 128.85, 127.99, 127.82, 127.36, 127.02, 126.26, 123.75, 122.78, 121.76, 121.21, 120.90, 120.38, 84.39, 35.66, 34.39, 31.88, 31.39, 25.15 ppm.

MS (ESI$^+$, MeOH/$CHCl_3$): *m/z* 636.14 $[M+H]^+$; calculated for $C_{42}H_{42}BNO_4$: 635.32.

UV-Vis (DCM): λ_{max} (*ε*) = 489 (*35464*), 514 (*36990*) nm.

Fluorescence (DCM, λ_{exc} 495 nm): 552 nm. **ϕ:** 63%.

IR-Spectrum (cm^{-1}, ATR): 2965 *ν*(C–H aliphatic), 1700 *ν*(C═O), 1660 *ν*(C═O), 1590 *ν*(C═C aromatic), 1575 *ν*(C═C aromatic), 1505 *ν*(C═C aromatic), 1460, 1410, 1330, 1245, 1140, 1110, 1045, 965, 855, 810, 750, 730.

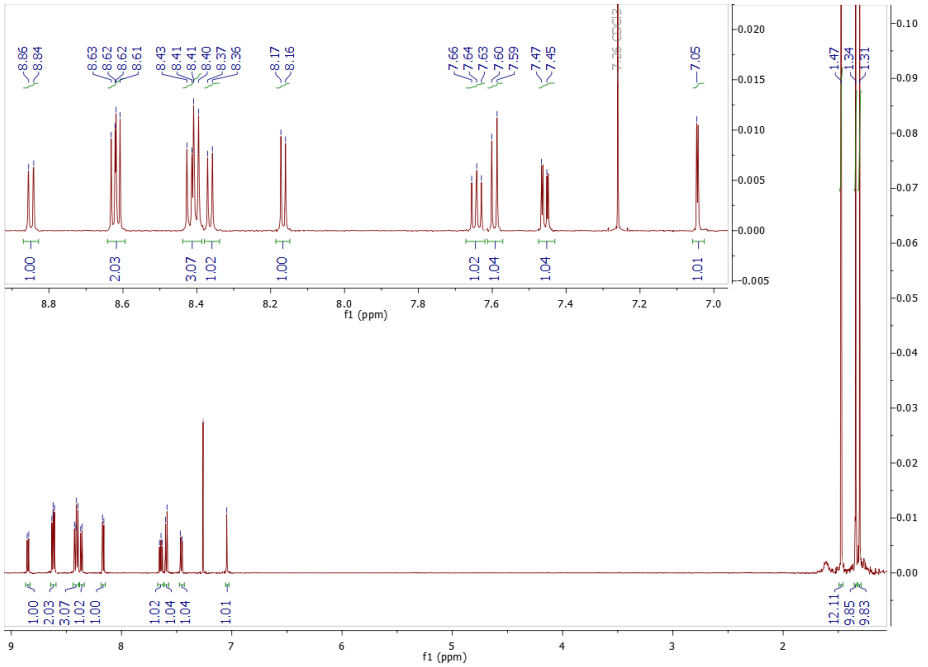

Figure 151 – ^{1}H-NMR in $CDCl_3$ of **313**.

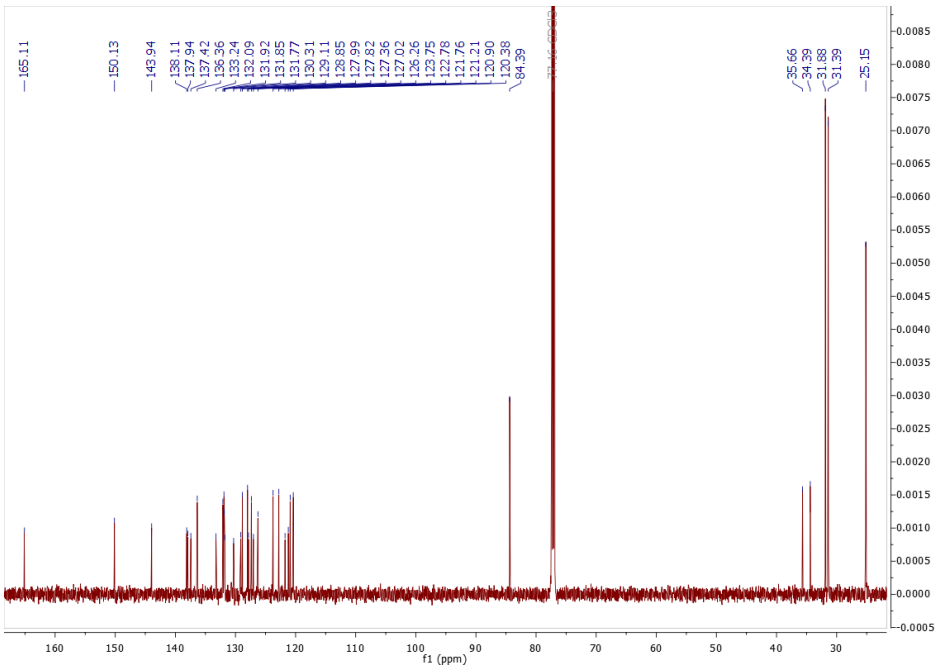

Figure 152 – ^{13}C-NMR in $CDCl_3$ of **313**.

Compound 314

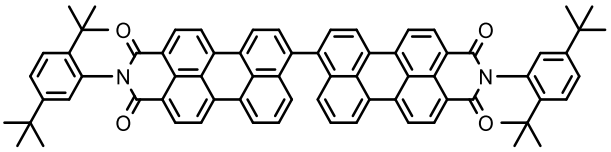

A mixture of **313** (200 mg, 0.31 mmol), **312** (260 mg, 0.45 mmol), $Pd(PPh_3)_4$ (20 mg, 0.02 mmol), potassium carbonate (180 mg, 1.33 mmol) and 15 mL of a solution toluene/ethanol/water (25:1:1) was stirred at 80 °C for 24 h under argon. After cooling to room temperature, the reaction mixture was extracted with dichloromethane and washed with brine. Removing the solvent under the vacuum afforded a dark purple solid. The desired product was purified by flash chromatography on silica gel using *n*-hexane/DCM (1/1) as eluent (246 mg, 78%). R_f (silica gel): 0.60 (DCM). M_p: > 200 °C.

^{1}H-NMR (600 MHz, $CDCl_3$, RT): δ 8.62-8.73 (m, 6H, Ar-H), 8.48-8.58 (m, 6H, Ar-H), 7.75-7.77 (m, 2H, Ar-H), 7.58-7.62 (m, 4H, Ar-H), 7.51-7.54 (m, 2H, Ar-H), 7.46-7.48 (m, 2H, Ar-H), 7.05 (d, *J* = 2.2 Hz, 1H, Ar-H), 1.33-1.34 (m, 36H, $-CH_3$) ppm.

^{13}C-NMR (151 MHz, $CDCl_3$, RT): δ 165.09, 150.18, 143.95, 140.67, 137.55, 137.34, 135.43, 135.20, 133.83, 133.40, 133.16, 132.28, 130.49, 129.79, 129.73, 129.43, 128.90, 128.45, 127.95, 127.60, 127.13, 126.34, 124.22, 123.58, 121.79, 121.71, 120.81, 120.68, 35.68, 34.38, 31.90, 31.39 ppm.

MS (ESI$^+$, MeOH/$CHCl_3$ + formic acid): *m/z* 1017.24 $[M+H]^+$; calculated for $C_{72}H_{60}N_2O_4$: 1016.46.

UV-Vis (DCM): λ_{max} (*ε*) = 527 (*99135*) nm.

Fluorescence (DCM, λ_{exc} 505 nm): 605 nm. **ϕ:** 63%.

IR-Spectrum (cm^{-1}, ATR): 2960 *ν*(C–H aliphatic), 2920 *ν*(C–H aliphatic), 2855 *ν*(C–H aliphatic), 1700 *ν*(C═O), 1655 *ν*(C═O), 1590 *ν*(C═C aromatic), 1570 *ν*(C═C aromatic), 1390, 1350, 1290, 1245, 1200, 1180, 1035, 920, 810, 755, 730.

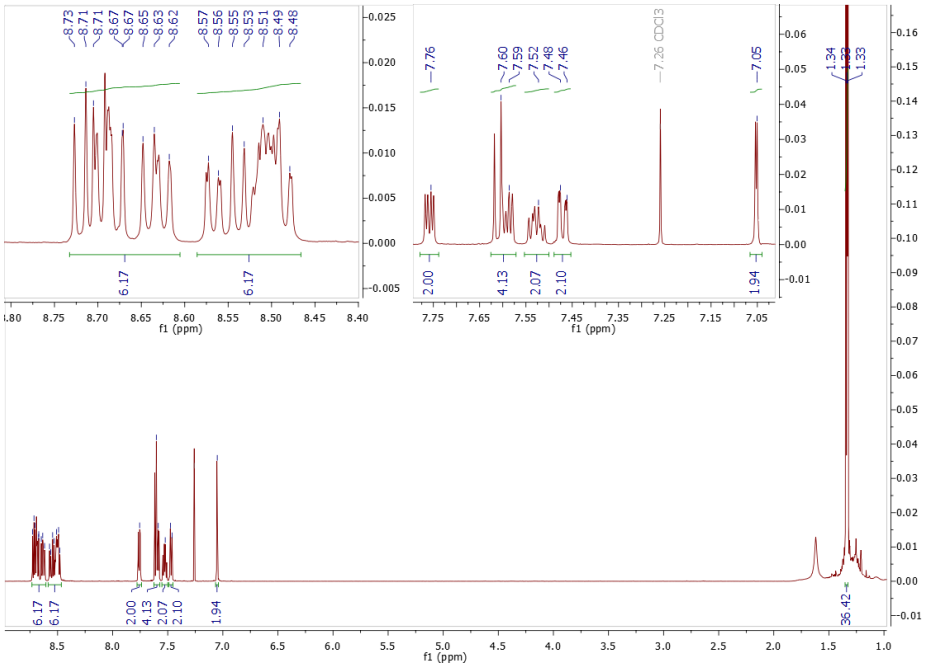

Figure 153 – ^{1}H-NMR in $CDCl_3$ of **314**.

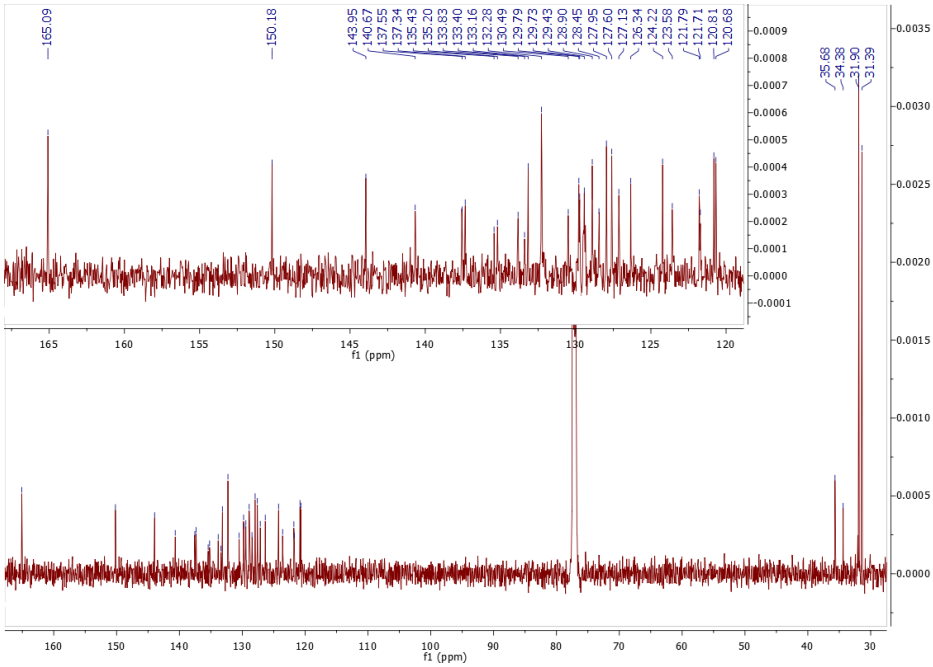

Figure 154 – ^{13}C-NMR in $CDCl_3$ of **314**.

Compound 315

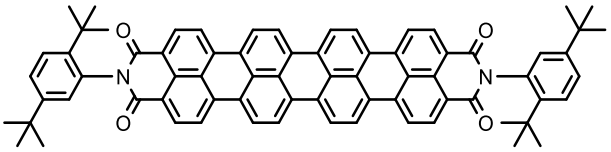

A mixture of **314** (250 mg, 0.25 mmol), potassium carbonate (50 mg, 0.37 mmol) and ethanolamine (3 mL), was stirred at 120 °C for 24 h. After cooling to room temperature, the reaction mixture was poured in 20 mL of cold ethanol. The resulting dark blue precipitate was filtered, washed with water and dried under vacuum. The desired product was purified by flash chromatography on silica gel using chloroform as eluent (178 mg, 70%). R_f (silica gel): 0.10 (DCM). M_p: > 200 °C. The crude material it wasn't characterized by NMR due to its poor solubility in the most common deuterated solvents even at high temperature. Furthermore, the poor solubility does not allow to perform ESI-MS experiments.

MS (ESI): Sample not detectable by ESI-MS.

UV-Vis (DCM): λ_{max} (ε) = 764 (*148190*) nm.

Fluorescence (DCM, λ_{exc} 755 nm): 790 nm. **ϕ:** 3%.

IR-Spectrum (cm^{-1}, ATR): 2950 *ν*(C–H aliphatic), 1695 *ν*(C═O), 1650 *ν*(C═O), 1565 *ν*(C═C aromatic), 1400, 1350, 1285, 1250, 1035, 805, 750, 735.

Compound 316

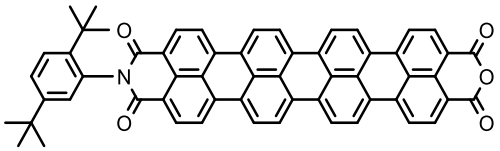

A mixture of **315** (25 mg, 0.03 mmol), potassium hydroxide (610 mg, 10.9 mmol) and *tert*-butanol (30 mL), was refluxed for 1 h. After one hour, 2 mL of acetic acid were added and the resulting mixture was refluxed for 1 h. After cooling to room temperature, 2 mL of 2 N HCl aqueous solution was added and the mixture was stirred overnight. After, the reaction mixture was poured into 100 mL of cold water and the resulting blue precipitate was filtered (15 mg, 63%). R_f (silica gel): 0.05 (9:1 DCM/MeOH). M_p: > 200 °C. The crude material it wasn't characterized by NMR due to its poor solubility in the most common deuterated solvents.

HRMS (MALDI-TOF): *m/z* 827.1945 [M^+]; calculated for $C_{58}H_{37}NO_5$: 827.27.

UV-Vis (DCM): λ_{max} (ε) = 763 (*149601*) nm.

Fluorescence (DCM, λ_{exc} 755 nm): 799 nm. **ϕ:** 3%.

IR-Spectrum (cm^{-1}, ATR): 2920 *v*(C–H aliphatic), 2850 *v*(C–H aliphatic), 1750 *v*(C═O), 1690 *v*(C═O), 1650 *v* (C═O), 1500, 1460, 1400, 1345, 1280, 1220, 1125, 1010, 805, 750, 735.

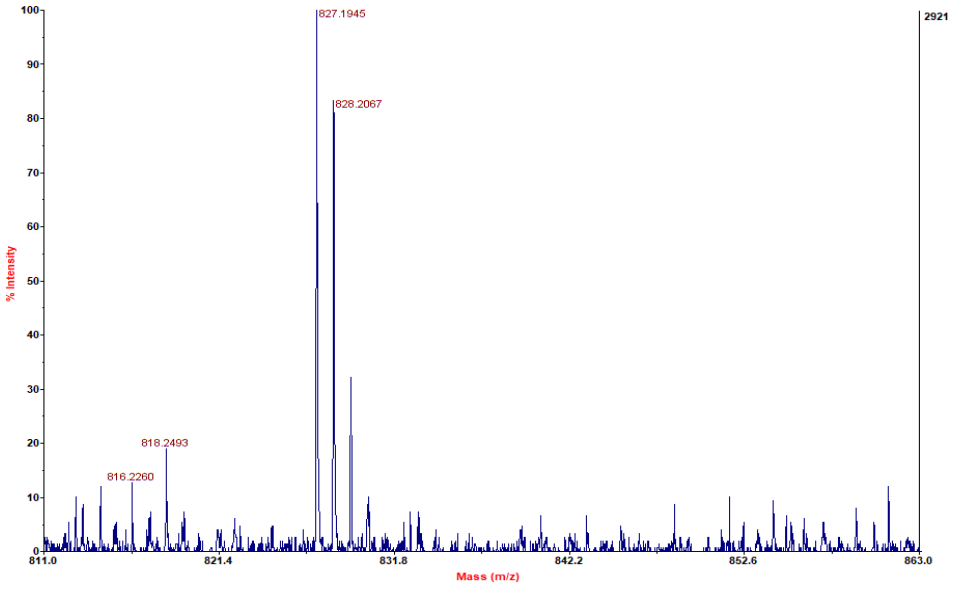

Figure 155 – HRMS MALDI-TOF mass spectrum of **316**.

Compound 317

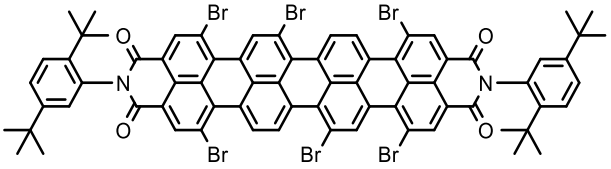

A mixture of **315** (20 mg, 0.02 mmol), bromine (1.32 g, 8.3 mmol, 0.42 mL) and chloroform (8 mL) was stirred at 55 °C for 2 days in the dark. After cooling to room temperature, the reaction mixture was washed with a solution of 0.15 g KOH and 0.1 g sodium sulfite in 20 mL of water. The organic phase was separated and dried over sodium sulfate. Removing the solvent under the vacuum afforded a dark-green solid. Crude material is a mixture of hexa-brominated regioisomers and slightly amount of other polybrominated derivatives (penta- and hepta-). These compounds are not separable and for this reason the crude material was used without any purification for the next step (20 mg, ≈65%). R_f (silica gel): 0.90 (DCM). M_p: > 200 °C.

MS (ESI): Sample not detectable by ESI-MS.

UV-Vis (DCM): λ_{max} (ε) = 746 (*99198*) nm.

Fluorescence (DCM, λ_{exc} 735 nm): 772 nm. **ϕ:** < 1%.

IR-Spectrum (cm^{-1}, ATR): 2960 *ν*(C–H aliphatic), 2925 *ν*(C–H aliphatic), 2870 *ν*(C–H aliphatic), 1715 *ν*(C═O), 1710 *ν*(C═O), 1700 *ν*(C═O), 1670 *ν*(C═O), 1590 *ν*(C═C aromatic), 1570 *ν*(C═C aromatic), 1470 *ν*(C═C aromatic), 1390, 1350, 1230, 1200, 1170, 1150, 1050, 840, 815, 795, 725.

Compound 318

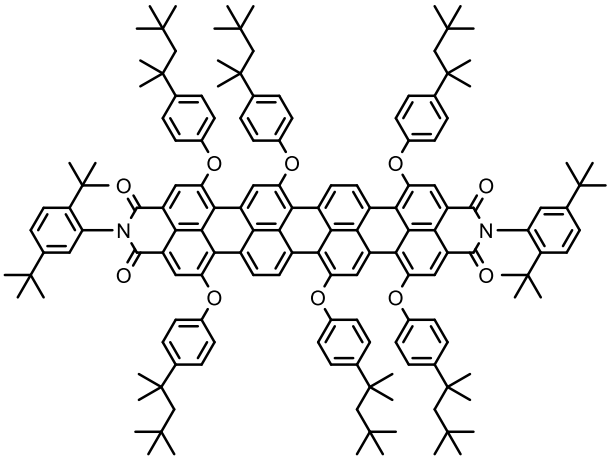

A mixture of **317** (20 mg, 0.015 mmol), *tert*-octylphenol (56 mg, 0.27 mmol), potassium carbonate (5 mg, 0.04 mmol) and NMP (2 mL) was stirred at 120 °C for 3 days. After cooling to room temperature, the reaction mixture was poured in 15 mL of 6 M HCl aqueous solution. The resulting greenish precipitate was filtered and washed with water. The crude material was purified by flash chromatography on silica gel using *n*-hexane/DCM (1:1) as eluent (10 mg, 30%). R_f (silica gel): 0.35 (1:1 *n*-hexane/DCM). M_p: > 200 °C.

^{1}H-NMR (600 MHz, $CDCl_3$, RT): δ 9.37-9.44 (m, 4H, Ar-H), 8.19-8.43 (m, 8H, Ar-H), 7.52-7.56 (m, 2H, Ar-H), 7.39-7.40 (d, *J* = 7.3 Hz, 12H, Ar-H), 7.07-7.08 (d, *J* = 7.1 Hz, 12H, Ar-H), 6.94-6.98 (m, 2H, Ar-H), 1.72 (s, 12H, -CH_2-), 1.37 (s, 36H, -CH_3), 0.86-0.89 (m, 36H, -CH_3), 0.74 (s, 54H, -CH_3) ppm.

^{13}C-NMR: Not enough sample to perform the experiment.

MS (ESI): Sample not detectable by ESI-MS.

UV-Vis (DCM): λ_{max} (ε) = 648 (*39693*), 713 (*79020*), 783 (*152233*) nm.

Fluorescence (DCM, λ_{exc} 750 nm): 806 nm. **ϕ:** 2%.

IR-Spectrum (cm^{-1}, ATR): 2960 *v*(C–H aliphatic), 2875 *v*(C–H aliphatic), 1705 *v*(C═O), 1670 *v*(C═O), 1595 *v*(C═C aromatic), 1500 *v*(C═C aromatic), 1335, 1210, 1040, 815, 745, 705.

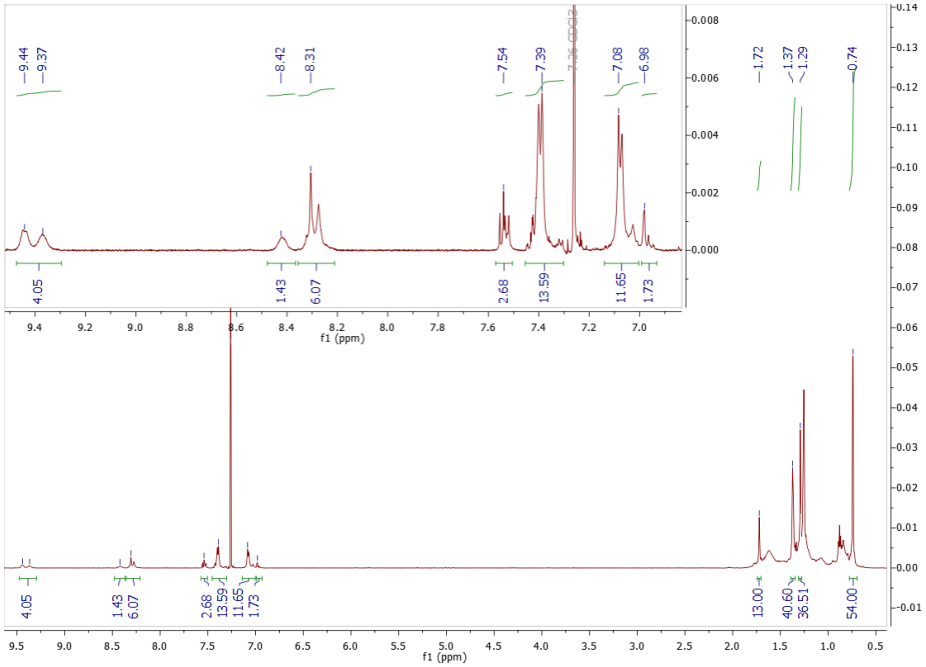

Figure 156 – ^{1}H-NMR in $CDCl_3$ of **318**.

Compound 319

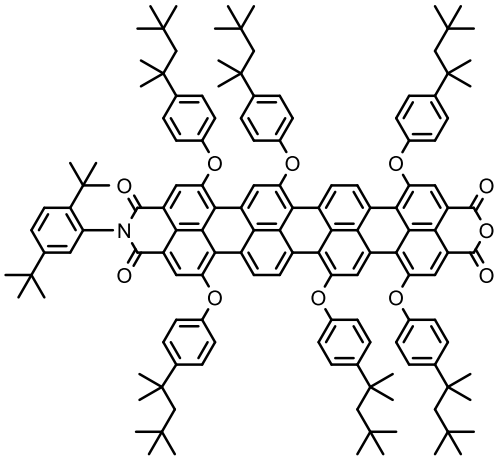

A mixture of **318** (9 mg, 0.004 mmol), potassium hydroxide (100 mg, 1.85 mmol) and *tert*-butanol (10 mL), was refluxed for 1 h. After one hour, 2 mL of acetic acid were added and the resulting mixture was refluxed for 1 h. After cooling to room temperature, 0.5 mL of 2 N HCl aqueous solution was added and the mixture was stirred overnight. After, the reaction mixture was poured into 10 mL of cold water and the resulting blue-greenish precipitate was filtered (2.1 mg, 25%). R_f (silica gel): 0.10 (1:1 *n*-hexane/DCM). M_p: > 200 °C.

^{1}H-NMR: Not enough sample to perform the experiment.

^{13}C-NMR: Not enough sample to perform the experiment.

HRMS (MALDI-TOF): *m/z* 2052.4609 [M^+]; calculated for $C_{142}H_{157}NO_{11}$: 2052.18.

UV-Vis (DCM): λ_{max} (ε) = 715 (*71485*), 784 (*155029*) nm.

Fluorescence (DCM, λ_{exc} 750 nm): 802 nm. **ϕ:** 2%.

IR-Spectrum (cm^{-1}, ATR): Not enough sample to perform the experiment.

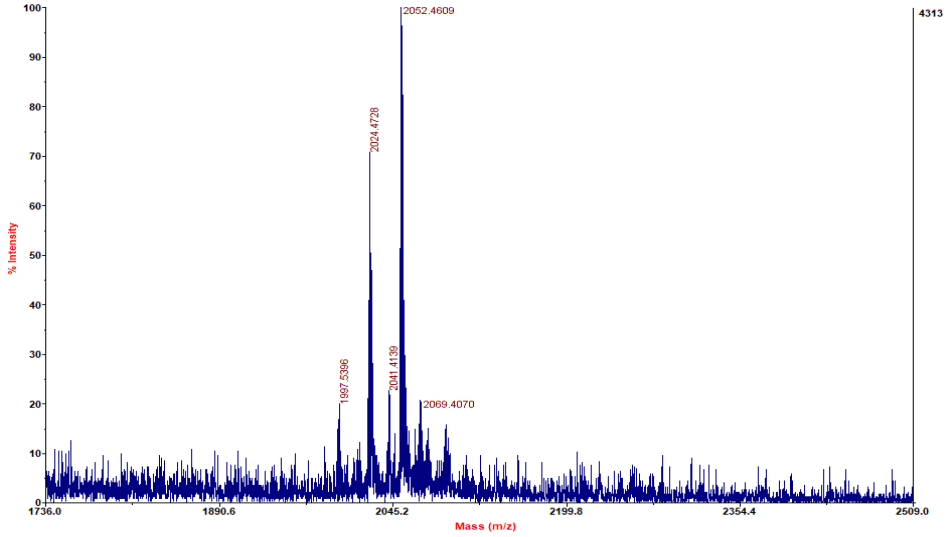

Figure 157 – HRMS MALDI-TOF mass spectrum of **319**.

1.2. Synthesis of Compound 321

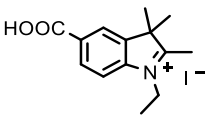

Synthesis of Compound **321** was performed as described in literature.[474] A mixture of **320** (2.0 g, 9.7 mmol), iodoethane (3.12 mL, 6.1 g, 38.9 mmol) and 12 mL of acetonitrile was introduced in a sealed 20 mL reaction vial and heated in a microwave reactor at 155 °C for 20 min. The reaction mixture is washed out of the vessel with acetonitrile and the total volume was reduced by ca. 50%. The resulting solution was poured in 200 mL of diethyl ether causing the precipitation of the desired compound. The precipitate was filtered, washed under stirring diethyl ether (3 x 200 mL) and dried under vacuum. The product was isolated as a light-yellow powder (3.03 g, 87%). R_f (silica gel): 0.20 (95:5 DCM/MeOH). M_p: > 200 °C.

^{1}H-NMR (600 MHz, DMSO-d$_6$, RT): δ 8.39 (s, 1H, Ar-H), 8.18-8.19 (d, *J* = 8.2 Hz, 1H, Ar-H), 8.08-8.09 (d, *J* = 8.3 Hz, 1H, Ar-H), 4.51-4.54 (q, J = 7.0 Hz, 2H, -CH$_2$-), 2.88 (s, 3H, -CH$_3$), 1.58 (s, 6H, -CH$_3$) ppm.

^{13}C-NMR (151 MHz, DMSO-d$_6$, RT): δ 199.18, 166.43, 143.95, 142.34, 131.67, 130.46, 124.42, 115.57, 54.47, 43.45, 21.70, 14.33, 12.60 ppm.

MS (ESI$^+$, MeOH): *m/z* 232.48 $[M+H]^+$; calculated for $C_{14}H_{18}NO_2^+$: 232.13.

UV-Vis (EtOH): λ_{max} (ε) = 325 (*9699*) nm.

Fluorescence (EtOH, λ_{exc} 315 nm): 411 nm. **ϕ:** 14%.

IR-Spectrum (cm^{-1}, ATR): 2975 *v*(C–H aliphatic), 1720 *v*(C═O), 1590, 1430, 1370, 1200, 1165, 1110, 940, 855, 775, 710.

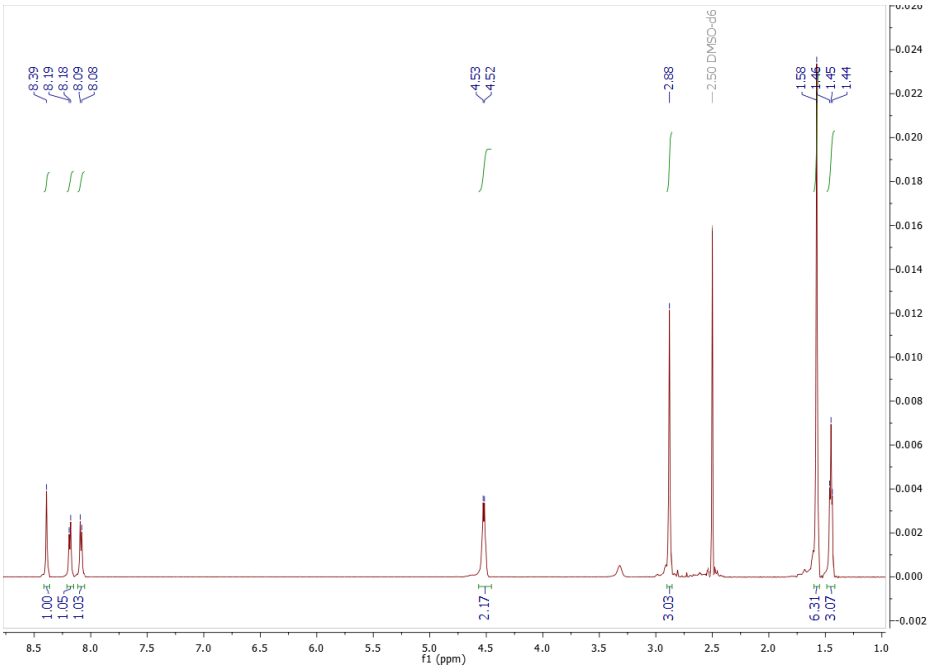

Figure 158 – ^{1}H-NMR in DMSO-d_6 of **321**.

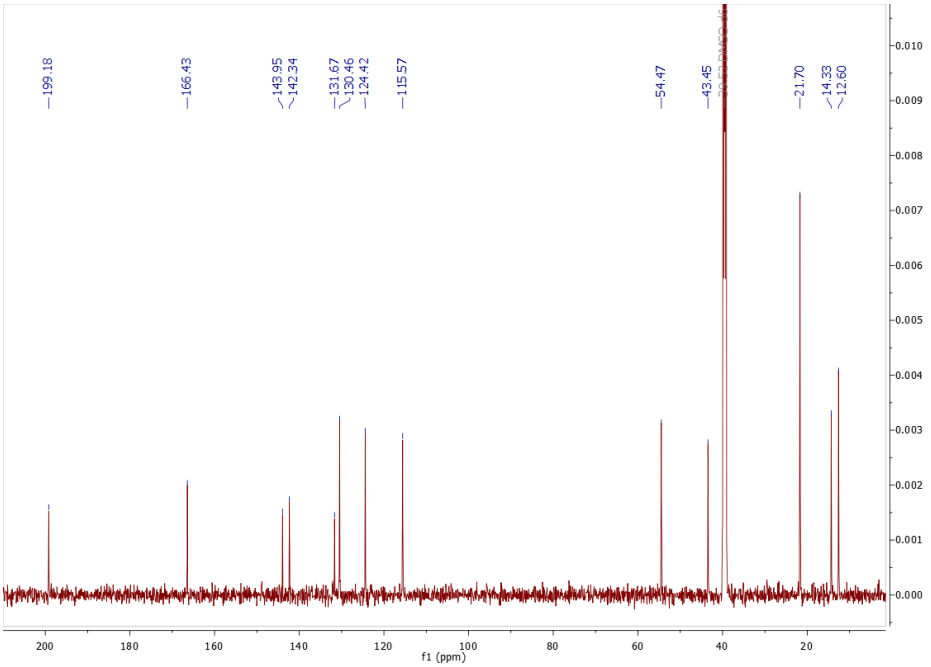

Figure 159 – ^{13}C-NMR in DMSO-d_6 of **321**.

1.3. Synthesis of Compound 326

Compound 325

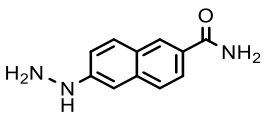

Synthesis of **325** was performed as described in literature.[87] **324** (40 g, 0.21 mol) was cooled to 0 °C and then monohydrate hydrazine (60 mL, 1.23 mol) was slowly added dropwise. After the addition, the resulting turbid light-orange solution was heated at 130 °C for 24 h under argon. After, the reaction mixture was cooled to 60 °C and 200 mL of 2-propanol was added to obtain a yellow precipitate which was filtered (during the filtration the yellow solid should not be completely dried to avoid explosion risks). The resulting solid was used as it for the next step without any purification. Due to the explosion risks the compound was not isolated and characterized.

Compound 326

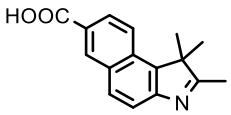

Synthesis of **326** was performed as described in literature.[87] A mixture of **325** (raw material) and 120 mL of acetic acid was cooled to 0 °C and then 150 mL of 3-methyl-3-butanone was added dropwise. After the addition, the resulting red solution was stirred at room temperature for one night and then distilled to remove all the solvent. At the remaining viscous solution, 150 mL of HCl 32% was added and the resulting mixture was refluxed for 12 h. After cooling to room temperature, the resulting light-brown precipitate was filtered, washed with cold 2-propanol and dried under vacuum. The resulting light-brown solid was poured in a saturated aqueous solution of sodium bicarbonate and then acidified to pH 5 by 1 M HCl aqueous solution. The resulting precipitate was filtered, washed with diethyl ether and dried under vacuum. The product was isolated as a light-brown powder (34.4 g, 65% from starting material 6-hydroxy-2-naphthoic acid). R_f (silica gel): 0.20 (95:5 DCM/MeOH). M_p: > 200 °C.

^{1}H-NMR (600 MHz, DMSO-d$_6$, RT): δ 8.68 (d, *J* = 1.6 Hz, 1H, Ar-H), 8.20-8.21 (d, *J* = 8.8 Hz, 1H, Ar-H), 8.11-8.12 (d, *J* = 8.8 Hz, 1H, Ar-H), 8.04-8.05 (dd, *J* = 8.8 Hz, *J* = 1.7 Hz, 1H, Ar-H), 7.77-7.79 (d, *J* = 8.5 Hz, 1H, Ar-H), 2.33 (s, 3H, -CH_3), 1.48 (s, 6H, -CH_3) ppm.

^{13}C-NMR (151 MHz, DMSO-d$_6$, RT): δ 191.06, 167.53, 152.72, 138.87, 132.13, 130.77, 130.40, 130.06, 126.47, 125.87, 122.95, 120.46, 55.00, 22.01, 15.05 ppm.

MS (ESI$^+$, MeOH + formic acid): *m/z* 254.32 $[M+H]^+$; calculated for $C_{16}H_{15}NO_2$: 253.11.

UV-Vis (EtOH): λ_{max} (ε) = 310 (*9543*), 318 (*9338*), 347 (*2879*) nm.

Fluorescence (EtOH, λ_{exc} 300 nm): 376 nm. **ϕ:** <1 %.

IR-Spectrum (cm^{-1}, ATR): 3445 *v*(O–H), 2955 *v*(C–H aliphatic), 1665 *v*(C═O), 1625 *v*(C═C aromatic), 1570 *v*(C═C aromatic), 1460, 1420, 1385, 1350, 1280 *δ*(O–H), 1245, 1215, 1190, 1155, 980, 905, 805, 755, 735.

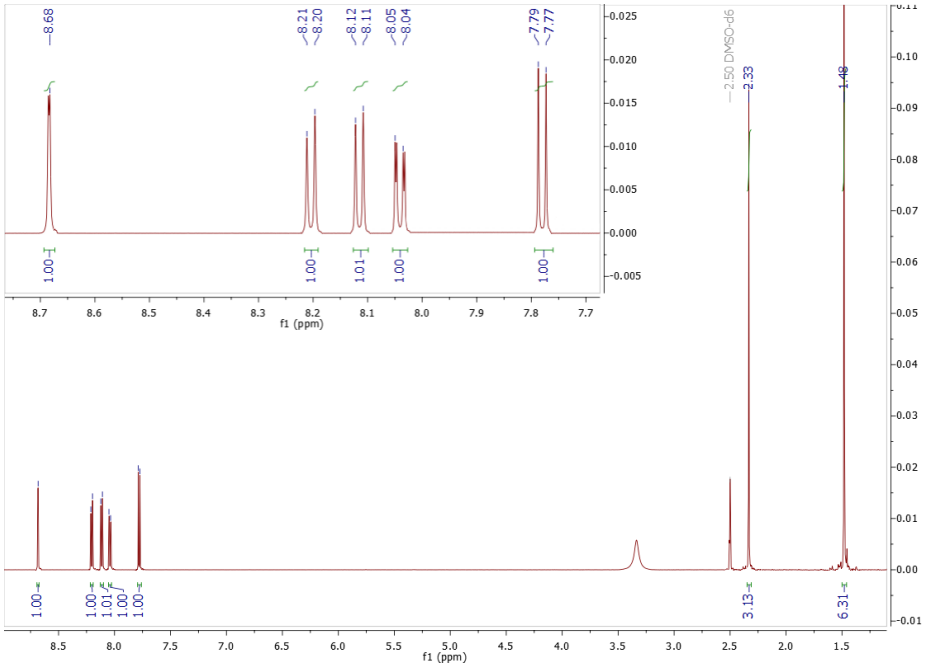

Figure 160 – ^{1}H-NMR in DMSO-d$_6$ of **326**.

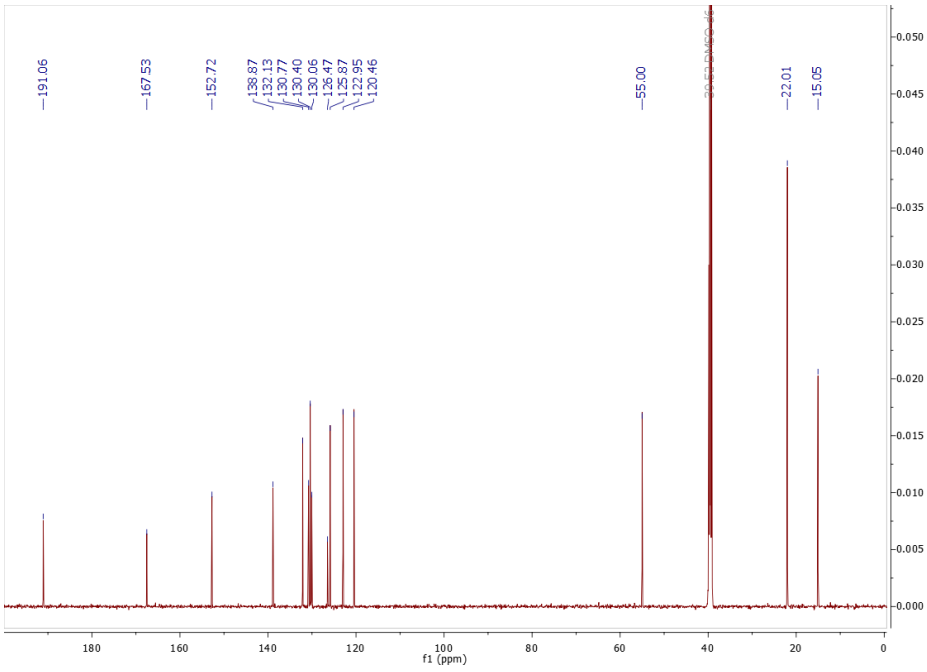

Figure 161 – ^{13}C-NMR in DMSO-d$_6$ of **326**.

1.4. General Synthesis of Carboxy Benzoindolium Iodide Salts

Carboxy-benzoindolium iodide salts **327**, **328** and **329** were synthetized according to the published general procedure.[87]

A mixture of **326** (4.0 g, 1.0 eq.), 1-iodoalkane (4.0 eq.) and 100 mL of acetonitrile was refluxed for 48 h. After cooling the reaction to room temperature, the total volume of the reaction mixture was reduced by ca. 50%. The resulting solution was poured in 250 mL of diethyl ether causing the precipitation of the desired compound. The precipitate was filtered, washed under stirring diethyl ether (3 x 400 mL) and dried under vacuum.

Compound 327

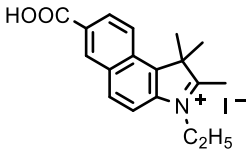

The product was isolated as a light-yellow powder (5.85 g, 84%). R_f (silica gel): 0.05 (95:5 DCM/MeOH). M_p: > 200 °C.

^{1}H-NMR (600 MHz, DMSO-d$_6$, RT): δ 8.87 (d, *J* = 1.5 Hz, 1H, Ar-H), 8.51-8.52 (d, *J* = 8.9 Hz, 1H, Ar-H), 8.47-8.48 (d, *J* = 8.8 Hz, 1H, Ar-H), 8.24-8.24 (d, *J* = 8.9 Hz, 1H, Ar-H), 8.20-8.21 (dd, *J* = 8.8 Hz, *J* = 1.7 Hz, 1H, Ar-H), 4.60-4.63 (q, *J* = 7.4 Hz, 2H, -CH_2-), 2.94 (s, 3H, -CH_3), 1.77 (s, 6H, -CH_3), 1.49-1.51 (t, J = 7.3 Hz, 3H, -CH_3) ppm.

^{13}C-NMR (151 MHz, DMSO-d$_6$, RT): δ 197.22, 166.93, 139.95, 136.95, 132.36, 132.28, 132.10, 129.11, 128.98, 127.41, 123.95, 114.12, 55.59, 43.48, 21.40, 13.84, 12.84 ppm.

MS (ESI$^+$, MeOH): *m/z* 282.41 $[M+H]^+$; calculated for $C_{18}H_{20}NO_2^+$: 282.15.

UV-Vis (EtOH): λ_{max} (ε) = 258 (*29948*), 319 (*8723*), 350 (*6516*) nm.

Fluorescence (EtOH, λ_{exc} 240 nm): 483 nm. **ϕ:** 8%.

IR-Spectrum (cm^{-1}, ATR): 2970 *v*(C–H aliphatic), 1715 *v*(C═O), 1680, 1615, 1465, 1300, 1160, 1100, 970, 815, 760, 705.

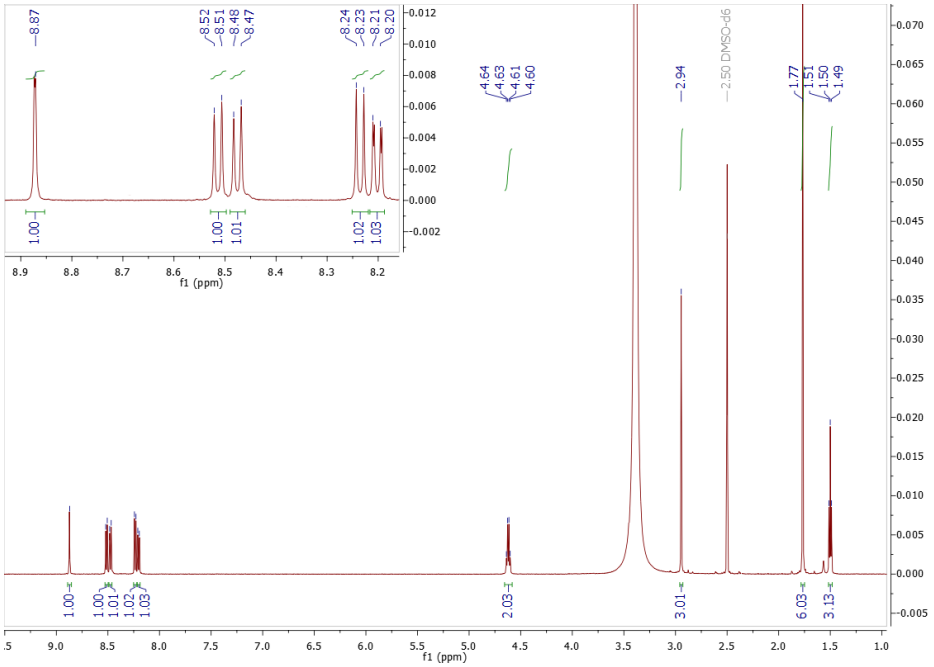

Figure 162 – ^{1}H-NMR in DMSO-d$_6$ of **327**.

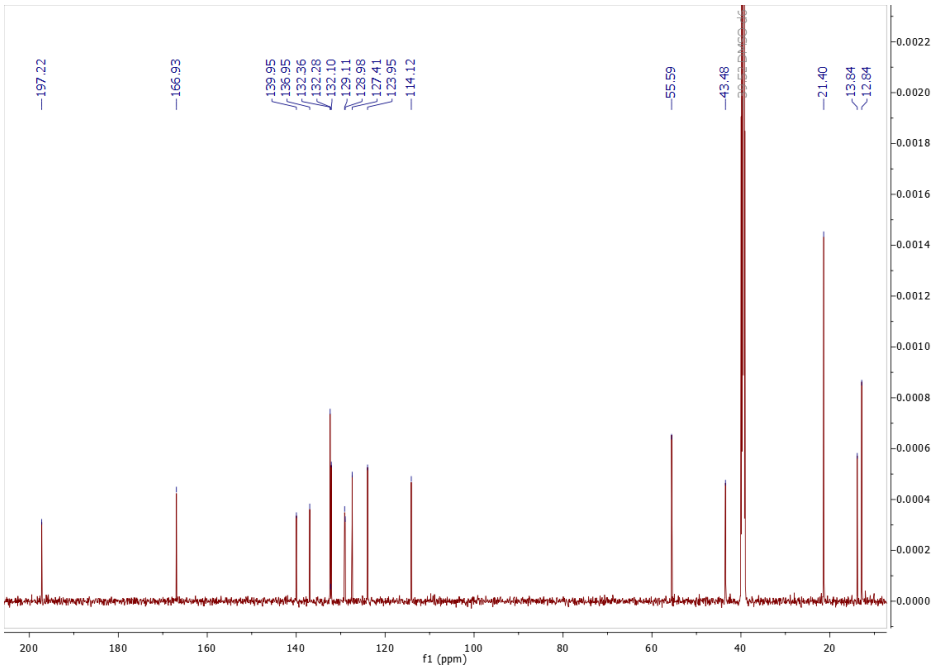

Figure 163 – ^{13}C-NMR in DMSO-d$_6$ of **327**.

Compound 328

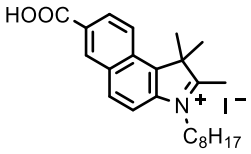

The product was isolated as a light-brown powder (5.84 g, 75%). R_f (silica gel): 0.10 (95:5 DCM/MeOH). M_p: > 200 °C.

^{1}H-NMR (600 MHz, DMSO-d$_6$, RT): δ 8.87 (d, *J* = 1.4 Hz, 1H, Ar-H), 8.50-8.52 (d, *J* = 8.9 Hz, 1H, Ar-H), 8.47-8.59 (d, *J* = 8.9 Hz, 1H, Ar-H), 8.23-8.24 (d, *J* = 8.9 Hz, 1H, Ar-H), 8.19-8.21 (dd, *J* = 8.8 Hz, *J* = 1.7 Hz, 1H, Ar-H), 4.56-4.58 (t, *J* = 7.7 Hz, 2H, -CH_2-), 2.95 (s, 3H, -CH_3), 1.86-1.91 (m, 2H, -CH_2-), 1.77 (s, 6H, -CH_3), 1.42-1.47 (m, 2H, -CH_2-), 1.31-1.35 (m, 2H, -CH_2-), 1.20-1.30 (m, 6H, -CH_2-), 0.83-0.85 (t, *J* = 6.7 Hz, 3H, -CH_3) ppm.

^{13}C-NMR (151 MHz, DMSO-d$_6$, RT): δ 197.50, 166.92, 140.23, 136.90, 132.38, 132.33, 132.09, 129.07, 129.02, 127.43, 123.97, 114.26, 55.62, 47.98, 31.14, 28.58, 28.45, 27.42, 25.87, 22.01, 21.54, 14.06, 13.92 ppm.

MS (ESI$^+$, MeOH): *m/z* 366.71 $[M+H]^+$; calculated for $C_{24}H_{32}NO_2^+$: 366.24.

UV-Vis (EtOH): λ_{max} (ε) = 258 (*33419*), 319 (*7689*), 349 (*5932*) nm.

Fluorescence (EtOH, λ_{exc} 240 nm): 484 nm. **ϕ:** 6%.

IR-Spectrum (cm^{-1}, ATR): 2920 *v*(C–H aliphatic), 1720 *v*(C═O), 1615, 1580, 1465, 1345, 1170, 995, 910, 820, 795, 705.

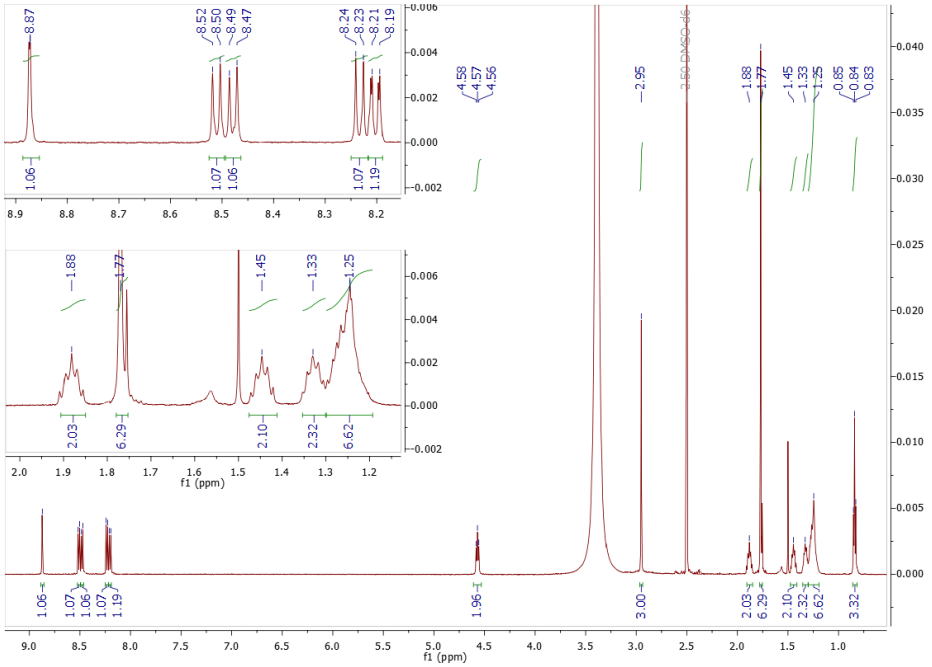

Figure 164 – ^{1}H-NMR in DMSO-d$_6$ of **328**.

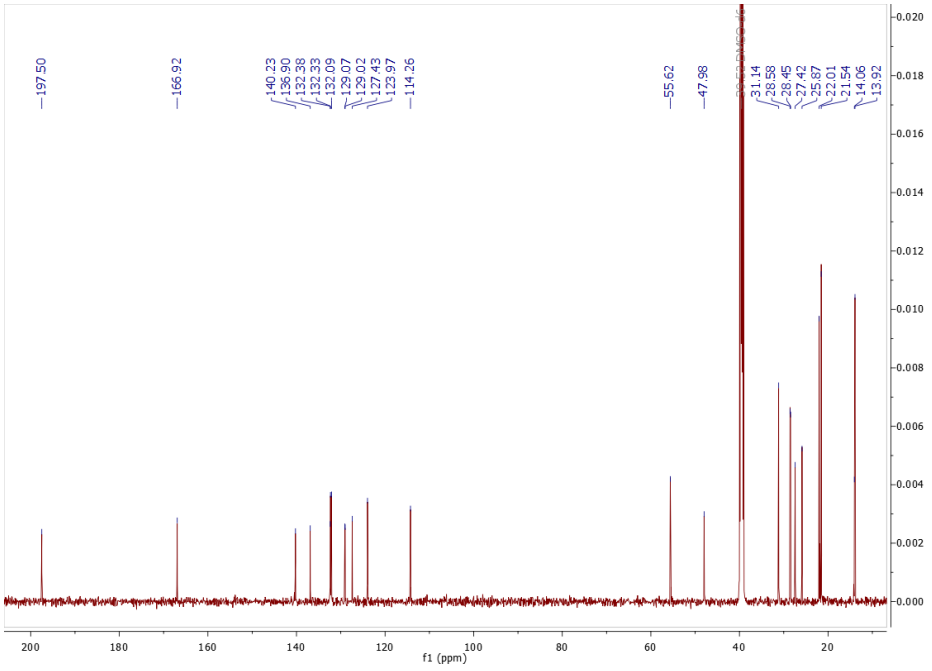

Figure 165 – ^{13}C-NMR in DMSO-d$_6$ of **328**.

Compound 329

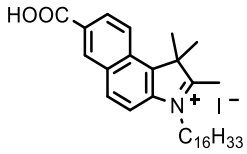

The product was isolated as a light gray powder (5.26 g, 55%). R_f (silica gel): 0.10 (95:5 DCM/MeOH). M_p: > 200 °C.

^{1}H-NMR (600 MHz, DMSO-d$_6$, RT): δ 8.87 (d, *J* = 1.2 Hz, 1H, Ar-H), 8.51-8.52 (d, *J* = 9.0 Hz, 1H, Ar-H), 8.48-8.49 (d, *J* = 8.9 Hz, 1H, Ar-H), 8.24-8.25 (d, *J* = 9.0 Hz, 1H, Ar-H), 8.19-8.21 (dd, *J* = 8.8 Hz, *J* = 1.6 Hz, 1H, Ar-H), 4.57-4.59 (q, J = 7.8 Hz, 2H, -CH_2-), 2.96 (s, 3H, -CH_3), 1.86-1.91 (m, 2H, -CH_2-), 1.77 (s, 6H, -CH_3), 1.41-1.46 (m, 2H, -CH_2-), 1.30-1.34 (m, 2H, -CH_2-), 1.19-1.26 (m, 22H, -CH_2-), 0.83-0.85 (t, J = 7.2 Hz, 3H, -CH_3) ppm.

^{13}C-NMR (151 MHz, DMSO-d$_6$, RT): δ 197.51, 166.91, 140.21, 136.89, 132.39, 132.32, 132.08, 129.07, 129.03, 127.43, 123.96, 114.25, 55.62, 47.98, 31.26, 28.99, 28.85, 28.73, 28.67, 28.58, 27.39, 25.81, 22.06, 21.53, 14.05, 13.92 ppm.

MS (ESI$^+$, MeOH): *m/z* 478.29[M+H]$^+$; calculated for $C_{32}H_{48}NO_2^+$: 478.37.

UV-Vis (EtOH): λ_{max} (ε) = 259 (*26990*), 319 (*7556*), 350 (*6353*) nm.

Fluorescence (EtOH, λ_{exc} 235 nm): 479 nm. **ϕ:** 6%.

IR-Spectrum (cm^{-1}, ATR): 2915 *v*(C–H aliphatic), 2850 *v*(C–H aliphatic), 1720 *v*(C═O), 1685, 1615, 1465, 1350, 1300, 1185, 815, 790, 750, 710.

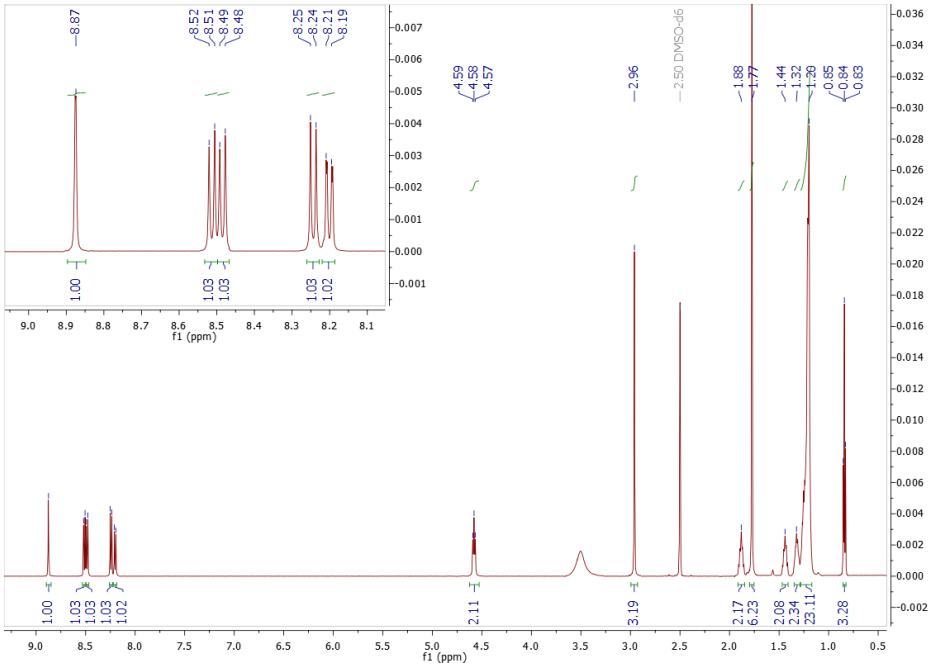

Figure 166 – ^{1}H-NMR in DMSO-d$_6$ of **329**.

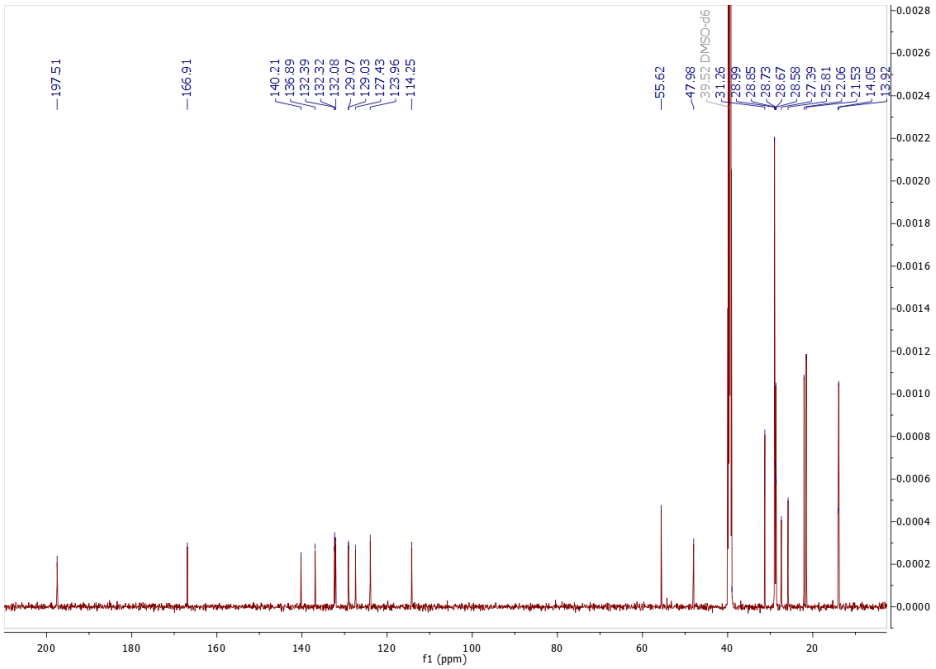

Figure 167 – ^{13}C-NMR in DMSO-d$_6$ of **329**.

1.5. Synthesis of Compound 322

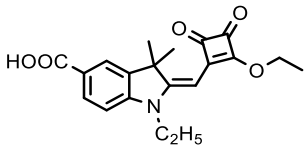

Synthesis of **322** was performed as described in literature.[474] A mixture of **321** (8.35 g, 23.25 mmol), 3,4-diethoxy-3- cyclobutene-1,2-dione (3.44 mL, 3.96 g, 23.25 mmol) and 200 mL of a solution ethanol/triethylamine (93:7) was refluxed for 15 min. After cooling the reaction to room temperature, the solvent was removed by evaporation under vacuum. The resulting solid was treated with saturated aqueous solution of citric acid and the mixture was extracted with dichloromethane. The organic layer was separated, dried over sodium sulphate and the solvent evaporated under vacuum. The desired product was purified by flash chromatography on silica gel using dichloromethane/methanol (97:3) as eluent. The product was isolated as a brown powder (6.78 g, 82%). R_f (silica gel): 0.15 (95:5 DCM/MeOH). M_p: > 200 °C.

^{1}H-NMR (600 MHz, DMSO-d$_6$, RT): δ 7.92-7.93 (d, *J* = 1.6 Hz, 1H, Ar-H), 7.90-7.92 (dd, *J* = 8.2 Hz, *J* = 1.6 Hz, 1H, Ar-H), 7.22-7.23 (d, *J* = 8.3 Hz, 1H, Ar-H), 5.74 (s, 1H, -CH=), 4.80-4.84 (q, *J* = 7.1 Hz, 2H, -CH_2-), 3.95-3.98 (q, *J* = 7.2 Hz, 2H, -CH_2-), 1.56 (s, 6H, -CH_3), 1.43-1.45 (t, *J* = 7.1 Hz, 3H, -CH_3), 1.19-1.21 (t, *J* = 7.1 Hz, 3H, -CH_3) ppm.

^{13}C-NMR (151 MHz, DMSO-d$_6$, RT): δ 191.87, 188.95, 187.27, 172.67, 167.16, 166.74, 145.87, 140.42, 130.39, 124.53, 122.94, 108.46, 82.03, 70.06, 46.95, 37.35, 26.43, 15.65, 11.07 ppm.

MS (ESI$^-$, MeOH + NH$_4$OH): *m/z* 354.31 $[M]^-$; calculated for $C_{20}H_{21}NO_5$: 355.14.

UV-Vis (EtOH): λ_{max} (ε) = 293 (*9769*), 425 (*73644*) nm.

Fluorescence (EtOH, λ_{exc} 405 nm): 461 nm. **ϕ:** < 1%.

IR-Spectrum (cm^{-1}, ATR): 2970 *ν*(C–H aliphatic), 1770 *ν*(C═O), 1710 *ν*(C═O), 1680 *ν*(C═O), 1600 *ν*(C═C aromatic), 1535, 1365, 1295, 1205 *δ*(O–H), 1115, 1055, 930, 820, 770.

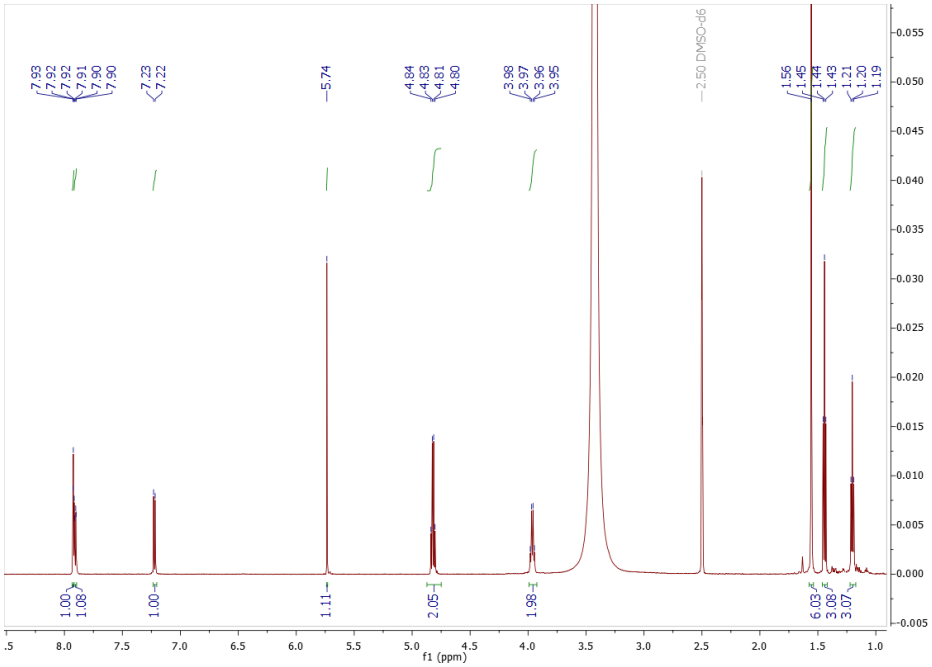

Figure 168 – ^{1}H-NMR in DMSO-d$_6$ of **322**.

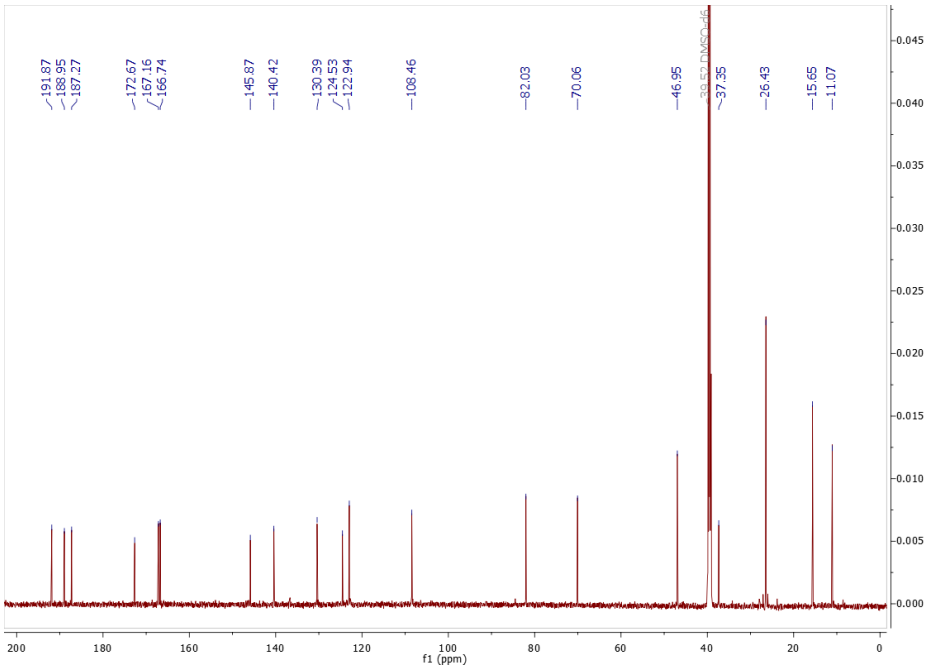

Figure 169 – ^{13}C-NMR in DMSO-d$_6$ of **322**.

1.6. Synthesis of Compound 323

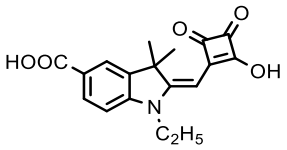

Synthesis of **323** was performed according to the published general procedure.[80] A mixture of **322** (3.0 g, 8.45 mmol), 200 mL of acetone and 15 mL of 2 N HCl aqueous solution was refluxed for 8 h. After cooling the reaction to room temperature, the solvent was removed by distillation and the title compound was obtained as a greenish-brown powder without any other purification (2.71 g, 98%). R_f (silica gel): 0.55 (9:1 DCM/MeOH). M_p: > 200 °C.

^{1}H-NMR (600 MHz, DMSO-d$_6$, RT): δ 7.87-7.88 (m, 2H, Ar-H), 7.13-7.14 (d, *J* = 8.9 Hz, 1H, Ar-H), 5.61 (s, 1H, -CH=), 3.90-3.94 (q, J = 7.1 Hz, 2H, -CH_2-), 1.57 (s, 6H, -CH_3), 1.19-1.22 (t, *J* = 7.1 Hz, 3H, -CH_3) ppm.

^{13}C-NMR (151 MHz, DMSO-d$_6$, RT): δ 192.81, 192.53, 187.28, 174.01, 167.27, 164.21, 146.31, 140.24, 130.42, 123.74, 122.91, 107.80, 83.03, 46.46, 37.16, 26.71, 11.07 ppm.

MS (ESI$^-$, MeOH + NH$_4$OH): *m/z* 326.52 $[M]^-$; calculated for $C_{18}H_{17}NO_5$: 327.11.

UV-Vis (EtOH): λ_{max} (ε) = 285 (*10551*), 424 (*74373*) nm.

Fluorescence (EtOH, λ_{exc} 405 nm): 463 nm. **ϕ:** < 1%.

IR-Spectrum (cm^{-1}, ATR): 3455 *ν*(O–H), 2970 *ν*(C–H aliphatic), 1770 *ν*(C═O), 1660 *ν*(C═O), 1505, 1360, 1295, 1190 *δ*(O–H), 1095, 1060, 930, 825, 770.

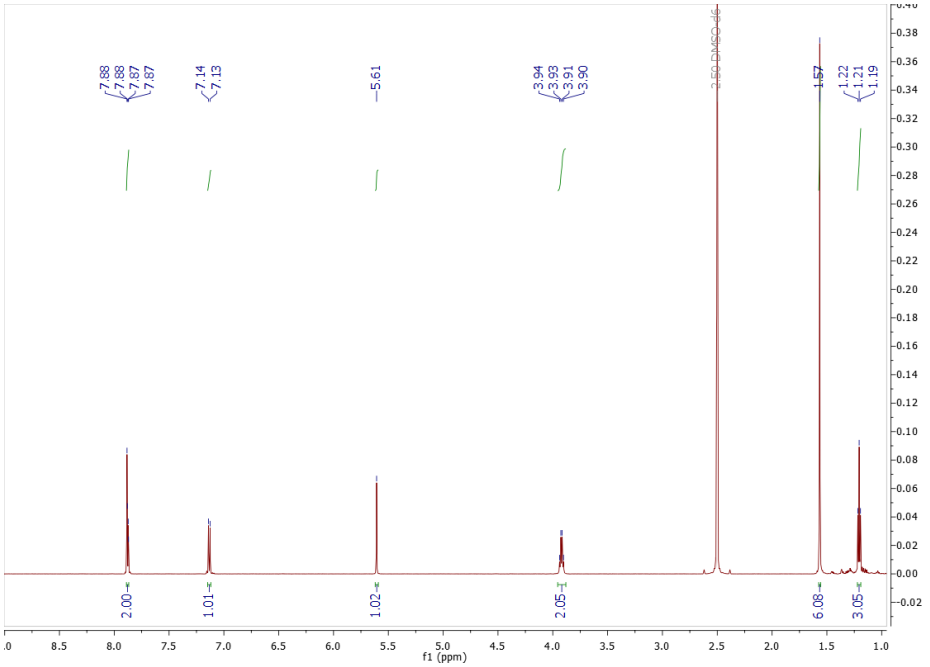

Figure 170 – ^{1}H-NMR in DMSO-d$_6$ of **323**.

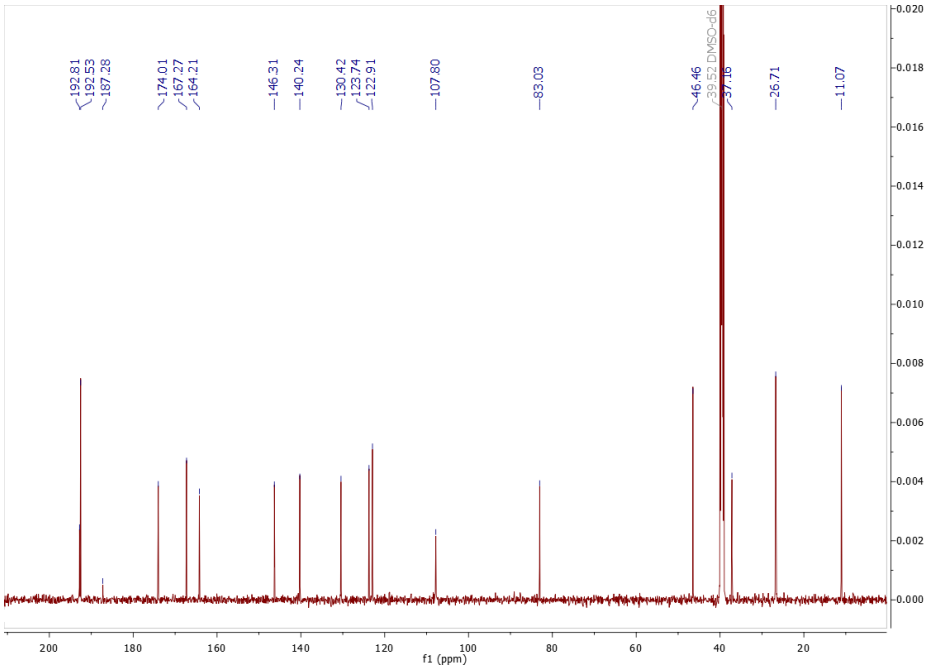

Figure 171 – ^{13}C-NMR in DMSO-d$_6$ of **323**.

1.7. General Synthesis of Carboxy Benzoindoline Emisquarates

Carboxy-benzoindoline emisquarates **330**, **331** and **332** were synthetized according to this general procedure.

A mixture of carboxy-benzoindolium iodide salts **330**-**332** (2.0 g, 1.0 eq.), 3,4-diethoxy-3- cyclobutene-1,2-dione (1.0 eq.) and 50 mL a solution ethanol/triethylamine (93:7) was refluxed for 12 h. After cooling the reaction to room temperature, the solvent was removed by evaporation under vacuum. The resulting solid was treated with saturated aqueous solution of citric acid and the mixture was extracted with dichloromethane. The organic layer was separated, dried over sodium sulphate and the solvent evaporated under vacuum. The desired product was purified by flash chromatography on silica gel using DCM/MeOH (99:1) as eluent.

Compound 330

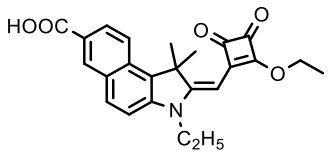

The product was isolated as a dark orange powder (1.62 g, 82%). R_f (silica gel): 0.20 (98:2 DCM/MeOH). M_p: > 200 °C.

^{1}H-NMR (600 MHz, DMSO-d$_6$, RT): δ 8.63 (d, *J* = 1.4 Hz, 1H, Ar-H), 8.23-8.25 (d, *J* = 8.9 Hz, 1H, Ar-H), 8.17-8.18 (d, *J* = 8.9 Hz, 1H, Ar-H), 8.00-8.01 (dd, *J* = 8,9 Hz, *J* = 1.6 Hz, 1H, Ar-H), 7.66-7.68 (d, *J* = 8.9 Hz, 1H, Ar-H), 5.44 (s, 1H, -CH=), 4.83-4.87 (q, *J* = 7.1 Hz, 2H, -CH_2-), 4.07-4.11 (q, J = 7.1 Hz, 2H, -CH_2-), 1.81 (s, 6H, -CH_3), 1.46-1.49 (t, *J* = 7.1 Hz, 3H, -CH_3), 1.24-1.27 (t, J = 7.2 Hz, 3H, -CH_3) ppm.

^{13}C-NMR (151 MHz, DMSO-d$_6$, RT): δ 192.20, 187.91, 186.59, 172.23, 168.62, 167.33, 141.56, 132.44, 131.53, 131.47, 129.79, 129.34, 126.50, 125.30, 122.22, 114.44, 80.76, 69.88, 48.96, 37.39, 26.13, 15.71, 11.50 ppm.

MS (ESI$^-$, MeOH + NH$_4$OH): *m/z* 404.21 $[M]^-$; calculated for $C_{24}H_{23}NO_5$: 405.16.

UV-Vis (EtOH): λ_{max} (ε) = 315 (*19057*), 371 (*9691*), 445 (*76326*) nm.

Fluorescence (EtOH, λ_{exc} 425 nm): 486 nm. **ϕ:** < 1%.

IR-Spectrum (cm^{-1}, ATR): 2970 *v*(C–H aliphatic), 2935 *v*(C–H aliphatic), 1785 *v*(C═O), 1680 *v*(C═O), 1550, 1510, 1460, 1365, 1335, 1295, 1250 *δ*(O–H), 1200, 1090, 1020, 975, 905, 875, 815, 750.

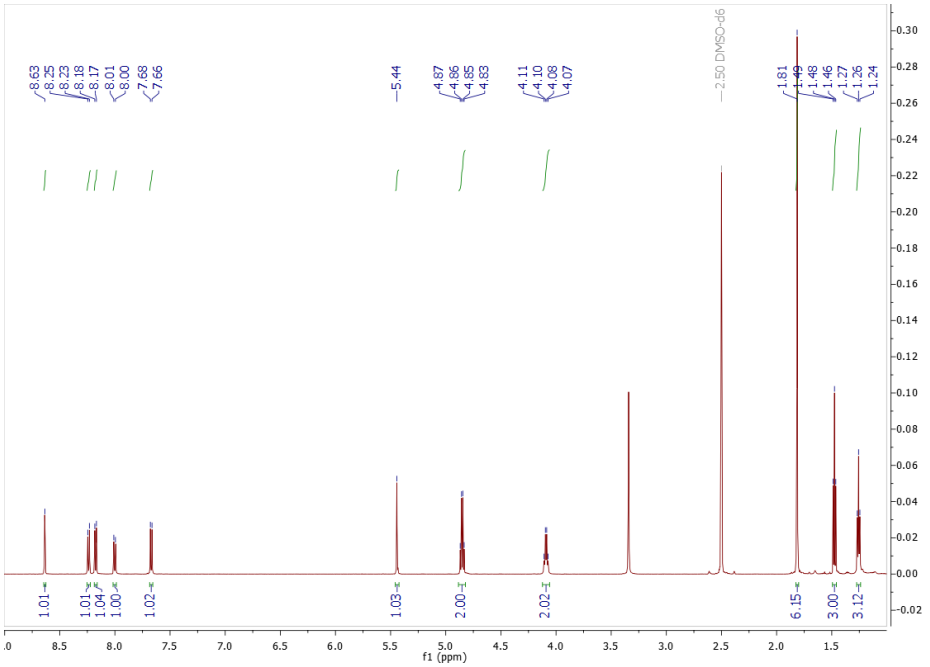

Figure 172 – ^{1}H-NMR in DMSO-d$_6$ of **330**.

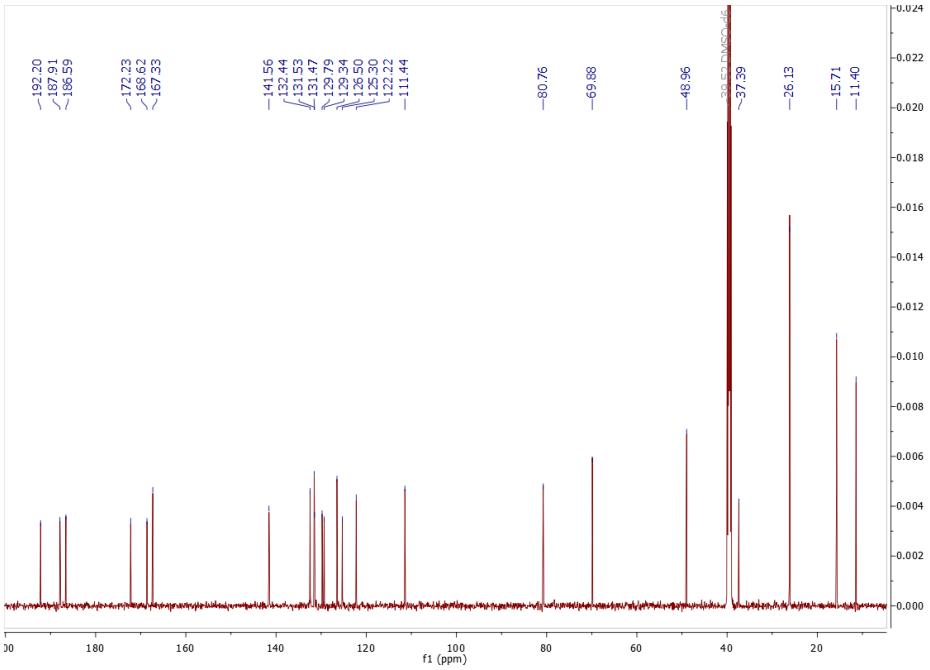

Figure 173 – ^{13}C-NMR in DMSO-d$_6$ of **330**.

Compound 331

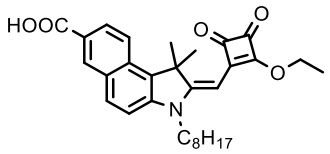

The product was isolated as a dark orange powder (1.47 g, 74%). R_f (silica gel): 0.65 (9:1 DCM/MeOH). M_p: > 200 °C.

^{1}H-NMR (600 MHz, DMSO-d$_6$, RT): δ 8.63 (d, *J* = 1.7 Hz, 1H, Ar-H), 8.23-8.24 (d, *J* = 9.0 Hz, 1H, Ar-H), 8.15-8.17 (d, *J* = 8.8 Hz, 1H, Ar-H), 8.00-8.01 (dd, *J* = 8.9 Hz, *J* = 1.7 Hz, 1H, Ar-H), 7.66-7.67 (d, *J* = 8.9 Hz, 1H, Ar-H), 5.45 (s, 1H, -CH=), 4.83-4.87 (q, *J* = 7.1 Hz, 2H, -CH_2-), 4.03-4.05 (t, *J* = 7.2 Hz, 2H, -CH_2-), 1.81 (s, 6H, -CH_3), 1.67-1.72 (m, 2H, -CH_2-), 1.46-1.48 (t, *J* = 7.1 Hz, 3H, -CH_3), 1.34-1.39 (m, 2H, -CH_2-), 1.29-1.34 (m, 2H, -CH_2-), 1.18-1.26 (m, 6H, -CH_2-), 0.81-0.83 (t, *J* = 7.1 Hz, 3H, -CH_3) ppm.

^{13}C-NMR (151 MHz, DMSO-d$_6$, RT): δ 192.19, 187.90, 186.56, 172.12, 168.98, 167.35, 142.07, 132.41, 131.44, 131.29, 129.75, 129.30, 126.52, 125.38, 122.22, 111.63, 81.10, 69.86, 54.90, 48.91, 42.26, 31.10, 28.54, 28.50, 26.20, 26.02, 25.98, 21.99, 15.67, 13.88 ppm.

MS (ESI$^-$, MeOH + NH$_4$OH): *m/z* 488.53 $[M]^-$; calculated for $C_{30}H_{35}NO_5$: 489.25.

UV-Vis (EtOH): λ_{max} (*ε*) = 316 (*19445*), 371 (*9249*), 446 (*77937*) nm.

Fluorescence (EtOH, λ_{exc} 430 nm): 487 nm. **ϕ:** < 1%.

IR-Spectrum (cm^{-1}, ATR): 2925 *ν*(C–H aliphatic), 2850 *ν*(C–H aliphatic), 1765 *ν*(C═O), 1710 *ν*(C═O), 1675 *ν*(C═O), 1530, 1470, 1420, 1260 *δ*(O–H), 1200, 1170, 1095, 1040, 940, 915, 820, 750, 730.

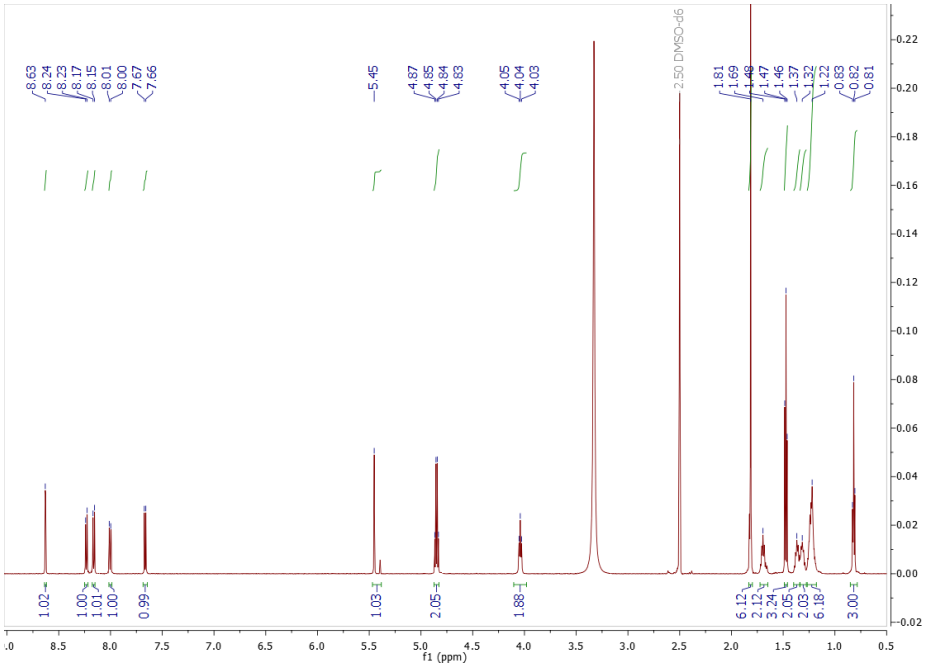

Figure 174 – ^{1}H-NMR in DMSO-d$_6$ of **331**.

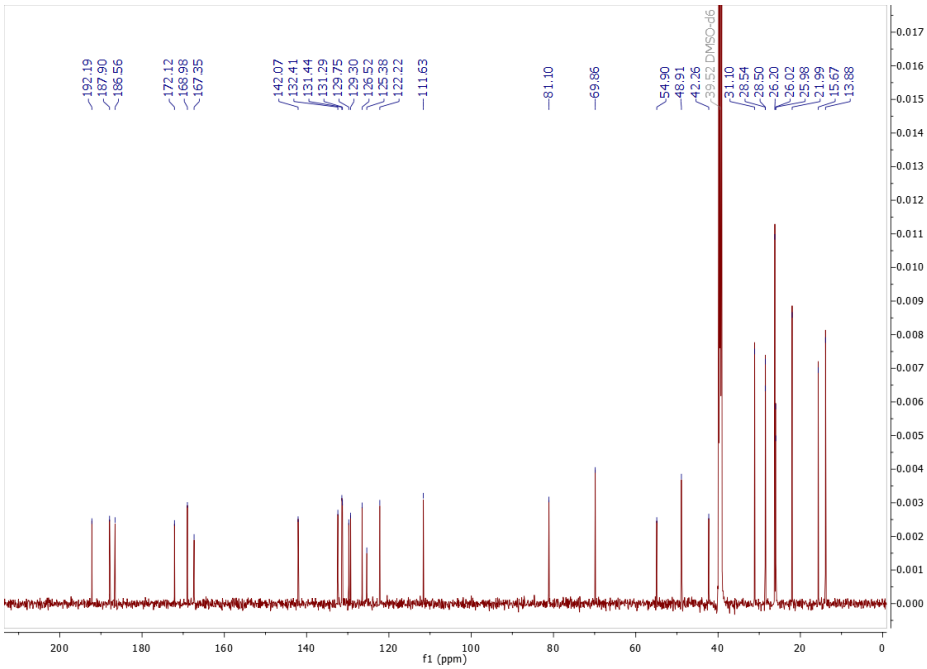

Figure 175 – ^{13}C-NMR in DMSO-d$_6$ of **331**.

Compound 332

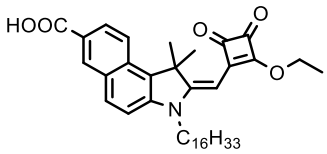

The product was isolated as an orange powder (1.55 g, 78%). R_f (silica gel): 0.25 (95:5 DCM/MeOH). M_p: 193-195 °C (decomposition).

^{1}H-NMR (600 MHz, DMSO-d$_6$, RT): δ 8.63 (d, *J* = 1.3 Hz, 1H, Ar-H), 8.23-8.24 (d, *J* = 9.0 Hz, 1H, Ar-H), 8.15-8.17 (d, *J* = 8.8 Hz, 1H, Ar-H), 7.99-8.01 (dd, *J* = 8.9 Hz, *J* = 1.6 Hz, 1H, Ar-H), 7.67-7.68 (d, *J* = 8.9 Hz, 1H, Ar-H), 5.45 (s, 1H, -CH=), 4.83-4.86 (q, *J* = 7.1 Hz, 2H, -CH_2-), 4.03-4.06 (t, *J* = 7.2 Hz, 2H, -CH_2-), 1.81 (s, 6H, -CH_3), 1.67-1.72 (m, 2H, -CH_2-), 1.46-1.48 (t, *J* = 7.0 Hz, 3H, -CH_3), 1.33-1.38 (m, 2H, -CH_2-), 1.28-1.32 (m, 2H, -CH_2-), 1.14-1.27 (m, 22H, -CH_2-), 0.83-0.85 (t, *J* = 7.1 Hz, 3H, -CH_3) ppm.

^{13}C-NMR (151 MHz, DMSO-d$_6$/CDCl$_3$ 2:1, RT): δ 191.88, 187.56, 186.51, 172.37, 168.86, 167.20, 141.74, 131.25, 131.16, 131.09, 129.72, 129.16, 126.31, 125.27, 121.74, 110.99, 81.10, 69.46, 54.25, 48.78, 42.32, 31.21, 28.95, 28.92, 28.87, 28.79, 28.73, 28.62, 28.56, 26.11, 26.08, 25.94, 22.00, 15.53, 13.75 ppm.

MS (ESI$^-$, MeOH + NH$_4$OH): *m/z* 600.61 $[M]^-$; calculated for $C_{38}H_{51}NO_5$: 601.38.

UV-Vis (EtOH): λ_{max} (*ε*) = 314 (*17770*), 371 (*8500*), 446 (*73561*) nm.

Fluorescence (EtOH, λ_{exc} 425 nm): 487 nm. **ϕ:** < 1%.

IR-Spectrum (cm^{-1}, ATR): 2920 *ν*(C–H aliphatic), 2850 *ν*(C–H aliphatic), 1770 *ν*(C═O), 1710 *ν*(C═O), 1670 *ν*(C═O), 1530, 1470, 1335, 1280 *δ*(O–H), 1200, 1045, 945, 820, 755, 730.

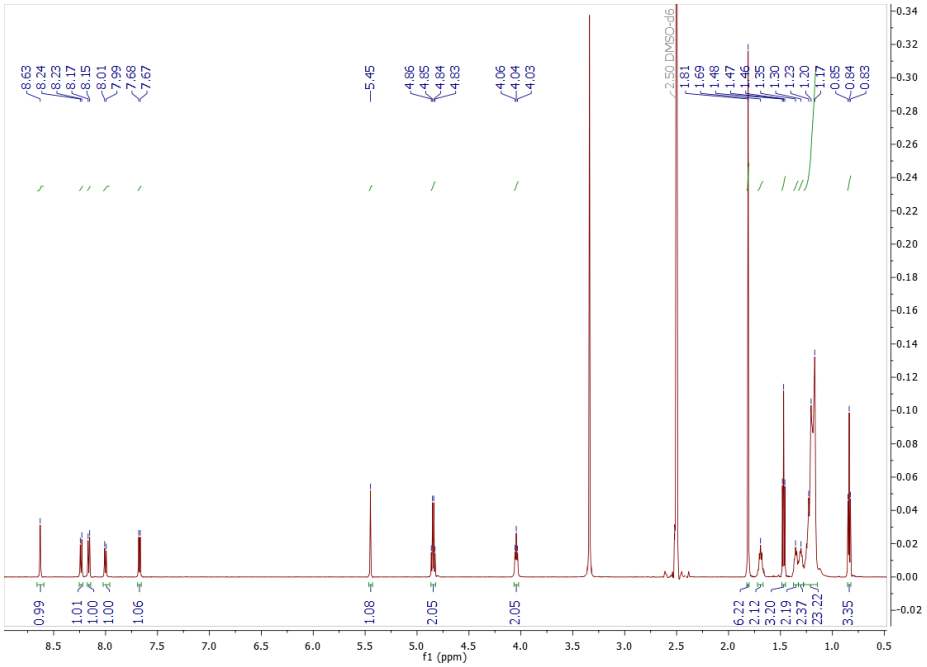

Figure 176 – ^{1}H-NMR in DMSO-d$_6$ of **332**.

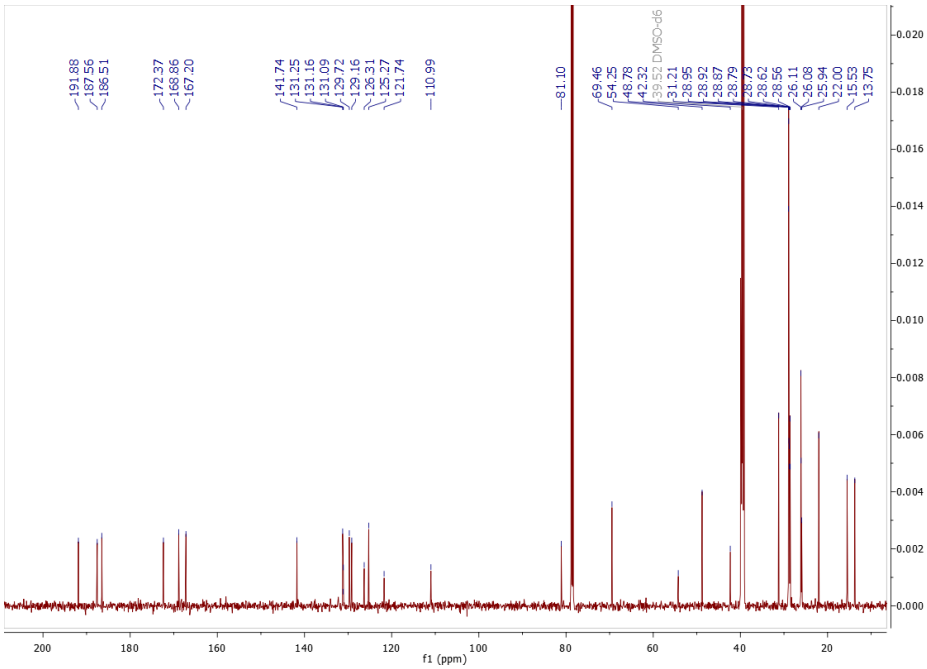

Figure 177 – ^{13}C-NMR in DMSO-d$_6$/CDCl$_3$ (2:1) of **332**.

1.8. General Synthesis of Carboxy Benzoindoline Emisquaraines

Carboxy-benzoindoline emisquaraines **333**, **334** and **335** were synthetized according to this general procedure.

A mixture of carboxy-benzoindoline emisquarate (1.0 g, 1.0 eq.), 60 mL of acetone and 5 mL of 2 N HCl aqueous solution was refluxed for 8 h. After cooling the reaction to room temperature, the solvent was removed by distillation and the product was obtained without any other purification.

Compound 333

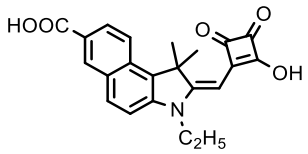

The product was isolated as a dark-brown powder (0.84 g, 90%). R_f (silica gel): 0.20 (9:1 DCM/MeOH). M_p: > 200 °C.

^{1}H-NMR (600 MHz, DMSO-d$_6$, RT): δ 8.60 (d, *J* = 1.1 Hz, 1H, Ar-H), 8.21-8.22 (d, *J* = 8.9 Hz, 1H, Ar-H), 8.13-8.14 (d, *J* = 8.8 Hz, 1H, Ar-H), 7.96-7.98 (dd, *J* = 8.8 Hz, *J* = 1.5 Hz, 1H, Ar-H), 7.60-7.61 (d, *J* = 8.8 Hz, 1H, Ar-H), 5.62 (s, 1H, -CH=), 4.02-4.06 (q, *J* = 7.1 Hz, 2H, -CH_2-), 1.82 (s, 6H, -CH_3), 1.24-1.27 (t, J = 7.2 Hz, 3H, -CH_3) ppm.

^{13}C-NMR (151 MHz, DMSO-d$_6$, RT): δ 192.10, 191.55, 173.63, 167.39, 166.38, 141.99, 132.48, 131.45, 130.86, 130.00, 129.02, 126.40, 124.89, 122.10, 111.21, 81.66, 48.55, 37.18, 30.69, 26.27, 11.39 ppm.

MS (ESI$^-$, MeOH + NH$_4$OH): *m/z* 376.21 $[M]^-$; calculated for $C_{22}H_{19}NO_5$: 377.13.

UV-Vis (EtOH): λ_{max} (ε) = 296 (*12479*), 386 (*15387*), 448 (*53427*) nm.

Fluorescence (EtOH, λ_{exc} 430 nm): 484 nm. **ϕ:** < 1%.

IR-Spectrum (cm^{-1}, ATR): 2970 *ν*(C–H aliphatic), 2860 *ν*(C–H aliphatic), 1765 *ν*(C═O), 1675 *ν*(C═O), 1615, 1530, 1505, 1445, 1295, 1250, 1200 *δ*(O–H), 1130, 910, 785, 755.

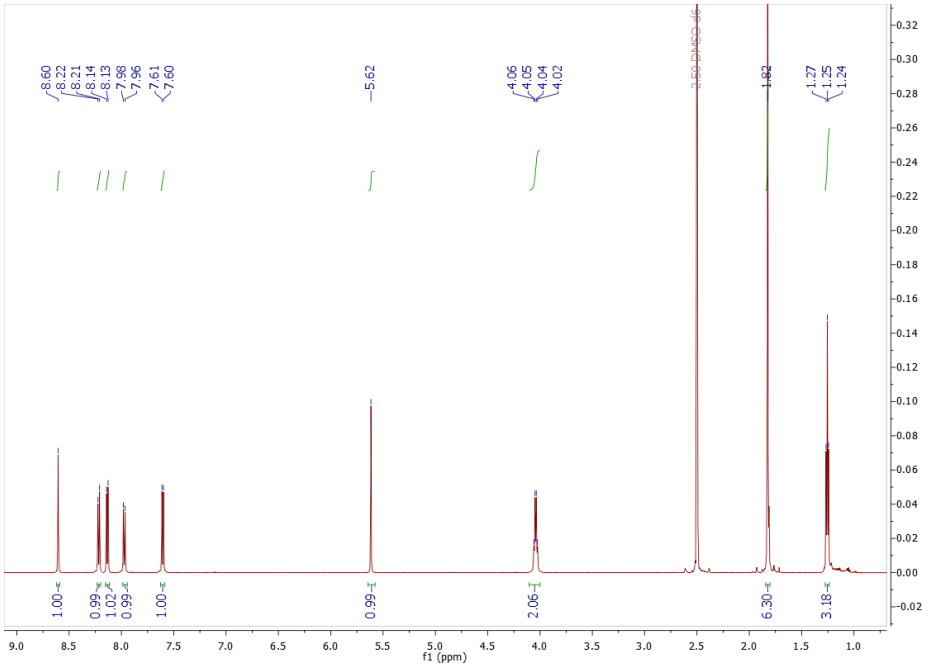

Figure 178 – ^{1}H-NMR in DMSO-d$_6$ of **333**.

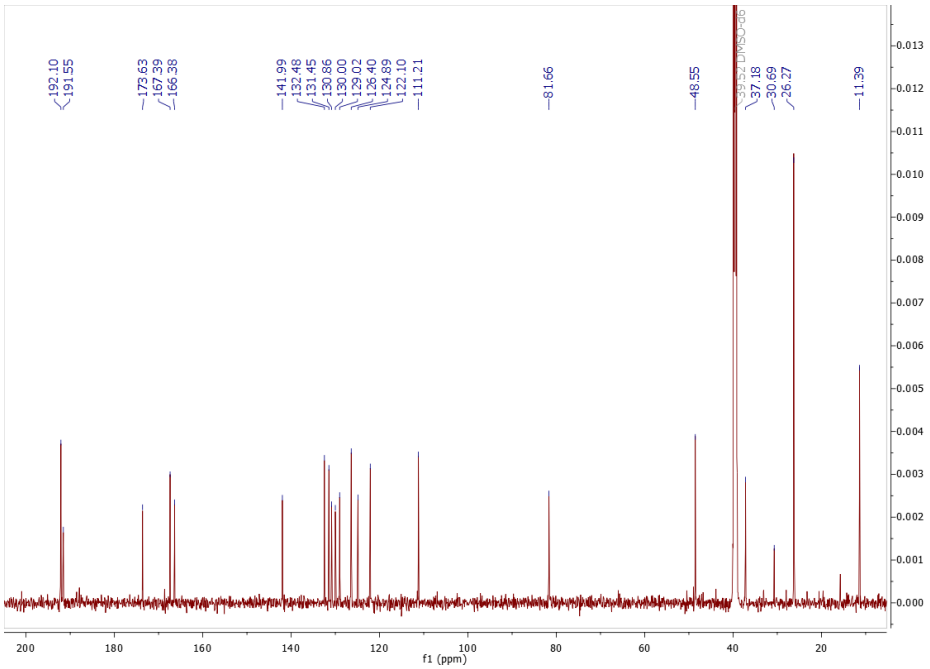

Figure 179 – ^{13}C-NMR in DMSO-d$_6$ of **333**.

Compound 334

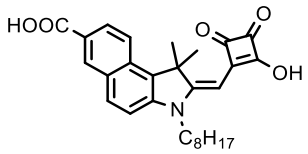

The product was isolated as a dark-brown powder (0.84 g, 89%). R_f (silica gel): 0.25 (9:1 DCM/MeOH). M_p: > 200 °C.

^{1}H-NMR (600 MHz, DMSO-d$_6$, RT): δ 8.60 (d, *J* = 1.6 Hz, 1H, Ar-H), 8.20-8.22 (d, *J* = 8.9 Hz, 1H, Ar-H), 8.11-8.13 (d, *J* = 8.8 Hz, 1H, Ar-H), 7.96-7-98 (dd, *J* = 8.9 Hz, *J* = 1.7 Hz, 1H, Ar-H), 7.59-7.60 (d, *J* = 8.9 Hz, 1H, Ar-H), 5.60 (s, 1H, -CH=), 3.97-4.00 (t, *J* = 7.4 Hz, 2H, -CH_2-), 1.82 (s, 6H, -CH_3), 1.66-1.71 (m, 2H, -CH_2-), 1.37-1.39 (m, 2H, -CH_2-), 1.29-1.34 (m, 2H, -CH_2-), 1.18-1.26 (m, 6H, -CH_2-), 0.80-0.82 (t, *J* = 7.1 Hz, 3H, -CH_3) ppm.

^{13}C-NMR (151 MHz, DMSO-d$_6$, RT): δ 192.08, 191.56, 173.54, 167.38, 166.72, 142.51, 132.45, 131.35, 130.69, 129.95, 128.98, 126.41, 124.90, 122.10, 111.42, 82.00, 48.51, 42.15, 31.12, 28.68, 28.57, 26.34, 26.14, 26.03, 22.01, 13.90 ppm.

MS (ESI$^-$, MeOH + NH$_4$OH): *m/z* 460.57 $[M]^-$; calculated for $C_{28}H_{31}NO_5$: 461.22.

UV-Vis (EtOH): λ_{max} (ε) = 290 (*14969*), 387 (*16584*), 449 (*57578*) nm.

Fluorescence (EtOH, λ_{exc} 430 nm): 485 nm. **ϕ:** < 1%.

IR-Spectrum (cm^{-1}, ATR): 2930 *v*(C–H aliphatic), 2855 *v*(C–H aliphatic), 1770 *v*(C═O), 1675 *v*(C═O), 1615, 1530, 1505, 1435, 1290, 1250 *δ*(O–H), 1200, 1155, 940, 910, 800.

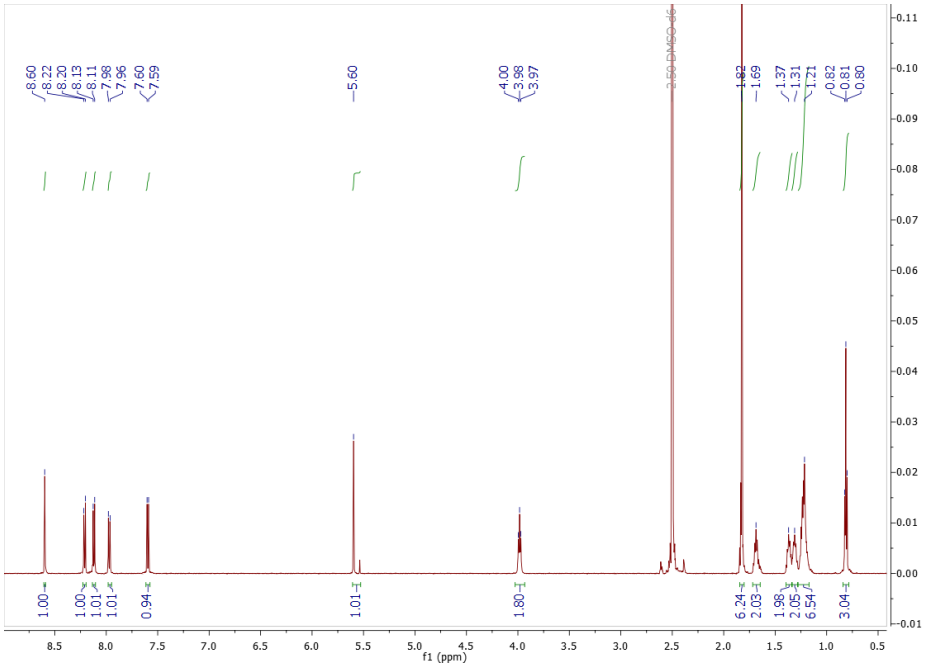

Figure 180 – ^{1}H-NMR in DMSO-d$_6$ of **334**.

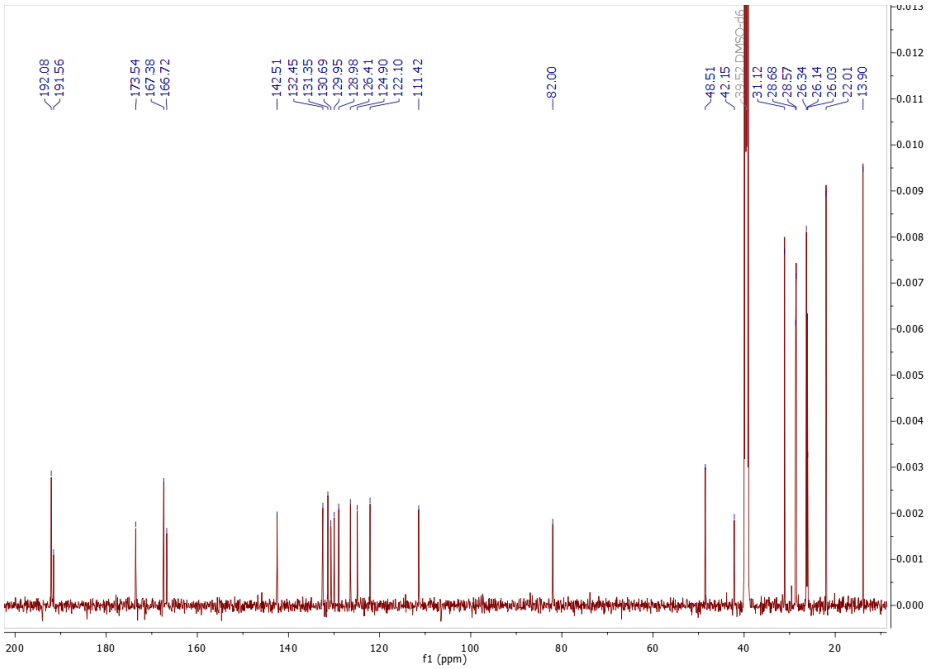

Figure 181 – ^{13}C-NMR in DMSO-d$_6$ of **334**.

Compound 335

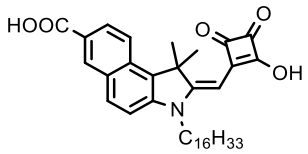

The product was isolated as a dark-brown powder (0.89 g, 93%). R_f (silica gel): 0.30 (9:1 DCM/MeOH). M_p: > 200 °C.

^{1}H-NMR (600 MHz, DMSO-d$_6$, RT): δ 8.59 (s, 1H, Ar-H), 8.19-8.21 (d, *J* = 8.9 Hz, 1H, Ar-H), 8.10-8.11 (d, *J* = 8.8 Hz, 1H, Ar-H), 7.95-7.97 (d, *J* = 9.0 Hz, 1H, Ar-H), 7.58-7.59 (d, *J* = 8.8 Hz, 1H, Ar-H), 5.61 (s, 1H, -CH=), 3.97-3.99 (br, 2H, -CH_2-), 1.82 (s, 6H, -CH_3), 1.66-1.71 (br, 2H, -CH_2-), 1.33-1.40 (br, 2H, -CH_2-), 1.27-1.31 (br, 2H, -CH_2-), 1.17-1.26 (br, 22H, -CH_2-), 0.82-0.85 (t, *J* = 6.8 Hz, 3H, -CH_3) ppm.

^{13}C-NMR (151 MHz, DMSO-d$_6$, RT): δ 192.10, 191.63, 173.55, 167.37, 166.66, 142.50, 132.44, 131.32, 130.67, 129.96, 128.98, 126.40, 124.90, 122.06, 111.36, 82.01, 48.49, 42.14, 31.27, 28.99, 28.98, 28.96, 28.91, 28.81, 28.79, 28.68, 26.33, 26.08, 26.01, 22.07, 13.91 ppm.

MS (ESI$^-$, MeOH + NH$_4$OH): *m/z* 572.50 $[M]^-$; calculated for $C_{36}H_{47}NO_5$: 573.35

UV-Vis (EtOH): λ_{max} (*ε*) = 290 (*15198*), 387 (*16943*), 450 (*57640*) nm.

Fluorescence (EtOH, λ_{exc} 430 nm): 485 nm. **ϕ:** < 1%.

IR-Spectrum (cm^{-1}, ATR): 2920 *ν*(C–H aliphatic), 2850 *ν*(C–H aliphatic), 1765 *ν*(C═O), 1675 *ν*(C═O), 1615, 1505, 1440, 1290, 1250 *δ*(O–H), 1200, 940, 910, 805, 755.

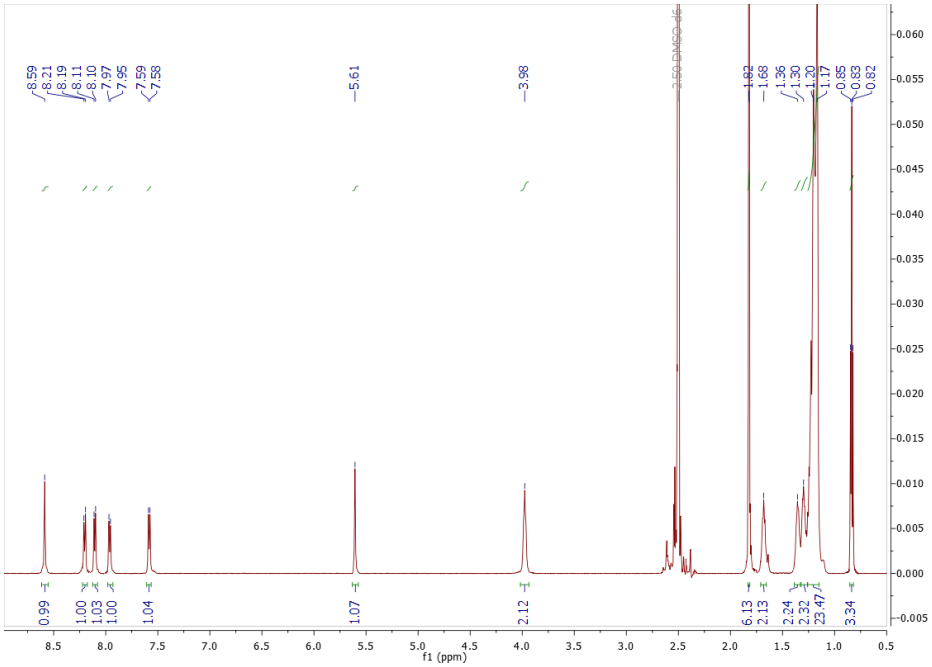

Figure 182 – ^{1}H-NMR in DMSO-d$_6$ of **335**.

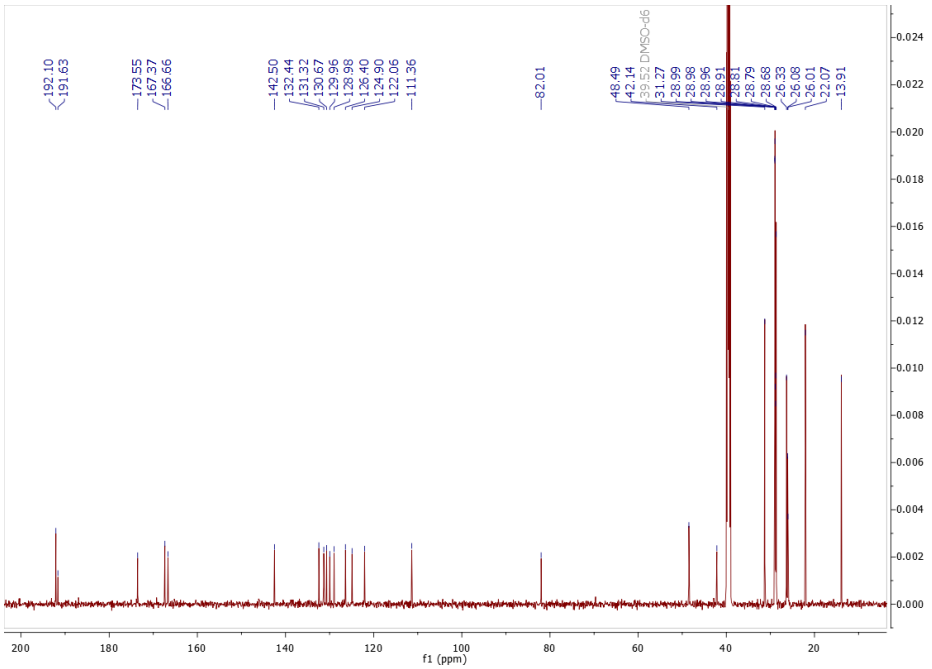

Figure 183 – ^{13}C-NMR in DMSO-d$_6$ of **335**.

1.9. General Synthesis of Mono- and Di-substituted DHPs

Mono- and di-substituted DHP were synthetized according to this general procedure.

A mixture of 1,8-diamminonaphtalene **336** (3.0 g, 18.96 mmol), ketone or aldehyde (19.90 mmol), *p*-toluene sulfonic acid (0.16 g, 0.57 mmol) in 30 mL of toluene was refluxed in a Dean-Stark apparatus for 16 hours. After cooling the reaction to room temperature, the solvent was removed and the crude material was purified by flash chromatography.

Compound 337

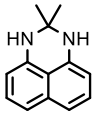

The crude was purified by flash chromatography on silica gel using DCM/*n*-hexane (8:2) as eluent. The product was isolated as a pale pink powder (2.79 g, 74%). R_f (silica gel): 0.40 (DCM). M_p: 115-117 °C.

^{1}H-NMR (600 MHz, $CDCl_3$, RT): δ 7.23-7.25 (t, *J* = 8.2 Hz, 2H, Ar-H), 7.15-7.17 (d, *J* = 8.3 Hz, 2H, Ar-H), 6.47-6.48 (dd, *J* = 7.3 Hz, *J* = 0.8 Hz, 2H, Ar-H), 4.17 (br, 2H, -NH), 1.50 (s, 6H, -CH_3) ppm.

^{13}C-NMR (151 MHz, $CDCl_3$, RT): δ 140.57, 134.95, 127.35, 117.45, 113.29, 106.29, 64.90, 29.17 ppm.

MS (ESI$^+$, MeOH): *m/z* 199.53 $[M-H]^+$; calculated for $C_{13}H_{14}N_2$: 198.12.

UV-Vis (DCM): λ_{max} (*ε*) = 336 (*14847*), 349 (*15912*) nm.

Fluorescence (DCM, λ_{exc} 330 nm): 402 nm. **ϕ:** 7%.

IR-Spectrum (cm^{-1}, ATR): 3355 *ν*(N–H), 3275 *ν*(N–H), 3040 *ν*(C–H aromatic), 2970 *ν*(C–H aliphatic), 1735, 1590 *δ*(N–H), 1495, 1420, 1400, 1375, 1360, 1215, 1200, 1160, 1065, 1030, 855, 810 *δ*(N–H), 760, 745, 705.

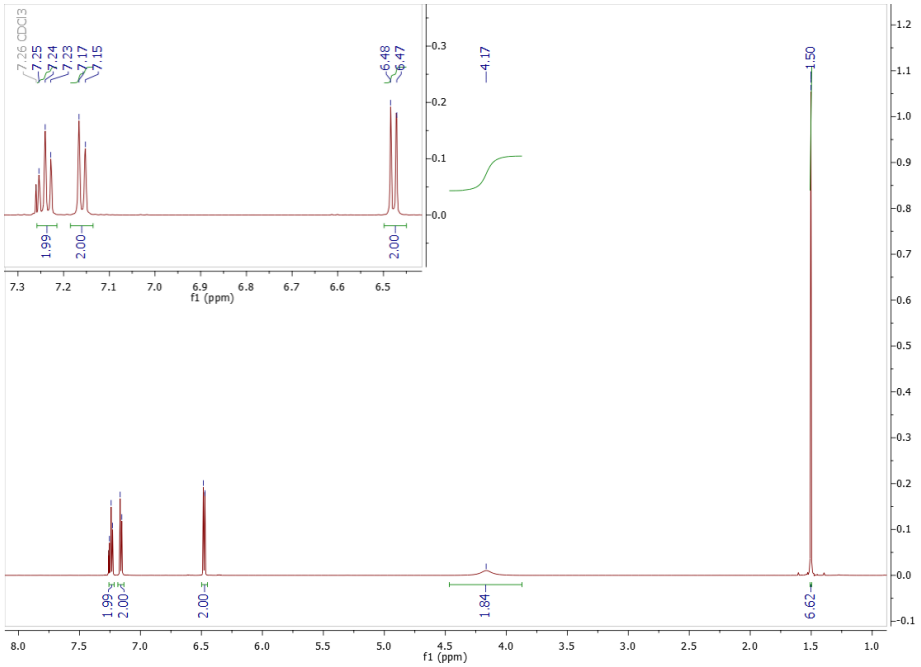

Figure 184 – ^{1}H-NMR in $CDCl_3$ of **337**.

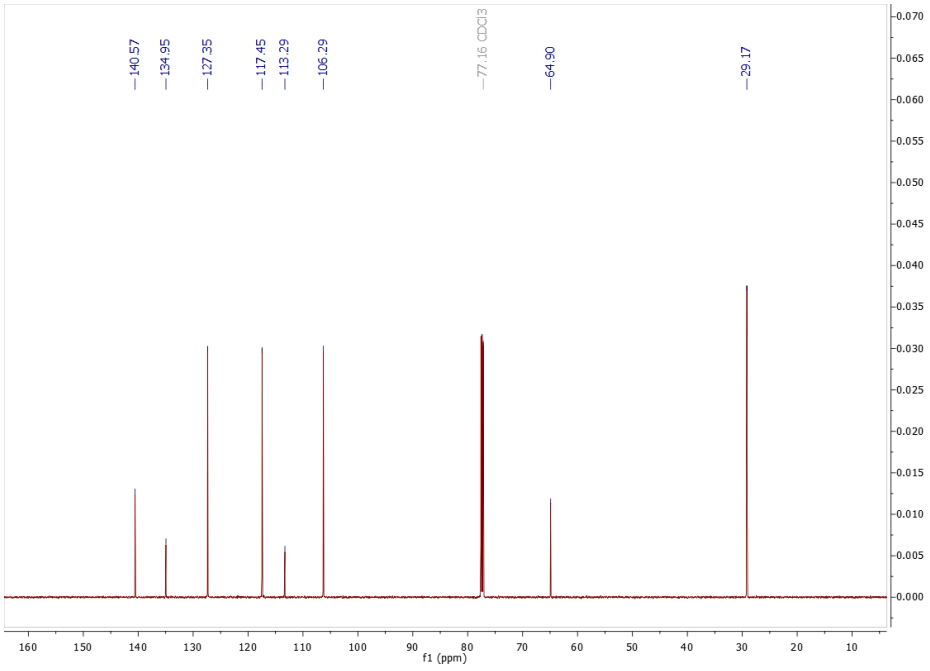

Figure 185 – ^{13}C-NMR in $CDCl_3$ of **337**.

Compound 338

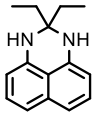

The crude was purified by flash chromatography on silica gel using DCM/*n*-hexane (1:1) as eluent. The product was isolated as a pale pink powder (3.12 g, 73%). R_f (silica gel): 0.75 (DCM). M_p: 93-95 °C.

^{1}H-NMR (600 MHz, $CDCl_3$, RT): δ 7.20-7.23 (t, *J* = 7.4 Hz, 2H, Ar-H), 7.10-7.11 (dd, *J* = 8.3 Hz, *J* = 0.6 Hz, 2H, Ar-H), 6.45-6.47 (dd, *J* = 7.4 Hz, *J* = 0.7 Hz, 2H, Ar-H), 4.24 (br, 2H, -NH), 1.72-1.76 (q, *J* = 7.4 Hz, 4H, $-CH_2-$), 0.95-0.97 (t, *J* = 7.5 Hz, 6H, $-CH_3$) ppm.

^{13}C-NMR (151 MHz, $CDCl_3$, RT): δ 140.41, 134.75, 127.20, 116.76, 113.01, 105.69, 69.06, 30.56, 7.90 ppm.

MS (ESI$^+$, MeOH): *m/z* 227.21 $[M-H]^+$; calculated for $C_{15}H_{18}N_2$: 226.15.

UV-Vis (DCM): λ_{max} (ε) = 337 (*13806*), 350 (*14848*) nm.

Fluorescence (DCM, λ_{exc} 330 nm): 418 nm. **ϕ:** 9%.

IR-Spectrum (cm^{-1}, ATR): 3370 *ν*(N–H), 3360 *ν*(N–H), 3040 *ν*(C–H aromatic), 2965 *ν*(C–H aliphatic), 2930 *ν*(C–H aliphatic), 1740, 1595 *δ*(N–H), 1455, 1425, 1370, 1160, 1120, 1035, 955, 805 *δ*(N–H), 755.

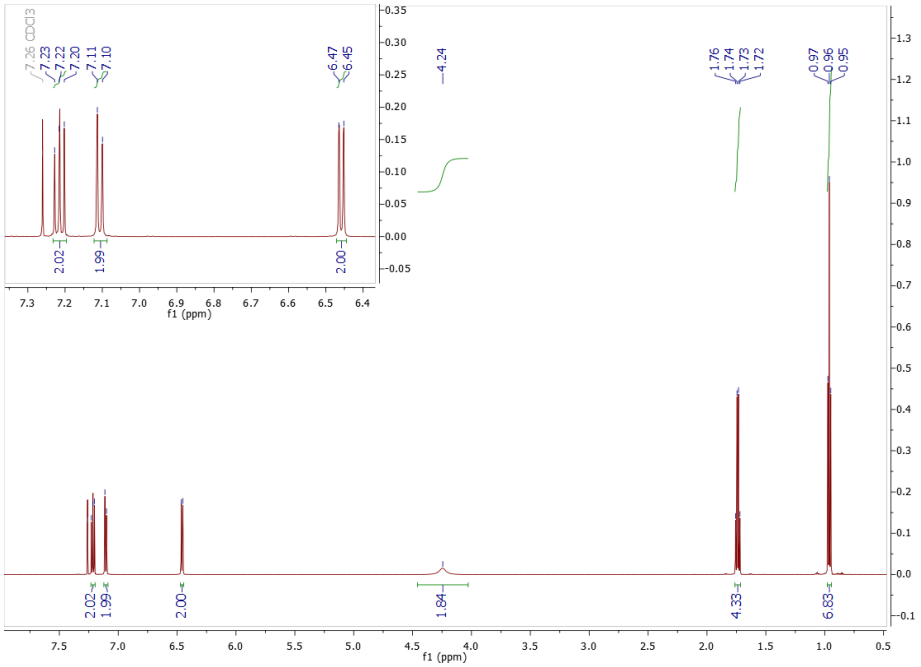

Figure 186 – ^{1}H-NMR in $CDCl_3$ of **338**.

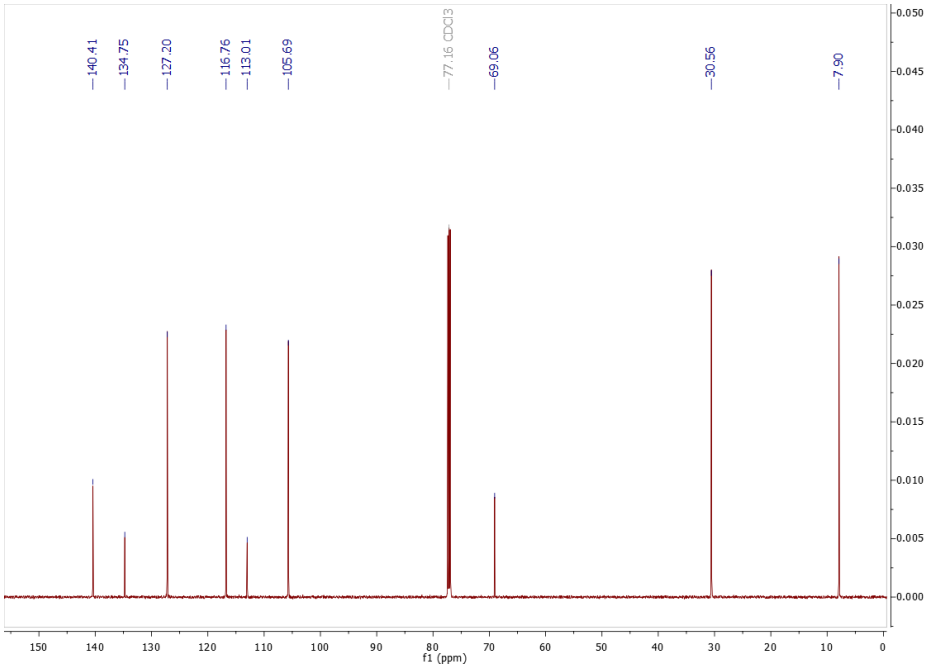

Figure 187 – ^{13}C-NMR in $CDCl_3$ of **338**.

Compound 339

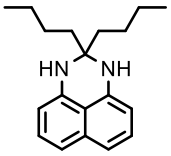

The crude was purified by flash chromatography on silica gel using *n*-hexane/DCM (8:2) as eluent. The product was isolated as a dark purple sticky oil (4.68 g, 87%). R_f (silica gel): 0.85 (DCM). M_p: < 20 °C

^{1}H-NMR (600 MHz, $CDCl_3$, RT): δ 7.20-7.23 (t, *J* = 7.4 Hz, 2H, Ar-H), 7.10-7.11 (d, *J* = 8.2 Hz, 2H, Ar-H), 6.44-6.45 (d, *J* = 7.3 Hz, 2H, Ar-H), 4.25 (br, 2H, -NH), 1.69-1.72 (m, 4H, -CH_2-), 1.36-1.41 (m, 4H, -CH_2-), 1.25-1.32 (m, 4H, -CH_2-), 0.88-0.90 (t, J = 7.3 Hz, 6H, -CH_3) ppm.

^{13}C-NMR (151 MHz, $CDCl_3$, RT): δ 140.45, 134.77, 127.21, 116.70, 112.94, 105.55, 68.66, 38.39, 25.85, 23.08, 14.24 ppm.

MS (ESI$^+$, MeOH): *m/z* 283.09 $[M-H]^+$; calculated for $C_{19}H_{26}N_2$: 282.21.

UV-Vis (DCM): λ_{max} (*ε*) = 338 (*14131*), 350 (*15275*) nm.

Fluorescence (DCM, λ_{exc} 330 nm): 415 nm. **ϕ:** < 9%.

IR-Spectrum (cm^{-1}, ATR): 3385 *ν*(N–H), 3040 *ν*(C–H aromatic), 2950 *ν*(C–H aliphatic), 2855 *ν*(C–H aliphatic), 1735, 1595 *δ*(N–H), 1490, 1410, 1375, 1160, 1085, 1040, 810 *δ*(N–H), 755, 730.

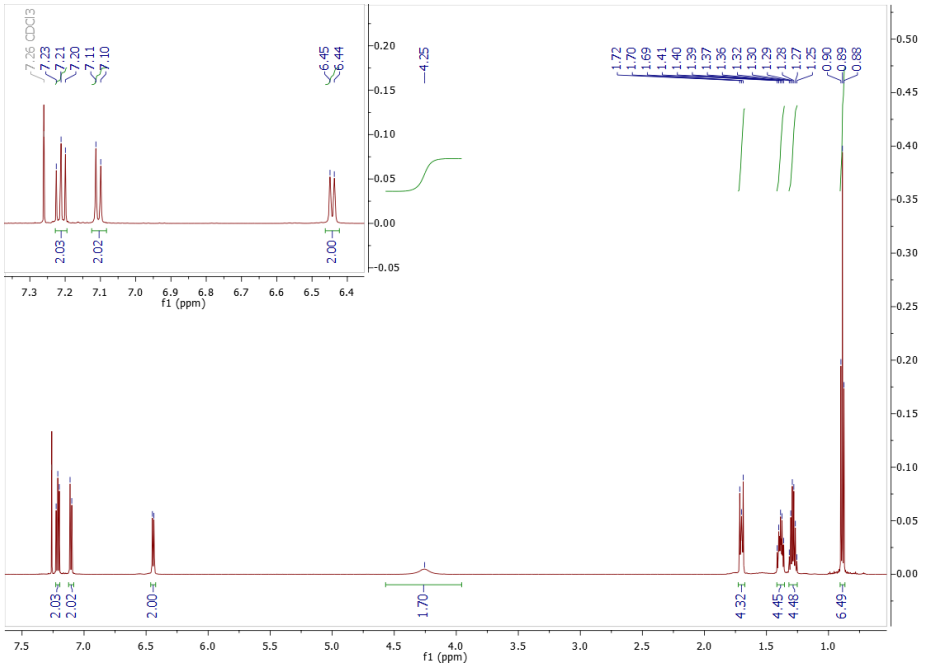

Figure 188 – ^{1}H-NMR in $CDCl_3$ of **339**.

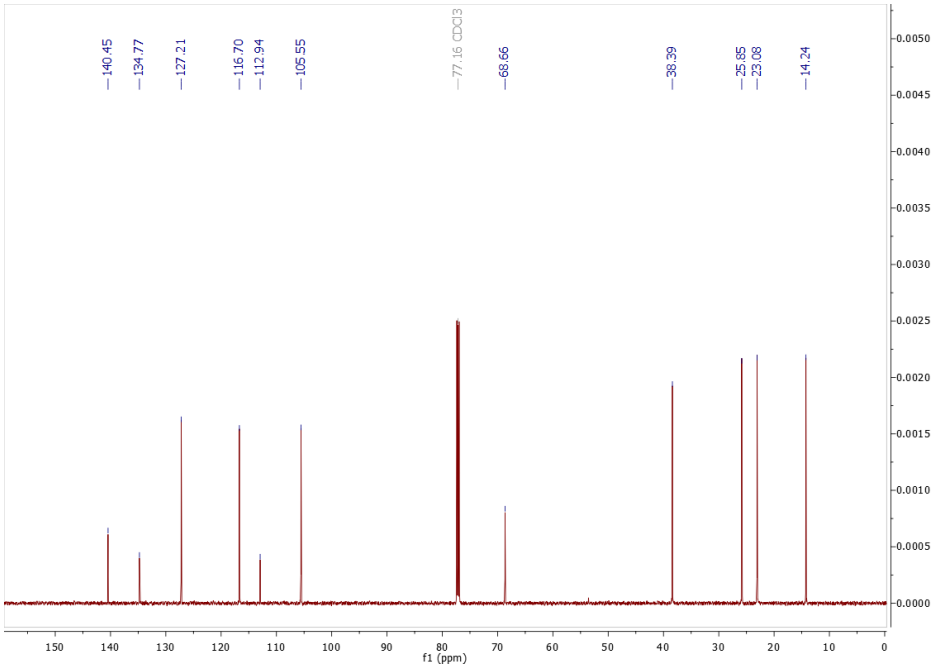

Figure 189 – ^{13}C-NMR in $CDCl_3$ of **339**.

Compound 340

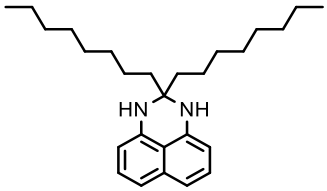

The crude was purified by flash chromatography on silica gel using *n*-hexane/DCM (9:1) as eluent. The product was isolated as a dark purple sticky oil (6.75 g, 90%). R_f (silica gel): 0.95 (DCM). M_p: < 20 °C

^{1}H-NMR (600 MHz, $CDCl_3$, RT): δ 7.21-7.23 (t, *J* = 7.4 Hz, 2H, Ar-H), 7.11-7.13 (d, *J* = 8.2 Hz, 2H, Ar-H), 6.45-6.47 (d, *J* = 7.3 Hz, 2H, Ar-H), 4.28 (br, 2H, -NH), 1.68-1.71 (m, 4H, -CH_2-), 1.38-1.41 (m, 4H, -CH_2-), 1.25-1.30 (m, 20H, -CH_2-), 0.86-0.89 (t, *J* = 7.2 Hz, 6H, -CH_3) ppm.

^{13}C-NMR (151 MHz, $CDCl_3$, RT): δ 140.49, 134.79, 127.21, 116.69, 112.97, 105.55, 68.70, 38.65, 31.98, 29.97, 29.68, 29.35, 23.65, 22.78, 14.23 ppm.

MS (ESI$^+$, MeOH): *m/z* 395.42 $[M-H]^+$; calculated for $C_{27}H_{42}N_2$: 394.33.

UV-Vis (DCM): λ_{max} (*ε*) = 339 (*12903*), 351 (*13961*) nm.

Fluorescence (DCM, λ_{exc} 330 nm): 417 nm. **ϕ:** 8%.

IR-Spectrum (cm^{-1}, ATR): 3375 *ν*(N–H), 3030 *ν*(C–H aromatic), 2920 *ν*(C–H aliphatic), 2850 *ν*(C–H aliphatic), 1735, 1600 *δ*(N–H), 1465, 1410, 1375, 1215, 1165, 1090, 810 *δ*(N–H), 755.

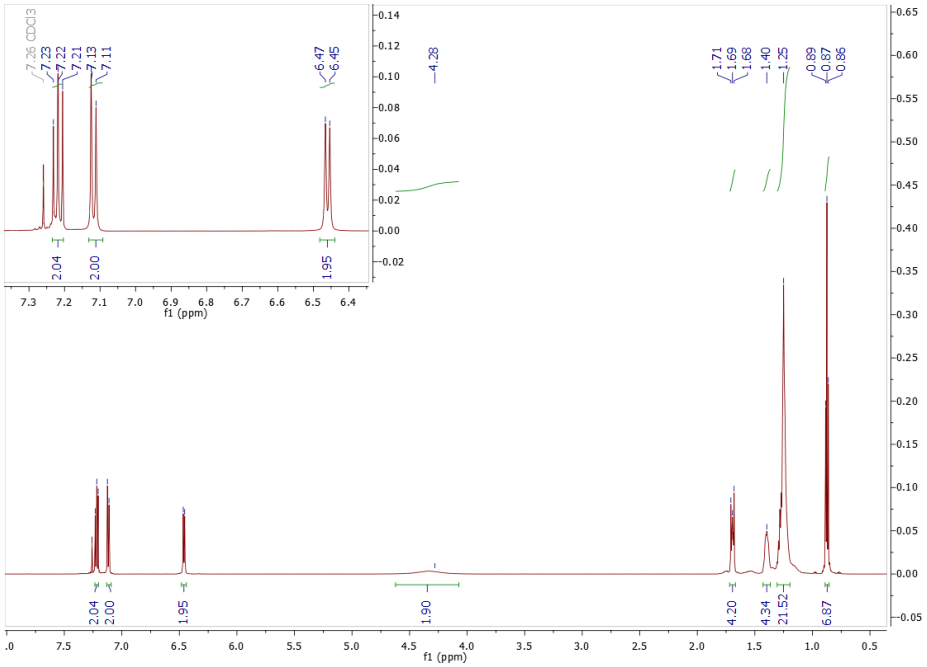

Figure 190 – ^{1}H-NMR in $CDCl_3$ of **340**.

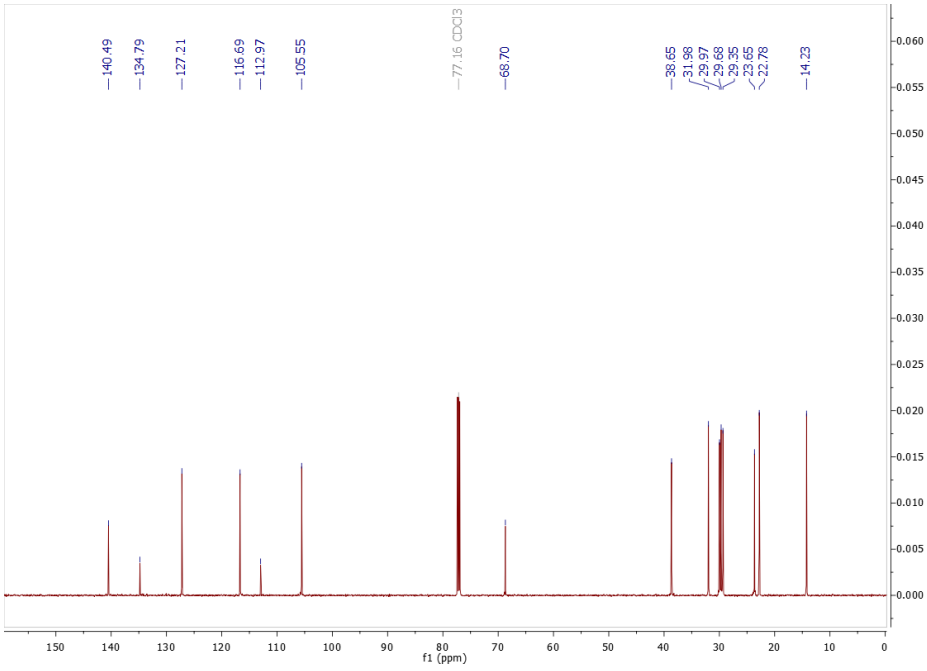

Figure 191 – ^{13}C-NMR in $CDCl_3$ of **340**.

Compound 396

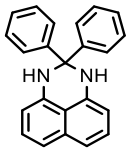

The crude was purified by flash chromatography on silica gel using DCM/*n*-hexane (1:1) as eluent. The product was isolated as a light-brown powder (3.73 g, 61%). R_f (silica gel): 0.75 (DCM). M_p: > 200 °C.

^{1}H-NMR (600 MHz, $CDCl_3$, RT): δ 7.42-7.43 (m, 4H, Ar-H), 7.22-7.27 (m, 6H, Ar-H), 7.17-7.19 (t, *J* = 7.5 Hz, 2H, Ar-H), 7.07-7.09 (d, *J* = 8.2 Hz, 2H, Ar-H), 6.52-6.54 (d, *J* = 7.3 Hz, 2H, Ar-H), 5.14 (br, 2H, -NH) ppm.

^{13}C-NMR (151 MHz, $CDCl_3$, RT): δ 145.05, 140.40, 134.70, 128.43, 128.15, 127.92, 127.14, 117.63, 113.93, 106.08, 73.31 ppm.

MS (ESI$^+$, MeOH): *m/z* 323.42 $[M-H]^+$; calculated for $C_{23}H_{18}N_2$: 322.15.

UV-Vis (DCM): λ_{max} (ε) = 337 (*14896*), 351 (*15259*) nm.

Fluorescence (DCM, λ_{exc} 330 nm): 414 nm. **ϕ:** 6%.

IR-Spectrum (cm^{-1}, ATR): 3390 *ν*(N–H), 3370 *ν*(N–H), 3025 *ν*(C–H aromatic), 2970 *ν*(C–H aliphatic), 1740, 1595 *δ*(N–H), 1475, 1445, 1400, 1215, 1165, 1070, 980, 810 *δ*(N–H), 790, 755, 700.

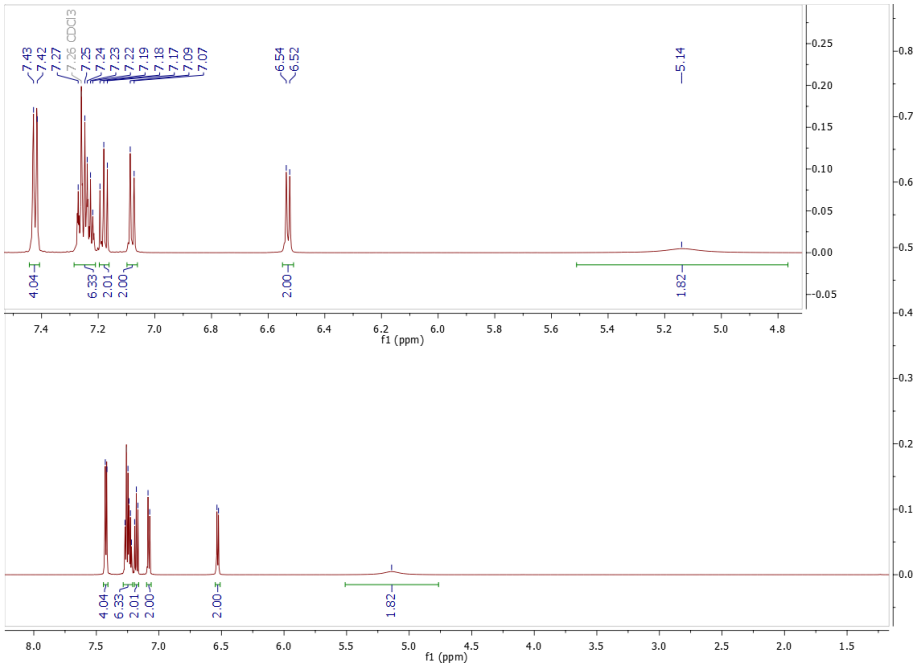

Figure 192 – ^{1}H-NMR in $CDCl_3$ of **396**.

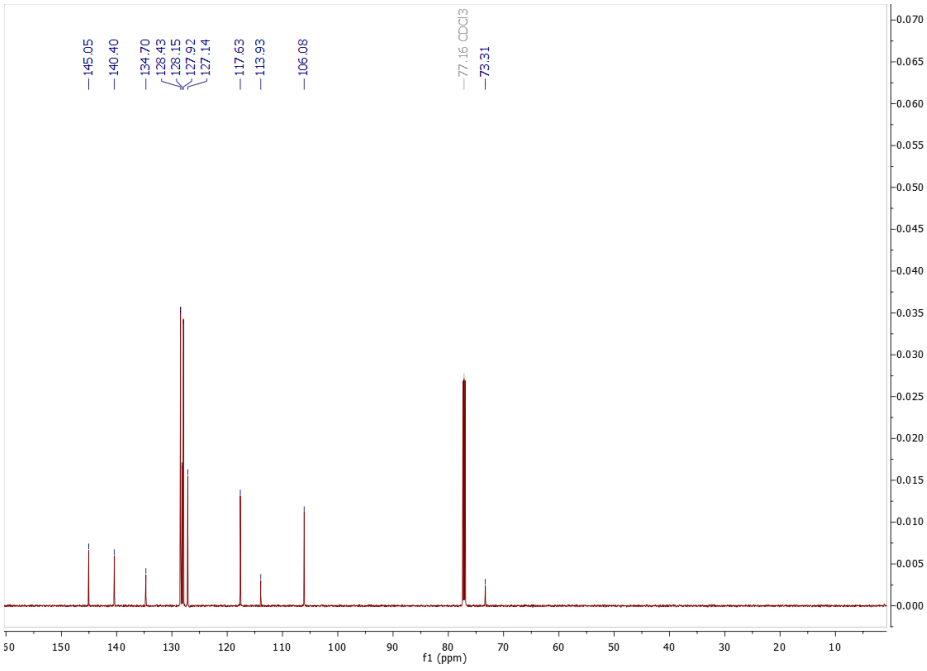

Figure 193 – ^{13}C-NMR in $CDCl_3$ of **396**.

Compound 383

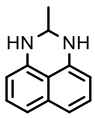

The crude was purified by flash chromatography on silica gel using DCM/*n*-hexane (7:3) as eluent. The product was isolated as a dark-brown powder (1.75 g, 50%). R_f (silica gel): 0.55 (95:5 DCM/MeOH). M_p: 71-73 °C.

^{1}H-NMR (600 MHz, DMSO-d$_6$, RT): δ 7.10-7.13 (t, *J* = 7.6 Hz, 2H, Ar-H), 6.92-6.94 (dd, *J* = 7.7 Hz, *J* = 0.7 Hz, 2H, Ar-H), 6.42 (s, 2H, -NH), 6.39-6.40 (dd, *J* = 7.4 Hz, *J* = 0.7 Hz, 2H, Ar-H), 4.42-4.44 (q, *J* = 5.6 Hz, 1H, -CH-), 1.34-1.35 (d, *J* = 5.6 Hz, 3H, -CH_3) ppm.

^{13}C-NMR (151 MHz, DMSO-d$_6$, RT): δ 143.43, 134.52, 126.80, 115.00, 112.68, 103.93, 59.85, 21.47 ppm.

MS (ESI$^+$, MeOH): *m/z* 185.21 $[M-H]^+$; calculated for $C_{12}H_{12}N_2$: 184.10.

UV-Vis (DCM): λ_{max} (ε) = 333 (*12564*), 347 (*12975*) nm.

Fluorescence (DCM, λ_{exc} 325 nm): 400 nm. **ϕ:** 6%.

IR-Spectrum (cm^{-1}, ATR): 3360 *ν*(N–H), 3325 *ν*(N–H), 3045 *ν*(C–H aromatic), 2970 *ν*(C–H aliphatic), 1740, 1595 *δ*(N–H), 1410, 1375, 1265, 1165, 1130, 1080, 1030, 810 *δ*(N–H), 755.

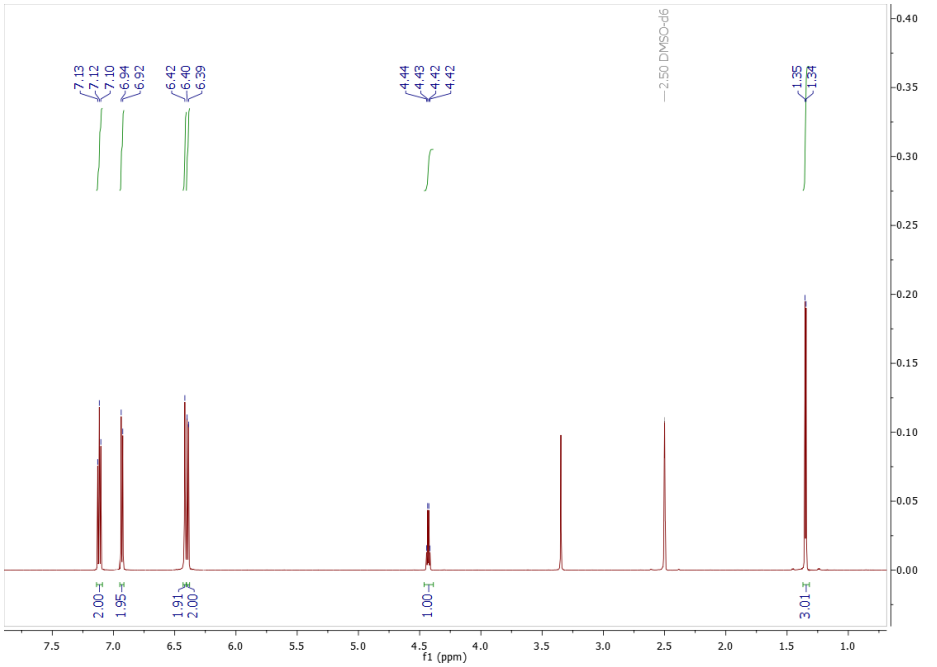

Figure 194 – ^{1}H-NMR in DMSO-d$_6$ of **383**.

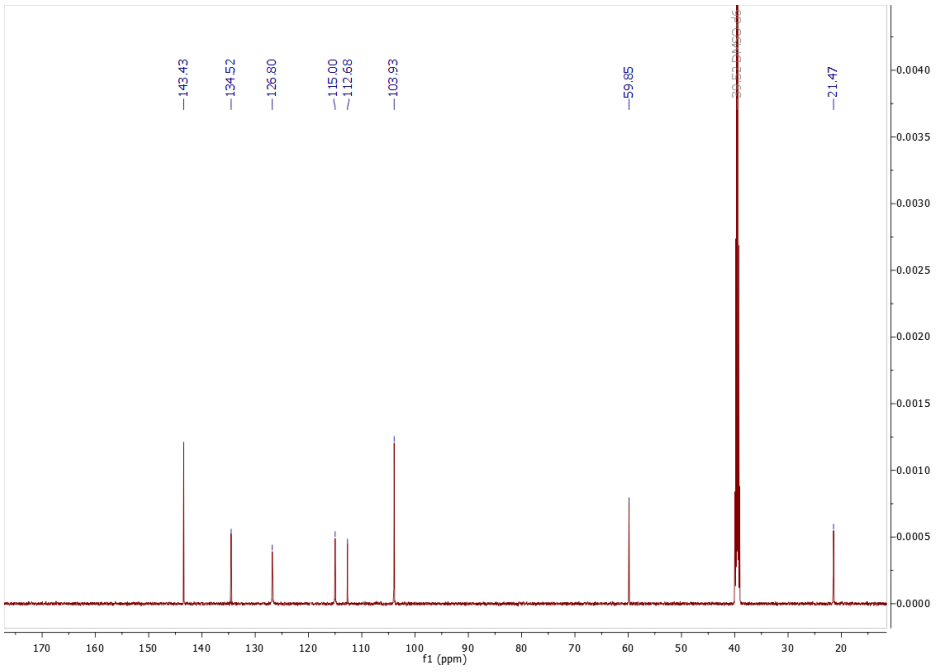

Figure 195 – ^{13}C-NMR in DMSO-d$_6$ of **383**.

Compound 394

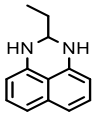

The crude was purified by flash chromatography on silica gel using dichloromethane as eluent. The product was isolated as a brown sticky oil (2.18 g, 58%). R_f (silica gel): 0.85 (95:5 DCM/MeOH). M_p: < 20 °C.

^{1}H-NMR (600 MHz, $CDCl_3$, RT): δ 7.23-7.25 (t, *J* = 7.2 Hz, 2H, Ar-H), 7.17-7.19 (dd, *J* = 8.3 Hz, *J* = 0.9 Hz, 2H, Ar-H), 6.52-6.53 (dd, *J* = 7.3 Hz, *J* = 1.0 Hz, 2H, Ar-H), 4.43-4.45 (t, *J* = 5.7 Hz, 1H, -CH-), 4.36 (br, 2H, -NH), 1.78-1.83 (m, 2H, $-CH_2-$), 1.10-1.13 (t, J = 7.6 Hz, 3H, $-CH_3$) ppm.

^{13}C-NMR (151 MHz, $CDCl_3$, RT): δ 142.06, 135.06, 126.97, 117.75, 114.10, 106.02, 66.03, 28.91, 8.80 ppm.

MS (ESI$^+$, MeOH): *m/z* 199.23 $[M-H]^+$; calculated for $C_{12}H_{12}N_2$: 198.12.

UV-Vis (DCM): λ_{max} (ε) = 334 (*13167*), 347 (*13882*) nm.

Fluorescence (DCM, λ_{exc} 325 nm): 400 nm. **ϕ:** 5%.

IR-Spectrum (cm^{-1}, ATR): 3360 *ν*(N–H), 3035 *ν*(C–H aromatic), 2960 *ν*(C–H aliphatic), 1735, 1595 *δ*(N–H), 1415, 1375, 1260, 1160, 1080, 1035, 810 *δ*(N–H), 755.

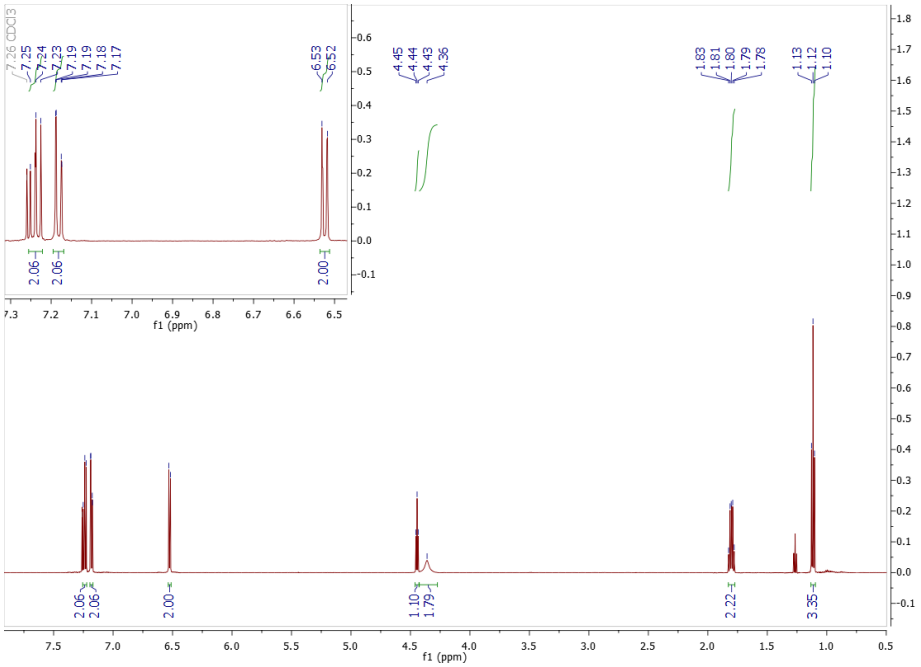

Figure 196 – ^{1}H-NMR in $CDCl_3$ of **394**.

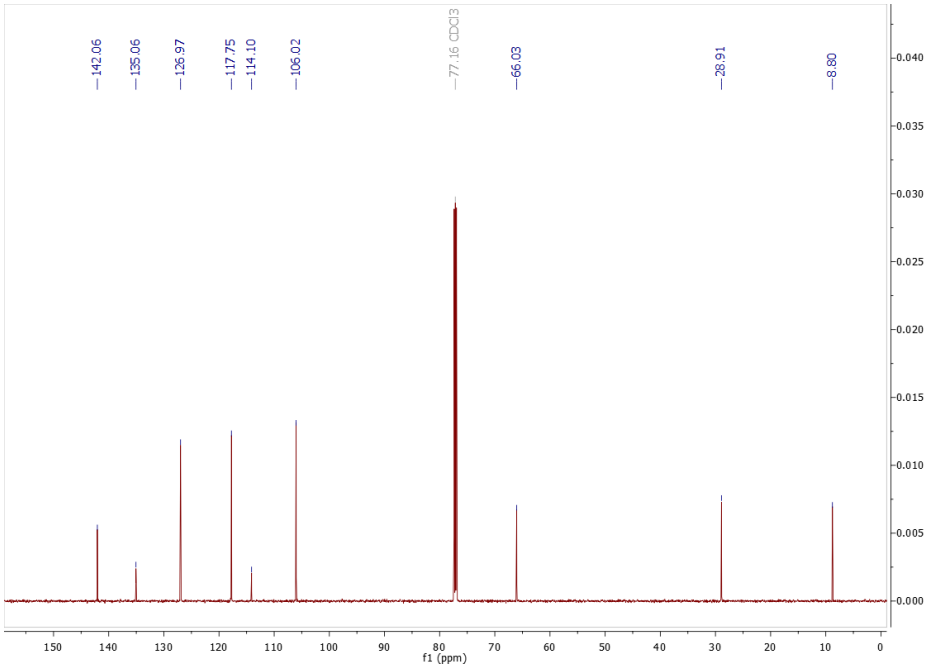

Figure 197 – ^{13}C-NMR in $CDCl_3$ of **394**.

Compound 385

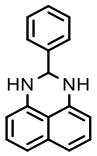

The crude was purified by flash chromatography on silica gel using DCM/*n*-hexane (8:2) as eluent. The product was isolated as a light-brown powder (2.47 g, 53%). R_f (silica gel): 0.40 (DCM). M_p: 128-130 °C.

^{1}H-NMR (600 MHz, $CDCl_3$, RT): δ 7.64-7.66 (m, 2H, Ar-H), 7.45-7.46 (m, 3H, Ar-H), 7.26-7.28 (m, 2H, Ar-H), 7.23-7.24 (dd, *J* = 8.3 Hz, *J* = 1.1 Hz, 2H, Ar-H), 6.53-6.54 (dd, *J* = 7.1 Hz, *J* = 1.1 Hz, 2H, Ar-H), 5.48 (s, 1H, -CH-), 4.56 (br, 2H, -NH) ppm.

^{13}C-NMR (151 MHz, $CDCl_3$, RT): δ 142.24, 140.22, 135.04, 129.74, 128.98, 128.04, 127.01, 118.02, 113.59, 105.96, 68.53 ppm.

MS (ESI$^+$, MeOH): *m/z* 247.25 $[M-H]^+$; calculated for $C_{12}H_{12}N_2$: 246.12.

UV-Vis (DCM): λ_{max} (*ε*) = 333 (*13794*), 347 (*14267*) nm.

Fluorescence (DCM, λ_{exc} 325 nm): 394 nm. **ϕ:** 8%.

IR-Spectrum (cm^{-1}, ATR): 3380 *ν*(N–H), 3355 *ν*(N–H), 3035 *ν*(C–H aromatic), 2970 *ν*(C–H aliphatic), 1735, 1595 *δ*(N–H), 1480, 1415, 1380, 1260, 1160, 1070, 1020, 810 *δ*(N–H), 750, 705.

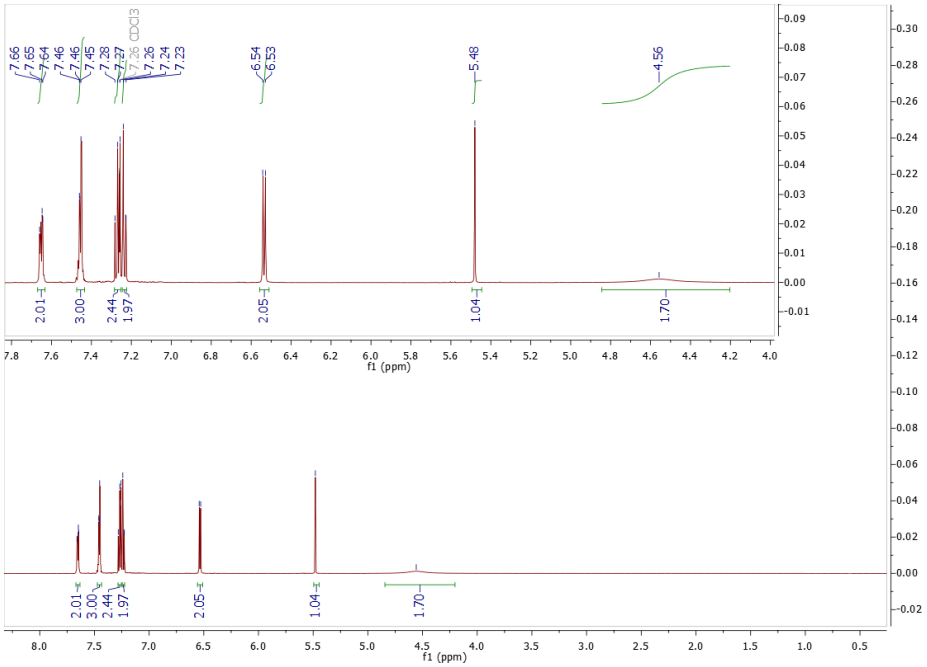

Figure 198 – ^{1}H-NMR in $CDCl_3$ of **385**.

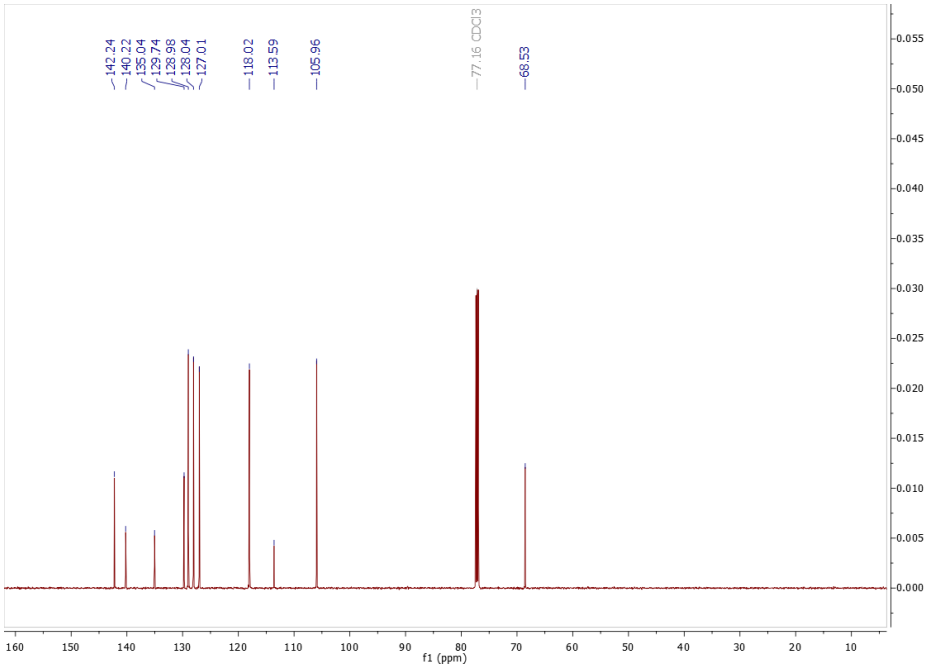

Figure 199 – ^{13}C-NMR in $CDCl_3$ of **385**.

1.10. General Synthesis of CI-SQ with Di-substituted DHPs

The synthesis of CI-SQ dyes **341**-**344** and **397** with di-substituted DHP were performed according to the following procedure.

A mixture of CI-emisquaraine **323** (150 mg, 0.46 mmol), di-substituted DHP derivative (0.69 mmol) and 12 mL of a solution toluene/*n*-butanol (1:1) was introduced in a sealed 20 mL reaction vial and heated in a microwave reactor at 160 °C for 30 min. After cooling to room temperature, the reaction mixture was washed out of the reaction vessel with methanol and all the solvent was removed by evaporation under vacuum. The crude was purified by flash chromatography on silica gel using DCM/MeOH/acetic acid (94:5.5:0.5) as eluent.

Compound 341

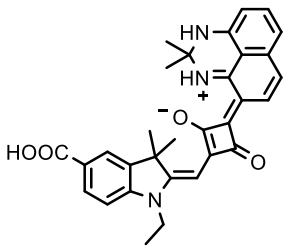

The product was isolated as a dark-blue powder (75 mg, 32%). R_f (silica gel): 0.60 (9:1 DCM/MeOH). M_p: > 200 °C.

^{1}H-NMR (600 MHz, DMSO-d$_6$, RT): δ 10.54 (s, 1H, -NH$^+$), 8.10 (d, *J* = 1.3 Hz, 1H, Ar-H), 8.00-8.01 (dd, *J* = 8.3 Hz, *J* = 1.5 Hz, 1H, Ar-H), 7.98-8.00 (d, *J* = 9.0 Hz, 1H, Ar-H), 7.53-7.55 (d, *J* = 8.4 Hz, 1H, Ar-H), 7.29-7.32 (t, *J* = 7.8 Hz, 1H, Ar-H), 7.20 (s, 1H, -NH), 6.81-6.83 (d, *J* = 7.6 Hz, 1H, Ar-H), 6.79-6.80 (d, *J* = 9.1 Hz, 1H, Ar-H), 6.48-6.50 (d, *J* = 7.7 Hz, 1H, Ar-H), 5.93 (s, 1H, -CH=), 4.23-4.26 (q, J = 7.3 Hz, 2H, -CH$_2$-), 1.73 (s, 6H, -CH$_3$), 1.52 (s, 6H, -CH$_3$), 1.30-1.33 (t, *J* = 7.3 Hz, 3H, -CH$_3$) ppm.

^{13}C-NMR (151 MHz, DMSO-d$_6$, RT): δ 178.55, 174.00, 171.79, 167.02, 147.68, 145.02, 144.28, 142.05, 136.34, 132.82, 130.33, 126.92, 124.33, 123.38, 116.77, 115.09, 110.84, 109.07, 108.92, 107.86, 88.34, 64.79, 49.21, 38.87, 28.29, 26.02, 11.97 ppm.

HRMS (ESI$^+$-TOF, MeOH): *m/z* 508.2231 [M-H]$^+$; calculated for $C_{31}H_{29}N_3O_4$: 508.2231 (+1).

UV-Vis (EtOH): λ_{max} (ε) = 277 (*22396*), 397 (*15698*), 463 (*12314*), 733 (*109343*) nm.

Fluorescence (EtOH, λ_{exc} 720 nm): 773 nm. **ϕ:** 1%.

IR-Spectrum (cm^{-1}, ATR): 2965 *ν*(C–H aliphatic), 2925 *ν*(C–H aliphatic), 1720 *ν*(C═O), 1685 *ν*(C═O), 1620, 1605, 1550, 1540, 1510, 1450, 1430, 1390, 1355, 1290, 1180, 1120, 1090, 1050, 940, 815, 770, 745.

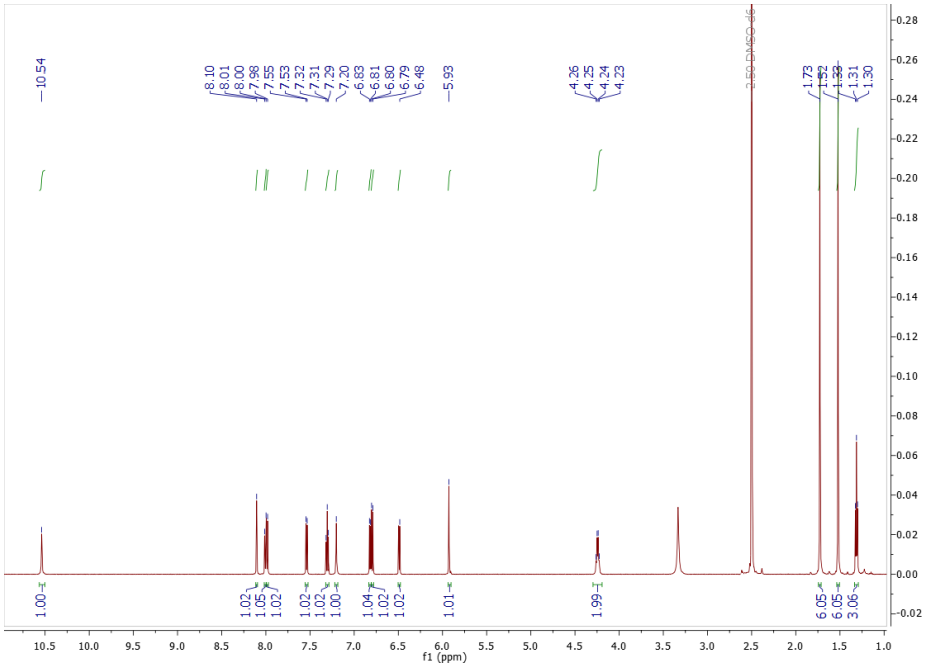

Figure 200 – ^{1}H-NMR in DMSO-d$_6$ of **341**.

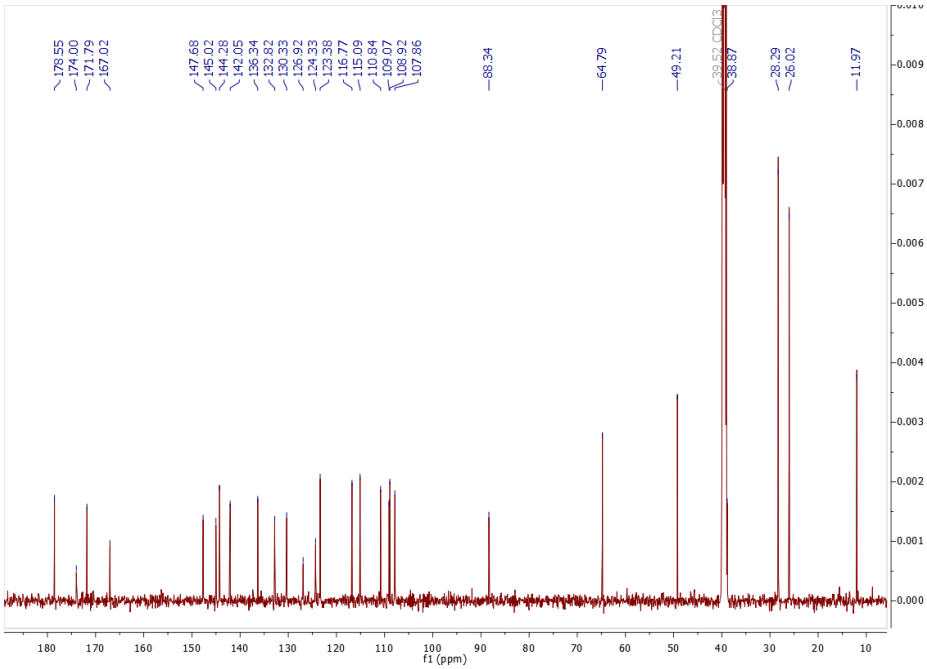

Figure 201 – ^{13}C-NMR in DMSO-d$_6$ of **341**.

Compound 342

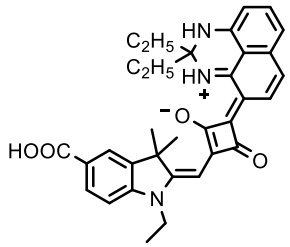

The product was isolated as a dark-blue powder (142 mg, 58%). R_f (silica gel): 0.30 (95:5 DCM/MeOH). M_p: > 200 °C.

^{1}H-NMR (600 MHz, DMSO-d$_6$, RT): δ 10.52 (s, 1H, -NH$^+$), 8.09 (s, 1H, Ar-H), 7.99-8.00 (d, *J* = 8.4 Hz, 1H, Ar-H), 7.96-7.97 (d, *J* = 8.9 Hz, 1H, Ar-H), 7.50-7.52 (d, *J* = 8.4 Hz, Ar-H), 7.27-7.29 (t, *J* = 7.8 Hz, 1H, Ar-H), 7.11 (s, 1H, -NH), 6.74-6.76 (m, 2H, Ar-H), 6.51-6.52 (d, *J* = 7.9 Hz, 1H, Ar-H), 5.90 (s, 1H, -CH=), 4.21-4.24 (q, *J* = 7.3 Hz, 2H, -CH$_2$-), 1.74-1.82 (m, 4H, -CH$_2$-), 1.72 (s, 6H, -CH$_3$), 1.29-1.32 (t, *J* = 7.3 Hz, 3H, -CH$_3$), 0.94-0.96 (t, *J* = 7.4 Hz, 6H, -CH$_3$) ppm.

^{13}C-NMR (151 MHz, DMSO-d$_6$, RT): δ 177.56, 174.11, 171.11, 167.02, 148.70, 145.15, 144.86, 141.97, 136.29, 133.13, 130.35, 126.60, 124.29, 123.37, 116.65, 114.51, 110.63, 108.65, 108.41, 107.71, 88.22, 70.11, 49.04, 38.72, 31.56, 26.07, 11.96, 7.66 ppm.

HRMS (ESI$^+$-TOF, MeOH): *m/z* 536.2528 [M-H]$^+$; calculated for $C_{33}H_{33}N_3O_4$: 536.2544 (+1).

UV-Vis (EtOH): λ_{max} (ε) = 276 (*32969*), 398 (*17172*), 467 (*12703*), 746 (*108086*) nm.

Fluorescence (EtOH, λ_{exc} 730 nm): 778 nm. **ϕ:** 1%.

IR-Spectrum (cm^{-1}, ATR): 2915 *v*(C–H aliphatic), 2850 *v*(C–H aliphatic), 1700 *v*(C═O), 1580, 1535, 1510, 1450, 1390, 1355, 1280, 1235, 1190, 1085, 1045, 935, 815, 770.

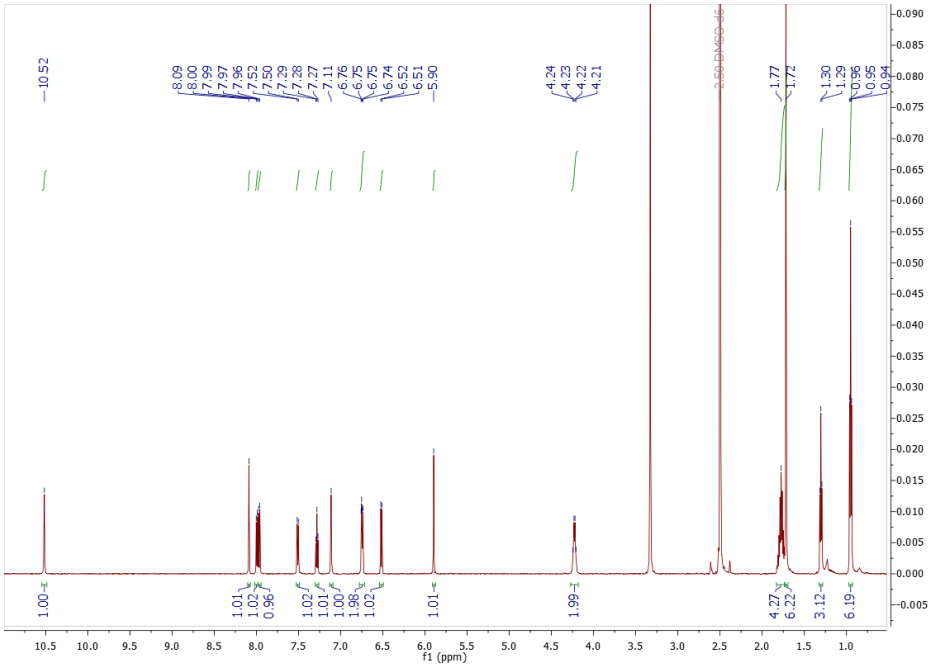

Figure 202 – ^{1}H-NMR in DMSO-d$_6$ of **342**.

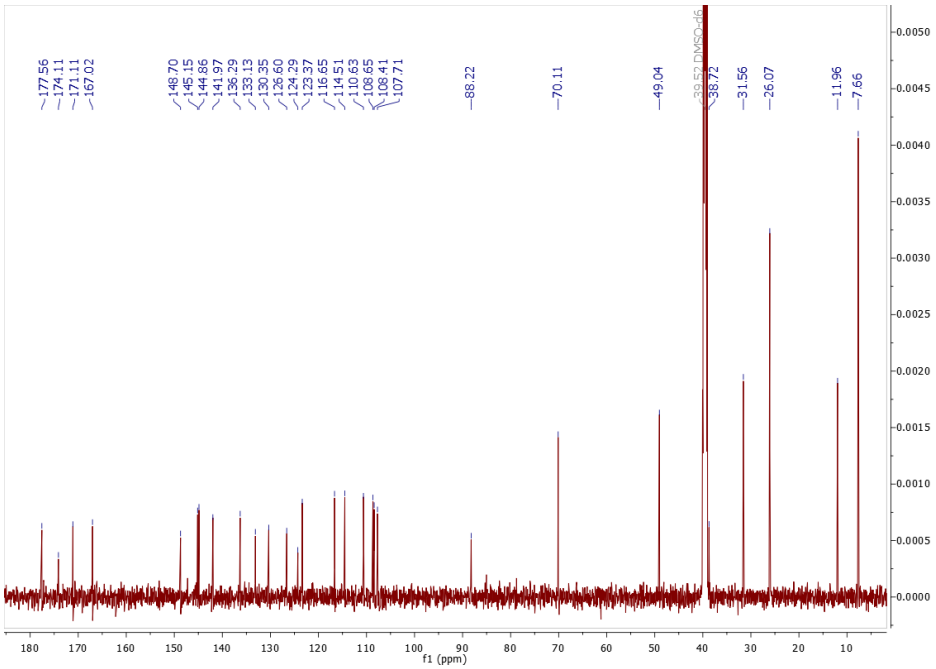

Figure 203 – ^{13}C-NMR in DMSO-d$_6$ of **342**.

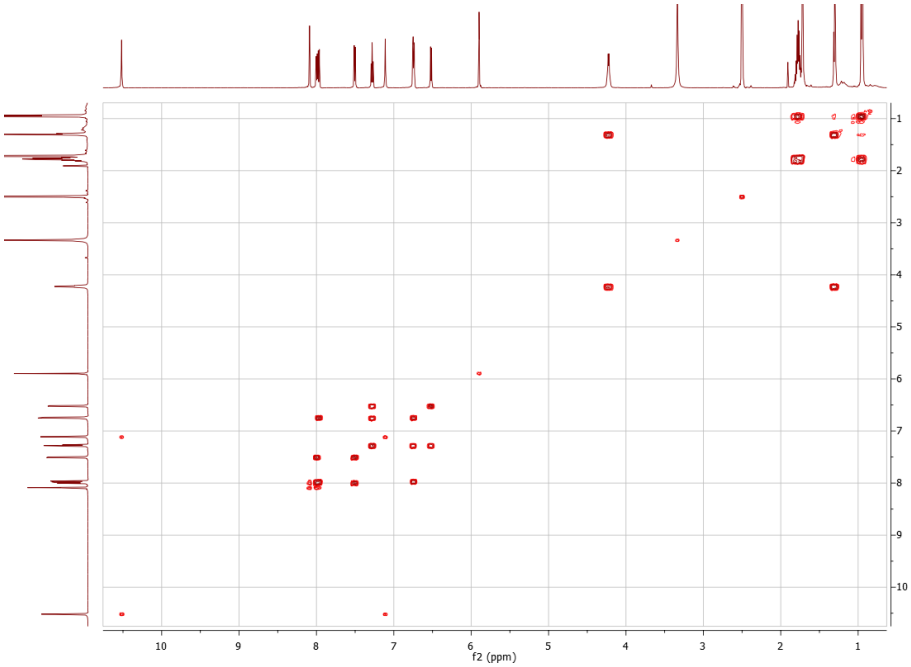

Figure 204 – COSY in DMSO-d_6 of **342**.

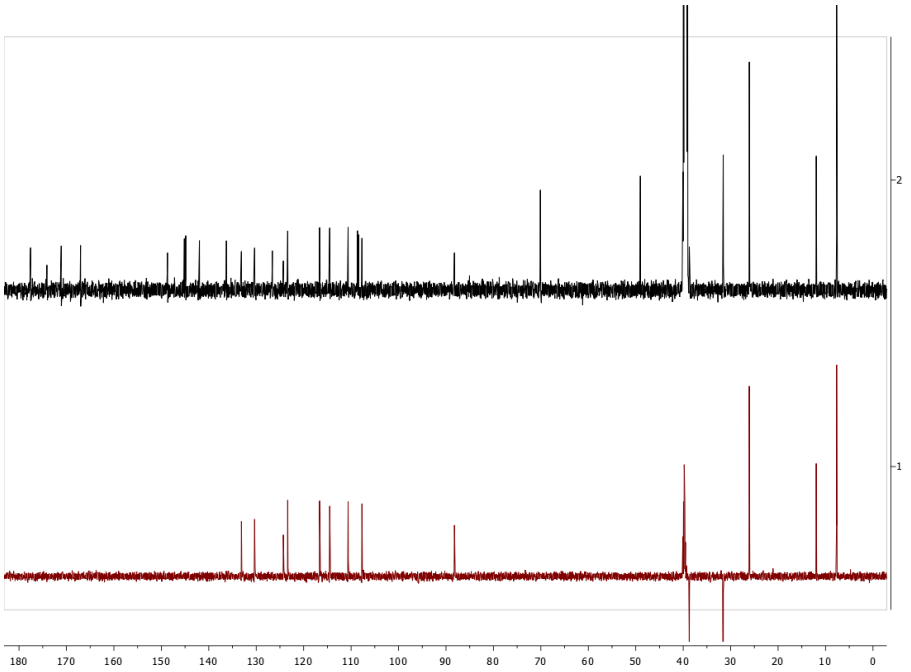

Figure 205 – DEPT-135 (red) *vs*. ^{13}C-NMR (black) in DMSO-d_6 of **342**.

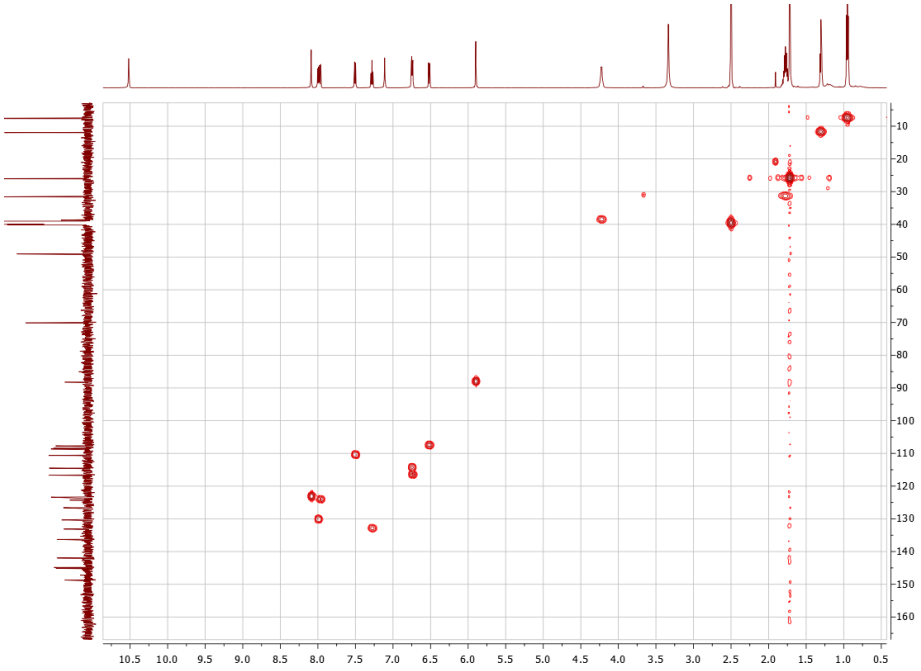

Figure 205 – HSQC in DMSO-d_6 of **342**.

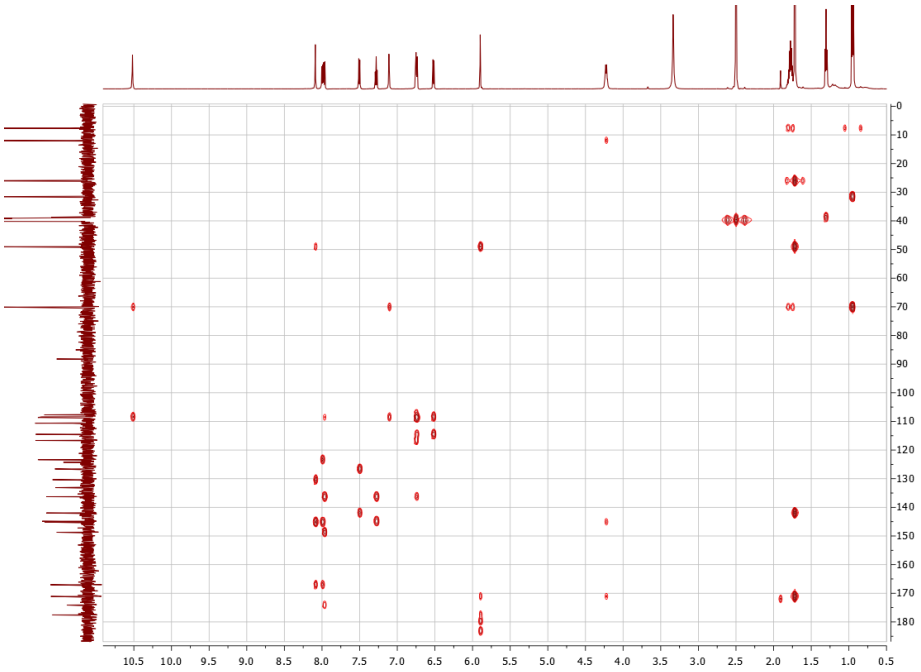

Figure 207 – HMBC in DMSO-d_6 of **342**.

Compound 343

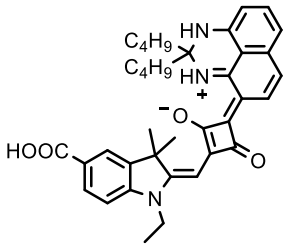

The product was isolated as a dark-blue powder (127 mg, 47%). R_f (silica gel): 0.65 (9:1 DCM/MeOH). M_p: > 200 °C.

^{1}H-NMR (600 MHz, DMSO-d$_6$, RT): δ 10-54 (s, 1H, -NH$^+$), 8.09 (s, 1H, Ar-H), 7.99-8.00 (dd, *J* = 8.2 Hz, *J* = 1.1 Hz, 1H, Ar-H), 7.96-7.97 (d, J = 8.9 Hz, 1H, Ar-H), 7.50-7.51 (d, *J* = 8.5 Hz, 1H, Ar-H), 7.26-7.29 (t, *J* = 7.7 Hz, 1H, Ar-H), 7.13 (s, 1H, -NH), 6.73-6.75 (m, 2H, Ar-H), 6.49-6.50 (d, *J* = 7.9 Hz, 1H, Ar-H), 5.90 (s, 1H, -CH=), 4.21-4.25 (q, *J* = 7.1 Hz, 2H, -CH$_2$-), 1.73-1.79 (m, 4H, -CH$_2$-), 1.72 (s, 6H, -CH$_3$), 1-42-1.48 (m, 2H, -CH$_2$-), 1.34-1.41 (m, 2H, -CH$_2$-), 1.26-1.31 (m, 7H, -CH$_2$- and -CH$_3$), 0.84-0.86 (t, J = 7.3 Hz, 6H, -CH$_3$) ppm.

^{13}C-NMR (151 MHz, DMSO-d$_6$, RT): δ 177.38, 174.08, 171.00, 167.02, 148.51, 145.13, 144.73, 141.97, 136.26, 133.15, 130.33, 126.60, 124.27, 123.33, 116.63, 114.47, 110.58, 108.57, 108.21, 107.65, 88.24, 69.60, 49.02, 38.69, 26.06, 25.07, 22.37, 14.00, 11.97 ppm.

HRMS (ESI$^+$-TOF, MeOH): *m/z* 592.3148 [M-H]$^+$; calculated for $C_{37}H_{41}N_3O_4$: 592.3170 (+1).

UV-Vis (EtOH): λ_{max} (ε) = 277 (*24966*), 398 (*16066*), 466 (*11666*), 745 (*107612*) nm.

Fluorescence (EtOH, λ_{exc} 730 nm): 778 nm. **ϕ:** 1%.

IR-Spectrum (cm^{-1}, ATR): 2970 *v*(C–H aliphatic), 2925 *v*(C–H aliphatic), 2855 *v*(C–H aliphatic), 1705 *v*(C═O), 1540, 1505, 1445, 1390, 1350, 1280, 1230, 1185, 1120, 1085, 1040, 935, 815, 765.

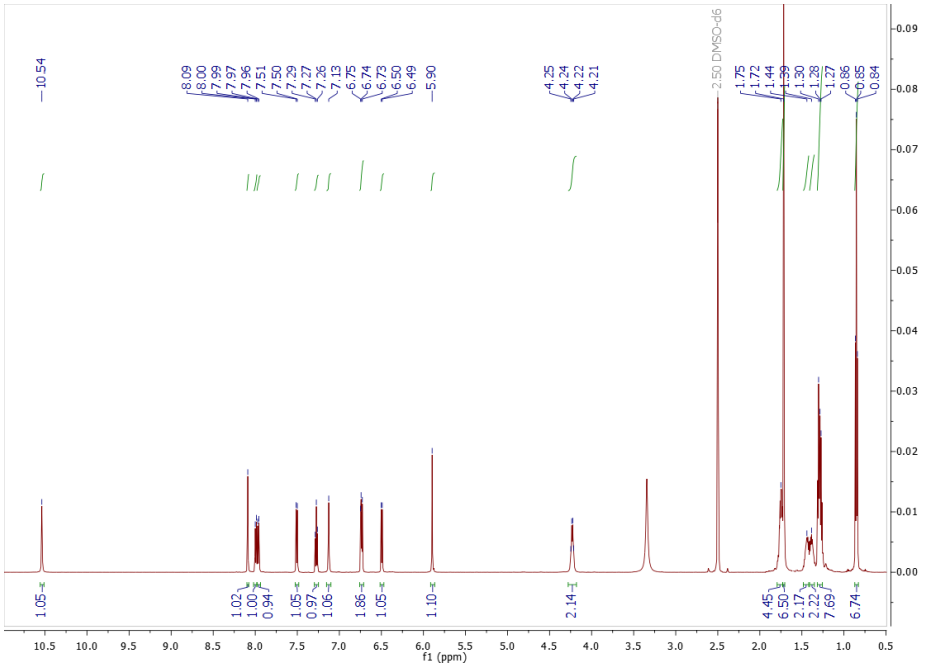

Figure 208 – ^{1}H-NMR in DMSO-d$_6$ of **343**.

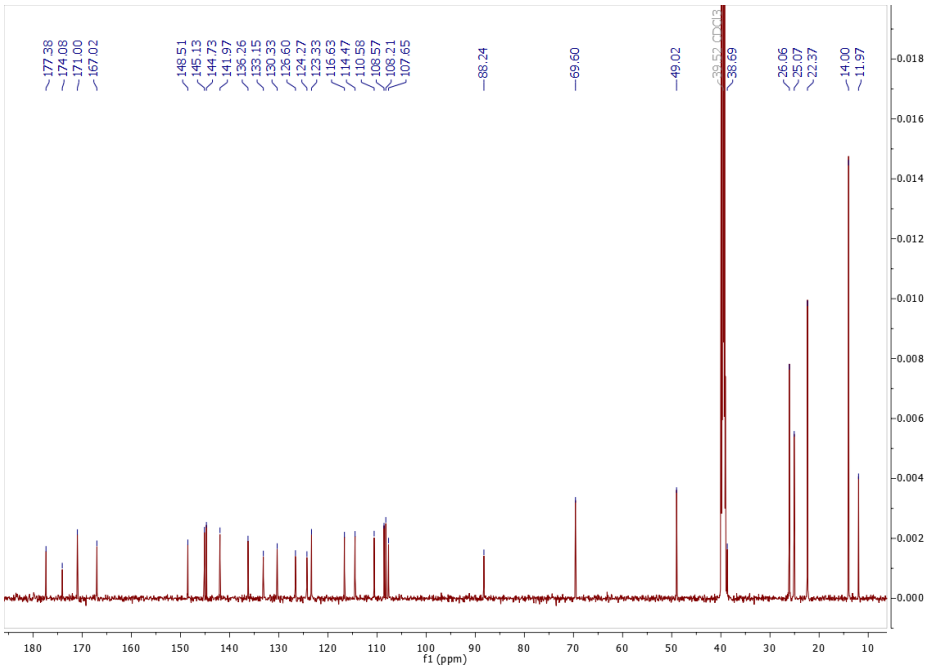

Figure 209 – ^{13}C-NMR in DMSO-d$_6$ of **343**.

Compound 344

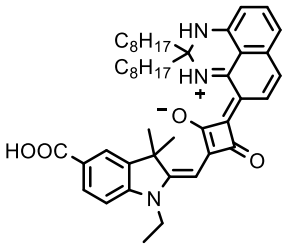

The product was isolated as a dark-blue powder (80 mg, 25%). R_f (silica gel): 0.70 (9:1 DCM/MeOH). M_p: 170-172 °C.

^{1}H-NMR (600 MHz, DMSO-d$_6$, RT): δ 10.56 (s, 1H, -NH$^+$), 8.08 (d, *J* = 1.4 Hz, 1H, Ar-H), 7.98-8.00 (dd, *J* = 8.3 Hz, *J* = 1.6 Hz, 1H, Ar-H), 7.95-7.97 (d, *J* = 9.0 Hz, 1H, Ar-H), 7.49-7.51 (d, *J* = 8.5 Hz, 1H, Ar-H), 7.25-7.28 (t, *J* = 7.8 Hz, 1H, Ar-H), 7,10 (s, 1H, -NH), 6.72-6.74 (m, 2H, Ar-H), 6.48-6.50 (d, *J* = 7.8 Hz, 1H, Ar-H), 5.89 (s, 1H, -CH=), 4.20-4.23 (q, *J* = 6.5 Hz, 2H, -CH_2-), 1.71-1.78 (m, 10H, -CH_2- and -CH_3), 1.44-1.49 (m, 2H, -CH_2-), 1.35-1.42 (m, 2H, -CH_2-), 1.28-1.30 (t, *J* = 7.2 Hz, 3H, -CH_3), 1.12-1.24 (m, 20H, -CH_2-), 0.79-0.81 (t, *J* = 7.1 Hz, 6H, -CH_3) ppm.

^{13}C-NMR (151 MHz, DMSO-d$_6$, RT): δ 177.40, 174.29, 170.86, 166.99, 148.59, 145.13, 144.73, 141.92, 136.27, 133.13, 130.34, 126.53, 124.28, 123.29, 116.65, 114.48, 110.56, 108.67, 108.28, 107.69, 88.17, 69.66, 48.96, 38.65, 31.26, 29.08, 28.82, 28.51, 26.08, 22.62, 22.09, 13.93, 11.91 ppm.

HRMS (ESI$^+$-TOF, MeOH): *m/z* 704.4391 [M-H]$^+$; calculated for $C_{45}H_{57}N_3O_4$: 704.4422 (+1).

UV-Vis (EtOH): λ_{max} (ε) = 398 (*13633*), 466 (*9748*), 744 (*93359*) nm.

Fluorescence (EtOH, λ_{exc} 730 nm): 776 nm. **ϕ:** 1%.

IR-Spectrum (cm^{-1}, ATR): 2920 *v*(C–H aliphatic), 2850 *v*(C–H aliphatic), 1710 *v*(C═O), 1575, 1535, 1510, 1450, 1395, 1355, 1285, 1235, 1180, 1120, 1085, 1045, 940, 815, 770.

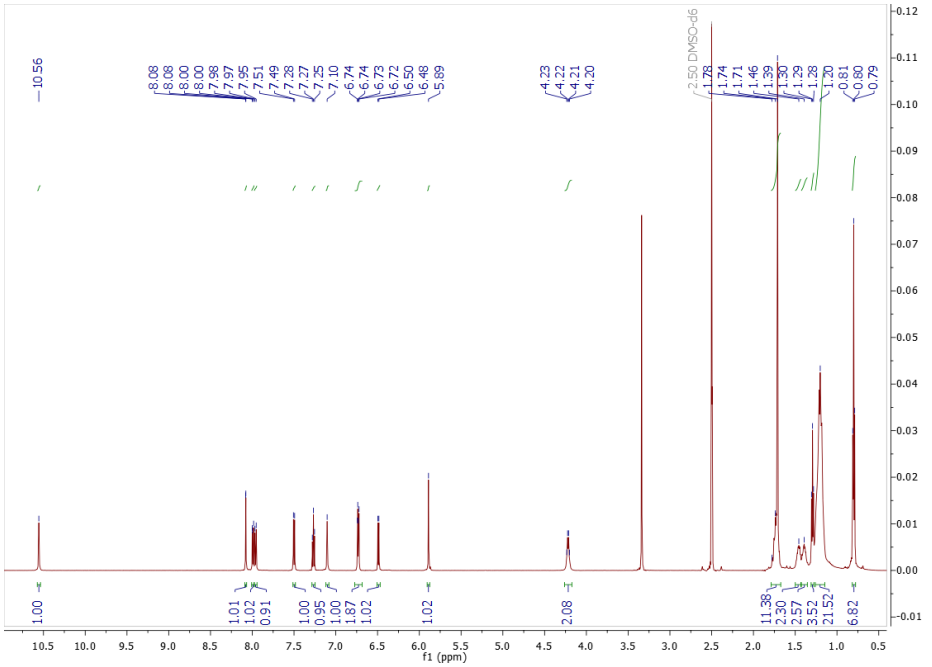

Figure 210 – ^{1}H-NMR in DMSO-d$_6$ of **344**.

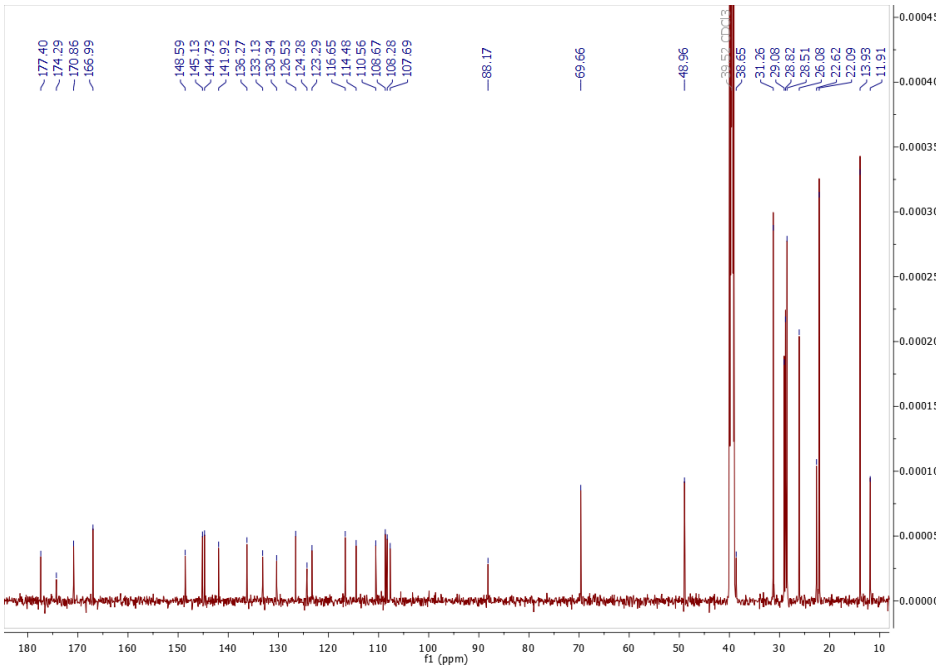

Figure 211 – ^{13}C-NMR in DMSO-d$_6$ of **344**.

Compound 397

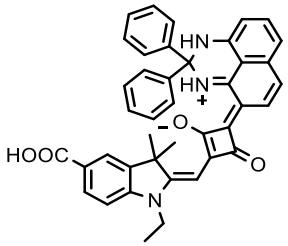

The product was isolated as a dark-blue powder (188 mg, 65%). R_f (silica gel): 0.60 (9:1 DCM/MeOH). M_p: > 200 °C.

^{1}H-NMR (600 MHz, DMSO-d$_6$, RT): δ 11.19 (s, 1H, -NH$^+$), 8.32 (s, 1H, -NH), 8.14 (d, *J* = 1.4 Hz, 1H, Ar-H), 8.05-8.06 (d, *J* = 8.9 Hz, 1H, Ar-H), 8.02-8.03 (dd, *J* = 8.3 Hz, *J* = 1.6 Hz, 1H, Ar-H), 7.59-7.61 (d, *J* = 8.5 Hz, 1H, Ar-H), 7.51-7.53 (m, 4H, Ar-H), 7.38-7.41 (m, 4H, Ar-H), 7.30-7.34 (m, 3H, Ar-H), 6.83-6.85 (m, 2H, Ar-H), 6.74-6.76 (dd, *J* = 7.8 Hz, *J* = 0.7 Hz, 1H, Ar-H), 6.00 (s, 1H, -CH=), 4.27-4.31 (q, *J* = 7.2 Hz, 2H, -CH$_2$-), 1.74 (s, 6H, -CH$_3$), 1.30-1.32 (t, *J* = 7.3 Hz, 3H, -CH$_3$) ppm.

^{13}C-NMR (151 MHz, DMSO-d$_6$, RT): δ 180.87, 173.47, 172.72, 172.05, 166.97, 146.47, 144.78, 144.62, 144.04, 142.41, 136.04, 132.31, 130.32, 128.26, 128.09, 127.49, 124.23, 123.46, 117.11, 115.59, 111.42, 110.46, 109.33, 107.75, 89.26, 73.02, 49.69, 40.05, 25.72, 21.07, 12.18 ppm.

HRMS (ESI$^+$-TOF, MeOH): *m/z* 632.2379 [M-H]$^+$; calculated for $C_{41}H_{33}N_3O_4$: 632.2398 (+1).

UV-Vis (EtOH): λ_{max} (ε) = 396 (*20355*), 450 (*13490*), 732 (*93693*) nm.

Fluorescence (EtOH, λ_{exc} 720 nm): 778 nm. **ϕ:** 2%.

IR-Spectrum (cm^{-1}, ATR): 3270 *v*(N–H), 2965 *v*(C–H aliphatic), 2935 *v*(C–H aliphatic), 1705 *v*(C═O), 1600, 1515, 1440, 1360, 1290, 1240, 1180, 1090, 1050, 935, 840, 770, 750.

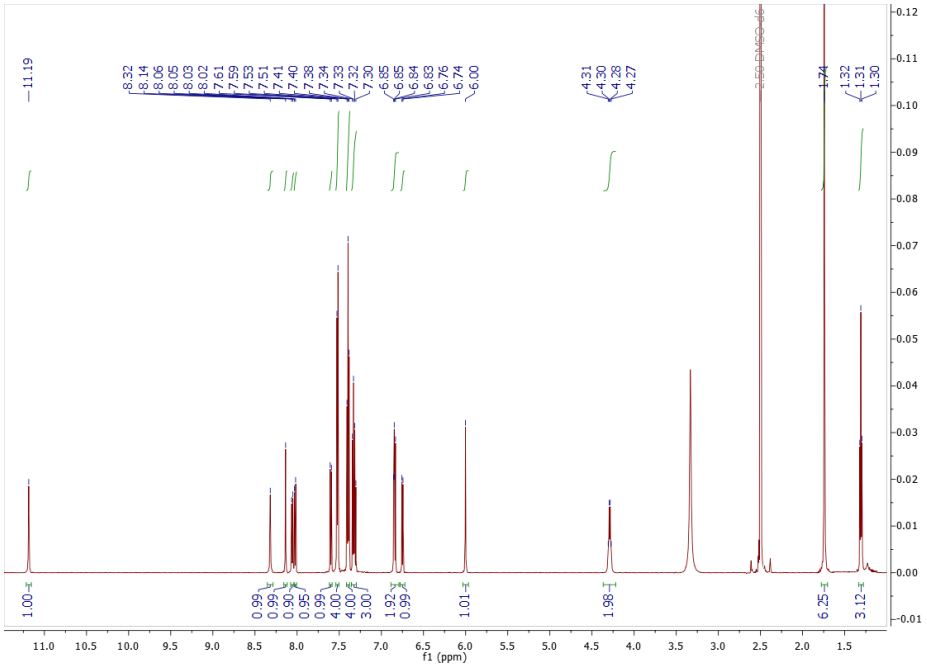

Figure 212 – ^{1}H-NMR in DMSO-d$_6$ of **397**.

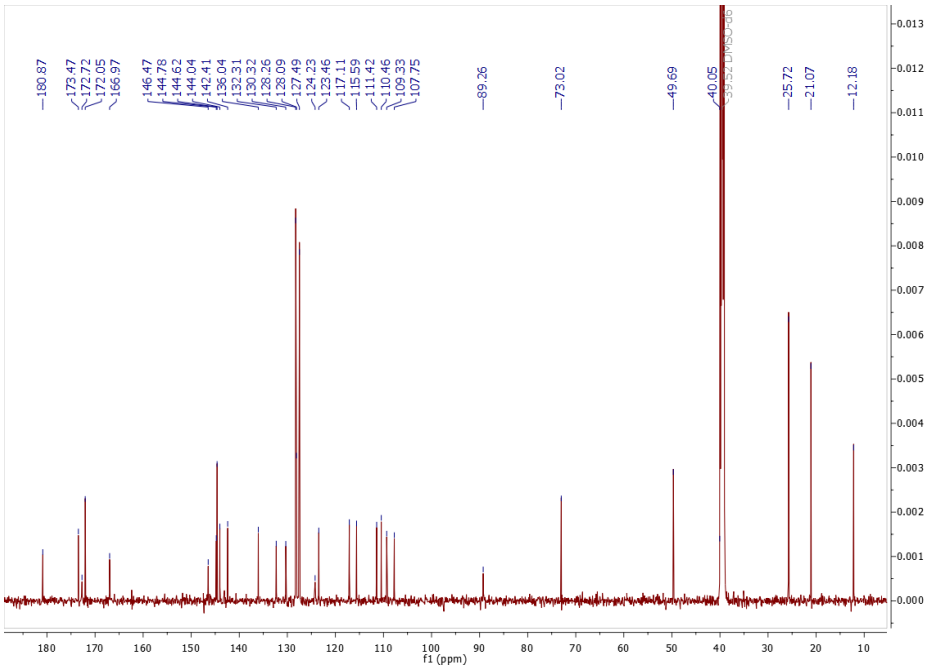

Figure 213 – ^{13}C-NMR in DMSO-d$_6$ of **397**.

1.11. General Synthesis of CBI-SQ Dyes with Di-substituted DHPs

The synthesis of CBI-SQ dyes **345**-**350** with di-substituted DHP were performed according to the following procedure.

A mixture of CBI-emisquaraines **333**-**335** (150 mg, 1.0 eq.), di-substituted DHP derivative (1.5 eq.) and 12 mL of a solution toluene/*n*-butanol (1:1) was introduced in a sealed 20 mL reaction vial and heated in a microwave reactor at 160 °C for 40 min. After cooling to room temperature, the reaction mixture was washed out of the reaction vessel with methanol and all the solvent was removed by evaporation under vacuum. The crude was purified by flash chromatography on silica gel using DCM/MeOH/acetic acid (94:5.7:0.3) as eluent.

Compound 345

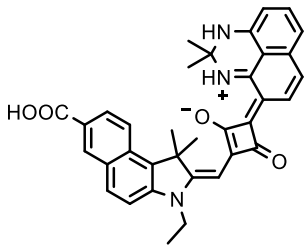

The product was isolated as a dark-blue powder (75 mg, 32%). R_f (silica gel): 0.50 (9:1 DCM/MeOH). M_p: > 200 °C.

^{1}H-NMR (600 MHz, DMSO-d$_6$, RT): δ 10.33 (s, 1H, -NH$^+$), 8.73 (d, *J* = 0.7 Hz, 1H, Ar-H), 8.39-8.41 (d, *J* = 8.6 Hz, 1H, Ar-H), 8.30-8.31 (d, *J* = 8.9 Hz, 1H, Ar-H), 8.10-8.11 (dd, *J* = 8.7 Hz, *J* = 1.4 Hz, 1H, Ar-H), 8.03-8.05 (d, *J* = 8.8 Hz, 1H, Ar-H), 7.91-7.93 (d, *J* = 8.9 Hz, 1H, Ar-H), 7.27-7.30 (t, *J* = 7.7 Hz, 1H, Ar-H), 7.12 (s, 1H, -NH), 6.80-6.84 (m, 2H, Ar-H), 6.47-6.49 (d, *J* = 7.7 Hz, 1H, Ar-H), 6.01 (s, 1H, -CH=), 4.39-4.42 (q, *J* = 7.1 Hz, 2H, -CH$_2$-), 1.98 (s, 6H, -CH$_3$), 1.52 (s, 6H, -CH$_3$), 1.37-1.39 (t, *J* = 7.3 Hz, 3H, -CH$_3$) ppm.

^{13}C-NMR (151 MHz, DMSO-d$_6$, RT): δ 183.29, 178.70, 173.71, 172.04, 167.25, 146.60, 144.02, 140.74, 136.10, 134.68, 132.35, 132.12, 131.89, 130.63, 129.55, 126.94, 126.80, 124.52, 122.97, 116.34, 114.98, 112.53, 109.39, 108.79, 107.40, 87.99, 64.58, 51.39, 40.06, 28.32, 25.68, 12.41 ppm.

HRMS (ESI$^+$-TOF, MeOH): *m/z* 558.2367 [M-H]$^+$; calculated for $C_{35}H_{31}N_3O_4$: 558.2367 (+1).

UV-Vis (EtOH): λ_{max} (ε) = 360 (*11093*), 404 (*10739*), 463 (*8025*), 743 (*95370*) nm.

Fluorescence (EtOH, λ_{exc} 730 nm): 784 nm. **ϕ:** 1%.

IR-Spectrum (cm^{-1}, ATR): 2965 *v*(C–H aliphatic), 2915 *v*(C–H aliphatic), 1705 *v*(C═O), 1540, 1505, 1445, 1415, 1385, 1285, 1235, 1180, 1125, 1035, 965, 935, 815, 800, 750.

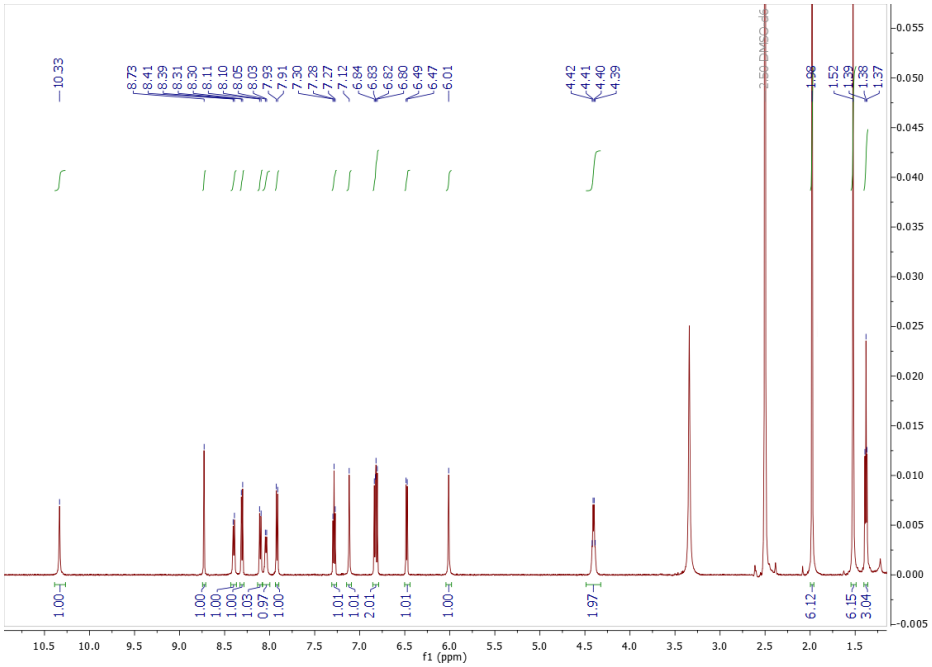

Figure 214 – ^{1}H-NMR in DMSO-d$_6$ of **345**.

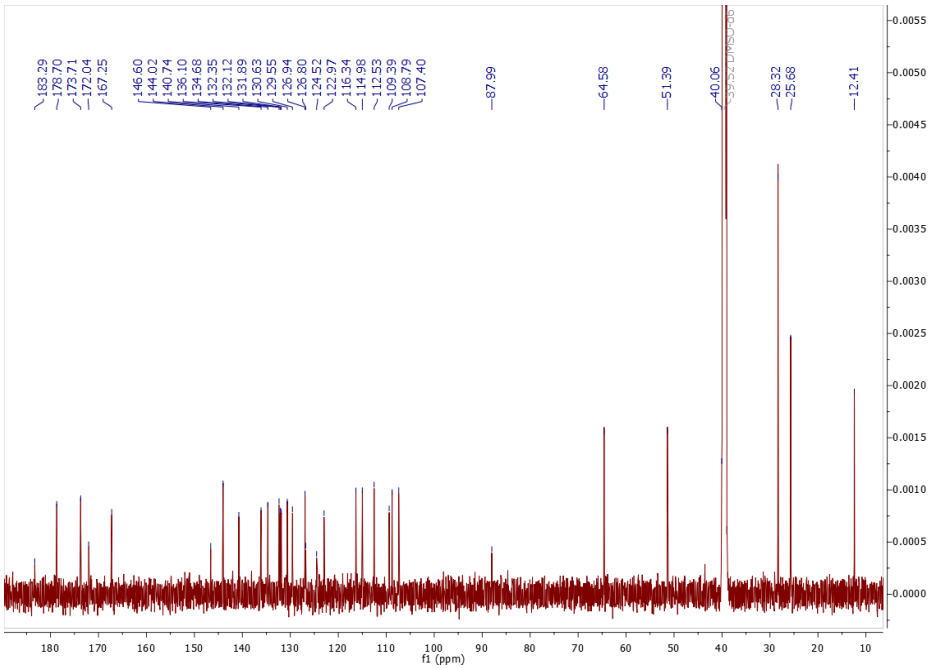

Figure 215 – ^{13}C-NMR in DMSO-d$_6$ of **345**.

Compound 346

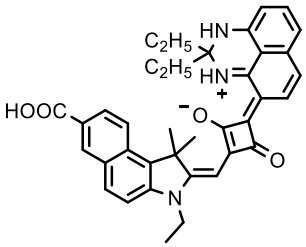

The product was isolated as a dark-blue powder (140 mg, 60%). R_f (silica gel): 0.40 (9:1 DCM/MeOH). M_p: > 200 °C.

^{1}H-NMR (600 MHz, DMSO-d$_6$, RT): δ 10.32 (s, 1H, -NH$^+$), 8.72 (d, *J* = 1.3 Hz, 1H, Ar-H), 8.37-8.39 (d, *J* = 8.9 Hz, 1H, Ar-H), 8.29-8.30 (d, *J* = 8.9 Hz, 1H, Ar-H), 8.09-8.11 (dd, *J* = 8.8 Hz, *J* = 1.5 Hz, 1H, Ar-H), 8.02-8.03 (d, *J* = 8.6 Hz, 1H, Ar-H), 7.89-7.91 (d, *J* = 8.9 Hz, 1H, Ar-H), 7.25-7.27 (t, *J* = 7.7 Hz, 1H, Ar-H), 7.03 (s, 1H, -NH), 6.75-6.77 (m, 2H, Ar-H), 6.50-6.51 (d, *J* = 7.8 Hz, 1H, Ar-H), 5.98 (s, 1H, -CH=), 4.37-4.41 (q, *J* = 7.3 Hz, 2H, -CH$_2$-), 1.97 (s, 6H,-CH$_3$), 1.73-1.82 (m, 4H, -CH$_2$-), 1.36-1.38 (t, *J* = 7.3 Hz, 3H, -CH$_3$), 0.95-0.97 (t, *J* = 7.4 Hz, 6H, -CH$_3$) ppm.

^{13}C-NMR (151 MHz, DMSO-d$_6$, RT): δ 177.88, 173.14, 172.04, 167.27, 147.57, 144.55, 140.82, 136.06, 134.45, 132.39, 131.86, 130.53, 129.59, 126.92, 126.69, 122.91, 116.15, 114.39, 112.46, 108.78, 108.47, 107.22, 87.81, 69.81, 51.24, 40.05, 31.47, 25.70, 12.39, 7.68 ppm.

HRMS (ESI$^+$-TOF, MeOH): *m/z* 586.2673 [M-H]$^+$; calculated for $C_{37}H_{35}N_3O_4$: 586.2700 (+1).

UV-Vis (EtOH): λ_{max} (ε) = 359 (*9073*), 404 (*8960*), 471 (*7576*), 749 (*102549*) nm.

Fluorescence (EtOH, λ_{exc} 735 nm): 784 nm. **ϕ:** 1%.

IR-Spectrum (cm^{-1}, ATR): 2970 *v*(C–H aliphatic), 2925 *v*(C–H aliphatic), 1700 *v*(C═O), 1540, 1505, 1445, 1420, 1390, 1280, 1230, 1190, 1125, 1035, 1010, 960, 930, 805, 750.

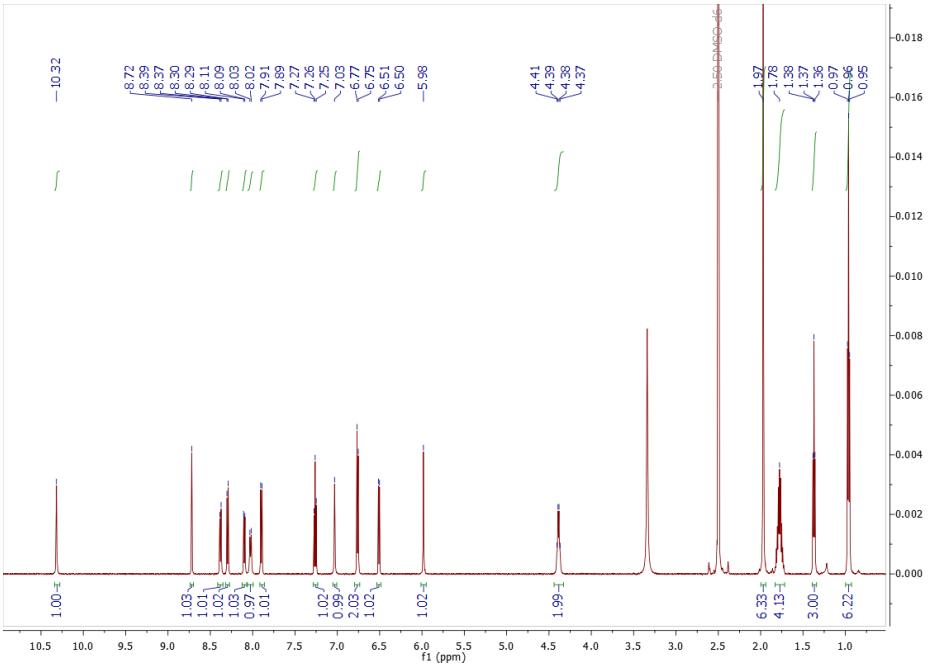

Figure 216 – ^{1}H-NMR in DMSO-d$_6$ of **346**.

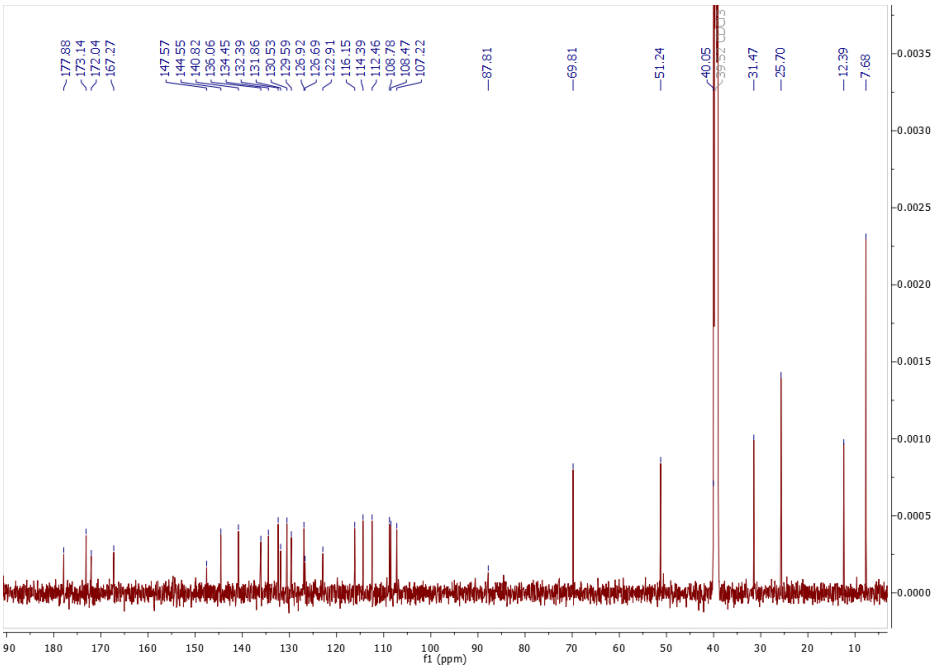

Figure 217 – ^{13}C-NMR in DMSO-d$_6$ of **346**.

Compound 347

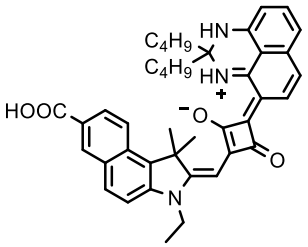

The product was isolated as a dark-blue powder (127 mg, 50%). R_f (silica gel): 0.45 (9:1 DCM/MeOH). M_p: > 200 °C.

^{1}H-NMR (600 MHz, DMSO-d$_6$, RT): δ 10.31 (s, 1H, -NH$^+$), 8.70 (d, *J* = 1.0 Hz, 1H, Ar-H), 8.34-8.36 (d, *J* = 8.9 Hz, 1H, Ar-H), 8.28-8.29 (d, *J* = 8.9 Hz, 1H, Ar-H), 8.10-8.12 (dd, *J* = 8.7 Hz, *J* = 1.1 Hz, 1H, Ar-H), 8.02-8.03 (d, *J* = 8.5 Hz, 1H, Ar-H), 7.89-7.90 (d, *J* = 8.9 Hz, 1H, Ar-H), 7.24-7.27 (t, *J* = 7.7 Hz, 1H, Ar-H), 7.04 (s, 1H, -NH), 6.74-6.76 (m, 2H, Ar-H), 6.48-6.49 (d, *J* = 7.7 Hz, 1H, Ar-H), 5.98 (s, 1H, -CH=), 4.38-4.41 (q, *J* = 7.1 Hz, 2H, -CH$_2$-), 1.97 (s, 6H, -CH$_3$), 1.71-1.79 (m, 4H, -CH$_2$-), 1.36-1.48 (m, 7H, -CH$_2$- and -CH$_3$), 1.25-1.32 (m, 4H, -CH$_2$-), 0.85-0.87 (t, *J* = 7.3 Hz, 6H, -CH$_3$) ppm.

^{13}C-NMR (151 MHz, DMSO-d$_6$, RT): δ 177.75, 173.06, 172.04, 167.32, 147.36, 144.43, 140.79, 136.05, 134.45, 132.42, 132.34, 131.84, 130.53, 129.56, 126.94, 126.80, 124.46, 122.82, 116.13, 114.35, 112.43, 108.57, 108.40, 107.15, 87.86, 69.32, 51.23, 40.05, 25.68, 25.11, 22.42, 14.03, 12.41 ppm.

HRMS (ESI$^+$-TOF, MeOH): *m/z* 642.3326 [M-H]$^+$; calculated for $C_{41}H_{43}N_3O_4$: 642.3326 (+1).

UV-Vis (EtOH): λ_{max} (ε) = 359 (*7500*), 404 (*7500*), 472 (*6119*), 749 (*101239*) nm.

Fluorescence (EtOH, λ_{exc} 735 nm): 783 nm. **ϕ:** 1%.

IR-Spectrum (cm^{-1}, ATR): 2950 *ν*(C–H aliphatic), 2925 *ν*(C–H aliphatic), 2855 *ν*(C–H aliphatic), 1710 *ν*(C═O), 1540, 1505, 1450, 1420, 1390, 1290, 1230, 1190, 1125, 1035, 1015, 965, 935, 815, 800, 750.

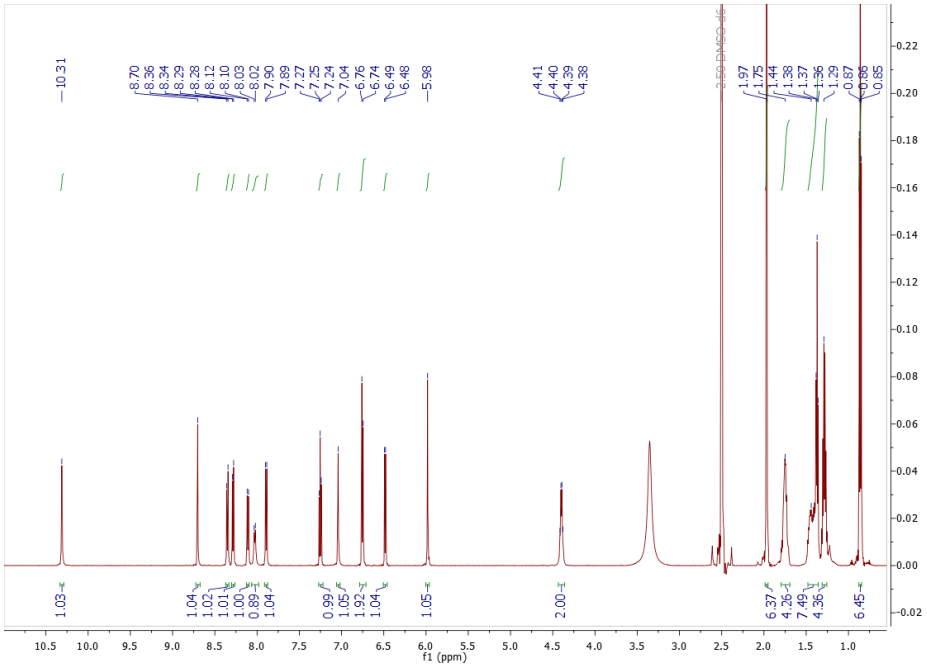

Figure 218 – ^{1}H-NMR in DMSO-d$_6$ of **347**.

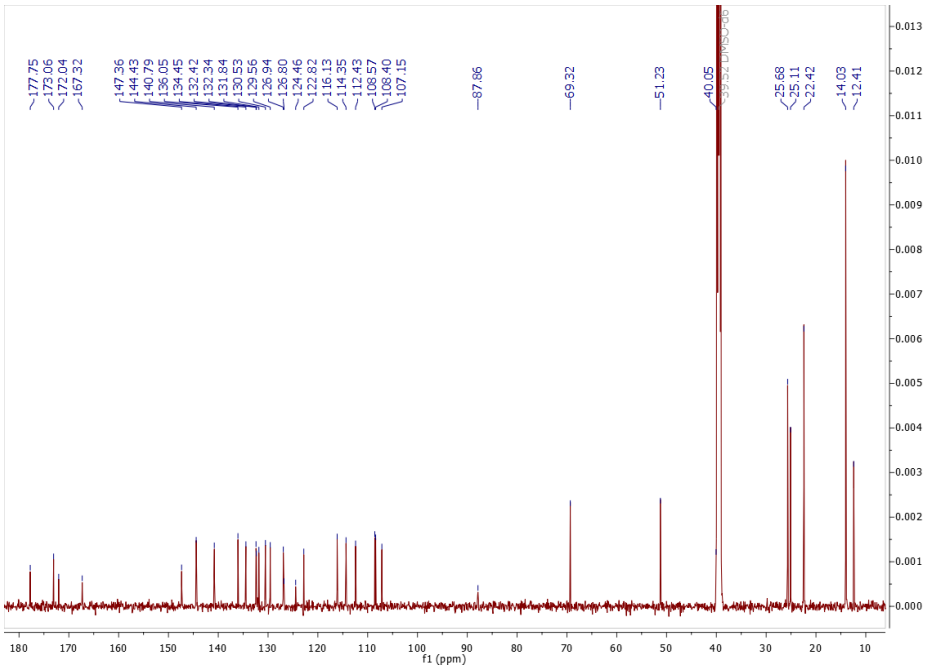

Figure 219 – ^{13}C-NMR in DMSO-d$_6$ of **347**.

Compound 348

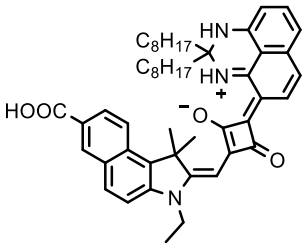

The product was isolated as a dark-blue powder (103 mg, 35%). R_f (silica gel): 0.50 (9:1 DCM/MeOH). M_p: 169-171 °C.

^{1}H-NMR (600 MHz, DMSO-d$_6$, RT): δ 10.35 (s, 1H, -NH$^+$), 8.72 (d, *J* = 1.0 Hz, 1H, Ar-H), 8.35-8.36 (d, *J* = 8.9 Hz, 1H, Ar-H), 8.28-8.30 (d, *J* = 8.9 Hz, 1H, Ar-H), 8.08-8.10 (dd, *J* = 8.8 Hz, *J* = 1.0 Hz, 1H, Ar-H), 8.01-8.03 (d, *J* = 9.2 Hz, 1H, Ar-H), 7.88-7.90 (d, *J* = 9.0 Hz, 1H, Ar-H), 7.24-7.26 (t, *J* = 7.7 Hz, 1H, Ar-H), 7.02 (s, 1H, -NH), 6.74-6.75 (m, 2H, Ar-H), 6.48-6.49 (d, *J* = 7.7 Hz, 1H, Ar-H), 5.98 (s, 1H, -CH=), 4.36-4.40 (q, *J* = 6.9 Hz, 2H, -CH$_2$-), 1.96 (s, 6H, -CH$_3$), 1.69-1.78 (m, 4H, -CH$_2$-), 1.35-1.51 (m, 7H, -CH$_2$- and -CH$_3$), 1.14-1.29 (m, 20H, -CH$_2$-), 0.79-0.81 (t, *J* = 7.1 Hz, 1H, -CH$_3$) ppm.

^{13}C-NMR (151 MHz, DMSO-d$_6$, RT): δ 177.77, 172.92, 172.07, 167.27, 147.46, 144.43, 140.80, 136.05, 134.37, 132.40, 131.85, 130.51, 129.56, 128.90, 128.21, 126.89, 124.50, 122.76, 116.51, 114.36, 112.41, 108.65, 108.49, 107.20, 87.78, 69.38, 51.17, 38.97, 31.26, 29.13, 28.85, 28.52, 25.70, 22.65, 22.10, 13.93, 12.34 ppm.

HRMS (ESI$^+$-TOF, MeOH): *m/z* 754.4556 [M-H]$^+$; calculated for $C_{49}H_{59}N_3O_4$: 754.4578 (+1).

UV-Vis (EtOH): λ_{max} (ε) = 362 (*8778*), 406 (*8663*), 449 (*8778*), 749 (*102695*) nm.

Fluorescence (EtOH, λ_{exc} 735 nm): 783 nm. **ϕ:** 1%.

IR-Spectrum (cm^{-1}, ATR): 2920 *v*(C–H aliphatic), 2845 *v*(C–H aliphatic), 1720 *v*(C═O), 1535, 1505, 1445, 1420, 1390, 1325, 1290, 1230, 1185, 1125, 1095, 1035, 1015, 965, 930, 795, 750.

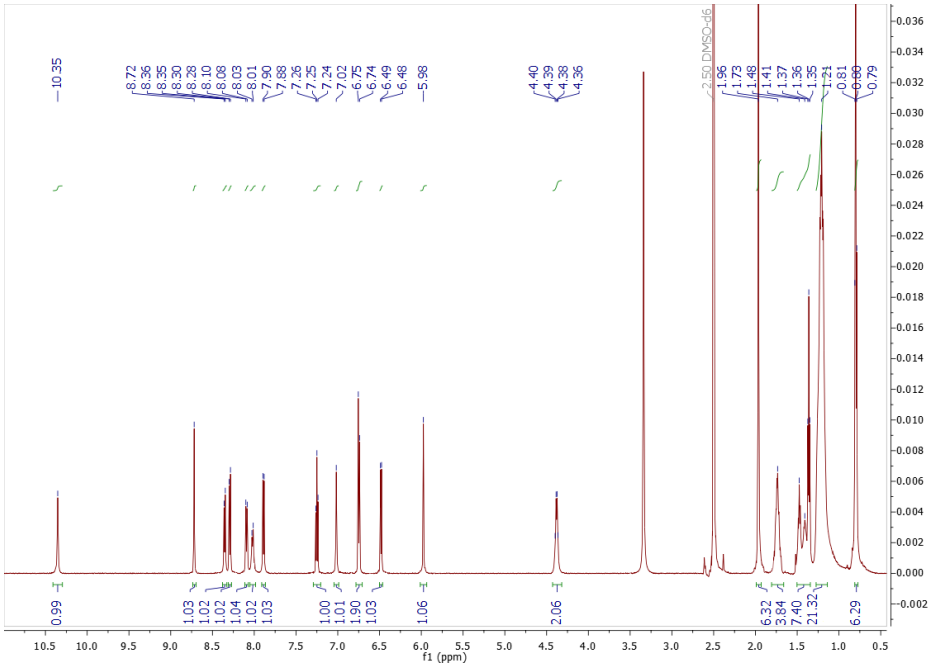

Figure 220 – ^{1}H-NMR in DMSO-d$_6$ of **348**.

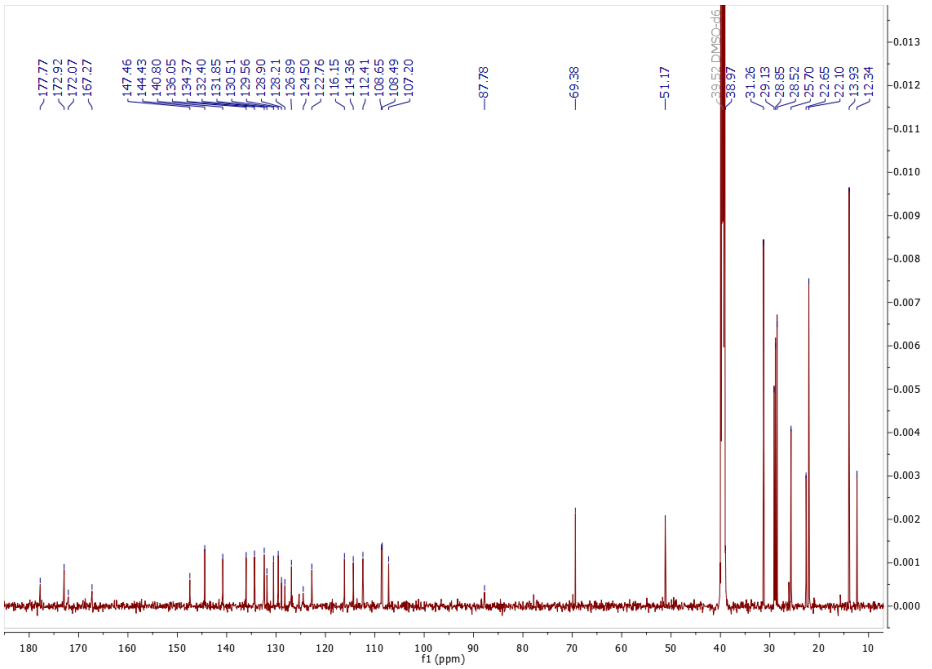

Figure 221 – ^{13}C-NMR in DMSO-d$_6$ of **348**.

Compound 349

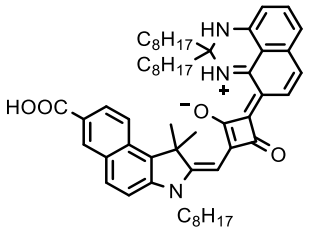

The product was isolated as a dark-blue powder (79 mg, 50%). R_f (silica gel): 0.80 (9:1 DCM/MeOH). M_p: 153-155 °C.

^{1}H-NMR (600 MHz, $CDCl_3$, RT): δ 10.58 (s, 1H, -NH^+), 8.75 (s, 1H, Ar-H), 8.22-8.28 (m, 3H, Ar-H), 8.02-8.03 (d, *J* = 8.9 Hz, 1H, Ar-H), 7.37-7.38 (d, *J* = 8.9 Hz, 1H, Ar-H), 7.26-7.29 (t, *J* = 7.8 Hz, 1H, Ar-H), 6.87-6.89 (d, *J* = 7.7 Hz, 1H, Ar-H), 6.80-6.82 (d, *J* = 9.0 Hz, 1H, Ar-H), 6.40-6.41 (d, *J* = 7.6 Hz, 1H, Ar-H), 6.08 (s, 1H, -CH=), 4.19 (br, 2H, -CH_2-), 2.08 (s, 6H, -CH_3), 1.82-1.93 (m, 6H, -CH_2-), 1.17-1.59 (m, 36H, -CH_2-), 0.82-0.84 (m, 9H, -CH_3) ppm.

^{13}C-NMR (151 MHz, $CDCl_3$, RT): δ 177.65, 174.95, 173.41, 170.58, 148.86, 143.56, 141.60, 137.42, 135.21, 133.73, 132.54, 131.85, 130.98, 130.64, 127.34, 125.94, 125.77, 122.91, 117.11, 116.72, 111.34, 110.14, 107.77, 88.45, 70.33, 51.67, 45.83, 44.33, 39.86, 31.97, 31.83, 29.93, 29.64, 29.45, 29.39, 29.22, 27.74, 27.08, 26.78, 23.48, 22.78, 22.69, 14.21 ppm.

MS (ESI$^-$, MeOH + NH_4OH): *m/z* 836.61 $[M]^-$; calculated for $C_{55}H_{71}N_3O_4$: 837.54.

UV-Vis (EtOH): λ_{max} (*ε*) = 404 (*7996*), 473 (*6584*), 755 (*99072*) nm.

Fluorescence (EtOH, λ_{exc} 735 nm): 788 nm. **ϕ:** 1%.

IR-Spectrum (cm^{-1}, ATR): 2920 *v*(C–H aliphatic), 2850 *v*(C–H aliphatic), 1715 *v*(C═O), 1535, 1505, 1450, 1420, 1390, 1290, 1230, 1180, 1125, 1035, 1010, 935, 800, 750.

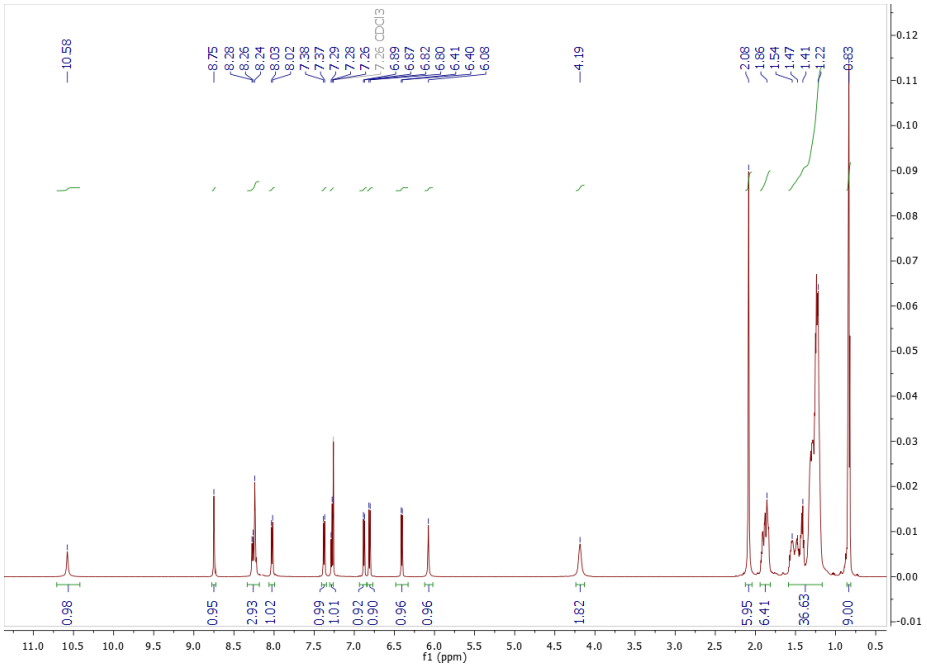

Figure 222 – ^{1}H-NMR in $CDCl_3$ of **349**.

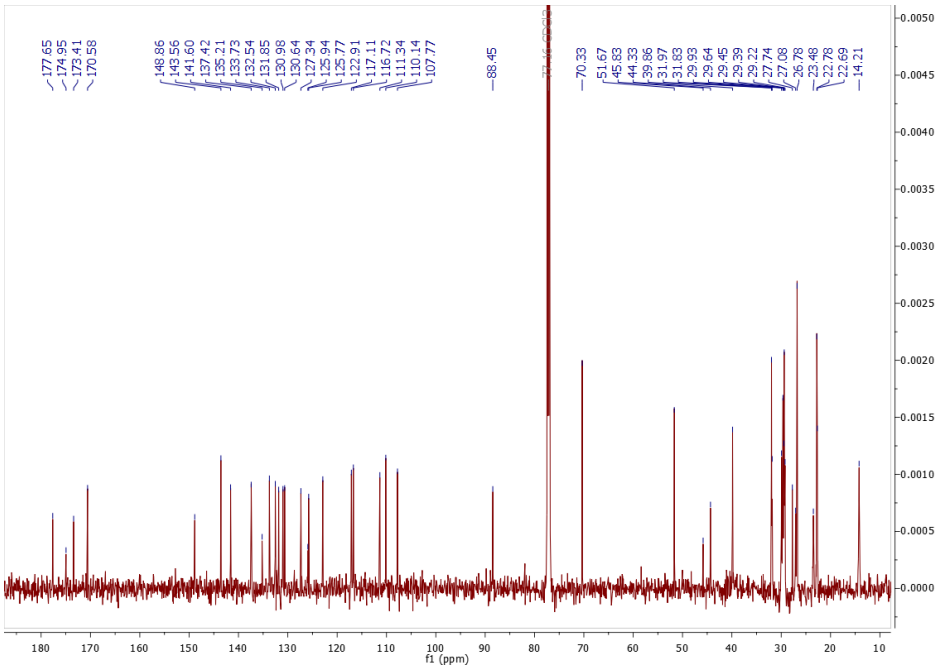

Figure 223 – ^{13}C-NMR in $CDCl_3$ of **349**.

Compound 350

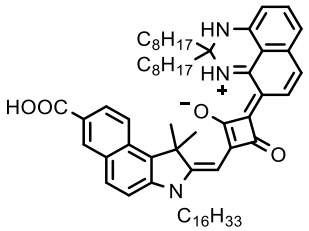

The product was isolated as a dark-blue powder (154 mg, 62%). R_f (silica gel): 0.85 (9:1 DCM/MeOH). M_p: 137-139 °C.

^{1}H-NMR (600 MHz, $CDCl_3$, RT): δ 10.60 (s, 1H, -NH^+), 8.75 (s, 1H, Ar-H), 8.21-8.27 (m, 3H, Ar-H), 8.02-8.04 (d, *J* = 8.8 Hz, 1H, Ar-H), 7.37-7.39 (d, *J* = 8.9 Hz, 1H, Ar-H), 7.27-7.29 (t, *J* = 7.7 Hz, 1H, Ar-H), 6.87-6.89 (d, *J* = 7.6 Hz, 1H, Ar-H), 6.80-6.82 (d, *J* = 9.1 Hz, 1H, Ar-H), 6.39-6.40 (d, *J* = 7.6 Hz, 1H, Ar-H), 6.04 (s, 1H, -CH=), 4.18 (br, 2H, -CH_2-), 2.08 (s, 6H, -CH_3), 1.83-1.93 (m, 6H, -CH_2-), 1.19-1.57 (m, 58H, -CH_2-), 0.83-0.89 (m, 9H, -CH_3) ppm.

^{13}C-NMR (151 MHz, $CDCl_3$, RT): δ 177.69, 175.16, 173.34, 170.74, 148.90, 143.56, 141.68, 140.64, 137.45, 135.20, 133.82, 132.56, 131.87, 131.05, 130.61, 127.31, 125.50, 122.95, 117.14, 116.74, 111.40, 110.19, 110.09, 107.78, 88.44, 70.35, 51.66, 44.33, 39.87, 32.06, 31.98, 29.93, 29.83, 29.81, 29.71, 29.65, 29.58, 29.50, 29.45, 29.39, 27.75, 27.10, 26.80, 23.49, 22.83, 22.79, 14.25 ppm.

MS (ESI^-, MeOH + NH_4OH): *m/z* 948.42 $[M]^-$; calculated for $C_{63}H_{87}N_3O_4$: 949.67.

UV-Vis (EtOH): λ_{max} (ε) = 404 (*9185*), 474 (*6908*), 756 (*95794*) nm.

Fluorescence (EtOH, λ_{exc} 735 nm): 787 nm. **ϕ:** 1%.

IR-Spectrum (cm^{-1}, ATR): 2920 *v*(C–H aliphatic), 2845 *v*(C–H aliphatic), 1705 *v*(C═O), 1580, 1535, 1510, 1450, 1420, 1390, 1290, 1230, 1180, 1125, 1040, 1015, 935, 815, 800, 750.

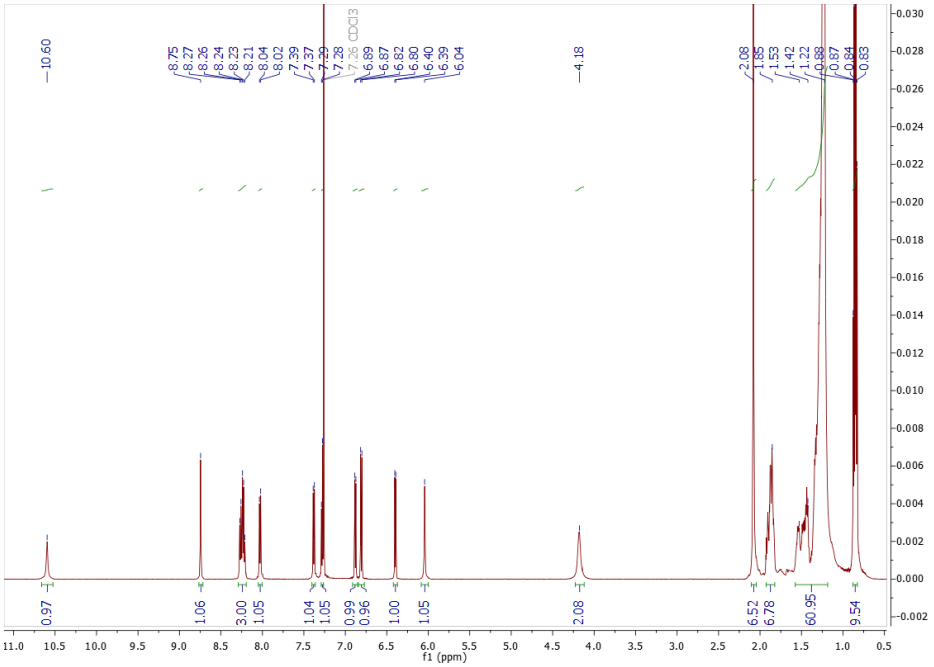

Figure 224 – ^{1}H-NMR in $CDCl_3$ of **350**.

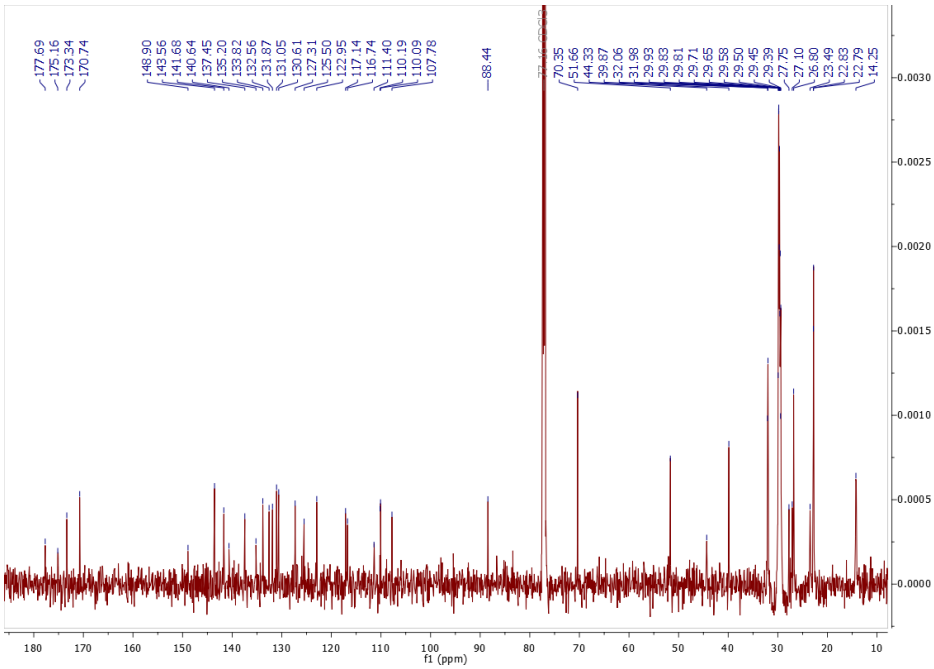

Figure 225 – ^{13}C-NMR in $CDCl_3$ of **350**.

1.12. General Synthesis of CI-SQ Dyes with Mono-substituted DHPs

The synthesis of CI-SQ dyes with mono-substituted DHP were performed according to the following procedure.

A mixture of CI-emisquaraine **323** (150 mg, 0.46 mmol), mono-substituted DHP derivative (0.69 mmol) and 12 mL of a solution toluene/*n*-butanol (1:1) was introduced in a sealed 20 mL reaction vial and heated in a microwave reactor at 160 °C for 30 min. After cooling to room temperature, the reaction mixture was washed out of the reaction vessel with methanol and all the solvent was removed by evaporation under vacuum. The crude was purified by flash chromatography on silica gel using DCM/MeOH/acetic acid (94:5.5:0.5) as eluent.

Compound 393

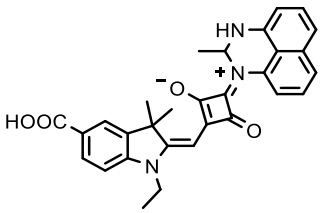

The product was isolated as a dark-purple powder (25 mg, 11%). R_f (silica gel): 0.55 (9:1 DCM/MeOH). M_p: > 200 °C.

^{1}H-NMR (600 MHz, DMSO-d$_6$, RT): δ 8.02 (s, 1H, Ar-H), 7.95-7.96 (d, *J* = 8.3 Hz, 1H, Ar-H), 7.71-7.73 (t, *J* = 7.5 Hz, 2H, Ar-H), 7.53-7.55 (t , *J* = 8.0 Hz, 1H, Ar-H), 7.37-7.39 (m, 2H, Ar-H), 7.29-7.30 (d, *J* = 8.2 Hz, 1H, Ar-H), 7.25 (d, *J* = 3.2 Hz, 1H, -NH), 6.77-6.78 (d, *J* = 7.4 Hz, 1H, Ar-H), 6.72-6.75 (m, 1H, -CH-), 5.81 (s, 1H, -CH=), 4.10 (br, 2H, -CH_2-), 1.70 (s, 3H, -CH_3), 1.67 (s, 3H, -CH_3), 1.36-1.37 (d, *J* = 6.2 Hz, 3H, -CH_3), 1.26-1.28 (t, *J* = 7.2 Hz, 3H, -CH_3) ppm.

^{13}C-NMR (151 MHz, DMSO-d$_6$, RT): δ 180.10, 178.76, 175.66, 168.62, 167.09, 145.52, 141.25, 137.81, 133.50, 130.29, 128.37, 128.20, 127.73, 126.00, 125.74, 125.40, 123.13, 117.87, 116.66, 114.00, 108.90, 85.83, 63.08, 48.15, 37.98, 26.85, 26.61, 20.01, 11.47 ppm.

HRMS (ESI$^-$-TOF, MeOH): *m/z* 492.1944 $[M]^-$; calculated for $C_{30}H_{27}N_3O_4$: 492.1929 (-1).

UV-Vis (EtOH): λ_{max} (ε) = 542 (*44511*) nm.

Fluorescence (EtOH, λ_{exc} 525 nm): 568 nm. **ϕ:** <1 %.

IR-Spectrum: Not enough sample to perform the experiment.

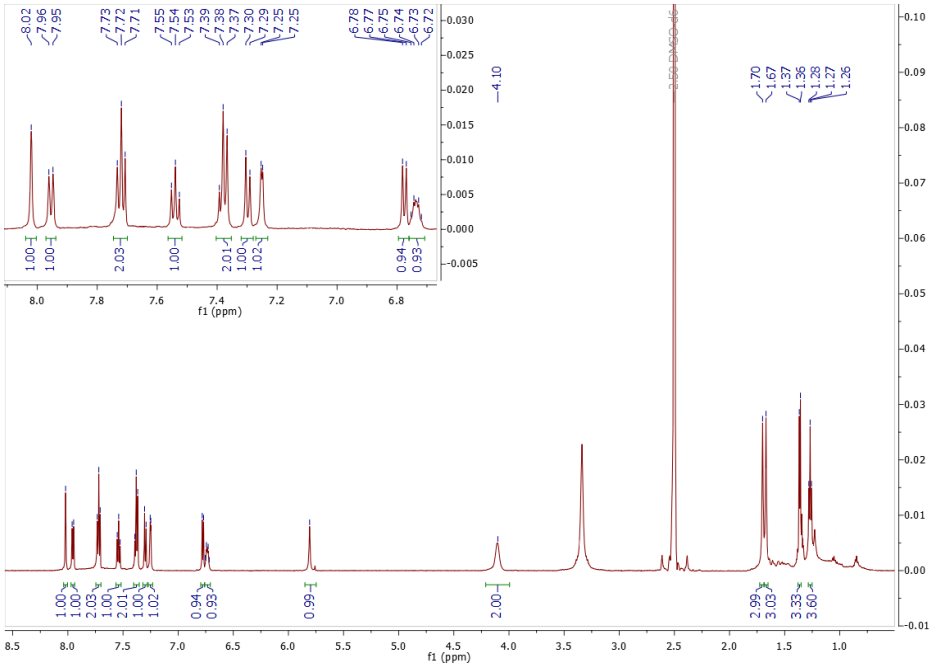

Figure 226 – ^{1}H-NMR in DMSO-d$_6$ of **393**.

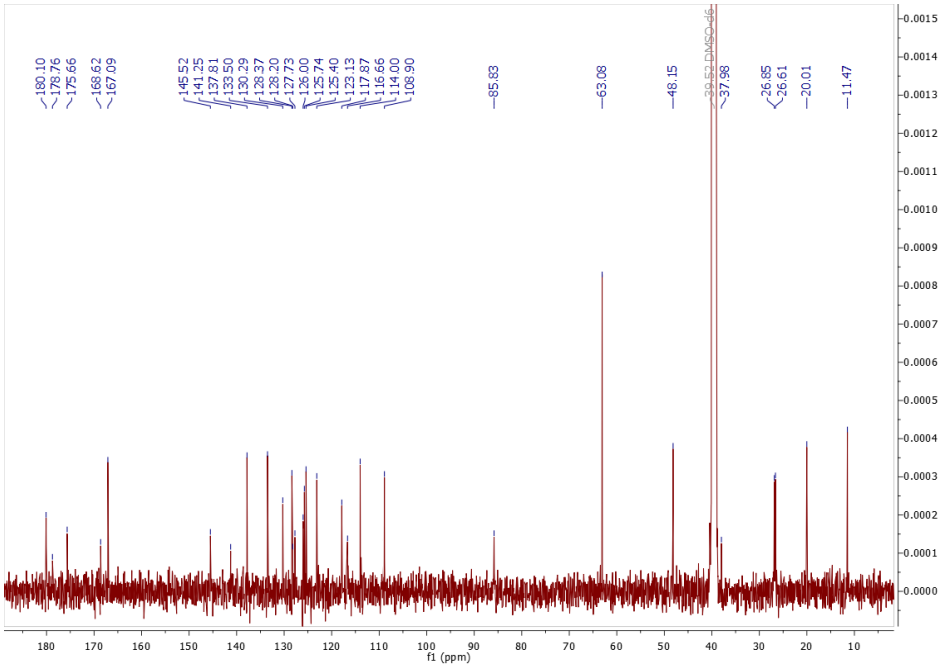

Figure 227 – ^{13}C-NMR in DMSO-d$_6$ of **393**.

Compound 392

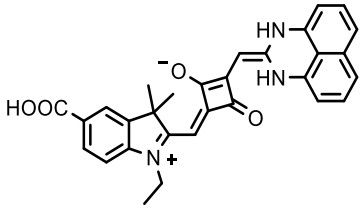

The product was isolated as a dark-purple powder (18 mg, 8%). R_f (silica gel): 0.45 (9:1 DCM/MeOH). M_p: > 200 °C.

^{1}H-NMR (600 MHz, DMSO-d$_6$, RT): δ 7.84-7-86 (m, 2H, Ar-H), 7.28-7.31 (t, *J* = 7.7 Hz, 2H, Ar-H), 7.24-7.26 (d, *J* = 8.3 Hz, 2H, Ar-H), 7.04-7.05 (d, *J* = 8.4 Hz, 1H, Ar-H), 6.62-6.63 (d, *J* = 7.2 Hz, 2H), 5.39 (s, 1H, -CH=), 5.27 (s, 1H, -CH=), 3.86-3.89 (q, *J* = 7.0 Hz, 2H, -CH_2-), 1.62 (s, 6H, -CH_3), 1.18-1.20 (t, *J* = 7.2 Hz, 3H, -CH_3) ppm.

^{13}C-NMR (151 MHz, DMSO-d$_6$, RT): δ 182.96, 180.59, 167.33, 159.93, 153.71, 146.82, 140.14, 134.42, 130.36, 128.62, 122.78, 120.09, 117.82, 106.96, 84.96, 45.97, 36.80, 27.11, 11.10 ppm.

HRMS (ESI$^-$-TOF, MeOH): *m/z* 490.1781 $[M]^-$; calculated for $C_{30}H_{25}N_3O_4$: 490.1772 (-1).

UV-Vis (EtOH): λ_{max} (ε) = 572 (*38858*) nm.

Fluorescence (EtOH, λ_{exc} 560 nm): 614 nm. **ϕ:** <1 %.

IR-Spectrum (cm^{-1}, ATR): 2970 *ν*(C–H aliphatic), 1670 *ν*(C═O), 1645 *ν*(C═O), 1600, 1535, 1490, 1415, 1360, 1290, 1235, 1195, 1105, 1065, 930, 815, 760, 715.

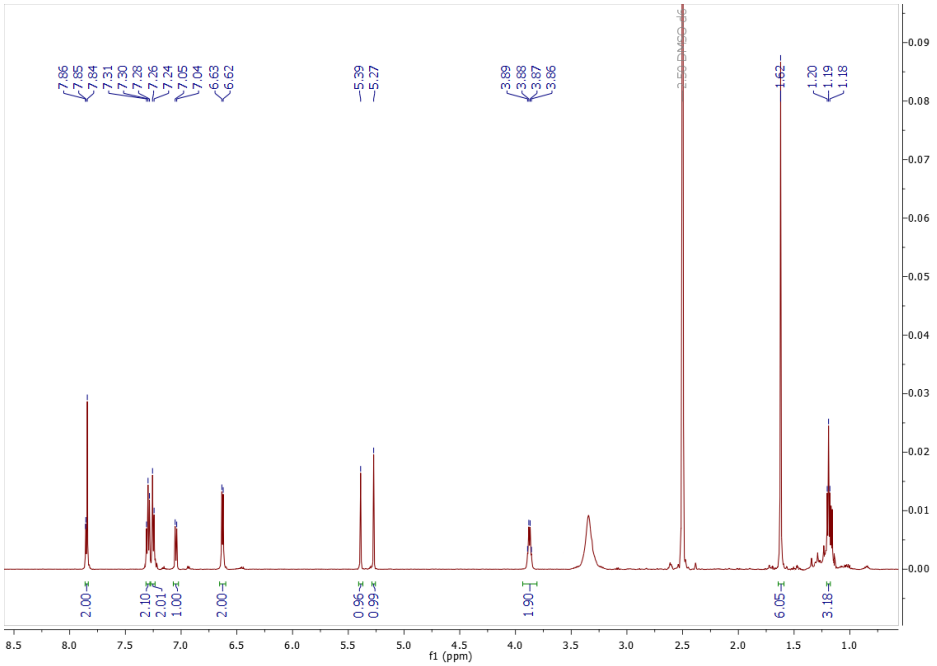

Figure 228 – ^{1}H-NMR in DMSO-d$_6$ of **392**.

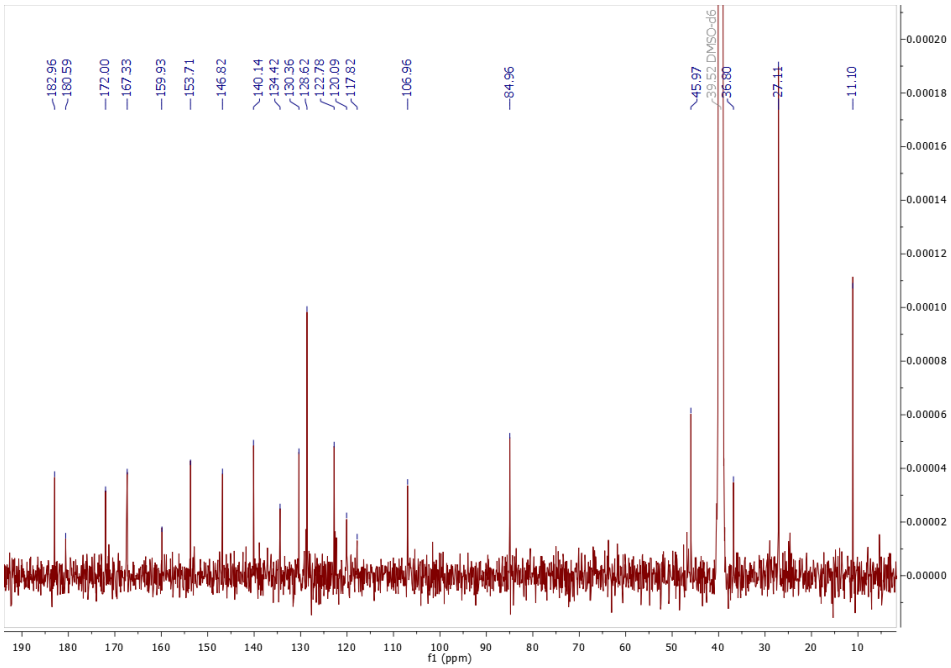

Figure 229 – ^{13}C-NMR in DMSO-d$_6$ of **392**.

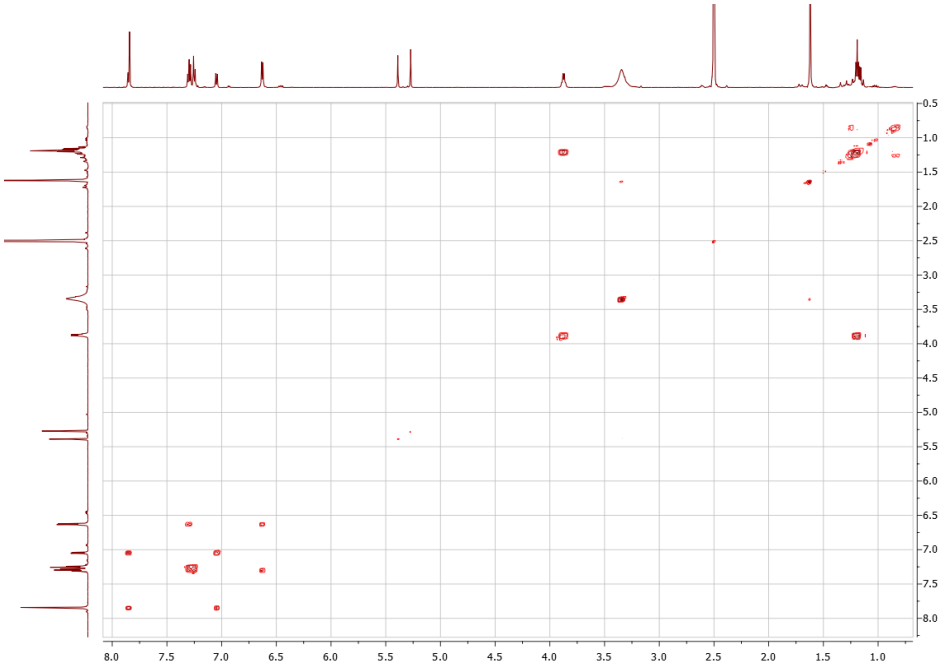

Figure 230 – COSY in DMSO-d_6 of **392**.

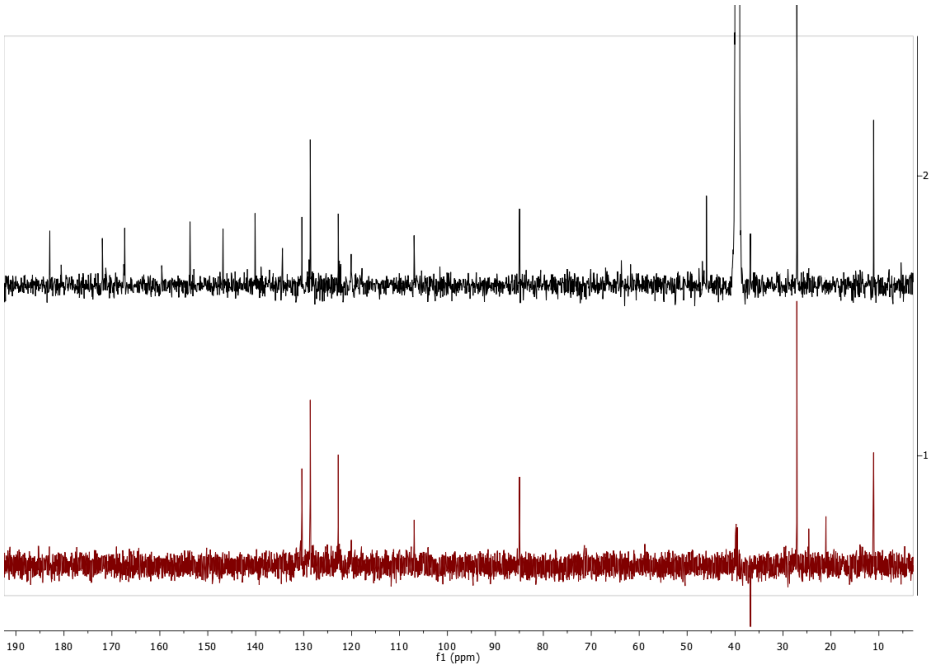

Figure 231 – DEPT-135 (red) *vs*. ^{13}C-NMR (black) in DMSO-d_6 of **392**.

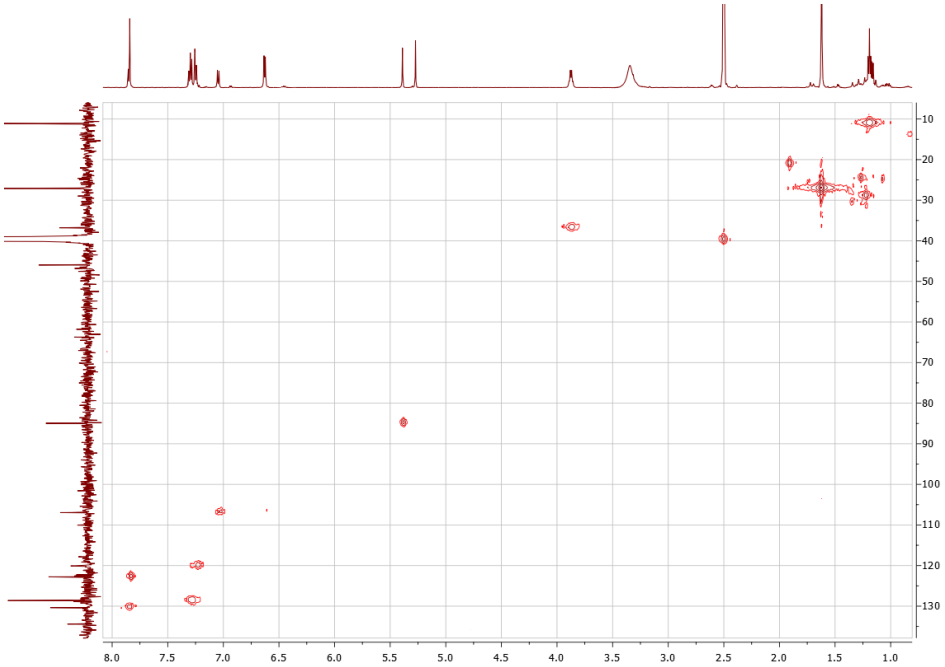

Figure 232 – HSQC in DMSO-d_6 of **392**.

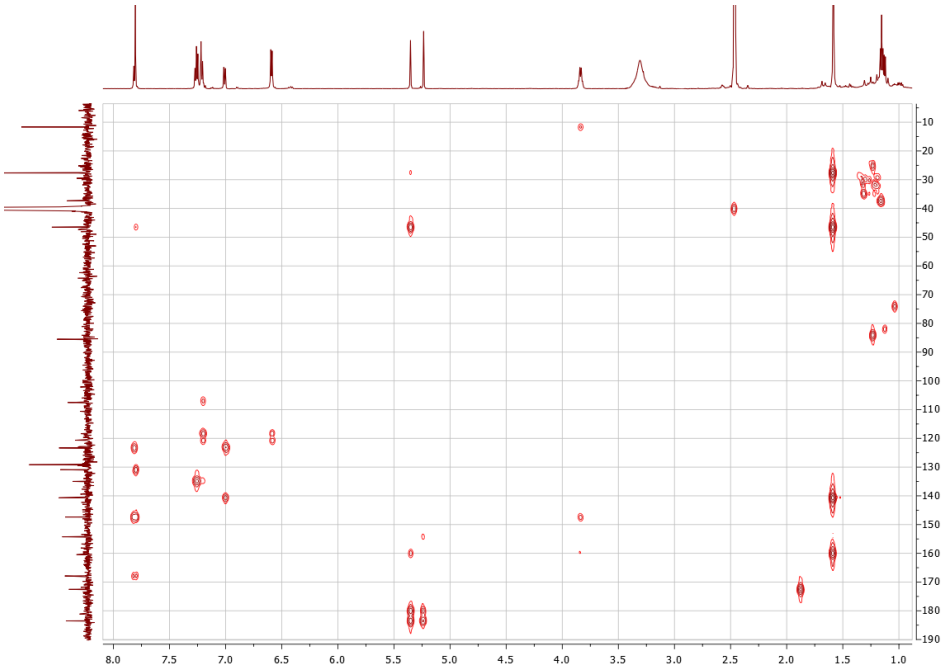

Figure 233 – HMBC in DMSO-d_6 of **392**.

Compound 395

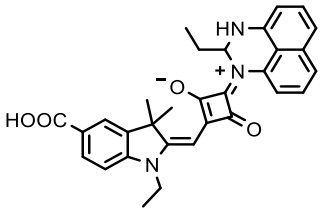

The product was isolated as a dark-purple powder (37 mg, 16%). R_f (silica gel): 0.75 (9:1 DCM/MeOH). M_p: > 200 °C.

^{1}H-NMR (600 MHz, DMSO-d$_6$, RT): δ 8.01 (s, 1H, Ar-H), 7.95-7.96 (dd, *J* = 8.3 Hz, *J* = 1.5 Hz, 1H, Ar-H), 7.71-7.72 (d, *J* = 8.3 Hz, 1H, Ar-H), 7.68-7-69 (d, *J* = 7.1 Hz, 1H, Ar-H), 7.52-7.54 (t, *J* = 8.0 Hz, 1H, Ar-H), 7.39-7-40 (d, J = 3.7 Hz, 1H, -NH), 7.35-7.38 (m, 2H, Ar-H), 7.27-7.28 (d, *J* = 8.0 Hz, 1H, Ar-H), 6.77-6.79 (d, *J* = 7.1 Hz, 1H, Ar-H), 6.46-6.49 (m, 1H, -CH-), 5.81 (s, 1H, -CH=), 4.09-4.10 (m, 2H, -CH_2-), 1.71 (s, 3H, -CH_3), 1.66 (s, 3H, -CH_3), 1.60-1.64 (m, 2H, -CH_2-), 1.26-1.28 (t, *J* = 7.1 Hz, 3H, -CH_3), 0.89-0.91 (t, *J* = 7.4 Hz, 3H, -CH_3) ppm.

^{13}C-NMR (151 MHz, DMSO-d$_6$, RT): δ 180.18, 176.13, 174.97, 168.64, 167.14, 141.11, 138.01, 133.46, 130.27, 128.89, 128.37, 128.20, 127.74, 125.96, 125.78, 125.31, 123.15, 117.85, 116.47, 114.41, 109.40, 108.63, 85.74, 66.70, 48.16, 37.98, 26.88, 26.60, 25.82, 11.49, 8.60 ppm.

HRMS (ESI$^-$-TOF, MeOH): *m/z* 506.2067 $[M]^-$; calculated for $C_{31}H_{29}N_3O_4$: 506.2085 (-1).

UV-Vis (EtOH): λ_{max} (ε) = 543 (*48012*) nm.

Fluorescence (EtOH, λ_{exc} 525 nm): 570 nm. **ϕ:** <1 %.

IR-Spectrum (cm^{-1}, ATR): 2960 *v*(C–H aliphatic), 2920 *v*(C–H aliphatic), 2850 *v*(C–H aliphatic), 1680 *v*(C═O), 1595, 1495, 1440, 1350, 1295, 1260, 1205, 1095, 1065, 1050, 945, 815, 755.

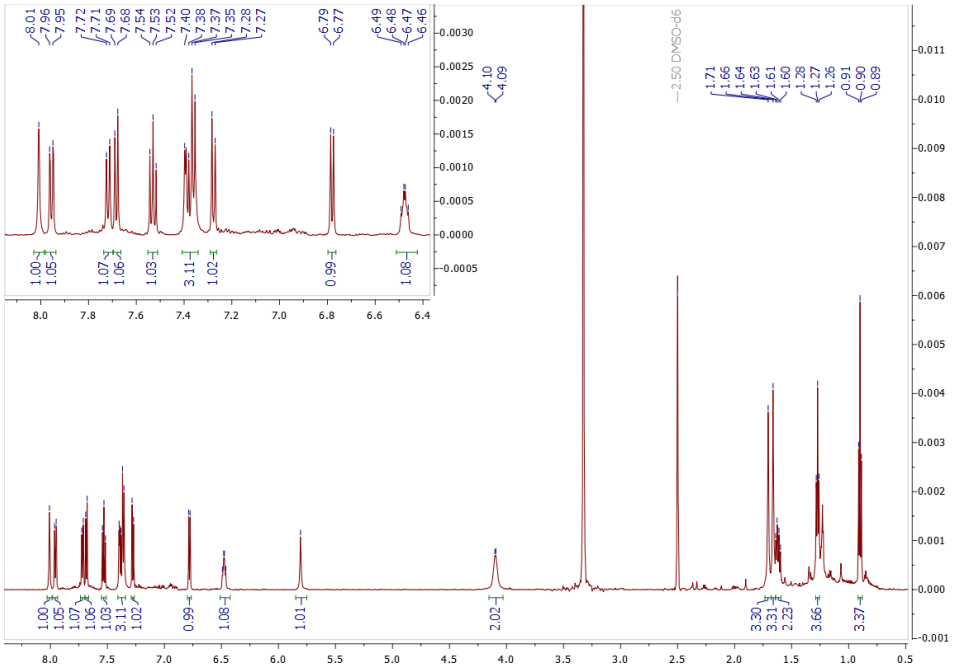

Figure 234 – ^{1}H-NMR in DMSO-d$_6$ of **395**.

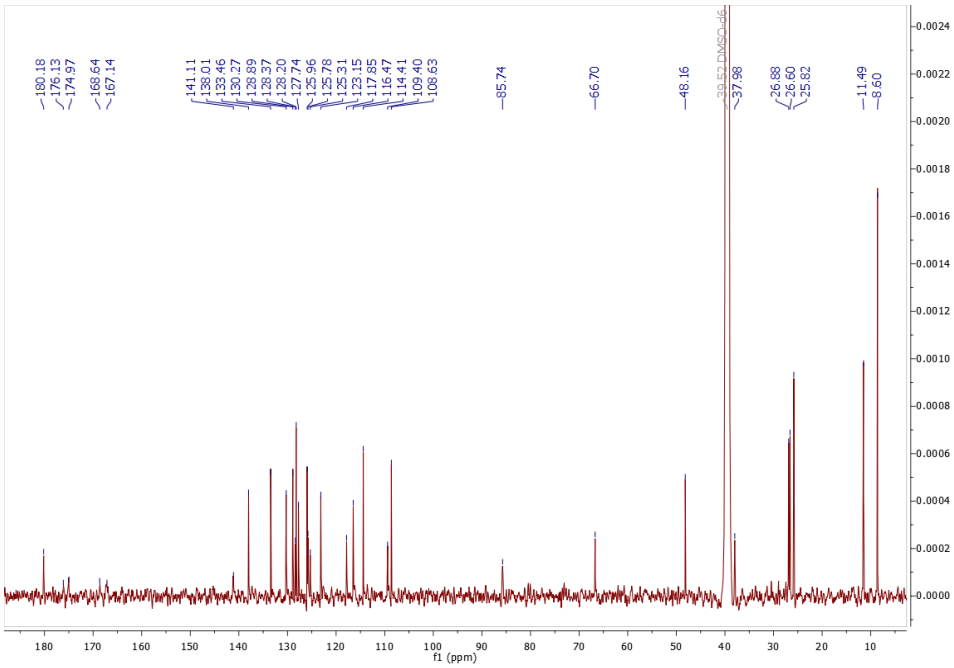

Figure 235 – ^{13}C-NMR in DMSO-d$_6$ of **395**.

Compound 391

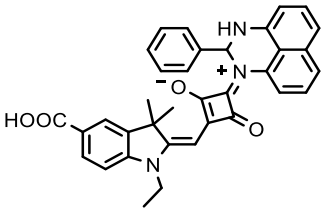

The product was isolated as a dark-purple powder (66 mg, 26%). R_f (silica gel): 0.30 (95:5 DCM/MeOH). M_p: > 200 °C.

^{1}H-NMR (600 MHz, DMSO-d$_6$, RT): δ 8.14 (d, *J* = 4.3 Hz, 1H, -NH), 8.04 (d, *J* = 1.5 Hz, 1H, Ar-H), 7.96-7.98 (dd, *J* = 8.3 Hz, *J* = 1.6 Hz, 1H), 7.67-7.68 (m, 2H, Ar-H and -CH-), 7.62-7.63 (d, *J* = 8.0 Hz, 1H, Ar-H), 7.44-7.47 (t, *J* = 7.9 Hz, 1H, Ar-H), 7.37-7.42 (m, 4H, Ar-H), 7.23-7.26 (m, 3H, Ar-H), 7.16-7.19 (t, *J* = 7.3 Hz, 1H, Ar-H), 6.96-6.97 (d, *J* = 7.3 Hz, 1H, Ar-H), 5.89 (s, 1H, -CH=), 4.13 (m, 2H, -CH_2-), 1.73 (s, 3H, -CH_3), 1.69 (s, 3H, -CH_3), 1.27-1.30 (t, *J* = 7.3 Hz, 3H, -CH_3) ppm.

^{13}C-NMR (151 MHz, DMSO-d$_6$, RT): δ 180.81, 175.72, 169.25, 167.11, 145.46, 141.41, 139.31, 138.38, 133.48, 130.32, 129.09, 128.58, 128.04, 127.78, 126.36, 125.97, 125.69, 125.65, 123.19, 117.95, 116.95, 114.81, 109.70, 108.86, 86.12, 65.96, 48.35, 38.12, 26.83, 26.57, 11.55 ppm.

HRMS (ESI$^-$-TOF, MeOH): *m/z* 554.2065 $[M]^-$; calculated for $C_{35}H_{29}N_3O_4$: 554.2085 (-1).

UV-Vis (EtOH): λ_{max} (*ε*) = 546 (*71618*) nm.

Fluorescence (EtOH, λ_{exc} 525 nm): 571 nm. **ϕ:** <1 %.

IR-Spectrum (cm^{-1}, ATR): 3380 *ν*(N–H), 3325 *ν*(N–H), 3055 *ν*(C–H aliphatic), 2975 *ν*(C–H aliphatic), 1670, 1605 *ν*(C═C aromatic), 1490, 1445, 1405, 1360, 1290, 1245, 1200, 1100, 1070, 1045, 950, 810, 755, 705.

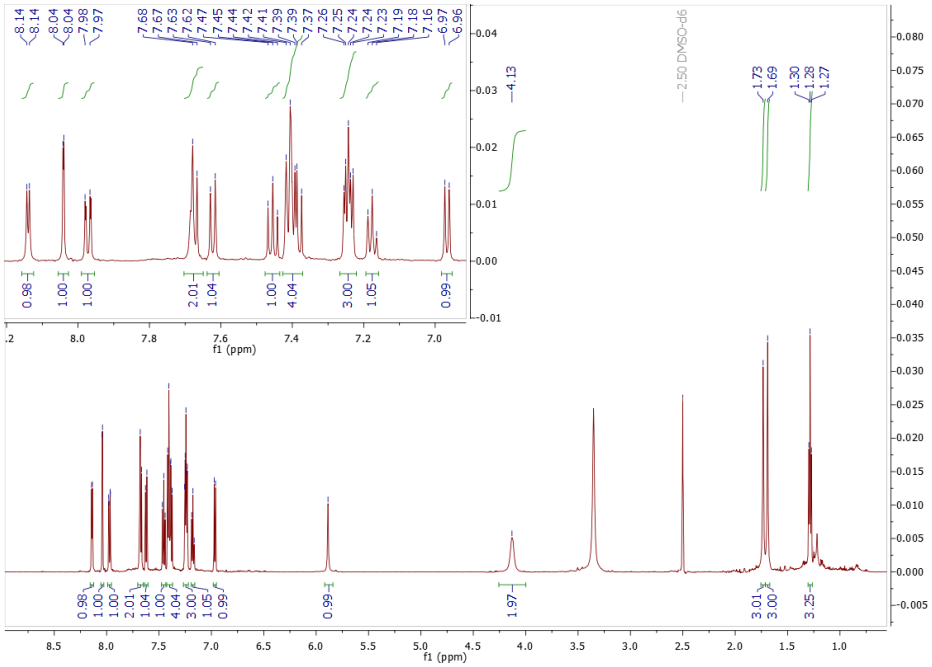

Figure 236 – ^{1}H-NMR in DMSO-d$_6$ of **391**.

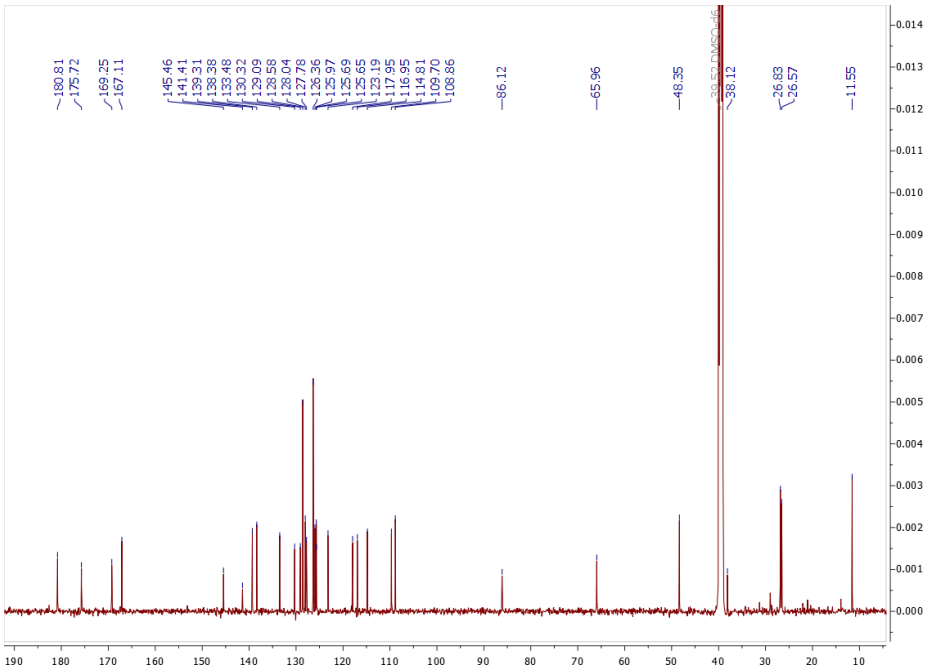

Figure 237 – ^{13}C-NMR in DMSO-d$_6$ of **391**.

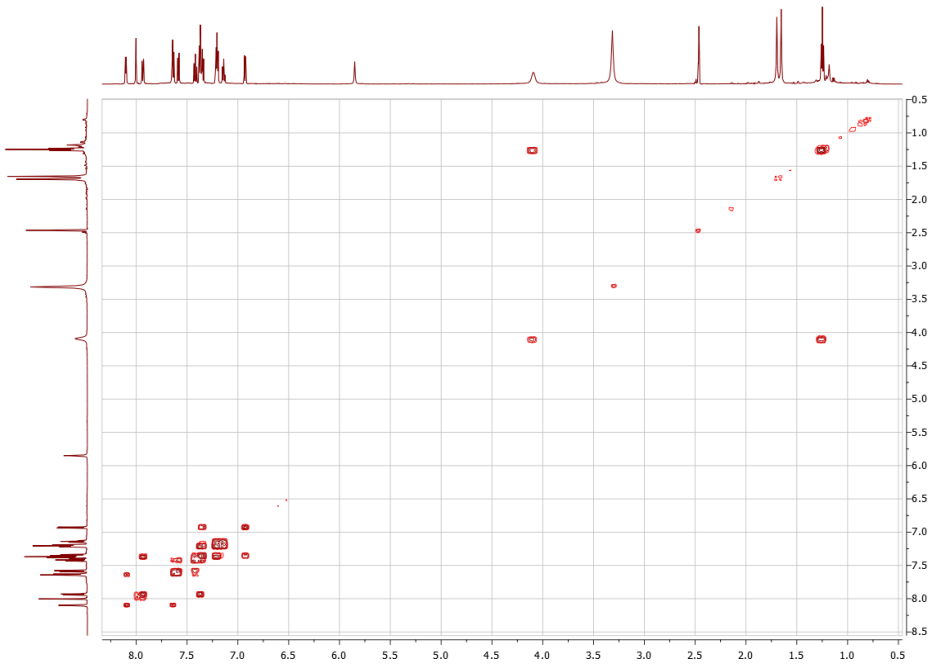

Figure 238 – COSY in DMSO-d_6 of **391**.

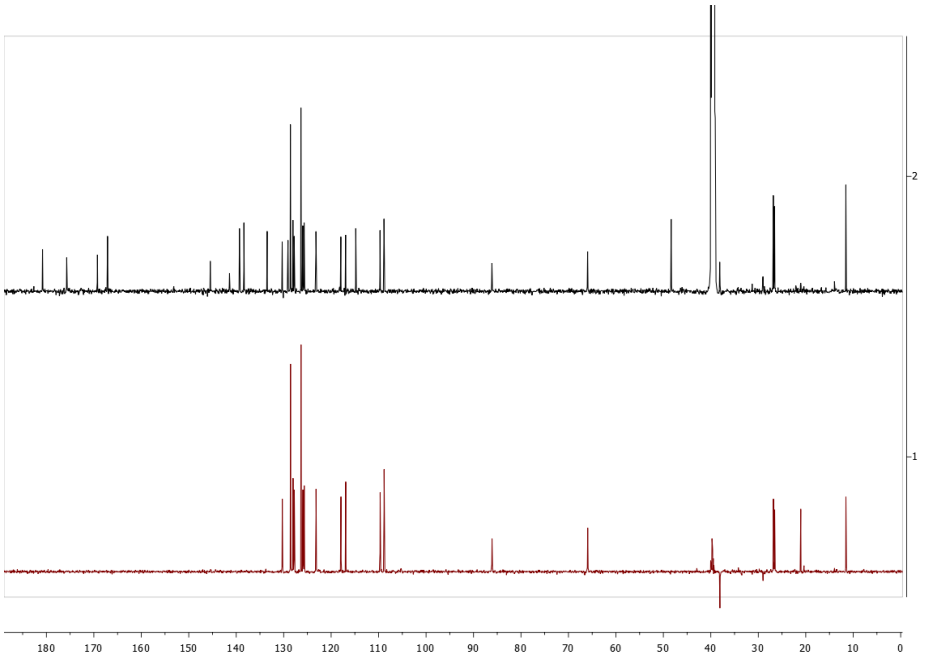

Figure 239 – DEPT-135 (red) *vs*. ^{13}C-NMR (black) in DMSO-d_6 of **391**.

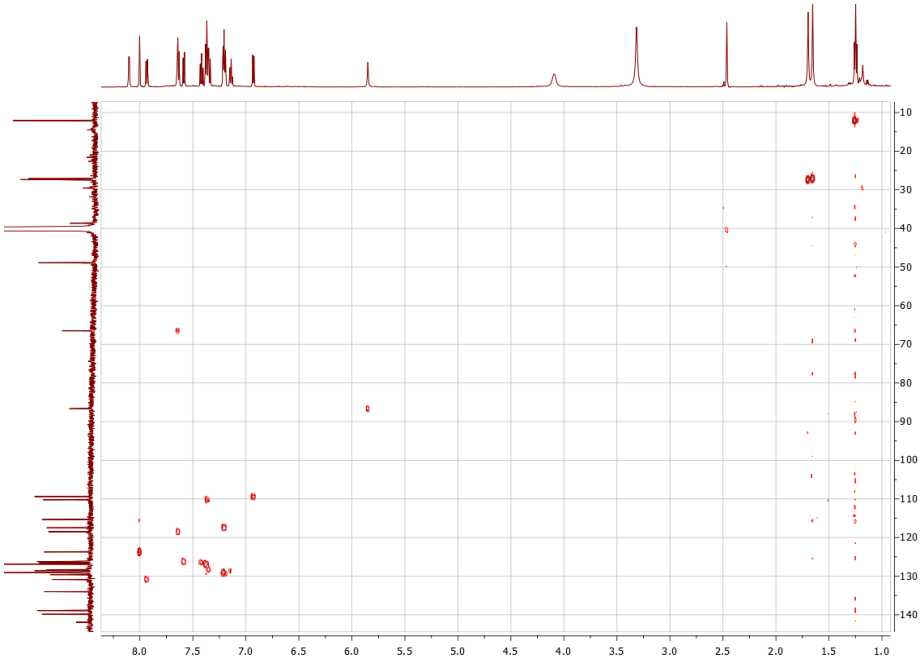

Figure 240 – HSQC in DMSO-d_6 of **391**.

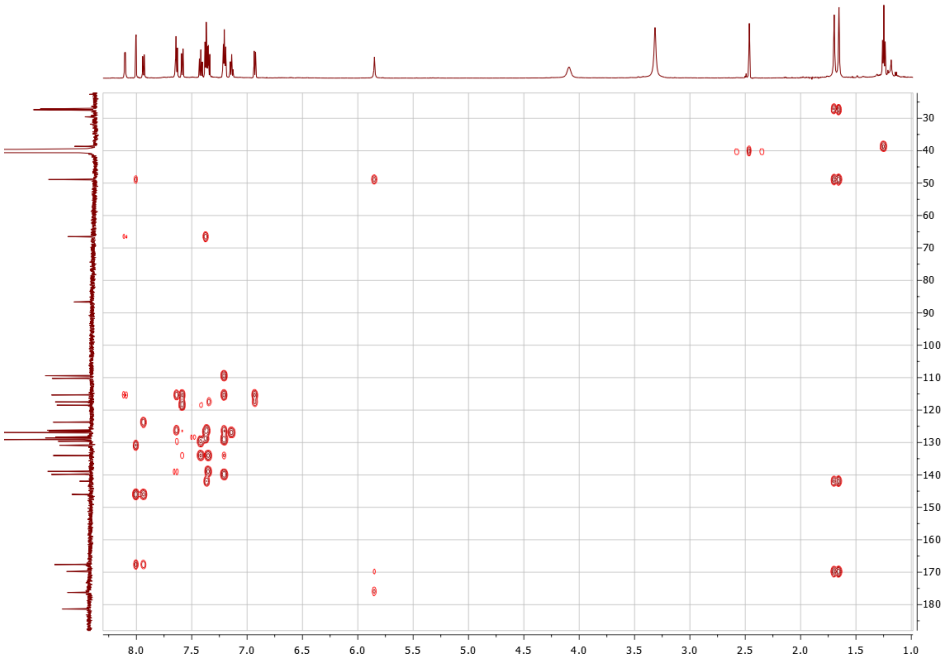

Figure 241 – HMBC in DMSO-d_6 of **391**.

1.13. General Synthesis of Mono-substituted *Impy* Ligands

Mono-substituted *Impy* ligands were synthetized according to the published general procedures.[496,511]

A mixture of di(pyridin-2-yl)methanone **352** (2.0 g, 10.9 mmol), 2-substituted benzaldehyde (16.3 mmol) and ammonium acetate (4.3 g, 54.5 mmol) and 150 mL of acetic acid was refluxed for 12 h. After, the reaction mixture was cooled to room temperature and acetic acid was removed by evaporation under vacuum. The resulting solid was dissolved in a saturated aqueous solution of sodium carbonate and the mixture was extracted with dichloromethane. The organic layer was separated, dried over sodium sulphate and the solvent evaporated under vacuum. The desired product was purified by flash chromatography on silica gel using DCM/MeOH (98:2) as eluent.

Compound 353

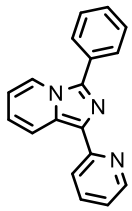

The product was isolated as a light-brown powder (2.96 g, 94%). R_f (silica gel): 0.30 (95:5 DCM/MeOH). M_p: 91-93 °C.

^{1}H-NMR (600 MHz, $CDCl_3$, RT): δ 8.70-8.72 (dt, *J* = 9.2 Hz, *J* = 1.2 Hz, 1H, Ar-H), 8.63-8.64 (dq, *J* = 4.9 Hz, *J* = 0.9 Hz, 1H, Ar-H), 8.25-8.27 (m, 2H, Ar-H), 7.84-7.86 (m, 2H, Ar-H), 7.70-7.73 (m, 1H, Ar-H), 7.54-7.57 (m, 2H, Ar-H), 7.45-7.48 (tt, *J* = 7.4 Hz, *J* = 1.2 Hz, 1H, Ar-H), 7.09-7.11 (m, 1H, Ar-H), 6.91-6.94 (m, 1H, Ar-H), 6.64-6.67 (m, 1H, Ar-H) ppm.

^{13}C-NMR (151 MHz, $CDCl_3$, RT): δ 155.17, 149.09, 138.20, 136.38, 130.69, 130.35, 130.27, 129.18, 129.05, 128.52, 121.97, 121.73, 121.17, 120.57, 120.07, 114.04 ppm.

HRMS (ESI$^+$-TOF, MeOH): *m/z* 272.1188 $[M+H]^+$; calculated for $C_{18}H_{13}N_3$: 272.1182 (+1).

UV-Vis (DCM): λ_{max} (ε) = 323 (*11615*) nm.

Fluorescence (DCM, λ_{exc} 340 nm): 463 nm. **ϕ:** 18%.

IR-Spectrum (cm^{-1}, ATR): 3065 *ν*(C–H aromatic), 1585 *ν*(C═C aromatic), 1530 *ν*(C═C aromatic), 1505 *ν*(C═C aromatic), 1475 *ν*(C═C aromatic), 1440, 1425, 1400, 1355, 1300, 1245, 1135, 1120, 1070, 1005, 950, 785, 770, 735.

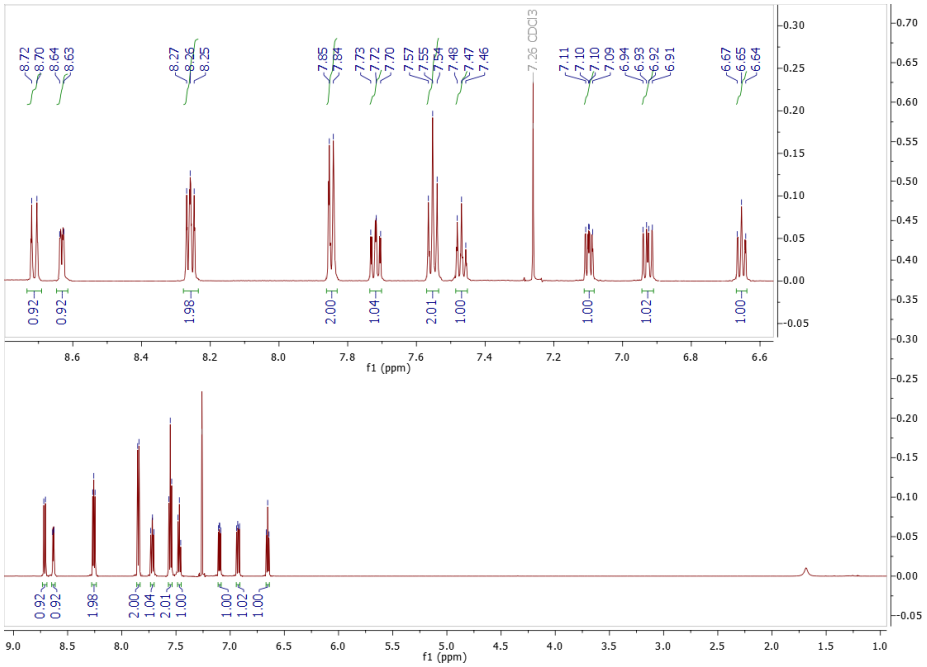

Figure 242 – ^{1}H-NMR in $CDCl_3$ of **353**.

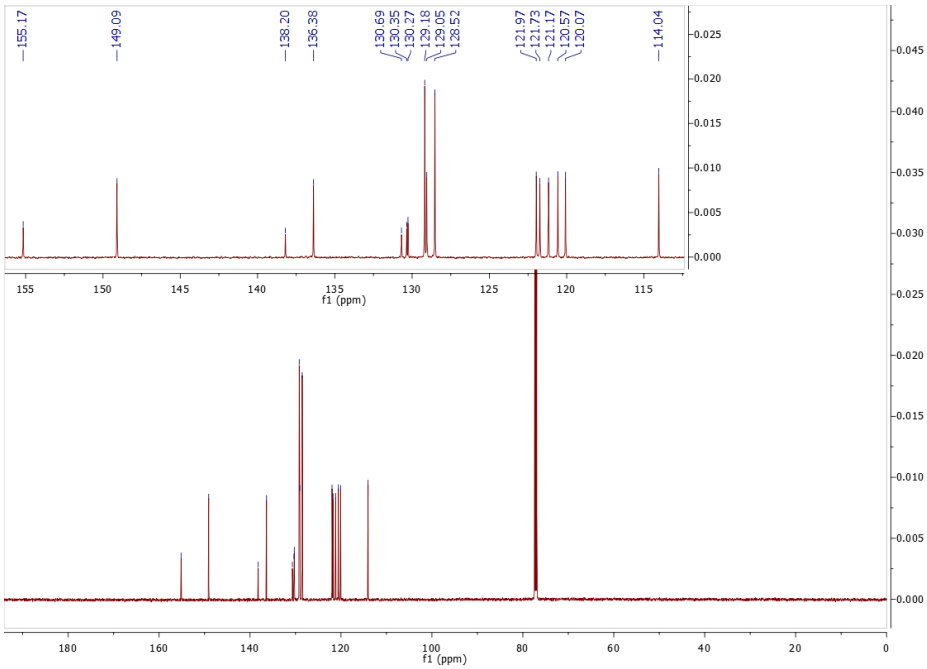

Figure 243 – ^{13}C-NMR in $CDCl_3$ of **353**.

Compound 354

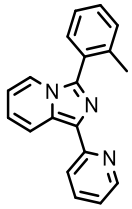

The product was isolated as a light-brown powder (2.89 g, 93%). R_f (silica gel): 0.30 (95:5 DCM/MeOH). M_p: 111-113 °C.

^{1}H-NMR (600 MHz, $CDCl_3$, RT): δ 8.70-8.72 (d, *J* = 9.2 Hz, 1H, Ar-H), 8.63-8.64 (dq, *J* = 4.9 Hz, *J* = 0.9 Hz, 1H, Ar-H), 8.23-8.24 (d, *J* = 8.0 Hz, 1H, Ar-H), 7.70-7.72 (td, *J* = 7.9 Hz, *J* = 1.8 Hz, 1H, Ar-H), 7.63-7.65 (d, *J* = 7.1 Hz, 1H, Ar-H), 7.50-7.51 (d, *J* = 7.5 Hz, 1H, Ar-H), 7.38-7.43 (m, 2H, Ar-H), 7.33-7.36 (td, *J* = 7.4 Hz, *J* = 0.9 Hz, 1H, Ar-H), 7.08-7.11 (m, 1H, Ar-H), 6.92-6.95 (m, 1H, Ar-H), 6.60-6.62 (m, 1H, Ar-H), 2.26 (s, 3H, -CH_3) ppm.

^{13}C-NMR (151 MHz, $CDCl_3$, RT): δ 155.32, 149.09, 138.73, 137.88, 136.38, 130.99, 130.78, 130.02, 129.82, 129.40, 129.30, 126.29, 121.83, 121.74, 121.06, 120.45, 120.00, 113.70, 19.88 ppm.

HRMS (ESI$^+$-TOF, MeOH): *m/z* 286.1338 $[M+H]^+$; calculated for $C_{19}H_{15}N_3$: 286.1339 (+1).

UV-Vis (DCM): λ_{max} (*ε*) = 299 (*16961*), 319 (*17003*), 367 (*11755*) nm.

Fluorescence (DCM, λ_{exc} 340 nm): 460 nm. **ϕ:** 32%.

IR-Spectrum (cm^{-1}, ATR): 3040 *v*(C–H aromatic), 1590 *v*(C═C aromatic), 1535 *v*(C═C aromatic), 1510 *v*(C═C aromatic), 1480 *v*(C═C aromatic), 1400, 1355, 1315, 1140, 1110, 1090, 1005, 940, 790, 775, 755, 745, 725, 710.

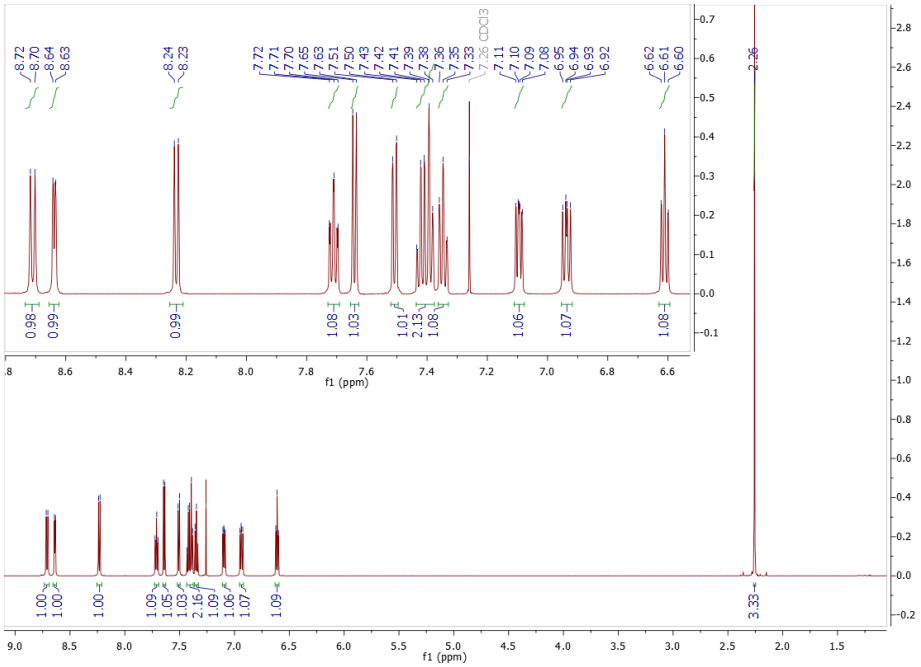

Figure 244 – ^{1}H-NMR in $CDCl_3$ of **354**.

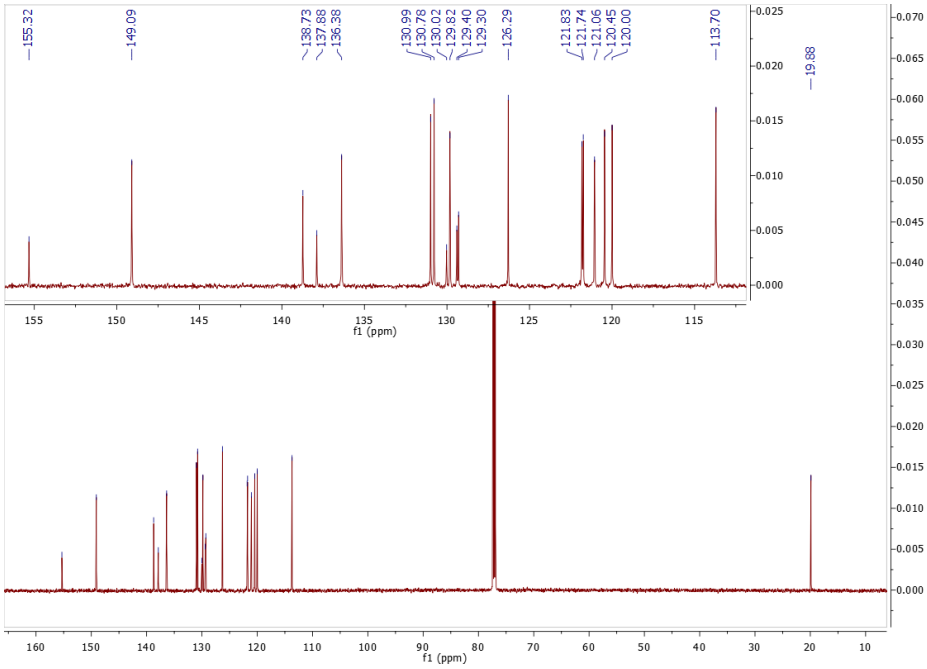

Figure 245 – ^{13}C-NMR in $CDCl_3$ of **354**.

Compound 355

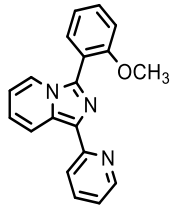

The product was isolated as a light-yellow powder (2.99 g, 91%). R_f (silica gel): 0.35 (95:5 DCM/MeOH). M_p: 130-132 °C.

^{1}H-NMR (600 MHz, $CDCl_3$, RT): δ 8.69-8.71 (d, *J* = 9.2 Hz, 1H, Ar-H), 8.62-8.63 (d, *J* = 4.6 Hz, 1H, Ar-H), 8.23-8.25 (d, *J* = 8.0 Hz, 1H, Ar-H), 7.66-7.71 (m, 2H, Ar-H), 7.61-7.62 (d, *J* = 7.1 Hz, 1H, Ar-H), 7.48-7.51 (m, 1H, Ar-H), 7.13-7.15 (t, *J* = 7.4 Hz, 1H, Ar-H), 7.05-7.08 (m, 2H, Ar-H), 6.93-6.95 (m, 1H, Ar-H), 6.60-6.62 (t, *J* = 7.0 Hz, 1H, Ar-H), 3.81 (s, 3H, -CH_3) ppm.

^{13}C-NMR (151 MHz, $CDCl_3$, RT): δ 157.72, 155.42, 149.06, 136.32, 136.27, 132.92, 131.14, 130.30, 130.13, 123.43, 121.40, 121.39, 121.02, 120.31, 120.00, 119.23, 112.86, 111.36, 55.72 ppm.

HRMS (ESI$^+$-TOF, MeOH): *m/z* 302.1286 $[M+H]^+$; calculated for $C_{19}H_{15}ON_3$: 302.1288 (+1).

UV-Vis (DCM): λ_{max} (*ε*) = 317 (*17247*), 365 (*11880*) nm.

Fluorescence (DCM, λ_{exc} 340 nm): 454 nm. **ϕ:** 53%.

IR-Spectrum (cm^{-1}, ATR): 3005 *v*(C–H aromatic), 1590 *v*(C═C aromatic), 1525 *v*(C═C aromatic), 1510 *v*(C═C aromatic), 1460, 1430, 1400, 1355, 1315, 1270, 1240, 1110, 1025, 1005, 950, 785, 735, 705.

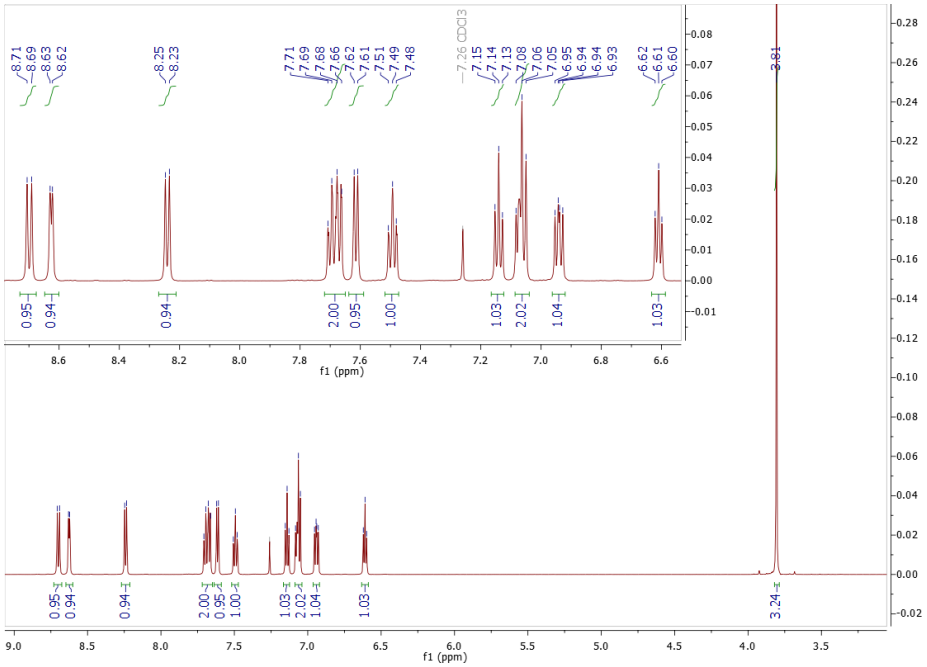

Figure 246 – ^{1}H-NMR in $CDCl_3$ of **355**.

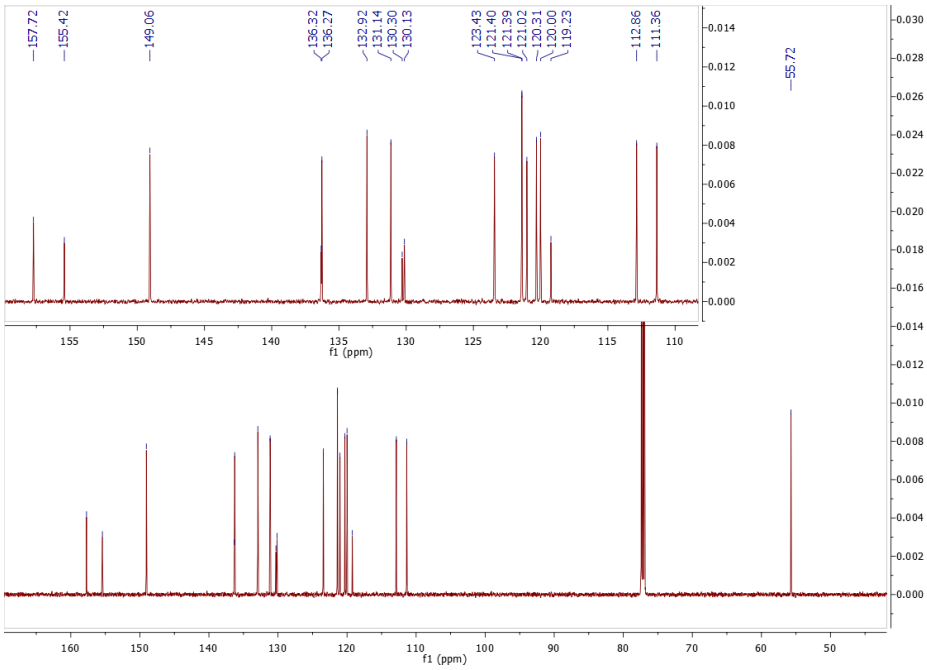

Figure 247 – ^{13}C-NMR in $CDCl_3$ of **355**.

Compound 356

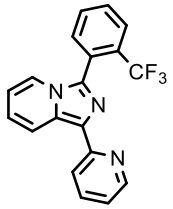

The product was isolated as a brown powder (2.92 g, 79%). R_f (silica gel): 0.45 (95:5 DCM/MeOH). M_p: 134-136 °C.

^{1}H-NMR (600 MHz, $CDCl_3$, RT): δ 8.69-8.71 (dt, *J* = 9.3 Hz, *J* = 1.2 Hz, 1H, Ar-H), 8.63-8.64 (dq, *J* = 4.8 Hz, *J* = 0.9 Hz, 1H, Ar-H), 8.19-8.20 (dt, *J* = 8.0 Hz, *J* = 1.0 Hz, 1H, Ar-H), 7.89-7.91 (d, *J* = 7.7 Hz, 1H, Ar-H), 7.66-7.73 (m, 3H, Ar-H), 7.62-7.63 (d, *J* = 7.4 Hz, 1H, Ar-H), 7.55-7.56 (d, *J* = 7.1 Hz, 1H, Ar-H), 7.09-7.11 (m, 1H, Ar-H), 6.93-6.95 (m, 1H, Ar-H), 6.59-6.61 (m, 1H, Ar-H) ppm.

^{13}C-NMR (151 MHz, $CDCl_3$, RT): δ 155.13, 149.09, 136.42, 134.37, 133.04, 132.29, 130.51, 130.30, 129.66, 128.52, 127.30, 127.27, 124.57, 122.75, 121.71, 121.60, 121.26, 120.62, 120.11 ppm.

HRMS (ESI$^+$-TOF, MeOH): *m/z* 340.1076 $[M+H]^+$; calculated for $C_{19}H_{12}F_3N_3$: 340.1056 (+1).

UV-Vis (DCM): λ_{max} (*ε*) = 295 (*10089*), 328 (*12982*), 356 (*10369*) nm.

Fluorescence (DCM, λ_{exc} 340 nm): 454 nm. **ϕ:** 33%.

IR-Spectrum (cm^{-1}, ATR): 3065 *v*(C–H aromatic), 1590 *v*(C═C aromatic), 1535 *v*(C═C aromatic), 1510 *v*(C═C aromatic), 1480, 1440, 1400, 1360, 1310, 1135 *v*(C–F), 1055, 1030, 1005, 950, 830, 785, 770, 735, 705.

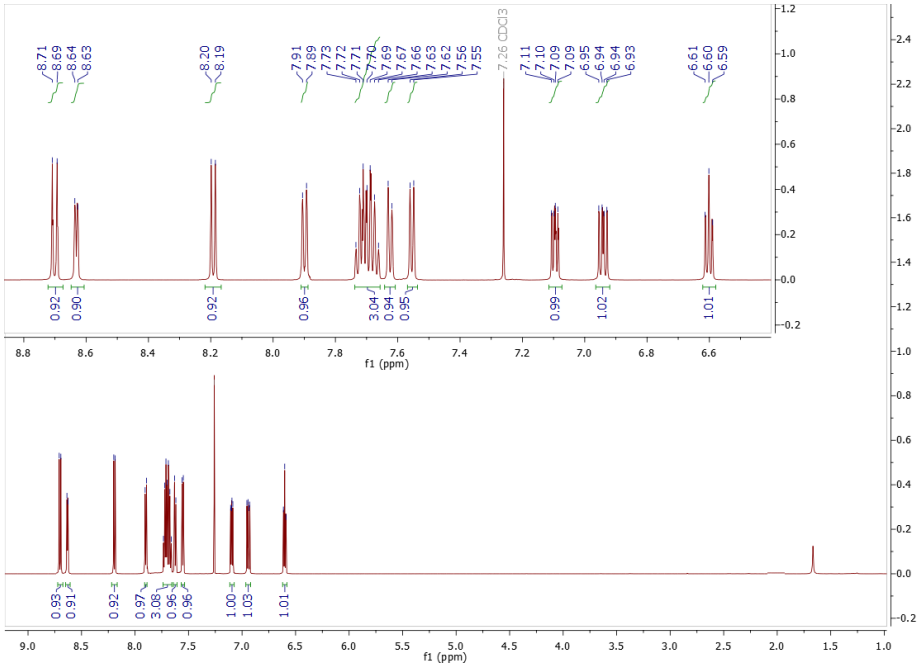

Figure 248 – ^{1}H-NMR in $CDCl_3$ of **356**.

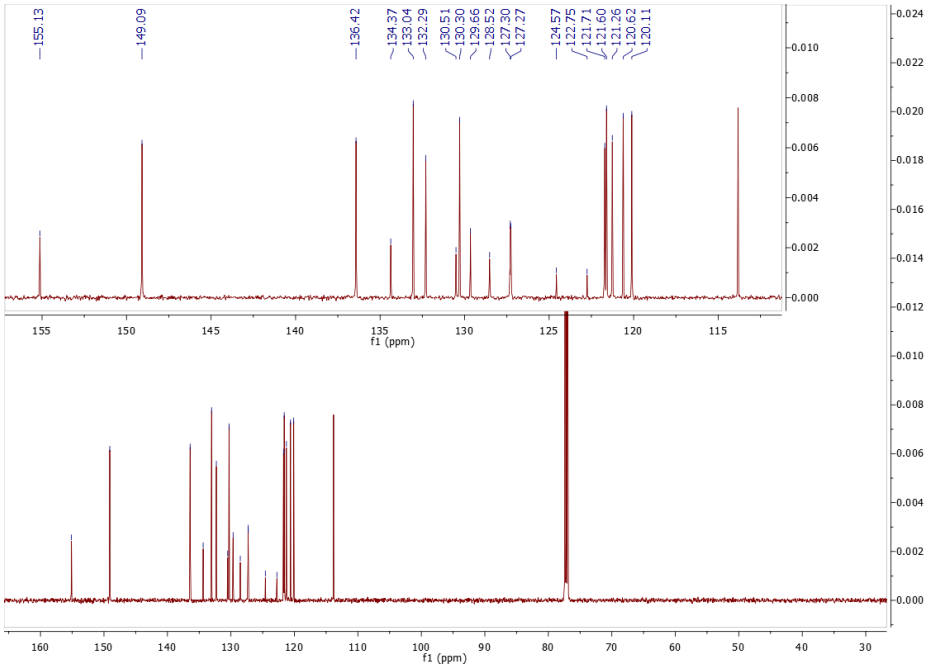

Figure 249 – ^{13}C-NMR in $CDCl_3$ of **356**.

1.14. General Synthesis of Substituted DPKs

Substituted di(pyridine-2-yl)methanone derivative, in particular bis(6-methylpyridin-2-yl)methanone **359** and bis(6-methoxypyridin-2-yl)methanone **360**, were synthetized according to the published general procedures.[496]

A mixture of 2-bromo-6-substituted pyridine (40.7 mmol, 2.2 eq.) and 150 mL of anhydrous THF was cooled to -78 °C under argon. After, a solution of *n*-butyl lithium (2.5 M in *n*-hexane) (24.4 mL, 60.5 mmol, 3.3 eq) was added dropwise over 20 minutes under vigorous stirring. The resulting mixture was left at -78° C for 30 minutes and after diethyl carbonate (4.5 mL, 37 mmol, 2.0 eq) was added dropwise over 5 minutes. After, the reaction was stirred for 2 h without cooling. Reached the room temperature, the reaction was quenched with 30 mL of an aqueous solution of HCl 10%, then basified until pH 8.0 with an aqueous saturated solution of sodium bicarbonate and the mixture was extracted with dichloromethane. The organic layer was separated, dried over sodium sulphate and the solvent evaporated under vacuum. The desired product was purified by flash chromatography on silica gel using DCM/MeOH (99:1) as eluent.

Compound 359

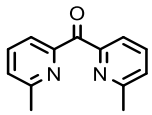

The product was isolated as yellowish crystals (3.02 g, 78%). R_f (silica gel): 0.30 (99:1 DCM/MeOH). M_p: 61-63 °C.

^{1}H-NMR (600 MHz, $CDCl_3$, RT): δ 7.88-7.90 (d, *J* = 7.7 Hz, 2H, Ar-H), 7.72-7.75 (t, *J* = 7.7 Hz, 2H, Ar-H), 7.32-7.34 (d, *J* = 7.7 Hz, 2H, Ar-H), 2.62 (s, 6H, $-CH_3$) ppm.

^{13}C-NMR (151 MHz, $CDCl_3$, RT): δ 192.74, 158.01, 153.32, 136.33, 125.84, 122.67, 24.28 ppm.

MS (ESI^+, MeOH): *m/z* 213.18 $[M+H]^+$; calculated for $C_{13}H_{12}N_2O$: 212.09.

UV-Vis (DCM): λ_{max} (*ε*) = 282 (*8155*) nm.

IR-Spectrum (cm^{-1}, ATR): 3055 *ν*(C–H aromatic), 2960 *ν*(C–H aliphatic), 2925 *ν*(C–H aliphatic), 1680 *ν*(C═O), 1585, 1450, 1375, 1310, 1255, 1225, 1155, 1090, 1040, 990, 960, 795, 755, 705.

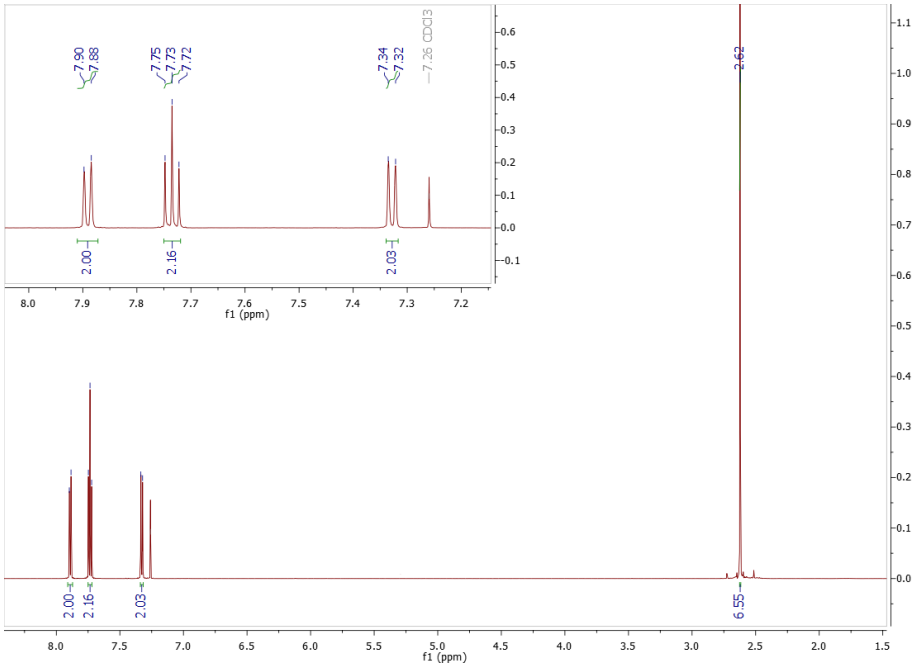

Figure 250 – ^{1}H-NMR in $CDCl_3$ of **359**.

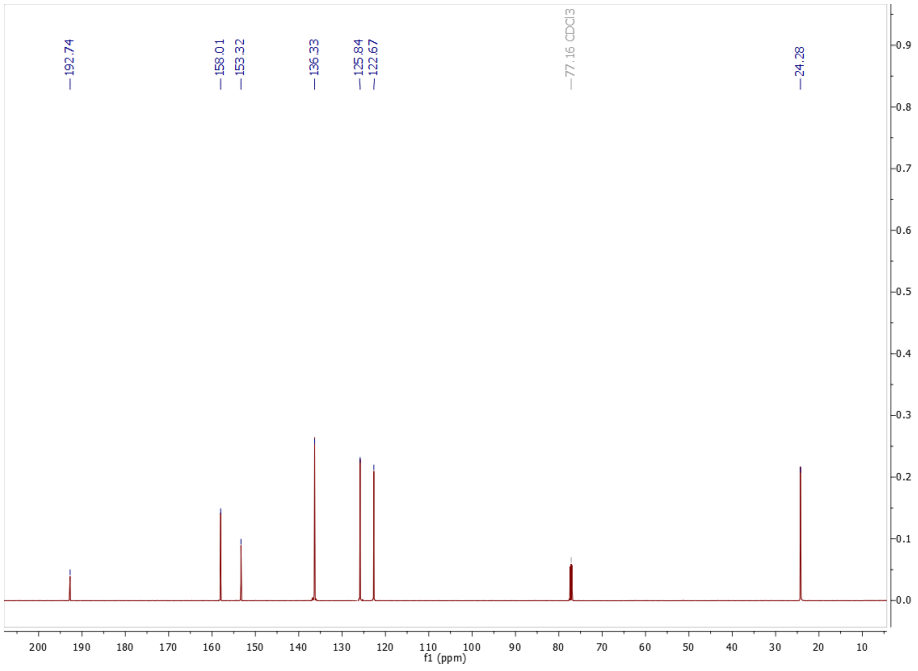

Figure 251 – ^{13}C-NMR in $CDCl_3$ of **359**.

Compound 360

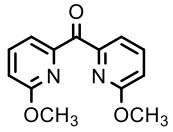

The product was isolated as yellow oil (2.51 g, 56%). R_f (silica gel): 0.25 (DCM). M_p: < 20 °C.

^{1}H-NMR (600 MHz, $CDCl_3$, RT): δ 7.69-7.74 (m, 4H, Ar-H), 6.93-6.94 (dd, *J* = 7.9 Hz, *J* = 1.1 Hz, 2H, Ar-H), 3.91 (s, 6H, -CH_3) ppm.

^{13}C-NMR (151 MHz, $CDCl_3$, RT): δ 192.11, 163.33, 151.74, 138.72, 118.95, 114.58, 53.61 ppm.

MS (ESI$^+$, MeOH): *m/z* 245.38 $[M+H]^+$; calculated for $C_{13}H_{12}N_2O_3$: 244.08.

UV-Vis (DCM): λ_{max} (*ε*) = 310 (*5136*) nm.

IR-Spectrum (cm^{-1}, ATR): 3075 *ν*(C–H aromatic), 2950 *ν*(C–H aliphatic), 2850 *ν*(C–H aliphatic), 1680 *ν*(C═O), 1585, 1460, 1410, 1335, 1310, 1250, 1150, 1025, 980, 830, 800, 765, 735.

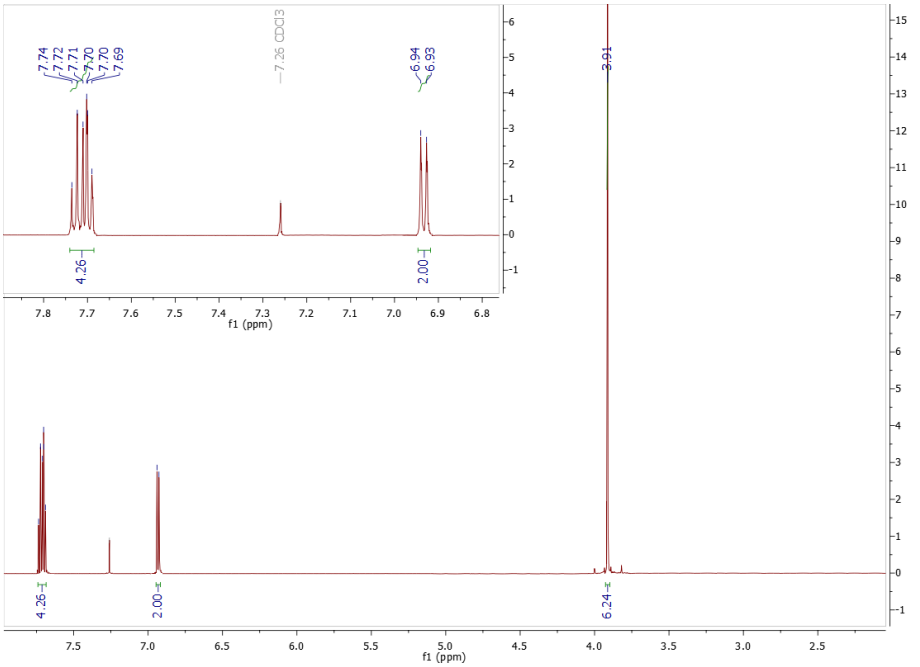

Figure 252 – ^{1}H-NMR in $CDCl_3$ of **360**.

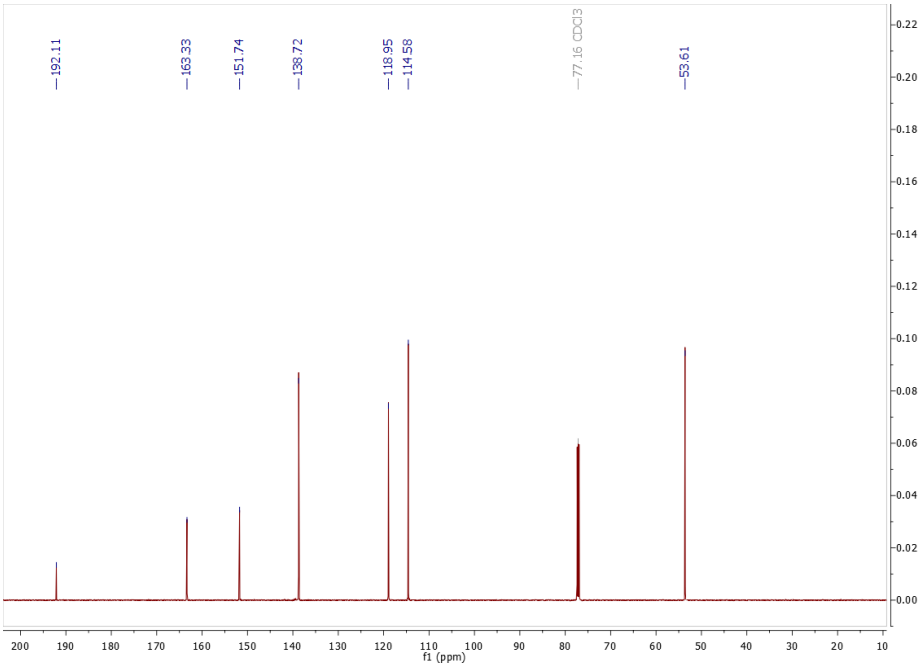

Figure 253 – ^{13}C-NMR in $CDCl_3$ of **360**.

1.15. General Synthesis of *Tris*-substituted *Impy* Ligands

Tris-substituted *Impy* ligands, in particular **361** and 5-methoxy-3-(2-methoxyphenyl)-1-(6-methoxypyridin-2-yl)imidazo[1,5-*a*]pyridine **362** were synthetized according to the published general procedures.[496]

A mixture of substituted di(pyridin-2-yl)methanone (2 g, 1.0 eq.), the desired 2-substituted benzaldehyde (1.5 eq.) and ammonium acetate (5.0 eq.) and 200 mL of acetic acid was refluxed for 12 h. After, the reaction mixture was cooled to room temperature and acetic acid was removed by evaporation under vacuum. The resulting solid was dissolved in a saturated aqueous solution of sodium carbonate and the mixture was extracted with dichloromethane. The organic layer was separated, dried over sodium sulphate and the solvent evaporated under vacuum. The desired product was purified by flash chromatography on silica gel using DCM/MeOH (99:1) as eluent.

Compound 361

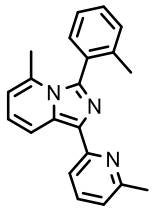

The product was isolated as a light-orange powder (2.51 g, 85%). R_f (silica gel): 0.50 (95:5 DCM/MeOH). M_p: 155-157 °C.

^{1}H-NMR (600 MHz, $CDCl_3$, RT): δ 8.73-8.75 (d, *J* = 9.2 Hz, 1H, Ar-H), 7.99-8.00 (d, *J* = 7.9 Hz, 1H, Ar-H), 7.57-7.60 (t, *J* = 7.7 Hz, 1H, Ar-H), 7.46-7.48 (dd, *J* = 8.0 Hz, *J* = 1.4 Hz, 1H, Ar-H), 7.37-7.40 (td, *J* = 8.2 Hz, *J* = 1.3 Hz, 1H, Ar-H), 7.24-7.26 (m, 2H, Ar-H), 6.95-6.96 (d, *J* = 7.5 Hz, 1H, Ar-H), 6.83-6.86 (m, 1H, Ar-H), 6.34-6.35 (dt, *J* = 6.5 Hz, *J* = 1.1 Hz, 1H, Ar-H), 2.67 (s, 3H, -CH_3), 2.07 (s, 3H, -CH_3), 2.00 (s, 3H, -CH_3) ppm.

^{13}C-NMR (151 MHz, $CDCl_3$, RT): δ 157.45, 154.62, 139.53, 138.06, 136.62, 133.85, 133.08, 131.69, 130.86, 129.70, 129.51, 129.48, 125.10, 121.22, 119.95, 119.80, 117.31, 114.54, 24.86, 20.77, 20.04 ppm.

HRMS (ESI$^+$-TOF, MeOH): *m/z* 314.1669 $[M+H]^+$; calculated for $C_{21}H_{19}N_3$: 314.1652 (+1).

UV-Vis (DCM): λ_{max} (*ε*) = 294 (*12879*), 334 (*13568*), 366 (*15677*) nm.

Fluorescence (DCM, λ_{exc} 340 nm): 445 nm. **ϕ:** 59%.

IR-Spectrum (cm^{-1}, ATR): 2925 *ν*(C–H aliphatic), 1585 *ν*(C═C aromatic), 1570 *ν*(C═C aromatic), 1530 *ν*(C═C aromatic), 1470, 1430, 1325, 1305, 1140, 1060, 840, 800, 770, 740, 730.

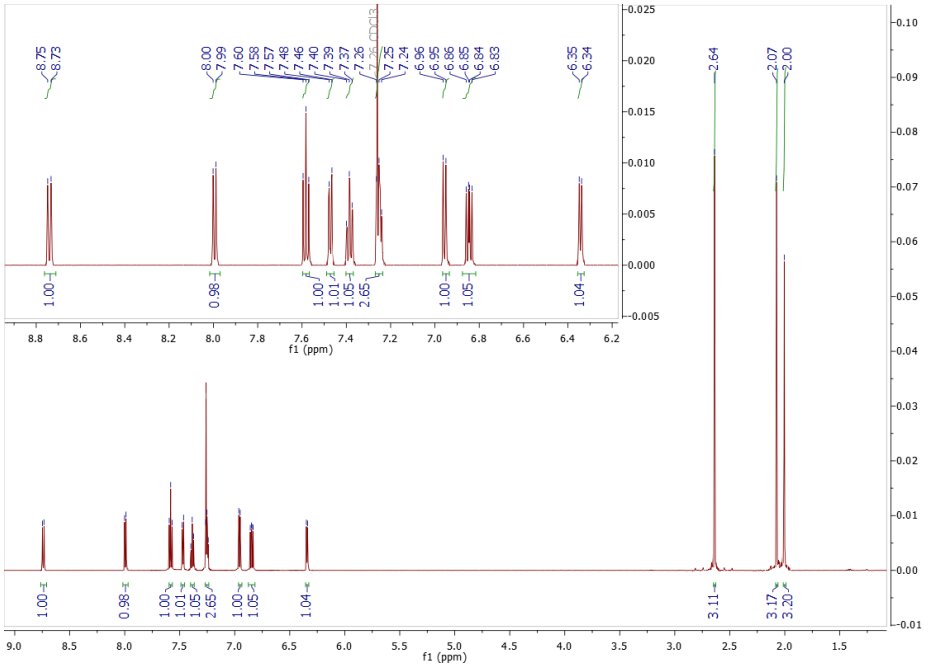

Figure 254 – ^{1}H-NMR in $CDCl_3$ of **361**.

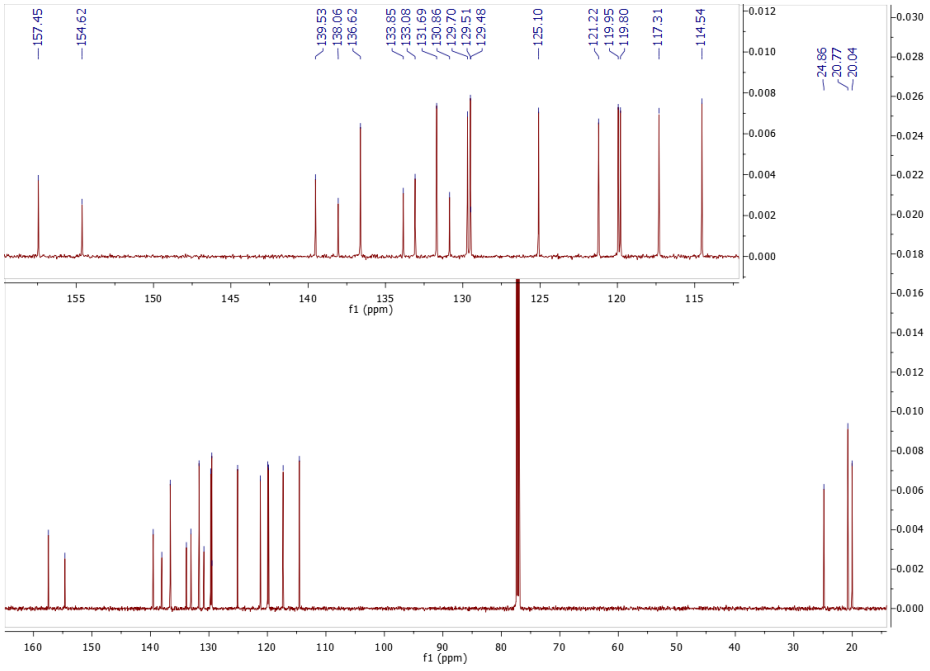

Figure 255 – ^{13}C-NMR in $CDCl_3$ of **361**.

Compound 362

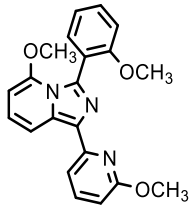

The product was isolated as a dark-yellow powder (1.83 g, 62%). R_f (silica gel): 0.60 (95:5 DCM/MeOH). M_p: 157-159 °C.

^{1}H-NMR (600 MHz, $CDCl_3$, RT): δ 8.37-8.38 (d, *J* = 9.0 Hz, 1H, Ar-H), 7.84 (br, 1H, Ar-H), 7.57-7.60 (t, *J* = 7.9 Hz, 1H, Ar-H), 7.53-7.54 (dd, *J* = 7.3 Hz, *J* = 1.1 Hz, 1H, Ar-H), 7.39-7.42 (td, *J* = 8.3 Hz, *J* = 1.6 Hz, 1H, Ar-H), 7.02-7.05 (t, *J* = 7.4 Hz, 1H, Ar-H), 6.90-6.93 (m, 2H, Ar-H), 6.55-6.56 (d, *J* = 8.0 Hz, 1H, Ar-H), 5.81-5.82 (d, *J* = 6.9 Hz, 1H, Ar-H), 4.10 (s, 3H, -CH_3), 3.70 (s, 3H, -CH_3), 3.69 (s, 3H, -CH_3) ppm.

^{13}C-NMR (151 MHz, $CDCl_3$, RT): δ 163.54, 158.85, 152.77, 149.96, 138.93, 134.82, 132.03, 131.36, 130.15, 129.53, 123.83, 122.62, 119.99, 113.43, 112.73, 109.96, 106.90, 88.79, 56.09, 55.51, 53.56 ppm.

HRMS (ESI$^+$-TOF, MeOH): *m/z* 362.1510 $[M+H]^+$; calculated for $C_{21}H_{19}N_3O_3$: 362.1499 (+1).

UV-Vis (DCM): λ_{max} (*ε*) = 294 (*11696*), 375 (*22601*) nm.

Fluorescence (DCM, λ_{exc} 470 nm): 435 nm. **ϕ:** 42%.

IR-Spectrum (cm^{-1}, ATR): 2970 *ν*(C–H aliphatic), 1635, 1575 *ν*(C═C aromatic), 1530 *ν*(C═C aromatic), 1520 *ν*(C═C aromatic), 1460, 1405, 1320, 1240, 1110, 1020, 985, 900, 845, 805, 740, 725.

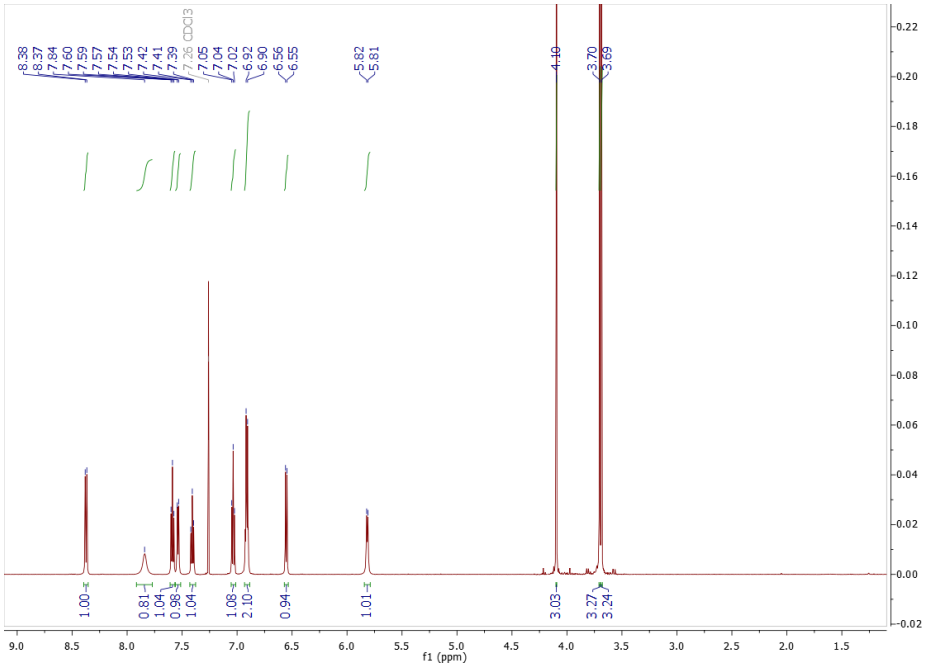

Figure 256 – ^{1}H-NMR in $CDCl_3$ of **362**.

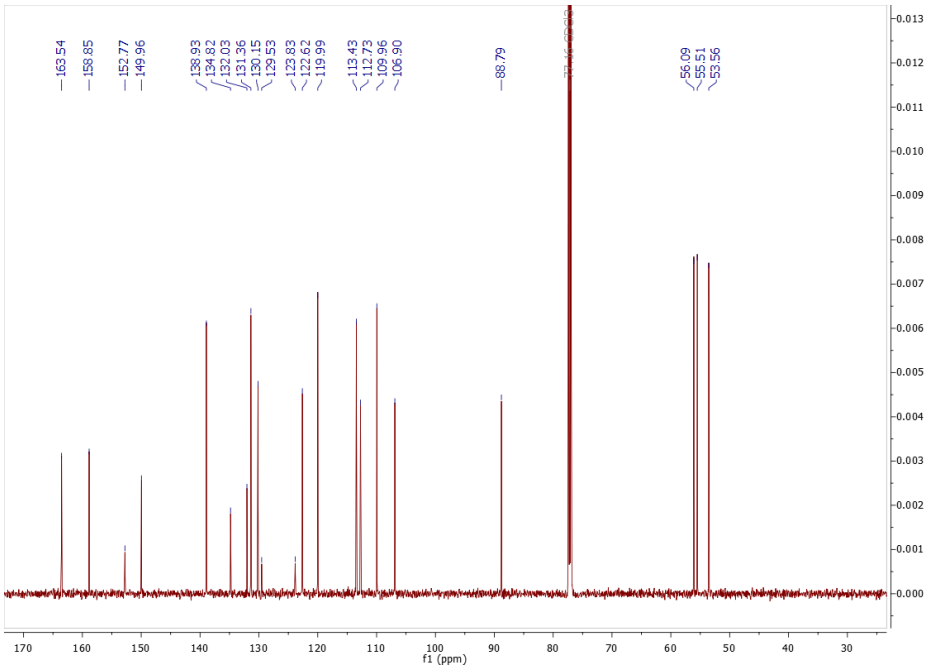

Figure 257 – ^{13}C-NMR in $CDCl_3$ of **362**.

1.16. Synthesis of Compound 368 Tris-CF_3 *Impy* Ligand

As discussed in Section 2 of Chapter 4, tris-substituted *Impy* ligand **368** cannot be synthetized with the classical procedure by the reaction between a substituted di(pyridin-2-yl)methanone and the desired benzaldehyde. *Impy* ligand **368** was prepared following a different multi-step synthetic pathway according to the published general procedure.[514-516]

Compound 364

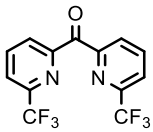

A mixture of 2-bromo-6-(trifluoromethyl)pyridine **363** (3.6 g, 16.0 mmol, 2.0 eq.) and 100 mL of anhydrous tetrahydrofuran was cooled to -78 °C under argon. After, a solution of *n*-butyl lithium (2.5 M in *n*-hexane) (6.0 mL, 15.2 mmol, 1.9 eq) was added dropwise over 20 minutes under vigorous stirring. The resulting mixture was left at -78 °C for 30 minutes and after ethyl chloroformate (0.76 mL, 8.0 mmol, 1.0 eq) was added dropwise over 2 minutes. After, the reaction was stirred for 2 h without cooling. Reached the room temperature, the reaction was quenched with 20 mL of an aqueous solution of HCl 10%, then basified until pH 8.0 with an aqueous saturated solution of sodium bicarbonate and the mixture was extracted with dichloromethane. The organic layer was separated, dried over sodium sulphate and the solvent evaporated under vacuum. The desired product was purified by flash chromatography on silica gel using *n*-hexane/DCM (6:4) as eluent afforded a white-yellow powder (1.15 g, 46%). R_f (silica gel): 0.75 (1:1 *n*-hexane/DCM). M_p: 97-99 °C.

^{1}H-NMR (600 MHz, $CDCl_3$, RT): δ 8.32-8.33 (d, *J* = 7.9 Hz, 2H, Ar-H), 8.10-8.13 (t, *J* = 7.9 Hz, 2, Ar-H), 7.89-7.90 (dd, *J* = 7.9 Hz, *J* = 0.9 Hz, 2H, Ar-H) ppm.

^{13}C-NMR (151 MHz, $CDCl_3$, RT): δ 190.27, 153.73, 147.78, 138.57, 127.56, 123.29, 122.11, 120.29 ppm.

MS (ESI$^+$, MeOH): *m/z* 321.48 $[M+H]^+$; calculated for $C_{13}H_6F_6N_2O$: 320.04.

UV-Vis (DCM): λ_{max} (ε) = 269 (*6923*) nm.

IR-Spectrum (cm^{-1}, ATR): 1695 *ν*(C═O), 1425, 1340, 1240, 1180, 1130 *ν*(C–F), 1105 *ν*(C–F), 1080 *ν*(C–F), 990, 970, 840, 820, 765, 740, 725.

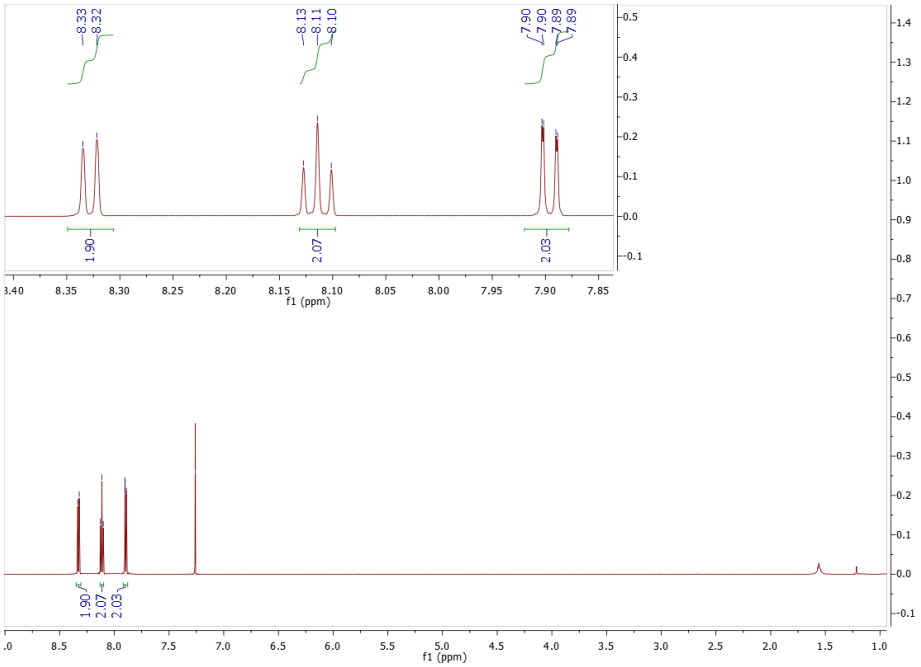

Figure 258 – ^{1}H-NMR in $CDCl_3$ of **364**.

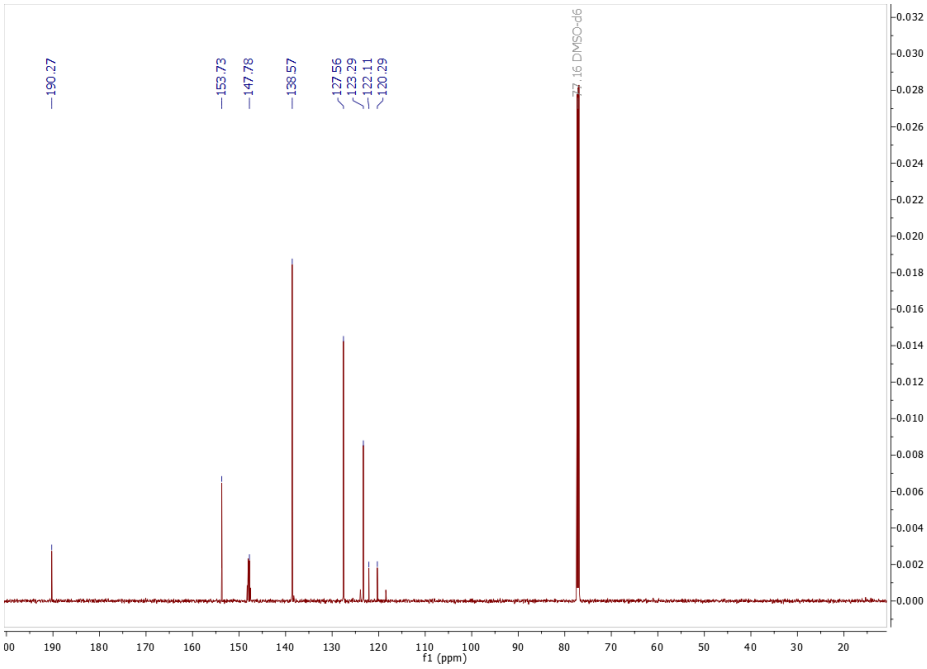

Figure 259 – ^{13}C-NMR in $CDCl_3$ of **364**.

Compound 365

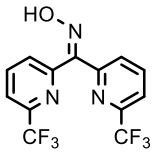

A mixture of hydroxylamine hydrochloride (1.22 g, 17.50 mmol), triethylamine (3.66 mL, 2.65 g, 26.25 mmol) and 35 mL of ethanol was stirred for 1 h at room temperature. After, **364** (0.70 g, 2.19 mmol) was added in one portion and the resulting mixture was refluxed overnight. After cooling to room temperature, the reaction mixture was washed with 30 mL of water and extracted with ethyl acetate. The organic layer was separated, dried over sodium sulphate and the solvent evaporated under vacuum. The desired product was purified by flash chromatography on silica gel using *n*-hexane/DCM (1:1) as eluent afforded a white powder (0.59 g, 80%). R_f (silica gel): 0.15 (1:1 *n*-hexane/DCM). M_p: 151-153 °C.

^{1}H-NMR (600 MHz, $CDCl_3$, RT): δ 8.08-8.14 (m, 3H, Ar-H), 7.98-8.01 (t, *J* = 7.9 Hz, Ar-H), 7.84-7.85 (dd, *J* = 7.6 Hz, *J* = 1.1 Hz, 1H, Ar-H), 7.73-7.75 (d, *J* = 7.4 Hz, 1H, Ar-H) ppm.

^{13}C-NMR (151 MHz, $CDCl_3$, RT): δ 154.40, 150.72, 149.68, 147.40, 146.03, 139.20, 138.59, 128.22, 126.34, 122.29, 121.90, 121.59, 120.53, 120.08 ppm.

MS (ESI$^+$, MeOH): *m/z* 336.17 $[M+H]^+$; calculated for $C_{13}H_7F_6N_3O$: 335.05.

UV-Vis (DCM): λ_{max} (ε) = 258 *shoulder* (*8951*) nm.

IR-Spectrum (cm^{-1}, ATR): 3255 *v*(O–H), 1590 *v*(C═C aromatic), 1470, 1335, 1310, 1250, 1190, 1110 *v*(C–F), 1090 *v*(C–F), 1040, 995, 980, 845, 815, 790, 740, 705.

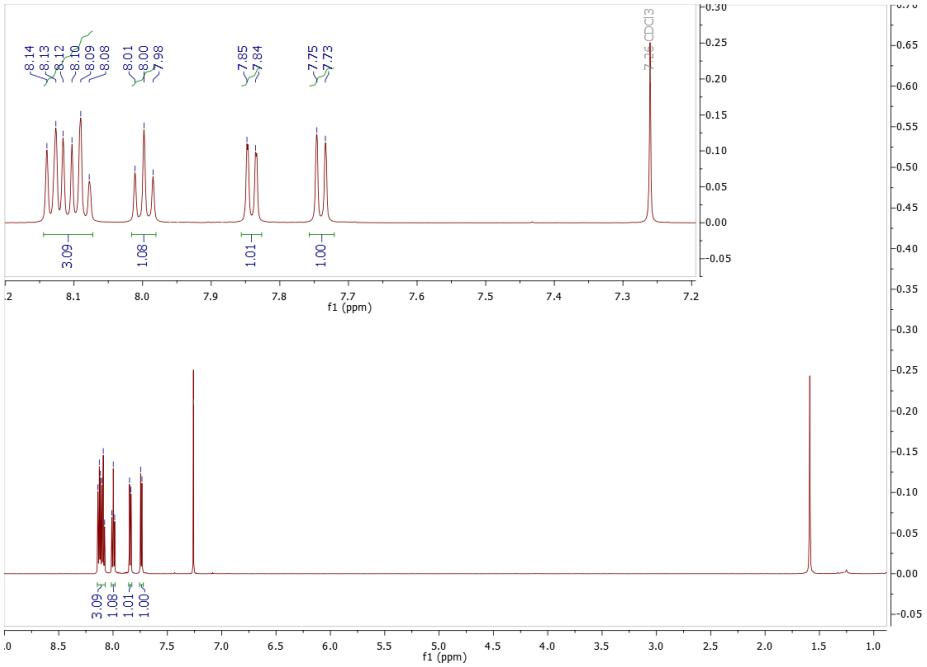

Figure 260 – ^{1}H-NMR in $CDCl_3$ of **365**.

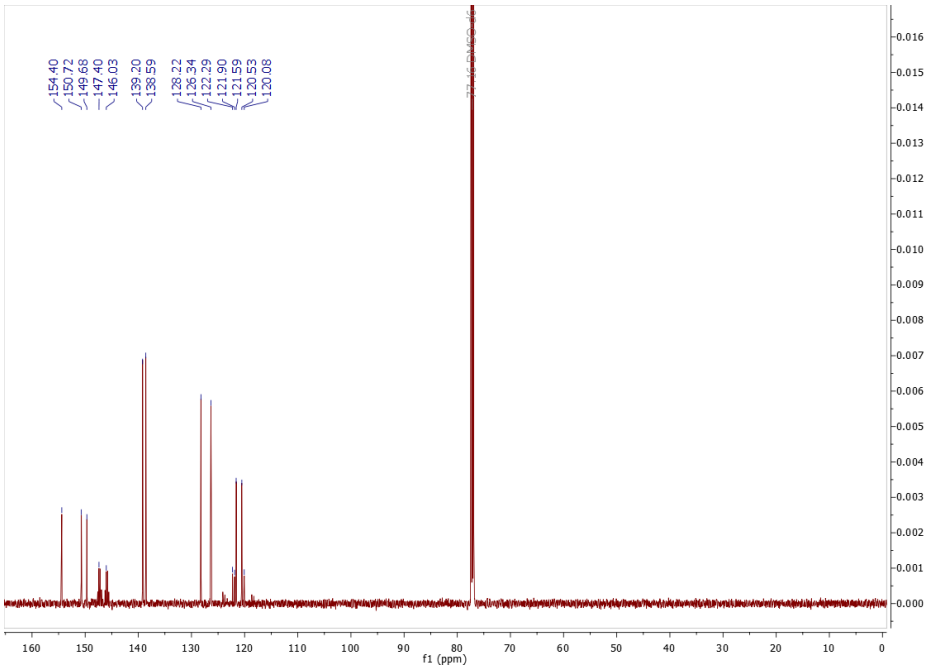

Figure 261 – ^{13}C-NMR in $CDCl_3$ of **365**.

Compound 366

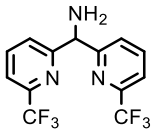

A mixture of **365** (0.50 g, 1.5 mmol), zinc dust (0.48 g, 12 mmol), ammonium acetate (0.10 g, 1.6 mmol), ammonium hydroxide 25% (2.5 mL) and 10 mL of ethanol was refluxed for 3 h. After cooling to room temperature, the reaction mixture was filtered on celite-545 and the mixture was concentrated under vacuum. The resulting solid was dissolved in 2 M NaOH aqueous solution and the mixture was extracted with dichloromethane. The organic layer was separated, dried over sodium sulphate and the solvent evaporated under vacuum. The product was isolated as a sticky-yellow oil without any other purification (0.45 g, 94%). R_f (silica gel): 0.05 (DCM). M_p: < 20 °C.

^{1}H-NMR (600 MHz, $CDCl_3$, RT): δ 7.81-7.84 (t, *J* = 7.8 Hz, 2H, Ar-H), 7.66-7.68 (d, *J* = 7.9 Hz, 2H, Ar-H), 7.55-7.56 (d, *J* = 7.7 Hz, 2H, Ar-H), 5.48 (s, 1H, -CH-), 2.49 (br, 2H, -NH_2) ppm.

^{13}C-NMR (151 MHz, $CDCl_3$, RT): δ 163.00, 147.46, 138.24, 124.92, 122.48, 119.19, 61.66 ppm.

MS (ESI$^+$, MeOH): *m/z* 322.48 $[M+H]^+$; calculated for $C_{13}H_9F_6N_3$: 321.07.

UV-Vis (DCM): λ_{max} (*ε*) = 261 (*3716*) nm.

IR-Spectrum (cm^{-1}, ATR): 3320 *ν*(N–H), 3025 *ν*(C–H aliphatic), 1595 *ν*(C═O), 1460, 1430, 1335, 1185, 1135 *ν*(C–F), 1110 *ν*(C–F), 1090, 995, 815, 745.

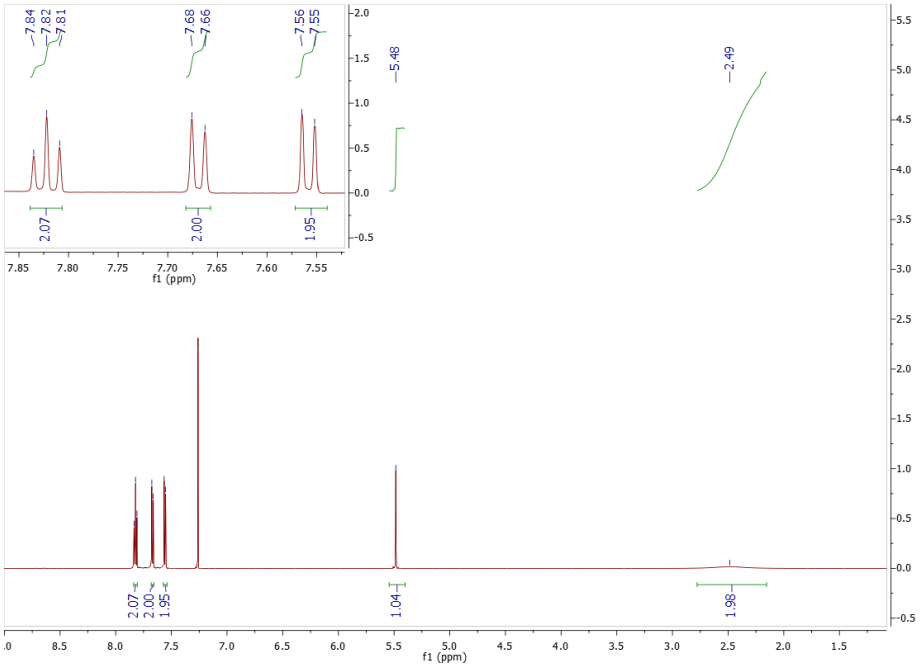

Figure 262 – ^{1}H-NMR in $CDCl_3$ of **366**.

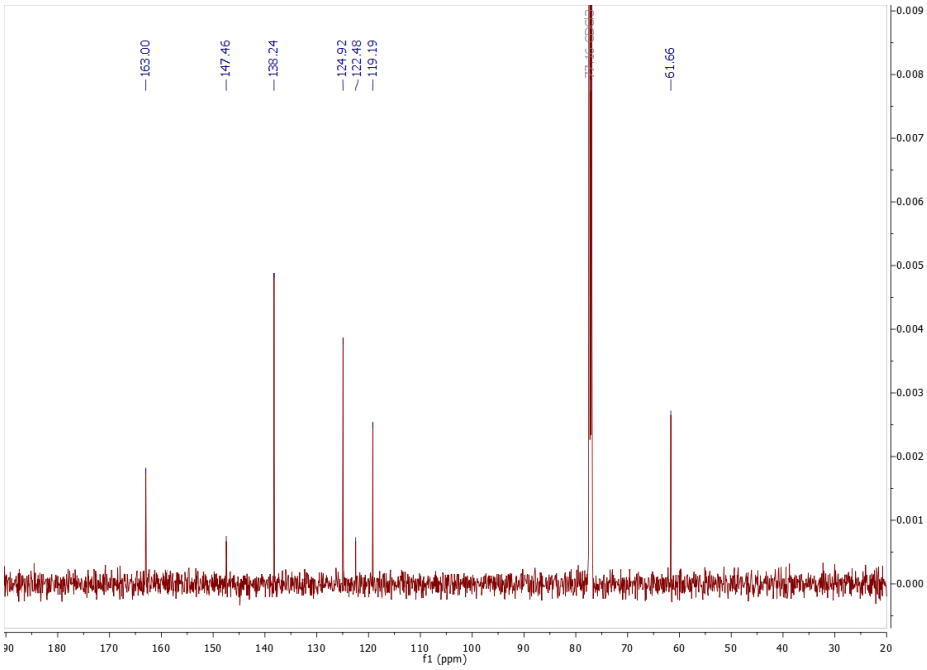

Figure 263 – ^{13}C-NMR in $CDCl_3$ of **366**.

Compound 367

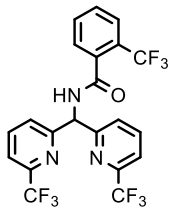

A mixture of **366** (1.86 g, 5.8 mmol), 2-(trifluoromethyl)benzoic acid (1.13 g, 5.8 mmol), 23 mL of propylphosphonic anhydride (50% in ethyl acetate) and 70 mL of butyl acetate was refluxed for 16 h. After cooling to room temperature, the solvent was removed by evaporation under vacuum. The resulting sticky-oil was dissolved in a saturated aqueous solution of sodium carbonate and the mixture was extracted with dichloromethane. The organic layer was separated, dried over sodium sulphate and the solvent evaporated under vacuum. The desired product was purified by flash chromatography on silica gel using DCM/*n*-hexane (8:2) as eluent. The product was isolated as a white-yellow powder (1.73 g, 60%). R_f (silica gel): 0.75 (95:5 DCM/MeOH).

^{1}H-NMR (600 MHz, $CDCl_3$, RT): δ 8.24-8.25 (d, *J* = 6.2 Hz, 1H, -NH-), 7.87-7.90 (t, *J* = 7.9 Hz, 2H, Ar-H), 7.80-7.81 (d, *J* = 8.0 Hz, 2H, Ar-H), 7.77-7.78 (d, *J* = 7.8 Hz, 1H, Ar-H), 7.65-7.70 (m, 2H, Ar-H), 7.60-7.61 (m, 3H, Ar-H), 6.58-6.59 (d, *J* = 6.4 Hz, 1H, -CH-) ppm.

^{13}C-NMR (151 MHz, $CDCl_3$, RT): δ 167.55, 158.55, 158.50, 147.80, 147.57, 138.66, 135.39, 132.37, 130.45, 129.03, 127.84, 127.63, 126.76, 124.89, 122.30, 120.48, 119.89, 119.77, 119.76, 119.70, 59.16 ppm.

MS (ESI$^+$, MeOH): *m/z* 494.56 $[M+H]^+$; calculated for $C_{21}H_{12}F_9N_3O$: 493.08.

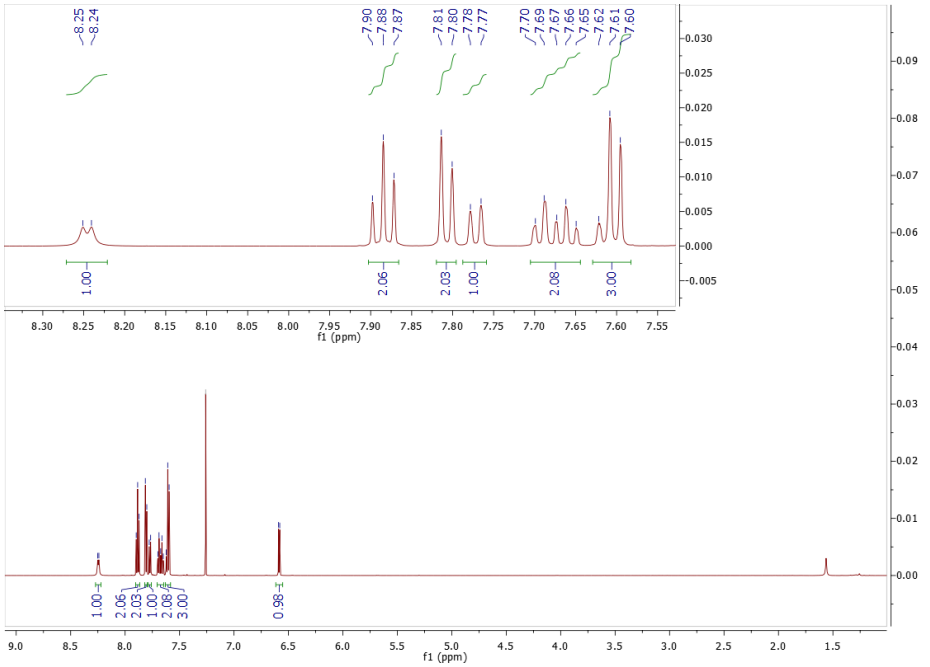

Figure 264 – ^{1}H-NMR in $CDCl_3$ of **367**.

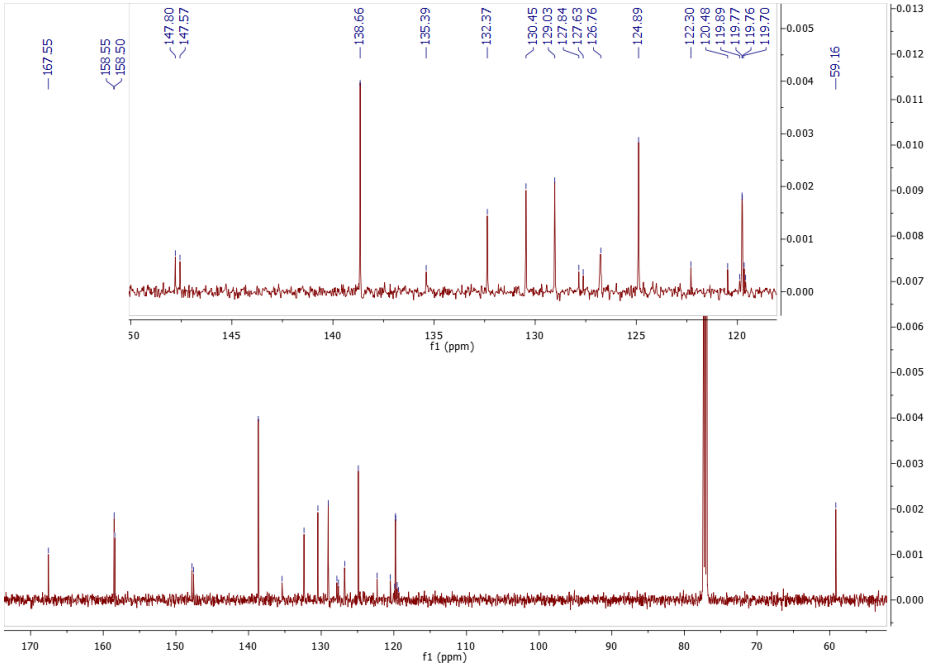

Figure 265 – ^{13}C-NMR in $CDCl_3$ of **367**.

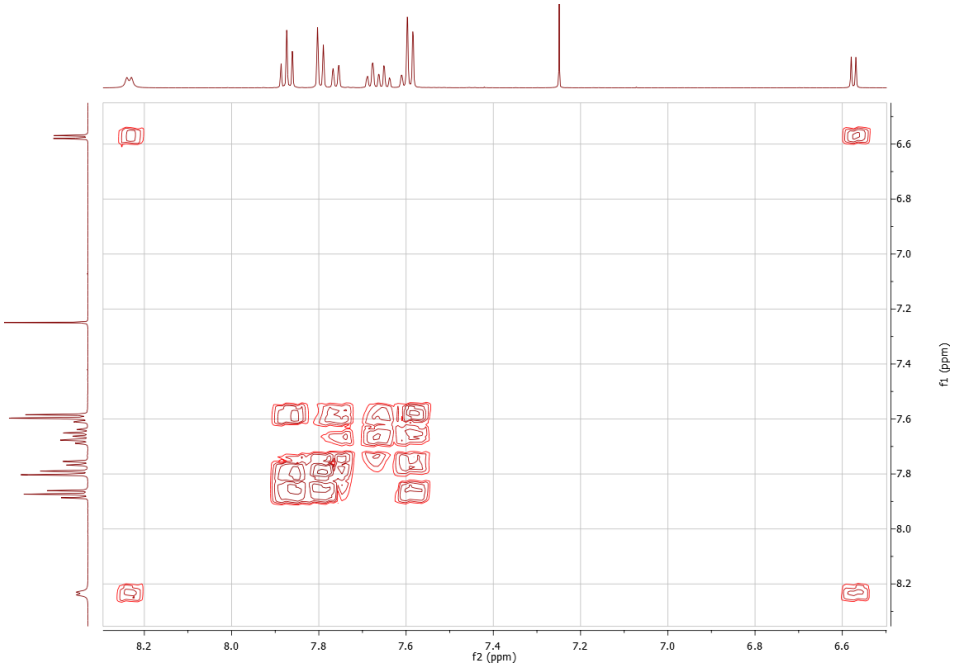

Figure 266 – COSY in $CDCl_3$ of **367**.

Compound 368

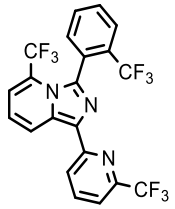

A mixture of **367** (1.65 g, 3.35 mmol) and 16 mL of propylphosphonic anhydride (50% in ethyl acetate) was introduced in a sealed 20 mL reaction vial and heated in a microwave reactor at 180 °C for 1 h. After cooling to room temperature, the solvent was removed by evaporation under vacuum. The resulting sticky-oil was dissolved in a saturated aqueous solution of sodium carbonate and the mixture was extracted with dichloromethane. The organic layer was separated, dried over sodium sulphate and the solvent evaporated under vacuum. The desired product was purified by flash chromatography on silica gel using DCM/*n*-hexane (8:2) as eluent. The product was isolated as a yellow powder (0.76 g, 48%). R_f (silica gel): 0.80 (98:2 DCM/MeOH). M_p: 130-132 °C.

^{1}H-NMR (600 MHz, $CDCl_3$, RT): δ 9.12-9.14 (d, *J* = 9.1 Hz, 1H, Ar-H), 8.38-8.39 (d, *J* = 8.1 Hz, 1H, Ar-H), 7.87-7.89 (t, *J* = 7.8 Hz, 1H, Ar-H), 7.81-7.82 (m, 1H, Ar-H), 7.66-7.68 (m, 2H, Ar-H), 7.60-7.61 (br, 1H, Ar-H), 7.52-7.53 (d, *J* = 7.6 Hz, 1H, Ar-H), 7.27-7.28 (d, *J* = 6.8 Hz, 1H. Ar-H), 7.04-7.06 (m, 1H, Ar-H) ppm.

^{13}C-NMR (151 MHz, $CDCl_3$, RT): δ 154.46, 147.36, 137.91, 135.90, 133.59, 133.58, 132.06, 131.15, 130.78, 130.45, 129.62, 126.53, 124.66, 123.25, 122.84, 119.58, 117.71, 117.70, 117.40, 117.36 ppm.

HRMS (ESI$^+$-TOF, MeOH): *m/z* 476.0836 $[M+H]^+$; calculated for $C_{21}H_{10}F_9N_3$: 476.0804 (+1).

UV-Vis (DCM): λ_{max} (*ε*) = 296 (*16192*), 376 (*10943*) nm.

Fluorescence (DCM, λ_{exc} 340 nm): 490 nm. **ϕ:** 67%.

IR-Spectrum (cm^{-1}, ATR): 1595 *ν*(C═C aromatic), 1545 *ν*(C═C aromatic), 1475, 1310, 1265, 1100 *ν*(C–F), 1055, 815, 790, 775, 730.

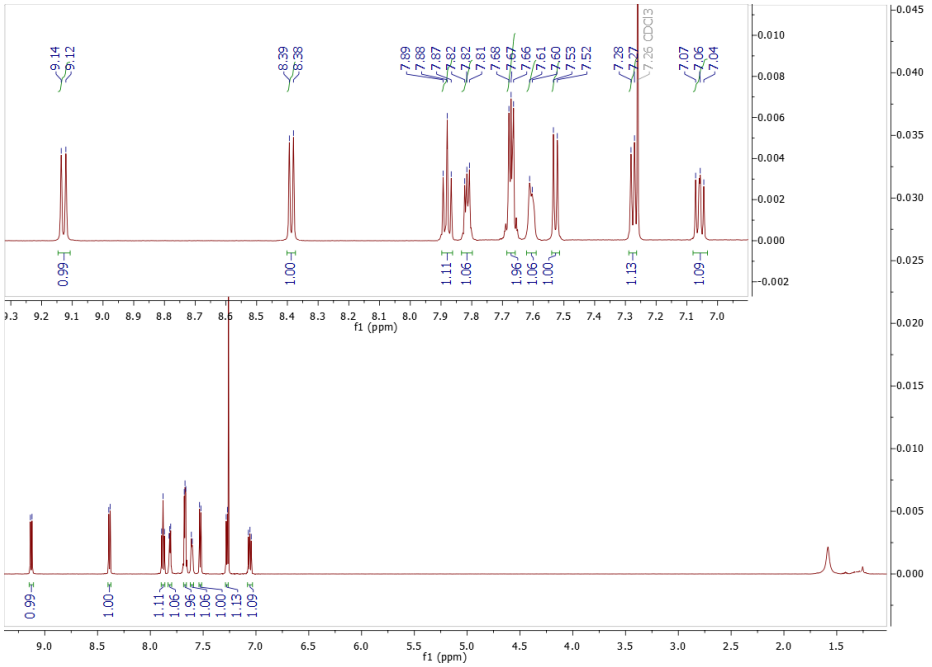

Figure 267 – ^{1}H-NMR in $CDCl_3$ of **368**.

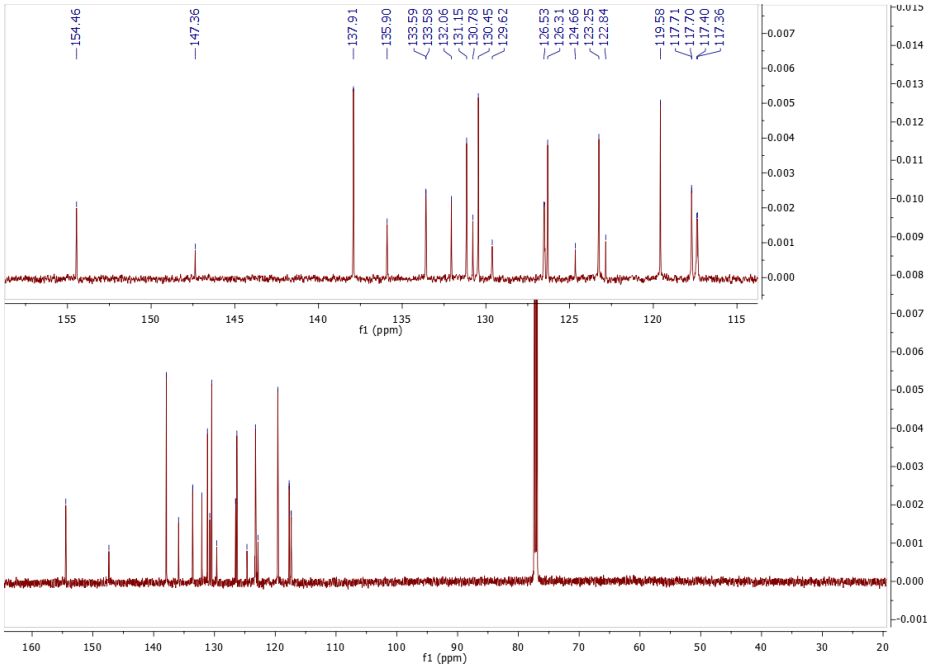

Figure 268 – ^{13}C-NMR in $CDCl_3$ of **368**.

1.17. General Synthesis of *Impy*-based Copper(I) Complexes

Copper(I) complexes **369**-**375** were synthetized according to the published general procedure.[292,295]

100 mg (2.2 eq.) of *Impy* ligand were dissolved in 5 mL of dichloromethane at room temperature. After the complete dissolution of the ligand, tetrakis(acetonitrile)copper(I) hexafluorophosphate (1.0 eq.) was added and the resulting mixture was refluxed for 2 h under argon. After cooling to room temperature, the reaction mixture was concentrated and the raw material purified by repeated washings with a diethyl ether/*n*-hexane solution (1:1). For all copper(I) complexes it was not possible to acquire the ^{13}C NMR spectra due to their low solubility in deuterated acetone alongside the presence of coordination equilibria. On **370** have been performed different experiments raising both the number of scans and the relaxation time but the obtained spectra show broad signals with a very poor intensity. The broadening of signals could be cause by traces of copper(II) paramagnetic species due to the oxidation in solution of the copper(I) complex during the spectrum acquisition. Below it is reported the best ^{13}C NMR spectrum obtained for **370**.

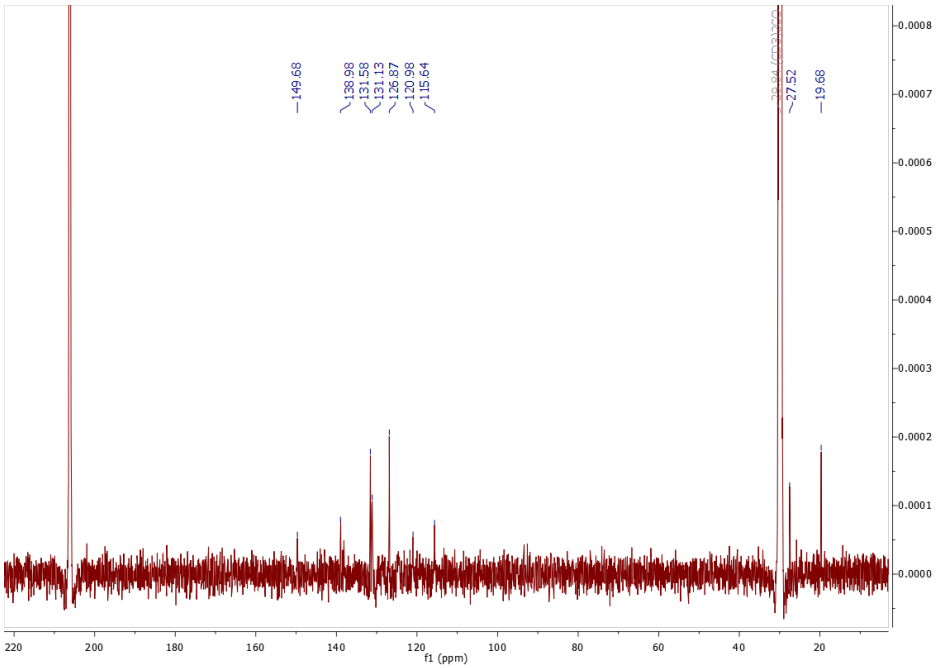

Figure 269 – ^{13}C-NMR in acetone-d_6 of **370** performed at room temperature with high number of scan and long relaxation time.

Compound 369

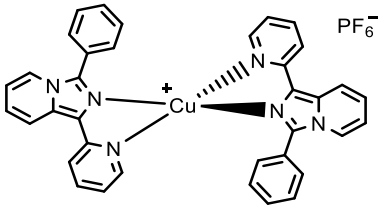

The product was isolated as a yellow powder (94 mg, 75%). R_f (silica gel): 0.65 (9:1 DCM/MeOH). M_p: > 200 °C.

^{1}H-NMR (600 MHz, Acetone-d$_6$, RT): δ 8.57-8.58 (d, *J* = 6.8 Hz, 2H, Ar-H), 8.51 (d, *J* = 3.0 Hz, 2H, Ar-H), 8.36-8.37 (d, *J* = 9.1 Hz, 2H, Ar-H), 8.31-8.32 (d, *J* = 7.8 Hz, 2H, Ar-H), 8.08-8.10 (t, *J* = 7.3 Hz, 2H, Ar-H), 7.62-7.64 (d, *J* = 7.1 Hz, 2H, Ar-H), 7.36-7.40 (br, 4H, Ar-H), 7.25-7.27 (br, 2H, Ar-H), 7.18-7.20 (br, 4H, Ar-H), 7.06-7.08 (t, *J* = 6.0 Hz, 2H, Ar-H) ppm.

HRMS (ESI$^+$-TOF, MeOH): *m/z* 605.1551 [M]$^+$; calculated for $C_{36}H_{26}CuN_6^+$: 605.1509.

UV-Vis (DCM): λ_{max} (*ε*) = 303 (*46973)*, 364 (*31089*) nm.

Fluorescence (DCM, λ_{exc} 380 nm): 460 nm. **ϕ:** 1%.

IR-Spectrum (cm^{-1}, ATR): 3105 *ν*(C–H aromatic), 1600, 1545, 1510, 1475, 1325, 1250, 1145, 835, 785, 740, 700.

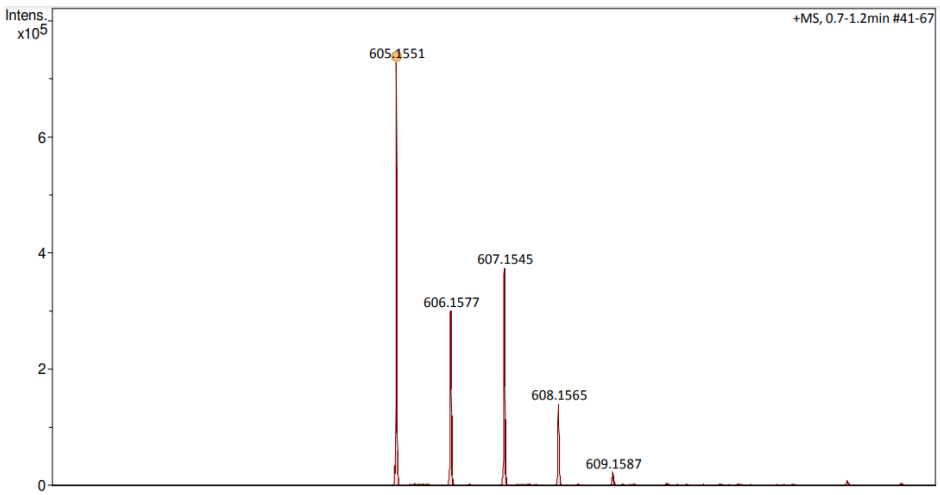

Figure 270 – HRMS-ESI$^+$ mass spectrum in MeOH of **369**.

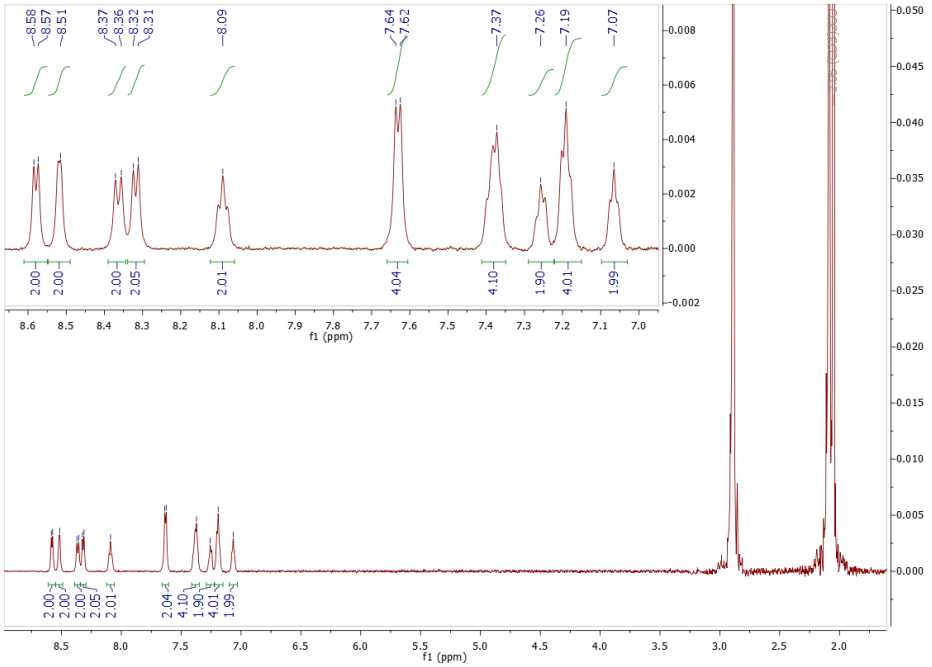

Figure 271 – ^{1}H-NMR in acetone-d$_6$ of **369**.

Compound 370

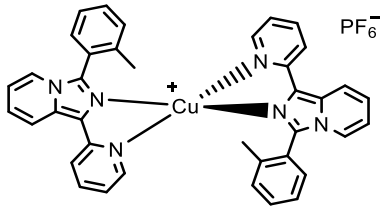

The product was isolated as a bright orange-red powder (86 mg, 69%). R_f (silica gel): 0.45 (9:1 DCM/MeOH). M_p: > 200 °C.

^{1}H-NMR (600 MHz, Acetone-d$_6$, RT): δ 8.41 (br, 2H, Ar-H), 8.32 (br, 2H, Ar-H), 8.22-8.24 (d, *J* = 7.4 Hz, 2H, Ar-H), 8.02 (br, 2H, Ar-H), 7.90-7.91 (d, *J* = 5.1 Hz, 2H, Ar-H), 7.25-7.35 (br, 10H, Ar-H), 7.11 (br, 2H, Ar-H), 7.02 (br, 2H, Ar-H), 2.07 (s, 6H, -CH$_3$) ppm.

HRMS (ESI$^+$-TOF, MeOH): *m/z* 633.1864 [M]$^+$; calculated for $C_{38}H_{30}CuN_6^+$: 633.1822.

UV-Vis (DCM): λ_{max} (*ε*) = 297 (*33151*), 374 (*29714*) nm.

Fluorescence (DCM, λ_{exc} 380 nm): 458 nm. **ϕ:** 4%.

IR-Spectrum (cm^{-1}, ATR): 3050 *ν*(C–H aromatic), 2920 *ν*(C–H aliphatic), 1600, 1510, 1475, 1325, 1245, 1145, 1110, 1005, 955, 830, 780, 735, 705.

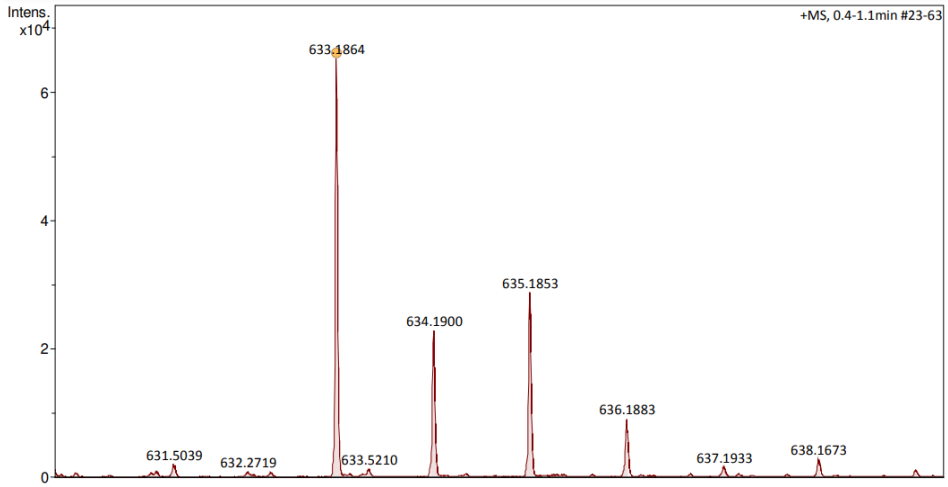

Figure 272 – HRMS-ESI$^+$ mass spectrum in MeOH of **370**.

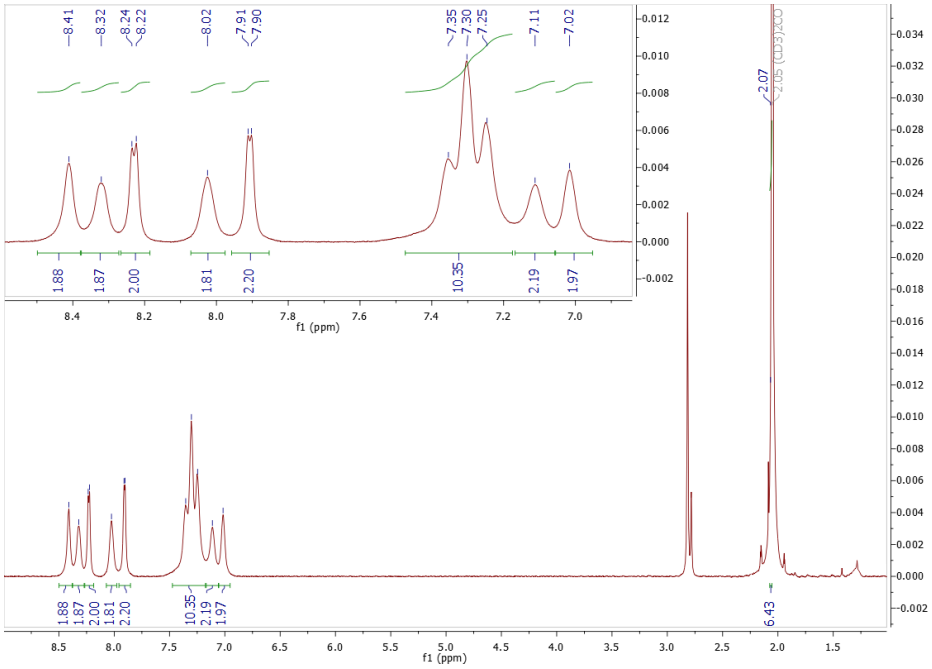

Figure 273 – ^{1}H-NMR in acetone-d$_6$ of **370**.

Compound 371

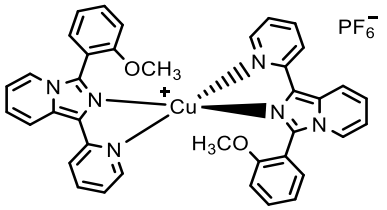

The product was isolated as a bright orange-red powder (86 mg, 70%). R_f (silica gel): 0.50 (9:1 DCM/MeOH). M_p: > 200 °C.

^{1}H-NMR (600 MHz, Acetone-d$_6$, RT): δ 8.45 (br, 2H, Ar-H), 8.33 (br, 2H, Ar-H), 8.24 (br, 2H, Ar-H), 8.03 (br, 2H, Ar-H), 7.95 (br, 2H, Ar-H), 7.17-7.44 (br, 10H, Ar-H), 7.08 (br, 2H, Ar-H), 7.02 (br, 2H, Ar-H), 6.59 (br, 2H, Ar-H), 3.80 (s, 6H, -CH_3) ppm.

HRMS (ESI$^+$-TOF, MeOH): *m/z* 665.1743 $[M]^+$; calculated for $C_{38}H_{30}CuN_6O_6^+$: 665.1721.

UV-Vis (DCM): λ_{max} (ε) = 298 (*34466*), 376 (*28766*) nm.

Fluorescence (DCM, λ_{exc} 380 nm): 454 nm. **ϕ:** 13%.

IR-Spectrum (cm^{-1}, ATR): 2945 *v*(C–H aliphatic), 2840 *v*(C–H aliphatic), 1600, 1510, 1470, 1435, 1325, 1245, 1110, 1015, 835, 735, 700.

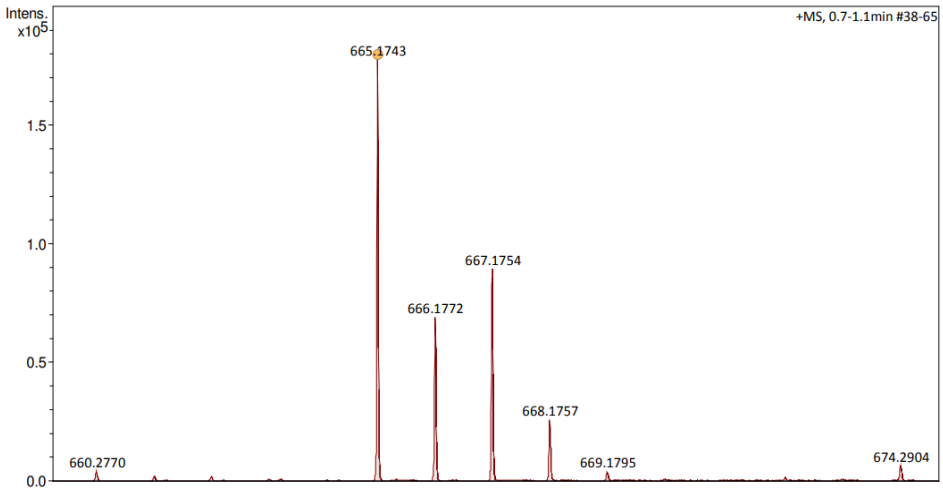

Figure 274 – HRMS-ESI$^+$ mass spectrum in MeOH of **371**.

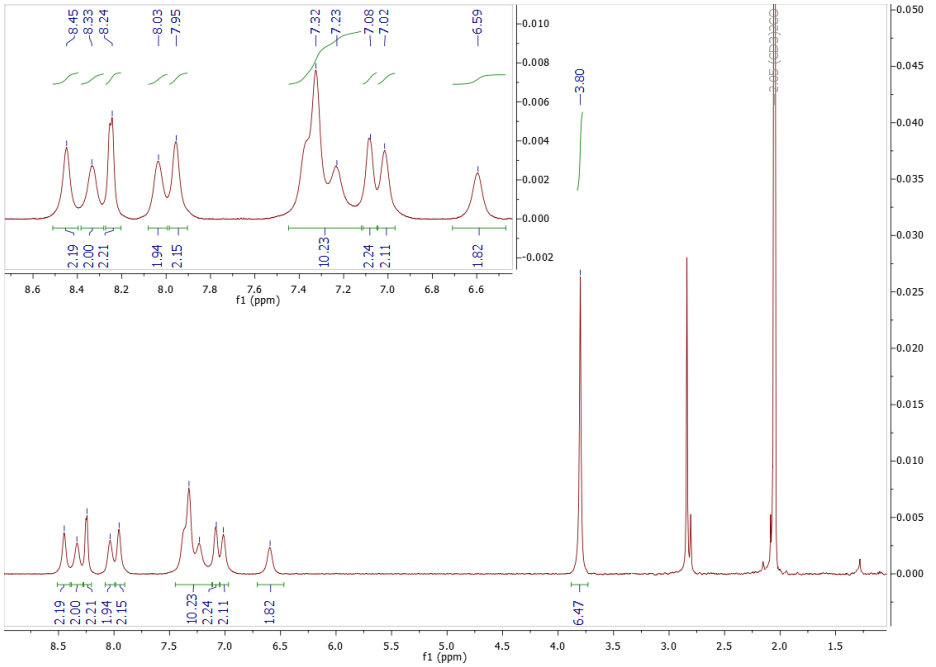

Figure 275 – ^{1}H-NMR in acetone-d_6 of **371**.

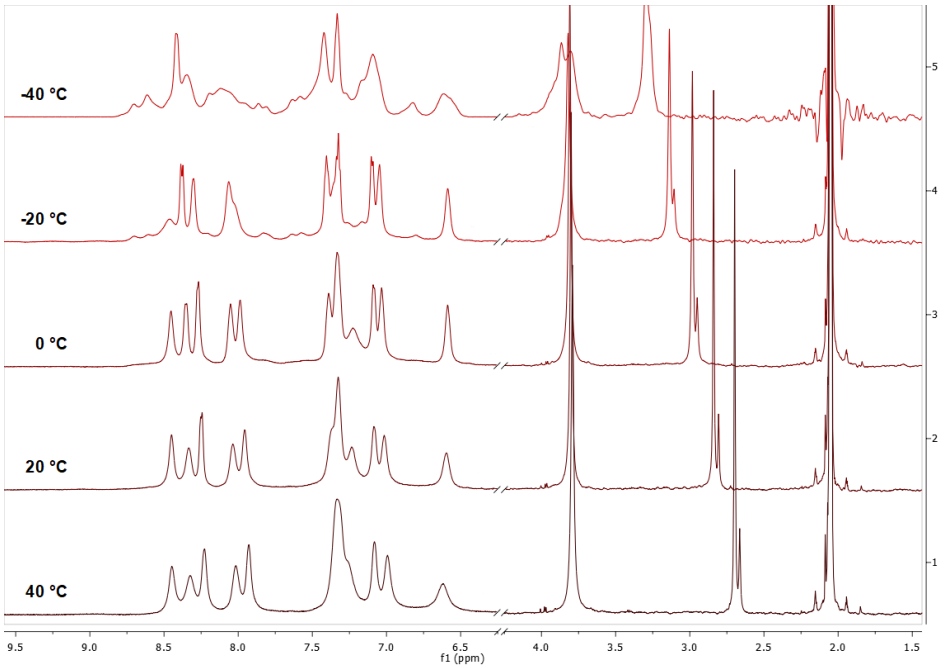

Figure 276 – Variable-temperature ^{1}H-NMR spectra in acetone-d_6 of **371**.

Compound 372

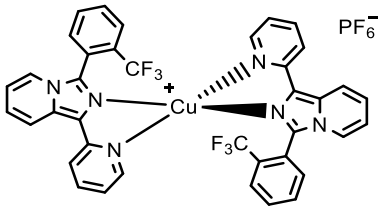

The product was isolated as a light-brown powder (64 mg, 54%). R_f (silica gel): 0.40 (9:1 DCM/MeOH). M_p: > 200 °C.

^{1}H-NMR (600 MHz, Acetone-d$_6$, RT): δ 8.40 (br, 2H, Ar-H), 8.30 (br, 2H, Ar-H), 8.19 (br, 2H, Ar-H), 8.02 (br, 2H, Ar-H), 7.82-7.88 (br, 4H, Ar-H), 7.72 (br, 4H, Ar-H), 7.58 (br, 2H, Ar-H), 7.33-7.41 (br, 4H, Ar-H), 6.99 (br, 2H, Ar-H) ppm.

HRMS (ESI$^+$-TOF, MeOH): *m/z* 741.1311 $[M]^+$; calculated for $C_{38}H_{24}CuF_6N_6^+$: 741.1257.

UV-Vis (DCM): λ_{max} (ε) = 298 (*28261*), 360 (*30792*), 369 (*31692*) nm.

Fluorescence (DCM, λ_{exc} 380 nm): 454 nm. **ϕ:** 9%.

IR-Spectrum (cm^{-1}, ATR): 3095 *ν*(C–H aromatic), 1600, 1510, 1475, 1445, 1315, 1170, 1110 *ν*(C–F), 1060, 1035, 835, 780, 740, 705.

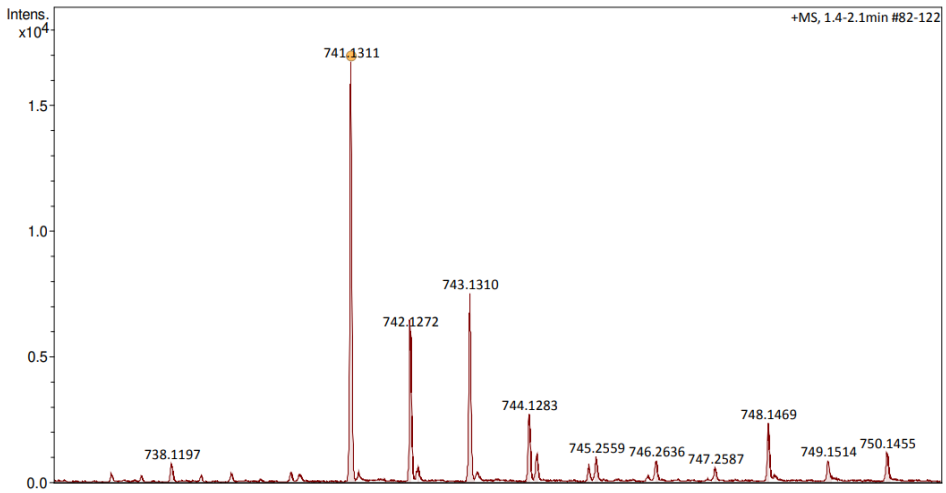

Figure 277 – HRMS-ESI$^+$ mass spectrum in MeOH of **372**.

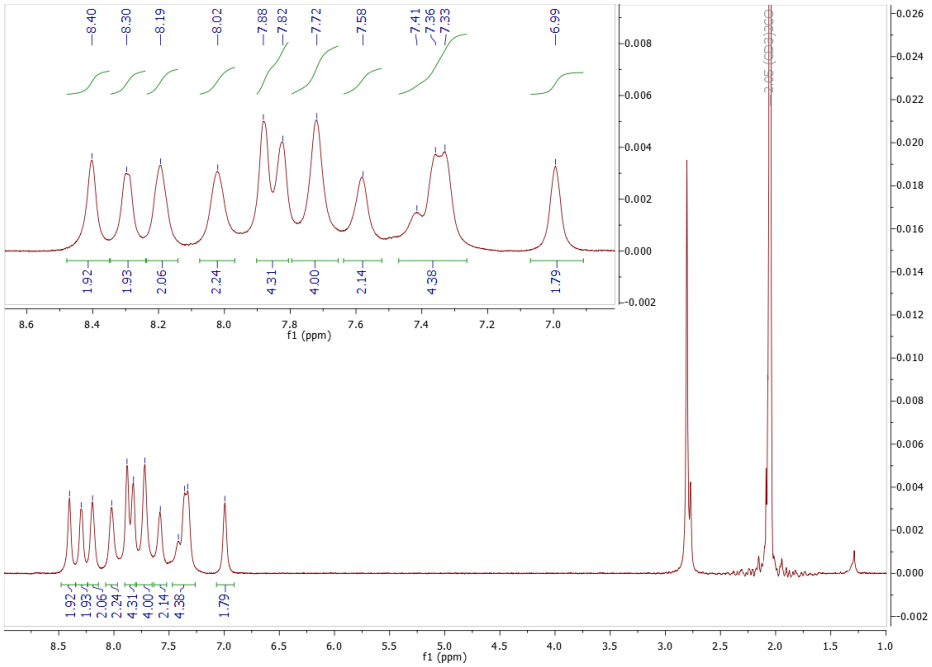

Figure X28 – ^{1}H-NMR in acetone-d_6 of **372**.

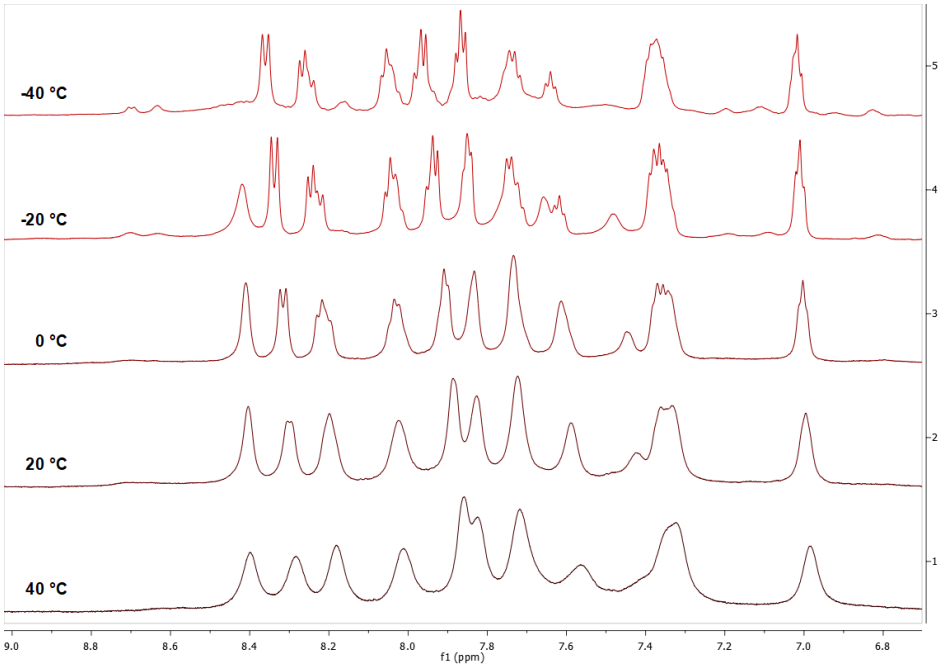

Figure 279 – Variable-temperature ^{1}H-NMR spectra in acetone-d_6 of **372**.

Compound 373

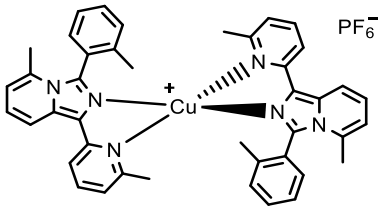

The product was isolated as a yellow powder (57 mg, 47%). R_f (silica gel): 0.75 (9:1 DCM/MeOH). M_p: > 200 °C.

^{1}H-NMR (600 MHz, Acetone-d$_6$, RT): δ 8.15-8.21 (m, 2H, Ar-H), 7.86-8.04 (m, 4H, Ar-H), 6.85-7.25 (m, 12H, Ar-H), 6.75-6.78 (m, 2H, Ar-H), 2.26-2.32 (m, 6H, -CH$_3$), 2.07-2.09 (m, 6H, -CH$_3$), 1.71-1.89 (m, 6H, -CH$_3$) ppm.

HRMS (ESI$^+$-TOF, MeOH): *m/z* 689.2489. [M]$^+$; calculated for $C_{42}H_{38}CuN_6^+$: 689.2448.

UV-Vis (DCM): λ_{max} (ε) = 299 (*20250*), 375 (*24918*) nm.

Fluorescence (DCM, λ_{exc} 380 nm): 444 nm. **ϕ:** 15%.

IR-Spectrum (cm^{-1}, ATR): 2930 *v*(C–H aliphatic), 2850 *v*(C–H aliphatic), 1640, 1600, 1570, 1530, 1475, 1320, 1150, 1095, 835, 790, 770, 735.

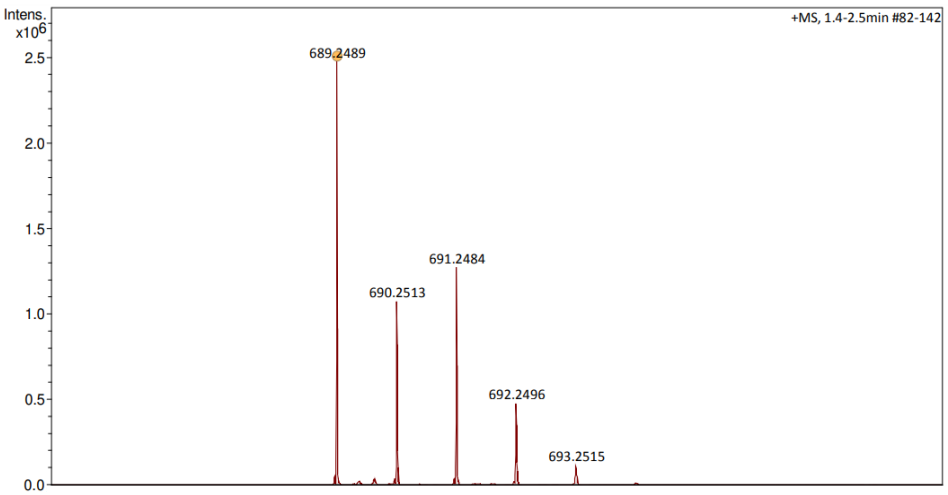

Figure 280 – HRMS-ESI$^+$ mass spectrum in MeOH of **373**.

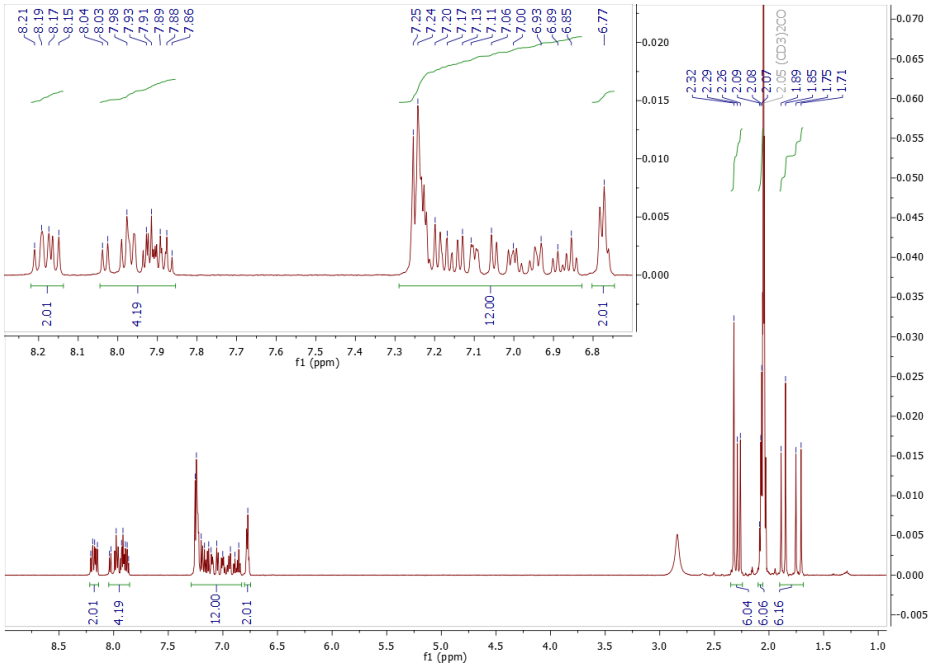

Figure 281 – ^{1}H-NMR in acetone-d$_6$ of **373**.

Compound 374

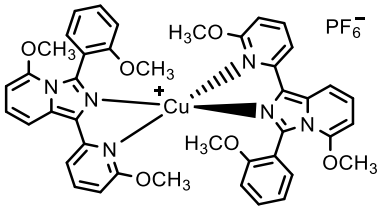

The product was isolated as a bright-orange powder (100 mg, 85%). R_f (silica gel): 0.70 (9:1 DCM/MeOH). M_p: > 200 °C.

^{1}H-NMR (600 MHz, Acetone-d$_6$, RT): δ 7.63-7.78 (br, 6H, Ar-H), 7-16-7.27 (br, 6H, Ar-H), 6.30-6.84 (br, 8H, Ar-H), 3.62-3.79 (br, 18H, -CH$_3$) ppm.

HRMS (ESI$^+$-TOF, MeOH): *m/z* 785.2179 [M]$^+$; calculated for $C_{42}H_{38}CuN_6O_6^+$: 785.2143.

UV-Vis (DCM): λ_{max} (ε) = 293 (*17224*), 375 (*29409*) nm.

Fluorescence (DCM, λ_{exc} 380 nm): 435 nm. **ϕ:** 25%.

IR-Spectrum (cm^{-1}, ATR): 2940 *v*(C–H aliphatic), 2835 *v*(C–H aliphatic), 1635, 1570, 1530, 1465, 1425, 1400, 1275, 1245, 1135, 1010, 985, 830, 790, 750, 715.

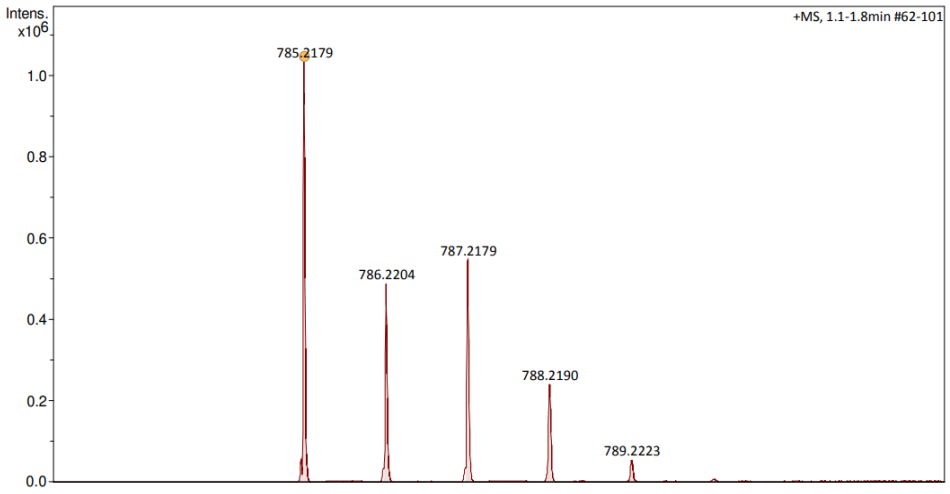

Figure 282 – HRMS-ESI$^+$ mass spectrum in MeOH of **374**.

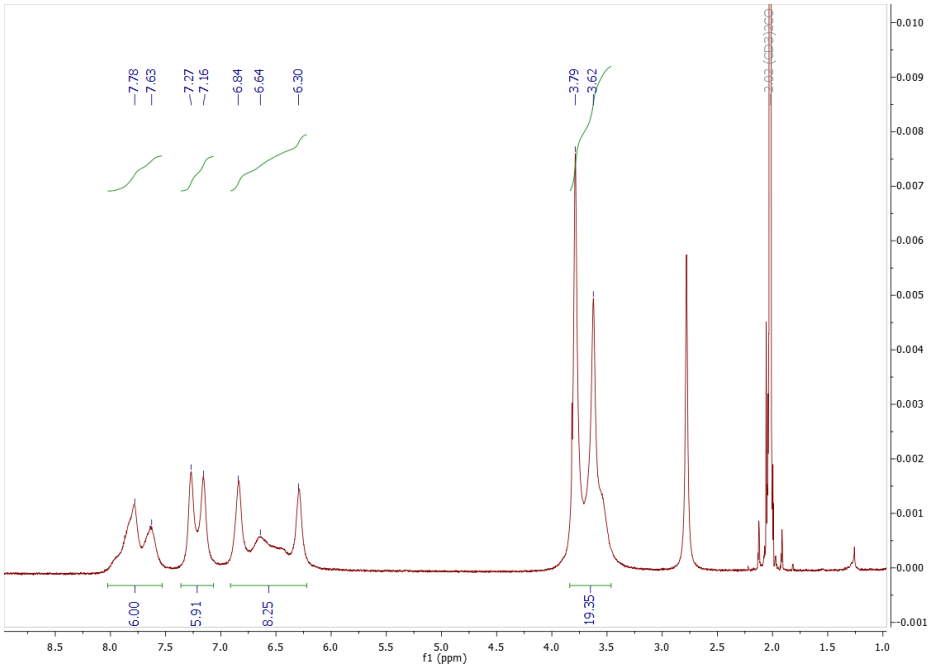

Figure 283 – ^{1}H-NMR in acetone-d_6 of **374**.

Compound 375

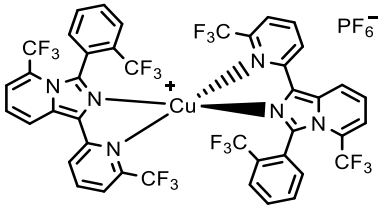

The product was isolated as a light-orange powder (103 mg, 93%). R_f (silica gel): 0.80 (9:1 DCM/MeOH). M_p: > 200 °C.

^{1}H-NMR (600 MHz, Acetone-d$_6$, RT): δ 8.30-8.80 (br, 6H, Ar-H), 7.00-7.90 (br, 14H, Ar-H) ppm.

HRMS (ESI$^+$-TOF, MeOH): *m/z* 1013.0780 [M]$^+$; calculated for $C_{42}H_{20}CuF_{18}N_6^+$: 1013.0753.

UV-Vis (DCM): λ_{max} (ε) = 296 (*18122*), 373 (*14784*) nm.

Fluorescence (DCM, λ_{exc} 380 nm): 488 nm. **ϕ:** 13%.

IR-Spectrum (cm^{-1}, ATR): 3115 *ν*(C–H aromatic), 1605, 1480, 1310, 1115 *ν*(C–F), 1060, 835, 815, 770, 725, 700.

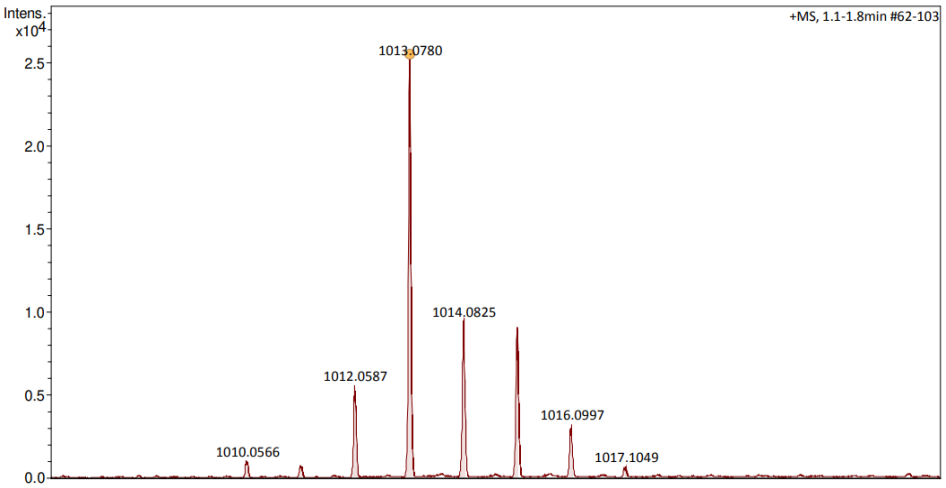

Figure 284 – HRMS-ESI$^+$ mass spectrum in MeOH of **375**.

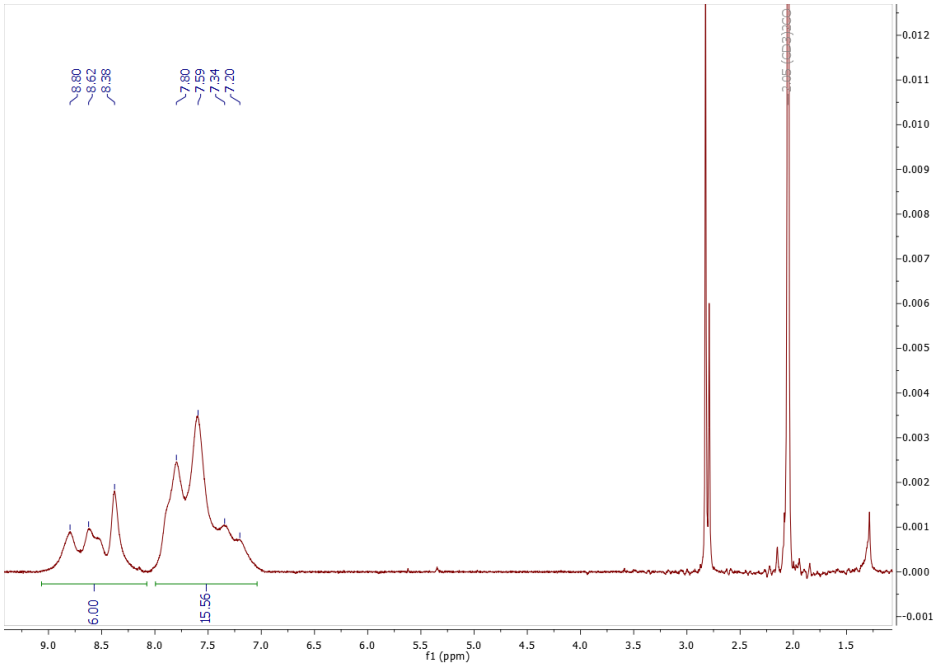

Figure 285 – ^{1}H-NMR in acetone-d_6 of **375**.

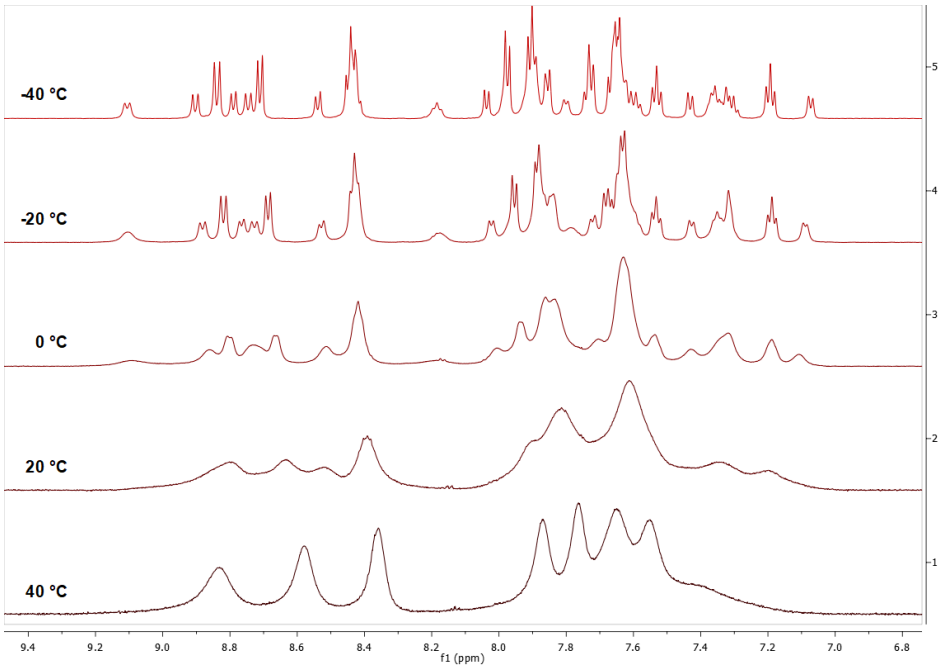

Figure 286 – Variable-temperature ^{1}H-NMR spectra in acetone-d_6 of **375**.

1.18. Synthesis of TPA-based Asymmetrical Cyanine

Compound 403

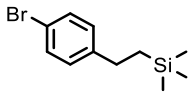

Compound **403** was synthetized according to the published procedure.[523] A mixture of **402** (4.4 g, 21.99 mmol), DIPEA (5.3 mL, 4.0 g, 30.6 mmol) and 35 mL of DCM was cooled at 0 °C and after TMSCl (3.9 mL, 3.3 g, 30.6 mmol) was added. The resulting mixture was warmed at RT and stirred overnight. After the reaction, potassium carbonate (1.4 g) was added and the resulting mixture was stirred for an additional 3 h at RT. The solid were then filtered off and the solvent was removed by evaporation under vacuum. The resulting colorless sticky-oil was purified by flash chromatography on silica gel using *n*-hexane/ethyl acetate (95:5). The product was isolated as colorless oil (4.52 g, 80%). R_f (silica gel): 0.85 (85:15 *n*-hexane/ethyl acetate).

^{1}H-NMR (600 MHz, $CDCl_3$, RT): δ 7.39-7.41 (d, *J* = 8.3 Hz, 2H, Ar-H), 7.07-7-09 (d, *J* = 8.5 Hz, 2H, Ar-H), 3.75 (t, *J* = 8.2 Hz, 2H, -CH_2-), 2.78 (t, *J* = 7.0 Hz, 2H, -CH_2-), 0.06 (s, 9H, -CH_3) ppm.

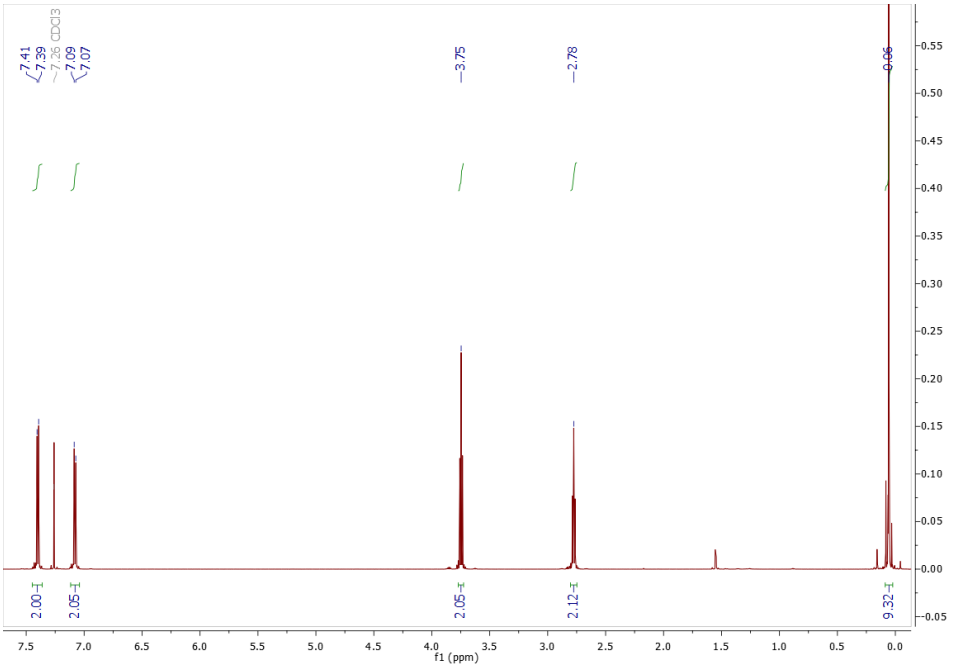

Figure 287 – ^{1}H-NMR in $CDCl_3$ of **403**.

Compound 404

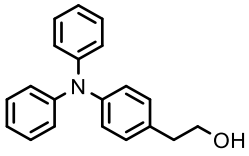

Compound **404** was synthetized according to the published procedure.[524] A mixture of tris(dibenzylideneacetone)dipalladium(0) (410 mg, 0.45 mmol), sodium *tert*-butoxide (1.93 g, 20.1 mmol) and 25 mL of anhydrous toluene was carefully deoxygenated three vacuum/argon cycles at room temperature. After, 1.34 mL of a solution 1.0 M of tri-*tert*-butyl phosphine in toluene was added and the resulting mixture was stirred for 15 min. After, a mixture of **403** (2.43 g, 8.9 mmol), diphenylamine (2.27 g, 13.4 mmol) and 20 mL of anhydrous toluene was added and the resulting reaction mixture was refluxed overnight. After, the reaction mixture was cooled to room temperature and 24 mL of 2 N HCl aqueous solution was added and the resulting mixture was stirred for 30 min at RT. The resulting mixture was concentrated under vacuum and then extracted with dichloromethane. The organic layer was separated, dried over sodium sulphate and the solvent evaporated under vacuum. The desired product was purified by flash chromatography on silica gel using *n*-hexane/ethyl acetate (9:1) as eluent. The product was isolated brown sticky oil (2.17 g, 84%). R_f (silica gel): 0.10 (85:15 *n*-hexane/ethyl acetate).

^{1}H-NMR (600 MHz, $CDCl_3$, RT): δ 7.22-7.25 (m, 4H, Ar-H), 6.98-7.12 (m, 10H, Ar-H), 3.87 (t, *J* = 6.5 Hz, 2H, -CH_2-), 2.83 (t, *J* = 6.5 Hz, 2H, -CH_2-) ppm.

MS (ESI^+, MeOH): *m/z* 290.28 $[M]^+$; calculated for $C_{20}H_{19}NO$: 289.15.

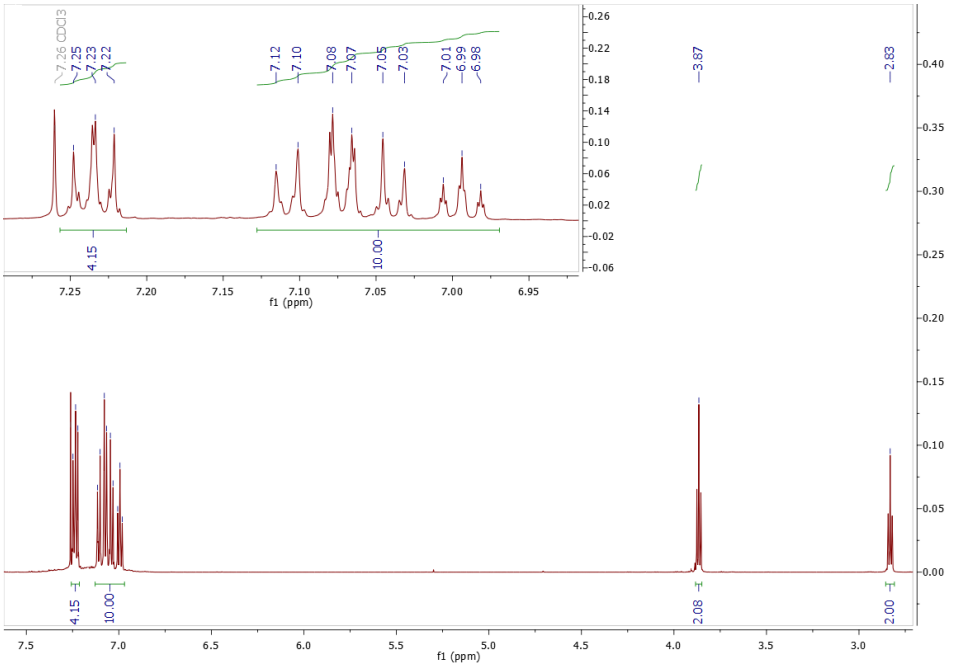

Figure 288 – ^{1}H-NMR in $CDCl_3$ of **404**.

Compound 405

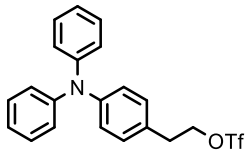

A mixture of **404** (0.2 g, 0.7 mmol), 2,6-lutidine (0.12 mL, 0.11 g, 1.0 mmol) and 5 mL of DCM was cooled to -78 °C and then trifluoromethanesulfonic anhydride (0.13 mL, 0.22 g, 0.7 mmol) was added dropwise. After the addition, the resulting mixture was stirred for 5 min at -78 °C. Then, 3 mL of an aqueous solution 0.5 M of sulfuric acid and 1.5 mL of *n*-hexane were added to the reaction mixture and readily extracted. The organic phase was separated, dried over a sodium sulfate in a Gooch funnel and collected. The resulting light-pink solution was immediately used as it for the next step without any purification.

Compound 407

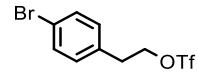

A mixture of **402** (7.0 mL, 10.0 g, 49.7 mmol), 2,6-lutidine (9.0 mL, 8.6 g, 79.6 mmol) and 120 mL of DCM was cooled to -78 °C and then trifluoromethanesulfonic anhydride (10.0 mL, 16.8 g, 59.7 mmol) was added dropwise. After the addition, the resulting mixture was stirred for 5 min at -78 °C. Then, 200 mL of an aqueous solution 0.5 M of sulfuric acid and 50 mL of *n*-hexane were added to the reaction mixture and readily extracted. The organic phase was separated, dried over sodium sulfate in a Gooch funnel and collected. The resulting light-pink solution was immediately used as it for the next step without any purification.

Compound 408

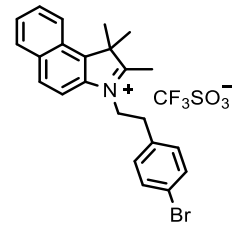

A mixture of **407** (raw material) and 1,1,2-trimethyl-1*H*-benzo[*e*]indole (2.5 g, 11.94 mmol) was refluxed for 1 h. After cooling the reaction to room temperature, the solvent was removed and the crude material was purified by flash chromatography on silica gel using DCM/MeOH (93:7) as eluent. The product was isolated as a greenish powder (5.14 g, 79%). R_f (silica gel): 0.40 (9:1 DCM/MeOH). M_p: 174-176 °C (decomposition).

^{1}H-NMR (600 MHz, $CDCl_3$, RT): δ 8.14-8.15 (d, *J* = 8.8 Hz, 1H, Ar-H), 8.07 (t, *J* = 9.1 Hz, 1H, Ar-H), 7.84-7.85 (d, *J* = 8.9 Hz, 1H, Ar-H), 7.74-7.77 (m, 1H, Ar-H), 7.68-7.71 (m, 1H, Ar-H), 7.36-7.37 (d, *J* = 8.3 Hz, 2H, Ar-H), 6.89-6.91 (d, *J* = 8.3 Hz, 2H, Ar-H), 4.99-5.01 (t, *J* = 6.4 Hz, 2H, -CH_2-), 3.32-3.34 (t, *J* = 6.4 Hz, 2H, -CH_2-), 2.31 (s, 3H, -CH_3), 1.66 (s, 6H, -CH_3) ppm.

^{13}C-NMR (151 MHz, $CDCl_3$/DMSO-d_6 3:1, RT): δ 195.31, 136.68, 135.84, 133.83, 132.44, 130.82, 130.26, 130.07, 129.76, 128.87, 127.59, 126.60, 126.44, 121.85, 120.66, 120.37, 118.53, 111.55, 54.65, 48.33, 31.84, 21.07, 12.55 ppm.

MS (ESI$^+$, MeOH): *m/z* 394.02 $[M]^+$; calculated for $C_{23}H_{23}BrN^+$: 392.10.

UV-Vis (EtOH): λ_{max} (ε) = 265 (*24041*), 275 (*21497*), 304 (*6383*), 316 (*7232*) nm.

Fluorescence (EtOH, λ_{exc} 280 nm): 438 nm. **ϕ:** 11%.

IR-Spectrum (cm^{-1}, ATR): 2990 *ν*(C–H aliphatic), 1635, 1580, 1490, 1280, 1250 *ν*(S=O), 1220, 1140, 1030, 820, 750.

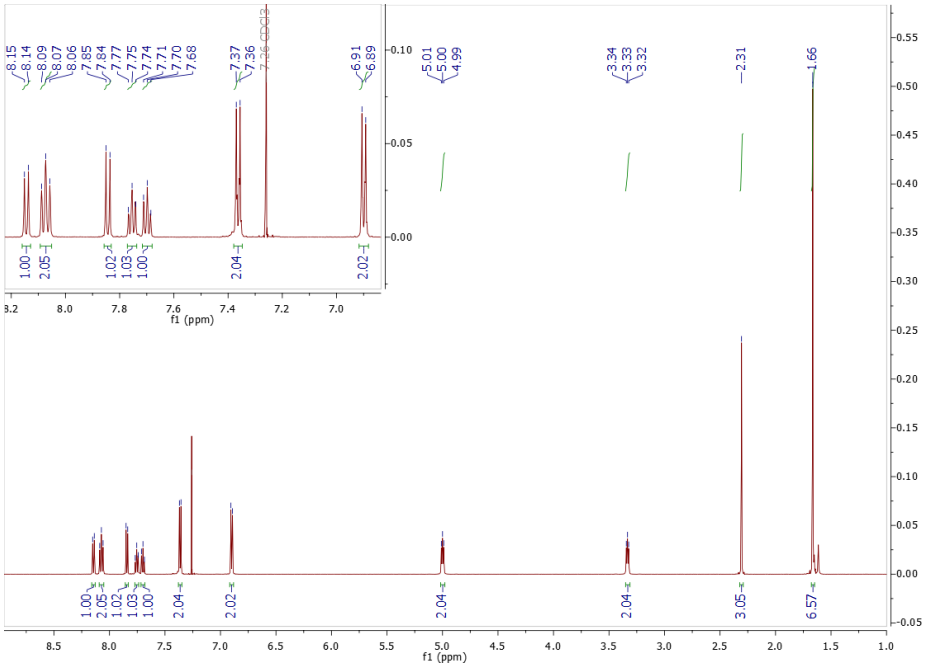

Figure 289 – ^{1}H-NMR in $CDCl_3$ of **408**.

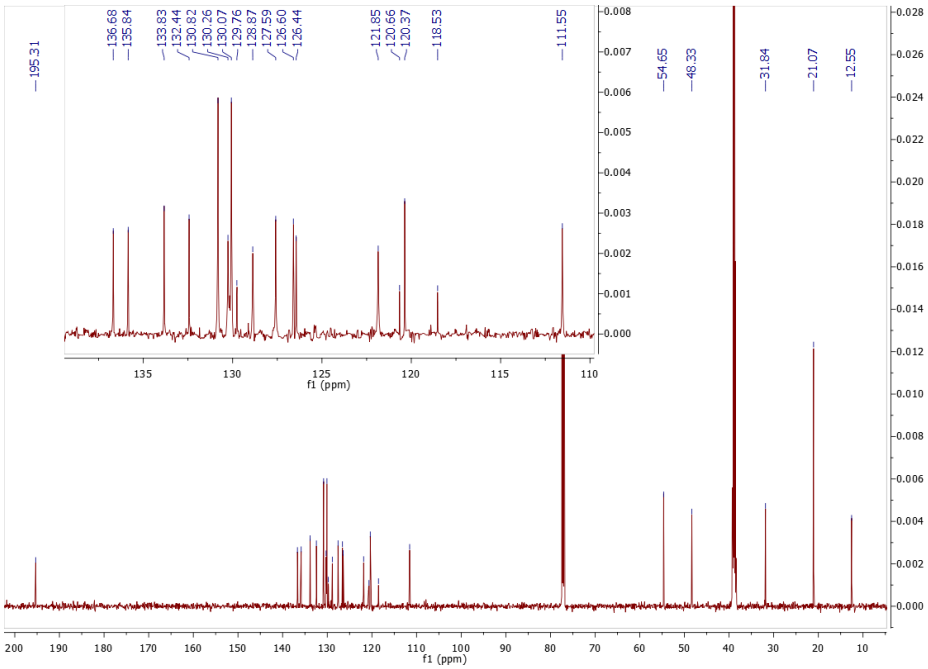

Figure 290 – ^{13}C-NMR in $CDCl_3$/DMSO-d_6 (3:1) of **408**.

Compound 406

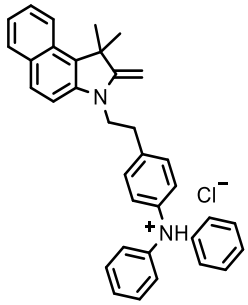

A mixture of tris(dibenzylideneacetone)dipalladium(0) (80 mg, 0.09 mmol), sodium *tert*-butoxide (0.4 g, 4.16 mmol) and 5 mL of anhydrous toluene was carefully deoxygenated three vacuum/argon cycles at room temperature. After, 0.28 mL of a solution 1.0 M of tri-*tert*-butyl phosphine in toluene was added and the resulting mixture was stirred for 15 min. After, a mixture of **408** (1.0 g, 1.85 mmol), diphenylamine (0.47 g, 0.28 mmol) and 16 mL of anhydrous toluene was added and the resulting reaction mixture was refluxed overnight. After cooling to room temperature, 1 mL of HCl 4 M in 1,4-dioxane was added and the mixture was stirred for 15 min. After, the solvent was removed under vacuum and the crude was purified by flash chromatography on silica gel using DCM/MeOH (97/3) as eluent. The product was isolated as a greenish powder (0.17 g, 18%). R_f (silica gel): 0.35 (95:5 DCM/MeOH). Due to the low stability of the product, all compound was directly used for the synthesis of the asymmetrical cyanine **410**. Only basic chemical characterization was performed.

^{1}H-NMR (600 MHz, $CDCl_3$, RT): δ 7.93-7.96 (m, 1H, Ar-H), 7.73-7.76 (m 1H, Ar-H), 7.58-7.63 (m, 1H, Ar-H), 7.36-7.40 (m, 1H, Ar-H), 7.14-7.19 (m, 4H, Ar-H), 7.07-7.11 (m, 2H, Ar-H), 6.93-6-97 (m, 6H, Ar-H), 6.72-6.83 (m, 1H, Ar-H), 3.97-3.98 (m, 2H, $=CH_2$), 3.82-3.83 (m, 2H, $-CH_2-$), 2.89-2.94 (m, 2H, $-CH_2-$), 1.65 (s, 6H, $-CH_3$) ppm.

MS (ESI$^+$, MeOH + formic acid): *m/z* 481.10 $[M-H]^+$; calculated for $C_{35}H_{32}N_2^+$: 480.26.

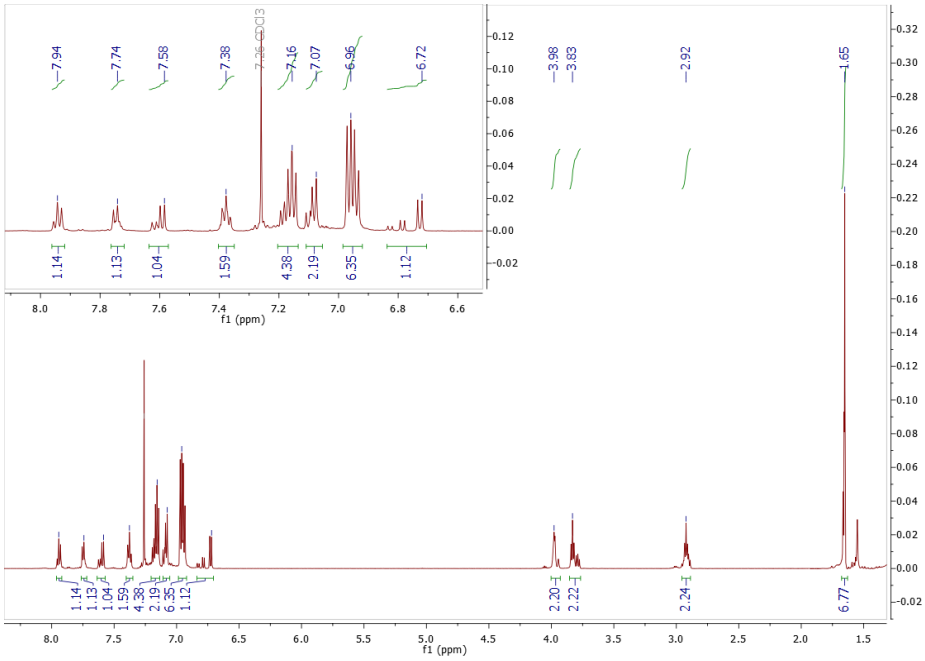

Figure 291 – ^{1}H-NMR in DMSO-d_6 of **406**.

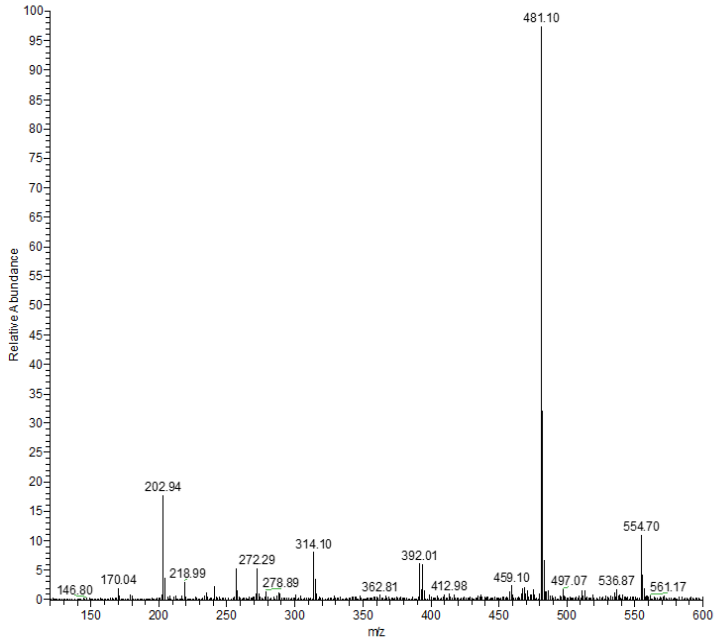

Figure 292 – ESI^{+} mass spectrum in MeOH of **406**.

Compound 409

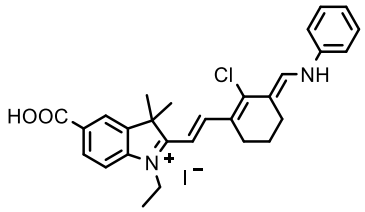

A mixture of **321** (5.0 g, 13.9 mmol), *N*-[(3-(Anilinomethylene)-2-chloro-1-cyclohexen-1-yl)methylene]aniline monohydrochloride (7.5 g, 20.9 mmol) and 125 mL of ethanol was refluxed for 1 h in the dark under argon. After cooling to room temperature, the solvent was removed under vacuum and the crude was purified by flash chromatography on silica gel using a *n*-hexane/ethyl acetate (6:4) as eluent. The product was isolated as a dark-green powder (0.53 g, 6%). R_f (silica gel): 0.45 (9:1 DCM/MeOH). M_p: > 200 °C.

^{1}H-NMR (600 MHz, DMSO-d$_6$, RT): δ 8.74 (s, 1H, -CH=), 7.82-7.86 (m, 3H, Ar-H and -NH), 7.54-7.56 (d, *J* = 12 Hz, 1H, -CH=), 7.37-7.40 (t, *J* = 7.8 Hz, 2H, Ar-H), 7.20-7.22 (t, *J* = 7.4 Hz, 1H, Ar-H), 7.14-7.16 (d, *J* = 7.5 Hz, 2H, Ar-H), 6.92-6.93 (d, *J* = 8.7 Hz, 1H, Ar-H), 5.70-5.72 (d, *J* = 12.7 Hz, 1H, -CH=), 3.83-3.86 (q, *J* = 7.0 Hz, 2H, -CH_2-), 2.69-2.70 (t, *J* = 5.9 Hz, 2H, -CH_2-), 2.63-2.65 (t, *J* = 5.7 Hz, 2H, -CH_2-), 1.76-1.78 (t, *J* = 5.9 Hz, 2H, -CH_2-), 1.59 (s, 6H, -CH_3), 1.15-1.18 (t, *J* = 7.1 Hz, 3H, -CH_3) ppm.

^{13}C-NMR (151 MHz, DMSO-d$_6$, RT): δ 189.55, 167.25, 166.87, 160.84, 147.16, 145.30, 141.28, 130.71, 129.79, 129.75, 129.72, 125.79, 125.61, 123.49, 122.91, 122.80, 121.87, 118.92, 118.73, 111.17, 106.95, 48.85, 27.36, 25.50, 25.19, 19.96, 12.19 ppm.

MS (ESI$^+$, MeOH): *m/z* 461.08 $[M]^+$; calculated for $C_{28}H_{30}ClN_2O_2^+$: 461.20.

UV-Vis (EtOH): λ_{max} (ε) = 393 (*11241*), 469 (*17910*), 658 (*35826*) nm.

Fluorescence (EtOH, λ_{exc} 630 nm): 686 nm. **ϕ:** 4%.

IR-Spectrum (cm^{-1}, ATR): 2930 *v*(C–H aliphatic), 1700 *v*(C═O), 1625, 1550, 1520, 1470, 1430, 1405, 1340, 1235, 1155, 1110, 1060, 1035, 905, 835, 745.

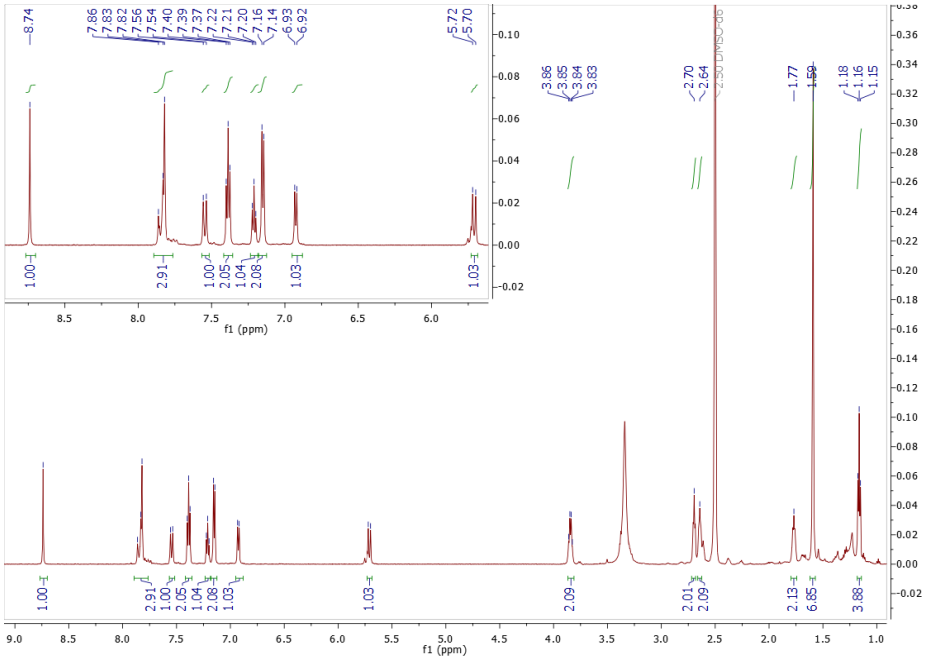

Figure 293 – ^{1}H-NMR in DMSO-d$_6$ of **409**.

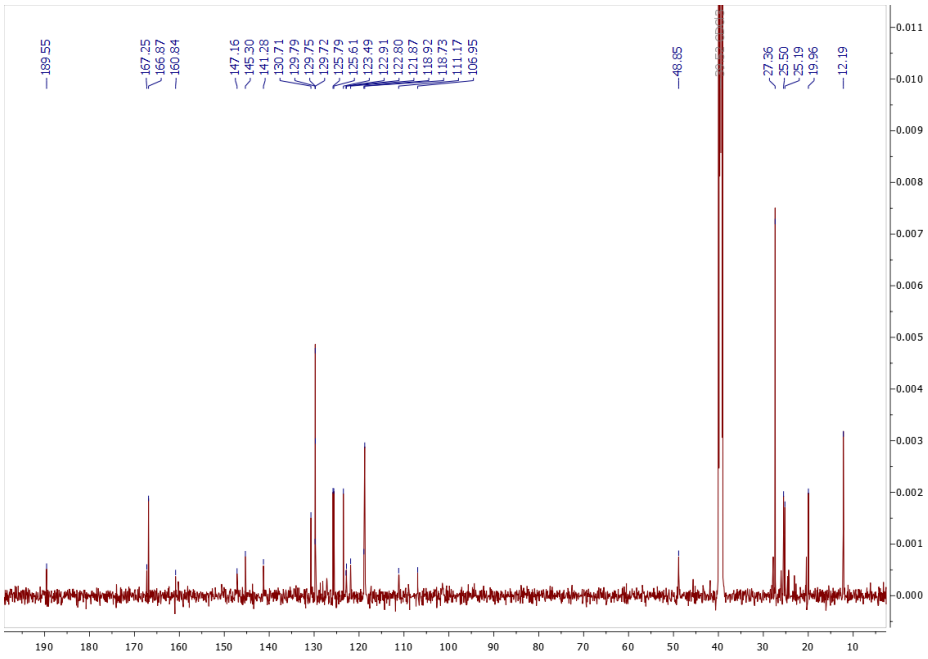

Figure 294 – ^{13}C-NMR in DMSO-d$_6$ of **409**.

Compound 410

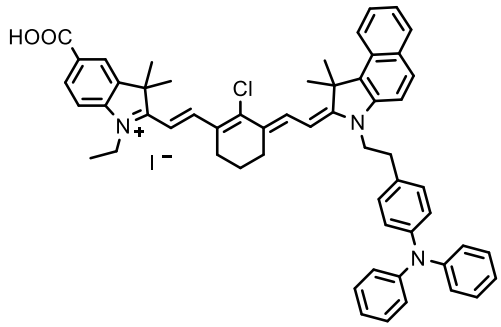

A mixture of **406** (135 mg, 0.23 mmol), **409** (170 mg, 0.33 mmol), anhydrous potassium acetate (46 mg, 0.47 mmol) and 10 mL of absolute ethanol was refluxed overnight under argon. After cooling to room temperature, the reaction mixture was filtered to separate the poor soluble di-TPA-based symmetrical cyanine and the resulting solution was concentrated under vacuum. The crude was purified by flash chromatography silica gel using DCM/MeOH/acetic acid (92:7.7:0.3) as eluent. The product was isolated as a dark-green powder (4 mg, 2%). R_f (silica gel): 0.15 (94:6 DCM/MeOH).

^{1}H-NMR (600 MHz, $CDCl_3$, RT): δ 8.62-8.70 (m, 1H, Ar-H), 8.45-8.48 (d, *J* = 14.7 Hz, -CH=), 8.03-8.15 (m, 4H, Ar-H and -CH=), 7.57-7.71 (m, 5H, Ar-H), 7.06-7.16 (m, 6H, Ar-H), 6.99-7.00 (d, *J* = 8.3 Hz, 2H, Ar-H), 6.91-6.93 (t, *J* = 7.4 Hz, 3H, Ar-H), 6.84-6.86 (m, 6H, Ar-H), 6.34-6.37 (d, *J* = 15.5 Hz, 1H, -CH=), 5.89-5.91 (d, *J* = 13.4 Hz, 1H, -CH=), 5.00 (br, 2H, $-CH_2-$), 3.98-3.99 (m, 2H, $-CH_2-$), 3.30-3.32 (t, *J* = 5.4 Hz, 2H, $-CH_2-$), 2.69-2.71 (t, *J* = 5.2 Hz, 2H, $-CH_2-$), 2.60-2.62 (m, 2H, $-CH_2-$), 1.94 (s, 6H, $-CH_3$), 1.87-1.92 (m, 2H, $-CH_2-$), 1.38-1.41 (t, *J* = 7.1 Hz, 3H, $-CH_3$) ppm.

^{13}C-NMR: Not enough sample to perform the experiment.

MS (ESI$^+$, MeOH): *m/z* 848.51 $[M]^+$; calculated for $C_{57}H_{55}ClN_3O_2^+$: 848.40.

UV-Vis (EtOH): λ_{max} (ε) = 307 (*51560*), 389 (*13814*), 562 (*8706*), 810 (*142746*) nm.

Fluorescence (EtOH, λ_{exc} 770 nm): 836 nm. **ϕ:** 4%.

IR-Spectrum: Not enough sample to perform the experiment.

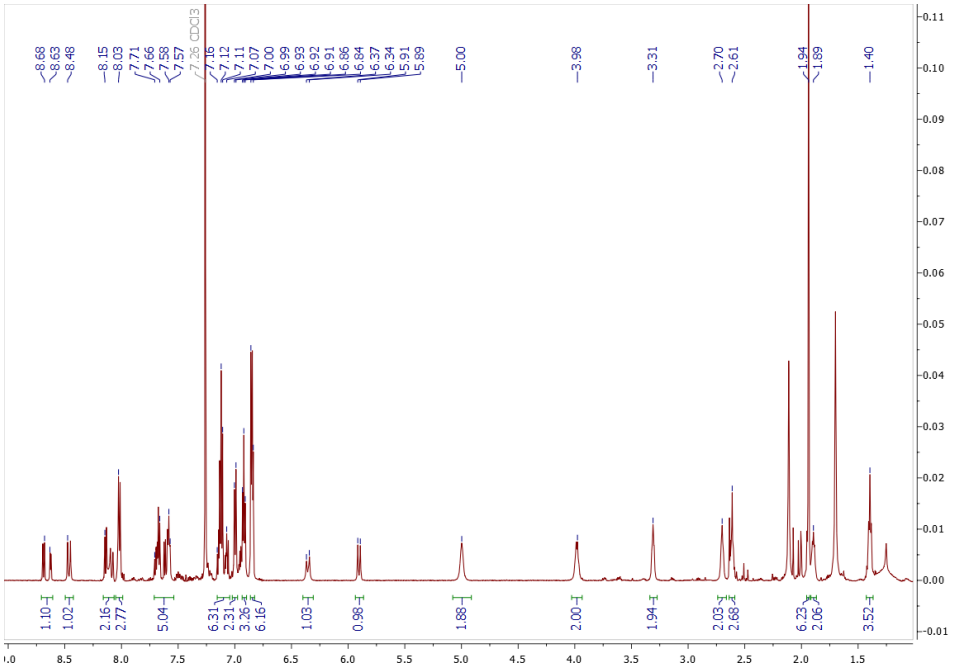

Figure 295 – ^{1}H-NMR in $CDCl_3$ of **410**.

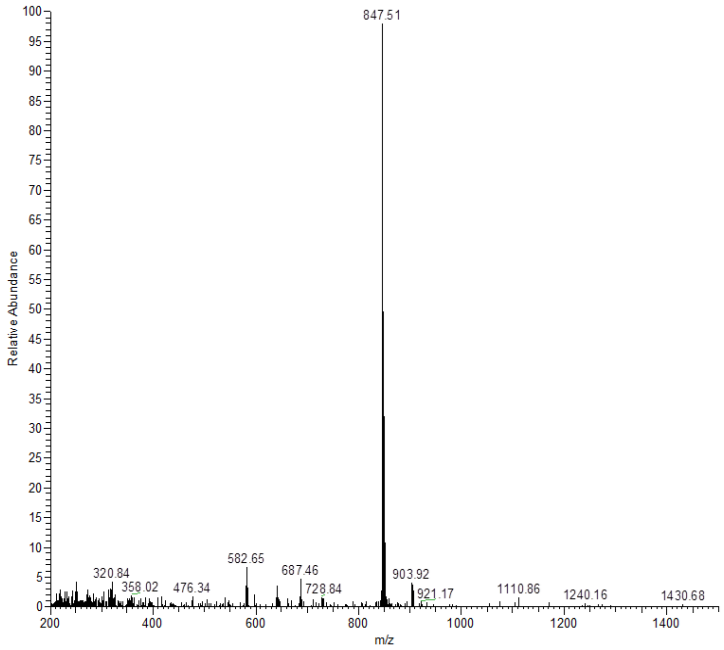

Figure 296 – ESI^{+} mass spectrum in MeOH of **410**.

2. Photophysical Characterization

All the anhydrous solvents used for the absorption and emission spectroscopy measurements were purchased from Sigma Aldrich, VWR and Carlo Erba.

For each compounds a stock solution was prepared and stored at -20 °C in the dark. In particular: (i) the stock solutions of the perylene-, quaterrylene-based compounds and DHPs were prepared in toluene, (ii) the stock solutions of the indole-based iodide salts, the emisquarates, the emisquaraines and the SQs were prepared in DMSO (except for **350**, in which toluene was used due to its insolubility in DMSO) and (iii) the stock solutions of *impy* ligands and copper complexes in DCM. Prepared stock solutions have concentrations between $2 \cdot 10^{-4}$ and $6 \cdot 10^{-3}$ M.

The samples concentration was adjusted to have an absorbance between 0.1 and 1 at the λ_{max} for the absorption spectroscopy experiments, while for the fluorescence spectroscopy measurements the sample concentrations were adapted to have an absorbance lower than 0.1 at the excitation wavelength (λ_{ex}).

All the photophysical measurements were carried out in a 1 cm four-sided quartz cuvette from Hellma Analitics.

Absorption spectra were measured on a Shimadzu UV-1900i UV-Vis Spectrophotometer, using a resolution of 0.5 nm.

Steady state emission spectra were measured on a Shimadzu RF6000. The excitation and the emission slits were set at 5 and 10 nm respectively (for squaraines **391**-**393** and **395** emission slits were set at 20 and 20 nm), while the resolution at 1 nm.

Table 32 – Physical properties of different solvents.

Solvent	Refractive Index (at 20 °C)	$E_T(30)$ [kcal mol^{-1}]
EtOH	1.3614	51.9
ACN	1.3441	45.6
DMF	1.4305	43.2
Acetone	1.3587	42.2
DCM	1.4242	40.7
EtOAc	1.3724	38.1
THF	1.4072	37.4
Dioxane	1.4224	36.0
Toluene	1.4969	33.9

Fluorescence quantum yield (QY) were evaluated compared on three different external standards: (i) Coumarin 153 (QY = 0.38 in EtOH, λ_{ex} = 421 nm), (ii) Rhodamine 6G (QY = 0.94 in EtOH, λ_{ex} = 488 nm) and (iii) Quinine (QY = 0.55 in 0.5 M H_2SO_4, λ_{ex} = 366 nm). The relative QY was calculated by the equation 11:

$$QY = QY_{std}\frac{I}{I_{std}}\frac{Abs_{std}}{Abs}\frac{n^2}{{n_{std}}^2} \qquad (11)$$

Where QY_{std} is the fluorescence quantum yield of the standard, I and I_{std} are the integrated area of the emission band of the sample and the standard, respectively. Abs and Abs_{std} are the absorbance at the excitation wavelength for the sample and the standard, respectively. n and n_{std} are the solvent refractive indexes of the sample and the standard solutions, respectively.

The refractive indexes for the QY calculation and the E_T30 values for solvatochromism used are reported in Tab. 32.[536]

2.1. Additional Data for the DHP-SQs of the Chapter 3

In this section are reported all the absorption and steady state emission spectra and their photophysical properties of DHP-SQs **341**-**350** in different solvents. In addition, Reichardt's Plots for each dye are reported.

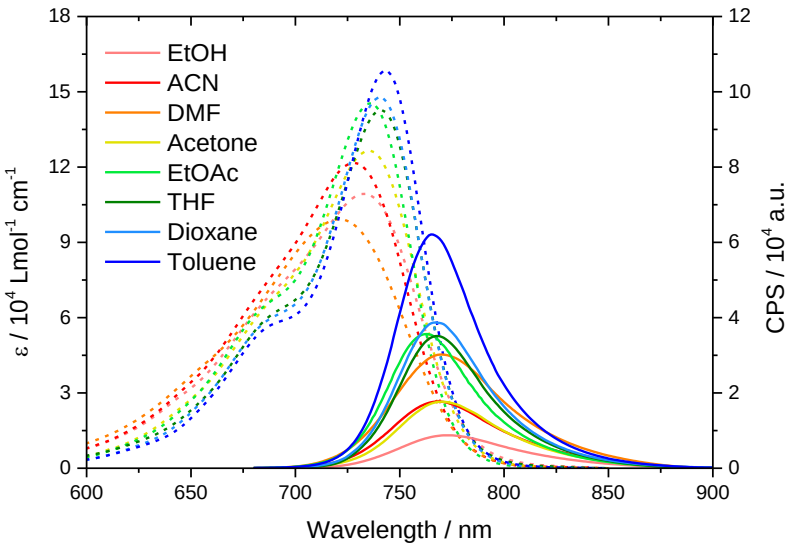

Figure 297 – Absorption and steady state emission spectra of **341** in different solvents.

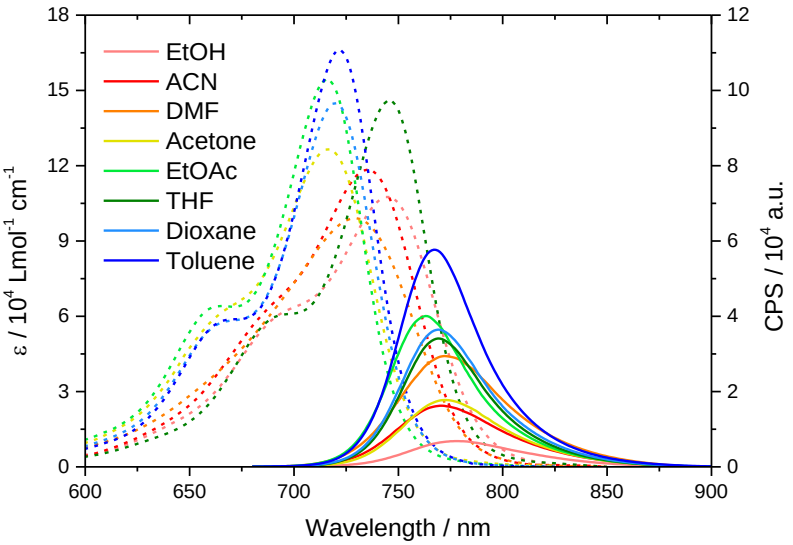

Figure 298 – Absorption and steady state emission spectra of **343** in different solvents.

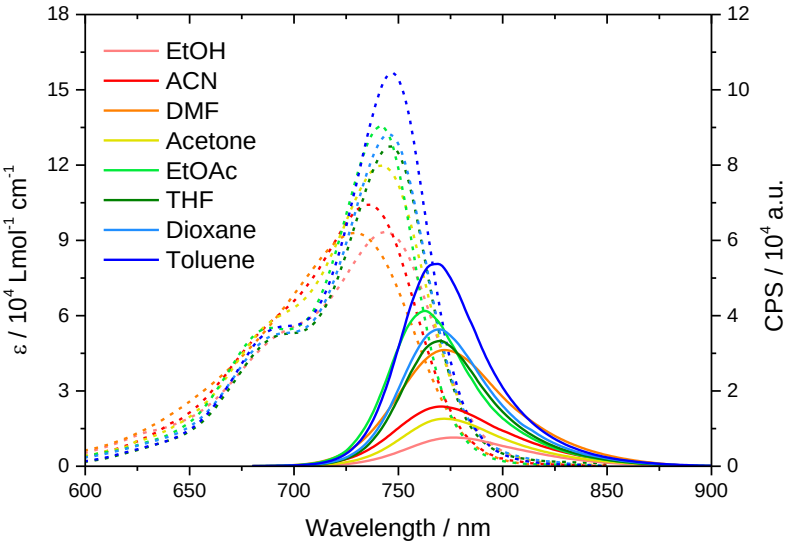

Figure 299 – Absorption and steady state emission spectra of **344** in different solvents.

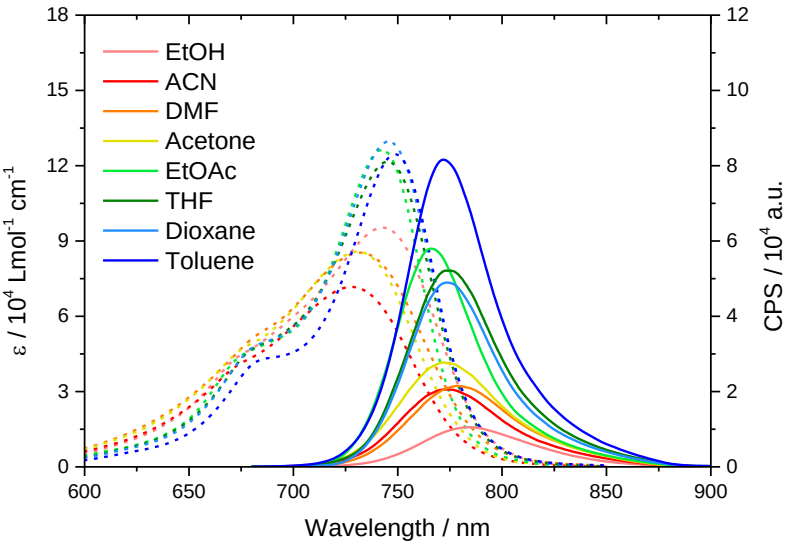

Figure 300 – Absorption and steady state emission spectra of **345** in different solvents.

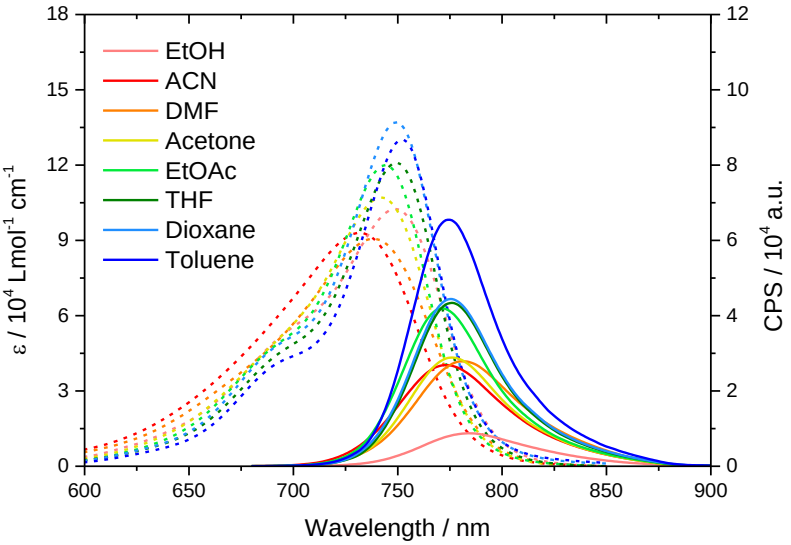

Figure 301 – Absorption and steady state emission spectra of **346** in different solvents.

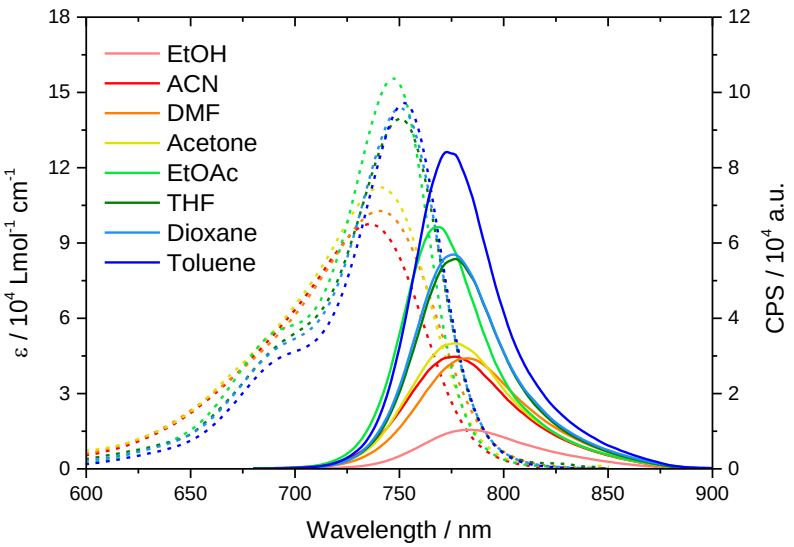

Figure 302 – Absorption and steady state emission spectra of **347** in different solvents.

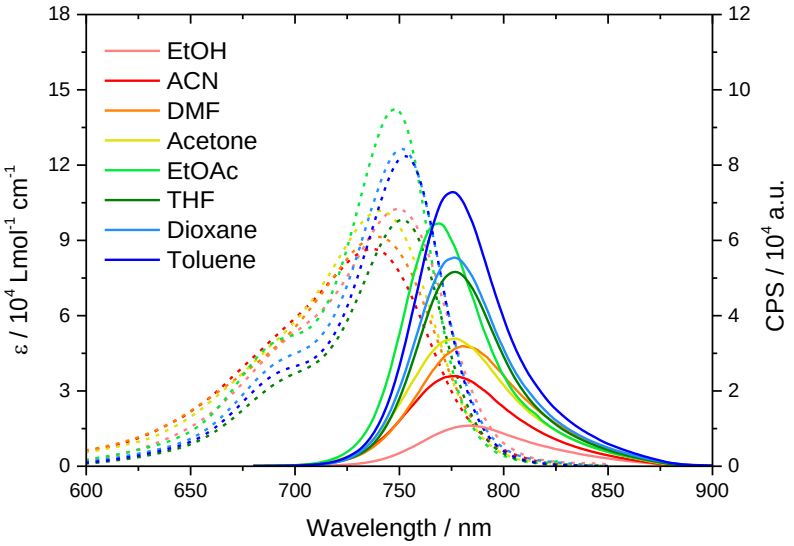

Figure 303 – Absorption and steady state emission spectra of **348** in different solvents.

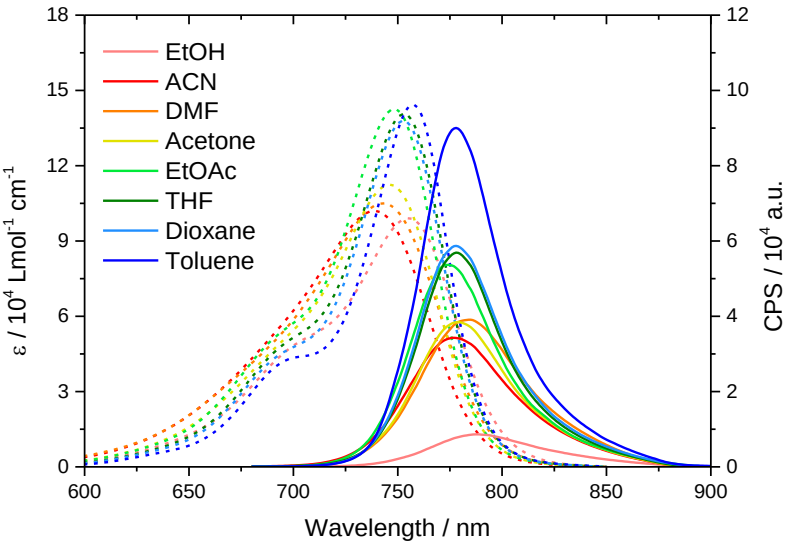

Figure 304 – Absorption and steady state emission spectra of **349** in different solvents.

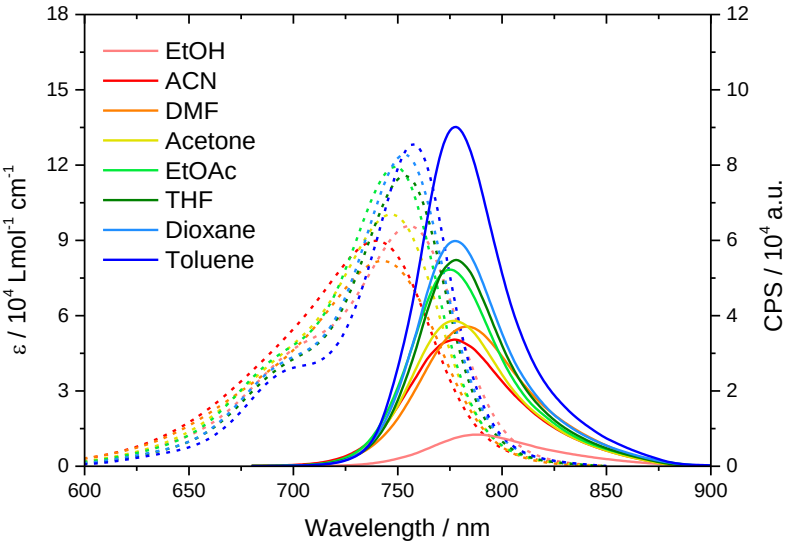

Figure 305 – Absorption and steady state emission spectra of **350** in different solvents.

Table 33 – Photophysical properties of **341** in different solvents.

Solvent	λ_{max} [nm]	λ_{em} [nm]	ε [M^{-1} cm^{-1}]	Stokes shift [cm^{-1}]	QY [%]	Brightness [M^{-1} cm^{-1}]
EtOH	733	773	109 343	706	1.0	1 080
ACN	728	768	121 673	715	1.9	2 307
DMF	721	770	99 199	883	6.4	5 449
Acetone	735	770	126 525	618	1.8	2 331
EtOAc	736	763	145 424	481	3.3	4 758
THF	741	768	145 424	474	3.4	4 836
Dioxane	741	767	147 817	457	3.9	5 693
Toluene	743	765	158 427	387	6.4	10 166

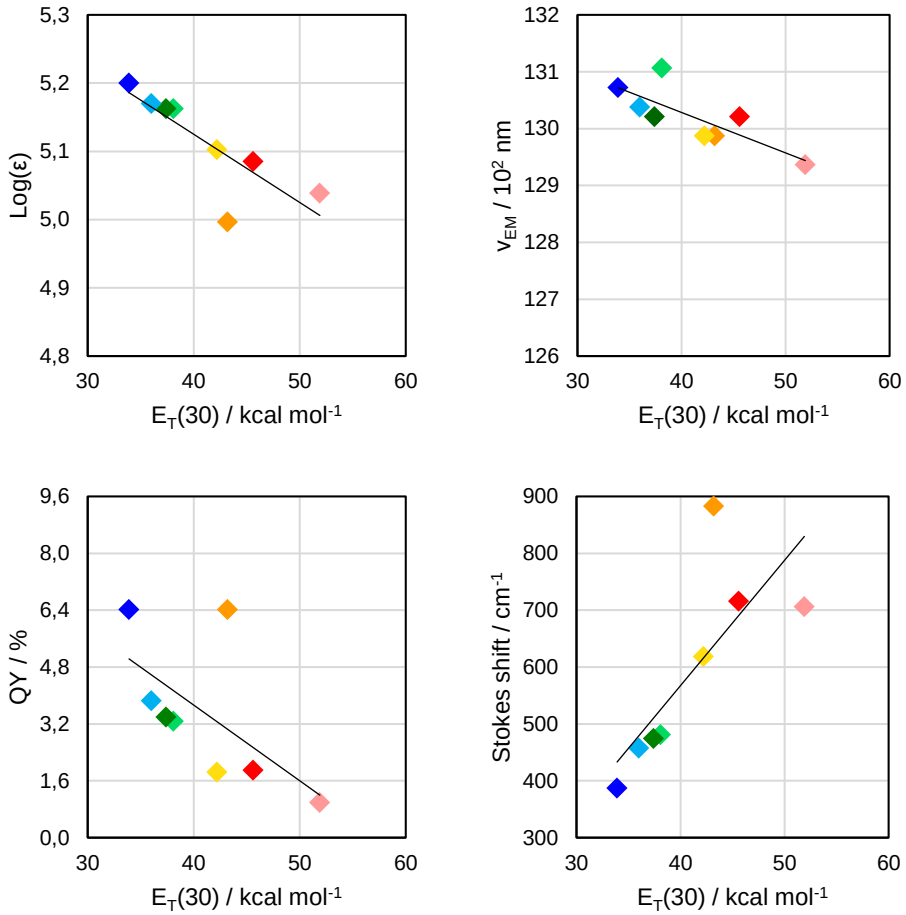

Figure 306 – Photophysical properties of **341** *vs*. $E_T(30)$. a) ν_{EM} *vs*. $E_T(30)$. b) Log(ε) *vs*. $E_T(30)$. c) QY *vs*. $E_T(30)$. d) Stokes shift *vs*. $E_T(30)$. Solvents: Toluene is blue, 1,4-Dioxane is light blue, THF is dark green, EtOAc is light green, Acetone is yellow, DMF is orange, ACN is red, EtOH is pink.

Table 34 – Photophysical properties of **342** in different solvents.

Solvent	λ_{max} [nm]	λ_{em} [nm]	ε [M^{-1} cm^{-1}]	Stokes shift [cm^{-1}]	QY [%]	Brightness [M^{-1} cm^{-1}]
EtOH	746	778	108 086	551	0.7	728
ACN	730	766	101 679	644	2.1	2 185
DMF	729	772	92 191	764	3.3	3 033
Acetone	739	770	113 170	545	2.0	2 222
EtOAc	739	765	129 579	460	2.9	3 786
THF	744	769	132 280	437	3.2	4 290
Dioxane	768	768	132 958	420	3.6	4 850
Toluene	767	767	135 359	367	5.8	7 830

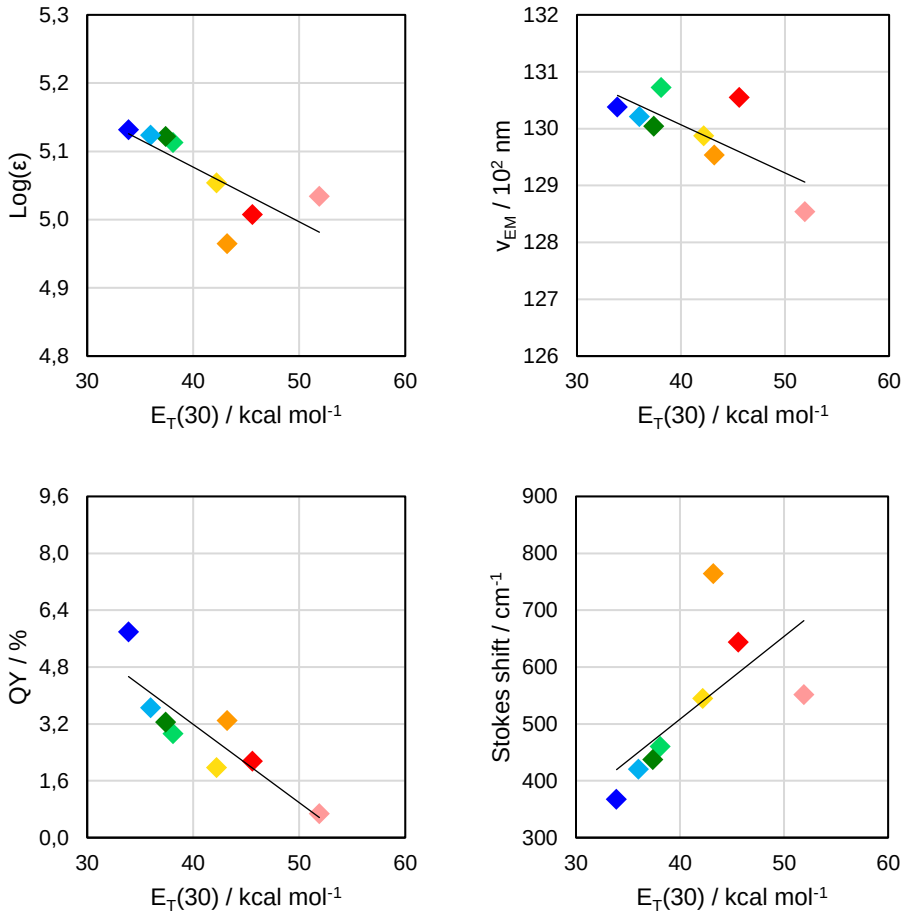

Figure 307 – Photophysical properties of **342** *vs.* $E_T(30)$. a) ν_{EM} *vs.* $E_T(30)$. b) Log(ε) *vs.* $E_T(30)$. c) QY *vs.* $E_T(30)$. d) Stokes shift *vs.* $E_T(30)$. Solvents: Toluene is blue, 1,4-Dioxane is light blue, THF is dark green, EtOAc is light green, Acetone is yellow, DMF is orange, ACN is red, EtOH is pink.

Table 35 – Photophysical properties of **343** in different solvents.

Solvent	λ_{max} [nm]	λ_{em} [nm]	ε [M^{-1} cm^{-1}]	Stokes shift [cm^{-1}]	QY [%]	Brightness [M^{-1} cm^{-1}]
EtOH	745	778	107 612	569	0.7	806
ACN	735	771	118 411	635	1.7	1 988
DMF	729	772	99 092	764	3.5	3 421
Acetone	741	772	126 576	542	1.8	2 253
EtOAc	741	763	154 372	389	3.5	5 375
THF	746	769	145 965	401	3.2	4 639
Dioxane	745	769	144 938	419	3.5	5 130
Toluene	746	767	166 084	367	5.9	9 751

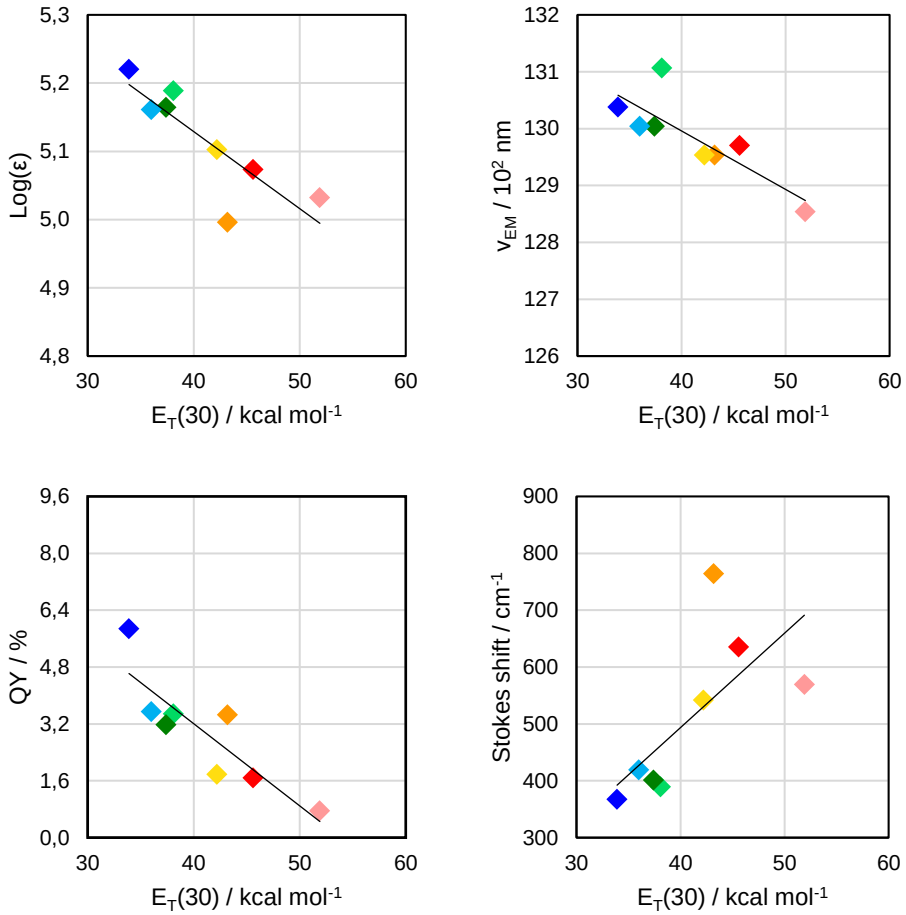

Figure 308 – Photophysical properties of **343** *vs*. $E_T(30)$. a) ν_{EM} *vs*. $E_T(30)$. b) Log(ε) *vs*. $E_T(30)$. c) QY *vs*. $E_T(30)$. d) Stokes shift *vs*. $E_T(30)$. Solvents: Toluene is blue, 1,4-Dioxane is light blue, THF is dark green, EtOAc is light green, Acetone is yellow, DMF is orange, ACN is red, EtOH is pink.

Table 36 – Photophysical properties of **344** in different solvents.

Solvent	λ_{max} [nm]	λ_{em} [nm]	ε [M^{-1} cm^{-1}]	Stokes shift [cm^{-1}]	QY [%]	Brightness [M^{-1} cm^{-1}]
EtOH	744	776	93 359	554	0.8	780
ACN	736	770	104 210	600	1.7	1 744
DMF	730	772	92 986	745	3.6	3 382
Acetone	742	772	119 795	524	1.3	1 555
EtOAc	742	763	135 553	371	3.6	4 813
THF	746	770	127 546	418	3.1	3 963
Dioxane	746	770	132 323	418	3.5	4 688
Toluene	747	769	156 728	383	5.5	8 680

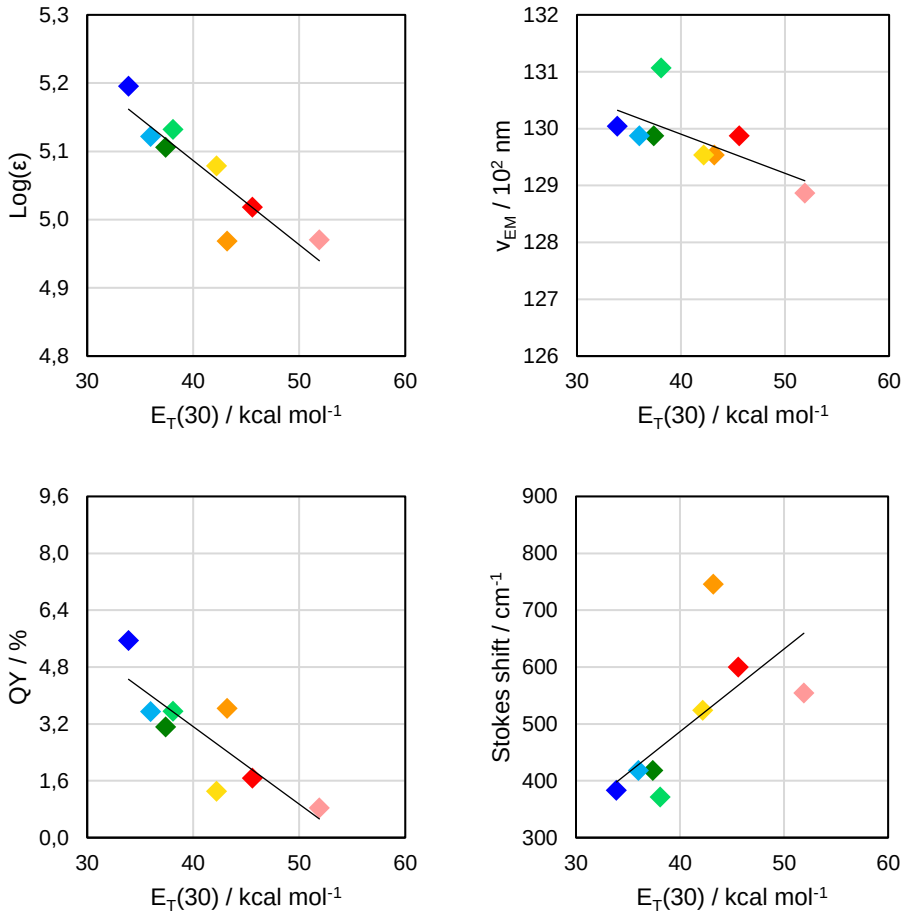

Figure 309 – Photophysical properties of **344** *vs.* $E_T(30)$. a) ν_{EM} *vs.* $E_T(30)$. b) Log(ε) *vs.* $E_T(30)$. c) QY *vs.* $E_T(30)$. d) Stokes shift *vs.* $E_T(30)$. Solvents: Toluene is blue, 1,4-Dioxane is light blue, THF is dark green, EtOAc is light green, Acetone is yellow, DMF is orange, ACN is red, EtOH is pink.

Table 37 – Photophysical properties of **345** in different solvents.

Solvent	λ_{max} [nm]	λ_{em} [nm]	ε [M^{-1} cm^{-1}]	Stokes shift [cm^{-1}]	QY [%]	Brightness [M^{-1} cm^{-1}]
EtOH	743	784	95 370	704	1.4	1 312
ACN	728	774	71 721	816	4.2	2 989
DMF	732	779	85 397	824	4.3	3 677
Acetone	731	772	85 765	727	4.6	3 979
EtOAc	742	766	126 320	422	5.0	6 258
THF	745	773	121 657	486	5.2	6 332
Dioxane	746	774	129 680	485	4.9	6 303
Toluene	749	772	124 618	398	8.8	10 975

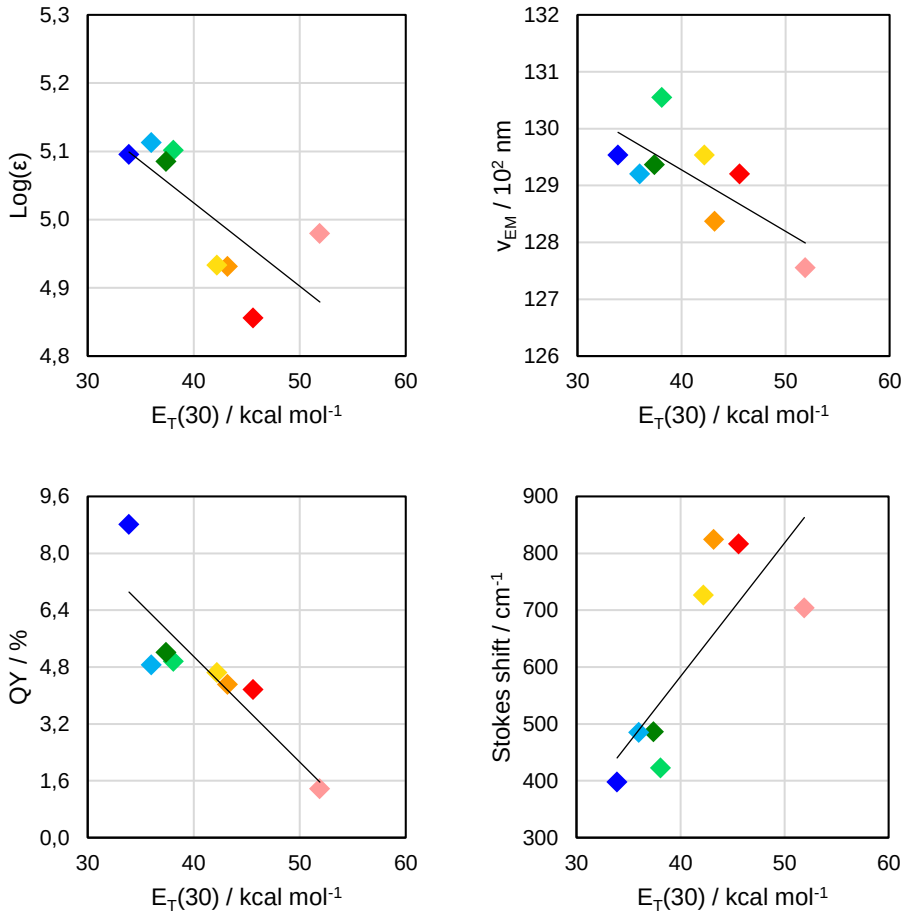

Figure 310 – Photophysical properties of **345** *vs*. $E_T(30)$. a) ν_{EM} *vs*. $E_T(30)$. b) Log(ε) *vs*. $E_T(30)$. c) QY *vs*. $E_T(30)$. d) Stokes shift *vs*. $E_T(30)$. Solvents: Toluene is blue, 1,4-Dioxane is light blue, THF is dark green, EtOAc is light green, Acetone is yellow, DMF is orange, ACN is red, EtOH is pink.

Table 38 – Photophysical properties of **346** in different solvents.

Solvent	λ_{max} [nm]	λ_{em} [nm]	ε [M^{-1} cm^{-1}]	Stokes shift [cm^{-1}]	QY [%]	Brightness [M^{-1} cm^{-1}]
EtOH	749	784	102 549	596	0.9	971
ACN	732	773	93 009	725	2.8	2 648
DMF	738	781	90 654	746	3.3	2 998
Acetone	742	776	107 093	590	2.9	3 055
EtOAc	744	771	119 988	471	3.9	4 715
THF	749	776	120 895	465	4.2	5 074
Dioxane	749	774	137 072	465	2.8	6 094
Toluene	753	774	130 207	378	7.0	9 086

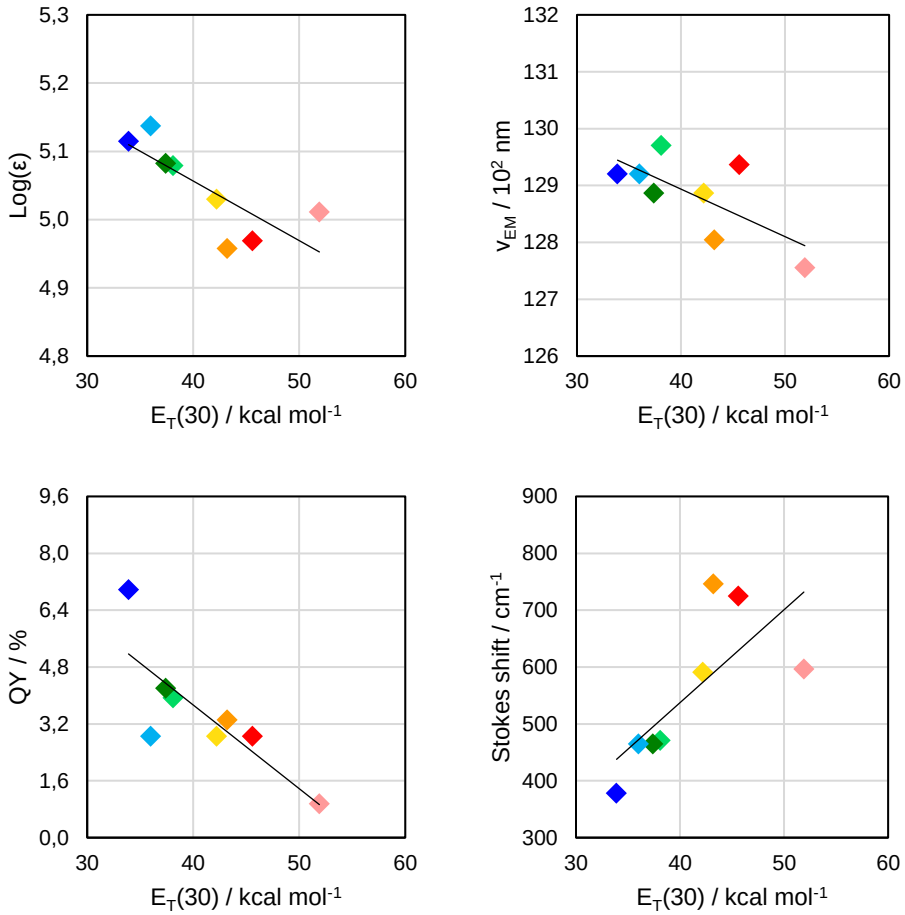

Figure 311 – Photophysical properties of **346** *vs.* $E_T(30)$. a) ν_{EM} *vs.* $E_T(30)$. b) Log(ε) *vs.* $E_T(30)$. c) QY *vs.* $E_T(30)$. d) Stokes shift *vs.* $E_T(30)$. Solvents: Toluene is blue, 1,4-Dioxane is light blue, THF is dark green, EtOAc is light green, Acetone is yellow, DMF is orange, ACN is red, EtOH is pink.

Table 39 – Photophysical properties of **347** in different solvents.

Solvent	λ_{max} [nm]	λ_{em} [nm]	ε [M^{-1} cm^{-1}]	Stokes shift [cm^{-1}]	QY [%]	Brightness [M^{-1} cm^{-1}]
EtOH	749	783	101 239	580	1.1	1 139
ACN	736	777	97 560	717	3.1	3 023
DMF	740	782	102 821	726	3.4	3 546
Acetone	741	777	112 248	625	3.4	3 808
EtOAc	747	769	155 669	383	5.5	8 600
THF	750	777	139 508	463	5.3	7 422
Dioxane	750	776	143 854	447	5.6	8 081
Toluene	752	773	145 856	361	5.9	8 621

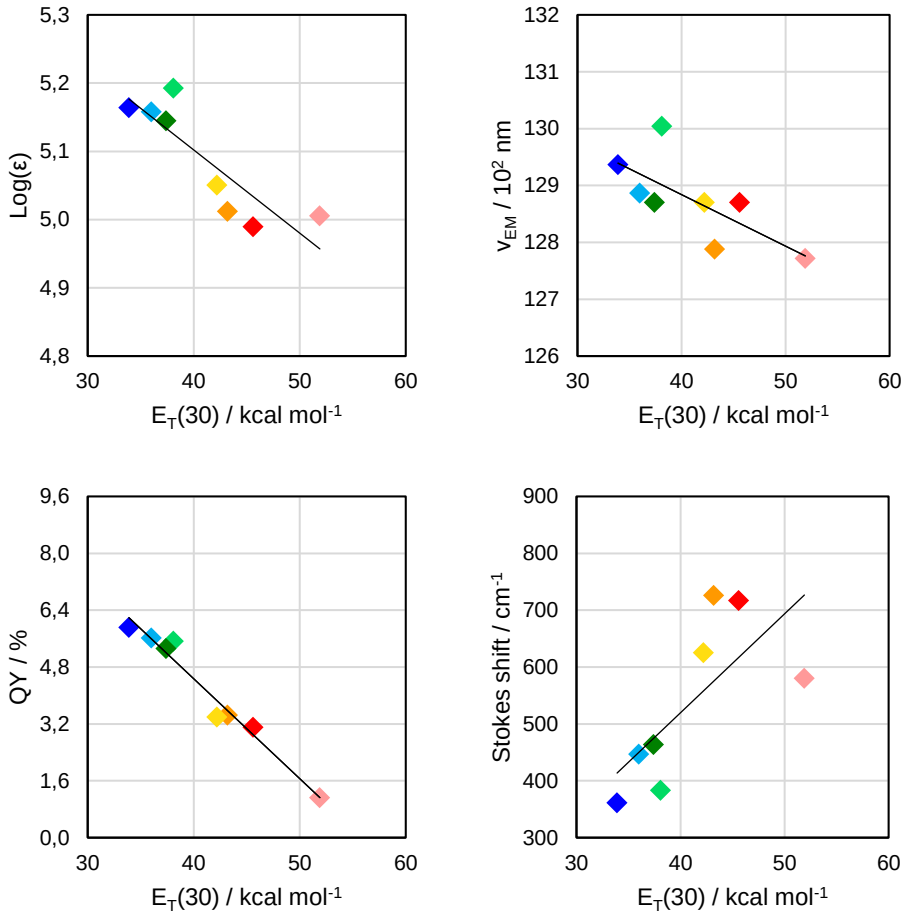

Figure 312 – Photophysical properties of **347** *vs*. $E_T(30)$. a) ν_{EM} *vs*. $E_T(30)$. b) Log(ε) *vs*. $E_T(30)$. c) QY *vs*. $E_T(30)$. d) Stokes shift *vs*. $E_T(30)$. Solvents: Toluene is blue, 1,4-Dioxane is light blue, THF is dark green, EtOAc is light green, Acetone is yellow, DMF is orange, ACN is red, EtOH is pink.

Table 40 – Photophysical properties of **348** in different solvents.

Solvent	λ_{max} [nm]	λ_{em} [nm]	ε [M^{-1} cm^{-1}]	Stokes shift [cm^{-1}]	QY [%]	Brightness [M^{-1} cm^{-1}]
EtOH	749	783	102 695	580	1.2	1 204
ACN	737	777	86 582	699	2.5	2 147
DMF	740	780	91 440	693	3.7	3 393
Acetone	741	777	101 813	625	3.5	3 532
EtOAc	748	769	142 339	365	5.5	7 864
THF	751	777	98 154	446	4.9	4 817
Dioxane	751	777	126 526	446	5.5	6 931
Toluene	753	776	123 636	394	7.8	9 617

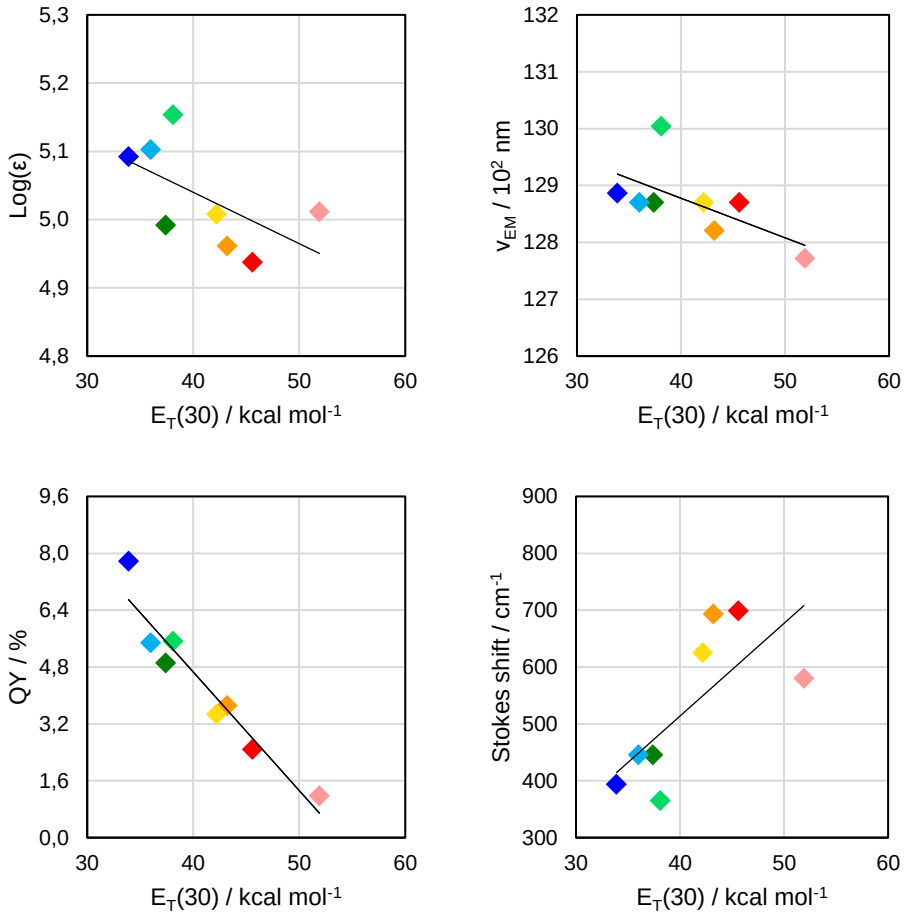

Figure 313 – Photophysical properties of **348** *vs.* $E_T(30)$. a) ν_{EM} *vs.* $E_T(30)$. b) Log(ε) *vs.* $E_T(30)$. c) QY *vs.* $E_T(30)$. d) Stokes shift *vs.* $E_T(30)$. Solvents: Toluene is blue, 1,4-Dioxane is light blue, THF is dark green, EtOAc is light green, Acetone is yellow, DMF is orange, ACN is red, EtOH is pink.

Table 41 – Photophysical properties of **349** in different solvents.

Solvent	λ_{max} [nm]	λ_{em} [nm]	ε [M^{-1} cm^{-1}]	Stokes shift [cm^{-1}]	QY [%]	Brightness [M^{-1} cm^{-1}]
EtOH	755	788	99 072	555	0.9	935
ACN	739	777	101 995	662	3.5	3 606
DMF	743	785	105 025	720	4.5	4 737
Acetone	746	779	112 449	568	3.7	4 213
EtOAc	748	774	142 575	449	5.0	7 091
THF	753	778	140 587	427	5.4	7 532
Dioxane	753	778	137 923	427	5.7	7 907
Toluene	757	778	144 363	357	9.2	13 226

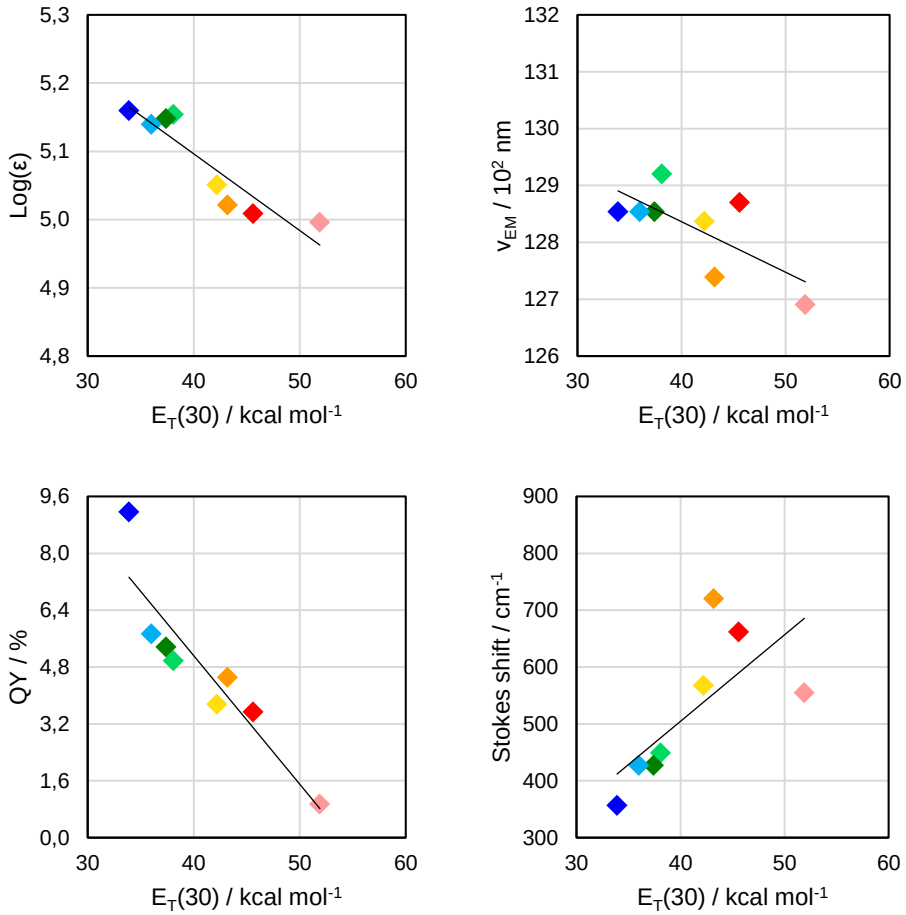

Figure 314 – Photophysical properties of **349** *vs*. $E_T(30)$. a) ν_{EM} *vs*. $E_T(30)$. b) Log(ε) *vs*. $E_T(30)$. c) QY *vs*. $E_T(30)$. d) Stokes shift *vs*. $E_T(30)$. Solvents: Toluene is blue, 1,4-Dioxane is light blue, THF is dark green, EtOAc is light green, Acetone is yellow, DMF is orange, ACN is red, EtOH is pink.

Table 42 – Photophysical properties of **350** in different solvents.

Solvent	λ_{max} [nm]	λ_{em} [nm]	ε [M^{-1} cm^{-1}]	Stokes shift [cm^{-1}]	QY [%]	Brightness [M^{-1} cm^{-1}]
EtOH	756	787	95 794	521	0.9	880
ACN	740	777	89 864	644	3.5	3 106
DMF	743	783	81 847	688	4.3	3 508
Acetone	747	777	100 374	517	3.8	3 809
EtOAc	749	775	119 368	448	4.8	5 784
THF	753	778	115 766	427	5.2	6 011
Dioxane	753	777	124 266	410	5.9	7 296
Toluene	758	778	128 293	339	9.3	11 877

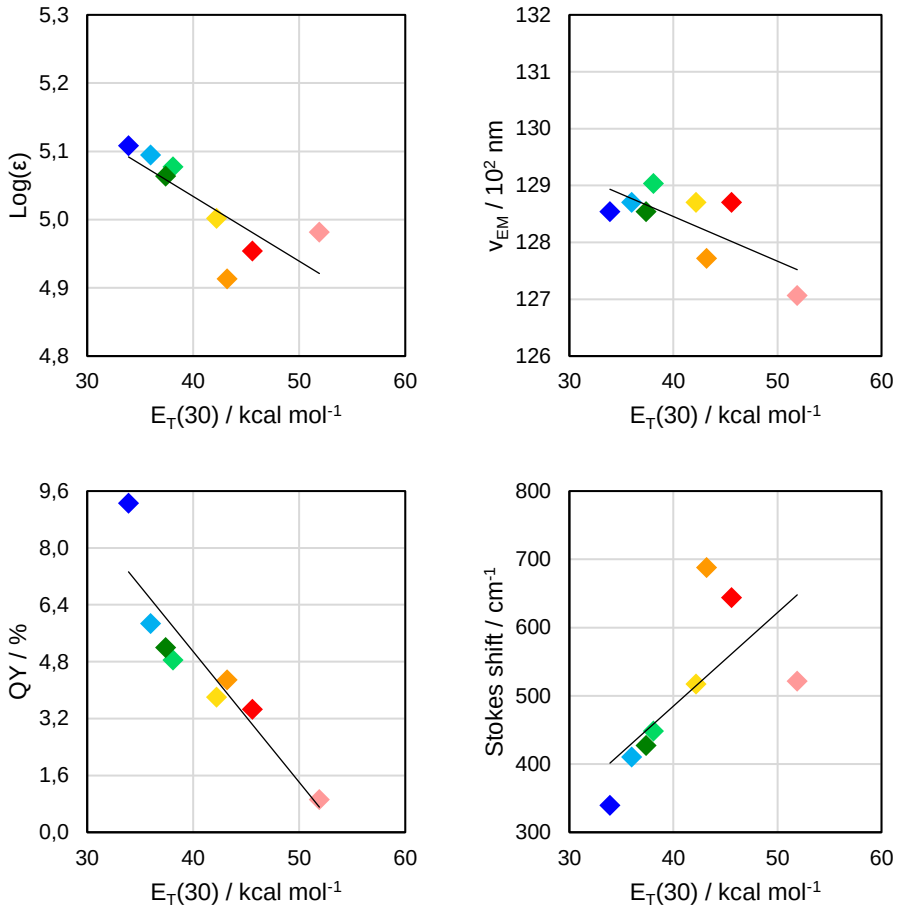

Figure 315 – Photophysical properties of **350** *vs*. $E_T(30)$. a) ν_{EM} *vs*. $E_T(30)$. b) Log(ε) *vs*. $E_T(30)$. c) QY *vs*. $E_T(30)$. d) Stokes shift *vs*. $E_T(30)$. Solvents: Toluene is blue, 1,4-Dioxane is light blue, THF is dark green, EtOAc is light green, Acetone is yellow, DMF is orange, ACN is red, EtOH is pink.

2.2. Additional Data for the DHP-SQs of the Chapter 5

In this section are reported all the absorption and steady state emission spectra and their photophysical properties of all DHP-SQs of Chapter 5 in different solvents. In addition, Reichardt's Plots for squaraine **397** are reported.

Table 43 – Absorption properties of squaraines **391**, **393** and **395**.

	391		**393**		**395**	
Solvent	**λ_{max} [nm]**	**ε [M^{-1} cm^{-1}]**	**λ_{max} [nm]**	**ε [M^{-1} cm^{-1}]**	**λ_{max} [nm]**	**ε [M^{-1} cm^{-1}]**
EtOH	546	71 618	542	44 511	543	48 012
ACN	545	78 700	541	45 199	541	53 263
DMF	555	73 877	553	41 812	550	46 771
Acetone	547	75 524	543	43 189	544	51 278
EtOAc	546	70 852	543	42 508	543	46 757
THF	550	68 535	547	41 571	547	45 442
Dioxane	548	77 567	545	42 241	545	45 859
Toluene	552	65 397	550	40 431	549	45 618

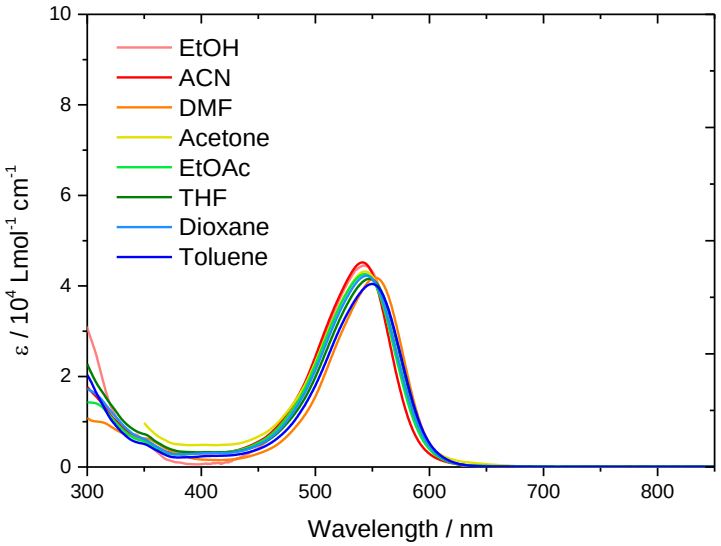

Figure 316 – Absorption spectra of **393** in different solvents.

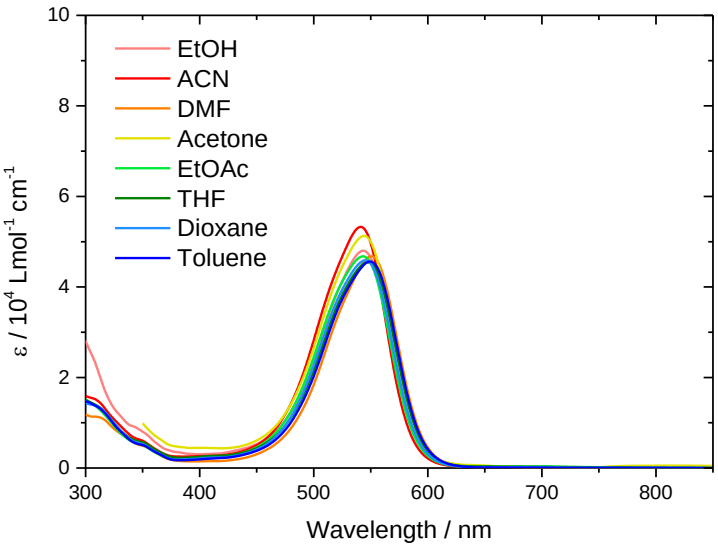

Figure 317 – Absorption spectra of **395** in different solvents.

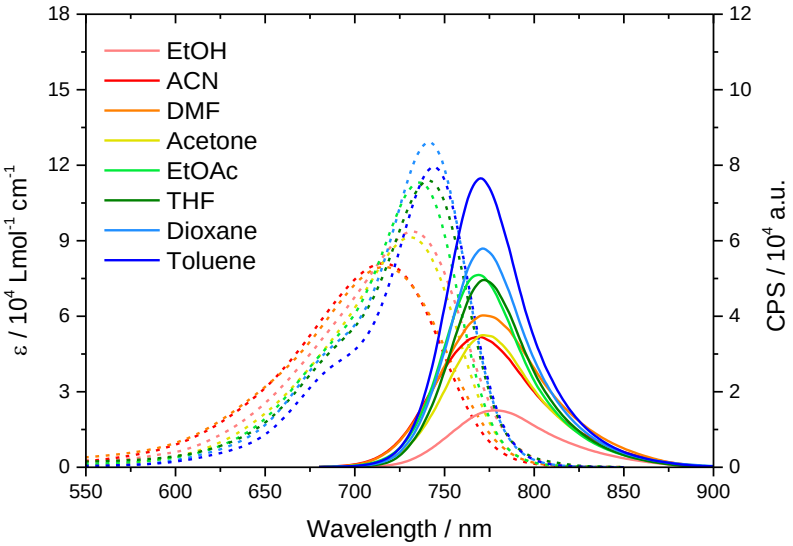

Figure 318 – Absorption and steady state emission spectra of **397** in different solvents.

Table 44 – Photophysical properties of **397** in different solvents.

Solvent	λ_{max} [nm]	λ_{em} [nm]	ε [M^{-1} cm^{-1}]	Stokes shift [cm^{-1}]	QY [%]	Brightness [M^{-1} cm^{-1}]
EtOH	732	778	93 693	808	1.7	1 600
ACN	716	770	81 064	979	3.9	3 190
DMF	717	770	79 586	994	5.2	4 122
Acetone	731	772	91 401	710	3.7	3 364
EtOAc	736	769	113 190	583	4.9	5 539
THF	741	772	113 938	542	4.9	5 602
Dioxane	741	771	129 101	525	5.9	7 586
Toluene	744	770	119 336	454	8.3	9 864

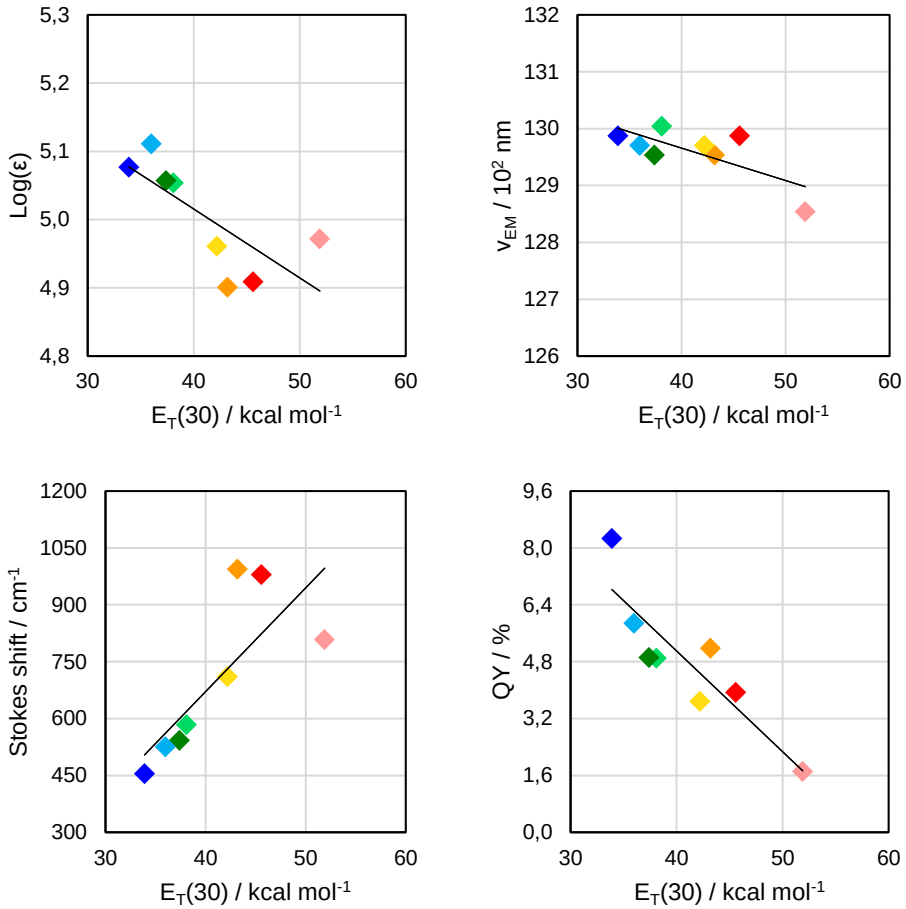

Figure 319 – Photophysical properties of **397** *vs*. $E_T(30)$. a) ν_{EM} *vs*. $E_T(30)$. b) Log(ε) *vs*. $E_T(30)$. c) QY *vs*. $E_T(30)$. d) Stokes shift *vs*. $E_T(30)$. Solvents: Toluene is blue, 1,4-Dioxane is light blue, THF is dark green, EtOAc is light green, Acetone is yellow, DMF is orange, ACN is red, EtOH is pink.

3. Electrochemical Characterization

Anhydrous solvents, tetrabutylammonium hexafluorophosphate and ferrocene used for CVs experiments were purchased from Sigma Aldrich.

Cyclic voltammetry experiments were performed using Metrohm Autolab 302 N potentiostat. The electrochemical cell was a single-compartment cell equipped with a standard three-electrode set-up: a glassy carbon working electrode (Ø = 1 mm), a Pt-wire counter electrode and an Ag/AgCl (KCl 3 M) reference electrode. All measurements were carried out in DCM with tetrabutylammonium hexafluorophosphate 0.1 M as supporting electrolyte under argon and at 50 mV/s scan rate.

Redox potentials were primarily referenced versus the ferrocene/ferrocenium standard redox couple (measured $E_{1/2}$ Fc^+/Fc = +0.499 V in DCM *vs*. Ag/AgCl, $E_{1/2}$ Fc^+/Fc = +0.433 V in ACN *vs*. Ag/AgCl) employed as internal standard. Potentials referenced *vs*. Fc^+/Fc were referenced to *NHE* following the reported relationship ($E_{1/2}$ Fc^+/Fc = +0.624 V *vs*. *NHE*).[454]

3.1. Additional Data for QDI-dyes and DHP-SQs

In this section are reported the voltammograms of QDI-dyes **316** and **319** with those ones of the DHP-SQs **341**-**350** and **391**-**393**, **395**, **397**.

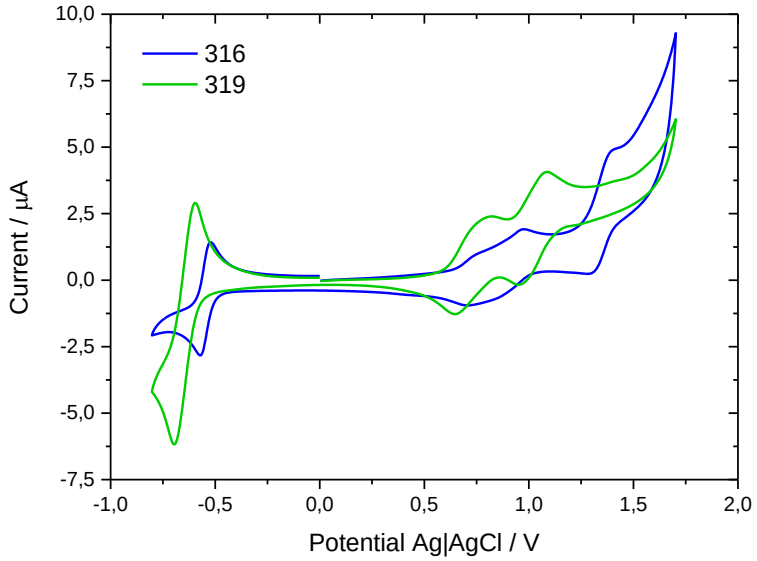

Figure 320 – Cyclic voltammetry curves of **316** and **319** in DCM. Scan rate: 50 mV/s.

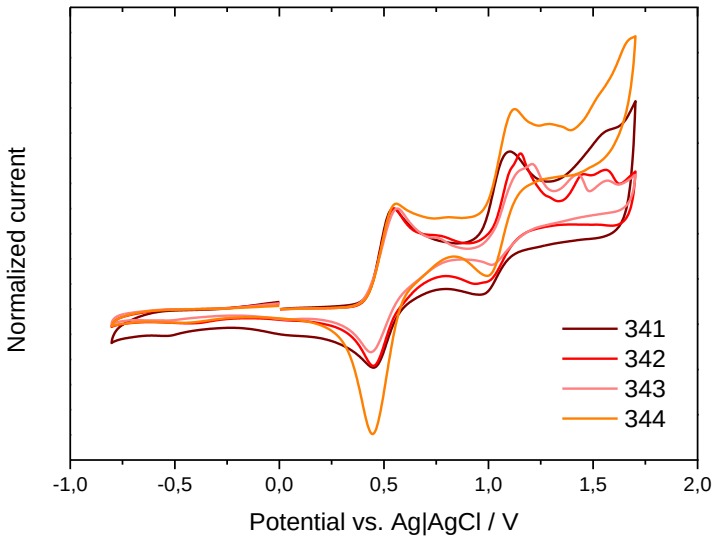

Figure 321 – Cyclic voltammetry curves of CI-based DHP-SQs **341**-**344** in DCM. Scan rate: 50 mV/s.

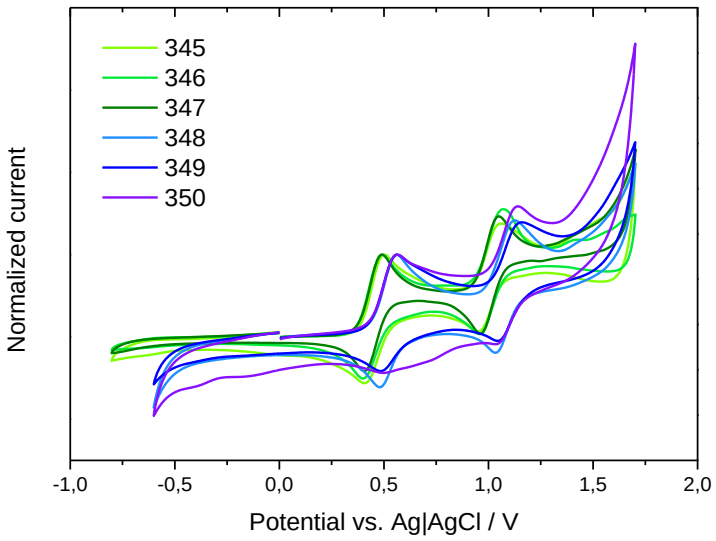

Figure 322 – Cyclic voltammetry curves of CBI-based DHP-SQs **345**-**350** in DCM. Scan rate: 50 mV/s.

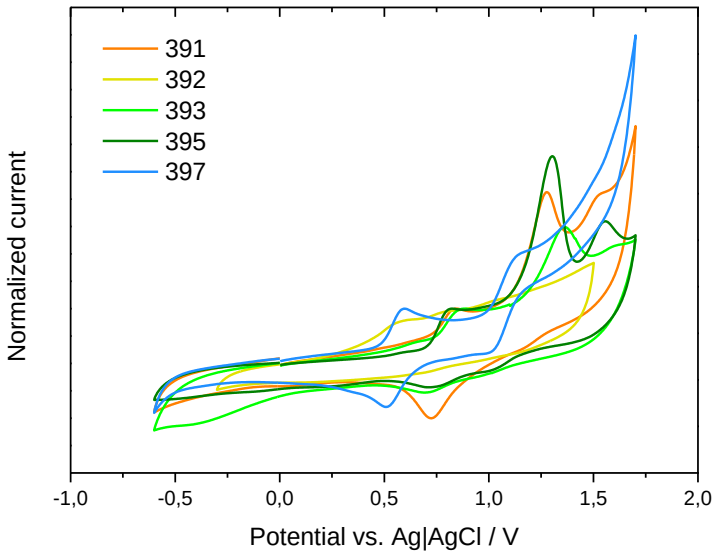

Figure 323 – Cyclic voltammetry curves of Cl-based DHP-SQs **341**-**344** in DCM. Scan rate: 50 mV/s.

4. NMR-Spectroscopy Characterization

All the deuterated solvents used for the NMR-spectroscopy measurements were purchased from Sigma Aldrich and Euriso-top.

^{1}H- and ^{13}C-NMR spectra alongside COSY, DEPT-135, HSQC and HMBC 2D-experiments were recorded on a JEOL JNM-ECZR600 spectrometer (^{1}H-NMR operating frequency 600 MHz, ^{13}C-NMR operating frequency 151 MHz). Chemical shifts are reported relative to TMS (δ = 0 ppm) and referenced against solvent residual peaks.

The following abbreviations are used: s (singlet), d (doublet), t (triplet), dd (doublet of doublets), m (multiplet).

5. Mass Spectrometry Characterization

ESI-MS and ESI-TOF HRMS mass spectra were recorded on a Thermo-Finnigan Advantage Max Ion Trap Spectrometer and on a Bruker maXis 4G Mass Spectrometers, respectively. Methanol was used to perform all the analysis and formic acid (MS-grade) and ammonium-hydroxide 30% were sometimes used as additives to protonate or de-protonate target molecules, respectively.

MALDI-TOF mass spectra were recorded on a Bruker Daltonics MALDI-ToF Autoflex III mass spectrometer. Sample's preparation for MALDI-TOF MS experiments has been different between compound **316** and **319**.

For **316**, the compound was dissolved in toluene, diluted in ethanol and then add in matrix solution: DAN 10 mg/mL in ACN/water 70/30 with 0.1% of TFA.

For **319**, the compound was dissolved in toluene, diluted in ethanol and then add in matrix solution: HCCA 10 mg/mL in ACN/water 70/30 with 0.1% of TFA.

6. IR-Spectroscopy Characterization

All the IR transmittance spectra were carried out on a Thermo Fisher Nicolet iS 5 FT-IR Spectrometer by ATR technique. Generally, roughly 1 mg of compound was used to perform the measurement.

The following abbreviations are used: (*ν*) general stretching vibration mode and (*δ*) general bending vibration mode.

7. Photoanodes' Solid-State Absorption Characterization

In this section is reported the detailed description of the preparation of the dye-loading solutions and the solid-state absorption measurements procedure of the photoanodes sensitized with squaraines **341**-**348**.

The dye-loading solution were prepared using ethanol abs. purchased from Sigma Aldrich, CDCA purchased from TCI and squaraine **341**-**350** synthetized in Chapter 3. For each squaraines a stock solution was prepared in ethanol abs. and stored at -20 °C in the dark.

A 25 mM CDCA stock solution was prepared dissolving 4.91 g of CDCA in 500 mL of ethanol abs. and stored in fridge. The different dye-loading solutions with the different ratio concentration CDCA/dye were prepared by properly mixing the respective dye stock-solution, the CDCA stock-solution and ethanol abs. to obtain 8 mL of dye-loading solution.

The photoanodes used for solid-state absorption measurements were prepared following the procedure reported in the Section 8.2 of SI. To reduce the unavoidable slightly variations in the measurements due to the different morphologies of each TiO_2 films, all the photoanodes used for solid-state absorption measurements (even the un-sensitized one used like blank) were from the same batch.

For these measurements, the dye-loading process of photoanodes was performed for 6 h, at RT and in the dark. After the sensitization, the photoanodes were carefully washed with ethanol abs., dried by compressed air and immediately measured.

Solid-state absorption spectra were measured on an Agilent Cary 60 UV-Vis spectrophotometer, using the Cary 60 Solid Sample Holder (diameter of the circular slot: 4 mm). Spectra were recorded with a resolution of 1.0 nm.

7.1. Solid-State Absorption Spectra of Other Squaraines

In this section are reported the solid-state absorption spectra of other DHP-SQs (**342**, **343**, **346** and **347**).

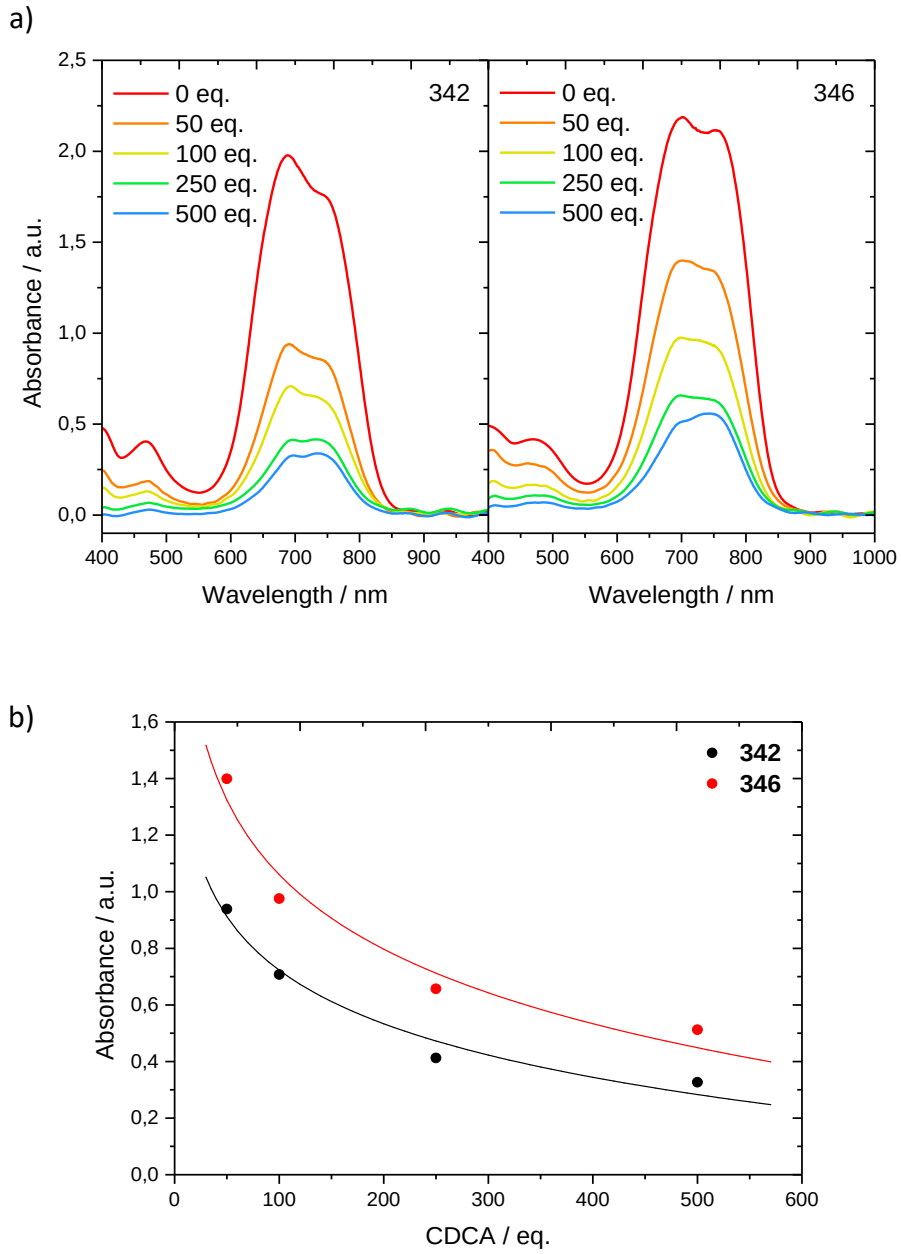

Figure 324 – a) Solid-state absorption spectra of photoanodes sensitized with **342** (left) and **346** (right) in presence of different concentrations of CDCA. b) Solid-state absorbance *vs*. CDCA concentration trend for the photoanodes sensitized with **342** and **346**.

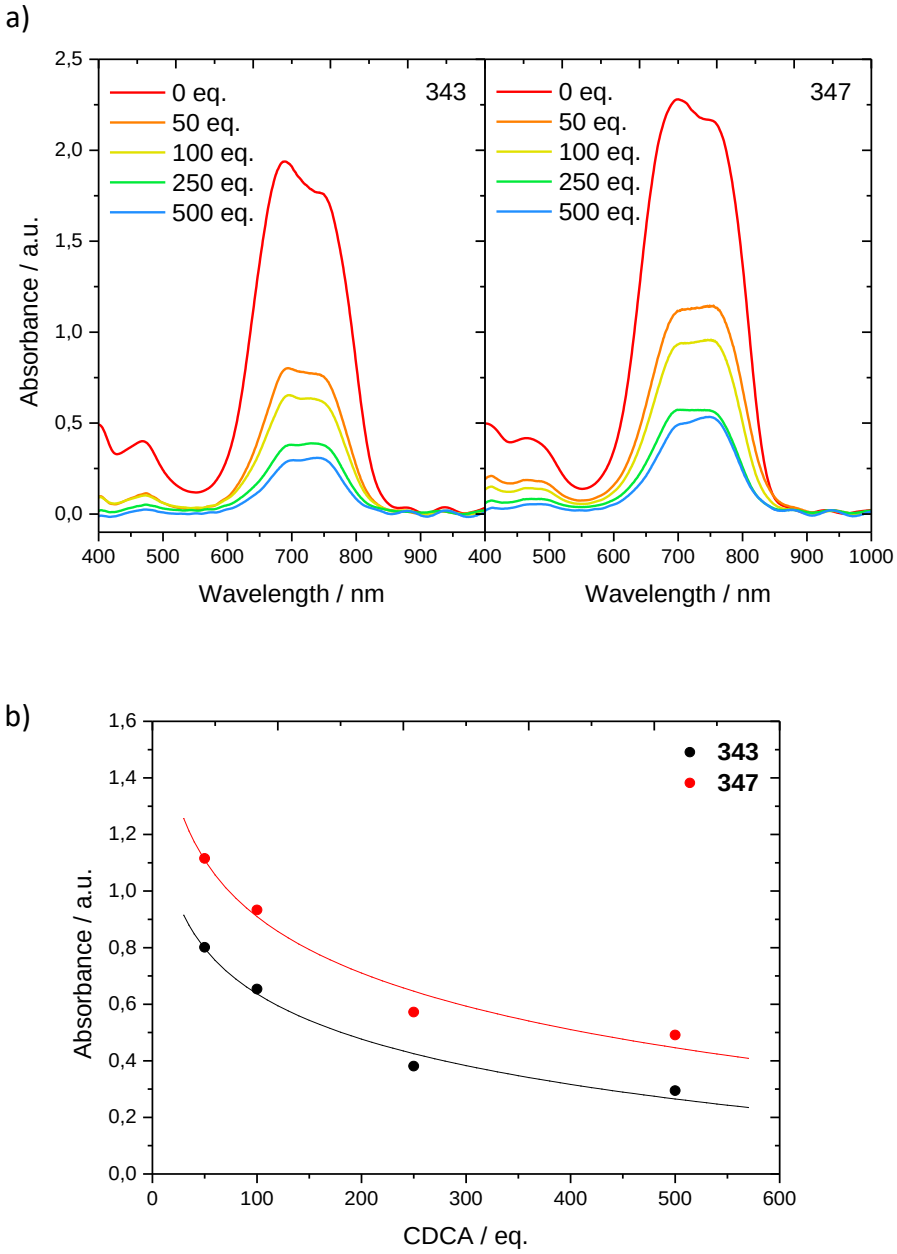

Figure 325 – a) Solid-state absorption spectra of photoanodes sensitized with **343** (left) and **347** (right) in presence of different concentrations of CDCA. b) Solid-state absorbance *vs*. CDCA concentration trend for the photoanodes sensitized with **343** and **347**.

7.2. Solid-State Absorption Spectra of 348

In this section are reported the comparison of all solid-state absorption spectra of **348** with different concentration of CDCA.

a)

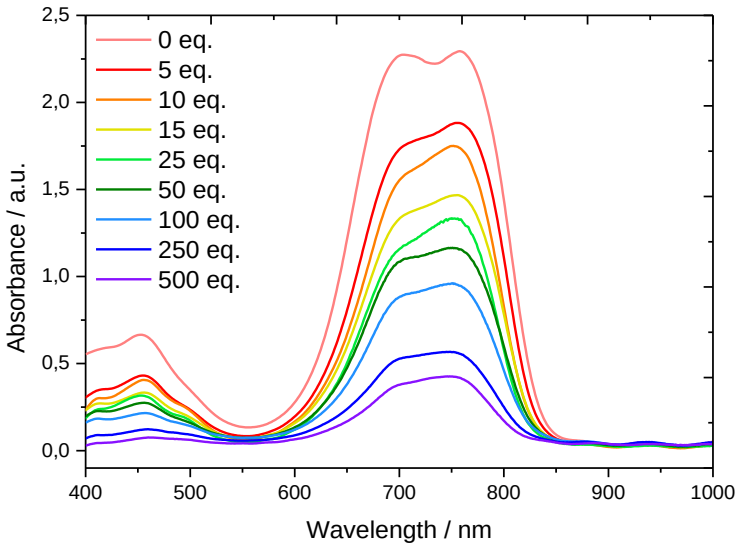

b)

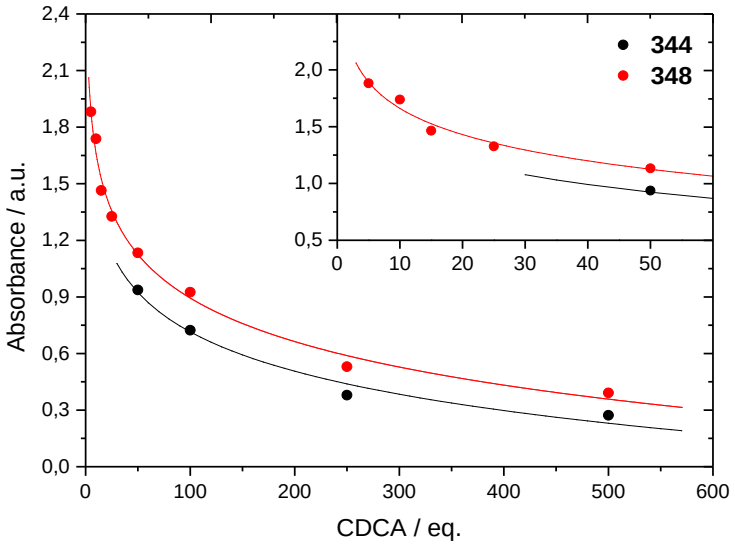

Figure 326 – a) Solid-state absorption spectra of photoanodes sensitized with **348** in presence of different concentrations of CDCA. b) Solid-state absorbance *vs*. CDCA concentration trend for the photoanodes sensitized with **344** and **348**.

8. Solar Cells Fabrication

In this section is reported the detailed description of the procedure used for the fabrication of DSSCs with quaterrylene-based dye **316** and with DHP-SQs **341**-**350**.

All the anhydrous solvents, iodine, lithium iodide, TBP, GuSCN, DMII, hexachloroplatinic acid and titanium(IV) chloride used in the solar cell's fabrication were purchased from Sigma Aldrich while CDCA was purchased from TCI. A schematic representation of the structure of a DSSC is reported in Fig. 327.

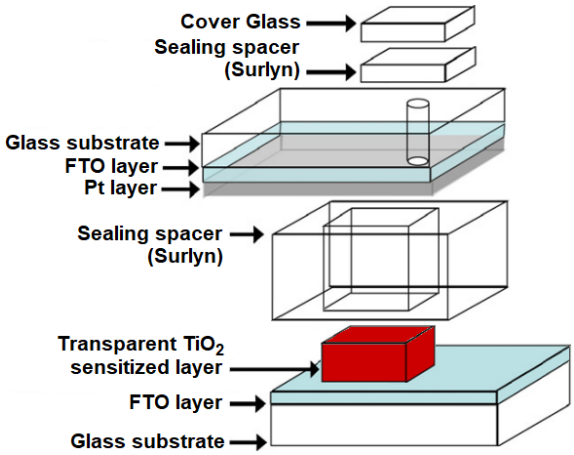

Figure 327 – Schematic representation of the structure of a DSSC.[235]

8.1. Solar Cell Fabrication with Sensitizer 316

The mesoporous TiO_2 electrodes were fabricated following the literature procedure.[235] The FTO glass (purchased from Sigma Aldrich, thickness 2.3 mm, 13 Ω/cm^2 sheet resistance) was thoroughly cleaned with water, acetone, and ethanol in sequence. Then the substrates were treated under ultraviolet/O_3 for 15 min. The TiO_2 paste (18NR-T from Dyesol) was deposited on the above FTO glass by screen-printing technology. The TiO_2 films were patterned in square spots (0.25 x 0.25 cm) with the area of 0.25 cm^2. The mesoporous TiO_2 films composed of ~6.0 µm transparent layer was obtained after the films was dried in oven at 110 °C for 15 minutes and successively sintered at 450 °C for 30 minutes. After sintering, the substrates were treated by 50 mM $TiCl_4$ aqueous solution at 70 °C for 50 min. The obtained mesoporous TiO_2 electrodes were stained by immersing them into dye solutions before sintered at 500 °C in air for 30 min and cooled down to 80 °C. Dye solutions were prepared dissolving 0.5 mM of sensitizers **316** in anhydrous dichloromethane. The sensitization process was performed in the dark for 48 h at RT. The Pt-based counter electrode was prepared by spreading a drop of 5.0 mM solution of hexachloroplatinic acid in *iso*-propanol onto the conductive side of FTO glass and the heating up to 450 °C for 30 min. This procedure was repeated twice. Device was assembled mechanically pressing both electrodes together with a Surlyn thermoplastic

gasket (internal area 0.6 x 0.6 cm) as spacer (≈ 22 µm thickness), taking care of the overlapping of the active areas. Then, iodine-based electrolyte (Greatcell Solar Materials' EL-HPE High Performance Electrolyte) was added by vacuum back-filling method through a hole in the Surlyn frame, which was then sealed by commercial epoxy glue.

8.2. Solar Cell Fabrication with Sensitizers 341-350

The mesoporous TiO_2 electrodes were fabricated following the literature procedure.[235] The FTO glass (Nippon Sheet Glass, NSG, thickness 2.2 mm, 10 Ω/cm^2 sheet resistance) was thoroughly cleaned with water, acetone, and ethanol in sequence. Then the substrates were treated under ultraviolet/O_3 for 15 min. The TiO_2 paste (Greatcell Solar Materials' 30 NR-D Transparent Titania Paste) was deposited on the above FTO glass by screen-printing technology. The TiO_2 films were patterned in round spots with the area of 0.158 cm2. The mesoporous TiO_2 films composed of ~4.0 µm transparent layer was obtained after the films was dried in oven at 110 °C for 15 minutes and successively sintered at 450 °C for 30 minutes. After sintering, the substrates were treated by 50 mM $TiCl_4$ aqueous solution at 70 °C for 50 min. The obtained mesoporous TiO_2 electrodes were stained by immersing them into dye solutions before sintered at 500 °C in air for 30 min and cooled down to 80 °C. Dye solutions were prepared dissolving 0.1 mM corresponding sensitizers **341**-**350** in anhydrous ethanol. Sensitization processes were performed in the dark with different concentration of CDCA, temperature and time as reported in Chapter 3. CDCA were added at the specific concentration by saturated CDCA ethanol solution. The Pt-based counter electrode was prepared by spreading a drop of 5.0 mM solution of hexachloroplatinic acid in *iso*-propanol onto the conductive side of drilled FTO glass and the heating up to 450 °C for 30 min. This procedure was repeated twice. Device was assembled mechanically pressing both electrodes together with a ring Surlyn thermoplastic gasket (OD 0.9 cm, ID 0.8 cm) as spacer (≈ 22 µm thickness), taking care of the overlapping of the active areas. Then, iodine-based electrolyte was added by vacuum back-filling method through the hole in the count electrode. The iodine-based electrolyte was prepared with different formulations as reported in Chapter 3. After the fabrication, the hole of the counter electrode was sealed with a circle Surlyn thermoplastic gasket (OD 0.8 cm) clothed by a cover glass (thickness 0.15 mm, OD 1 cm).

9. Solar Cells Characterization

Photoelectrochemical performances of DSSC with **316** were tested using a solar simulator Solar Test 1200 KHS at 1000 W/m^{-2} (artificial solar spectrum AM 1.5G).

Contrarily, DSSCs with sensitizers 341-350 were tested using solar simulator Oriel equipped with 300 W Xenon light source and SchottK113 Tempax sunlight filter to match the emission spectrum of the lamp to the AM1.5G standard.

In this section are also reported all the additional 3D-plots and trends of the photovoltaic parameters for the squaraines **341**-**350** of the Chapter 3.

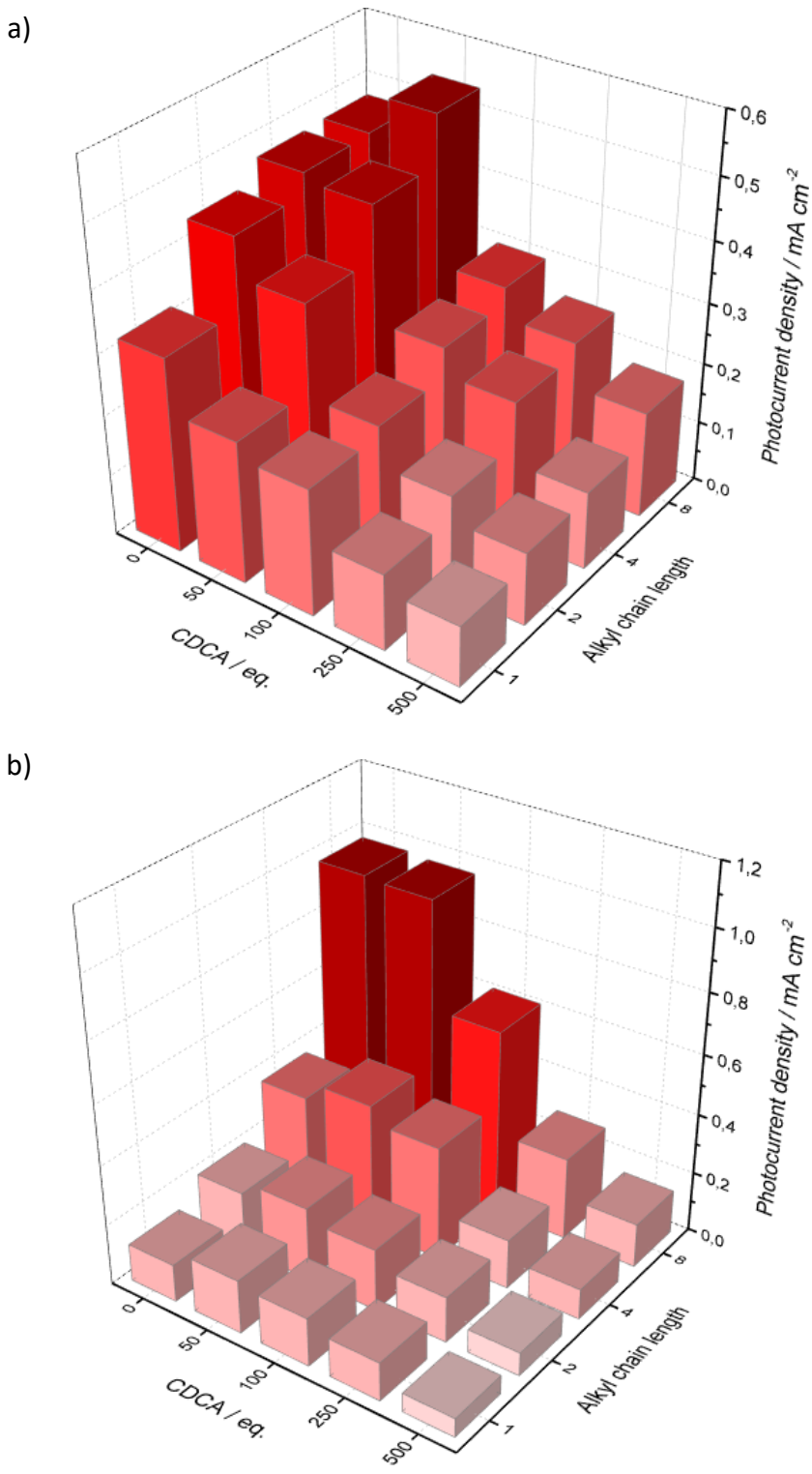

Figure 328 – 3D-plots photocurrent density *vs*. CDCA concentration *vs*. alkyl chains length of (a) SQ-CI series and (b) SQ-CBI series.

a)

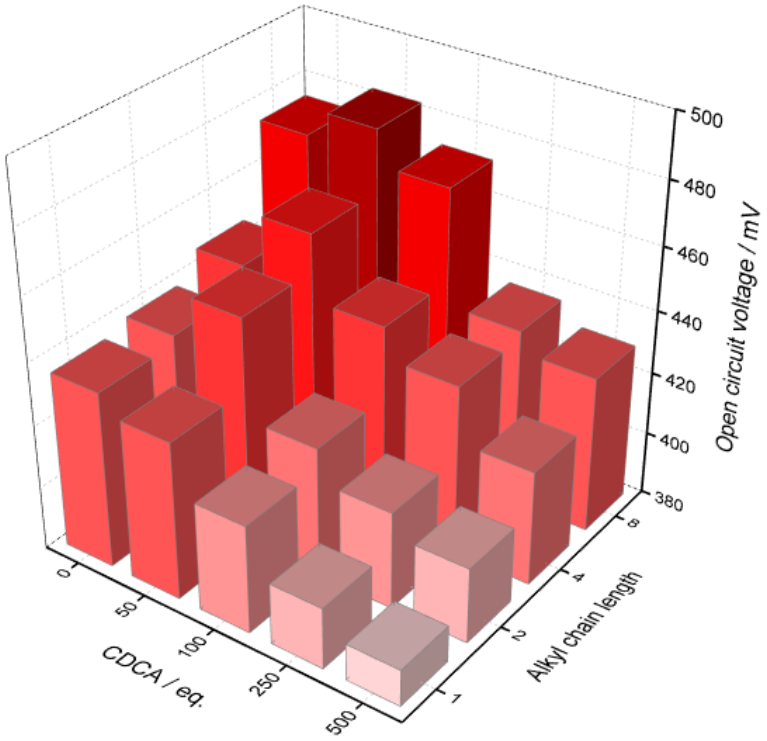

b)

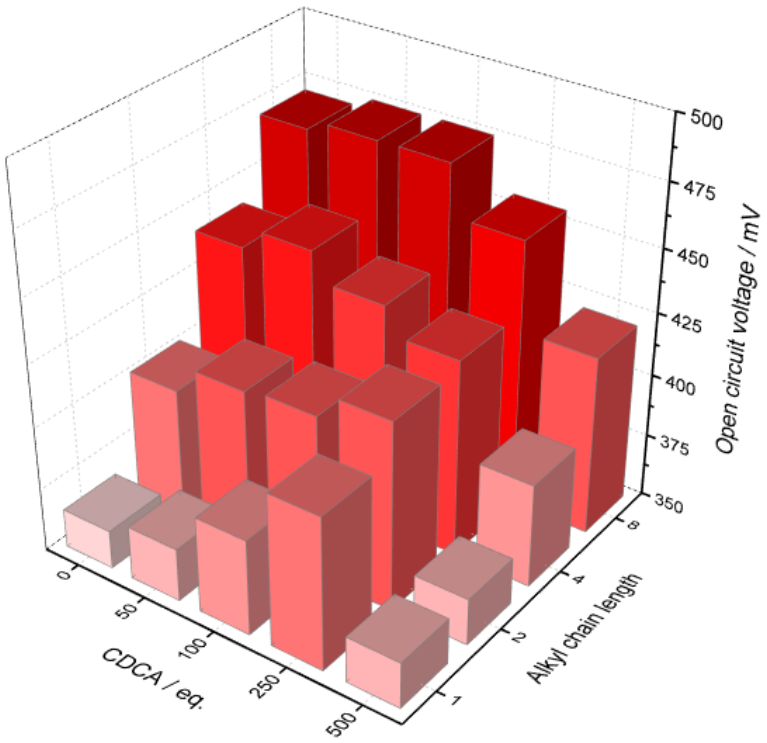

Figure 329 – 3D-plots open circuit voltage *vs*. CDCA concentration *vs*. alkyl chains length of (a) SQ-CI series and (b) SQ-CBI series.

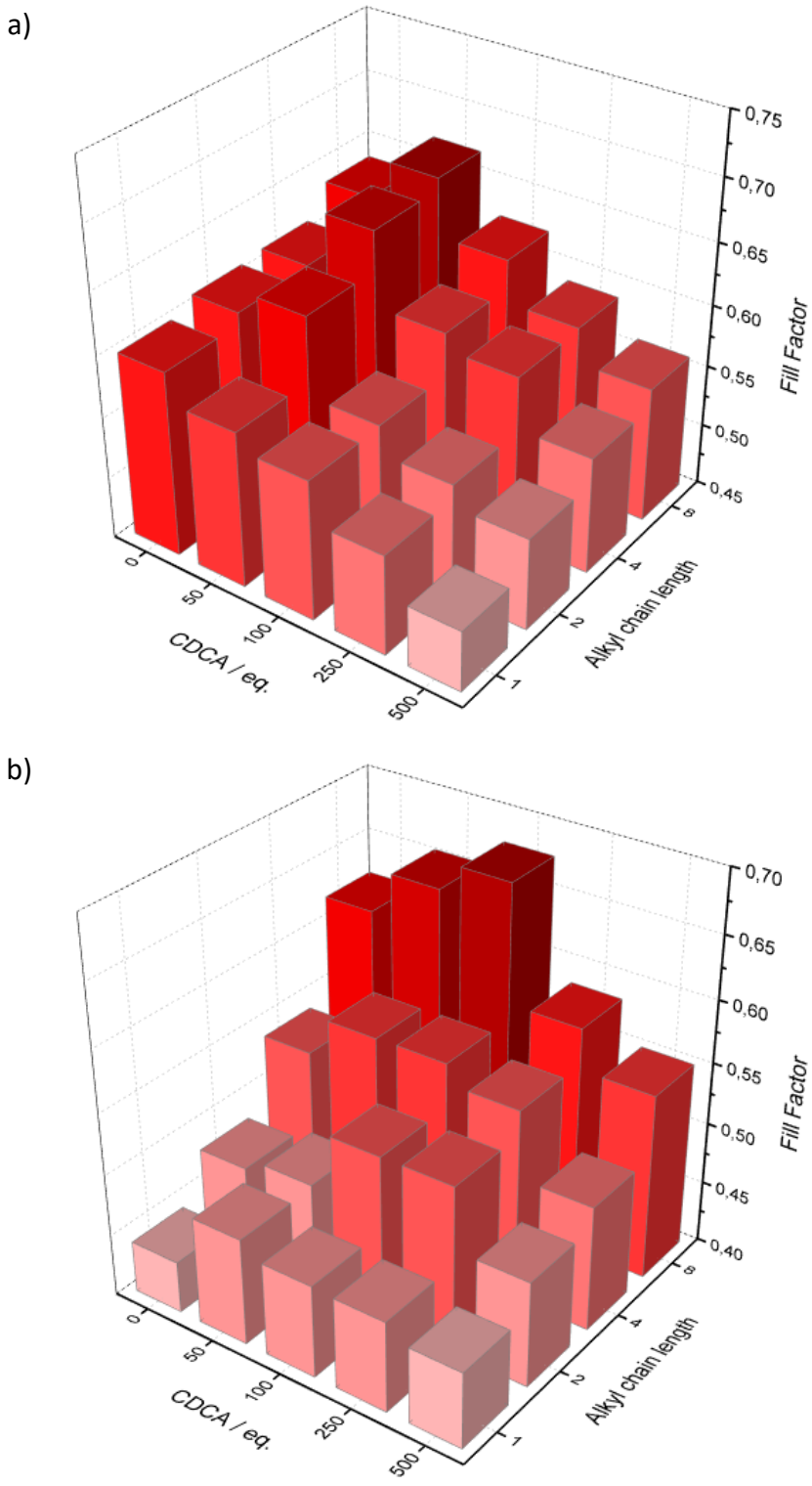

Figure 330 – 3D-plots FF *vs*. CDCA concentration *vs*. alkyl chains length of (a) SQ-CI series and (b) SQ-CBI series.

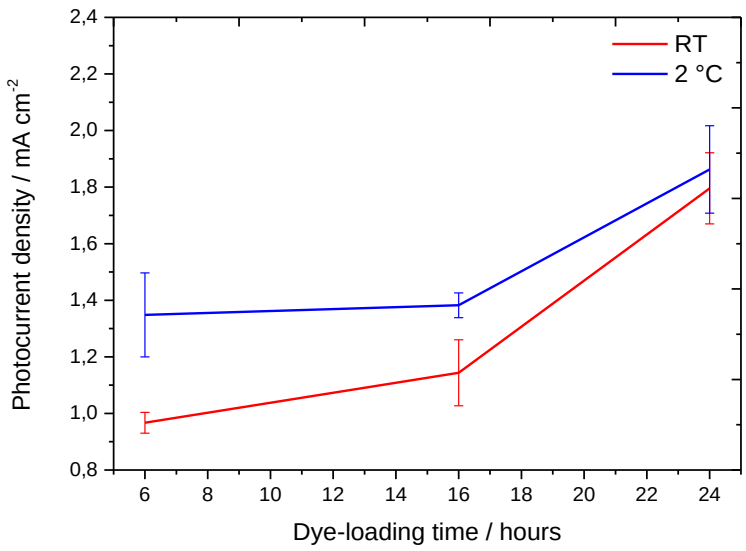

Figure 331 – Photocurrent density *vs.* dye-loading time at RT and at 2 °C for squaraine **348**.

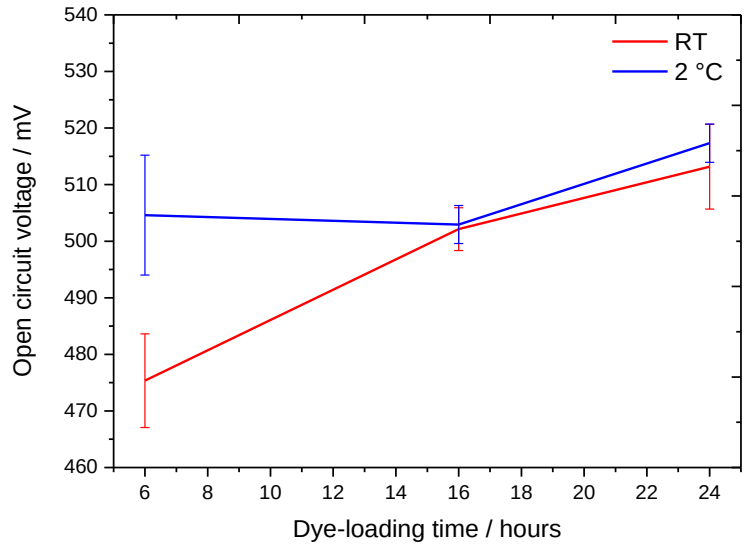

Figure 332 – Open circuit voltage *vs*. dye-loading time at RT and at 2 °C for squaraine **348**.

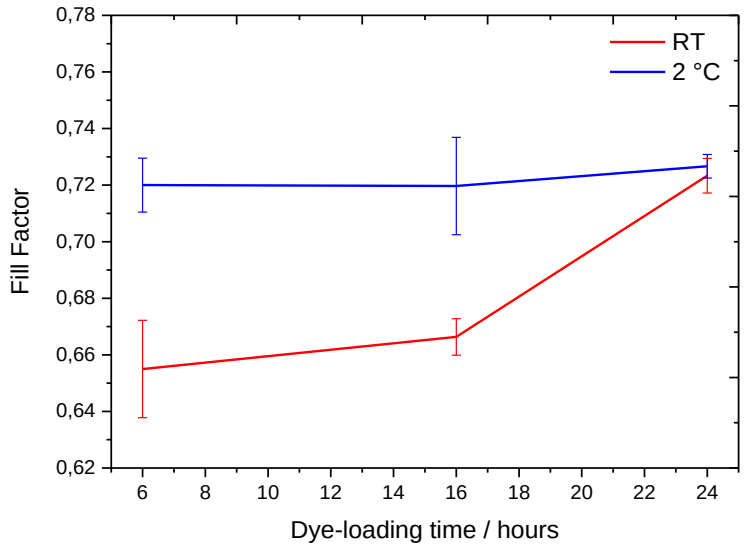

Figure 333 – FF *vs*. dye-loading time at RT and at 2 °C for squaraine **348**.

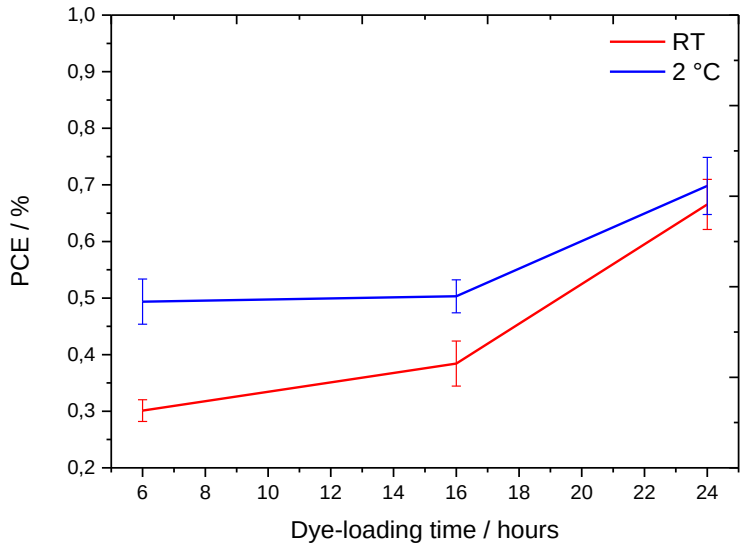

Figure 334 – PCE *vs*. dye-loading time at RT and at 2 °C for squaraine **348**.

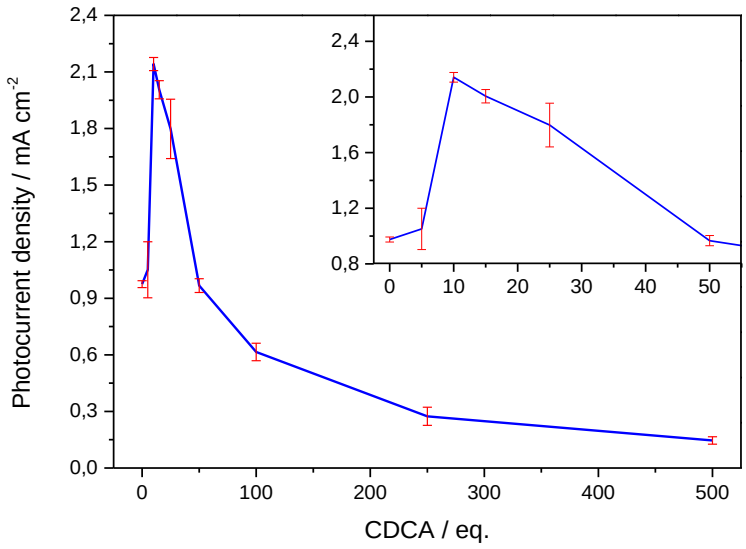

Figure 335 – Photocurrent density *vs*. CDCA concentration in dye-loading solution for squaraine **348**.

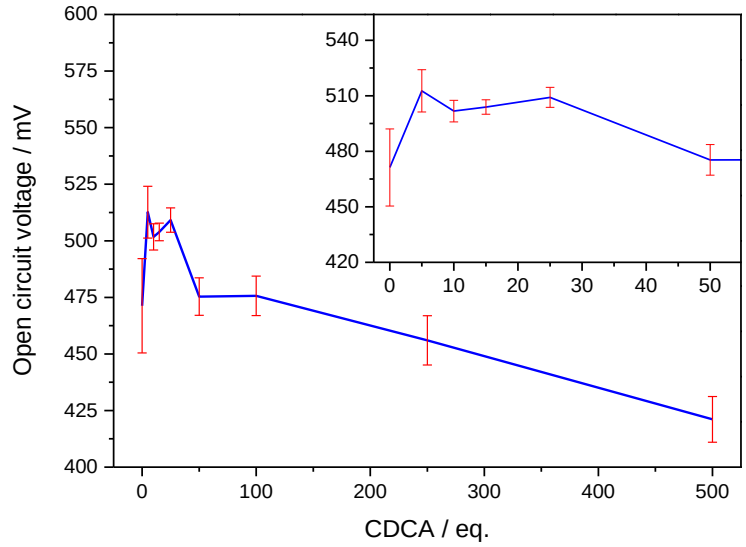

Figure 336 – Open circuit voltage *vs*. CDCA concentration in dye-loading solution for squaraine **348**.

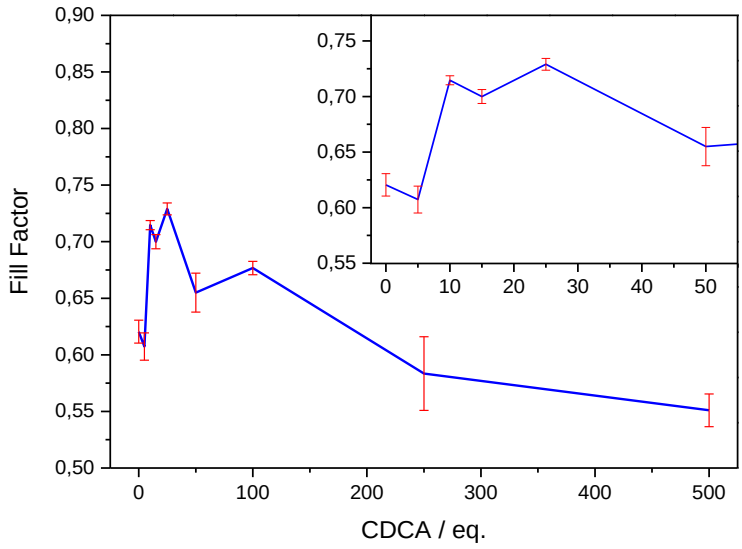

Figure 337 – FF *vs*. CDCA concentration in dye-loading solution for squaraine **348**.

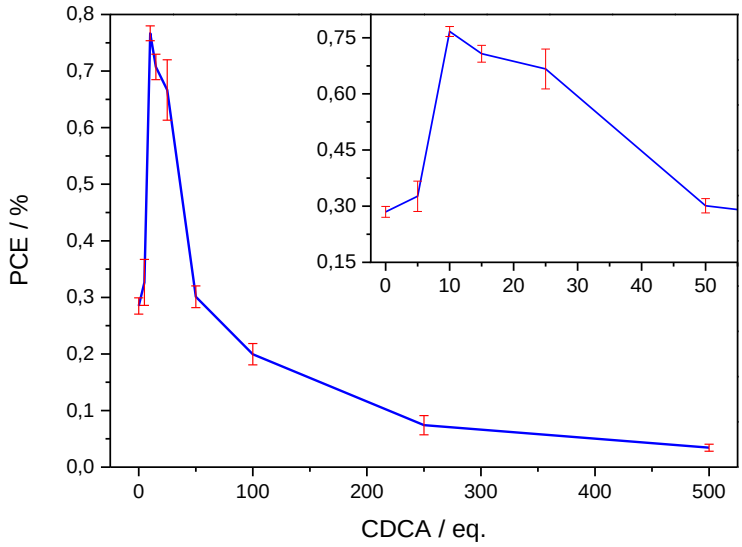

Figure 338 – PCE *vs*. CDCA concentration in dye-loading solution for squaraine **348**.

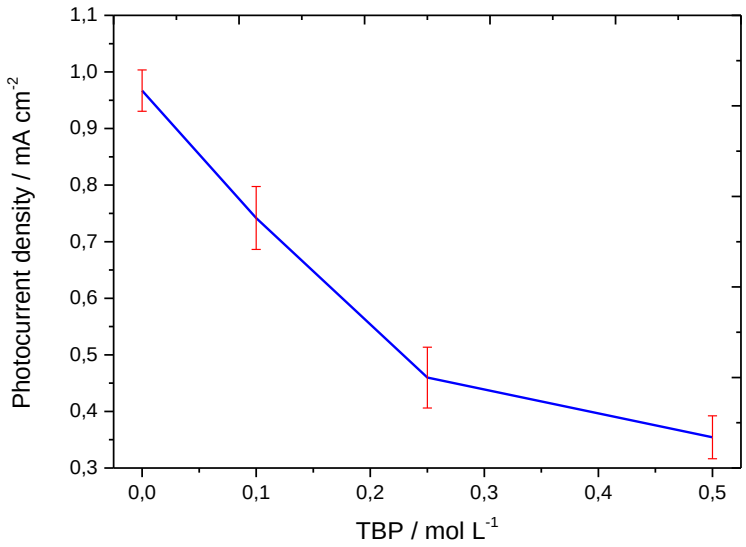

Figure 339 – Photocurrent density *vs*. TBP concentration in the electrolyte solution for squaraine **348**.

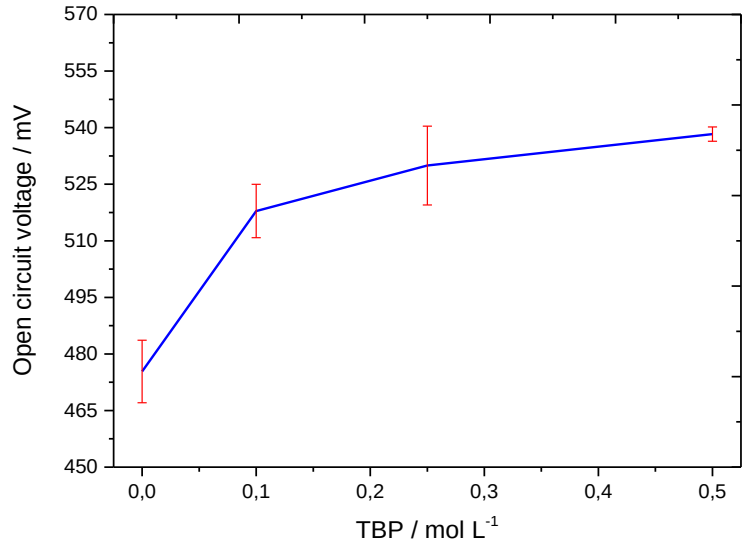

Figure 340 – Open circuit voltage *vs*. TBP concentration in the electrolyte solution for squaraine **348**.

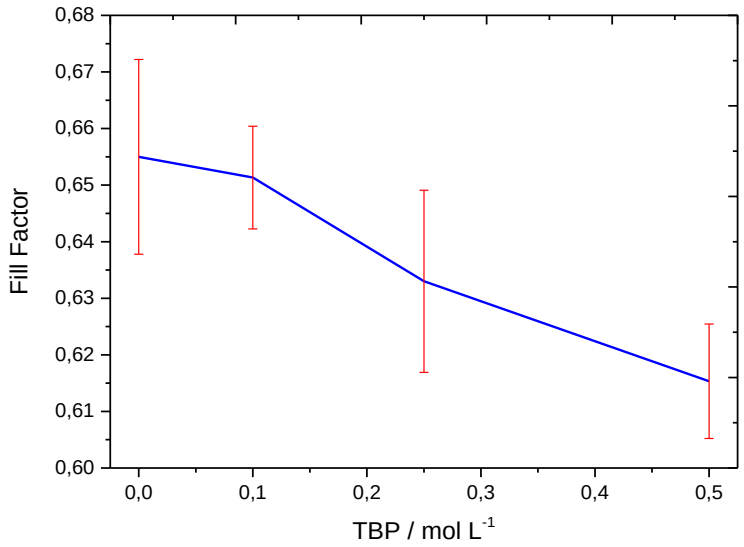

Figure 341 – FF *vs*. TBP concentration in the electrolyte solution for squaraine **348**.

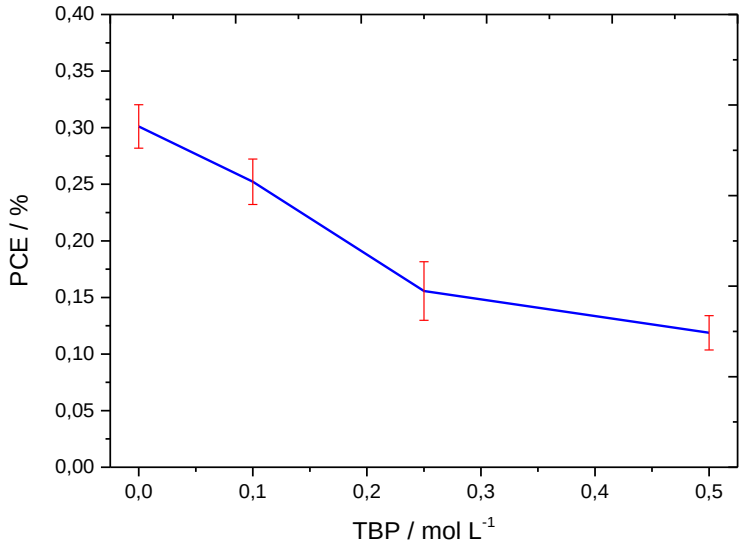

Figure 342 – FF *vs*. TBP concentration in the electrolyte solution for squaraine **348**.

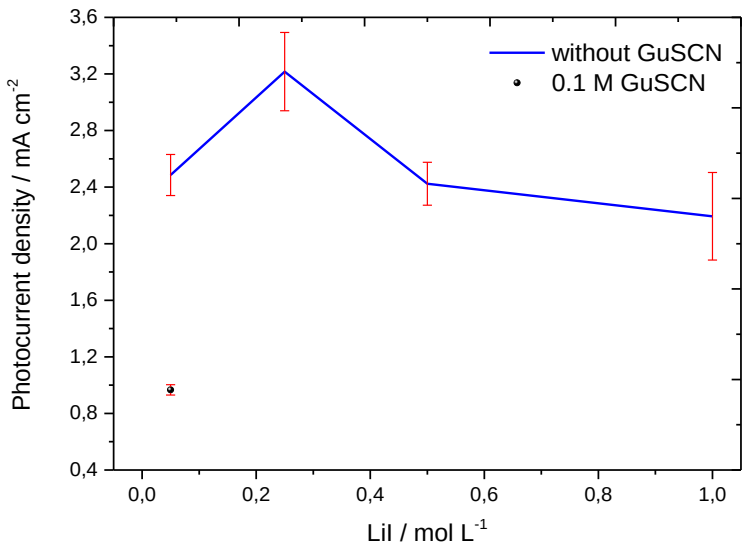

Figure 343 – Photocurrent density *vs*. LiI concentration in the electrolyte solution for squaraine **348**.

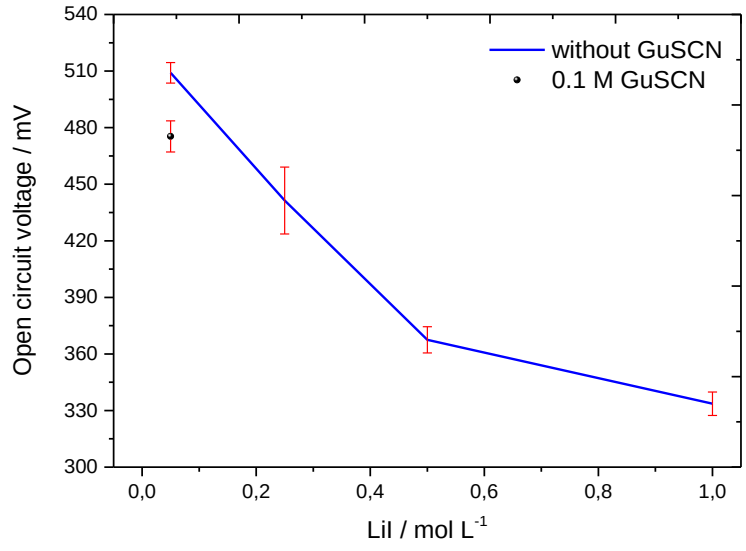

Figure 344 – Open circuit voltage *vs*. LiI concentration in the electrolyte solution for squaraine **348**.

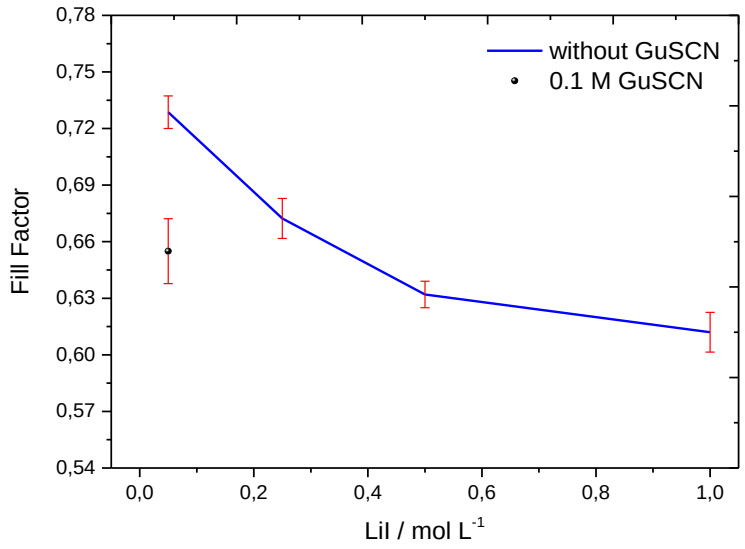

Figure 345 – FF *vs*. LiI concentration in the electrolyte solution for squaraine **348**.

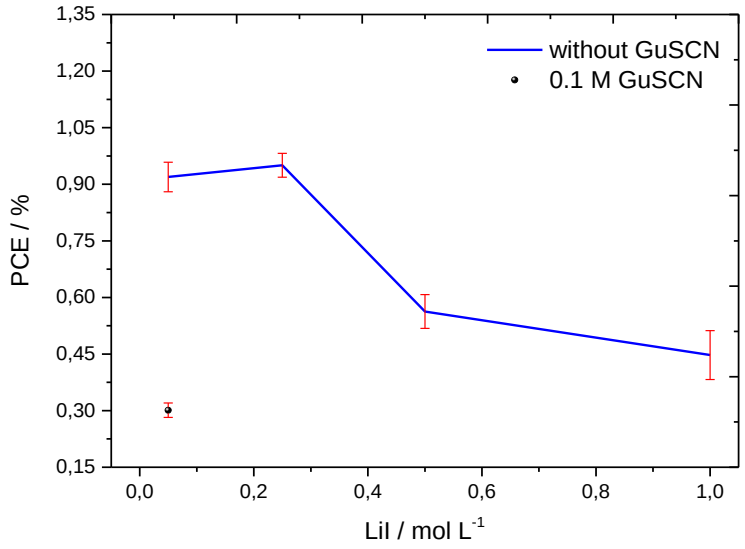

Figure 346 – PCE *vs*. LiI concentration in the electrolyte solution for squaraine **348**.

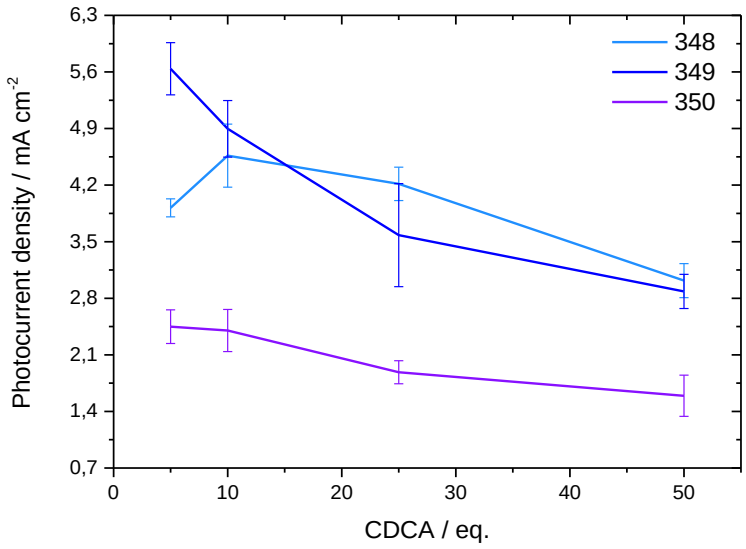

Figure 347 – Photocurrent density *vs*. CDCA concentration in the dye-loading solution for squaraine **348**-**350** with the optimized electrolyte.

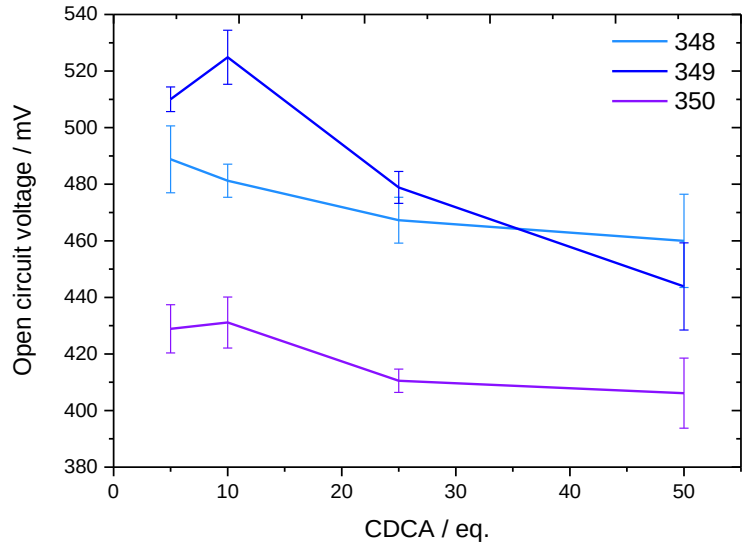

Figure 348 – Open circuit voltage *vs*. CDCA concentration in the dye-loading solution for squaraine **348**-**350** with the optimized electrolyte.

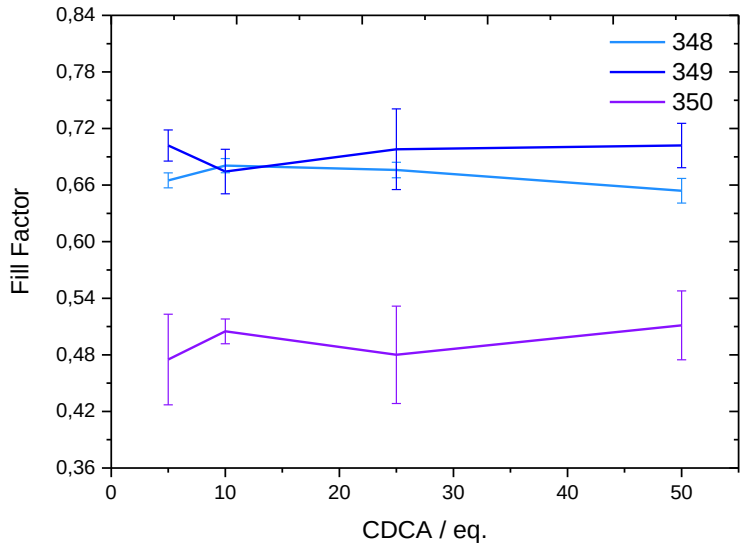

Figure 349 – FF *vs*. CDCA concentration in the dye-loading solution for squaraine **348**-**350** with the optimized electrolyte.

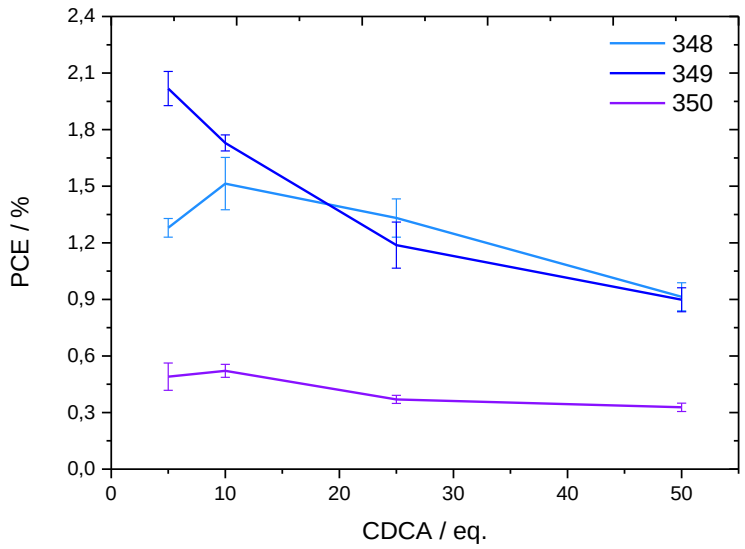

Figure 350 – PCE *vs*. CDCA concentration in the dye-loading solution for squaraine **348**-**350** with the optimized electrolyte.

10. Studies of Liposomes

10.1. DOPC LUVs Preparation

A fine lipid film was prepared by slow rotary evaporation (30°C) of a DOPC (25.0 mg, 0.03 mmol) solution in MeOH/$CHCl_3$ 1:1 (2.0 mL), followed by a final draining (5 h) *in vacuo*. The prepared film was hydrated with 1.0 mL buffer (10 mM phosphate, 100 mM NaCl, pH 7.4) for 30 min at RT, subjected to freeze-melt cycles (7×, liquid N_2, 40 °C water bath) and extrusions (17×) through a polycarbonate membrane (pore size, 100 nm) at RT. Final conditions: ~32 mM DOPC; 10 mM phosphate, 100 mM NaCl, pH 7.4. The vesicles were used by 7 days after the extrusion.

10.2. DPPC LUVs Preparation

A fine lipid film was prepared by slow rotary evaporation (50°C) of a DPPC (22.5 mg, 0.03 mmol) solution in MeOH/$CHCl_3$ 1:1 (2.0 mL), followed by a final draining (5 h) *in vacuo*. The prepared film was hydrated with 1.0 mL buffer (10 mM phosphate, 100 mM NaCl, pH 7.4) for 30 min at 55°C, subjected to freeze-melt cycles (7×, liquid N_2, 55°C °C water bath) and extrusions (21×) through a polycarbonate membrane (pore size, 100 nm) at 55° C. Final conditions: ~31 mM DPPC; 10 mM phosphate, 100 mM NaCl, pH 7.4. The vesicles were used by 7 days after the extrusion.

10.3. Kinetic Measurements

In a typical procedure, to a 2.9 mL buffer (10 mM phosphate, 100 mM NaCl, pH 7.4 at RT) in a quartz cuvette was added DOPC LUVs (100 µL, 1.1 mM DOPC final) or DPPC LUVs (100 µL, 1.02 mM DPPC final). All the probes (10 µL, ≈0.11 mM in DMSO, ≈0.35µM final) were added in separated experiments. Each solution was mixed at RT and monitored acquiring the emission spectra every 1 minute during the first 20 minutes, then after 5 minutes up to 1 h. Depending on the specific kinetic of each probe and on the experiment itself, the monitoring is adjusted and continued for a longer time

10.4. Temperature-dependent Measurements

In a typical procedure, to a 2.9 mL buffer (10 mM phosphate, 100 mM NaCl, pH 7.4 at rt) in a quartz cuvette were added DOPC LUVs (100 µL, 1.1 mM DOPC final) or DPPC LUVs (100 µL, 1.02 mM DPPC final) and aliquots of the tested probes' DMSO solutions (10 µL, ≈0.11 mM in DMSO, ≈0.35µM final) were added in separated experiments. The solution was mixed at RT, and the emission/excitation spectra were acquired after the respective equilibration time at RT calculated by the time dependence measurements. The solution was kept at 25±1 °C for 15 minutes before the spectra acquisition, the cuvette was then warmed to 55±1 °C using a hot plate and a sand bath, and the solution was kept at this temperature for 15 minutes before the spectra acquisition. Then the temperature was lowered to 25±1 °C, and the spectra were acquired after 15 minutes. The described temperature cycle was repeated a second time, collecting five measurements for each probe.

PhD ACTIVITIES SUMMARY

Publications

- G. Volpi, C. Garino, E. Fresta, E. Casamassa, **M. Giordano**, C. Barolo, G. Viscardi. Strategies to increase the quantum yield: luminescent methoxylated imidazo[1,5-*a*]pyridines. *Dyes Pigm.* **2021**, *192*, 109455.
- **M. Giordano**, G. Renno, P. Quagliotto, C. Barolo, G. Cravotto, A. Fin, G. Viscardi. Solid-Phase Synthesis of Asymmetric Cyanine Dyes. *Curr. Org. Chem.* **2021**, *25*, 1739-1754.
- **M. Giordano**, G. Volpi, M. Bonomo, P. Mariani, C. Garino, G. Viscardi. Methoxy-Substituted Copper Complexes as possible Redox Mediators in Dye Sensitized Solar Cells. *New J. Chem.* **2021**, *45*, 15303-15311.
- F. Grifoni, M. Bonomo, W. Naim, N. Barbero, T. Alnasser, I. Dzeba, **M. Giordano**, A. Tsaturyan, M. Urbani, T. Torres, C. Barolo, F. Sauvage. Towards sustainable, colorless and transparent photovoltaics: state of the art and perspectives for the development of selective near-infrared dye-sensitized solar cells. *Adv. Energy Mat.* **2021**, 2101598.
- **M. Giordano**, G. Volpi, C. Garino, F. Cardano, C. Barolo, G. Viscardi, A. Fin. New fluorescent derivatives from papaverine: Two mechanisms to increase the quantum yield. *Dyes Pigm.* **2023**, *218*, 111482.

Posters and Presentations

- F. Cardano, N. Barbero, **M. Giordano**, M. Bonomo, Y. Ren, F. Grifoni, W. Naim, R. Borrelli, G. Viscardi, F. Sauvage, S. M. Zakeeruddin, M. Grätzel, C. Barolo. Low cost Near-infrared absorbing dyes for building integrated applications. Oral presentation at: *Central European Conference on Photochemistry CECP 2020*. Bad Hofgastein, Austria. 9th-13th February 2020.
- **M. Giordano**, G. Giobbio, F. Cardano, A. Fin, N. Barbero, R. Borrelli, Y. Ren, S. M. Zakeeruddin, M. Grätzel, C. Barolo, G. Viscardi, F. Sauvage. Synthesis of NIR Rylene Dyes and Cobalt-based Redox Couple for Colourless Dye-sensitized Solar Cells. Poster presented at: *2nd Congress of the Interdivisional Group on Chemistry for Renewable Energy of the Italian Chemical Society – SCI ENERCHEM-2*. Padova, Italy. 12th-14th February 2020.
- F. Cardano, R. Borrelli, F. Grifoni, Y. Ren, **M. Giordano**, G. Giobbio, M. Bonomo, A. Fin, W. Naim, S. M. Zakeeruddin, N. Barbero, M. Gratzel, F. Sauvage, C. Barolo. Low cost NIR dyes for transparent Dye-Sensitized Solar Cells. Oral presentation at: *2nd Congress of the Interdivisional Group on Chemistry for Renewable Energy of the Italian Chemical Society – SCI ENERCHEM-2*. Padova, Italy. 12th-14th February 2020.
- **M. Giordano**, A. Fin, M. Bonomo, N. Barbero, C. Barolo, G. Viscardi. Synthesis of Near Infrared Quaterrylene-based Dyes for Colourless Dye-sensitized Solar Cells. Poster presented at: *1st Virtual Symposium for Young Organic Chemists of Societá Chimica Italiana*. Online. 3rd-6th November 2020.

- **M. Giordano**, A. Fin, M. Bonomo, N. Barbero, C. Barolo, G. Viscardi. Synthesis of Quaterrylene-based Dyes as possible NIR sensitizers in Dye-Sensitized Solar Cells. Poster presented at: *2021 #RSC Poster Twitter Conference*. Online. 2nd March 2021.
- **M. Giordano**, A. Fin, M. Bonomo, N. Barbero, C. Barolo, G. Viscardi. Synthesis of Quaterrylene-Based Dyes for NIR Dye-Sensitized Solar Cells. Oral presentation at: *NSM21 - nanoGe Spring Meeting 2021*. Online. 8th-12th March 2021.
- N. Barbero, R. Borrelli, F. Grifoni, A. Velardo, W. Naim, **M. Giordano**, Y. Ren, S. M. Zakeeruddin, F. Matteocci, T. Alnasser, M. Bonomo, I. Nikolinanos, S. Haacke, A. Di Carlo, M. Gratzel, C. Barolo, F. Sauvage. NIR functional dyes for transparent and colourless Dye-Sensitized Solar Cells. Oral presentation at: *NSM21 - nanoGe Spring Meeting 2021*. Online. 8th-12th March 2021.
- G. Renno, **M. Giordano**, N. Barbero, P. Quagliotto, G. Cravotto, G. Viscardi, A. Fin. NIR squaraine dyes for cell bilayer bioimaging: a structure-activity investigation. Poster presented at: *XXVII Congresso Nazionale Della Società Chimica Italiana.* Online. 14th-23rd September 2021.
- A. Antenucci, F. Grifoni, **M. Giordano**, A. Velardo, R. Borrelli, W. Naim, T. Alnasser, M. Bonomo, N. Barbero, G. Viscardi, F. Sauvage, C. Barolo. NIR dyes for transporter and building integrated photovoltaic devices. Poster presented at: *Giornate Italiane di Fotochimica del GIF 2021*. Online. 23rd-24th September 2021.
- G. Volpi, C. Garino, E. Fresta, E. Casamassa, **M. Giordano**, C. Barolo, G. Viscardi. Investigation on molecular modification of luminescent methoxylated imidazo[1,5-*a*]pyridines. Poster presented at: *Giornate Italiane di Fotochimica del GIF 2021*. Online. 23rd-24th September 2021.
- G. Renno, **M. Giordano**, N. Barbero, G. Cravotto, P. Quagliotto, G. Viscardi, C. Barolo, A. Fin. Perimidine-based NIR squaraine dyes as cell membrane probes: a structure-to-function investigation in liposomes. Poster presented at: *Giornate Italiane di Fotochimica del GIF 2021*. Online. 23rd-24th September 2021.
- **M. Giordano**, F. Grifoni, A. Velardo, R. Borrelli, N. Barbero, C. Barolo, G. Viscardi, F. Sauvage. Modulation of charge-transfer and recombination processes by a nonconjugate triphenylamine moiety in cyanine sensitizer for NIR-DSSCs. Short-oral presentation at: *HOPE-PV 2021 – 3rd International School on Hybrid, Organic and Perovskite Photovoltaics*. Online. 22nd-25th November 2021.
- **M. Giordano**, G. Renno, N. Barbero, G. Cravotto, P. Quagliotto, C. Barolo, G. Viscardi, A. Fin. Novel perimidine-based squaraine dyes as cell membrane probes: a structure-function investigation in liposomes. Poster presented at: *Italian Photochemistry Meeting 2021.* Torino, Italy. 16th-18th December 2021.
- **M. Giordano**, G. Volpi, N. Barbero, S. M. Zakeeruddin, M. Grätzel, C. Barolo, A. Fin, G. Viscardi. Imidazo[1,5-*a*]pyridine-based copper complexes as possible redox mediators in NIR-DSSCs. Poster presented at: *2022 #RSC Poster Twitter Conference.* Online, 1st March 2022.

- **M. Giordano**, G. Renno, N. Barbero, S. M. Zakeeruddin, M. Grätzel, C. Barolo, A. Fin, G. Viscardi. Effect of Out-of-Plane Alkyl Chains in Dye-Sensitized Solar Cell Efficiency: A Structure-Property Relationship in Novel Perimidine-Based Squaraine Dyes. Oral presentation at: *15th International Conference on Hybrid and Organic Photovoltaics.* Valencia, Spain. 19th-25th May 2022.
- C. Barolo, N. Barbero, M. Bonomo, **M. Giordano**, A. Y. Segura Zarate, S. Galliano, W. Naim, F. Grifoni, R. Borrelli, F. Matteocci, P. Chotard, S. Ceurstemont, F. Barath, A. Di Carlo, F. Sauvage. Toward non-intrusive BIPV: strategies for NIR-selective DSSCs. Oral presentation at: *15th International Conference on Hybrid and Organic Photovoltaics.* Valencia, Spain. 19th-25th May 2022.

Congresses, Conferences, Seminars

- *2nd Congress of the Interdivisional Group on Chemistry for Renewable Energy of the Italian Chemical Society – SCI ENERCHEM-2*. Padova, Italy. 12th-14th February 2020.
- *1st Virtual Symposium for Young Organic Chemists of Societá Chimica Italiana*. Online. 3rd-6th November 2020.
- *2021 #RSC Poster Twitter Conference*. Online. 2nd March 2021.
- *NSM21 - nanoGe Spring Meeting 2021*. Online. 8th-12th March 2021.
- *Italian Photochemistry Meeting 2021.* Torino, Italy. 16th-18th December 2021.
- *2022 #RSC Poster Twitter Conference.* Online, 1st March 2022.
- *15th International Conference on Hybrid and Organic Photovoltaics.* Valencia, Spain. 19th-25th May 2022.

Attended PhD Courses

- Electrochemical Energy Storage and Conversion Systems. Dott. M. Sgroi. Chemistry Department, University of Turin. 2020.
- Solid state NMR: basics and applications. Prof. R. Gobetto, Prof. M. R. Chierotti. Chemistry Department, University of Turin. 2020.
- The vitreous state. Prof. Battezzati. Chemistry Department, University of Turin. 2020.
- Chemical Sensors for Scientific Research and Everyday Life. Prof. O. Abollino. Chemistry Department, University of Turin. 2020.
- Carbanion Chemistry in Organic Synthesis. Prof. V. Pace. Chemistry Department, University of Turin. 2020.
- Organic Chemistry for Chemical Biology and Biomedical Applications. Prof. A. Fin. Chemistry Department, University of Turin. 2021.
- Organic and Hybrid Materials for Biochemical Applications. Prof. N. Barbero. Chemistry Department, University of Turin. 2021.
- Materials in optoelectronic applications for energy generation. Prof. J. Yum, Dott. M. Bonomo. Chemistry Department, University of Turin. 2022.

Schools

- 3rd International School on Hybrid, Organic and Perovskite Photovoltaics 2021. Organized by "Institute of Problems of Chemical Physics of Russian Academy of Sciences (IPCP RAS)". Online. 22nd-25th November 2021.

Teaching Assistances

- May 2019, Tutorato in aula di Chimica Organica (Corso A), Laurea triennale in Scienze Biologiche (Università degli Studi di Torino), Prof. Nadia Barbero.
- May 2019, Tutorato in aula di Chimica Organica (Corso A), Laurea triennale in Chimica e Tecnologie Chimiche (Università degli Studi di Torino), Prof. Guido Viscardi.
- October 2020, Assistenza in Laboratorio di Sintesi Organiche di Interesse Industriale, Laurea triennale in Chimica e Tecnologie chimiche (Università degli Studi di Torino), Prof. Guido Viscardi.
- February 2021, Docente a contratto, Chimica Organica B, Laurea in Scienze Strategiche (SUISS – Scuola Universitaria Interdipartimentale in Scienze Strategiche (Università degli Studi di Torino), Prof. Vittorio Pace.
- December 2021, Assistenza in Laboratorio di Sintesi Organiche di Interesse Industriale, Laurea triennale in Chimica e Tecnologie chimiche (Università degli Studi di Torino), Prof. Guido Viscardi.
- February 2022, Docente a contratto, Chimica Organica B, Laurea in Scienze Strategiche (SUISS – Scuola Universitaria Interdipartimentale in Scienze Strategiche (Università degli Studi di Torino), Prof. Vittorio Pace.

ACKNOWLEDGEMENTS

First, I would like to thank all the team of the MOF group for the last years spent together. In particular, I need to do special thanks to my supervisor, Prof. Viscardi, for his constant support as well as his countless teachings (not only scientific) that made me a scientist and a better person. And what about Andrea? He is the guy that convinced me almost five years ago to jump in the PhD life, the guy that first believed in me, who taught me everything I know and who is more than a tutor, is a friend. I do not want miss to thank Giorgio, for having given me a lot of teachings, nicknames (how can I ever forget Giordy and Missile???) and for having the possibility to work with him with the mythical GVs!!! He is the first person that passed me the passion and the curiosity for the synthesis.

Thanks to Claudio, Federica, and Ivan for their valuable help during these years; without them I couldn't achieve the results showed discussing the copper complexes and the green-pink squaraines. Thanks to Dr. Yameng Ren and Prof. Michael Grätzel for having offered me the great opportunity to spent six months in their laboratories at the EPFL to learn everything about the DSSCs.

Now is arriving the moment to thank some special people I met during this journey in the MOF Lab. I would like thanks Anna, Bap, Daniel, Fabio, Francesca, Gingi, "il" Mattia, Nicole, Onur, Pablo, Vale, Viktoria; without them the journey wouldn't been the same. I need to reserve some special thanks for two guys that in these years became more than friends, they became brothers for me! Thanks Giacomino and "il Sindaco" Matteo, you two guys have been fundamental and provided me constant help and support. We shared together a lot of memorable moments… the Friday's Pizzas, the "solvent battles" with Giacomo, the angry "Sindaco" with its proverbial "SOTTO CAPPA", the Olympic Lab Game with the bottles' caps and many other epic moments with you two guys. These years would not been the same without you.

I cannot miss to thank Ale and Vale, the guys endured me during these years, I hope I helped you in your thesis works.

Finally, I would like to thank the people always supported me after every bad day, my girlfriend Francesca and my family. Francesca in these three years we growth together and I'm sure this journey wouldn't been the same without you. Now it's the time to start another trip and I can't wait to start it with you. A warm thanks to whole my family and especially to my mother and my father. Mom and dad, all results and achievements I have reached are even yours. Without you, everything I did from my first steps at school till' now wouldn't been possible. All your teachings, all your help, all your support have allowed this day became true. I hope to become like you!

Thank at all!!!

REFERENCES

1. *World Energy Outlook 2022*, IEA Publications, **2022**.
2. Q. Schiermeier, J. Tollefson, T. Scully, A. Witze, O. Morton, *Nature* **2008**, *454*, 816-823.
3. N. Lewis, *Science* **2007**, *315*, 798-801.
4. V. Smil, (Ed.); *General Energetics: Energy in the Biosphere and Civilization,* John Wiley, **1991**.
5. A. Goetzberger, J. Luther, G. Willeke, *Sol. Energy Mater. Sol. Cells* **2002**, *74*, 1-11.
6. A. Cristobal, A. M. Vega, A. L. López, (Ed.); *Next Generation of Photovoltaics: New Concepts*, Springer, **2012**.
7. D. Chapin, C. Fuller, G. Pearson, *J. Appl. Phys.* **1954**, *25*, 676-677.
8. M. A. Green, Y. Hishikawa, W. Warta, E. D. Dunlop, D. H. Levi, J. Hohl-Ebinger, A. W. H. Ho-Baillie, *Prog. Photovoltaics Res. Appl.* **2017**, *25*, 668-676.
9. M. Lira-Cantu, (Ed.); *The Future of Semiconductor Oxides in Next-Generation Solar Cells*, Elsevier, **2018**.
10. Shah, P. Torres, R. Tscharner, N. Wyrsch, H. Keppner, *Science* **1999**, *285*, 692-698.
11. M. Grätzel, *J. Photochem. Photobiol. C: Photochem. Rev.* **2003**, *4*, 145-153.
12. M. Grätzel, *Acc. Chem. Res.* **2009**, *42*, 1788-1798
13. A. Hagfeldt, G. Boschloo, L. Sun, L. Kloo, H. Pettersson, *Chem. Rev.* **2010**, *110*, 6595-6663.
14. H. Hoppe, N. Sariciftci, S. Niyazi, *J. Mater. Res.* **2004**, *19*, 1924-1945.
15. L. Dou, J. You, Z. Hong, Z. Xu, G. Li, R. A. Street, Y. Yang, *Adv. Mater.* **2013**, *25*, 6642-6671.
16. J. Hou, O. Inganas, R. H. Friend, F. Gao, *Nat. Mater.* **2018**, *17*, 119-128.
17. J. Nozik, *Physica* **2002**, *14*, 115-120.
18. P. Kamat, *J. Phys. Chem. Lett.* **2013**, *4*, 909-918.
19. G. H. Carey, A. L. Abdelhady, Z. Ning, S. M. Thon, O. M. Bakr, E. H. Sargent, *Chem. Rev.* **2015**, *115*, 12732-12763.
20. M. A. Green, A. Ho-Baillie, H. J. Snaith, *Nat. Photon.* **2014**, *8*, 50-–514.
21. J. Correa-Baena, A. Abate, M. Saliba, W. Tress, J. T. Jesper, M. Grätzel, A. Hagfeldt, *Energy Environ. Sci.* **2017**, *10*, 710-727.
22. https://www.nrel.gov/pv/cell-efficiency.html.
23. K. Kakiage, Y. Aoyama, T. Yano, K. Oya, J. Fujisawa, M. Hanaya, *Chem. Commun.* **2015**, *51*, 15894-15897.
24. H. Pettersson, T. Gruszecki, *Sol. Energy Mater. Sol. Cells* **2001**, *70*, 203-212.
25. M. Freitag and G. Boschloo, *Curr. Opin. Electrochem.* **2017**, *2*, 111-119
26. A. B. Muñoz-García, I. Benesperi, G. Boschloo, J. J. Concepcion, J. H. Delcamp, E. A. Gibson, G. J. Meyer, M. Pavone, H. Pettersson, A. Hagfeldt, M. Freitag, *Chem. Soc. Rev.* **2021**, 50, 12450-12550.
27. T. M. W. J. Bandara, J. M. C. Hansadi, F. Bella, *Ionics* **2022**, *28*, 2563-2583.

28. C. Dupraz, H. Marrou, G. Talbot, L. Dufour, A. Nogier, Y. Ferad, *Renew. Energ.* **2011**, 36, 2725-2732.
29. F. Grifoni, M. Bonomo, W. Naim, N. Barbero, T. Alnasser, I. Dzeba, M. Giordano, A. Tsaturyan, M. Urbani, T. Torres, C. Barolo, F. Sauvage, *Adv. Energy Mat.* **2021**, 2101598.
30. B. O'Regan, M. Grätzel, *Nature* **1991**, *353*, 737-740.
31. M. Grätzel, *Nature* **2001**, *414*, 338-344.
32. A. Listorti, B. O'Regan, J.R. Durrant, *Chem. Mater.* **2011**, *23*, 3381-3399.
33. C. Martín, M. Ziółek, A. Douhal, *J. Photochem. Photobiol. C: Photochem. Rev.* 2016, 26, 1-30.
34. R. Katoh, A. Furube, *J. Photochem. Photobiol. C: Photochem. Rev.* **2014**, *20*, 1-16.
35. J. N. Clifford, E. Martínez-Ferrero, A. Viterisi, E. Palomares, *Chem. Soc. Rev.* **2011**, *40*, 1635-1646.
36. A. Islam, H. Sugihara, H. Arakawa, *J. Photochem. Photobiol. A: Chem.* **2003**, *158*, 131-138.
37. A. O. Adeloye, P. A. Ajibade, *Molecules* **2014**, *19*, 12421-12460.
38. S. Mathew, A. Yella, P. Gao, R. Humphry-Baker, B. F. E. Curchod, N. Ashari-Astani, I. Tavernelli, U. Roethlisberger, M. K. Nazeeruddin, M. Grätzel, *Nat. Chem.* **2014**, *6*, 242-247.
39. L. Li, E. W.G. Diau, *Chem. Soc. Rev*. **2013**, *42*, 291-304.
40. M. Urbani, M.-E. Ragoussi, M. K. Nazeeruddin, T. Torres, *Coord. Chem. Rev.* **2019**, *381*, 1-64.
41. M. V. Martinez-Diaz, G. de la Torre, T. Torres, *Chem. Commun.* **2010**, *46*, 7090-7108.
42. K. Hara, M. Kurashige, Y. Dan-ho, C. Kasada, A. Shinpo, S. Suga, K. Sayama, H. Arakawa, *New J. Chem.* **2003**, *27*, 783-785.
43. T. Horiuchi, H. Miura, K. Sumioka, S. Uchida, *J. Am. Chem. Soc.* **2004**, *126*, 12218-12219.
44. D. P. Hagberg, T. Edvinsson, T. Marinado, G. Boschloo, A. Hagfeldt, L. Sun, *Chem. Commun.* **2006**, 2245-2247.
45. A. Burke, L. Schmidt-Mende, S. Ito, M. Grätzel, *Chem. Commun.* **2007**, 234-236.
46. D. Saccone, S. Galliano, N. Barbero, P. Quagliotto, G. Viscardi, C. Barolo, *Eur. J. Org. Chem.* **2016**, 2244-2259.
47. C. Li, H. Wonneberger, *Adv. Mater.* **2012**, *24*, 613-636.
48. Z. Yao, C. Yan, M. Zhang, R. Li, Y. Cai, P. Wang, *Adv. Energy Mater.* **2014**, *4*, 1400244.
49. J. L. Bricks, A. D. Kachkovskii, Y. L. Slominskii, A. O. Gerasov, S. V. Popov, *Dyes Pigm.* **2015**, *121*, 238-255.
50. H. Vogel, *Ber. Dtsch. Chem. Ges.* **1873**, *6*, 1302-1306.
51. V. Voiciuk, K. Redeckas, N. A. Derevyanko, A. V. Kulinich, M. Barkauskas, M. Vengris, V. Sirutkaitis, A. A. Ishchenko, *Dyes Pigm.* **2014**, *109*, 120-126.
52. D. Valeur, *Principles of fluorescent probe design for ion recognition*. In: *Topics in fluorescence spectroscopy. Probe design and chemical sensing, vol. 4*. JR. Lacowicz (Ed.); Plenum, **1994**.
53. M. Y. Berezin, S. Achilefu, *Chem. Rev.* **2010**, *110*, 2641-2684.

54. Z. Guo, S. Park, J. Yoon, I. Shin, Chem. Soc. Rev. **2014**, *43*, 16-28.
55. D. M. Dereje, C. Pontremoli, M. J. Moran Plata, S. Visentin, N. Barbero, *Photochem. Photobiol. Sci.* **2022**, *21*, 397-419.
56. J. M. Hales, S. Barlow, H. Kim, S. Mukhopadhyay, J. Brédas, J. W. Perry, S. R. Marder, *Chem. Mater.* **2014**, *26*, 549-560.
57. C. Qin, W. Wong, L. Han, *Chem. Asian J.* **2013**, *8*, 1706-1719.
58. M. Giordano, G. Renno, P. Quagliotto, C. Barolo, G. Cravotto, A. Fin, G. Viscardi, *Curr. Org. Chem.* **2021**, *25*, 1739-1754.
59. D. E. Lynch, D. G. Hamilton, *Eur. J. Org. Chem.* **2017**, 3897-3911.
60. L. Zhang, J. M. Cole, *J. Mater. Chem. A* **2017**, *5*, 19541-19559.
61. W. Naim, V. Novelli, I. Nikolinakos, N. Barbero, I. Dzeba, F. Grifoni, Y. Ren, T. Alnasser, A. Velardo, R. Borrelli, S. Haacke, S. M. Zakeeruddin, M. Grätzel, C. Barolo, F. Sauvage, *JACS Au* **2021**, *1*, 409-426.
62. J. H. Yum, S. J. Moon, R. Humphry-Baker, P. Walter, T. Geiger, F. Nüesch, M. Grätzel, M. K. Nazeeruddin, *Nanotechnology* **2008**, *19*, 424005.
63. L. Beverina, P. Salice, *Eur. J. Org. Chem.* **2010**, 1207-1225.
64. S. Sreejith, P. Carol, P. Chithra, A. Ajayaghosh, *J. Mater. Chem.* **2008**, *18*, 264-274.
65. J. Jiang, C. Sun, Z. Shi, H. Zhang, *RSC Adv.* **2014**, *4*, 32987-32996.
66. S. Khopkar, G. Shankarling, *Dyes Pigm.* **2019**, *170*, 107645.
67. J. H. Yum, P. Walter, S. Huber, D. Rentsch, T. Geiger, F. Nüesch, F. De Angelis, M. Grätzel, M. K. Nazeeruddin, *J. Am. Chem. Soc.* **2007**, *129*, 10320-10321.
68. T. Geiger, S. Kuster, J.-H. Yum, S.-J. Moon, M. K. Nazeeruddin, M. Grätzel, F. Nüesch, *Adv. Funct. Mater.* **2009**, *19*, 2720-2727.
69. S. Kuster, F. Sauvage, M. K. Nazeeruddin, M. Grätzel, F. A. Nüesch, T. Geiger, *Dyes Pigm.* **2010**, *87*, 30-38.
70. T. Maeda, Y. Hamamura, K. Miyanaga, N. Shima, S. Yagi, H. Nakazumi, *Org. Lett.* **2011**, *13*, 5994-5997.
71. T. Maeda, S. Arikawa, H. Nakao, S. Yagi, H. Nakazumi, *New J. Chem.* **2013**, *37*, 701-708.
72. C. Magistris, S. Martiniani, N. Barbero, J. Park, C. Benzi, A. Anderson, C. H. Law, C. Barolo, B. O'Regan, *Renew. Energ.* **2013**, *60*, 672-678.
73. T. Maeda, S. Nitta, Y. Sano, S. Tanaka, S. Yagi, H. Nakazumi, *Dyes Pigm.* **2015**, *122*, 160-167.
74. Y. Haishima, Y. Kubota, K. Manseki, J. Jin, Y. Sawada, T. Inuzuka, K. Funabiki, M. Matsui, *J. Org. Chem.* **2018**, *83*, 4389-4401.
75. S. Kim, G. K. Mor, M. Paulose, O. K. Varghese, C. Baik, C. A. Grimes, *Langmuir* **2010**, *26*, 13486-13492.
76. J. Li, C. Chen, W. Ho, S. Chen, C. Wu, *Org. Lett.* **2012**, *14*, 5420-5423.
77. K. Funabiki, H. Mase, Y. Saito, A. Otsuka, A. Hibino, N. Tanaka, H. Miura, Y. Himori, T. Yoshida, Y. Kubota, M. Matsui, *Org. Lett.* **2012**, *14*, 1246-1249.
78. N. Karjule, M. Fairoos M. K., J. Nithyanandhan, *J. Mater. Chem. A* **2016**, *4*, 18910-18921.
79. R. Bisht, M. Fairoos M. K., J. Nithyanandhan, *Chem. Eur. J.* **2018**, *24*, 16368-16378.

80. R. Bisht, V. Sudhakar, M. Fairoos M. K., N. Karjule, J. Nithyanandhan, *ACS Appl. Mater. Interfaces* **2018**, *10*, 26335-26347.
81. P. F. Santos, L. V. Reis, P. Almeida, A. S. Oliveira, L. F. Vieira Ferreira, *J. Photochem. Photobiol. A: Chem.* **2003**, 160, 159-161.
82. L. Zhang, J. M. Cole, *ACS Appl. Mater. Interfaces* **2015**, *7*, 3427−3455.
83. A L. Tatarets, I. A. Fedyunyaeva, E. Terpetschnig, L. D. Patsenker, *Dyes Pigm.* **2005**, *64*, 125-134.
84. J. Park, C. Barolo, F. Sauvage, N. Barbero, C. Benzi, P. Quagliotto, S. Coluccia, D. Di Censo, M. Grätzel, M. K. Nazeeruddin, G. Viscardi, *Chem. Commun.* **2012**, *48*, 2782-2784.
85. C. H. Lee, H. J. Yun, M. R. Jung, J. G. Lee, S. H. Kim, J. H. Kim, *Electrochim. Acta* **2014**, *138*, 148-154.
86. C. Qin, Y. Numata, S. Zhang, X. Yang, A. Islam, K. Zhang, H. Chen, L. Han, *Adv. Funct. Mater.* **2014**, 24, 3059-3066.
87. J. Park, N. Barbero, J. Yoon, E. Dell'Orto, S. Galliano, R. Borrelli, J.-H. Yum, D. Di Censo, M. Grätzel, M. K. Nazeeruddin, C. Barolo, G. Viscardi, *Phys. Chem. Chem. Phys.* **2014**, *16*, 24173-24177.
88. U. Mayerhöffer, M. Gsänger, M. Stolte, B. Fimmel, F. Würthner, *Chem. Eur. J.* **2013**, *19*, 218-232.
89. L. Beverina, R. Ruffo, C. M. Mari, G. A. Pagani, M. Sassi, F. De Angelis, S. Fantacci, J.-H. Yum, M. Grätzel, M. K. Nazeeruddin, *ChemSusChem* **2009**, *2*, 621-624.
90. D. Keil, H. Hartmann, *Dyes Pigm.* **2001**, *49*, 161-179.
91. T. Maeda, S. Mineta, H. Fujiwara, H. Nakao, S. Yagia, H. Nakazumi, *J. Mater. Chem. A* **2013**, *1*, 1303-1309.
92. C. Qin, Y. Numata, S. Zhang, A. Islam, X. Yang, K. Sodeyama, Y. Tateyama, L. Han, *Adv. Funct. Mater.* **2013**, *23*, 3782-3789.
93. S. Galliano, V. Novelli, N. Barbero, A. Smarra, G. Viscardi, R. Borrelli, F. Sauvage, C. Barolo, *Energies* **2016**, *9*, 486.
94. V. Punitharasu, M. Fairoos M. K., J. Nithyanandhan, *ACS Appl. Mater. Interfaces* **2018**, *10*, 16541-16551.
95. I. Venditti, N. Barbero, M. V. Russo, A. Di Carlo, F. Decker, I. Fratoddi, C. Barolo, D. Dini, *Mater. Res. Express* **2014**, 1, 015040.
96. S. M. Feldt, E. A. Gibson, E. Gabrielsson, L. Sun, G. Boschloo, A. Hagfeldt, *J. Am. Chem. Soc.* **2010**, *132*, 16714-16724.
97. S. S. Pandey, T. Inoue, N. Fujikawa, Y. Yamaguchi, S. Hayase, *J. Photochem. Photobiol. A* **2010**, 214, 269-275.
98. S. S. Pandey, T. Inoue, N. Fujikawa, Y. Yamaguchi, S. Hayase, *Thin Solid Films* **2010**, *519*, 1066-1071.
99. Y. Shi, R. B. M. Hill, J. Yum, A. Dualeh, S. Barlow, M. Grätzel, S. R. Marder, M. K. Nazeeruddin, *Angew. Chem.* **2011**, *50*, 6619-6621.
100. J. H. Delcamp, Y. Shi, J. Yum, T. Sajoto, E. Dell'Orto, S. Barlow, M. K. Nazeeruddin, S. R. Marder, M. Grätzel, *Chem. Eur. J.* **2013**, *19*, 1819-1827.

101. A. Dualeh, J. H. Delcamp, M. K. Nazeeruddin, M. Grätzel, *Appl. Phys. Lett.* **2012**, 100, 173512.
102. G. M. Shivashimpi, S. S. Pandey, R. Watanabe, N. Fujikawa, Y. Ogomi, Y. Yamaguchi, S. Hayase, *J. Photochem. Photobiol. A: Chem.* **2014**, *273*, 1-7.
103. F. M. Jradi, X. Kang, D. O'Neil, G. Pajares, Y. A. Getmanenko, P. Szymanski, T. C. Parker, M. A. El-Sayed, S. R. Marder, *Chem. Mater.* **2015**, *27*, 2480-2487.
104. G H. Rao, P. J. S. Rana, A. Islam, S. P. Singh, *ACS Appl. Energy Mater.* **2018**, *1*, 4786-4793.
105. R. Bisht, M. Fairoos M. K., A. K. Singh, J. Nithyanandhan, *J. Org. Chem.* **2017**, *82*, 1920-1930.
106. A. Alagumalai, M. Fairoos M. K., P. Vellimalai, M. C. Sil, J. Nithyanandhan, *ACS Appl. Mater. Interfaces* **2016**, *8*, 35353-35367.
107. H. Chen, M. S. Farahat, K.-Y. Law, D. G. Whitten, *J. Am. Chem. Soc.* **1996**, *118*, 2584-2594.
108. A. K. Singh, M. Fairoos M. K., J. Nithyanandhan, *ACS Appl. Mater. Interfaces* **2020**, *12*, 2555-2565.
109. V. Punitharasu, M. Fairoos M. K., A. K. Singh, J. Nithyanandhan, *ACS Appl. Energy Mater.* **2019**, 2, 8464-8472.
110. S. Alex, U. Santhosh, S. Das, *J. Photochem. Photobiol. A*. **2005**, 172, 63-71.
111. G. H. Rao, A. Venkateswararao, L. Giribabua, S. P. Singh, *Photochem. Photobiol. Sci.* **2016**, 15, 287-296.
112. A. Burke, L. Schmidt-Mende, S. Ito, M. Grätzel, *Chem. Commun.* **2007**, 234-236.
113. A. K. Singh, A. Maibam, B. H. Javaregowda, R. Bisht, A. Kudlu, S. Krishnamurty, K. Krishnamoorthy, J. Nithyanandhan, *J. Phys. Chem. C* **2020**, *124*, 18436-18451.
114. A. K. Singh, J. Nithyanandhan, *ACS Appl. Energy Mater.* **2021**, 4, 13932-13942.
115. K. Ilina, M. Henary, *Chem. Eur. J.* **2021**, *27*, 4230-4248.
116. A. P. Demchenko, (Ed.); *Advanced fluorescence reporters in chemistry and biology I*, Springer, **2010**.
117. F. M. Hamer, (Ed.); *The Cyanine Dyes and Related Compounds,* Interscience Publishers, **1964**.
118. L. Strekowski, (Ed.); *Heterocyclic Polymethine Dyes*, Springer, **2008**.
119. D. M. Sturmer, Syntheses and Properties of Cyanine and Related Dyes. *Chemistry of Heterocyclic Compounds* **1977**, *30*, 441-587.
120. M. Mojzych, M. Henary, *Synthesis of Polymethine Dyes,* Topics in Heterocyclic Chemistry, Springer, **2008**, *14*, 1-9.
121. Y. Nagao, T. Sakai, K. Kozawa, T. Urano, *Dyes Pigm.* **2007**, *73*, 344-352.
122. W. West, *Photogr. Sci. Eng.* **1974**, *18*, 35-48.
123. W. Sun, S. Guo, C. Hu, J. Fan, X. Peng, *Chem. Rev.* **2016**, *116*, 7768-7817.
124. B. A. Armitage, *Top. Curr. Chem.* **2005**, *253*, 55-76.
125. M. Levitus, S. Ranjit, *Q. Rev. Biophys.* **2011**, *44*, 123-151.
126. A. P. Gorka, R. R. Nani, M. J. Schnermann, *Acc. Chem. Res.* **2018**, *51*, 3226-3235.
127. R.K.Pandey, N. James, Y. Chen, M. P. Dobhal, *Top.Heterocycl.Chem.* **2008**, *14*, 41-74.
128. A. Ehret, L. Stuhl, M. T. Spitler, *J. Phys. Chem. B* **2001**, 105, 9960-9965.

129. K. Sayama, S. Tsukagoshi, T. Mori, K. Hara, Y. Ohga, A. Shinpou, Y. Abe, S. Suga, H. Arakawa, *Sol. Energy Mater. Sol. Cells* **2003**, *80*, 47-71.
130. M. Guo, P. Diao, Y.J. Rena, F. Meng, H. Tian, S.-M. Cai, *Sol. Energy Mater. Sol. Cells* **2005**, *88*, 23-35.
131. W. Wu, F. Meng, J. Li, X. Teng, J. Hua, *Synth. Met.* **2009**, 159, 1028-1033.
132. W. Wu, W. Zhan, J. Hua, H. Tian, *Res. Chem. Intermed.* **2008**, *34*, 241-248.
133. W. Wu, J. Hua, Y. Jin, W. Zhan, H. Tian, *Photochem. Photobiol. Sci.* **2008**, *7*, 63-68.
134. X. Ma, J. Hua, W. Wu, Y. Jin, F. Meng, W. Zhan, H. Tian, *Tetrahedron* **2008**, *64*, 345-350.
135. J. Tang, W. Wu, J. Hua, J. Li, X. Li, H. Tian, *Energy Environ. Sci.* **2009**, *2*, 982-990.
136. W. Wu, F. Guo, J. Li, J. He, J. Hua, *Synth. Met.* **2010**, *160*, 1008-1014.
137. Y. Jin, J. Hua, W. Wu, X. Ma, F. Meng, *Synth. Met.* **2008**, *158*, 64-71.
138. T. Ono, T. Yamaguchi, H. Arakawa, *Sol. Energy Mater. Sol. Cells* **2009**, *93*, 831-835.
139. K. Pydzinska, M. Ziółek, *Dyes Pigm.* **2015**, 122, 272-279.
140. K. Funabiki, H. Mase, A. Hibino, N. Tanaka, N. Mizuhata, Y. Sakuragi, A. Nakashima, T. Yoshida, Y. Kubota, M. Matsui, *Energy Environ. Sci.* **2011**, *4*, 2186-2192.
141. T. Geiger, I. Schoger, D. Rentsch, A. C. Véron, F. Oswald, T. Meyer, F. Nüesch, *Int. J. Photoenergy* **2014**, 258984.
142. F. Sauvage, J.-D. Decoppet, M. Zhang, S. M. Zakeeruddin, P. Comte, M. K. Nazeeruddin, P. Wang, M. Grätzel, *J. Am. Chem. Soc.* **2011**, *133*, 9304-9310.
143. A. Ghosh, P. Selvaraj, S. Sundaram, T. K. Mallick, *Sol. Energy* **2018**, *163*, 537-544.
144. T. Baron, W. Naim, I. Nikolinakos, B. Andrin, Y. Pellegrin, D. Jacquemin, S. Haacke, F. Sauvage, F. Odobel, *Angew. Chem.* **2022**, *61*, e202207459.
145. G. M. Fischer, A. P. Ehlers, A. Zumbusch, E. Daltrozzo, *Angew. Chem.* **2007**, *46*, 3750-3753.
146. G. M. Fischer, M. Isomki-Krondahl, I. Gçttker-Schnetmann, E. Daltrozzo, A. Zumbusch, *Chem. Eur. J.* **2009**, *15*, 4857-4864.
147. G. M. Fischer, M. K. Klein, E. Daltrozzo, A. Zumbusch, *Eur. J. Org. Chem.* **2011**, 3421-3429.
148. S. Huang, C. Yang, J. Huang, X. Wang, M. Wang, *Dyes Pigm.* **2018**, *154*, 269-274.
149. C. Yang, X. Wang, M. Wang, K. Xu, C. Xu, *Chem. Eur. J.* **2017**, *23*, 4310-4319.
150. S. Huang, W. Liu, J. Huang, X. Wang, C. Yang, H. Bohra, Q. Liu, M. Wang, *ACS Appl. Bio Mater.* **2018**, *1*, 1109-1117.
151. M. Bai, S. Achilefu, *Heterocycl. Commun.* **2010**, *16*, 213-216.
152. K. Karl, R. Guilard, K. M. Smith, (Ed.); *The Porphyrin Handbook: Phthalocyanines: Spectroscopic and Electrochemical Characterization: Volume 16*, Academic Press, **2003**.
153. C. C. Leznoff, A. B. P. Lever, (Ed.); *Phthalocyanines: Properties and Applications*, John Wiley & Sons Inc, **1996**.
154. A. W. Snow, *109-Phthalocyanine aggregation*. In: *The Porphyrin Handbook*. K. Karl, R. Guilard, K. M. Smith, (Ed.); Academic Press, **2003**.
155. G. Bottari, G. de la Torre, D. M. Guldi, T. Torres, *Chem. Rev.* **2010**, *110*, 6768-6816.

156. O. A. Melville, B. H. Lessard, T. P. Bender, *ACS Appl. Mater. Interfaces* **2015**, *7*, 13105-13118.
157. M. V. Martínez-Diaz, T. Torres, *On the Significance of Phthalocyanines in Solar Cells*. In: *Handbook of Porphyrin Science: Volume 10*, K. Karl, K. M. Smith, R. Guilard, (Ed.); World Scientific, **2010**.
158. A. Sorokin, *Chem. Rev.* **2013**, *113*, 8152-8191.
159. P.-C. Lo, M. S. Rodríguez-Morgade, R. K. Pandey, D. K. P. Ng, T. Torres, F. Dumoulin, *Chem. Soc. Rev.* **2020**, *49*, 1041-1056.
160. L. Martín-Gomis, F. Fernández-Lázaro, and A. Sastre-Santos, *J. Mater. Chem. A* **2014**, *2*, 15672-15682.
161. V. K. Singh, R. K. Kanaparthi, L. Giribadu, *RSC Adv.* **2014**, *4*, 6970-6984.
162. D. Schlettwein, T. Nyokong, *Phthalocyanines as Sensitizers in Dye-Sensitized Solar Cells*. In: *Handbook of Porphyrin Science: Volume 10*, K. Karl, K. M. Smith, R. Guilard, (Ed.); World Scientific, **2010**.
163. T. Ikeuchi, H. Nomoto, N. Masaki, M. J. Griffith, S. Mori, M. Kimura, *Chem. Commun.* **2014**, *50*, 1941-1943.
164. Y. Shen, L. Wang, Z. Lu, Y Wei, Q. Zhou, H. Mao, H. Xu, *Thin Solid Films* **1995**, *257*, 144-146.
165. M. K. Nazeeruddin, R. Humphry-Baker, M. Grätzel, D. Wöhrle, G. Schnurpfeil, G. Schneider, A. Hirth, N. Trombach, *J. Porphyr. Phthalocyanines* **1999**, *3*, 230-237.
166. J.-J. Cid, J.-H. Yum, S.-R. Jang, M. K. Nazeeruddin, E. Martínez-Ferrero, E. Palomares, J. Ko, M. Grätzel, T. Torres, *Angew. Chem.* **2007**, *119*, 8510-8514.
167. P. Y. Reddy, L. Giribabu, C. Lyness, H. J. Snaith, C. Vijaykumar, M. Chandrasekharam, M. Lakshmikantam, J. H. Yum, K. Kalyanasundaram, M. Grätzel, M. K. Nazeeruddin, *Angew. Chem.* **2007**, *46*, 373-380.
168. G. Pozzi, S. Quici, M. C. Raffo, C. A. Bignozzi, S. Caramori, M. Orlandi*, J. Phys. Chem. C* **2011**, *115*, 3777-3788.
169. M. Ince, F. Cardinali, J. H. Yum, M. V. Martínez-Díaz, M. K. Nazeeruddin, M. Grätzel, T. Torres, *Chem. Eur. J.* **2012**, *18*, 6343-6348.
170. H. Huang, Z. Cao, X. Li, L. Zhang, X. Liu, H. Zhao, S. Tan, *Synth. Met.* **2012**, *162*, 2316-2323.
171. S. Eu, T. Katoh, T. Umeyama, Y. Matano, H. Imahori, *Dalton Trans.* **2008**, 5476-5483.
172. N. Masilela, N. Nombona, T. Loewenstein, T. Nyokong, D. Schlettwein, *J. Porphyr. Phthalocyanines* **2010**, *14*, 985-992.
173. M Kimura, H. Nomoto, N. Masaki, S. Mori, *Angew. Chem. Int. Ed.* **2012**, *51*, 4371-4374.
174. S. Yamamoto, T. Ikeuchi, S. Mori, M. Kimura, *Asian J. Org. Chem.* **2014**, *3*, 1083-1088.
175. S. Tortelli, M. Cavazzini, S. Orlandi, G. Pozzi, I. Pecnikaj, S. Caramori, R. Boaretto, *J. Fluor. Chem.* **2016**, *188*, 110-116.
176. L. Tejerina, E. Caballero, M. V. Martínez-Díaz, M. K. Nazeeruddin, M. Grätzel, T. Torres, *J. Porphyr. Phthalocyanines* **2016**, *20*, 1361-1367.
177. R. Milan, G. S. Selopal, M. Cavazzini, S. Orlandi, R. Boaretto, S. Caramori, I. Concina, G. Pozzi, *Sci. Rep.* **2017**, *7*, 1-10.

178. D. G. Solğun, S. Horoz, M. S. Ağırtaş, *Inorg. Nano-Met. Chem.* **2018**, *10*, 508-514.
179. B. Ghazal, K. Azizi, E. F. Ewies, A. S. A. Youssef, V. M. Mwalukuku, R. Demadrille, T. Torres, S. Makhseed, *Molecules* **2020**, *25*, 1692.
180. K. Harmandar, K. Granados-Tavera, M. Gezgin, M. Nebioğlu, I. Şişman, G. Cárdenas-Jíron, D. Attila, A. G. Gürek, *New J. Chem.* **2022**, *46*, 714-725.
181. M. Kimura, H. Suzuki, Y. Tohata, T. Ikeuchi, S. Yamamoto, N. Kobayashi, *Asian J. Org. Chem.* **2017**, *6*, 544-550.
182. L. Martín-Gomis, C. Parejo, J. C. Álvarez, F. Fernández-Lázaro, Á. Sastre-Santos, *Inorganica Chim. Acta* **2017**, *468*, 327-333.
183. L. Giribabu, C. V. Kumar, V. Gopal, P. Yella, C Srinivasa, S. Jang, J. H. Yum, M. K. Nazeeruddin, M. Grätzel, *Sol. Energy Mater. Sol. Cells* **2007**, *91*, 1611-1617.
184. L. Giribabu, C. V. Kumar, M. Raghavender, K. Somaiah, P. Yella, P. Venkateswara, *J. Nano Res.* **2008**, *2*, 39-48.
185. S. Cogal, S. Erten-Ela, K. Ocakoglu, A. U. Oksuz, *Dyes Pigm.* **2015**, 113, 474-480.
186. H. E. A. Ali, A. Altındal, S. Altun, Z. Odabaş, *Dyes Pigm.* **2016**, 124, 180-187.
187. E. Fazio, J. Jaramillo-García, M. Medel, M. Urbani, M. Grätzel, M. K. Nazeerudin, G. de la Torre, T. Torres, *ChemistryOpen* **2017**, *6*, 121-127.
188. L. Tejerina, M. Victoria Martínez-Díaz, M. K. Nazeeruddin, M. Grätzel, T. Torres, *ChemPlusChem* **2017**, *82*, 132-135.
189. T. Baron, X. Zarate, Y. Hidalgo-Rosa, M. Zambrano-Angulo, K. Mall-Haidaraly, R. Pino-Rios, Y. Pellegrin, F. Odobel, G. Cárdenas-Jíron, *C. R. Chimie* **2021**, *24*, 157-170
190. S. Mori, M. Nagata, Y. Nakahata, K. Yasuta, R. Goto, M. Kimura, M. Taya, *J. Am. Chem. Soc.* **2010**, *132*, 4054-4055.
191. M. Ince, R. Kuboi, T. Ince, K. Yoshimura, D. Motoyoshi, M. Sonobe, R. Kudo, S. Mori, M. Kimura, T. Torres, *Sustain.* **2021**, *5*, 584-589.
192. G. Tunç, E. Güzel, I. Şişman, V. Ahsen, G. Cárdenas-Jíron, A. G. Gürek, *New J. Chem.* **2019**, *43*, 14390-14401.
193. Ismael López-Duarte, M. Wang, R. Humphry-Baker, M. Ince, M. V. Martínez-Díaz, M. K. Nazeeruddin, T. Torres, M. Grätzel, *Angew. Chem. Int. Ed.* **2012**, *51*, 1895-1898.
194. M.-E. Ragoussi, J. Cid, J. H. Yum, G. de la Torre, D. Di Censo, M. Grätzel, M. K. Nazeeruddin, T. Torres, *Angew. Chem. Int. Ed.* **2012**, *51*, 4375-4378.
195. J. Cid, M. Garca-Iglesias, J. H. Yum, A. Forneli, J. Albero, E. Martínez-Ferrero, P. Vázquez, M. Grätzel, M. K. Nazeeruddin, E. Palomares, T. Torres, *Chem. Eur. J.* **2009**, *15*, 5130-5137.
196. F. Silvestri, M. García-Iglesias, J. H. Yum, P. Vázquez, M. V. Martínez-Díaz, M. Grätzel, M. K. Nazeeruddin, T. Torres, *J. Porphyr. Phthalocyanines* **2009**, *13*, 369-375.
197. G. Zanotti, N. Angelini, A. M. Paoletti, G. Pennesi, G. Rossi, A. A. Bonapasta, G. Mattioli, A. Di Carlo, T. M. Brown, A. Lembo, A. Reale, *Dalton Trans.* **2011**, *40*, 38-40.
198. M. Garca-Iglesias, J. Cid, J. H. Yum, A. Forneli, P. Vázquez, M. K. Nazeeruddin, E. Palomares, M. Grätzel, T. Torres, *Energy Environ. Sci.* **2011**, *4*, 189-194.
199. M.-E. Ragoussi, J. H. Yum, A. K. Chandiran, M. Ince, G. de la Torre, M. Grätzel, M. K. Nazeeruddin, T. Torres, *ChemPhysChem* **2014**, *15*, 1033-1036.

200. M. Ince, J. H. Yum, Y. Kim, S. Mathew, M. Grätzel, T. Torres, M. K. Nazeeruddin, J. *Phys. Chem. C* **2014**, *118*, 17166-17170.
201. J. S. Pita, M. Urbani, G. Bottari, M. Ince, S. A. Kumar, A. K. Chandiran, J. H. Yum, M. Grätzel, M. K. Nazeeruddin, T. Torres, *ChemPlusChem* **2017**, *82*, 1057-1061.
202. J. A. Stratton, (Ed.); *Electromagnetic Theory*, McGraw-Hill Book Company, **1941**.
203. Y. Bai, I. Mora-Seró, F. De Angelis, J. Bisquert, P. Wang, *Chem. Rev.* **2014**, *114*, 10095-10130.
204. D. Sengupta, P. Das, B. Mondal, K. Mukherjee, *Renew. Sust. Energ. Rev.* **2016**, *60*, 356-376.
205. M. S. Ahmad, A. K. Pandey, N. Abd Rahima, *Renew. Sust. Energ. Rev.* **2017**, *77*, 89-108.
206. S. M. Gupta, M. Tripathi, *Cent. Eur. J. Chem.* **2012**, *10*, 279-294.
207. M. A. Ahmad, B. Prelot, F. Dufour, O. Durupthy, A. Razafitianamaharavo, J. M. Douillard, C. Chaneac, F. Villiéras, J. Zajac, *J. Phys. Chem. C* **2013**, *117*, 4459-4469.
208. A. N. Banerjee, *Nanotechnol. Sci. Appl.* **2011**, *4*, 35-65.
209. J. Maçaira, L. Andrade, A. Mendes, *Renew. Sust. Energ. Rev.* **2013**, *27*, 334-349.
210. J. S. Shaikh, N. S. Shaikh, S. S. Mali, J. V. Patil, K. K. Pawar, P. Kanjanaboos, C. K. Hong, J. H. Kim, P. S. Patil, *Nanoscale* **2018**, *10*, 4987.5034.
211. G. Zhang, S. Finefrock, D. Liang, G. G. Yadav, H. Yang, H. Fang, Y. Wu, *Nanoscale* **2011**, *3*, 2430-2443.
212. C. Cavallo, F. Di Pascasio, A. Latini, M. Bonomo, D. Dini, *J. Nanomater.* **2017**, 5323164.
213. L. Zhu, Y. L. Zhao, X. P. Lin, X. Q. Gu, Y. H. Qiang, *Superlattices Microstruct.* **2014**, *65*, 152-160.
214. R. Jose, V. Thavasi, S. Ramakrishna, *J. Am. Ceram. Soc.* **2009**, *92*, 289-301.
215. R. G. Breckenridge, W. R. Hosler, *Phys. Rev.* **1953**, *91*, 793-802.
216. D. F. Watson, G. J. Meyer, *Coord. Chem. Rev.* **2004**, *248*, 1391-1406.
217. B. Roose, S. Pathak, U. Steiner, *Chem. Soc. Rev.* **2015**, *44*, 8326-8349.
218. A. K. Chandiran, F. Sauvage, M. Casas-Cabanas, P. Comte, S. M. Zakeeruddin, M. Grätzel, *J. Phys. Chem. C* **2010**, *114*, 15849-15856.
219. R. Vittal, K.-C. Ho, Renew. *Sust. Energ. Rev.* **2017**, *70*, 920-935.
220. R. Kumar, A. Umar, G. Kumar, H. S. Nalwa, A. Kumar, M. S. Akhtar, *J. Mater. Sci.* **2017**, *52*, 4743-4795.
221. V. Consonni, J. Briscoe, E. Kärber, X. Li, T. Cossuet, *Nanotechnology* **2019**, *30*, 362001.
222. H.-Y. Chen, D.-B. Kuang, C.-Y. Su, *J. Mater. Chem.* **2012**, *22*, 15475-15489.
223. Q. Wali, A. Fakharuddin, R. Jose, *J. Power Sources* **2015**, *293*, 1039-1052.
224. K. Sayama, H. Sugihara, H. Arakawa, *Chem. Mater.* **1998**, *10*, 3825-3832.
225. C. Magne, F. Dufour, F. Labat, G. Lancel, O. Durupthy, S. Cassaignon, T. Pauporté, *J. Photochem. Photobiol. A* **2012**, *232*, 22-31.
226. A. Alizadeh, M. Roudgar-Amoli, S.-M. Bonyad-Shekalgourabi, Z. Shariatinia, M. Mahmoudi, F. Saadat, *Renew. Sust. Energ. Rev.* **2022**, *157*, 112047.
227. B. Tan, E. Toman, Y. Li, Y. Wu, *J. Am. Chem. Soc.* **2007**, *129*, 4162-4163.

228. Y. Suzuki, Y. Okamoto, N. Ishii, *J. Phys. Conf. Ser.* **2015**, *596*, 012001.
229. A. Janotti, C. G. Van de Walle, *Rep. Prog. Phys.* **2009**, *72*, 126501.
230. C. G. Fonstad, R. H. Rediker, *J. Appl. Phys.* **1971**, *42*, 2911-2918.
231. A. N. M. Green, E. Palomares, S. A. Haque, J. M. Kroon, J. R. Durrant, *J. Phys. Chem. B* **2005**, *109*, 12525-12533.
232. P. Tiwana, P. Docampo, M. B. Johnston, H. J. Snaith, L. M. Herz, *ACS Nano* **2011**, *5*, 5158-5166.
233. P. Pratim Das, A. Roy, S. Das, P. S. Devi, *Phys. Chem. Chem. Phys.* **2016**, *18*, 1429-1438.
234. T. J. Coutts, D. L. Young, X. Li, W. P. Mulligan, X. Wu, *J. Vac. Sci. Technol. A* **2000**, *18*, 2646-2660.
235. S. Ito, T. N. Murakami, P. Comte, P. Liska, C. Grätzel, M. K. Nazeeruddin, M. Grätzel, *Thin Solid Films* **2008**, *516*, 4613-4619.
236. M. K. Nazeeruddin, A. Kay, I. Rodicio, R. Humphry-Baker, E. Müller, P. Liska, N. Vlachopoulos, M. Grätzel, *J. Am. Chem. So*c. **1993**, *115*, 6382-6390.
237. S. Ito, P. Liska, R. Charvet, P. Comte, P. Péchy, M. K. Nazeeruddin, S. M. Zakeeruddin, M. Grätzel, *Chem. Commun.* **2005**, 4351-4353.
238. P. Wang, S.M. Zakeeruddin, P. Comte, R. Charvet, R. Humphry-Baker, M. Grätzel, *J. Phys. Chem. B* **2003**, *107*, 14336-14341.
239. Z. Zhang, S. Ito, B. O'Regan, D. Kuang, S. M. Zakeeruddin, P. Liska, R. Charvet, P. Comte, M. K. Nazeeruddin, P. Péchy, R. Humphry-Baker, T. Koyanagi, T. Mizuno, M. Grätzel, *Z. Phys. Chem.* **2007**, *221*, 319-327.
240. S. Ito, M. K. Nazeeruddin, P. Liska, P. Comte, R. Charvet, P. Péchy, M. Jirousek, A. Kay, S. M. Zakeeruddin, M. Grätzel, *Prog. Photovolt.* **2006**, *14*, 589-601.
241. M. Wang, C. Grätzel, S. M. Zakeeruddin, M. Grätzel, *Energy Environ. Sci.* **2012**, *5*, 9394-9405.
242. J. Wu, Z. Lan, J. Lin, M. Huang, Y. Huang, L. Fan, G. Luo, *Chem. Rev.* **2015**, *115*, 2136-2173.
243. I. Benesperi, H. Michaels, M. Freitag, *J. Mater. Chem. C* **2018**, *6*, 11903-11942.
244. D. P. Hagberg, J. H. Yum, H. J. Lee, F. De Angelis, T. Marinado, K. M. Karlsson, R. Humphry-Baker, L. Sun, A. Hagfeldt, M. Grätzel, M. K. Nazeeruddin, *J. Am. Chem. Soc.* **2008**, *130*, 6259-6266.
245. C. A. Bignozzi, R. Argazzi, R. Boaretto, E. Busatto, S. Carli, F. Ronconi, S. Caramori, *Coord. Chem. Rev.* **2013**, *257*, 1472-1492.
246. J. G. Rowley, B. H. Farnum, S. Ardo, G. J. Meyer, *J. Phys. Chem. Lett.* **2010**, *1*, 3132-3140.
247. M. Bonomo, A. Di Carlo, D. Dini, *J. Electrochem. Soc.* **2018**, *165*, H889.
248. Y. Saygili, M. Stojanovic, N. Flores-Díaz, S. M. Zakeeruddin, N. Vlachopoulos, M. Grätzel, A. Hagfeldt, *Inorganics* **2019**, *7*, 30.
249. J. Cong, X. Yang, L. Kloo, L. Sun, *Energy Environ. Sci.* **2012**, *5*, 9180-9194.
250. J. Baillargeon, Y. Xie, A. L. Raithel, B. Ghaffari, R. J. Staples, T. W. Hamann, *Inorg. Chem.* **2018**, *57*, 11633-11645.

251. E. Mosconi, J. H. Yum, F. Kessler, C. J. Gómez García, C. Zuccaccia, A. Cinti, M. K. Nazeeruddin, M. Grätzel, F. De Angelis, *J. Am. Chem. Soc.* **2012**, *134*, 19438-19453.
252. H. Nusbaumer, J. E. Moser, S. M. Zakeeruddin, M. K. Nazeeruddin, M. Grätzel, *J. Phys. Chem. B* **2001**, *105*, 10461-10464.
253. H. Nusbaumer, S. M. Zakeeruddin, J. E. Moser, M. Grätzel, *Chem. Eur. J.* **2003**, *9*, 3756-3763.
254. P. J. Cameron, L. M. Peter, S. M. Zakeeruddin, M. Grätzel, *Coord. Chem. Rev.* **2004**, *248*, 1447-1453.
255. S. A. Sapp, C. M. M. Elliott, C. Contado, S. Caramori, S. Bignozzi, *J. Am. Chem. Soc.* **2002**, *124*, 11215-11222.
256. F. Bella, S. Galliano, C. Gerbaldi, G. Viscardi, *Energies* **2016**, *9*, 384.
257. T. W. Hamann, *Dalton Trans.* **2012**, *41*, 3111-3115.
258. S. M. Feldt, P. W. Lohse, F. Kessler, M. K. Nazeeruddin, M. Grätzel, G. Boschloo, A. Hagfeldt, *Phys. Chem. Chem. Phys.* **2013**, *15*, 7087-7097.
259. N. A. Lee, B. A. Frenzel, J. Rochford, S. E. Hightower, *Eur. J. Inorg. Chem.* **2015**, 3843-3849.
260. K. B. Aribia , T. Moehl , S. M. Zakeeruddin, M. Grätzel, *Chem. Sci.* **2013**, *4*, 454-459.
261. Z.-Z. Sun, K.-M. Zheng, Q.-S. Li, Z.-S. Li, *RSC Adv.* **2014**, *4*, 31544-31551.
262. J. H. Yum, E. Baranoff, F. Kessler, T. Moehl, S. Ahmad, T. Bessho, A. Marchioro, E. Ghadiri, J.-E. Moser, C. Yi, M. K. Nazeeruddin, M. Grätzel, *Nat. Commun.* **2012**, *3*, 631.
263. J. Burschka, A. Dualeh, F. Kessler, E. Baranoff, N. Cevey-Ha, C. Yi, M. K. Nazeeruddin, M. Grätzel, *J. Am. Chem. Soc.* **2011**, *133*, 18042-18045.
264. S.M. Feldt, E. A. Gibson, E. Gabrielsson, L. Sun, G: Boschloo, A. Hagfeldt, *J. Am. Chem. Soc.* **2010**, *132*, 16714-16724.
265. S. M. Feldt, G. Wang, G. Boschloo, A. Hagfeldt, *J. Phys. Chem. C* **2011**, *115*, 21500-21507.
266. J. T. Kirner, C. M. Elliott, *J. Phys. Chem. C* **2015**, *119*, 17502-17514.
267. S. Koussi-Daoud, D. Schaming, L. Fillaud, G. Trippé-Allard, F. Lafolet, E. Polanski, K. Nonomura, N. Vlachopoulos, A. Hagfeldt, J.-C. Lacroix, *Electrochim. Acta* **2015**, *179*, 237-240.
268. J. Gao, M. B. Achari, L. Kloo, *Chem. Commun.* **2014**, 50, 6249-6251.
269. M. K. Kashif, J. C. Axelson, N. W. Duffy, C. M. Forsyth, C. J. Chang, J. R. Long, L. Spiccia, U. Bach, *J. Am. Chem. Soc.* **2012**, *134*, 16646-16653.
270. M. K. Kashif, M. Nippe, N. W. Duffy, C. M. Forsyth, C. J. Chang, J. R. Long, L. Spiccia, U. Bach, *Angew. Chem. Int. Ed.* **2013**, *52*, 5527-5531
271. M. Nasr-Esfahani, M. Zendehdel, N. Yaghoobi Nia, B. Jafari, M. Khosravi Babadi, *RSC Adv.* **2014**, *4*, 15961-15967.
272. T. G. Appleton, *J. Chem. Educ.* **1977**, *54*, 443-444.
273. Y. Xie, J. Baillargeon, T. W. Hamann, *J. Phys. Chem. C* **2015**, *119*, 28155-28166.
274. N. Mariotti, M. Bonomo, L. Fagiolari, N. Barbero, C. Gerbaldi, F. Bella, C. Barolo, *Green Chem.* **2020**, *22*, 7168-7218.
275. K. S. Srivishnu, S. Prasanthkumar, L. Giribabu, *Mater. Adv.* **2021**, *2*, 1229-1247.

276. A. Colombo , C. Dragonetti, D. Roberto, F. Fagnani, *Molecules* **2021**, *26*, 194.
277. C. E. Housecroft, E. C. Constable, *Chem. Sci.* **2022**, *13*, 1225-1262.
278. M. Magni, P. Biagini, A. Colombo, C. Dragonetti, D. Roberto, A. Valore, *Coord. Chem. Rev.* **2016**, *322*, 69-93.
279. C. M. Groeneveld, S. Dahlin, B. Reinhammar, G. W. Canters, *J. Am. Chem. Soc.* **1987**, *109*, 3247-3250.
280. A.G. Sykes, *Adv. Inorg. Chem.* **1991**, *107*, 377-480.
281. P. Kyritsis, C. Dennison, W. J. Ingledew, W. McFarlane, A. G. Sykes, *Inorg. Chem.* **1995**, *34*, 5370-5374.
282. S. Hattori, Y. Wada, S. Yanagida, S. Fukuzumi, *J. Am. Chem. Soc.* **2005**, *127*, 9648-9654.
283. Y. Saygili, M. Söderberg, N. Pellet, F. Giordano, Y. Cao, A. B. Muñoz-García, S. M. Zakeeruddin, N. Vlachopoulos, M. Pavone, G. Boschloo, L. Kavan, J.-E. Moser, M. Grätzel, A. Hagfeldt, M. Freitag, *J. Am. Chem. Soc.* **2016**, *138*, 15087-15096.
284. M. Freitag, J. Teuscher, Y. Saygili, X. Zhang, F. Giordano, P. Liska, J. Hua, S. M. Zakeeruddin, J.-E. Moser, M. Grätzel, A. Hagfeldt, *Nat. Photonics* **2017**, *11*, 372–378.
285. D. Zhang, M. Stojanovic, Y. Ren, Y. Cao, F. T. Eickemeyer, E. Socie, N. Vlachopoulos, J.-E. Moser, S. M. Zakeeruddin, A. Hagfeldt, M. Grätzel, *Nat. Commun.* **2021**, *12*, 1777.
286. M. Brugnati, S. Caramori, S. Cazzanti, L. Marchini, R. Argazzi, C. A. Bignozzi, *Int. J. Photoenergy* **2007**, 1-10.
287. T. Higashino, H. Iiyama, S. Nimura, Y. Kurumisawa, H. Imahori, *Inorg. Chem.* **2020**, *59*, 452-459.
288. A. Colombo, R. Ossola, M. Magni, D. Roberto, D. Jacquemin, C. Castellano, F. Demartina, C. Dragonetti, *Dalton Trans.* **2018**, *47*, 1018-1022.
289. C. Dragonetti, M. Magni, A. Colombo, F. Melchiorre, P. Biagini, D. Roberto, *ACS Appl. Energy Mater.* **2018**, *1*, 751-756.
290. E. Benazzi, M. Magni, A. Colombo, C. Dragonetti, S. Caramori, C. A. Bignozzi, R. Grisorio, G Suranna, M. P. Cipolla, M. Manca, D. Roberto, *Electrochim. Acta* **2018**, *271*, 180-189.
291. A. Colombo, C. Dragonetti, M. Magni, D. Roberto, F. Demartin, S. Caramori, C. A. Bignozzi, *ACS Appl. Mater. Interfaces* **2014**, *6*, 13945-13955.
292. M. Magni, R. Giannuzzi, A. Colombo, M. P. Cipolla, C. Dragonetti, S. Caramori, S. Carli, R. Grisorio, G. Suranna, C. A. Bignozzi, D. Roberto, M. Manca, *Inorg. Chem.* **2016**, *55*, 5245-5253.
293. A. Colombo, G. Di Carlo, C. Dragonetti, M. Magni, A. Orbelli Biroli, M. Pizzotti, D. Roberto, F. Tessore, E. Benazzi, C. A. Bignozzi, L. Casarin, S. Caramori, *Inorg. Chem.* **2017**, *56*, 14189-14197.
294. J. Li, X. Yang, Z. Yu, G. G. Gurzadyan, M. Cheng, F. Zhang, J. Cong, W. Wang, H. Wang, X. Li, L. Kloo, M. Wang, L. Sun, *RSC Adv.* **2017**, *7*, 4611-4615.
295. M. Giordano, G. Volpi, M. Bonomo, P. Mariani, C. Garino, G. Viscardi, *New J. Chem.* **2021**, *45*, 15303-15311.

296. Y. Cao, Y. Saygili, A. Ummadisingu, J. Teuscher, J. Luo, N. Pellet, F. Giordano, S. M Zakeeruddin, J.-E. Moser, M. Freitag, A. Hagfeldt, M. Grätzel, *Nat. Commun.* **2017**, *8*, 15390.
297. M. Karpacheva, F. J. Malzner, C. Wobill, A. Büttner, E. C. Constable, C. E. Housecroft, *Dyes Pigm.* **2018**, *156*, 410-416.
298. Y. Saygili, M. Stojanovic, H.-S. Kim, J. Teuscher, R. Scopelliti, M. Freitag, S. M. Zakeeruddin, J.-E. Moser, M. Grätzel, A. Hagfeldt, *J. Phys. Chem. C* **2020**, *124*, 7071-7081.
299. Y. Bai, Q. Yu, N. Cai, Y. Wang, M. Zhang, P. Wang, *Chem. Commun.* **2011**, *47*, 4376-4378.
300. M. Freitag, F. Giordano, W. Yang, M. Pazoki, Y. Hao, B. Zietz, M. Grätzel, A. Hagfeldt, G. Boschloo, *J. Phys. Chem. C* **2016**, *120*, 9595-9603.
301. A. K. Ichinaga, J. R. Kirchhoff, D. R. McMillin, C. O. Dietrich-Buchecker, P. A. Marnot, J. P. Sauvage, *Inorg. Chem.* **1987**, *26*, 4290-4292.
302. J. Cong, d. Kinschel, Q. Daniel, m. Safdari, E. Gabrielsson, H. Chen, P. H. Svensson, L. Sun, L. Kloo, *J. Mater. Chem. A* **2016**, *4*, 14550-14554.
303. B. Selvaraj, G. Shanmugam, S. Kamaraj, A. Gunasekaran, A. Sambandam, *Inorg. Chem.* **2021**, *60*, 1937-1947.
304. Y. Wang, T. W. Hamann, *Chem. Commun.* **2018**, *54*, 12361-12364.
305. S. O. Fürer, R. A. Milhuisen, M. K. Kashif, S. R. Raga, S. S. Acharya, C. Forsyth, M. Liu, L. Frazer, N. W. Duffy, C. A. Ohlin, A. M. Funston, Y. Tachibana, U. Bach, *Adv. Energy Mater.* **2020**, *10*, 2002067.
306. K. Kannankutty, C.-C. Chen, V. S. Nguyen, Y.-C. Lin, H.-H. Chou, C.-Y. Yeh, T.-C. Wei, *ACS Appl. Mater. Interfaces* **2020**, **12**, 5812-5819.
307. L. Kavan, Y. Saygili, M. Freitag, S. M. Zakeeruddin, A. Hagfeldt, M. Grätzel, *Electrochim. Acta* **2017**, *227*, 194-202.
308. P. Ferdowsi, Y. Saygili, S. M. Zakeeruddin, J. Mokhtari, M. Grätzel, A. Hagfeldt, L. Kavan, *Electrochim. Acta* **2018**, *265*, 194-201.
309. W. L. Hoffeditz, M. J. Katz, P. Deria, G. E. Cutsail, M. J. Pellin, O. K. Farha, J. T. Hupp, *J. Phys. Chem. C* **2016**, *120*, 3731-3740.
310. H. Michaels, I. Benesperi, T. Edvinsson, A. B. Muñoz-García, M. Pavone, G. Boschloo, M. Freitag, *Inorganics* **2018**, *6*, 53.
311. R. R. Rodrigues, J. M. Lee, N. S. Taylor, H. Cheema, L. Chen, R. C. Fortenberry, J. H. Delcamp, J. W. Jurss, *Dalton Trans.* **2020**, *49*, 343-355.
312. M. Hu, J. Shen, Z. Yu, R.-Z. Liao, G. G. Gurzadyan, X. Yang, A. Hagfeldt, M. Wang, L. Sun, *ACS Appl. Mater. Interfaces* **2018**, *10*, 30409-30416.
313. H. Rui, J. Shen, Z. Yu, L. Li, H. Han, L. Sun, *Angew. Chem. Int. Ed.* **2021**, *60*, 16156-16163.
314. T. J. Kealy, P. L. Pauson, *Nature* **1951**, *168*, 1039-1040.
315. D. Astruc, *Eur. J. Inorg. Chem.* **2017**, 6-29.
316. B. Gregg, F. Pichot, S. Ferrere and C. Fields, *J. Phys. Chem. B* **2001**, *105*, 1422-1429.
317. S. Feldt, U. Cappel, E. J. Johansson, G. Boschloo and A. Hagfeldt, *J. Phys. Chem. C* **2010**, *114*, 10551-10558.

318. T. Daeneke, T.-H. Kwon, A. B. Holmes, N. W. Duffy, U. Bach, L. Spiccia, *Nat. Chem.* **2011**, *3*, 211-215.
319. I. Noviandri, K. N. Brown, D. S. Fleming, P. T. Gulyas, P. A. Lay, A. F. Masters, L. Phillips, *J. Phys. Chem. B* **1999**, *103*, 6713-6722.
320. K. N. Brown, P. T. Gulyas, P. A. Lay, N. S. McAlpine, A. F. Masters, L. Phillips, *J. Chem. Soc. Dalton Trans.* **1993**, 835-840.
321. A. Paul, R. Borrelli, H. Bouyanfif, S. Gottis, F. Sauvage, *ACS Omega* **2019**, *4*, 14780-14789.
322. T. Daeneke, A. J. Mozer, T.-H. Kwon, N. W. Duffy, A. B. Holmes, U. Bach, L. Spiccia, *Energy Environ. Sci.* **2012**, *5*, 7090-7099.
323. T. Daeneke, Y. Uemura, N. W. Duffy, A. J. Mozer, N. Koumura, U. Bach, L. Spiccia, *Adv. Mater.* **2012**, *24*, 1222-1225.
324. I. A. Rutkowska, A. Andrearczyk, S. Zoladek, M. Goral, K. Darowicki, P. J. Kulesza, *J. Solid State Electrochem.* **2011**, *15*, 2545-2552.
325. R. R. Rodrigues, H. Cheema, J. H. Delcamp, *Angew. Chem. Int. Ed.* **2018**, *57*, 5472-5476.
326. M. M. Morrison, D. T. Sawyer, *Inorg. Chem.* **1978**, *17*, 333-337.
327. I. R. Perera, A. Gupta, W. Xiang, T. Daeneke, U. Bach, R. A. Evans, C. A. Ohlin, L. Spiccia, *Phys. Chem. Chem. Phys.* **2014**, *16*, 12021-12028.
328. S. Carli, E. Benazzi, L. Casarin, T. Bernardi, V. Bertolasi, R. Argazzi, S. Caramori, C. A. Bignozzi, *Phys. Chem. Chem. Phys.* **2016**, *18*, 5949-5956.
329. J. Takaichi, Y. Morimoto, K. Ohkubo, C. Shimokawa, T. Hojo, S. Mori, H. Asahara, H. Sugimoto, N. Fujieda, N. Nishiwaki, *Inorg. Chem.* **2014**, *53*, 6159-6169.
330. T. C. Li, A. M. Spokoyny, C. She, O. K. Farha, C. A. Mirkin, T. J. Marks, J. T. Hupp, *J. Am. Chem. Soc.* **2010**, *132*, 4580-4582.
331. M. F. Hawthorne, J. I. Zink, J. M. Skelton, M. J. Bayer, C. Liu, E. Livshits, R. Baer, D. Neuhauser, *Science* **2004**, *303*, 1849-1851.
332. A. M. Spokoyny, T. C. Li, O. K. Farha, C. W. Machan, C. She, C. L. Stern, T. J. Marks, J. T. Hupp, C. A. Mirkin, *Angew. Chem. Int. Ed.* **2010**, *49*, 5339-5343.
333. A. Apostolopoulou, M. Vlasiou, P. A. Tziouris, C. Tsiafoulis, A. C. Tsipis, D. Rehder, T. A. Kabanos, A. D. Keramidas, E. Stathatos, *Inorg. Chem.* **2015**, *54*, 3979-3988.
334. K. Oyaizu, N. Hayo, Y. Sasada, F. Kato, H. Nishide, *Dalt. Trans.* **2013**, *42*, 16090-16095.
335. Z. Zhang, P. Chen, T. N. Murakami, S. M. Zakeeruddin, M. Grätzel, *Adv. Funct. Mater.* **2008**, *18*, 341-346.
336. D. Li, H. Li, Y. Luo, K. Li, Q. Meng, M. Armand, L. Chen, *Adv. Funct. Mater.* **2010**, *20*, 3358-3365.
337. S. Yang, H. Kou, H. Wang, K. Cheng, J. Wang, *New J. Chem.* **2010**, *34*, 313-317.
338. Z. Ku, X. Li, G. Liu, H. Wang, Y. Rong, M. Xu, L. Liu, M. Hu, Y. Yang, H. Han, *J. Mater. Chem. A* **2013**, *1*, 237-240.
339. K. Funabiki, Y. Saito, M. Doi, K. Yamada, Y. Yoshikawa, K. Manseki, Y. Kubota, M. Matsui, *Tetrahedron* **2014**, *70*, 6312-6317.
340. X. Li, Z. Ku, Y. Rong, G. Liu, L. Liu, T. Liu, M. Hu, Y. Yang, H. Wang, M. Xu, P. Xiang, H. Han, *Phys. Chem. Chem. Phys.* **2012**, *14*, 14383-14390.

341. H. Tian, E. Gabrielsson, P. W. Lohse, N. Vlachopoulos, L. Kloo, A. Hagfeldt, L. Sun, *Energy Environ. Sci.* **2012**, *5*, 9752-9755.
342. A. Hilmi, T. A. Shoker, T. H. Ghaddar, *ACS Appl. Mater. Interfaces* **2014**, *6*, 8744-8753.
343. H. Tian, L. Sun, *J. Mater. Chem.* **2011**, *21*, 10592-10601.
344. H. Tian, X. Jiang, Z. Yu, L. Kloo, A. Hagfeldt, L. Sun, *Angew. Chem.* **2010**, *122*, 7486-7489.
345. M. M. Rahman, J. Wang, N. C. D. Nath, J. J. Lee, *Electrochim. Acta* **2018**, *286*, 39-46.
346. Y. Zhang, Z. Sun, C. Shi, F. Yan, *RSC Adv.* **2016**, *6*, 70460-70467.
347. T. C. Li, F. Fabregat-Santiago, O. K. Farha, A. M. Spokoyny, S. R. Raga, J. Bisquert, C. A. Mirkin, T. J. Marks, J. T. Hupp, *J. Phys. Chem. C* **2011**, *115*, 11257-11264.
348. A. Hauch, A. Georg, *Electrochim. Acta* **2001**, *46*, 3457-3466.
349. U. Ahmed, M. Alizadeh, N. A. Rahim, S. Shahabuddin, M. S. Ahmed, A. K. Pandey, *Sol. Energy* **2018**, *174*, 1097-1125.
350. J. Wu, Z. Lan, J. Lin, M. Huang, Y. Huang, L. Fan, G. Luo, Y. Lin, Y. Xie, Y. Wei, *Chem. Soc. Rev.* **2017**, *46*, 5975-6023.
351. M. Wu, T. Ma, *J. Phys. Chem. C* **2014**, *118*, 16727-16742.
352. E. Olsen, G. Hagen, S. E. Lindquist, *Sol. Energy Mater. Sol. Cells* **2000**, *63*, 267-273.
353. C. H. Yoon, R. Vittal, J. Lee, W. S. Chae, K. J. Kim, *Electrochim. Acta* **2008**, *53*, 2890-2896.
354. G. Calogero, P. Calandra, A. Irrera, A. Sinopoli, I. Citro, G. Di Marco, *Energy Environ. Sci.* **2011**, *4*, 1838-1844.
355. M. Saifullah, J. Gwak, J. H. Yun, *J. Mater. Chem. A*, **2016**, *4*, 8512-8540.
356. L. J. Brennan, M. T. Byrne, M. Bari, Y. K. Gun'ko, *Adv. Energy Mater.* **2011**, *1*, 472-485.
357. M. Wu, M. Sun, H. Zhou, J.-Y. Ma, T. Ma, *Adv. Funct. Mater.* **2020**, *30*, 1906451.
358. K. Saranya, Md. Rameez, A. Subramania, *Eur. Polym. J.* **2015**, *66*, 207-227.
359. S. Yun, A. Hagfeldt, T. Ma, *Adv. Mater.* **2014**, *26*, 6210-6237.
360. J. D. Roy-Mayhew, I. A. Aksay, *Chem. Rev*. **2014**, *114*, 6323-6348.
361. H. Choi, S. Hwang, H. Bae, S. Kim, H. Kim, M. Jeon, *Electron. Lett.* **2011**, *47*, 281-285.
362. J. Huo, J. Wu, M. Zheng, Y. Tu, Z. Lan, *Electrochim. Acta* **2016**, *187*, 210-217.
363. J. Song, G. R. Li, C. Y. Wu, X. P. Gao, *J. Power Sources* **2014**, *266*, 464-470.
364. Y. Duan, Q. Tang, J. Liu, B. He, L. Yu, *Angew. Chem. Int. Ed.* **2014**, *53*, 14569-14574.
365. J. Liu, Q. Tang, B. He, L. Yu, *J. Power Sources* **2015**, *282*, 79-86.
366. S. S. Kim, J. W. Lee, J. M. Yun, S. I. Na, *J. Ind. Eng. Chem.* **2015**, *29*, 71-77.
367. P. Li, Q. Tang, *J. Power Sources* **2016**, *317*, 43-48.
368. J. Ou, B. Hu, S. He, W. Wang, Y. Han, *Sol. Energy* **2020**, *201*, 693-700.
369. E. Born, M. Wolf, (Ed.); *Principles of Optics Electromagnetic Theory of Propagation, Interference and Diffraction of Light*, Elsevier, **2002**.
370. P. Buskens, M. Burghoorn, M. C. D. Mourad, Z. Vroon, *Langmuir* **2016**, *32*, 6781-6793.
371. M. S. W. Vong, P. A. Sermon, *Thin Solid Films* **1997**, *293*, 185-195.
372. H. A. Macleod, (Ed.); *Thin-Film Optical Filters*, CRC Press, **2010**.

373. S. Chattopadhyay, Y. F. Huang, Y. J. Jen, A. Ganguly, K. H. Chen, L. C. Chen, *Mater. Sci. Eng. R Rep.* **2010**, *69*, 1-35.
374. U. Schulz, *Appl. Opt.* **2006**, *45*, 1608-1618.
375. H. K. Raut, V. A. Ganesh, A. S. Nair, S. Ramakrishna, *Energy Environ. Sci.* **2011**, *4*, 3779-3804.
376. X. Li, X. Yu, Y. Han, *J. Mater. Chem. C* **2013**, *1*, 2266-2285.
377. K. V. Yeole, *Paintindia* **2021**, *71*, 62-78.
378. H. Hanaei, M. K. Assadi, R. Saidur, *Renew. Sust. Energ. Rev.* **2016**, *59*, 620-635.
379. D. Chen, *Sol. Energy Mater. Sol. Cells* **2001**, *68*, 313-336.
380. W. Herbst, K. Hunger, (Ed.); *Industrial Organic Pigments: Production, Properties, Applications*, **1997**.
381. C. Huang, S. Barlow, S. R. Marder, *J. Org. Chem.* **2011**, *76*, 23862407.
382. B. A. Jones, A. Facchetti, M. R. Wasielewski, T.J. Marks, *J. Am. Chem. Soc.* **2007**, *129*, 15259-15278.
383. G. Horowitz, F. Kouki, P. Spearman, D. Fichou, C. Nogues, X. Pan, F. Garnier, *Adv. Mater.* **1996**, *8*, 242-244.
384. F. Würthner, *Chem. Commun.* **2004**, 1564-1579.
385. S. Becker, A. Böhm, K. Müllen, *Chem. Eur. J.* **2000**, *6*, 3984-3990.
386. C. Li, J. Schöneboom, Z. H. Liu, N. G. Pschirer, P. Erk, A. Herrmann, K. Müllen, *Chem. Eur. J.* **2009**, *15*, 878-884.
387. H. Langhals, *Heterocycles* **1995**, *40*, 477-500.
388. A. Hermann, K. Müllen, *Chem. Lett.* **2006**, *35*, 978-985.
389. Y. Avlasevich, C. Li, K. Müllen, *J. Mater. Chem.* **2010**, *20*, 3814-3826.
390. L. Chen, C. Li, K. Müllen, *J. Mater. Chem. C* **2014**, *2*, 1938-1956.
391. A. Nowak-Król, F. Würthner, *Org. Chem. Front.* **2019**, *6*, 1272-1318.
392. W. Jiang, H. Qian, Y. Li, Z. Wang, *J. Org. Chem.* **2008**, *73*, 7369-7372.
393. W. S. Shin, H. H. Jeong, M. K. Kim, S. H. Jin, M. R. Kim, J. K. Lee, J. W. Lee, Y.S. Gal, *J. Mater. Chem.* **2006**, *16*, 384-390.
394. E. Kozma, M. Catellani, *Dyes Pigm.* **2013**, *98*, 160-179.
395. Z. Liu, D. Zeng, X. Gao, P. Li, Q. Zhang, X. Peng, *Sol. Energy Mater Sol. Cells.* **2019**, *189*, 103-117.
396. A. Gerniski Macedo, L. P. Christopholi, A. E. X. Gavim, J. Ferreira de Deus, M. A. M. Teridi, A. R. M. Yusoff, W. J. da Silva, *J. Mater. Sci. Mater. Electron.* **2019**, *30*, 15803-15824.
397. X. Zhan, A. Facchetti, S. Barlow, T. J. Marks, M. A. Ratner, M. R. Wasielewski, S. R. Marder, *Adv. Mater.* **2011**, *23*, 268-284.
398. T. Weil, T. Vosch, J. Hofkens, K. Peneva, K. Müllen, *Angew. Chem. Int. Ed.* **2010**, *49*, 9068-9093.
399. C. Ji, W. Cheng, Q. Yuan, K. Müllen, M. Yin, *Acc. Chem. Res.* **2019**, *52*, 2266-2277.
400. N. G. Pschirer, C. Kohl, F. Nolde, J. Qu and K. Müllen, *Angew. Chem. Int. Ed.* **2006**, *45*, 1401-1404.
401. M. Kardos, DE 276357, **1913**.
402. M. Kardos, DE 276956, **1913**.

403. L. D. Wescott, D. L. Mattern, *J. Org. Chem.* **2003**, *68*, 10058-10066.
404. A. Rademacher, S. Märkle, H. Langhals, *Chem. Ber.* **1982**, *115*, 2927-2934.
405. V. Rogovik, L. Gutnik, *Zh. Org. Khim.* **1988**, *24*, 635-639.
406. P. Osswald, F. Würthner, *J. Am. Chem. Soc.* **2007**, *129*, 14319-14326.
407. M. Queste, C. Cadiou, B. Pagoaga, L. Giraudet, N. Hoffmann, *New J. Chem.* **2010**, *34*, 2537-2545.
408. M. Sadrai, L. Hadel, R. R. Sauers, S. Husain, K. Krogh-Jespersen, J. D. Westbrook, G. R. Bird, *J. Phys. Chem.* **1992**, *96*, 7988-7996.
409. A. Böhm, H. Arms, G. Henning, P. Blaschka, (BASF AG), DE19547209A1, **1997**.
410. F. Würthner, V. Stepanenko, Z. Chen, C. R. Saha-Möller, N. Kocher, D. Stalke, *J. Org. Chem.* **2004**, *69*, 7933-7939.
411. P. Rajasingh, R. Cohen, E. Shirman, L. J. W. Shimon, B. Rybtchinski, *J. Org. Chem.* **2007**, *72*, 5973-5979.
412. Y. Zhao, M. R. Wasielewski, *Tetrahedron Lett.* **1999**, *40*, 7047-7050.
413. Y. Nagao, T. Misono, *Bull. Chem. Jpn.* **1981**, *54*, 1191-1194.
414. Y. Nagao, T. Misono, *Bull. Chem. Jpn.* **1981**, *54*, 1575-1576.
415. L. Feiler, H. Langhals, K. Polborn, *Liebigs Ann.* **1995**,1229-1244.
416. K. Tomizaki, P. Thamyongkit, R. S. Loewe, J. S. Lindsey, *Tetrahedron* **2003**, *59*, 1191-1207.
417. Z. Yuan, S.-L. Lee, L. Chen, C. Li, K. S. Mali, S. De Feyter, K. Müllen, *Chem. Eur. J.* **2013**, *19*, 11842-11846.
418. H. Quante, K. Müllen, *Angew. Chem. Int. Ed.* **1995**, *34*, 1323-1325.
419. M. Grzybowski, K. Skonieczny, H. Butenschçn, D. T. Gryko, *Angew. Chem. Int. Ed.* **2013**, *52*, 9900-9930.
420. J. E. Anthony, *Chem. Re*v. **2006**, *106*, 5028-5048.
421. B. Burfeindt, T. Hannappel, W. Storck, F. Willig, *J. Phys. Chem.* **1996**, *100*, 16463-16465.
422. S. Ferrere, A. Zaban, B. A. Gregg, *J. Phys. Chem. B* **1997**, *101*, 4490-4493.
423. S. Wang, Y. L. Li, C. M. Du, Z. Q. Shi, S. X. Xiao, D. B. Zhu, E. Q. Gao, S. M. Cai, *Synt. Met.* **2002**, *128*, 299-304.
424. C. Zafer, M. Kus, G. Turkmen, H. Dincalp, S. Demic, B. Kuban, Y. Teoman, S. Icli, *Sol. Energy Mater. Sol. Cells* **2007**, *91*, 427-431.
425. J. E. Kroeze, N. Hirata, S. Koops, M. K. Nazeeruddin, L. Schmidt-Mende, M. Grätzel, J. R. Durrant, *J. Am. Chem. Soc* **2006**, *128*, 16376-16383.
426. Y. Shibano, T. Umeyama, Y. Matano, H. Imahori, *Org. Lett.* **2007**, *9*, 1971-1974.
427. J. Fortage, M. Severac, C. Houarner-Rassin, Y. Pellegrin, E. Blart, F. Odobel, *J. Photochem. Photobiol. A* **2008**, *197*, 156-169.
428. M. Planells, F. J. Céspedes-Guirao, L. Goncalves, A. Sastre-Santos, F. Fernandez-Lazaro, E. Palomares, *J. Mater. Chem.* **2009**, *19*, 5818-5825.
429. H. J. Snaith, S. M. Zakeeruddin, L. Schmidt-Mende, C. Klein, M. Grätzel, *Angew. Chem.* **2005**, *44*, 6413-6417.
430. M. Planells, F. J. Céspedes-Guirao, A. Forneli, A. Sastre-Santos, F. Fernández-Lázaro, E. Palomares, *J. Mater. Chem.* **2008**, *18*, 5802-5808.

431. G. D. Sharma, R. Kurchania, R. J. Ball, M. S. Roy, J. A. Mikroyannidis, *Int. J. Photoenergy* **2012**, 983081.
432. A. Kay, M. Grätzel, *J. Phys. Chem.* **1993**, *97*, 6272-6277.
433. H. Dinçalp, Z. Askar, C. Zafer, S. Icli, *Dyes Pigm.* **2011**, *91*, 182-191.
434. M. Liang, W. Xu, F. Cai, P. Chen, B. Peng, J. Chen, Z. Li, *J. Phys. Chem. C* **2007**, *117*, 4465-4472.
435. G. Li, K. Jiang, Y. Li, S. Li, L. Yang, *J. Phys. Chem. C* **2008**, *112*, 11591-11599.
436. Z. Ning, Q. Zhang, W. Wu, H. Pei, B. Liu, H. Tian, *J. Org. Chem.* **2008**, *73*, 3791-3797.
437. C. A. Echeverry, R. Cotta, A. Insuasty, A. Ortíz, N. Martín, L. Echegoyen, B. Insuasty, *Dyes Pigm.* **2018**, *153*, 182-188.
438. M. K. Nazeeruddin, F. De Angelis, S. Fantacci, A. Selloni, G. Viscardi, P. Liska, S. Ito, B. Takeru, M. Grätzel, *J. Am. Chem. Soc.* **2005**, *127*, 16835-16847.
439. N. Tasios, C. Grigoriadis, M. R. Hansen, H. Wonneberger, C. Li, H. W. Spiess, K. Müllen, G. Floudas, *J. Am. Chem. Soc.* **2010**, *132*, 7478-7487.
440. S. Ferrere, B. A. Gregg, *J. Phys. Chem. B* **2001**, *105*, 7602-7605.
441. S. Ferrere, B. A. Gregg, *New J. Chem.* **2002**, *26*, 1155-1160.
442. T. Dentani, K. Funabiki, J. Y. Jin, T. Yoshida, H. Minoura, M. Matsui, *Dyes Pigm.* **2007**, *72*, 303-307.
443. J. T. Otsuki, Y. Takaguchi, D. Takahashi, P. Kalimuthu, S. P. Singh, A. Islam, L. Han, *Adv. Optoelectron.* **2011**, 860486.
444. C. Li, J. H. Yum, S. J. Moon, A. Herrmann, F. Eickemeyer, N. G. Pschirer, P. Erk, J. Schöneboom, K. Müllen, M. Grätzel, M. K. Nazeeruddin, *ChemSusChem* **2008**, *1*, 615-618.
445. C. Li, Z. H. Liu, J. Schöneboom, F. Eickemeyer, N. G. Pschirer, P. Erk, A. Herrmann, K. Müllen, *J. Mater. Chem.* **2009**, *19*, 5405-5415.
446. A. Keerthi, Y. Liu, Q. Wang, S. Valiyaveettil, *Chem. Eur. J.* **2012**, *18*, 11669-11676.
447. T. Edvinsson, C. Li, N. Pschirer, J. Schöneboom, F. Eickemeyer, R. Sens, G. Boschloo, A. Herrmann, K. Müllen, A. Hagfeldt, *J. Phys. Chem. C* **2007**, *111*, 15137-15140.
448. S. Mathew, H. Imahori, *J. Mater. Chem.* **2011**, *21*, 7166-7174.
449. X. Zhao, Y. Xiong, J. Ma, Z. Yuan, *J. Phys. Chem. A* **2016**, *120*, 7554-7560.
450. C. O. Kappe, *Angew. Chem. Int. Ed.* **2004**, *43*, 6250-6284.
451. Y. Geerts, H. Quante, H. Platz, R. Mahrt, M. Hopmeier, A Böhm, K Müllen, *J. Mater. Chem.* **1998**, *8*, 2357-2369.
452. T. Edvinsson, N. Pschirer, J. Schöneboom, F. Eickemeyer, G. Boschloo, A. Hagfeldt, *Chem. Phys.* **2009**, *357*, 124-131.
453. Y. Avlasevich, S. Müller, P. Erk, K. Müllen, *Chem. Eur. J.* **2007**, *13*, 6555-6561.
454. N. Elgrishi, K. J. Rountree, B. D. McCarthy, E. S. Rountree, T. T. Eisenhart, J. L. Dempsey, *J. Chem. Educ.* **2018**, *95*, 197-206.
455. F. Sachs, *Liebigs Ann.* **1909**, *365*, 53-134.
456. R. A. Jeffreys, *J. Chem. Soc.* **1955**. 2394-2397.
457. M. Azam, I. Warad, S. I. Al-Resayes, N. Alzaqri, M. R. Khan, R. Pallepogu, S. Dwivedi, J. Musarrat, M. Shakir, *J. Mol. Struct.* **2013**, *1047*, 48-54.

458. M. Azam, I. Warad, S. Al-Resayes, M. Zahin, I. Ahmad, M. Shakir M, *Z. Anorg. Allg. Chem*. **2012**, *638*, 881-886.
459. F. A. Bassyouni, S. M. Abu-Bakr, K. H. Hegab, W. El-Eraky, A. A. El-Beih, M. E. A. Rehim, *Res. Chem. Intermed.* **2012**, *38*, 1527-1550.
460. M. F. Braña, M. Garrido, M. L. Lopez-Rodriguez, M. J. Morcillol, Y. Alvarez, Y. Valladares, G. Klebe, *Eur. J. Med. Chem.* **1990**, *25*, 209-215.
461. M. Jakubek, Z. Kejík, R. Kaplánek, H. Veselá, D. Sýkora, P. Martásek, V. Král, *Supramol. Chem.* **2018**, *30*, 218-226.
462. N. Sahiba, S. Agarwal, *Top. Curr. Chem*. **2020**, *378*, 44.
463. A. Ajayaghosh, *Acc. Chem. Res.* **2005**, *38*, 449-459.
464. K. A. Bello, N. Corns, J. Griffiths, *J. Chem. Soc. Chem. Commun.* **1993**, 452-454.
465. G.S. Bahra, J. Griffiths, W. Healy, V. Millar, S. J. Till, J. Till, *Mater. Res. Soc. Symp. Proc.* **1995**, *374*, 33-38.
466. D. Citterio, L. Jenny, S. Rkonyi, U. E. Spichiger, *Sens. Actuators B: Chem.* **1997**, *39*, 202-206.
467. P. Šimon, S. Sekretár, B.D. MacCraith, F. Kvasnik, *Sens. Actuators B: Chem.* **1997**, *39*, 252-255.
468. S.-H. Kima, J.-H. Kim, J.-Z. Cui, Y.-S. Gal, S.-H. Jin, K. Koh, *Dyes Pigm.* **2002**, *55*, 1-7.
469. K. Umezawa, D. Citterio, K. Suzuki, *Chem. Lett.* **2007**, *36*, 1424-1425.
470. K. Umezawa, D. Citterio, K. Suzuki, *Anal. Sci.* **2008**, *24*, 213-217.
471. K. C.W. Chong, M. A. Winnik, L. Gong, J. Nowicki, *Dyes Pigm.* **2008**, *79*, 200-204.
472. J. Mistol, S. Ernst, D. Keil, L. Hennig, *Dyes Pigm.* **2015**, *118*, 58-63.
473. S. Ernst , J. Mistol, B. Senns, L. Hennig, D. Keil, *Dyes Pigm.* **2018**, *154*, 216-228.
474. N. Barbero, C. Magistris, J. Park, D. Saccone, P. Quagliotto, R. Buscaino, C. Medana, C. Barolo, G. Viscardi, *Org. Lett.* **2015**, *17*, 3306-3309.
475. H. O. House, D. G. Koepsell, W. J. Campbell, *J. Org. Chem.* **1978**, *37*, 1003-1011.
476. S. C. Busman, R. J. Ellis, J. E. Haubrich, W. D. Ramsden, T. van Thien, G. D. Cuny, US RE38.251E, **2000**.
477. A. J. McKerrow, E. Buncel, P. K. Kazmaier, *Can. J. Chem.* **1995**, *73*, 1605-1615.
478. X. Chen, J. Guo, X. Peng, M. Guo, Y. Xu, L. Shi, C. Liang, L. Wang, Y. Gao, S. Sun, S. Cai, *J. Photochem. Photobiol. A* **2005**, *171*, 231-236.
479. G. Boschloo, L. Häggman, A. Hagfeldt, *J. Phys. Chem. B* **2006**, *110*, 13144-13150.
480. S. Y. Huang, G. Schlichthörl, M. Grätzel, A. J. Frank, *J. Phys. Chem. B* **1997**, *101*, 2576-2582.
481. G. Schlichthörl, S. Y. Huang, J. Sprague, A. J. Frank, *J. Phys. Chem. B* **1997**, *101*, 8141-8155.
482. S. Nakade, T. Kanzaki, W. Kubo, T. Kitamura, Y. Wada, S. Yanagida, *J. Phys. Chem. B* **2005**, 109, 3480-3487.
483. G. Boschloo, H. Lindström, E. Magnusson, A. Holmberg, A. Hagfeldt, *J. Photochem. Photobiol. A* **2002**, *148*, 11-15.
484. C. Zhang, Y. Huang, Z. Huo, S. Chen, S. Dai, *J. Phys. Chem. C* **2009**, *113*, 21779-21783.
485. C. A. Kelly, F. Farzad, D. W. Thompson, J. M. Stipkala, G. J. Meyer, *Langmuir* **1999**, *15*, 7047-7054.

486. N.-G. Park, S.-H. Chang, J. van de Lagemaat, K.-J. Kim, A. J. Frank, *Bull. Korean Chem. Soc.* **2000**, *21*, 985-988.
487. V. Novelli, N. Barbero, C. Barolo, G. Viscardi, M. Sliwa, F. Sauvage, *Phys. Chem. Chem. Phys.* **2017**, *19*, 27670-27681.
488. A. Kumar Singh, M. Fairoos M. K., A. J. Mozer, K. Krishnamoorthy, J. Nithyanandhan, *Langmuir* **2022**, *38*, 14808-14818.
489. F. Santos, D. Ivanou, A. Mendes, *Mater. Today Commun.* **2022**, *32*, 104030.
490. G. Volpi, R. Rabezzana, *New J. Chem.* **2021**, *45*, 5737-5743.
491. G. Volpi, *Asian J. Org. Chem.* **2022**, *11*, e202200171.
492. G. Volpi, C. Garino, E. Priola, C. Magistris, M. R. Chierotti, C. Barolo, *Dyes Pigm.* **2019**, *171*, 107713.
493. E. Yamaguchi, F. Shibahara, T. Murai, *J. Org. Chem.* **2011**, *76*, 6146-6158.
494. F. Shibahara, E. Yamaguchi, A. Kitagawa, A. Imai, T. Murai, *Tetrahedron* **2009**, *65*, 5062-5073.
495. A. Marchesi, S. Brenna, G. A. Ardizzoia, *Dyes Pigm.* **2019**, *161*, 457-463.
496. G. Volpi, C. Garino, E. Fresta, E. Casamassa, M. Giordano, C. Barolo, G. Viscardi, *Dyes Pigm.* **2021**, *192*, 109455.
497. S. Chen, H. Li, P. Hou, *Sens. Actuators B* **2018**, *256*, 1086-1092.
498. S. Chen, P. Hou, J. Sun, H. Wang, L. Liu, *Spectrochim. Acta Part A* **2020**, 225, 117508.
499. C. Garino, T. Ruiu, L. Salassa, A. Albertino, G. Volpi, C. Nervi, R. Gobetto, K. I. Hardcastle, *Eur. J. Inorg. Chem.* **2008**, 3587-3591.
500. G. Volpi, C. Garino, L. Salassa, J. Fiedler, K. I. Hardcastle, R. Gobetto, C. Nervi, *Chem. Eur. J.* **2009**, *15*, 6415-6427.
501. S. Durini, G. A. Ardizzoia, B. Therrien, S. Brenna, *New J. Chem.* **2017**, *41*, 3006-3014.
502. J.-J. Wu, M.-L. Cao, B.-H. Ye, *Chem. Commun.* **2010**, *46*, 3687-3689.
503. G. A. Ardizzoia, D. Ghiotti, B. Therrien, S. Brenna, *Inorg. Chim. Acta* **2018**, *471*, 384-390.
504. M. Strianese, S. Brenna, G. A. Ardizzoia, D. Guarnieri, M. Lamberti, I. D'Auria, C. Pellecchia, *Dalton Trans.* **2021**, *50*, 17075-17085.
505. E. Fresta, G. Volpi, M. Milanesio, C. Garino, C. Barolo, R. D. Costa, *Inorg. Chem.* **2018**, *57*, 10469-10479.
506. E. Fresta, G. Volpi, C. Garino, C. Barolo, R. D. Costa, *Polyhedron* **2018**, *140*, 129-137.
507. M. D. Weber, C. Garino, G. Volpi, E. Casamassa, M. Milanesio, C. Barolo, R. D. Costa, *Dalton Trans.* **2016**, *45*, 8984-8993.
508. G. Volpi, *Asian J. Org. Chem.* **2022**, *11*, e20220017.
509. R. Grigg, P. Kennewell, V. Savic, *Tetrahedron* **1994**, *50*, 5489-5494.
510. M. E. Bluhm, M. Ciesielski, H. Go, O. Walter, M. Do, *Inorg. Chem.* **2003**, *42*, 8878-8885.
511. J. Wang, L. Dyers, R. Mason, P. Amoyaw, X. R. Bu, *J. Org. Chem.* **2005**, *70*, 2353-2356.
512. G. Palazzo, G. Picconi, *Il Farm. Ed. Sci.* **1975**, *30*, 197-207.
513. A. P. Krapcho, J. R. Powell, *Tetrahedron Lett.* **1986**, *27*, 3713-3714.
514. J. M. Crawforth, M. Paoletti, *Tetrahedron Lett.* **2009**, *50*, 4916-4918.

515. D. Olbert, H. Gorls, D. Conrad, M. Westerhausen, *Eur. J. Inorg. Chem.* **2010**, 1791-1797.
516. D. V. Griffiths, Y.-K. Cheong, P. Duncanson, M. Motevalli, *Dalton Trans.* **2011**, *40*, 10215-10228.
517. L. Salassa, C. Garino, A. Albertino, G. Volpi, C. Nervi, R. Gobetto, K. I. Hardcastle, *Organometallics* **2008**, *27*, 1427-1435.
518. E. L. Eliel, S. H. Wilen, L. N. Mander, (Ed.); *Stereochemistry of Organic Compounds*, Wiley, **1994**.
519. N. Hirata, J.-J. Lagref, E. J. Palomares, J. R. Durrant, M. K. Nazeeruddin, M. Grätzel, D. Di Censo, *Chem. Eur. J.* **2004**, *10*, 595-602.
520. E. Ronchi, R. Ruffo, S. Rizzato, A. Albinati, L. Beverina, G. A. Pagani, *Org. Lett*. **2011**, *13*, 3166-3169.
521. T. S. Jarvis, C. G. Collins, J. M. Dempsey, A. G. Oliver, B. D. Smith, *J. Org. Chem.* **2017**, *82*, 5819-5825.
522. A. K. Singh, A. N. Veetil, J. Nithyanandhan, *ACS Appl. Energy Mater.* **2021**, *4*, 3182-3193.
523. C. Fotsch, M. D. Bartberger, E. A. Bercot, M. Chen, R. Cupples, M. Emery, J. Fretland, A. Guram, C. Hale, N. Han, D. Hickman, R. W. Hungate, M. Hayashi, R. Komorowski, Q. Liu, G. Matsumoto, D. J. St. Jean, Jr., S. Ursu, M. Véniant, G. Xu, Q. Ye, C. Yuan, J. Zhang, X. Zhang, H. Tu, M. Wang, *J. Med. Chem.* **2008**, *51*, 7953-7967.
524. M. H. Park, C. Yun, J. O. Huh, Y. Do, S. Yoo, M. H. Lee, *Synth. Met.* **2010**, *160*, 2000-2007.
525. A. Akbarzadeh, R. Rezaei-Sadabady, S. Davaran, S. Woo Joo, N. Zarghami, Y. Hanifehpour, M Samiei, M. Kouhi, K. Nejati-Koshki, *Nanoscale Res. Lett.* **2013**, *8*, 102.
526. S. H. Yun, S. J. J. Kwok, *Nat. Biomed. Eng.* **2017**, *1*, 8.
527. M. Collot, S. Pfister, A. S. Klymchenko, *Curr. Opin. Chem. Biol.* **2022**, *69*, 102161.
528. J. Wu, Z. Shi, L. Zhu, J. Li, X. Han, M. Xu, S. Hao, Y. Fan, T. Shao, H. Bai, B. Peng, W. Hu, X. Liu, C. Yao, L. Li, W. Huang, *Adv. Opt. Mater.* **2022**, *10*, 2102514.
529. I. A. Karpenko, M. Collot, L. Richert, C. Valencia, P. Villa, Y. Mély, M. Hibert, D. Bonnet, A. S. Klymchenko, *J. Am. Chem. Soc.* **2015**, *137*, 405-412.
530. T. Mukherjee, R. J. Martinez-Sanchez, K. T. Fam, S. Bou, L. Richert, D. Garnier, Y. Mély, S. Kanvah, A. S. Klymchenko, M. Collot, *Mater. Chem. Front.* **2021**, *5*, 2459-2469.
531. M. Collot, P. Ashokkumar, H. Anton, E. Boutant, O. Faklaris, T. Galli, Y. Mély, L. Danglot, A. S. Klymchenko, *Cell Chem. Biol.* **2019**, *26*, 600-614.
532. J. Karpenko, A. S. Klymchenko, S. Gioria, R. Kreder, I. Shulov, P. Villa, Y. Mély, M. Hibert, D. Bonnet, *Chem. Commun.* **2015**, *51*, 2960-2963.
533. M. Collot, R. Kreder, A. L. Tatarets, L. D. Patsenker, Y. Mely, A. S. Klymchenko, *Chem. Commun.* **2015**, *51*, 17136-17139.
534. G. Renno, F. Cardano, V. Ilieva, G. Viscardi, A. Fin, *Eur. J. Org. Chem.* **2022**, e202200833.
535. R. Koynova, M. Caffrey, *Biochim. Biophys. Acta - Rev. Biomembr.* **1998**, *1376*, 91.
536. C. Reichardt, (Ed.); *Solvents and Solvent Effects in Organic Chemistry*, Wiley, **2002**.